THERMAM 2014

International Conference on Thermophysical and Mechanical Properties of Advanced Materials

&

3rd Rostocker Symposium on Thermophysical Properties for Technical Thermodynamics

12-15 June 2014

Boyalik Beach Hotel, Cesme - Izmir / Turkey

Full Text Proceedings
ISBN: 978-605-84726-1-7

Edited by: Prof. Dr. Ismail TAVMAN

<u>Organizers:</u>

Dokuz Eylul University
Department of Mechanical Engineering,
Izmir – Turkey

University of Rostock
Institute of Technical Thermodynamics
Rostock, Germany

CONTENTS

Effect of Stamp Forming Pressure and Temperature on Polypropylene Sheets

Ertugrul Selçuk Erdogan [1], Olcay Eksi [2]

[1]Trakya University, Engineering and Architecture Faculty, Mechanical Engineering Department, EDIRNE, 22100-TURKEY, eselcuk@trakya.edu.tr

[2]Namık Kemal University, Engineering Faculty of CORLU, Mechanical Engineering Department, Corlu/TEKIRDAG, 59860-TURKEY

ABSTRACT: Materials that have been used in this work were formed with thermoforming technique known as stamp forming. Some required tools and distinctive equipments have been provided for this stamp forming operation. A stamp forming mould which has a shape that has rectangular geometry was designed and manufactured to use this mould in stamp forming operation. Polymer sheets were heated with an external heater to temperature which is close to melting limit but under melting point for each different material and formed by the mould which has been employed at room temperature to shape any parts from PP. Some useful parameters for stamp forming of the polymer sheets such as heating time of polymer sheets, mould velocity, stamping pressure e.c. were determined before the experimental operation started. These materials were formed in different temperature and pressure conditions. Some specimens were cut and taken from these sheets by machining. Tensile characteristics of these materials were investigated. According to tensile test results obtained from experimental stamp forming operations, after changing the stamp forming parameters as stamping pressure and stamping temperature, PP materials showed different characteristics in (%) elongation at break and ultimate tensile strength.

Keywords: Compression, Polypropylene(PP), Sheet, Strength, Thermoplastics.

INTRODUCTION

With the improvements about the plastic material compounds in the latest time, it is provided that plastic materials have advanced properties by reinforcing plastics with other materials. These developments provide the plastic matrix composites to have a usage as much as unreinforced plastic materials. Polymer composites reinforced with continuous fibers possess low weight plus high specific strength, stiffness, and environmental resistance. Furthermore, they are increasingly used for structural parts in aircraft and space applications, in the auto- mobile industry, and for sporting goods[4-15]. That makes stamp forming manufacturing technique well-known among the other producing techniques of thermoplastics and their composites.[21-25]

Polymers are based on long-chain polymer molecules and it is these long chains that are responsible for their characteristic mechanical and thermal properties, which distinguish them from other materials [2-9]. Peculiarities belong to different polymers are able to explored by looking at some common polymers and examples of design and failure. It is important to know how to design against polymer structure failure and how to work to the limit of the properties of polymers. There are countless man-made polymeric products. For this reason there are much more properties that are observed with most of the polymers such as synthetic fibers, engineering plastics and artificial rubber. [10-11] On the other hand, polymers have lower melting temperatures according to other material groups. That provides plastics to have a good formability. Increasing temperature make polymers become increasingly deformable. Also, the extent of polymer deformation is found to vary with time, temperature, stress and microstructure consistent with parallel observations for fully crystalline solids [1-3]. However, polymer sheets were used in this study are members of thermoplastic polymer group. In addition to this the most important advantage of thermoplastics may lie in their potential for rapid, low-cost, mass production of reinforced composites [2-12]. Thermoplastics have a linear structure of

molecular chains. As a result of this, thermoplastics are easy to process and shape with some special manufacturing methods above their melting and softening point. Thermoplastics can be easily fabricated by any other processing techniques using heat or pressure, when they don't include any filler or reinforcing material. However, in order to fabricate thermoplastic matrix composites it is needed seriously high processing temperature and forming pressure because of high melt viscosity peculiarity of thermoplastics. Therefore thermosetting resins are employed mainly to lessen the required parameters for the processing technique [16-20]. Fabrication techniques that are commonly applied for short glass fiber reinforced thermoplastic composite parts are pultrusion, roll forming, filament winding and thermoforming. There are lots of fabrication techniques that utilize the same forming method with thermoforming such as vacuum molding, pressure molding and stamp forming [19-22]. Every manufacturing process can be employed to create a new short glass fiber reinforced thermoplastic composite part. But the most effective forming technique for thermoplastic composite parts is stamp forming. Furthermore thermoforming is a manufacturing process that consists of many techniques for producing plastic articles from polymer sheets. In thermoforming producing technique, polymer sheet is heated and softened temporarily then this flat sheet is draped over a mold shape [17-18]. Thermoforming uses vacuum technique in order to form some kinds of polymer sheets. But with the stamp forming manufacturing process there is no need to use vacuum. That attribute is only the difference between thermoforming and stamp forming producing techniques [6]. Stamp forming has processing advantages over competitive processes such as blow molding, injection molding and rotational molding. Stamp forming needs relatively low forming pressures to change the shape of polymer material in to the final plastic product [23-24].

Thus large size parts can be economically manufactured. Parts which have small thicknesses can be easily fabricated. For these parts manufacturing period is extremely short. Stamp forming molds are subjected relatively low forces. For this reason stamp forming molds can be made of inexpensive materials and that makes fabrication time very short for preparing new molds [5-9]. Stamp forming consists of a couple of segments. These processing steps are clamping, heating, forming, cooling and trimming. Sheets that are used in stamp forming producing technique can be categorized as thin-gage and thick-gage. Thin gage sheets have thickness less than 0.25 mm, thick gage sheet have thickness greater than 0.25 mm. Thick gage sheet can be further separated as medium-weight sheet and heavy-gage sheet. Medium-weight sheet has a thickness of 0.25mm to 1.5 mm. Heavy gage sheet has thickness greater than 1.5 mm [14].

EXPERIMENTAL

Materials

Polypropylene sheets were used for this study. PP (Polypropylene) sheets manufactured by ROCHLING Germany which have thickness of about 3 mm. Stamp forming temperatures of the material used in this study were determined according to manufacturer catalog information. The temperature range for appropriate forming is given 320^0F - 350^0F. In order to investigate the condition of material arrangement, lines that are perpendicular to each other were drawn on the surface of the sheets before forming.

Equipment

The hydraulic press was used in this experimental study, has two working strokes, opening and compression during the closing. That hydraulic press can build up a maximum load of 150 kN in compression stroke. Forming press allows the mould to be closed on the pre-heated flat sheet with a constant velocity and mould has the same movement velocity during the forming operation. The entire stroke is 100 mm, in which 50 mm is the compression stroke. Desired stamping pressures can be adjusted by a computer which has software that controls the stroke of the hydraulic press and stamping pressure. Other important requirements are the devices that are needed to perform an experimental study. These devices are molds and heaters. In this experimental study as a stamp forming machine a couple of devices have been used to create an assembly called "stamp former device". This machine consists of stamp forming molds and a hydraulic press. Stamp forming molds were designed with a

specific purpose to investigate the sharp shape effect on tensile behaviour of plastics in stamp forming process. Stamp forming molds which have been used in this study were designed in CAD software. Although a stamp forming operation happens with these devices and equipments which are mentioned above, one more thing is needed to complete full stamp forming activity. This device is a 3 kW electrical heater. The heater was designed to heat and softened flat polymer sheets as desired. Heating zone of the heater consists of electrical rod heaters. That heating element is able to provide to heat two sides of the sheet. During heating, distance between heater rods and the PP sheet is about 10 mm. [6]

Processing Procedure

In this study stamp forming process has two important stages; loading the sheets that heated to required temperature in to the stamp former device, forming the part [7]. Before the experimental study, it is needed to prepare the flat sheets with their proper dimensions. These sheets have had their final shapes by machining. At the end of this stage they had a square of 300mm$x$300mm. Tensile test specimens have been cut and taken from these flat sheets by machining before and after the stamp forming operation. Heater device must heat the sheet desired and proper forming temperature. According to thermal properties of flat sheet material, temperature has changed among 150°C-300°C. After all these equipments are ready, experimental study can be performed. Firstly molds have positioned between the upper tool and lower tool of the hydraulic press. Then some adjustments have been made about the pressure value that is required for a successful stamp forming process. During these actions happened, thermoplastic flat sheet was heated to proper forming temperature by a 3 kW electrical heater. Then softened polymer sheet were taken from the heater and put between the two mold halves. Upper tool have moved through the lower tool. Two mold halves clamped completely. Thus softened sheet cooled and have taken the shape of clamped molds. After a while upper tool have moved reverse direction. Sheet was taken from the mold. [8-13] Before forming operation these sheets have a thickness of 3 mm. Because of this all of the flat sheets and this stamp forming operation can be called heavy-gage sheets and heavy-gage stamp forming respectively. The illustration of stamp forming producing technique is given in Figure-1.

Figure-1. Illustration of stamp forming producing technique.

CHARACTERIZATION

Tensile tests

Tensile tests were performed at 23 ^{o}C using a tensile testing machine set-up according to ASTM D638 standard. These tensile tests were performed at a constant velocity of 5 mm/min with ASTM D 638

type 4 tensile test specimens. At least ten specimens were tested for each processing condition. Results were obtained from specimens cut off from the flat sheet before and after forming operation.

RESULTS AND DISCUSSION

Tensile test results

Tensile test results of PP sheets before and after forming are given in Table-1 and Table-2 respectively.

Table-1. Tensile test results for PP sheets before formed with heat and pressure

PP sheets	• Ultimate tensile strength: 38.7 MPa • % Elongation at break: % 2.2

Table-2. Tensile test results for annealed unreinforced PP sheets after formed with heat and pressure (stamp forming)

Material	Applied force (kN)	Heated temperature (°C)	Holding time (sec)	Stroke (mm)	Ultimate tensile strength(MPa)	Elongation at break (%)
PP	200	200	200	50	39.9	2.5
PP	250	250	200	50	39.9	2.6

Also, the sheets were heated to proper temperature which is enough softened to shape. Then they were left for cooling at room temperature for five minutes in a water container in a certain time. Cooled PP sheets were taken and left for drying in room conditions. After that, the sheets were heated to desired temperature again. As a result they were formed by stamp forming manufacturing process. And then these results were obtained for tensile tests.

Effect of stamping pressure

Determining the effect of stamping pressure on mechanical properties especially on ultimate tensile strength and on (%) elongation at break is influenced phenomenon when it is one of the most important stamp forming operation parameters. Variation on ultimate tensile strength of PP sheets is shown with an illustration in Figure-2.
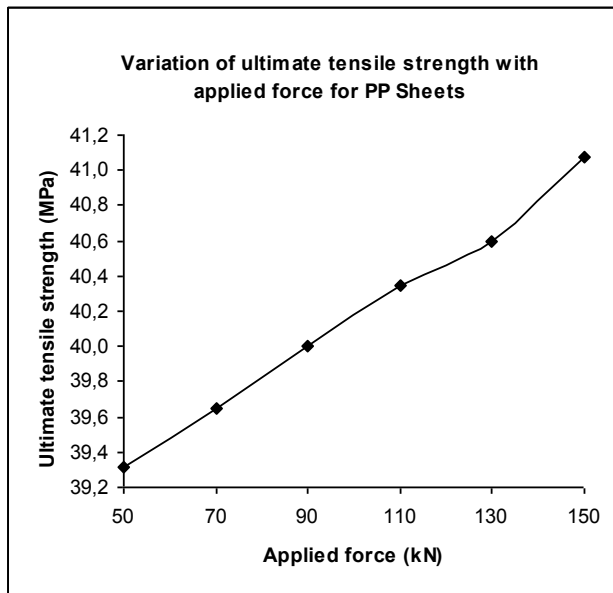
Figure-2. Variation of ultimate tensile strength with applied force for PP materials

Variation of (%) elongation at break with applied force for PP materials has been illustrated in Figure-3.
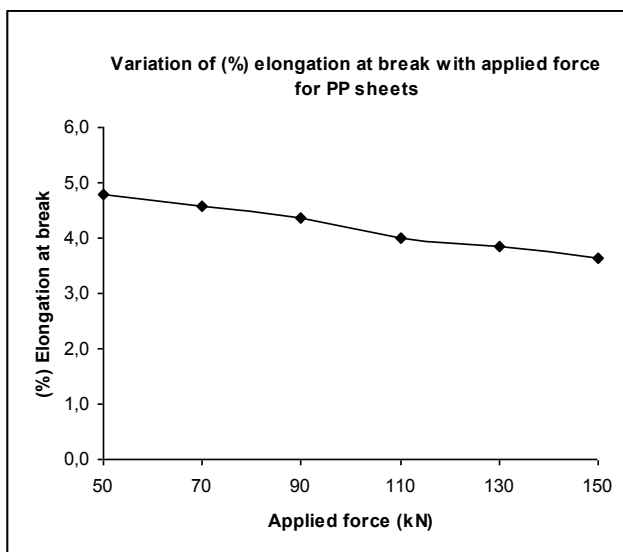
Figure-3. Variation of (%) elongation at break with applied force for PP material

Effect of stamping temperature

Stamping temperature is one of the most important parameters is able to influence the quality of the product deeply after finishing operation. Therefore in order to achieve best results from the stamp forming manufacturing process stamping temperature must be chosen carefully. In this experimental period different temperature values were determined according to material's melting point. Variation of ultimate tensile strength with stamping temperature for PP sheet materials is shown in Figure-4.
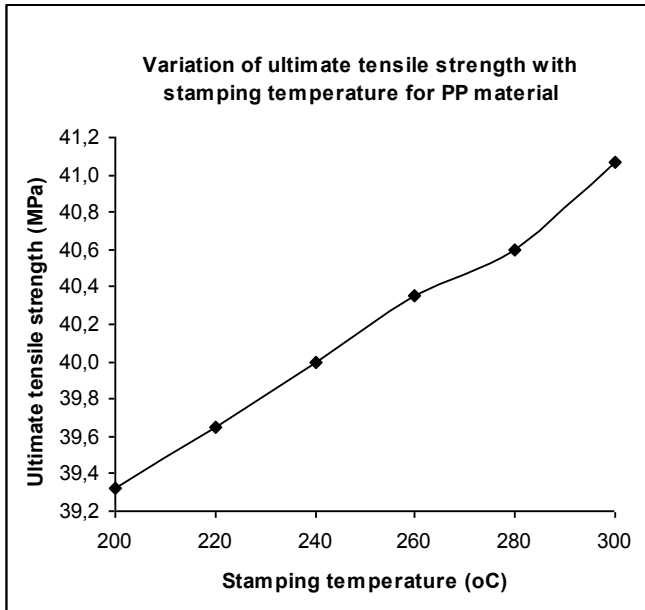
Figure-4. Variation of ultimate tensile strength with stamping temperature for PP material

Variation of (%) elongation at break with stamping temperature for PP sheet materials has been shown in Figure-5.
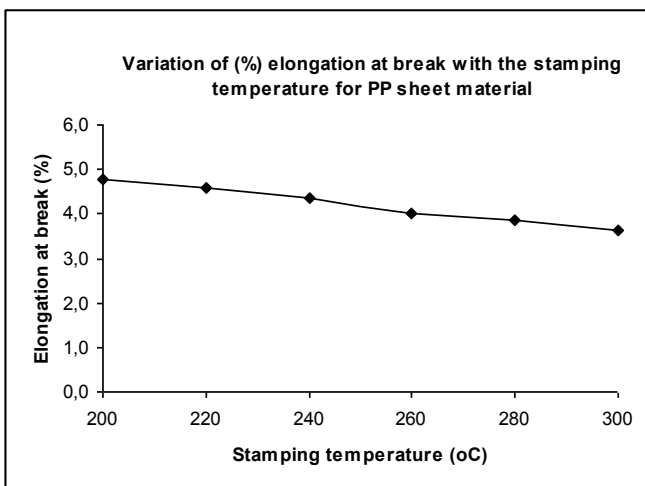
Figure-5. Variation of (%) elongation at break with stamping temperature for PP material

Figure-6 shows PP sheet after stamp forming process.
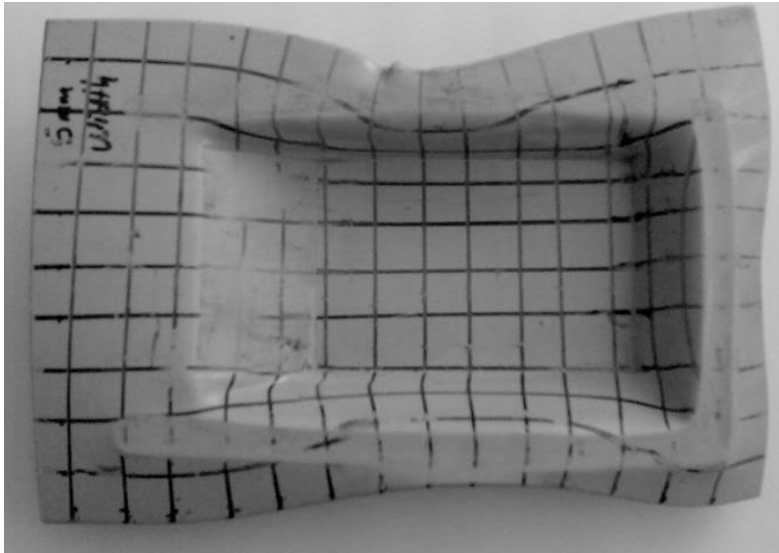
Figure-6. PP sheet material after stamp forming

CONCLUSIONS

In this study, the stamp forming process of PP sheets were investigated for simple mould geometry. Influence of stamping temperature and stamping pressure has been determined on the ultimate tensile strength and (%) elongation at break. It has seen from the test results for PP sheets that;

- Increasing applied force (stamping pressure) gives slightly increasing tensile strength
- Increasing applied force (stamping pressure) gives decreasing elongation at break
- Increasing stamping temperature gives slightly increasing tensile strength
- Increasing stamping temperature gives decreasing elongation at break

Observation of the tensile test results obtained from experimental stamp forming operations of distinct thermoplastic sheets showed that ultimate tensile strength and (%) elongation at break of PP sheets were changed similar for most of the stamping parameters like stamping temperature and stamping pressure.

SUGGESTED STUDIES FOR FUTURE

In this study PP extruded grades were formed in different temperature and pressure conditions. Some specimens were cut and taken from these sheets by machining. Tensile characteristics of these materials were investigated. According to tensile test results obtained from experimental stamp forming operations, after changing the stamp forming parameters as stamping pressure and stamping temperature, PP material showed different characteristics in (%) elongation at break and ultimate tensile strength. For future studies chopped fiber reinforced PP and common engineering thermoplastics will be formed by stamp forming process and different physical and rheological parameters of these grades will be investigated.

ACKNOWLEDGEMENT

REFERENCES

1. Weidmann, G.; Lewis, P.; Reid, N.; 1990, "Structural Materials", Butterworth/Heinemann, Materials Department, Open University, Milton Keynes, United Kingdom
2. Throne, J.L.; 1987, "Thermoforming" , Hanser Publishers, Munich
3. Groover, M. P.; 2002, "Fundamentals of Modern Manufacturing", John Wiley & Sons, Inc. , Second edition
4. Hou M., 1996, "Stamp forming of fabric-reinforced thermoplastic composites", Polymer Composites, Vol. 17, No.4. Page:596-603
5. Rosato, D.; Rosato, D.; 2003, "Plastics Engineered Product Design" , Elsevier, Oxford
6. EKSI O., 2007, "Determining the Stamp Forming Properties Of Plastic Based Materials" Master's Thesis, Trakya University, Graduate School of Natural and Applied Sciences.
7. Florian J., 1996, "Practical Thermoforming-Principles and Applications", 2nd Edition, Marcel Dekker, Inc., USA.
8. Gruenwald G., 1998, "Thermoforming-A Plastics Processing Guide", 2nd Edition, Technomic Publishing Company, Inc.
9. Harper C. A., 2006, "Handbook of Plastics Technologies", McGraw-Hill Companies, Inc.
10. Lokensgard E., 2004, "Industrial Plastics-Theory and Applications", 4th Edition, Thomson-Delmar Learning, USA
11. Margolis J.M., 2006, "Engineering Plastics Handbook", McGraw-Hill Companies, Inc.
12. Osswald T.A., 1998, "Polymer Processing Fundamentals", Hanser/Gardner Publications, Inc., USA.
13. Throne J.L., 1996, "Technology of Thermoforming", Hanser/Gardner Publications, Inc., USA.
14. Throne J.L., 2008, "Understanding Thermoforming", 2nd Edition, Hanser/Gardner Publications, Inc., USA.
15. Tucker N., Lindsey K., 2002, "Introduction to Automotive Composites", Rapra Technology Limited.
16. Hou M., Friedrich K., 1998, "Adjustable forming of thermoplastic composites for orthopaedic applications", Journal of Materials Science: Materials in Medicine, 9(1998), 83-88.
17. Friedrich K., Hou M., 1998, "On stamp forming of curved and flexible geometry components from continuous glass fiber/polypropylene composites", Composites Part A, 29A(1998).
18. Tulsian A., 2003, "Investigation of Plug-Assist Thermoforming of Polypropylene", Master of Science Thesis, University of Massachusetts Lowell, Plastics Engineering Department.
19. Rodgers B.N., 2004, "Multi-Layered Experimental and Numerical Analysis of Stamp Thermoforming Processing of Natural Fiber Reinforced Polypropylene Sheets", Master of Science Thesis, Michigan State University, Mechanical Engineering Department.
20. O'Connor C. P. J., Menary G., Martin P. J., McConville E., 2008, "Finite element analysis of the thermoforming of Polypropylene", International Journal of Material Forming, Suppl 1:779–782
21. Yankovich S.A., 2004, "Fabrication, Characterization and Stamp Thermoforming of Natural Fiber Polypropylene Composites Containing Kenaf Fibers", Master of Science Thesis, Michigan State University, Mechanical Engineering Department.
22. Shirani M., Agahi A., Sadough S.A., Biglari F.R., 2006, "Experimental study of thermoplastic reinforced composite sheet deep drawing", MATERIAUX 2006, Dijon,FRANCE
23. Martin P.J., Tan C.W., Tshai K.Y., McCool R., Menary G., Amstrong C.G., Harkin-Jones E.M.A., 2005, "Biaxial characterisation of materials for thermoforming and blow moulding", Plastics, Rubber and Composites, Vol.34, No:5/6
24. Sadighi M., Rabizadeh E.,Kermansaravi F., 2008, "Effects of laminate sequencing on thermoforming of thermoplastic matrix composites", Journal of Material Processing Technology, Vol.201, Page:725-730.
25. Bhattacharyya D., Bowis M., Jayaraman K., 2003, "Thermoforming woodfibre-polypropylene composite sheets", Composites Science and Technology, Vol.63, Page:353-365

Effect of Stamp Forming Pressure and Temperature on Polyvinylchloride Sheets

Ertugrul Selçuk Erdogan [1], Olcay Eksi [2]

[1]Trakya University, Engineering and Architecture Faculty, Mechanical Engineering Department, EDIRNE, 22100-TURKEY, eselcuk@trakya.edu.tr

[2]Namık Kemal University, Engineering Faculty of CORLU, Mechanical Engineering Department, Corlu/TEKIRDAG, 59860-TURKEY

ABSTRACT: Materials that have been used in this work were formed in stamp forming. A stamp forming mould which has a shape that has rectangular geometry was designed and manufactured to use this mould in this operation. Unreinforced polymer sheets were heated with an external heater to temperature which is close to melting limit but under melting point for each different material and formed by the mould which has been employed at room temperature to shape any parts from unreinforced PVC. Some useful parameters for stamp forming of the polymer sheets such as heating time of polymer sheets, mould velocity, stamping pressure etc. were determined before the experimental operation started. These materials were formed in different temperature and pressure conditions. Some specimens were cut and taken from these sheets by machining. Tensile characteristics of these materials were investigated. According to tensile test results obtained from experimental stamp forming operations, after changing the stamp forming parameters as stamping pressure and stamping temperature PVC materials showed different characteristics in (%)elongation at break and ultimate tensile strength.

Keywords: Compression, Temperature, Sheet, Polyvinylchloride (PVC), Strength, Thermoplastics.

INTRODUCTION

With the improvements about the plastic material compounds in the latest time, it is provided that plastic materials have advanced properties by reinforcing plastics with other materials. These developments provide the plastic matrix composites to have a usage as much as unreinforced plastic materials. Polymer composites reinforced with continuous fibers possess low weight plus high specific strength, stiffness, and environmental resistance. Furthermore they are increasingly used for structural parts in aircraft and space applications in the auto- mobile industry and for sporting goods.[4-15] That makes stamp forming manufacturing technique well-known among the other producing techniques of thermoplastics and their composites.

Polymers are based on long-chain polymer molecules and it is these long chains that are responsible for their characteristic mechanical and thermal properties, which distinguish them from other materials [1-2]. Peculiarities belong to different polymers are able to explored by looking at some common polymers and examples of design and failure. It is important to know how to design against polymer structure failure and how to work to the limit of the properties of polymers. There are countless man-made polymeric products. For this reason there are much more properties that are observed with most of the polymers such as synthetic fibres, engineering plastics and artificial rubber. [11-12] On the other hand, polymers have lower melting temperatures according to other material groups. That provides plastics to have a good formability. Increasing temperature make polymers become increasingly deformable. Also, the extent of polymer deformation is found to vary with time, temperature, stress and microstructure consistent with parallel observations for fully crystalline solids [3-9]. However, polymer sheets were used in this study are members of thermoplastic polymer group. In addition to this the most important advantage of thermoplastics may lie in their potential for rapid, low-cost, mass production of reinforced composites. Thermoplastics have a linear structure of molecular chains. As a result of this, thermoplastics are easy to process and shape with some special

manufacturing methods above their melting and softening point. Thermoplastics can be easily fabricated by any other processing techniques using heat or pressure, when they don't include any filler or reinforcing material. However, in order to fabricate thermoplastic matrix composites it is needed seriously high processing temperature and forming pressure because of high melt viscosity peculiarity of thermoplastics. Therefore thermosetting resins are employed mainly to lessen the required parameters for the processing technique [16]. Fabrication techniques that are commonly applied for short glass fibre reinforced thermoplastic composite parts are pultrusion, roll forming, filament winding and thermoforming. There are lots of fabrication techniques that utilize the same forming method with thermoforming such as vacuum molding, pressure molding and stamp forming. Every manufacturing process can be employed to create a new short glass fiber reinforced thermoplastic composite part. But the most effective forming technique for thermoplastic composite parts is stamp forming. Furthermore thermoforming is a manufacturing process that consists of many techniques for producing plastic articles from polymer sheets. In thermoforming producing technique, polymer sheet is heated and softened temporarily then this flat sheet is draped over a mold shape [17-18]. Thermoforming uses vacuum technique in order to form some kinds of polymer sheets. But with the stamp forming manufacturing process there is no need to use vacuum. That attribute is only the difference between thermoforming and stamp forming producing techniques [6-10]. Stamp forming has processing advantages over competitive processes such as blow molding, injection molding and rotational molding. Stamp forming needs relatively low forming pressures to change the shape of polymer material in to the final plastic product. Thus large size parts can be economically manufactured. Parts which have small thicknesses can be easily fabricated. For these parts manufacturing period is extremely short. Stamp forming molds are subjected relatively low forces. For this reason stamp forming molds can be made of inexpensive materials and that makes fabrication time very short for preparing new molds [5]. Stamp forming consists of a couple of segments. These processing steps are clamping, heating, forming, cooling and trimming. Sheets that are used in stamp forming producing technique can be categorized as thin-gage and thick-gage. Thin gage sheets have thickness less than 0.25 mm, thick gage sheet have thickness greater than 0.25 mm. Thick gage sheet can be further separated as medium-weight sheet and heavy-gage sheet. Medium-weight sheet has a thickness of 0.25mm to 1.5 mm. Heavy gage sheet has thickness greater than 1.5 mm [14].

EXPERIMENTAL

Materials

In this study polyvinyl chloride sheets were used. PVC (Trovidur PVC-U) sheets, manufactured by ROCHLING, Germany, have thickness of about 3 mm. Stamp forming temperatures of the material used in this study were determined according to manufacturer catalog information. The temperature range for appropriate forming is given 150^{0}C-180^{0}C. In order to investigate the condition of material arrangement, lines that are perpendicular to each other were drawn on the surface of the sheets before forming.

Equipment

The hydraulic press was used in this experimental study, has two working strokes, opening and compression during the closing. That hydraulic press can build up a maximum load of 150 kN in compression stroke. Forming press allows the mould to be closed on the pre-heated flat sheet with a constant velocity and mould has the same movement velocity during the forming operation. The entire stroke is 100 mm, in which 50 mm is the compression stroke. Desired stamping pressures can be adjusted by a computer which has software that controls the stroke of the hydraulic press and stamping pressure. Other important requirements are the devices that are needed to perform an experimental study. These devices are molds and heaters. In this experimental study as a stamp forming machine a couple of devices have been used to create an assembly called "stamp former device". This machine consists of stamp forming molds and a hydraulic press. Stamp forming molds were designed with a specific purpose to investigate the sharp shape effect on tensile behaviour of plastics in stamp forming process. Stamp forming molds which have been used in this study were designed in Solidworks CAD software. Although a stamp forming operation happens with these devices and equipments which are

mentioned above, one more thing is needed to complete full stamp forming activity. This device is a 3 kW electrical heater. The heater was designed to heat and softened flat polymer sheets as desired. Heating zone of the heater consists of electrical rod heaters. That heating element is able to provide to heat two sides of the sheet. During heating, distance between heater rods and the PVC sheet is about 10 mm.

Processing Procedure

In this study stamp forming process has two important stages; loading the sheets that heated to required temperature in to the stamp former device, forming the part [7]. Before the experimental study, it is needed to prepare the flat sheets with their proper dimensions. These sheets have had their final shapes by machining. At the end of this stage they had a square of 300mm*x*300mm. Tensile test specimens have been cut and taken from these flat sheets by machining before and after the stamp forming operation. Heater device employed in this experimental study must heat the sheet desired and proper forming temperature. According to thermal properties of flat sheet material, temperature has changed among 150°C-300°C. After all these equipments are ready, experimental study can be performed. Firstly molds have positioned between the upper tool and lower tool of the hydraulic press. Then some adjustments have been made about the pressure value that is required for a successful stamp forming process. During these actions happened, thermoplastic flat sheet was heated to proper forming temperature by a 3 kW electrical heater. Then softened polymer sheet were taken from the heater and put between the two mold halves. Upper tool have moved through the lower tool. Two mold halves clamped completely. Thus softened sheet cooled and have taken the shape of clamped molds. After a while upper tool have moved reverse direction. Sheet was taken from the mold. [8-13] Before forming operation these sheets have a thickness of 3 mm. Because of this all of the flat sheets and this stamp forming operation can be called heavy-gage sheets and heavy-gage stamp forming respectively. The illustration of stamp forming producing technique is given in Figure-1.

Figure-1. Illustration of stamp forming producing technique.

CHARACTERIZATION
Tensile tests

Tensile tests were performed at 23 °C using a tensile testing machine set-up according to ASTM D638 standard. These tensile tests were performed at a constant velocity of 5 mm/min with ASTM D 638 type 4 tensile test specimens. At least ten specimens were tested for each processing condition. Results were obtained from specimens cut off from the flat sheet before and after forming operation.

RESULTS AND DISCUSSION
Tensile test results

Tensile test results for PVC sheets are given in Table-1 and Table-2. Table 3 shows properties of Trovidur® PVC-U material.

Table-1. Tensile test results for PVC sheets before formed with heat and pressure

PVC sheets	• Ultimate tensile strength: 59.4 MPa • % Elongation at break: % 4.8

Table-2. Tensile test results PVC sheets after stamp forming

Material	Applied force (kN)	Heated temperature (^{o}C)	Holding time (sec)	Stroke (mm)	Ultimate tensile strength(MPa)	Elongation at break (%)
PVC	150	250	200	50	60.1	3.9
PVC	250	150	200	50	59.9	2.0

Table-3. Properties of Trovidur® PVC-U material(http://www.roechling.com/en/high-performance-plastics/thermoplastics/materials/trovidur/trovidur-pvc-u.html)

Density (g/cm^3)	DIN EN ISO 1183	1,44
Yield strength (MPa)	DIN EN ISO 527-1	50
Elongation (%)	DIN EN ISO 527-1	15
Elasticity modulus (MPa)	DIN EN ISO 527-1	3200
Sertlik(Shore D)	DIN EN ISO 868	80

Effect of stamping pressure

Determining the effect of stamping pressure on mechanical properties especially on ultimate tensile strength and on (%) elongation at break is influenced phenomenon when it is one of the most important stamp forming operation parameters. Variation of ultimate tensile strength with applied force of PVC sheets is shown with an illustration in Figure-2.
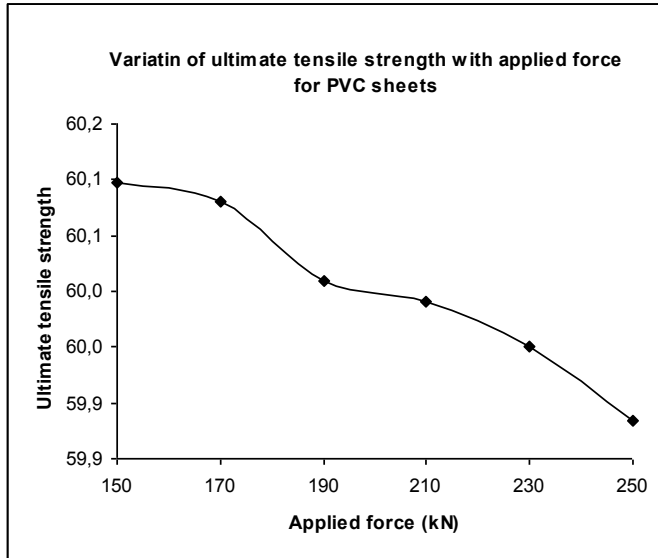
Figure-2. Variation of ultimate tensile strength with applied force for PVC materials

Variation of (%) elongation at break with applied force for PVC materials have been illustrated in Figure-3.
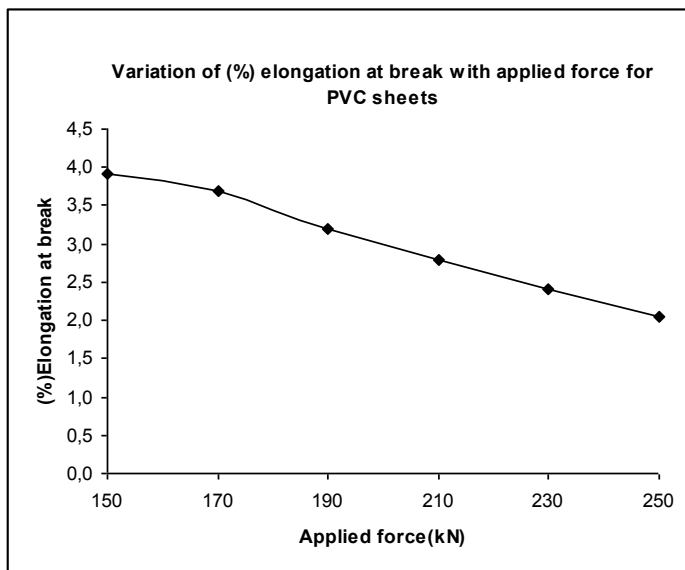
Figure-3. Variation of (%) elongation at break with applied force for PVC material

Effect of stamping temperature

Stamping temperature is one of the most important parameters is able to influence the quality of the product deeply after finishing operation. Therefore in order to achieve best results from the stamp forming manufacturing process stamping temperature must be chosen carefully. In this experimental period different temperature values were determined according to material's melting point. Variation of ultimate tensile strength with stamping temperature for PVC sheet materials are shown in Figure-4.
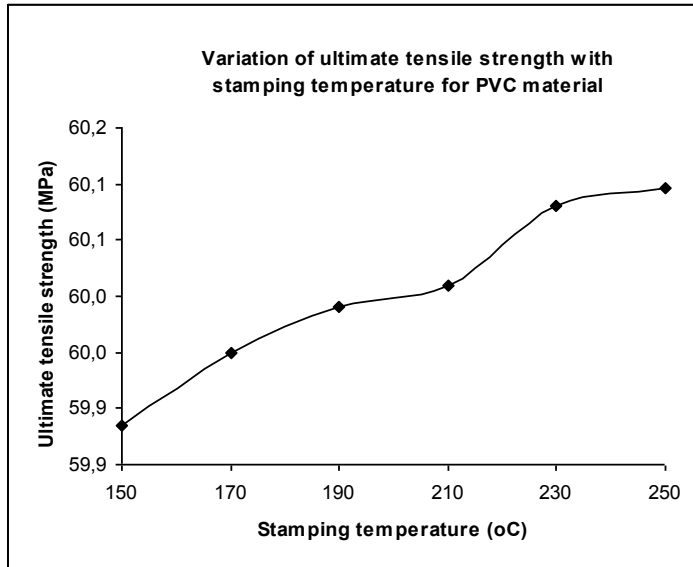
Figure-4. Variation of ultimate tensile strength with stamping temperature for PVC material

Variation of (%) elongation at break with stamping temperature for PVC sheet materials have been shown in Figure-5.
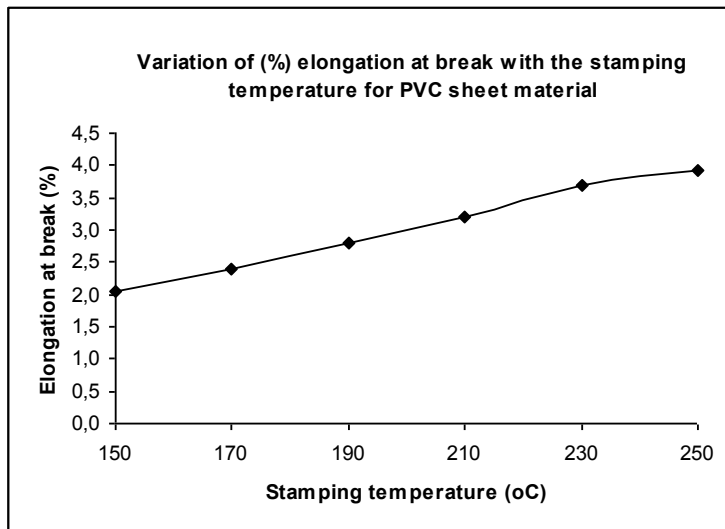
Figure-5. Variation of (%) elongation at break with stamping temperature for PVC material

Figure-6 shows PVC sheet after stamp forming process.
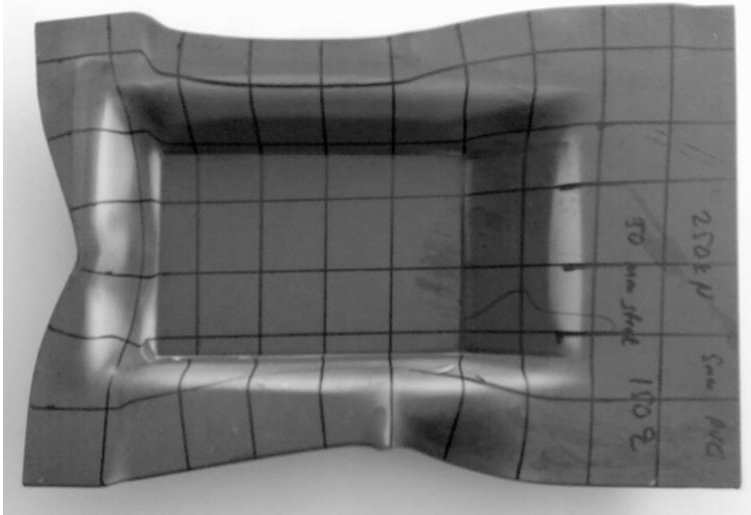
Figure-6. PVC sheet material after stamp forming

CONCLUSIONS

In this study, the stamp forming process of PVC sheets were investigated for simple mould geometry. Influence of stamping temperature and stamping pressure has been determined on the ultimate tensile strength and (%) elongation at break. It has seen from the test results for PVC sheets that;
- Increasing applied force (stamping pressure) gives slightly decreasing tensile strength
- Increasing applied force (stamping pressure) gives decreasing elongation at break
- Increasing stamping temperature gives slightly increasing tensile strength
- Increasing stamping temperature gives increasing elongation at break

Observation of the tensile test results obtained from experimental stamp forming operations of distinct thermoplastic sheets showed that ultimate tensile strength and (%) elongation at break of PVC sheets were changed similar for most of the stamping parameters like stamping temperature and stamping pressure.

SUGGESTED STUDIES FOR FUTURE

In this study PVC extruded grades were formed in different temperature and pressure conditions. Some specimens were cut and taken from these sheets by machining. Tensile characteristics of these materials were investigated. According to tensile test results obtained from experimental stamp forming operations after changing the stamp forming parameters as stamping pressure and stamping temperature PVC materials showed different characteristics in (%) elongation at break and ultimate tensile strength. For future studies chopped fiber reinforced PVC and common engineering thermoplastics will be formed by stamp forming process and different physical and rheological parameters of these grades will be investigated.

ACKNOWLEDGEMENT

REFERENCES

26. Weidmann, G.; Lewis, P.; Reid, N.; 1990, "Structural Materials", Butterworth/Heinemann, Materials Department, Open University, Milton Keynes, United Kingdom

27. Throne, J.L.; 1987, "Thermoforming" , Hanser Publishers, Munich

28. Groover, M. P.; 2002, "Fundamentals of Modern Manufacturing", John Wiley & Sons, Inc. , Second edition

29. Hou M., 1996, "Stamp forming of fabric-reinforced thermoplastic composites", Polymer Composites, Vol. 17, No.4. Page:596-603

30. Rosato, D.; Rosato, D.; 2003, "Plastics Engineered Product Design" , Elsevier, Oxford

31. EKSI O., 2007, "Determining the Stamp Forming Properties Of Plastic Based Materials" Trakya University, Graduate School of Natural and Applied Sciences.

32. Florian J., 1996, "Practical Thermoforming-Principles and Applications", 2nd Edition, Marcel Dekker, Inc., USA.

33. Gruenwald G., 1998, "Thermoforming-A Plastics Processing Guide", 2nd Edition, Technomic Publishing Company, Inc.

34. Harper C. A., 2006, "Handbook of Plastics Technologies", McGraw-Hill Companies, Inc.

35. Lokensgard E., 2004, "Industrial Plastics-Theory and Applications", 4th Edition, Thomson-Delmar Learning, USA

36. Margolis J.M., 2006, "Engineering Plastics Handbook", McGraw-Hill Companies, Inc.

37. Osswald T.A., 1998, "Polymer Processing Fundamentals", Hanser/Gardner Publications, Inc., USA.

38. Throne J.L., 1996, "Technology of Thermoforming", Hanser/Gardner Publications, Inc., USA.

39. Throne J.L., 2008, "Understanding Thermoforming", 2nd Edition, Hanser/Gardner Publications, Inc., USA.

40. Tucker N., Lindsey K., 2002, "Introduction to Automotive Composites", Rapra Technology Limited.

41. Hou M., Friedrich K., 1998, "Adjustable forming of thermoplastic composites for orthopaedic applications", Journal of Materials Science: Materials in Medicine, 9(1998), 83-88.

42. Taylor C.A., Delorenzi H.G., Kazmer D.O., 1992, "Experimental and Numerical Investigations of the Vacuum-Forming Process", Polymer Engineering and Science, Vol. 32, No.16

43. Nam G.J., Rhee H.W., Lee J.W., 1998, "Finite element Analysis of the Effect of Processing Conditions on Thermoforming", ANTEC'98, Conference Proceedings, Volume 1: Processing, Atlanta,Georgia.

Characterization Of Sintered %50ni-%48cr-%2ti Powder Mixtures Containing Intermetallics

*Ahmet YÖNETKEN [1] Ayhan EROL [2], İsmail YILDIZ [3]

[1]Afyon Kocatepe University, Engineering Faculty, 03200, Afyonkarahisar/ Turkey, yonetken@aku.edu.tr
[2]Afyon Kocatepe University, Technology Faculty, 03200, Afyonkarahisar/ Turkey aerol@aku.edu.tr,
[3] Vocational College of Iscehisar, Afyon Kocatepe University, Afyonkarahisar, Turkey iyildiz@aku.edu.tr
Phone:+902722281423 Fax:+902722281422
Corresponding Author*

Abstract: Intermetallic materials are among advanced technology materials that have outstanding mechanical and physical properties for high temperature applications. Especially creep resistance, low density and high hardness properties stand out in such intermetallics. The microstructure, mechanical properties of %50Ni-%48Cr and %2Ti powders were investigated using specimens produced by tube furnace sintering at 1000-1400°C temperature. A composite consisting of ternary additions, a metallic phase, Ti,Cr and Ni have been prepared under Ar shroud and then tube furnace sintered. XRD, SEM (Scanning Electron Microscope), were investigated to characterize the properties of the specimens. Experimental results carried out for composition %50Ni-%48Cr and %2Ti at 1400°C suggest that the best properties as 184HV and 6,24/cm^3 density were obtained at 1400°C

Keywords: Sintering, intermetallic, high temperature, composite

1 Introduction

Nickel-based alloys are commonly used as the substructure of metal–ceramic crowns and were introduced into dentistry as a possible replacement for precious alloys due to the increasing cost of gold throughout the 1980s. Ni-based alloys offer the advantage of an increased modulus of elasticity compared with gold that allows thinner sections of the alloy to be used, and consequently less sound tooth destruction during the crown preparation. In addition, the thermal expansion coefficient of Ni-based alloys is well matched to that of conventional veneering porcelain, whichmaintains the metal and ceramic crown to be intimately bonded during firing and prevents cracking of the veneer [1-4].

The Ni–Cr alloys have been shown to be an excellent alternative for noble alloys, for use primarily in metal-ceramic prostheses. The high modulus of elasticity of Ni– Cr alloys, approximately two times higher than the base alloy of gold, allows a reduction in cross-section of the piece, provides more space for the porcelain and less wear on the tooth [5-7].

In spite of the benefits, Ni–Cr alloys have some limitations. The immediate biocompatibility risk with nickel alloys seems to be allergic contact dermatitis. Like all non-precious alloys,

nickel alloys are subjected to corrosion products that might lead to soft tissue inflammation and contact dermatitis [8-11].

The purpose of this article is to present the results of an experimental study of the effect of titanium addition on the microstructure and some properties of Ni-Cr alloys. Hardness, density and shear strenght behaviour of the as-cast Ni–Cr–Ti alloys would be evaluated with a hope of developing an alloy suitable for biomedical application

2 Material-Method and Preparation Of Sample

Starting powders employed in this study were as follows: the purity of 99.8% for Ni powders with a particle size lower than 40 µm, the purity of 99.95% for Cr powders a particle size lower than 75 µm and the purity of 99.9% for Ti powders with a particle size lower than 150µm. The composition of %50Ni-%48Cr-%2Ti specimens was prepared in 10g rectangular compressed pre-form. They were mixed homogenously for 24 hours in a mixer following the weighing. The mixture was shaped by single axis cold hydraulic pressing using high strength steel die. A pressure of 300 Bar was used for the compacting all the powder mixtures. The cold pressed samples underwent for a sintering at 1000, 1100, 1200, 1300 and 1400°C for 2 hours in a traditional tube furnace using Argon gas atmosphere. The specimens were cooled in the furnace after sintering and their micro hardness and shear strengths measurements were carried out using METTEST-HT (Vickers) micro hardness tester and Shimadzu Autograph AG-IS 100KN universal tensile tester machine, respectively

Shimadzu XRD-6000 X-Ray Diffraction analyzer was operated with Cu K alpha radiation at the scanning rate of 2 degree per minute. LEO 1430 VP model Scanning Electron Microscope fitted with Oxford EDX analyzer was used for microstructural and EDX compositional analysis.

The volumetric changes of %50Ni-%48Cr-%2Ti composite material after sintering were calculated by using (d=m/V) formula (Fig. 1). The volume of post-sintered samples was measured with Archimedes principle. All the percentages and ratios are given in weight percent unless stated otherwise.

3 Experimental Results and Discussion

3.1 Characterization of specimens

In the study, the samples prepared and shape were sintered at temperatures ranging from 1000°C to 1400°C in conventional furnace and made ready for physical, mechanical and metallographic analyses. Density-temperature change curve is shown in Figure 1. The highest sintered density was achieved at 1400°C as 6,24gr/cm^3.
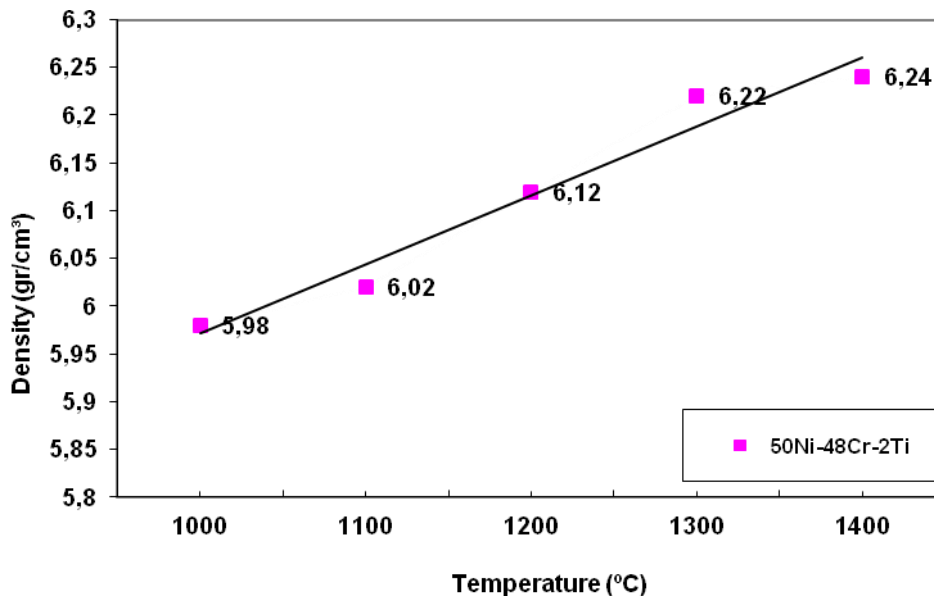
Fig.1: The density change with respect to sintering temperature

The micro hardness-temperature change diagram is shown in figure 2. The micro hardness values of the composite samples produced using conventional sintering technique within the temperature range 1000-1400°C. According to this, the highest micro hardness value in the composite samples produced using powder metallurgy method was observed to be 184HV at 1400°C.
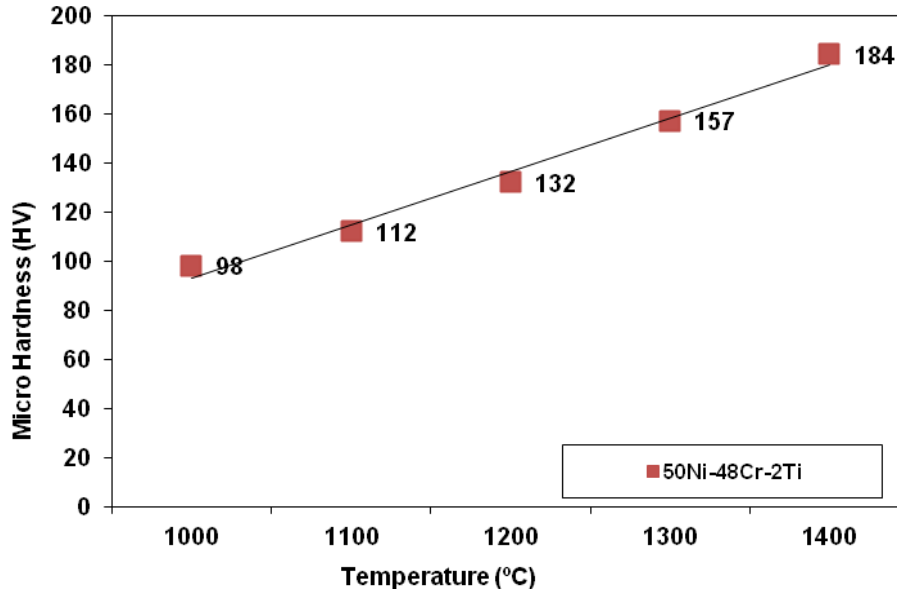
Fig. 2: The micro hardness tests results from sintered specimens treated at different temperatures

Shear strength and hardness of the metal-matrix composite specimens were also determined. The relation between the sintering temperatures and Shear strength values is shown in Figure 3. The shear strength value in the composite samples was observed to be 254.34 MPa at 1400°C.
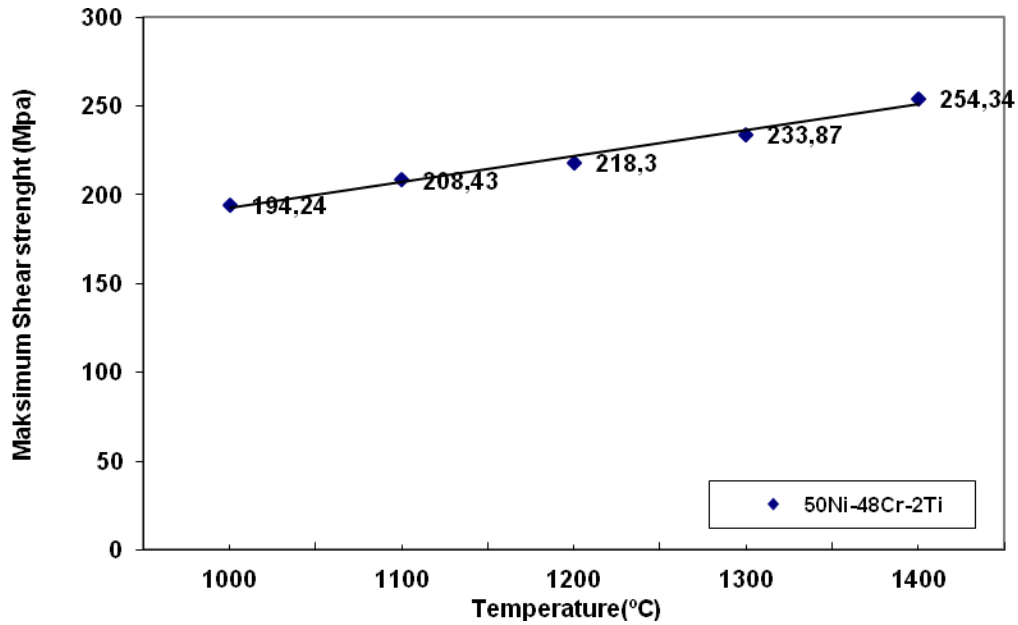
Fig. 3: Shear strength results from specimens sintered at different temperatures

3.1 Metallographic Analysis

The SEM analysis result of the metal matrix composite specimen obtained from Ni-Cr-Ti powders sintered at 1000ºC is shown in Figure 5. grain growth is observed and a homogeneous structure. In Figure 6, 1400 ºC to become apparent degree of grain boundaries and grain boundaries can be seen that the pores very smaller and circular shapes. Sintering is better understood at 1400 ºC temperature. This density, hardness and shear strength values are confirmed.
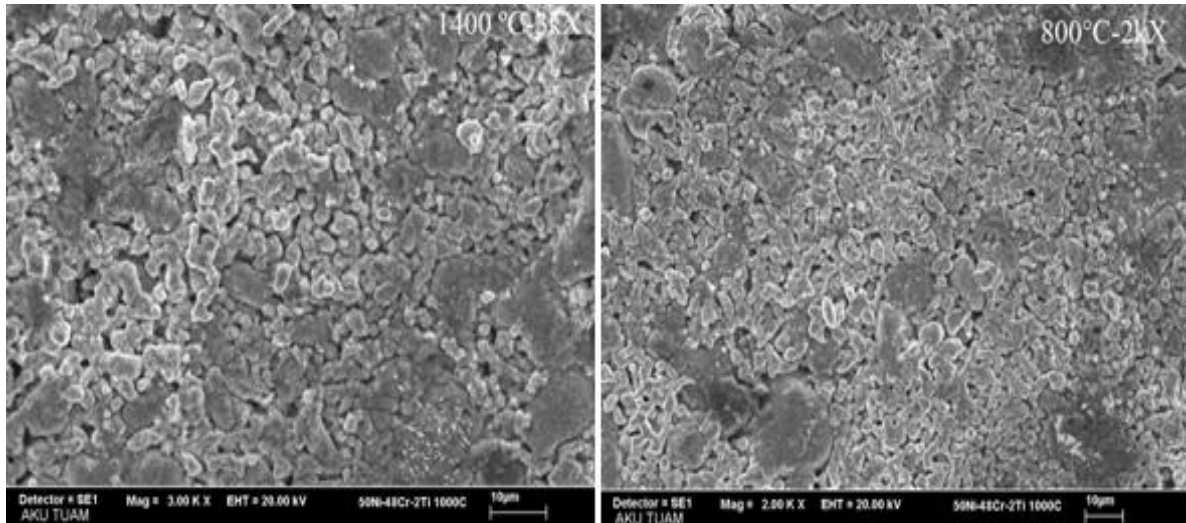
Fig. 5. SEM view of Ni-Cr-Ti composite 1000°C
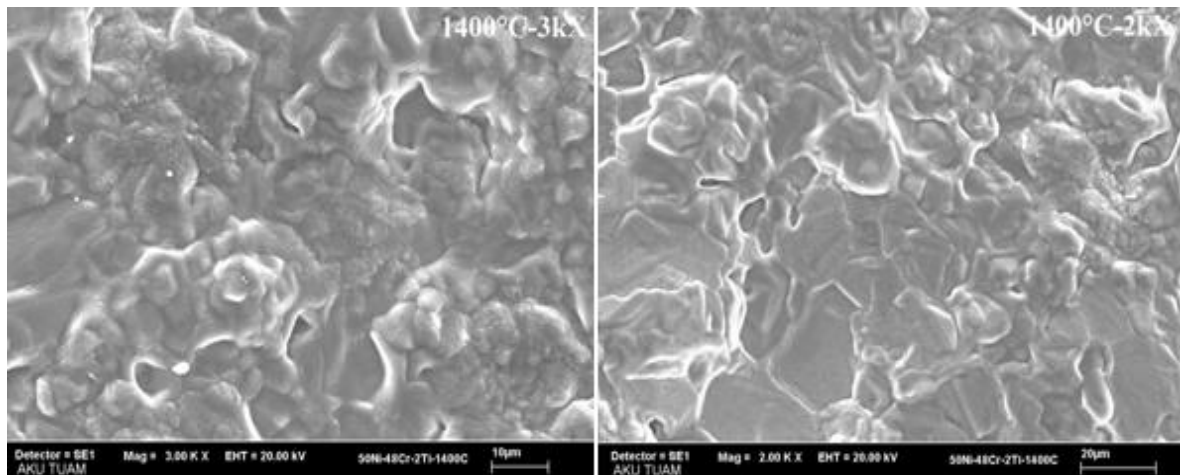
Fig. 6. SEM view of Ni-Cr-Ti composite 1400°C

3.2 XRD Analysis

In Figure 7, NiTi, Ni_3Cr_2, TiO, and Cr peaks can be seen in the XRD analysis from Ni-Cr-Ti composite sintered in tube furnace at 1000°C and 1400°C.
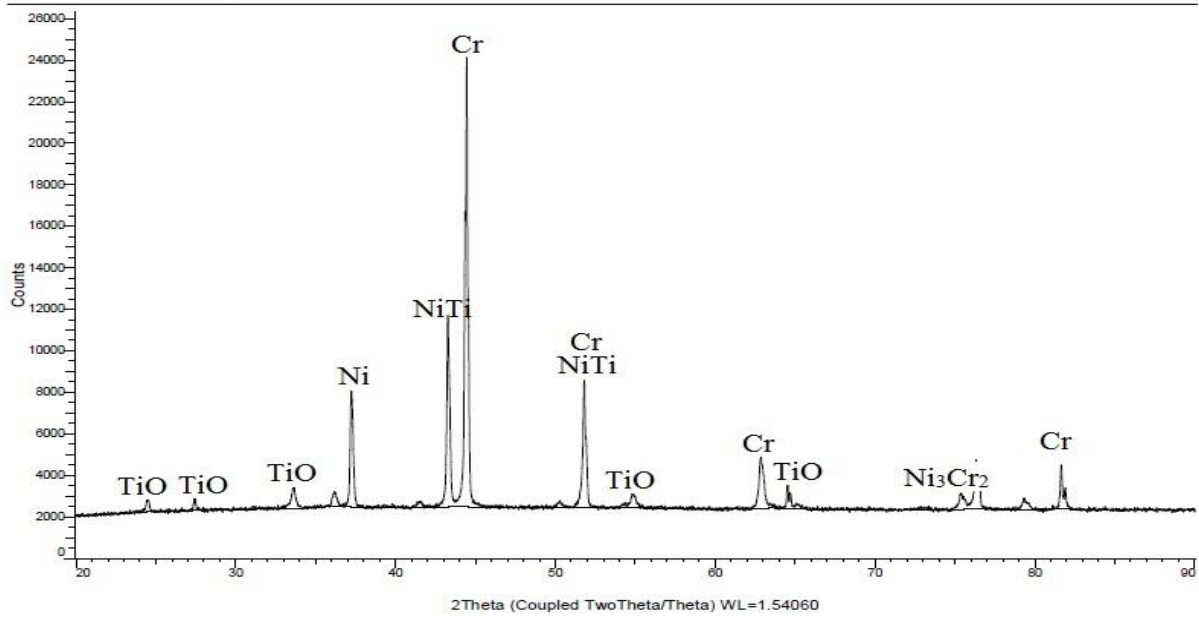
(a)
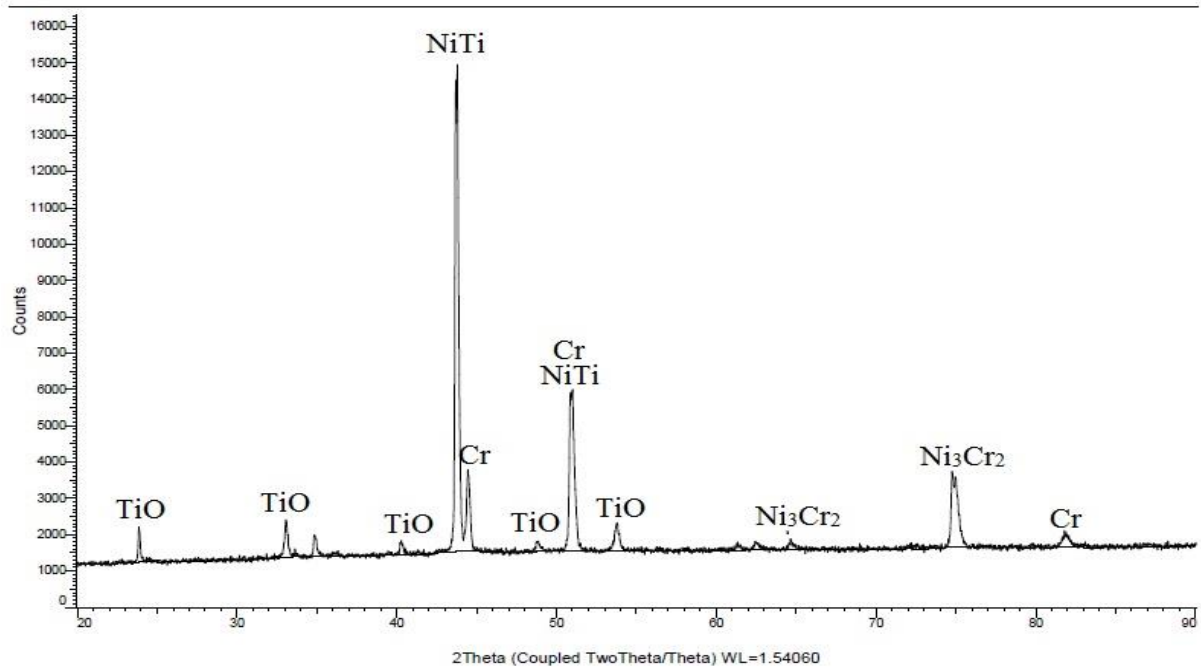
(b)

Fig.7: The XRD analysis Ni-Cr-Ti composites sintered at 1000°C and 1400°C

Ni-Cr-Ti powders were mixed and then sintered in a conventional furnace. After sintering, a considerable drop in the mechanical properties of specimens sintered at 1000°C and 1400°C were observed. It was concluded that Ni-Cr-Ti particles were occured by NiTi, and Ni_3Cr_2 intermetallic phase at 1400°C and Hardness test results suggest that Ni-Cr-Ti composite sintered at 1400°C shows Vickers micro hardness values respectively.

4 Conclusion

The following results were concluded from the experimental findings

- The highest density in composite made from Ni-Cr-Ti powders sintered at different temperatures was obtained as 1400°C The highest density sample was found as 6,24gr/cm^3 at 1400°C.

- The highest microhardness in Ni-Cr-Ti composite samples fabricated using powder metallurgy method was found as 184HV at 1400°C.

The highest Shear strength sample was obtained as 254,34MPa at 1400°C.

- It was also found out for composition %50Ni-%48Cr- %2Ti at 1400°C suggest that the best properties.

5 Acknowledgements

6 References

[1] C. M. Wylie, R. M. Shelton, G.J.P. Fleming, A. J. Davenport, Corrosion of nickel-based dental casting alloys, dental materials, vol. 23, pp. 714-723, 2007.

[2] Z. Tek, M.A. Gügör, E. Çal, M. Sonugelen, C. Artunç, A. Oztarhan, A study of the mechanical properties of TiN coating of Cr–Ni alloy, Surface & Coatings Technology, vol. 196, pp. 317-320, 2005.

[3] J. Bauer, J.F. Costa, C. N. Carvalho, R. H. M. Grande, A. D. Loguercio, A. Reis, Characterization of two Ni–Cr dental alloys and the influence of casting mode on mechanical properties, Journal of Prosthodontic Research, vol. 56, pp. 264-271, 2012.

[4] Z. Tek, M.A. Gungor, E. Çal, M. Sonugelen, C. Artunc, A. Oztarhan, Comparison of the mechanical properties of nitrogen ion implantation and micro-pulsed plasma nitriding techniques of Cr–Ni alloy, Surface & Coatings Technology, vol. 158-159, pp. 157-163, 2002.

[5] J. Liu, X.M. Qiu, S. Zhu, D.Q. Sun, Microstructures and mechanical properties of interface between porcelain and Ni–Cr alloy, Materials Science and Engineering, vol. 497, pp. 421-425, 2008.

[6] L. Reclaru, R.E. Unger, C.J. Kirkpatrick, C. Susz, P.Y. Eschler, M.-H. Zuercher, I. Antoniac, H. Lüthy, Ni–Cr based dental alloys; Ni release, corrosion and biological evaluation, Materials Science and Engineering, vol. 32, pp. 1452-1460, 2012.

[7] A. J. F. Neto, H. Panzeri, F. D. Neves, R. A. D. Prado, G. Mendonça, Bond Strength of Three Dental Porcelains to Ni-Cr and Co-Cr-Ti Alloys, Brazing Dental Journal, vol. 17, pp. 24-28, 2006.

[8] N. Espallargas, S. Mischler, Dry wear and tribocorrosion mechanisms of pulsed plasma nitrided Ni–Cr alloy, wear, vol. 270, pp. 464-471, 2011.

[9] E. L. McGinley, D. C. Coleman, G. P. Moran, G. J.P. Fleming, Effects of surface finishing conditions on the biocompatibility of a nickel–chromium dental casting alloy, Dental Materials, vol. 27, pp. 637-650, 2011.

[10] R. Venugopalan, R. L.W. Messer, The effect of a microcarrier suspension cell culture system on polarization measurements from Ni–Cr dental casting alloys, Dental Materials, vol. 21, pp. 993-998, 2005.

[11] H. Chao, L. Yong, W. Yan, L. Wei-jie, T. Hui-ping, Hot corrosion behavior of Ni−xCr−6.8Al based alloys, Transactions of Nonferrous Metals Society of China, vol. 21, pp. 2348-2357, 2011.

Mechanical Proporties of A Composite Produced From Electroless Ni Plated Cr And Ti Powders

[1] Ahmet YÖNETKEN [2] Ayhan EROL, [3] İsmail YILDIZ

[1] Faculty of Engineering, Afyon Kocatepe University, 03200, Afyonkarahisar, Turkey, yonetken@aku.edu.tr
[2] Afyon Kocatepe University, Technology Faculty, 03200, Afyonkarahisar/ Turkey aerol@aku.edu.tr,
[3] Vocational College of Iscehisar, Afyon Kocatepe University, Afyonkarahisar, Turkey, iyildiz@aku.edu.tr
Corresponding Author[1]

Abstract: Intermetallic materials such as NiTi, Ni_3Cr_2, CrTi are among advanced technology materials that have outstanding mechanical and physical properties for high temperature applications. Especially creep resistance, low density and high hardness properties stand out in such intermetallics. The microstructure, mechanical properties of %64Ni plated %32Cr and %4Ti powders were investigated using specimens produced by tube furnace sintering at 1000-1400°C temperature. A composite consisting of ternary additions, a metallic phase, NiTi and Ni_3Ti have been prepared under Ar shroud and then tube furnace sintered. XRD, SEM (Scanning Electron Microscope), were investigated to characterize the properties of the specimens. Experimental results carried out for composition %64Ni plated %32Cr- %4Ti at 1300°C suggest that the best properties as 208HV and $6,87/cm^3$ density were obtained at 1400°C

Keywords: Sintering, Intermetallic, Electroless plating, composite

1 Introduction

Electroless Ni plating is a deposition process by which Ni metal ions are transferred onto non-reacting substrate by a reducing agent in the plating solution. It is widely used in aerospace, automotive and electronic industries [1]. To increase its applicability, electroless metal plating of many ceramics has been successfully employed to form a strong binding between particles of ceramics and thus utilize the superior wear and chemical corrosion properties of ceramic phase in highly demanding conditions [2-5]. The coating of WC powders was studied for electroless deposition of Ni and other metals and Ni with P or B and the electrolytic deposition of Ni and onto WC particles and the effect of plating conditions with NiP were also investigated [6-10]. Nickel-based alloys are commonly used as the substructure of metal–ceramic crowns and were introduced into dentistry as a possible replacement for precious alloys due to the increasing cost of gold throughout the 1980s. Ni-based alloys offer the advantage of an increased modulus of elasticity compared with gold that allows thinner sections of the alloy to be used, and consequently less sound tooth destruction during the crown preparation. In addition, the thermal expansion coefficient of Ni-based alloys is well

matched to that of conventional veneering porcelain, whichmaintains the metal and ceramic crown to be intimately bonded during firing and prevents cracking of the veneer [11-14].

The Ni–Cr alloys have been shown to be an excellent alternative for noble alloys, for use primarily in metal-ceramic prostheses. The high modulus of elasticity of Ni– Cr alloys, approximately two times higher than the base alloy of gold, allows a reduction in cross-section of the piece, provides more space for the porcelain and less wear on the tooth [15-17]. In spite of the benefits, Ni–Cr alloys have some limitations. The immediate biocompatibility risk with nickel alloys seems to be allergic contact dermatitis. Like all non-precious alloys, nickel alloys are subjected to corrosion products that might lead to soft tissue inflammation and contact dermatitis [18-21].

The purpose of this article is to present the results of an experimental study of the effect of titanium addition on the microstructure and some properties of Ni-Cr alloys. Hardness, density and shear strenght behaviour of the as-cast Ni–Cr–Ti alloys would be evaluated with a hope of developing an alloy suitable for biomedical application

2 Material-Method and Preparation Of Sample

Starting powders employed in this study were as follows Cr powders a particle size lower than 75 µm and the purity of 99.9% for Ti powders with a particle size lower than 150µm. and Cr-Ti-Ni intermetallic composite was produced by electroless Ni plating of Cr-Ti powders.

Ni plating was achieved by suspending the starting Cr-Ti powders in a Ni containing solution ($NiCI_2.6H_2O$) at 90-95°C and by adding Hydrazine Hydrate ($N_2H_4.H_2O$) and 35 vol.% Ammonia solution while keeping the pH at 9-10. With increasing temperature, Ammonia evaporation rate increased rapidly, therefore, a dripper was used to add more ammonia for adjusting pH of the plating solution. In the mean time, the solution was continuously stirred and the pH was constantly monitored by using a Philips PW 9413 Ion-Activity Meter. The reaction was allowed to continue until sufficient Ni was added for plating all the Cr-Ti powders, then, Ni plated Cr-Ti powders were filtered out of the solution by using a paper filter and repeatedly washed off by distilled water and then oven dried at 105°C. and then followed by sintering The composition of %64Ni plated %32Cr-%4Ti specimens was prepared in 10g rectangular compressed pre-form. The Ni plated Cr-Ti powders were shaped by single axis cold hydraulic pressing using high strength steel die. A pressure of 300 Bar was used for the

compacting all the powder mixtures. The cold pressed samples underwent for a sintering at 1000, 1100, 1200, 1300 and 1400°C for 2 hours in a traditional tube furnace using Argon gas atmosphere. The specimens were cooled in the furnace after sintering and their micro hardness and shear strengths measurements were carried out using METTEST-HT (Vickers) micro hardness tester and Shimadzu Autograph AG-IS 100KN universal tensile tester machine, respectively

Shimadzu XRD-6000 X-Ray Diffraction analyzer was operated with Cu K alpha radiation at the scanning rate of 2 degree per minute. LEO 1430 VP model Scanning Electron Microscope fitted with Oxford EDX analyzer was used for microstructural and EDX compositional analysis.

The volumetric changes of %64Ni plated %32Cr-%4Ti composite material after sintering were calculated by using (d=m/V) formula (Fig. 1). The volume of post-sintered samples was measured with Archimedes principle. All the percentages and ratios are given in weight percent unless stated otherwise.

3 Experimental Results and Discussion

3.1. Characterization of specimens

In the study, the samples prepared and shape were sintered at temperatures ranging from 1000ºC to 1400ºC in conventional furnace and made ready for physical, mechanical and metallographic analyses. Density-temperature change curve is shown in Figure 1. The highest sintered density was achieved at 1400°C as 6,87gr/cm^3.
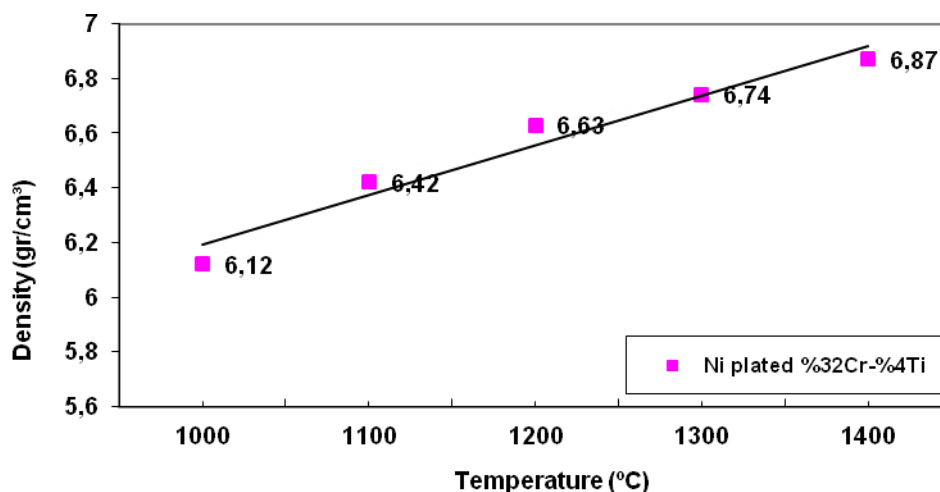
Fig. 1: Density results from sintered specimens treated at different temperatures

The micro hardness-temperature change diagram is shown in figure 2. The micro hardness values of the composite samples produced using conventional sintering technique within the temperature range 1000-1400°C. According to this, the highest micro hardness value in the composite samples produced using powder metallurgy method was observed to be 208HV at 1400°C.
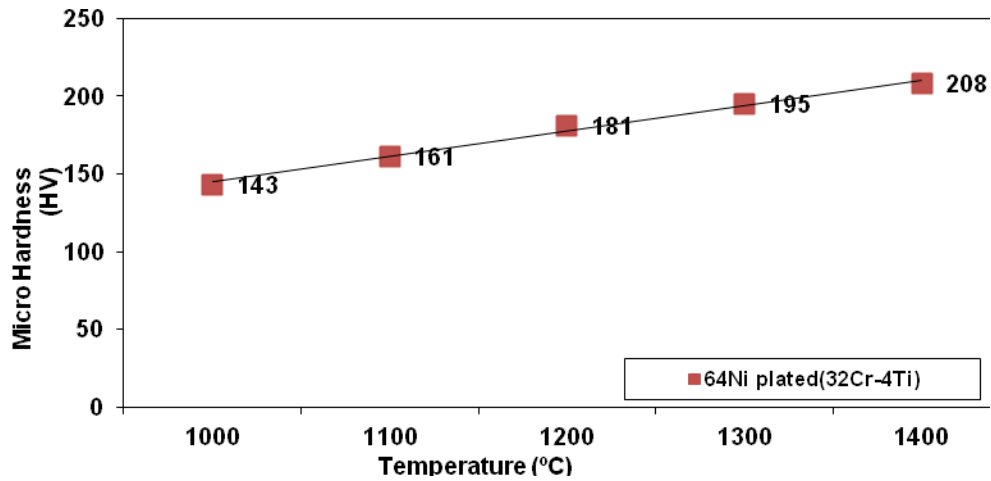
Fig. 2: The micro hardness tests results from sintered specimens treated at different temperatures

Shear strength and hardness of the metal-matrix composite specimens were also determined. The relation between the sintering temperatures and Shear strength values is shown in Figure 3. The shear strength value in the composite samples was observed to be 87.62 MPa at 1400°C.
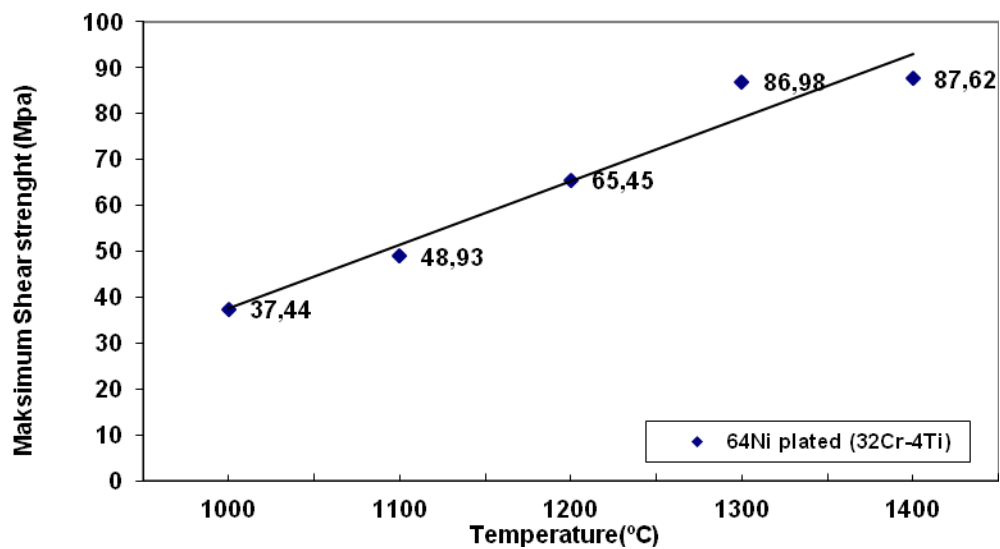
Fig. 3: Shear strength results from specimens sintered at different temperatures

3.1 Metallographic Analysis

The SEM analysis result of the metal matrix composite specimen obtained from Ni plated Cr-Ti powders sintered at 1000 ºC is shown in Figure 4d. grain growth is observed and a homogeneous structure. In Figure 4a, 1400 ºC to become apparent degree of grain boundaries and grain boundaries can be seen that the pores very smaller and circular shapes. Sintering is better understood at 1400 ºC temperature. This density, hardness and shear strength values are confirmed.
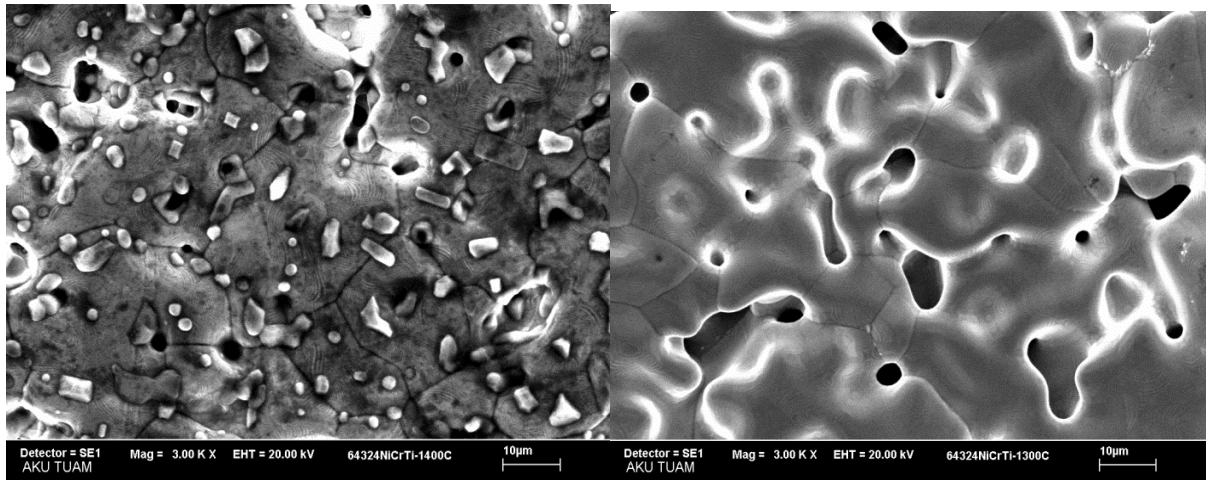
a)1400°C   b)1300°C
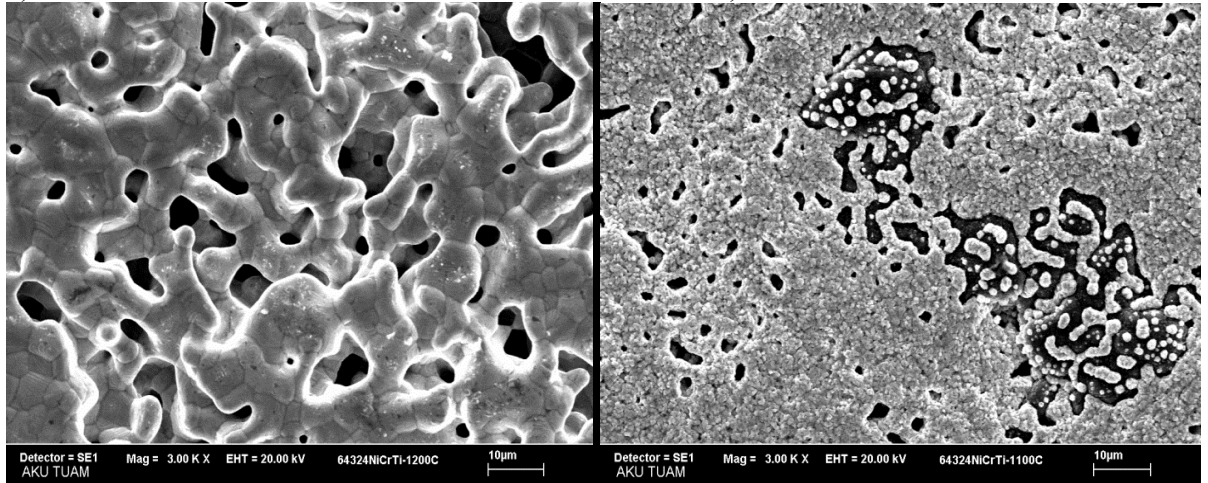
c)1200°C   d)1100°C
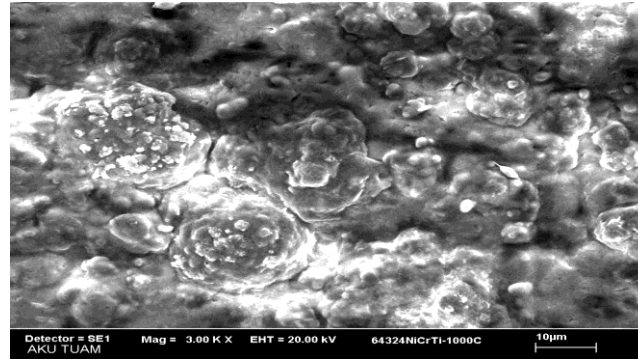
d)1000°C

Fig. 4. SEM view of Ni-Cr-Ti composite
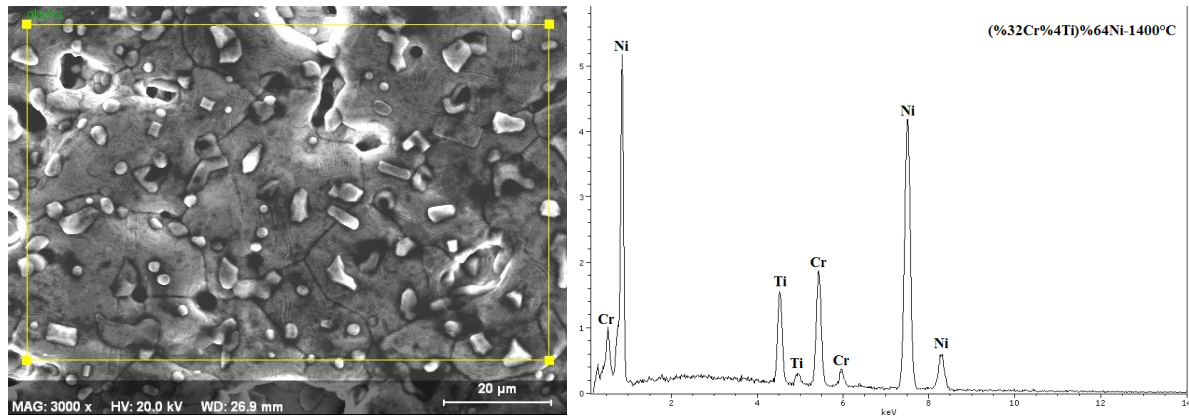
Fig. 5. 1400°C EDX analizi Ni plated (%32Cr-%4Ti)

EDX analysis results are given in Figure 5. Sintered at 1400°C Ni-Cr-Ti composite EDX analysis was conducted of the field. Ni, Cr, Ti elements were identified in the analysis results. The pure Ni element was prepared by coating in the Hydrazine bath.

4. Conclusion

The following results were concluded from the experimental findings

- The highest density in composite made from Ni-Cr-Ti powders sintered at different temperatures was obtained as 1400°C The highest density sample was found as 6,24gr/cm^3 at 1400°C.
- The highest microhardness in Ni-Cr-Ti composite samples fabricated using powder metallurgy method was found as 208HV at 1400°C.

The highest Shear strength sample was obtained as 87,62MPa at 1400°C.

- It was also found out for composition %64Ni plated%32Cr- %4Ti at 1400°C suggest that the best properties.

5. Acknowledgements

6. References

[1] Henry J.R., met. finish, 97 (1999), 424.

[2] Wu P., Du H.M., Chen X.L., li Z.Q., Bai H.L., and Jiang E.Y., wear, 257 (2004), 142.

[3] Farroq T., and Davies T.J., int. j. powder metall., 27 (1991), 347.

[4] Strafford K.N., Datta P.K., and O'donnell A.K., mater. design, 3 (1982), 608.

[5] Guozhi X., Jingxian Z., Yijun L., Keyu W., Xiangyin M., and Pinghua L., mater. sci. eng. a, 460 (2007), 461.

[6] Balaraju J.N., Narayanan T.S.N.S., and Seshadri S.K., j. appl. electrochem., 33 (2003), 1241.

[7] Giampaolo A.R., Ordonez J.G., Gugliemacci J.M., and Lira J., surf. coat. tech., 89 (1997), 127.

[8] Stroumbouli A., Gyftou P., Pavlatou E.A., and Spyrellis N., surf. coat. tech. 195 (2005), 325.

[9] Hamid Z.A., El Badry S.A., and Aal A.A., surf. coat. tech. 201(2007), 5948.

[10] Fernondes C.M., Senos A.M.R., Castanio J.M., and Vieira m.t., mater. sci. forum, 514-516 (2006), 633.

[11] C. M. Wylie, R. M. Shelton, G.J.P. Fleming, A. J. Davenport, Corrosion of nickel-based dental casting alloys, dental materials, vol. 23, pp. 714-723, 2007.

[12] Z. Tek, M.A. Gügör, E. Çal, M. Sonugelen, C. Artunç, A. Oztarhan, A study of the mechanical properties of TiN coating of Cr–Ni alloy, Surface & Coatings Technology, vol. 196, pp. 317-320, 2005.

[13] J. Bauer, J.F. Costa, C. N. Carvalho, R. H. M. Grande, A. D. Loguercio, A. Reis, Characterization of two Ni–Cr dental alloys and the influence of casting mode on mechanical properties, Journal of Prosthodontic Research, vol. 56, pp. 264-271, 2012.

[14] Z. Tek, M.A. Gungor, E. Çal, M. Sonugelen, C. Artunc, A. Oztarhan, Comparison of the mechanical properties of nitrogen ion implantation and micro-pulsed plasma nitriding techniques of Cr–Ni alloy, Surface & Coatings Technology, vol. 158-159, pp. 157-163, 2002.

[15] J. Liu, X.M. Qiu, S. Zhu, D.Q. Sun, Microstructures and mechanical properties of interface between porcelain and Ni–Cr alloy, Materials Science and Engineering, vol. 497, pp. 421-425, 2008.

[16] L. Reclaru, R.E. Unger, C.J. Kirkpatrick, C. Susz, P.Y. Eschler, M.-H. Zuercher, I. Antoniac, H. Lüthy, Ni–Cr based dental alloys; Ni release, corrosion and biological evaluation, Materials Science and Engineering, vol. 32, pp. 1452-1460, 2012.

[17] A. J. F. Neto, H. Panzeri, F. D. Neves, R. A. D. Prado, G.

The Effect of Filler Type on The Properties of In-Situ Polymerized PP Nanocomposites

O. Sultan [1], A Van Reenen [2]

[1] Dept. of Chemical Engineering, Faculty of Engineering, Zawia University, Libya
[2] Dept of Chemistry and Polymer Science, University of Stellenbosch, South Africa

Abstract

Polypropylene/filler nanocomposites were prepared by in-situ polymerization with MAO activated metallocene catalyst without supporting the catalyst on the filler. The effect of addition of MAO treated nanofiller, at different loads, on the polymerization kinetics and consequently on PP matrix microstructure was investigated. To this end, two different fillers (Silica and Calcium carbonate) were used in this study for the preparation of the PP nanocomposties. A C_2 symmetric metallocene catalyst *ansa* dimethylsilylbis(2-methyl benzoindenyl) zirconium dichloride (MBI) was used as the catalyst. Results show that the kinetic of the polymerizations were profoundly affected by the presence of the filler particles, in comparison to the kinetic of homogeneous polymerizations. Therefore, the microstructure of the polymer matrix was also influenced by the presence of treated nanofillers in the polymerization media. It was also evident that the different types of the filler affect the polymerization activity and the produced PP microstructure differently.

Keywords: Nanocomposites; PP microstructure; in-situ polymerization

1- Introduction

The properties of PP nanocomposites are largely determined by the microstructure of the polymer matrices, the nature of nanofillers, and the way in which the nanocomposites are prepared. Furthermore, the way in which the nanofillers are incorporated into the polymer matrix has a huge influence on the performance of the final product as it determines the dispersion of nanofillers in a polymer matrix and interactions with the matrix. The uniform dispersion of nanofillers in a polymer matrix is a general prerequisite for achieving the desired mechanical and physical characteristics.

In-situ polymerization of monomers in the presence of nanofillers is a useful method for achieving a more homogeneous distribution of inorganic nanoparticles, due to the close contact of polymer and filler during synthesis [1-5]. However, the in-situ preparation of the polymer matrix in the presence of the nanofillers will add new parameters to the

polymerization reaction and control over the polymer microstructure becomes more complicated.

One of the drawbacks of the in-situ polymerization is the uncontrolled and drastic decrease in the catalyst activity, which makes determining the final filler loading more complicated. In addition, the changes that occur in the polymer microstructure during polymerization due to the presence of the fillers could have a significant effect on the properties of the nanocomposites.

Although some authors have reported that there is no correlation between the presence of the nanofillers and the chemical properties of the polymer matrix [4, 6], others have found that the polymer matrix microstructure depends on the filler content [7, 8]. Thus, investigating the effect of the presence of fillers with different loadings on the catalyst activity and on the matrix microstructure obtained is essential.

This work deals with the effect of filler on the catalyst activity and on the produced polymers' microstructure. Comparison of the effect different filler characteristics during the in-situ polymerization is also addressed.

2- *Experimental*

2.1- *Materials*

All reactions were carried out under argon atmosphere. Nanosilica (15 nm) was obtained from Sigma-Aldrich. Uncoated calcium carbonate SOCAL® 31 (70 nm) was kindly donated by Solvay. The metallocene catalyst dimethylsilyl bis(2-methyl-4,5-benzo-indenyl)zirconium dichloride (rac-EZrCl$_2$) (MBI) was obtained from Boulder Scientific, and used as received. The cocatalyst MAO (10 % solution in toluene) was purchased from Sigma-Aldrich and used as received. Toluene was dried by refluxing over sodium/benzophenone, distilled under a nitrogen atmosphere, and then stored over 4 Å molecular sieve.

2.2- *Polymerization kinetics*

For the polymerization kinetics study, the stainless steel autoclave reactor was divided into four different minireactors of 30 mL each. Four reactions could therefore be performed simultaneously namely a homogeneous polymerization, an in-situ polymerization using

MAO-SiO$_2$, and using MAO-CaCO$_3$, and to eliminate experimental error, a homogenous reaction was performed in the fourth reactor as a reference. The empty reactor was pretreated under vacuum at high temperature to remove water and oxygen traces. In a typical polymerization reaction, 100 mg of MAO treated fille was reacted with 5.5 x 10^{-7} mol preactivated catalyst solution with MAO (reacted for 15 min) equivalent to Al/Zr 2000. This mixture was introduced into the minireactor. A continuous monomer pressure of 1.5 MPa was maintained throughout the duration of the polymerization. The reaction was stirred at room temperature to the designated period of time, after which the reactor was vented and then acidic methanol (10% HCl) was added.

2.3- *Synthesis of PP nanocomposites*

The polymerization reactions were carried out in a 300 mL stainless steel autoclave. The empty reactor was pretreated under vacuum at high temperature to remove water and oxygen traces. The desired amount of MAO treated filler was reacted with activated catalyst (MBI 2.2 x 10^{-6} mol; Al/Zr 2000) in a Schlenk tube for 6 h. Toluene (30 mL) was then added to the mixture, which was then transferred into the reactor via a syringe, under an argon atmosphere. The reactor was heated to the desired temperature then pressurized with propylene (1.5 MPa). The reaction mixture was stirred at the desired temperature for 1 h. In order to terminate the polymerization reaction the reactor was first vented and cooled, and then acidic methanol (10 % HCl) was added. The resulting polymer was filtered off, washed with methanol, and finally dried at 60 ^{o}C under reduced pressure.

2.4- *Characterization of nanocomposites*

The ^{13}C NMR spectra of the samples were recorded at 120 ^{o}C on a Varian VXR 600 MHz spectrometer, with a long repetition time of 0.82 seconds and a pulse angle of 45°. The samples were dissolved in a 9:1 mixture of 1,2,4- trichlorobenzene:C$_6$D$_6$ by using the C$_6$D$_6$ at δ=128.02 ppm as internal secondary reference. Mw and MWD of the polymers were determined by using HT-GPC. A PL-GPC 220 high temperature chromatograph was used at a solvent flow rate of 1 mL/min at 160 ^{o}C with a differential refractive index detector. Columns packed with a polystyrene/divinylbenzene copolymer (PL gel MIXED-B) from Polymer Laboratories were used. The PP samples were extracted from the nanocomposites using boiling xylene. The concentration of the samples was 0.75 mg/mL. 1,2,4-trichlorobenzene

(TCB), stabilized with 0.0125 wt% 2,6-di-tert-butyl-4-methylphenol (BHT), was used as solvent.

3- *Results and discussion*

3.1- *Effect of filler particles on polymerization kinetics*

Olefin polymerization catalyzed by a metallocene catalyst involves several steps: catalyst activation, propagation, and catalyst deactivation. The effect of the filler will only be on the propagation and the deactivation reactions. The effect of the filler on the activation step is, however, insignificant as the metallocene catalyst was allowed to react with the MAO for 15 min before the polymerization was carried out.

In this case there are two different active sites present in the polymerization media: one is supported on the filler and the other is a soluble active site. Previous studies indicate that the percentage and reactivity of the soluble active species are much higher than of the supported active species. Therefore, the latter should have little effect on the polymerization rate.

The polymerization rate (R_p) curve for each of the experiments was generated from the productivity of the catalyst at different polymerization times with continuous monomer pressure. The monomer pressure, amount of MAO-filler, Tp, and catalyst and cocatalyst concentrations were kept constant for all runs.

The R_p curves for the homogenous polymerization and in-situ polymerization in the presence of different fillers are shown in Figure 1. All the curves show a similar trend. The polymerization activities reach a maximum at the beginning of the reaction and then decreases over time. The induction period in the polymerization rate is due to the propylene monomer saturation. It has been explained as a slow rate of insertion of the first monomer unit in the Zr–methyl bond of the alkylated metallocene [9]. The reduction of the R_p after the maximum is reached is attributed to the formation of both reversibly and permanently deactivated sites [10, 11]. Some authors suggest that diffusion limitations might occur at longer times[12].

Figure 1 shows that at low polymerization times R_p of the homogenous polymerization is higher than that of the in-situ polymerizations and decreases more rapidly with polymerization time. The pathway of a polymerization reaction in which a metallocene

catalyst is used is complicated, and several different reactions can occur at the active centre. The relative values of the rate constants of these different possible reactions determine the activity of the catalyst and the microstructure of the polymer subsequently obtained under certain polymerization conditions. To understand the effect of the different fillers on the rate constants of these possible reactions it is essential to identify the parameters that control these rate constants and examine how the filler possibly influences these parameters.
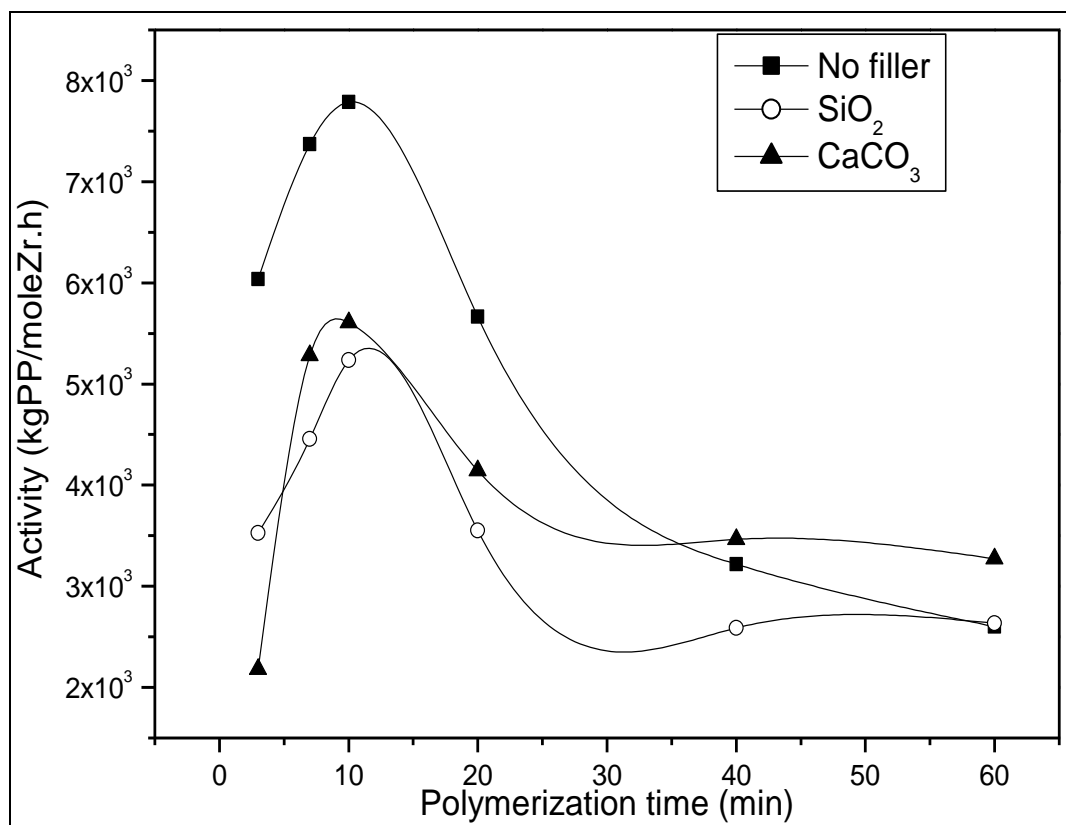
Figure 1: **Polymerization rate versus time profiles for propylene polymerizations with homogenous and in-situ polymerization.**

The R_p depends on the concentration of viable active sites [C*], the monomer concentration [M], and the average propagation rate constant (k_p), and can be expressed as:

$$R_p = k_p \, [C^*] \, [M]$$

If one assumes that no monomer diffusion limitations arise and that the monomer concentration is similar at all active sites and under similar polymerization conditions, the concentration of active sites determines the polymerization rate. The concentration of the active sites is affected by the number of deactivated sites and dormant sites (D).

$$[C^*] = [Zr] - [C\ dormant] - [C\ dead]$$

The lower R_p of the in-situ polymerization compared to that of the homogenous polymerization might be due to deactivation of the catalyst by the filler or the presence of dormant sites at low polymerization time, which will later become active. The slow decay of R_p of the in-situ polymerization compared with the fast decay of the R_p of the homogenous polymerization at high polymerization time confirms that the low R_p value for the in-situ polymerizations is caused by dormant sites which will be active later.

^{13}C NMR spectra of different PPs prepared via homogenous polymerization and in-situ polymerization in the presence of the filler are shown in Figure 2. A higher percentage of isolated secondary propylene units (2, 1 insertions) is evident in the in-situ polymerized PPs compared with the homogenous polymerized PP. These regiodefects have a strong effect in terms of reducing the propagation rate due to the lower monomer insertion rate at a secondary growing chain end [9].

This result supports the suggestion that the lower R_p of the in-situ polymerization at low polymerization times is due to the reversible switching of the soluble active site to a dormant site. Due to the nanoscale size of the filler particles, steric effects are most probably the cause of the regiodefects because the monomer concentration and the Tp have been reported to have no effect on the formation of regiodefects [9] and it is only the metallocene structure that determines their formation.
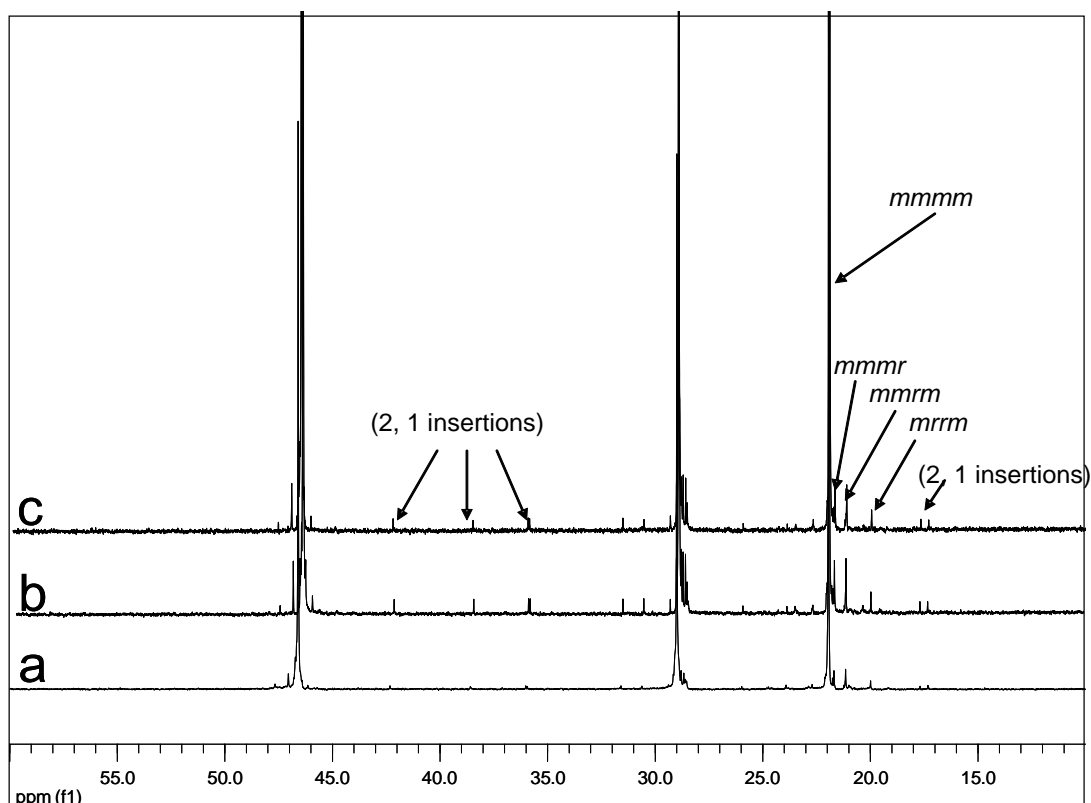
Figure 2: ^{13}**C NMR spectra of PP prepared with MBI catalyst: a) homogenous polymerization; b) in-situ polymerization using MAO-SiO$_2$; c) in-situ polymerization using MAO-CaCO$_3$.**

The slow decay of R_p of the in-situ polymerization compared with the fast decay of the R_p of the homogenous polymerization at high polymerization time could also be explained by monomer diffusion limitations. The regiodefects have a strong effect on reducing the crystallinity percentage of the formed PP and facilitates the monomer to reach the active site and hence a high polymerization rate over time is maintained for the in-situ polymerization. On the other hand, the high crystallinity of the formed polymer in the homogenous polymerization will restrict the monomer diffusion and consequently a decrease in R_p was obtained at high polymerization time.

3.2- *Effect of MAO treated filler on catalyst activity*

The effect of the initial amount of MAO-filler on the catalyst activity is shown in Figure 3. The Figure shows that at low filler feed there is an increase in the activity of the in-situ polymerization compared to the homogeneous polymerization. This could be explained by differences in monomer diffusion. Due to the presence of the filler, a PP with low tacticity and thus low crystallinity was obtained by the in-situ polymerization. This allows the

monomer to reach the active site, resulting in high activity. On the other hand, the restriction of the monomer diffusion, due to the high crystallinity of the high tacticity PP, results in low polymerization activity. The Figure also shows a decrease in catalyst activity at high filler feed. This might be due to the deactivation of the catalyst by the filler.
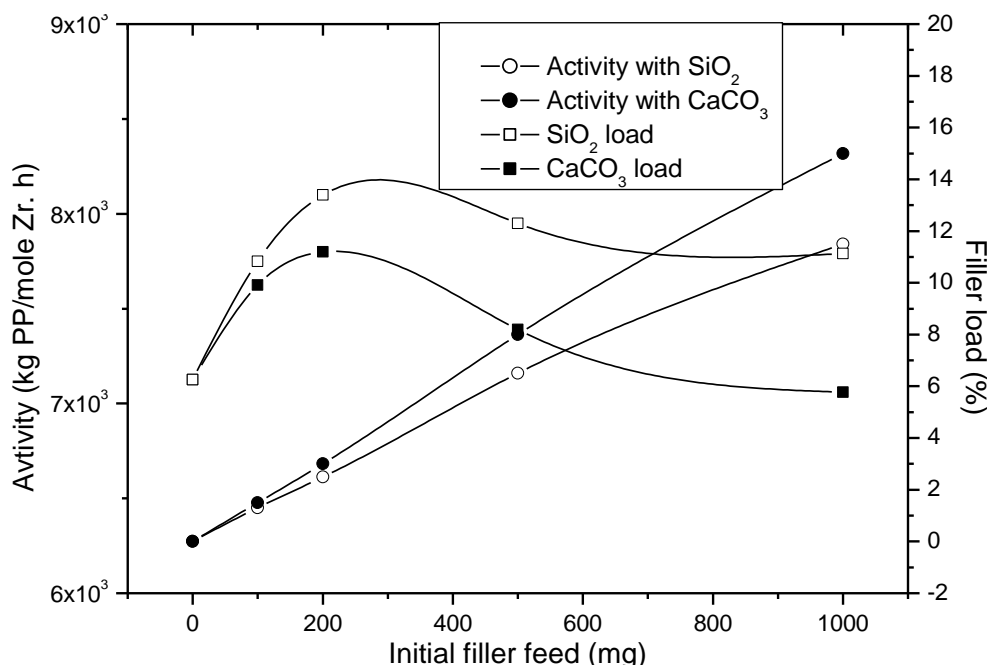
Figure 3:   Effect of MAO treated filler feed on the catalyst activity and the final filler load of the composites.

The Figure also shows that in-situ polymerization with MAO-CaCO$_3$ gives higher productivity than that with MAO-SiO$_2$. Thus the concentration of active sites plays an important role at high filler feeds. The rate of the deactivation of the catalyst is much higher in the in-situ polymerization with MAO-SiO$_2$ than with MAO-CaCO$_3$. This is attributed to the higher concentration of OH groups on the SiO$_2$ surface.

3.3-   *Effect of filler feed on PP tacticity*

Figure 4 illustrates the effect of MAO-filler load on the tacticity of the PP matrix. It is observed that the *mmmm* content decreased when the MAO-filler was increased. Possible reasons for this are a steric hindrance effect caused by the filler, which might change the characteristics of the available coordination site, or a low monomer concentration at the active site. It is also observed that PPs produced via in-situ polymerization with MAO-SiO$_2$ show lower tacticity than PPs produced with MAO-CaCO$_3$. The low average particle size of the

nanosilica (15 nm) compared with the $CaCO_3$ nanoparticle (70 nm) might be the reason for this effect.
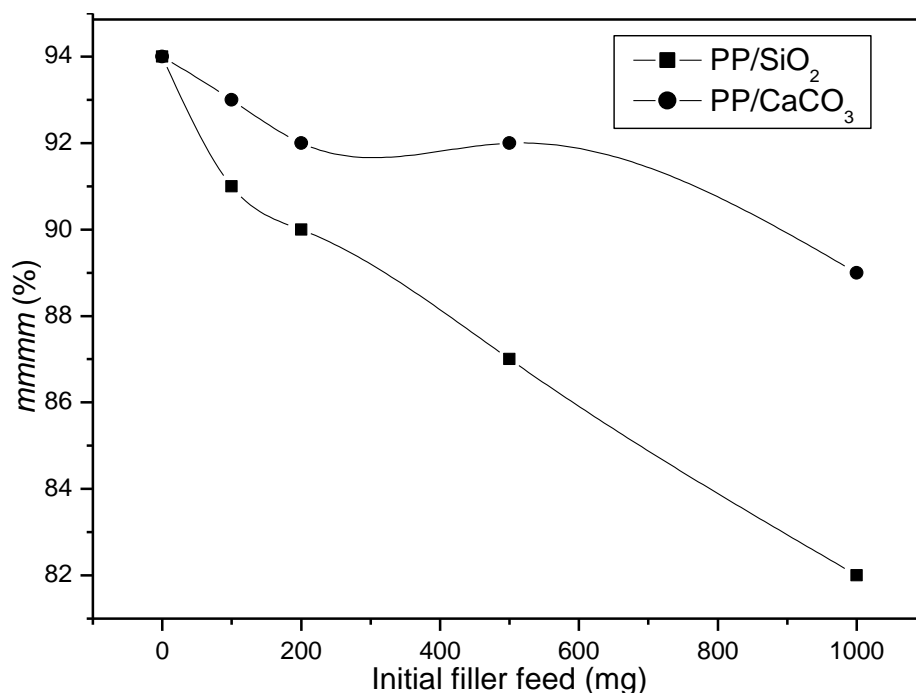
Figure 4: **Effect of MAO treated filler feed on the microstructure of PP of in-situ polymerized PP nanocomposites.**

3.4- *Effect of filler on the Mw and the MWD*

HT-GPC results show that the Mw of PP homopolymer (124 kg/mol) was slightly higher than the Mw of all the PP nanocomposites (approximately 100 kg/mol) produced under similar experimental conditions. The decrease in the Mw of PP nanocomposites can be explained by the high percentage of secondary insertions. Due to the lower monomer insertion rate at a chain end after secondary insertion, the probability for hydrogen transfer to the monomer is high, thus polymer with lower Mw and higher MWD is formed [9]. Furthermore, HT-GPC results show that increasing the filler content had no effect on the Mw as the Mw of the PP nanocomposites were in the range of 100 Kg/mol.

Figure 5 shows the effect of the initial filler feed on the MWD. Increasing the filler load leads to a broader MWD. This could be attributed to the random occurrence of the secondary insertion, which reduces the propagation rate and increases the probability of chain termination occurring.
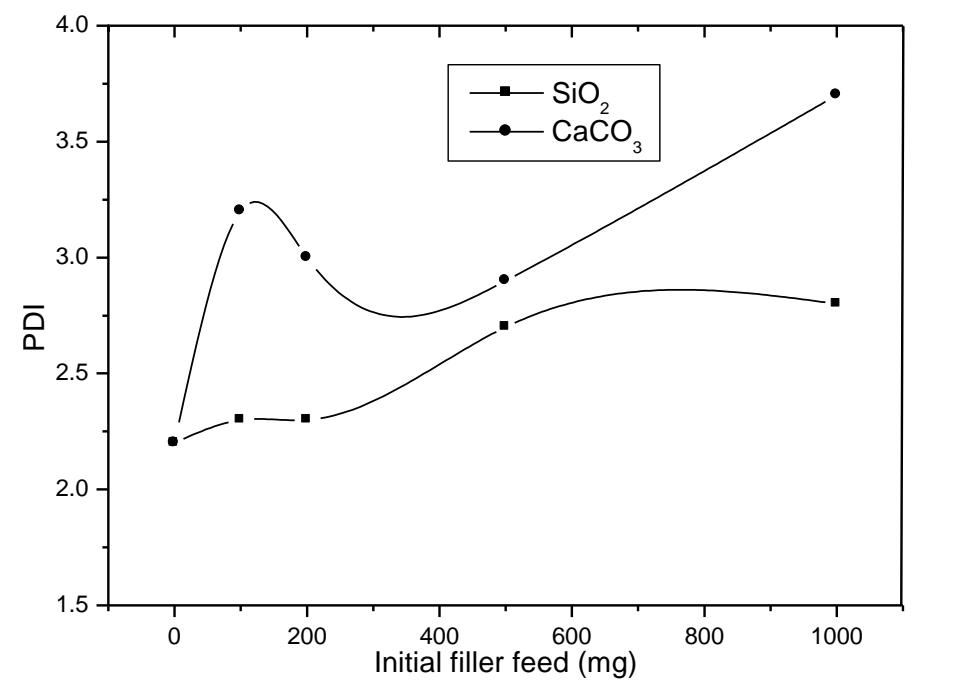
Figure 5:   **Effect of the initial filler feed on the MWD of PP prepared by in-situ polymerization.**

4- Conclusions

It was found that at low polymerization times the in-situ polymerization had lower R_p than that of the homogenous polymerization. However, as the polymerization time proceeds, the decay in the R_p of the homogenous polymerization was faster than that of the in-situ polymerization. It was also found that, due to the steric hindrance that arises from the presence of the filler nanoparticles and the change in the polymerization kinetics, the in-situ polymerization produced PP matrices with microstructures different from that of the homogenous polymerization. The *mmmm* content decreased with increasing MAO-filler content, for both fillers. Result also showed that in-situ polymerization performed with SiO_2 nanoparticles yielded an activity and PP microstructure that was slightly different from that of the in-situ polymerization performed with $CaCO_3$ nanoparticles.

5- References

1.   Ray, S.; Okamoto, M., *Prog. Polym. Sci.*, 2003. **28**: p. 1539.

2.   Sun, T.; Garces, J., *Adv. Mater.*, 2002. **14**: p. 128.

3.   Kaminsky, W.; Wiemann, K., *Compos. Interfaces*, 2006. **13**: p. 365.

4.   Funck, A.; Kaminsky, W., *Compos. Sci. Technol.*, 2007. **67**: p. 906.

5.   He, J.; Li, H.; Wang, X.; Gao, Y., *Eur. Polym. J.*, 2006. **42**: p. 1128.

6.   Scharlach, K.; Kaminsky, W., *Macromol. Symp.*, 2008. **261**: p. 10.

7.   Pavlidoua, S.; Papaspyrides, C., *Prog. Polym. Sci.*, 2008. **33**: p. 1119.

8.   Alfred, C.; Jong-Young, L., *Polym. Rev.*, 2007. **47**: p. 217.

9.   Resconi, L.; Cavallo, L.; Fait, A.; Piemontesi, F., *Chem. Rev.*, 2000. **100**: p. 1253.

10.   Ochoteco, E.; Vecino, M.; Montes, M.; de la Cal, J., *Chem. Eng. Sci.*, 2001. **56**: p. 4169.

11.   Fischer, D.; Mulhaupt, R., *J. Organomet. Chem.* , 1991. **417**: p. C7.

12.   Busico, V.; Cipullo, R.; Esposito, V., *Macromol. Rapid Commun.*, 1999. **20**: p. 116.

Calculation of Thermodynamic Properties of CO_2 Using The Combined Thermal Equation of State with A Small Number of Adjustable Parameters

Petr P. Bezverkhy [1], Victor G. Martynets [1] and Sergey V. Stankus [2]

[1] Nikolaev Institute of Inorganic Chemistry SB RAS, Novosibirsk, 630090 Russia, ppb@niic.nsc.ru
[2] Kutateladze Institute of Thermophysics SB RAS, Novosibirsk, 630090 Russia, stankus@itp.nsc.ru

Abstract: The new combined equation of state including regular and scaling parts was applied for calculation of thermodynamic properties of CO_2 in intervals $0 < \rho/\rho_c < 2$, 217 K $<T<$ 430 K, $0 < p \leq 25$ МПа, including the critical region. The total number of system-specific constants is 14. The description of $P\rho T$-data was achieved with an Rms error on pressure $\pm$ 0.63%. The heat capacity C_v calculated on isochores and isotherms including in the critical region using the constants of the combined equation of state. Also single-phase heat capacities C_v, C_p and sound velocity w calculated at T $<T_c$ along binodal. The calculating C_v -values describe the known experimental C_v data with an accuracy of $\pm$ 8%. The comparison is made with data from known referenced tables.

Keywords: Carbon dioxide, combined equation of state, scaling, heat capacities.

1 Introduction

As is known, the existing equations of state (ES) contain a lot of power terms with fractional exponents and terms of exponential type with a number of adjustable constants from 50 to 100 which are used to obtain the referenced tables on thermodynamic properties [1]. This causes difficulties in the practical application for calculations. All the data on the thermal and caloric properties are used generally to determine the adjustable constants. These equations of state are regular and do not contain completely the scaling theory achieves. Referenced tables based on regular ES contain no detailed information on the properties in the critical region. On the other hand, the existing crossover scaling ES are uncomfortable because of the implicit parametric form and complex for practical calculations [2]. If the experimental or tabulated data are absent in required intervals it is important to have the combined equation of state (CES), which you can easily apply to calculate both regular and critical behavior of thermodynamic properties. In this paper for the calculation of caloric properties the CES is proposed in explicit form with 14 adjustable constants which were found by using only p,ρ,T data.

2 Equation of state and calculation of heat capacities

The approximation p,ρ,T data of CO_2 was made in the intervals ($0 < \rho/\rho_c < 2$, 217 K $<T<$ 430 K, $0 < p \leq 25$ МПа) using the new combined equation of state [3]. In this equation, the pressure p is an explicit function of ρ and T. CES is written in the form

$$p/p_c = (1-Y)\, p_{reg}/p_c + Y\, p_{scal}/p_c.$$

(1)

It includes a new regular part p_{reg} for the approximation of p,ρ,T data in liquid and gaseous states for areas outside the critical region and the singular part p_{scal} which is scaling equation of state for the critical region, and crossover function $Y = \omega\, erfc(\sqrt{\lambda} \cdot |\tau|) \exp(-\mu(\Delta\rho)^2)$ to

combine these equations ($\tau = (T - T_c)/T_c$, $\omega = \rho/\rho_c$, $\Delta\rho = \omega - 1$, λ and μ are adjustable constants), $erfc(\sqrt{\lambda} \cdot |\tau|)$ is the Laplace error function which calculated with using the next series:

$$erfc(\sqrt{\lambda} \cdot |\tau|) = 1 - 2\sqrt{\lambda/\pi} \int_0^{|\tau|} \exp(-\lambda t^2)dt = 1 - (2/\sqrt{\pi})\exp(-\lambda\tau^2) \cdot \sum_{k=0}^{\infty} \frac{2^k(\sqrt{\lambda}|\tau|)^{2k+1}}{(2k+1)!!}.$$

Regular contribution p_{reg} consists of the sum of 8 terms of the equation including adjustable constants A_1 - A_8 [3], three of which (A_3, A_5, A_7) are calculated through the remaining 5 adjustable constants using the conditions at the critical point ($p_{reg}(\rho_c, T_c) = p_c$, $(\partial p_{reg}/\partial\rho)_{T_c} = 0$, $(\partial^2 p_{reg}/\partial\rho^2)_{T_c} = 0$):

$$p_{reg}/p_c = \frac{\omega t}{z_c}\{1 + A_1(f_1(t) - 1/t)\omega\varphi(\omega) - A_2\omega f(t) - A_3\frac{\omega}{t} + \frac{A_4\omega}{(1-A_6\omega)} + A_5\omega^4/(1-A_6\omega)^4 +$$

$$+ A_7\omega^5 t^3 e^{-5\omega-3t} + A_8(\omega_t - \omega)^3(3\omega - \omega_t)\omega^2(e^{5/t} - 1 - 5/t)\} \quad (2)$$

Here $\omega_t = \rho_{tr}/\rho_c$, ρ_{tr} is the liquid density at the triple point, $t = T/T_c$, $f(t) = exp(-1/t) - 1$, $f_1(t) = exp(1/t) - 1$, $z_c = p_c/\rho_c RT_c$ is the compressibility factor at the critical point, $\varphi(\omega) = (\omega_t - \omega)^2(4\omega - \omega_t)$.

The scaled (singular) part of the equation of state p_{scal}, containing the values of p_c, ρ_c, T_c and adjustable constant q, k, M-a_p, C_1, has the form for $P\rho T$- data treating taking into account the expansion of the integral term, see [3]:

$$p_{scal}/p_c = 1 - k(q_p - q)^\gamma \Delta\rho|\Delta\rho|^{\delta-1}(1 + \frac{\delta}{1+\delta}\Delta\rho) + k(\tau + q_p|\Delta\rho|^{1/\beta})^\gamma(\Delta\rho + \Delta\rho^2) -$$

$$k\tau|\tau|^{\gamma-1}\Delta\rho^2(\frac{1}{2} + \frac{\gamma\beta}{1+2\beta}\frac{q_p|\Delta\rho|^{1/\beta}}{\tau}) + (M - a_p)\tau + C_1\tau^2/2 \quad ,$$

$$(3)$$

where k is the compressibility coefficient in asymptotic dependence $p_c K_T = \tau^{-\gamma}/k$ on the critical isochore. The magnitude of q in (3) is a factor in binodal dependence $\Delta\rho = \pm(-\tau/q)^\beta$ $+B(-\tau)^{1-\alpha}$, $q_p = 4.0015q$, γ, β, δ are critical exponents, α - the index of the specific heat C_v at $\rho = \rho_c$; M-$a_p = s_c T_c/p_c - a_p$, s_c is critical entropy per unit volume, a_p is a constant of Pokrovsky transformations [4]. Values $\beta = 0.3255$, $\gamma = 1.239$, $\alpha = 0.11$ are taken in accordance with the 3-dimensional Ising model [5]. For CO_2, the critical parameters are taken from [1]: $T_c = 304.1282$ K, $\rho_c = 467.6$ кг/м³, $p_c = 7.3773$ MPa, $\omega_t = 2.520381$. The total number of system-specific constants - fourteen. To find them the minimization of a quadratic functional of relative deviations of pressure ($p_{i,exp}$ - $p_{i,calc})/p_{i,exp}$ was used. The array of p,ρ,T data for CO_2 (731 points) was formed using a tabulated data up to 25 MPa [1] which do not include the critical region, and in addition an experimental p, ρ, T − data [6], [7] in the wide vicinity of the critical point. Rms error on pressure is $\pm 0.63\%$ (AAD = 0.42%) in description of p,ρ,T CO_2 data over the entire region of gas and liquid states. The C_v was calculated on isochores and isotherms including the critical region and the binodal, using defined CES constants ($A_1 = 0.03526105$; $A_2 = 1.2189927$; $A_3 = 2.4763865$; $A_4 = 0.789272$; $A_5 = 0.0298947$; $A_6 = 0.0799580$; $A_7 = 69.729003$; $A_8 = 0.000073333$; M-$a_p = 7.280166$; $q = 0.110155$; $k = 9.7211647$; $\lambda = 152.318$; $\mu = 10.07$; $C_1 = -26.50$).

The well-known expression was applied to calculate C_v using CES constants:

$$C_\mathrm{v} = C_{\mathrm{v},reg} - z_c R t \int_0^\omega Y [\frac{\partial^2 (p_{scal} - p_{reg})/p_c}{\partial t^2}]_\omega \frac{d\omega}{\omega^2} - 2z_c R t \int_0^\omega [\frac{\partial (p_{scal} - p_{reg})/p_c}{\partial t}]_\omega \left(\frac{\partial Y}{\partial t}\right)_\omega \frac{d\omega}{\omega^2} -$$

$$z_c R t \int_0^\omega (p_{scal} - p_{reg})/p_c \left(\frac{\partial^2 Y}{\partial t^2}\right)_\omega \frac{d\omega}{\omega^2},$$

(4)

where the integrals can not be expressed in terms of elementary functions and are calculated numerically by using a simple program. In (4) $C_{\mathrm{v},reg}$ is expressed as

$$C_{\mathrm{v},reg} = C_{\mathrm{v},\ id} - Rt\{A_1 e^{(1/t)}/t^3 \cdot I_1 - A_2 e^{(-1/t)}/t^3 \cdot \omega + A_7 e^{(-3t)}\ 3t^2(4 - 8t + 3\ t^2) \cdot I_2 + 25\ A_8 e^{(5/t)}/t^3 \cdot I_3\},$$
(5)

where $I_1 = \omega(\omega - \omega_t)^3$, $I_2 = -e^{(-5\omega)}[24/5^4 + 24\omega/5^3 + 12\omega^2/25 + 4\omega^3/5 + \omega^4]/5 + 24/5^5$, $I_3 = -\omega^2(\omega_t - \omega)^4/2$; $C_{\mathrm{v},\ id}$ is contribution of rarefied gas heat capacity, which is calculated for CO_2 using interpolation formula [1]. To calculate the C_v (4) near and far from the critical point the following expressions for temperature derivatives of the p_{scal} were used:

$$(\partial p_{scal}/\partial t)_\omega / p_c = k\gamma(\tau + q_p \mid \Delta\rho \mid^{1/\beta})^{\gamma-1}(\Delta\rho + \Delta\rho^2) - k\gamma \int \Delta\rho(\tau + q_p \mid \Delta\rho \mid^{1/\beta})^{\gamma-1} d\Delta\rho + (M - a) + C_1\tau,$$

$$(\partial^2 (p_{scal}/p_c)/\partial t^2)_\omega = k\gamma(\gamma-1)(\tau + q_p \mid \Delta\rho \mid^{1/\beta})^{\gamma-2}(\Delta\rho + \Delta\rho^2) - k\gamma(\gamma-1)\int \Delta\rho(\tau + q_p \mid \Delta\rho \mid^{1/\beta})^{\gamma-2} d\Delta\rho + C_1.$$
(6)

For the numerical calculations integrals in expressions (6) replaced by convergent series which had a different shapes when $\tau < 0$ and $\tau > 0$ [3].

To calculate C_v along binodal the temperature dependence $\tau = -q\mid\Delta\rho\mid^{1/\beta}$ (in symmetric approximation) take into account in formulas (6) near the critical point. In this case, the derivatives (6) have forms:

$$(\partial p_{scal}/\partial t)_\omega / p_c = k\gamma(q_p - q)^{\gamma-1}[\Delta\rho + (1 - \beta/(1-\alpha))\Delta\rho^2] \mid \Delta\rho \mid^{(\gamma-1)/\beta} + (M - a_p) + C_1\tau,$$

$$(\partial^2 (p_{scal}/p_c)/\partial t^2)_\omega = k\gamma(\gamma-1)(q_p - q)^{\gamma-2}[\mid \Delta\rho \mid^{(\gamma-2)/\beta}(\Delta\rho + \Delta\rho^2) + \beta \mid \Delta\rho \mid^{-\alpha/\beta}/\alpha] + C_1.$$

3. Results

The calculation results shown in figures 1, 2 and 3 in comparison with the experimental C_v - data [8-10] along isochores. The coincidence of experimental and calculated C_v values along isochores is completely reasonable. The behavior of the calculated C_v (4) along the isotherms is shown in figure 4 in comparison with experimental values from [11, 12]. Contribution of $C_{\mathrm{v},reg}$ in accordance with the equation (5) is shown by a thin line at $T \approx T_c$ and dashed line far from T_c.
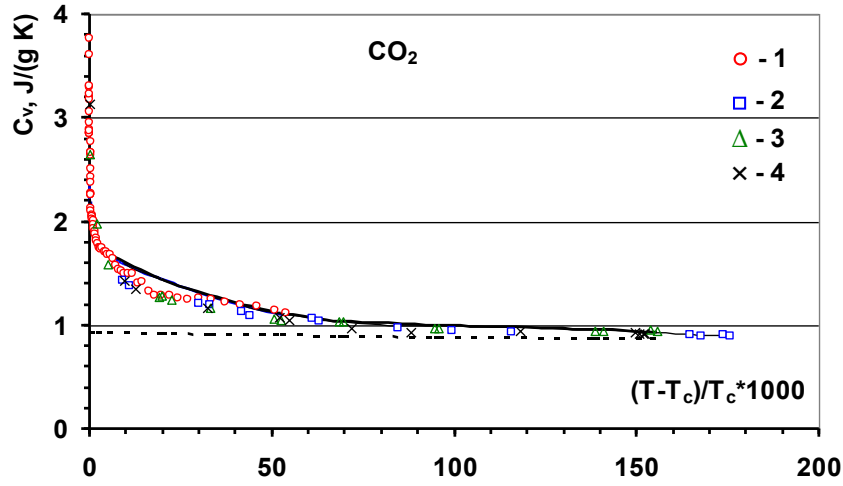
Figure 1. Specific heat C_v at near-critical isochores CO_2. Experiment: 1 – 468.57kg/m^3 [8], 2 – 467.5 kg/m^3, 3 - 470.1 kg/m^3, 4 – 461.2 kg/m^3 [9]. Solid curve is calculation by using CES constants at $\rho = \rho_c$, dashed line shows a regular
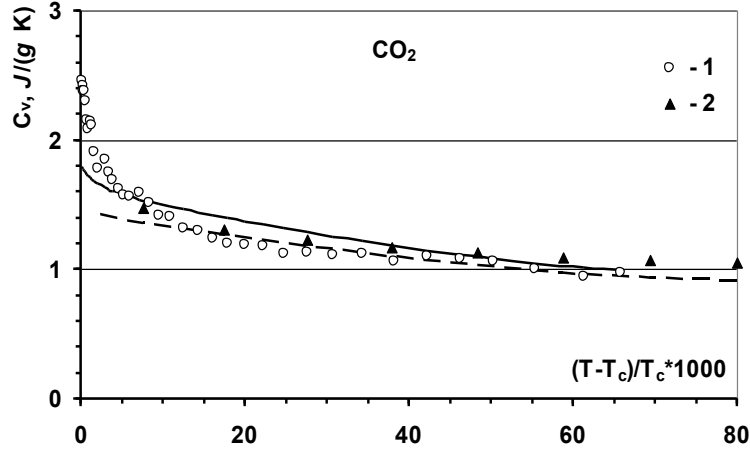
Figure 2. C_v along isochores $\rho < \rho_c$. Experiment: 1 – ρ = 412.13 kg/m^3 [8]; 2 – ρ = 368.4 kg/m^3, [10]. Solid (412 kg/m^3) and dashed (368.4 kg/m^3) lines are the calculated C_v using CES constants.
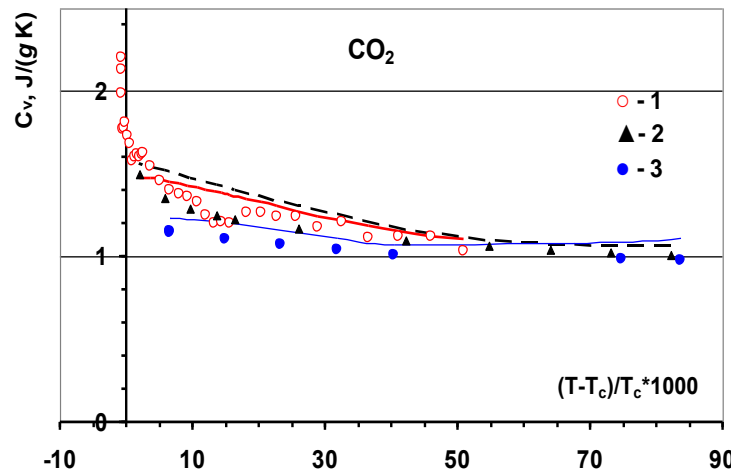
Figure 3. C_v along isochores $\rho > \rho_c$. Experiment: 1 – 549.79 kg/m^3 [8]; 2 – 533.6 kg/m^3, 3 - 615.4 kg/m^3 [10]. Bold (549.79 kg/m^3), dashed (533.6 kg/m^3) and thin (615.4 kg/m^3) lines are the calculated C_v (4) using CES constants.
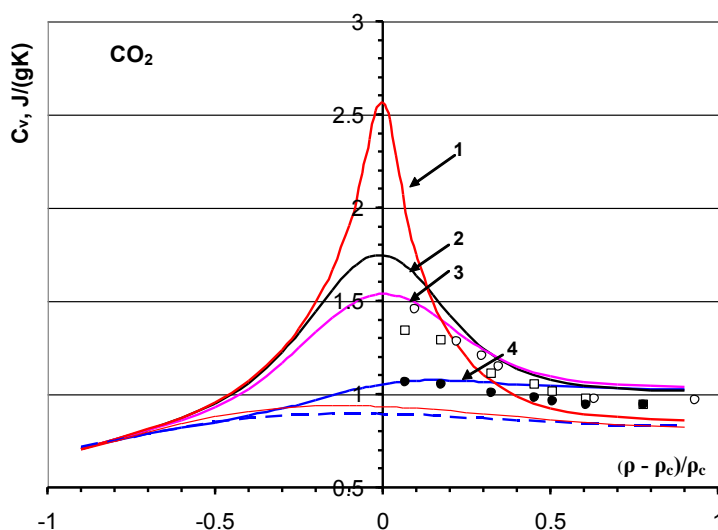
Figure 4. C_v along isotherms $T > T_c$. Experiment: ● − 323.087 K [8], □− 308.09 K [11], ○ − 305.09 K [12]; Solid curves are C_v –calculations (1 − 304.14K, 2 − 305.09K, 3 − 308.1K, 4 − 323.09K), dashed (323.09K) and thin (304.14K) lines show $C_{v,reg}$

In figure 5 it was shown the behavior of calculated C_v (4) along both gas and liquid binodal branches in comparison with the tabulated data [1]. Also calculated values of C_v along binodal are in satisfactory agreement with the referenced values of C_v calculated by the multiparametric equation of state [1] using 58 adjustable parameters and 35 different exponents only for residial part of the Helmholz energy. The main difference between the calculated values and the referenced data [1] occurs in the critical region. This can be clear because there is no complete accounting of scaling laws in the regular ES [1].

One can conclude from figures 1 - 5, the mean error at description of the known experimental C_v - data does not exceed ± 8% in all regions of states except isochor pieces adjacent to the binodal where it is possible the influence on the measured C_v values because the process of phase separation starts. In figure 6 it is shown the calculated sound velocity **w** coincide quite reasonable with the tabulated data [1] along the binodal.
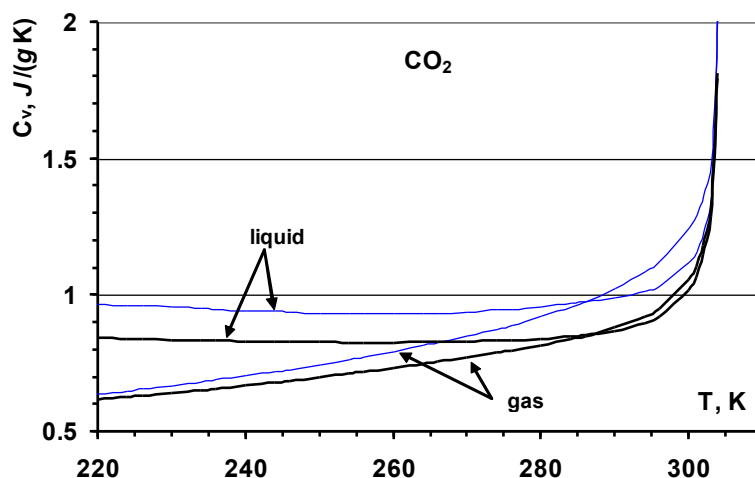
Figure 5. Comparison of the calculated C_v along the binodal (thick lines) with the tabulated data [1] (blue thin lines)
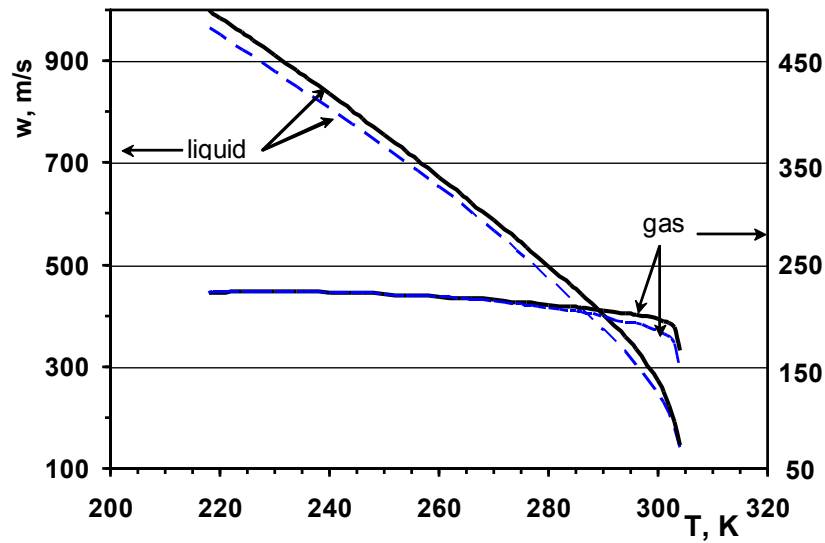
Figure 6. Comparison of the calculated sound velocity **w** (solid lines) with the tabulated data [1] (blue dashed lines) along the binodal.

The calculated single-phase values of heat capacities C_v, C_p and the sound speed **w** along the CO_2 binodal are shown in Table 1. Constants of CES (1) and the binodal densities [1] were used for calculations C_v (4). C_p and **w** were calculated using general equations:

$$C_p = C_v + \frac{p_c t}{\rho_c T_c \omega^2}(\partial(p/p_c)/\partial t)^2_{\Delta\ddot{o}}\Big/(\partial(p/p_c)/\partial\omega)_\tau\ ; \qquad w = \left\{ \left(\frac{\partial(p/p_c)}{\partial\omega}\right)_T + \frac{Z_c t}{\omega^2(C_v/R)}\left[\frac{\partial(p/p_c)}{\partial t}\right]^2_\omega \right\}^{0.5}.$$

Table 1. Calculated single-phase heat capacities C_v, C_p and the speed of sound **w** with using the constants of the CES (1) along binodal branches of CO_2 (the binodal densities were taken from [1]).

T, K	ρ_{liq}, kg/m^3	ρ_{gas}, kg/m^3	$C_{v,liq}$ J/(gK)	$C_{v,gas}$ J/(gK)	$C_{p,liq}$ J/(gK)	$C_{p,gas}$ J/(gK)	w_{liq}, m/s	w_{gas}, m/s
218	1173.4	14.384	0.84274	0.60787	1.8212	0.8811	999.24	223.09
220	1166.14	15.817	0.84140	0.61342	1.8283	0.8951	985.15	223.11
230	1128.68	23.271	0.83492	0.63900	1.8734	0.9639	911.85	223.45
240	1088.87	33.295	0.82953	0.66719	1.9344	1.0542	834.70	222.81
250	1045.97	46.644	0.82608	0.69816	2.0181	1.1769	754.59	221.21
260	998.89	64.417	0.82527	0.73226	2.1414	1.3524	671.92	218.68
270	945.83	88.374	0.82821	0.77038	2.3417	1.6243	586.49	215.28
274	922.30	100.32	0.83099	0.78725	2.4607	1.7804	551.39	213.68
276	909.90	106.95	0.83291	0.79622	2.5333	1.8744	533.59	212.82
280	883.58	121.74	0.83812	0.81545	2.7149	2.1060	497.38	210.99
284	854.74	139.09	0.84601	0.83722	2.9681	2.4250	460.13	208.94
286	839.12	148.98	0.85145	0.84952	3.1356	2.6351	440.99	207.82
290	804.67	171.96	0.86726	0.87866	3.6057	3.2269	401.15	205.33
294	764.09	201.06	0.89538	0.9192	4.4133	4.2769	357.77	202.37
296	740.28	219.14	0.91879	0.94818	5.0799	5.1889	333.49	200.64
300	679.24	268.58	1.01629	1.0537	8.1071	9.7053	271.62	196.32
301	658.69	286.15	1.06653	1.10456	10.0249	12.6749	250.32	194.79
302	633.69	308.15	1.14410	1.18149	13.8529	18.4868	224.48	192.60
303	599.86	339.00	1.28549	1.31963	25.8758	34.9293	191.56	188.26
304	530.30	406.42	1.79154	1.81397	211.418	335.798	145.40	166.10

4. Conclusion

We are proposed a unified description of thermal and caloric properties of CO_2 using a new type of thermal combined equation of state in the explicit form with a small number of adjustable parameters (only 14 coefficients). Coefficients of combined equation of state were found using the rms-approximation of p, ρ, T data without including data on C_v. In calculations the theoretical values of critical indices were used in accordance with three dimentional Ising model. The specific heats C_p, C_v and sound velocity were calculated in a wide range of single-phase state including the critical region and the binodal. Calculated values of these properties are in satisfactory agreement with the tabulated values and describe the known experimental C_v data with an accuracy of $\pm 8\%$. In our opinion this approach for equation of state including regular and scaled terms with a relatively small number of adjustable constants is promising. Combined thermal equation of state can provide both a description of thermodynamic properties with an accuracy not worse than the experimental one and a calculation of system properties in areas where there are no experimental data or the receiving of them are difficult.

5. References

[1] Span, R., Wagner, W. J. (1996). A New Equation of State for Carbon Dioxide Covering the Fluid Region from Triple-Point to 1100 K at Pressures up to 800 Mpa. *J. Phys. Chem. Ref. Data,* V. 25, No. 6, P. 1509-1596.

[2] Kiselev, S.B. (2004). Generalized crossover description of the thermodynamic and transport properties in pure fluids. *Fluid Phase Equilibr*., V. 222–223, P. 149-159.

[3] Bezverkhy, P.P., Martynets, V.G., Matizen, E.V., Kaplun, A.B., Meshalkin, A.B. (2012). Description of SF_6 behavior within the state range from the triple point to supercritical fluid. *Thermophysics and Aeromechanics*, V. 19, No. 4, P.679-689.

[4] Patashinsky, A.Z., Pokrovsky, V.L. (1979). *Fluctuation Theory of Phase Transitions.* Oxford. Pergamon Press. ISBN 0080216641.

[5] Agayan, V.A., Anisimov, M.A., Sengers, J.V. (2001). Crossover parametric equation of state for Ising-like systems. *Phys.Rev., E.* V. 64, 026125-1.

[6] Martynets, V.G., Matizen, E.V. (1979). *P,V,T,N-* data of argon solution in carbon dioxide near the vaporization critical point of solvent. *Thermophysical properties of substances and materials. GSSSD. Physical constants and properties of substances*. Moscow: Standarty. Issue 13. P. 13-23 (in Russian).

[7] Nowak, P., Tielkes, Th., Kleinrahm, R., Wagner, W.J. (1997). Supplementary measurements of the (p, ρ, T) relation of carbon dioxide in the homogeneous region at T =313 K and on the coexistence curve at T_304 K. *J. Chem. Thermod.*, V. 29, P. 885-889.

[8] Beck, L., Ernst, G., Gurtner, J. (2002). Isochoric heat capacity of carbon dioxide and sulfur hexafluoride in critical region. *J. Chem. Thermodyn.,* V.34, P. 277-292.

[9] Abdulagatov, I.M., Polikhronidi, N.G., Batyrova, R.G. (1994). Measurements of the isochoric heat capacities C_V of carbon dioxide in the critical region. *J. Chem. Thermodyn.,* V. 26, P. 1031-1045.

[10] Magee, J.W., Ely, J.F. (1986). Specific heats (C_v) of saturated and compressed liquid and vapor carbon dioxide. *Int. J. Thermophys.,* V. 7, No. 6, P. 1163-1182.

[11]. Amirkhanov, Kh.I., Polikhronidi, N.G., Batyrova, R.G. (1970). Experimental determination of heat capacity C_v of liquid carbon dioxide. *Teploenergetika,* No. 17(3), P. 70-72.

[12] Amirkhanov, Kh.I., Polikhronidi, N.G., Alibekov, B.G., Batyrova, R.G. (1971). Isochoric heat capacity C_v of carbon dioxide. *Teploenergetika,* No. 18, P.59.

Acknowledgements

Numerical Contribution to Heat Treatment of Wood

Ali Boumedien [1], Ramdane Younsi [2] and Youcef Bennouar [1]

[1] LTPMP-FGMGP-USTHB, Bp 32 El Alia Bab Ezzouar Alger, aboumedien@usthb.dz

[2] Ecole Polytechnique de Montréal, 2900 Bd Edouard Montpetit, Mtl,Qc,H3T1J4

Abstract. Heat treatment of wood which is a clean process may be an alternative to chemical treatments. The temperatures used are located on a range between 180 and 280°C, The gas temperature and duration of treatment are the parameters which determine the change in physical and chemical properties of wood. In this work, the Luikov model applied to a rectangular geometry with a numerical approach based on finite volumes is used. Distribution of temperature and humidity in the sample during heat treatment are analyzed. It is important to complete the heat treatment in order to determine the change of chemical properties, in a future work we will show some experimental results for the heat treatment of wood.

Keywords: Wood, moisture, heat treatment, temperature.

1. Introduction

Wood is a natural resource that can be used in many areas, including the construction and furniture. This material is available in large quantities in some parts of the world.

Treatments of wood are needed to make it resistant against various nature aggressions. Chemical treatments, after drying, which have always been used, may have adverse effects on the environment.

The thermal treatment of wood which is a clean process may be an alternative to chemical treatments. The temperatures used are located on a range between 180 and 280°C, which is an intermediate stage between the drying and the carbonization. The gas temperature and duration of treatment are the parameters which determine the change in physical and chemical properties of wood. These changes increase the dimensional stability, improve weather resistance and increase resistance to wood degrading agents (fungi, insects) [1].

Many numerical studies, in which the equations describing the drying process are solved [2] [3], show that more experimental high temperature treatment studies must be performed to determine the properties of wood and the interface conditions between wood and gas in the furnace.

Sandor Poncsak and Co [4] have examined in their study the transition temperature between the moisture removal and the start of the exothermic reactions (thermo-transformation) in the wood that alter its structure increase its bio-durability and give it some colors.

Many mathematical approaches modeled this phenomenon [5]. The diffusion model, which assumes diffusion of moisture and temperature is one of these models, the coupling is provided by coefficients involved in the equations and in the boundary conditions.

The model-based on Luikov approach [6] is another model where the coupling is in the equations through terms of Soret and Dufour. This model can be used in high temperature treatment when the initial moisture content is less than the fiber saturation [7].

The third model is the multiphase model which considers the heat transfer and mass transfer equations and taking into account the mass of all phases present.

In this work, the Luikov model applied to a rectangular geometry with a numerical approach based on finite volumes is used.

2. Governing equations

In our study a sample of wood assumed as porous medium with $2l \times 2h$ size is considered. This sample has an initial temperature (T0) and a moisture (M0), it is placed in an oven heated to a temperature (Tg), and a moisture content (Mg). Because of the symmetrical situation, the study is done on a quarter of the sample in the X, Z plane.
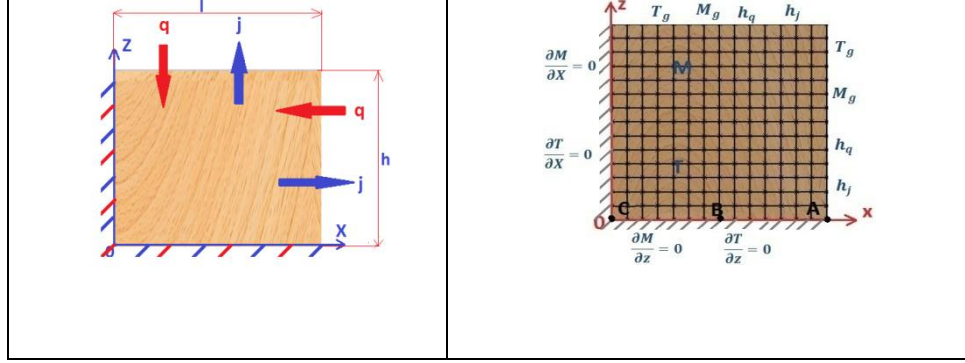
Figure 1 Physical domain

Heat and mass transfer are governing by the Luikov model equations given as follow.
Heat transfer:

$$\rho . \, Cp \frac{\partial T}{\partial t} = \nabla(k_{eff}. \nabla T) + \varepsilon. \, Q_1. \rho \frac{\partial M}{\partial t} \tag{1}$$

Mass transfer:

$$\rho \frac{\partial M}{\partial t} = \nabla[D_{eff}. \nabla M + D_{eff}. \delta \nabla T] \tag{2}$$

Combination of equations (1) and (2) gives:

$$\rho . \, C_p \frac{\partial T}{\partial t} = \nabla[(k_{eff} + \delta. \varepsilon. Q_1. D_{eff}) \nabla T + \varepsilon. Q_1. D_{eff}. \nabla M] \tag{3}$$

Initial conditions are:
$T = T_0$; $M = M_0$ at t=0
And boundary conditions are:
At $z = h$ and $0 \leq x \leq l$

Heat transfer: $keff \frac{\partial T}{\partial x} = h_q. (T - T_g) + (1 + \varepsilon). Q_1. h_j. (M - M_g)$

Mass transfer: $D_{eff}. \frac{\partial M}{\partial x} = h_j. (M - M_g) - D_{eff}. \delta. \frac{\partial T}{\partial x}$

At   x= l   and $0 \leq z \leq h$

Heat transfer: $k_{eff} \frac{\partial T}{\partial z} = h_q (T - T_g) + (1 + \varepsilon). Q_1. h_j. (M - M_g)$

Mass transfer: $D_{eff}. \frac{\partial M}{\partial z} = h_j. (M - M_g) - D_{eff}. \delta. \frac{\partial T}{\partial z}$

At   z =0   and $0 \leq x \leq l$

Heat transfer: $\frac{\partial T}{\partial z} = 0$

Mass transfer: $\frac{\partial M}{\partial z} = 0$

At   x = 0   and $0 \le z \le h$

Heat transfer: $\dfrac{\partial T}{\partial x} = 0$

Mass transfer: $\dfrac{\partial M}{\partial x} = 0$

The coupled equations of heat and mass transfer and boundary conditions are solved using the finite volume method. A system of N equations with N unknowns resulting from a mesh (M × N) is obtained. Uniform mesh in both directions X and Z is considered.

This system is solved using the Thomas algorithm for two-dimensional problem (2D). Direct method of the Thomas algorithm (TDMA) in one direction and the iterative Gauss-Seidel in the other direction are combined.

3. Results and discussion

Physical properties given by table 1 [4] are used in our study.

Table1: Properties and values

Properties and parameters	k_{eff} [W/m.K]	D_{eff} [m^2/s]	M_0 Kg$_{humid}$/kg$_{mixte}$[%]	Q_l [J/kg]	2l × 2h [m]	T_0 [^{0}C]	T_g [^{0}C]	M_g Kg$_{humid}$/kg$_{mixte}$[%]
Value	0.13	2.2×10^{-8}	10	2.5 × 10^6	0.2×0.15	25	240	1

Properties and parameters	h_q [W/mK]	h_j [Kg$_{bois}$/m^{2}s]	C_p [J/kg K]	δ [(Kg$_{humid}$/kg$_{mixte}$)/k]	ρ [kg/m^3]	E
Value	12	2.5 · 10^{-6}	2500	2	370	0.3

.

Results are presented in three parts. In the first part, the temperature and moisture evolution are represented during the heat treatment at different positions (A, B, C). The second part shows the temperature profile at different times. The third part concerns the evolution of drying rates as a function of time at different positions (A, B, C).
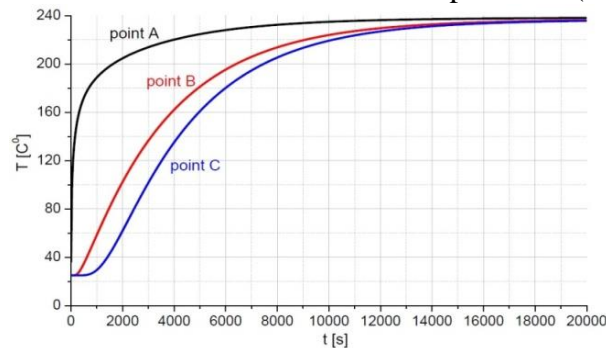
Figure 2 Temperature evolutions during the heat treatment

In Figure 2 we note that the temperature of the wood reaches the oven temperature more quickly for the extremity of the sample than the interior parts. All the parts of the wood become at the oven temperature later. In Figure 3, we find that moisture decreases more rapidly at the point on the boundary as internal points. This decrease of the moisture starts at

12% corresponding to dry wood and finishes at near zero corresponding to heat treated wood. The time to reach these values is given by the two figures.
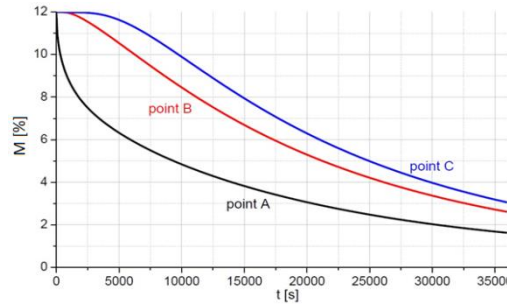
Figure 3 Moisture evolution
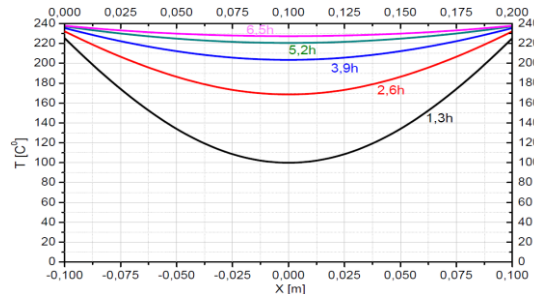
Figure 4 Temperature distributions along the entire sample

Figure 4 shows the temperature distribution along the entire sample as a function of exposure time in the oven, we notice that the temperature along the sample increases and tend to the oven temperature. The sample extremities reach this temperature earlier. Results obtained are approximately similar than the experimental results reported by Koceafe and Co [7], the difference is due to some simplifying assumptions in our model.
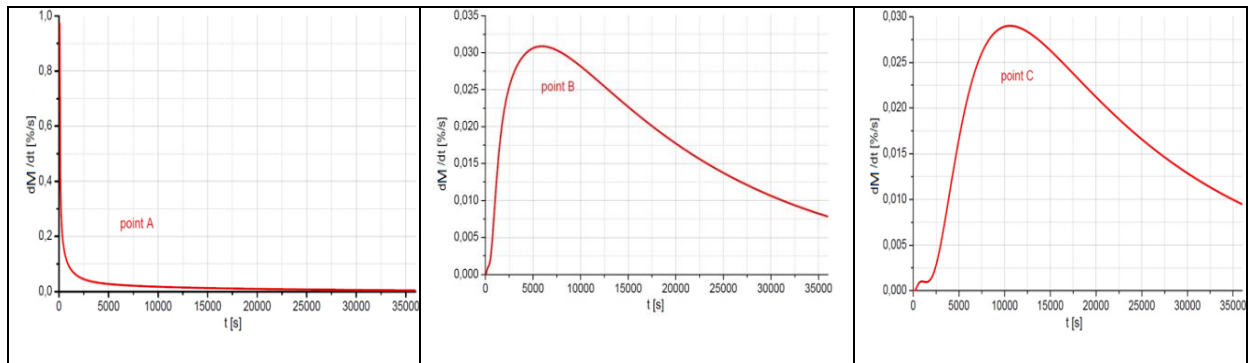
Figure 5 Drying speed for three reference points

In Figure 5, the drying speed is represented for the three reference points (extremity of the sample, an internal point and the middle of the sample). For the point A drying starts with a high speed and stabilizes quickly, for points B and C because of the drying is late, the speed starts increasing and after a certain time it decreases due to the reduction of moisture.

4. Conclusion

Distribution of temperature and humidity in the sample during heat treatment are analyzed. We note that the temperature increases until the oven temperature is reached and the moisture content decreases with time to a value close to zero. Removing moisture is the first stage of the heat treatment in order to preserve the wood from the different aggressions. The second

stage of the heat treatment is to give wood different colors and to ensure it dimensional stability.

Nomenclature

C_p : Equivalent specific heat capacity of the porous medium, (J/kg.K)

  D_{eff} : Effective mass diffusivity, (m^2/s)

h_q : Convective heat transfer coefficient, (W/m^2.K)

h_j :Convective mass transfer coefficient, (kg_{mixte}/m^2.s.M)

k_{eff} : Effective heat conductivity, (W/m.K)

M : Moisture content, ($kg_{moisture}$/$kg_{dry\ wood}$) [%]

Q_l : Latent heat of vaporization, (J/ kg)

  T   : Température, (^{0}C)

ε : Ratio of vapor diffusion coefficient to coefficient of total moisture diffusion

δ : thermal gradient coefficient, ([%]/K)

ρ : Dry wood density, (kg/m3)

5. References

[1]. Pavlo B, Niemz P, Effect of temperature on color and strength of spruce wood, Holzforschung 12:539–546, 2003

[2]. L. Aissani, N. Attaf et E. Mezaache, Thèse ; Etude de l'évolution de l'humidité et de laTempérature lors du séchage d'un milieu poreux: le bois ; Revue des Energies RenouvelablesCISM''08 Oum El Bouaghi (2008) 1 – 12.

[3]. R. Younsi, D. Kocaefe, S. Poncsak, Y. Kocaefe, Computational modelling of heat and mass transfer during the high-temperature heat treatment of wood, Applied Thermal Engineering 27 (2007) 1424–1431.

[4]. Sandor Poncsak, Duygu Kocaefe, Mohamed Bouazara and Andre Pichette, Effect of high temperature treatment on the mechanical properties of birch (Betula papyrifera), Wood Sci Technol, 2006.

[5] Duygu Kocaefe, Ramdane YounsiSandor Poncsak, Yasar Kocaefe, Comparison of different models for the high-temperature heat treatment of wood, International Journal of Thermal Sciences, 46, 707- 716, 2007.

[6] A.V. Luikov, Systems of differential equations of heat and mass transfer in capillary porous bodies, International Journal of Heat and Mass Transfer, Vol.18, N°1, pp. 1-17, 1975.

[7] Duygu Kocaefe, Ramdane Younsi Bushra Chaudry and Yasar Kocaefe, Modeling of heat and mass transfer during high temperature treatment of aspen, Wood Sci Technol, 2006..

The Modelling of Solar Air Collector with Thermal Efficiency Analysis and Artificial Neural Networks

Mesut ABUŞKA [1], Volkan ALTINTAŞ [2] and Mehmet Bahattin AKGÜL [3]

[1]Akhisar Vocational School, Dept of Machine, Celal Bayar Uni., Manisa, TURKEY, mesut.abuska@cbu.edu.tr
[2]Akhisar Vocational School, Dept of Computer Programming, Celal Bayar Uni., Manisa, TURKEY,
volkan.altintas@cbu.edu.tr
[3]Faculty of Engineering, Dept of Mechanical Engineering, Celal Bayar Uni., Manisa, TURKEY, mbakgul@gmail.com

Abstract: In this study, thermal performance of solar air collector with trapezoidal absorber plate is experimentally investigated. Experimental measurements are carried out under normal weather conditions. Global radiation value is measured with a pyranometer mounted on the collector. Temperatures of three points on the absorber plate and collector input-output air temperatures are recorded at regular intervals. Air flow rate at the collector output is measured by using hotwire type anemometer. As a result of all these measurements, thermal efficiency is determined. According to the data obtained in the experiments, a model of neural network of collector is created considering five inputs and two outputs data. The input variables of neural network model are the collector inlet air temperature, the global radiation and the temperatures of the absorber plate. The collector outlet air temperature and the thermal efficiency values of the collector constitute the output parameters. By training an artificial neural network with a part of the experimental data, the output parameters are estimated corresponding to different inputs data.

Keywords: Solar air collector, thermal efficiency analysis, artificial neural network.

1. Introduction

Solar air collectors are widely used from space heating to drying of agricultural products in many engineering applications. Despite solar air collectors have simple design and have a long life, thermal efficiencies are low. Many studies in the literature are performed to increase the thermal efficiency. Benli performed an experimental study to evaluate thermal performance of solar air collectors with different absorber plates. His experimental results show that the efficiency of air collector increases significantly depending on the surface geometry of the absorber plates [1]. Özgen et al. investigated experimentally the effect on efficiency by inserting an absorbing plate made of aluminum cans into the double-pass channel in a flat-plate solar air heater. They concluded that this method substantially improves the collector efficiency by increasing the air velocity and enhancing the heat transfer coefficient between the absorber plate and air [2]. Akpınar and Koçyiğit investigated thermal performance of solar air heater having different obstacles on absorber plates. They found that the efficiency of the collector with obstacles is significantly better than that of without obstacles [3]. Esen experimentally investigated energy and exergy analysis of a double-flow solar air heater having different obstacles on absorber plates. He reported that obstacles on the absorber plates increased thermal efficiency [4]. Benli studied on the determination of thermal performance of two different types of solar air collectors with the use of artificial neural networks. The results of this study showed that the artificial neural networks can be used to predict the thermal performance of solar air collectors as an accurate method [5]. Esen et al. used artificial neural network and wavelet neural network approaches for modelling a solar air heater. They concluded that wavelet neural network model can be used for estimating the some parameters of solar air heaters with reasonable accuracy [6].

In this paper, thermal performance of solar air collectors with trapezoidal absorber plate is experimentally investigated. According to the data obtained in the experiments, a model of neural network of collector is created considering five inputs and two outputs data. The input variables of neural network model are the collector inlet air temperature, the global radiation

and the temperatures of the absorber plate. The collector outlet air temperature and the thermal efficiency values of the collector constitute the output parameters. By training an artificial neural network with a part of the experimental data, the output parameters are estimated corresponding to different inputs data.

2. Material and methods

The experimental setup of the solar air collector is shown in Fig. 1. The system consists of metal frame, absorber plate, insulation material, transparent cover, air circulation fan and measurement devices. The main properties of the solar air collector is given in Table 1. Also, cross sectional view of the solar collector is presented in Fig. 2.

Table 1. Main properties of collector.

	Main Properties
Collector frame	Steel sheet (dimensions:1000x2000x200 mm)
Insulation	Glass wool (50 mm in thickness)
Absorber plate	Trapezoidal corrugated aluminum sheet (2 mm in thickness, surface area: 1000x2000 mm)
Transparent cover	Frosted glass (dimensions: 900x1900x3.2 mm)
Fans	15 W, 40 m^3/h, AC 220V, axial fans (3 pieces)
Sealant	EPDM rubber wick
Absorber coating	Selective solar paint (emissivity: 0.20-0.49, absorptivity: 0.88-0.94)

Figure 1. Experimental setup of the solar air collector
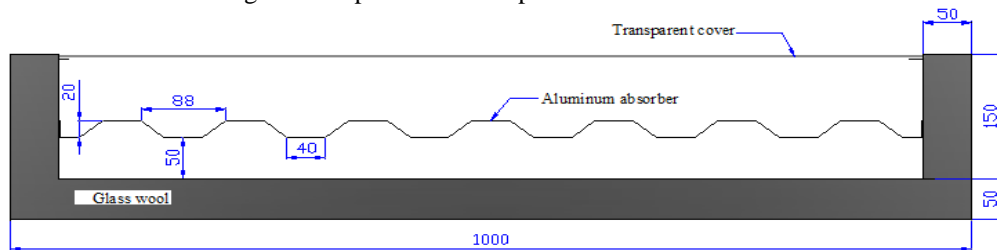
Figure 2. Cross sectional view of the solar collector

After installation of the experimental system, all tests began at 8.30 a.m. and ended at 17.30 p.m. under the normal weather conditions. Surface temperatures are measured at three points on the diagonal of the absorber plate as shown in Fig. 3. The total solar radiation incident is measured by using pyranometer mounted adjacent to the glazing cover. Air velocity is measured by a hot wire anemometer placed at the collector output. The collector outlet and ambient temperatures are measured by using pt1000 temperature probes. Slope of the collector is set to be 53°. All datas are recorded at the time intervals of 2 minutes. Schematic demonstration of the measurement points is given in Fig. 3. The following parameters are measured in the experimental setup.

1. Air velocity at the collector outlet (V)
2. Air temperature at the collector outlet (T_0)
3. Solar radiation incident (I)
4. Surface temperature of the absorber plate (T_1)
5. Surface temperature of the absorber plate (T_2)
6. Surface temperature of the absorber plate (T_3)
7. Air temperature at the collector inlet (T_i)
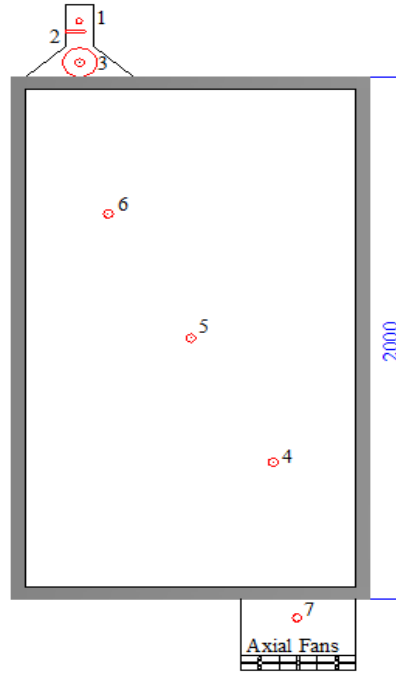
Figure 3. Measurement points

3. Thermal efficiency analysis

The useful energy in the solar air collector can be determined as follows

$$Q_u = \dot{m} c_p \left(T_o - T_i \right)$$
(3.1)

where $\dot{m}$ is the mass flow rate of the air, c_p is the specific heat of the air, T_o and T_i are the collector inlet and outlet temperatures, respectively.

The mass flow rate of the air can be written as

$$\dot{m} = \rho A_k V$$
$$(3.2)$$

where ρ is the density of the air, A_k is the cross sectional area at the collector outlet and V is the air velocity.

Thermal efficiency of the collector is defined as the ratio of the useful energy and the total solar radiation incident as

$$\eta = \frac{Q_u}{IA_c}$$
$$(3.3)$$

where A_c is the surface area of the collector.

4. Modelling of the solar air collector by using artificial neural networks

Artificial neural networks (ANN) can be defined as a method inspired by the operating system of the human brain. ANN is composed of interconnected many neural cells and usually arranged in layers [7]. ANN has a wide range of applications such as image recognition, prediction and classification. The ANN is formed in three layers called the input layer, hidden layer, and output layer as shown in Fig. 4.
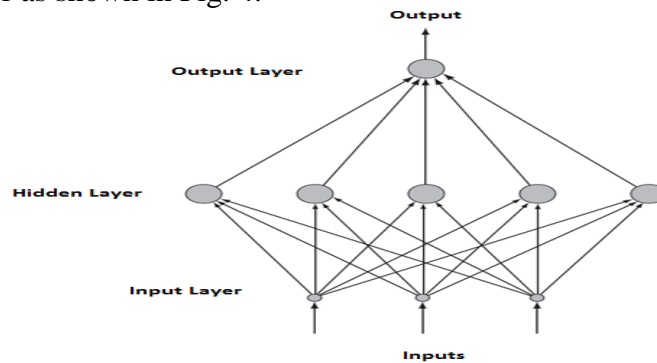
Figure 4. The structure of the ANN

The solar air heater collector system is modeled by ANN has five inputs and two outputs. The absorber plate surface temperatures (T_1, T_2 and T_3), solar radiation incident (I) and inlet temperature (T_i) are considered as input variables. The collector thermal efficiency and outlet temperature (T_o) are evaluated as output variables. Matlab 7.12 platform was used to train and test of the ANN. The information set contains 72 data patterns of input and output information of which 48 patterns were used for training of the ANN and the rest were evaluated in the test procedure. The structure of the ANN and training parameters are given in Table 2.

Table 2. The structure of the ANN and training parameters

	ANN
The number of layers	3
The number of neuron on the layers	8-8,10-2
The initial weights and biases	Random
Activation Functions	Tangent Sigmoid
Learning Rule	Backpropagation
Learning Rate	0.8
Mean-Squared Error	1e-06

The forecasting accuracy of the ANN was determined by the using of root mean square error (RMSE) and the coefficient of multiple determinations (R^2) as follows

$$RMSE = \sqrt{\frac{\sum_{m=1}^{n}\left(y_{pre,m} - t_{mea,m}\right)^2}{n}}$$
(4.1)

$$R^2 = 1 - \frac{\sum_{m=1}^{n}\left(y_{pre,m} - t_{mea,m}\right)^2}{\sum_{m=1}^{n}\left(t_{mea,m}\right)^2}$$
(4.2)

where, n is the total number of the data patterns, y_{pre} is the predicted value and t_{mea} indicates the true value.

5. Results and discussions

In the present study, thermal performance of a solar air collector with trapezoidal absorber plate is investigated experimentally and predicted by ANN.

Fig. 5. shows the hourly variation of the collector inlet and outlet temperatures. It is clear that temperature difference between inlet and outlet of the collector increases to a peak value from to noon and then gradually decreases with time.
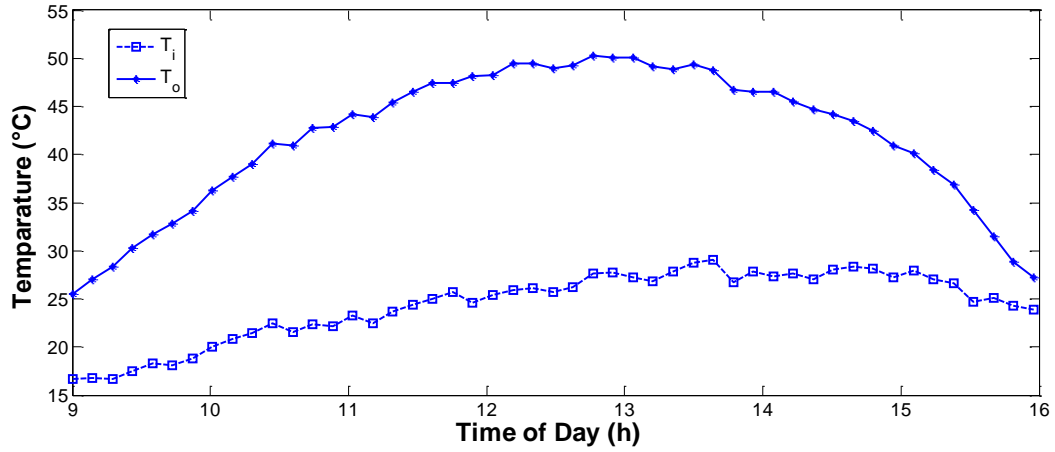
Figure 5. Inlet and outlet temperatures versus time of the day

The variation of solar radiation versus time of day is shown in Fig. 6. As expected, solar radiation shows a similar change to the temperature difference.
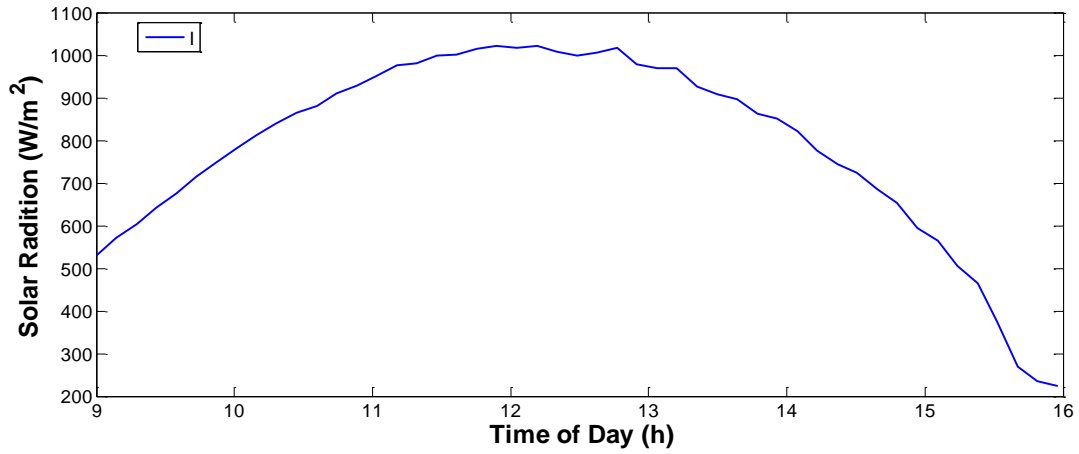
Figure 6. Solar radiation versus time of the day

The predicted and actual outlet temperatures for the number of samples are given in the Fig. 7. The predicted values of the ANN model are very close to the actual ones. Also, the ANN model for the outlet temperature has an accuracy of 99%.

Fig.8. shows the predicted and actual thermal efficiency values. It is clear that ANN model successfully predicts the thermal efficiency.
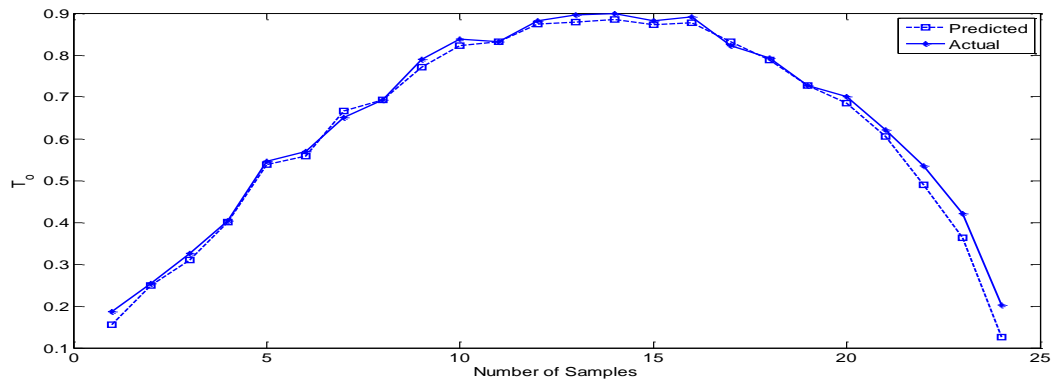
Figure 7. Predicted and actual outlet temperature values
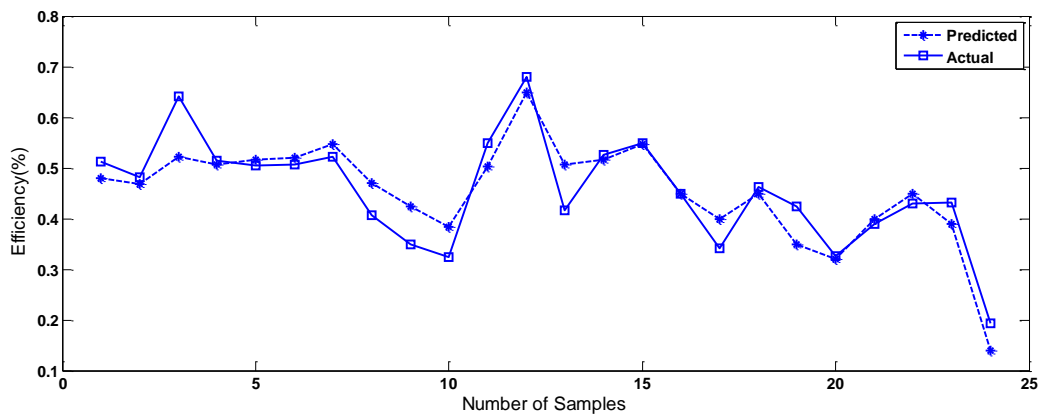
Figure 8. Predicted and actual outlet thermal efficiency values

6. Conclusions

In this paper, thermal performance of solar air collectors with trapezoidal absorber plate is experimentally investigated. According to the data obtained in the experiments, a model of neural network of collector is created considering five inputs and two outputs data. The input variables of neural network model are the collector inlet air temperature, the global radiation and the temperatures of the absorber plate. The collector outlet air temperature and the thermal efficiency values of the collector constitute the output parameters. By training an artificial neural network with a part of the experimental data, the output parameters are estimated corresponding to different inputs data. The ANN model can easily be implemented to predict thermal performance of solar air collector.

7. References

[1] Benli, H. (2013). Experimentally derived efficiency and exergy analysis of a new solar air heater having different surface shapes. *Renewable Energy*, 50, 58-67.
[2] Özgen, F. Esen, M. Esen, H. (2009). Experimental investigation of thermal performance of a double-flow solar air heater having aluminium cans. *Renewable Energy*, 34, 2391–2398.
[3] Akpinar, E.K. Koçyiğit, F. (2010). Experimental investigation of thermal performance of solar air heater having different obstacles on absorber plates. *Int. Com. In Heat and Mass Transfer*, 37, 416-421.
[4] Benli, H. (2013). Determination of thermal performance calculation of two different types solar air collectors with the use of artificial neural networks. *Int. Jo. of Heat and Mass Transfer*, 60, 1-7.
[5] Esen, H. (2008). Experimental energy and exergy analysis of a double-flow solar air heater having different obstacles on absorber plates. *Building and Environment*, 43, 1046-1054.

[6] Esen, H. Özgen, F. Esen, M. Sengur, A. (2009). Artificial neural network and wavelet neural network approaches for modelling of a solar air heater. *Expert System with Applications*, 36, 11240-11248.

[7] Özdemir, V. (2011). Determination of Turkey's carbonization index based on basic energy indicators by Artificial Neural Networks. *Journal of The Faculty of Engineering and Architecture of Gazi University,* 26, 1, 9-15.

A New Fatigue Damage Model for Mechanic Parts Subjected to High-Cycle Fatigue Loadings

H Guechichi [1], S Benkabouche [1], A Amrouche [2] and M Benkhettab [1]

[1] Laboratoire d'Elaboration et Caractérisation Physico Mécanique et Métallurgique des Matériaux, Department of mechanics, Faculty of science and Technology, Mostaganem university, B.P 188 - Mostaganem, Algeria, E-mail: hguechichi@hotmail.com

[2] Laboratoire de Génie Civil et géo Environnement LGCgE, faculty of applied sciences, University of Artois, Technoparc Futura 62400 Béthune, France

Abstract: The purpose of this work is to develop a numerical tool, based on the finite element method, in order to determine the cumulative damage evolution and the remaining lifetime for mechanic parts under HCF cyclic loadings. A nonlinear cumulative fatigue damage model, extended to multiaxial loading, taking into account the effects of the amplitude and sequence of variable-amplitude fatigue loadings is proposed. Various load histories were applied to a carbon steel type S 45 C specimen, and the resulting cumulative damage was evaluated using a numerical simulation. In order to demonstrate the features of the model, the results were compared to those obtained according to the Palmgren-Miner's rule. These comparisons indicate that the proposed model allows more accurate and reliable predictions of lifetime. The proposed model can be very useful tool for the lifetime prediction in the field of design and maintenance.

Keywords: Fatigue, high cycle fatigue, cumulative damage, finite element method.

1 Introduction

Damage in metals is mainly the process of the initiation and growth of micro-cracks and cavities. A reliable lifetime prediction is particularly important in the design, safety assessments, and optimization of engineering materials and structures. With the accumulation of fatigue damage, some accidents will occur.

Typical S-N curve, can be divided into three domains: Low Cycle Fatigue (LCF), the High Cycle Fatigue (HCF) and the Very High Cycle Fatigue (VHCF). The purpose of this work is to develop a numerical tool, based on the finite element method, in order to determine the damage evolution and the remaining lifetime for mechanic parts under HCF loadings. One should note that the proposed model is valid for proportional loadings with variable amplitudes. To derive the equivalent stress from the stress components, we can use fatigue criteria. The proposed fatigue damage model is based on the continuum damage mechanics [1]. Our approach belongs to the category of the nonlinear damage cumulative models. In this article, an effort was made to get a better life prediction capability and applicability of the proposed model. It was done by considering the influence of both static and cyclic loadings on damage and the effects of load sequence. An example is provided to demonstrate the applicability of the method.

2 Formulation of the proposed fatigue damage model

In order to determine the cumulative damage, it is necessary to replace the real sequence of cycles by an irregular loading with an assumed sequence of groups of uniform cycles. Each group, comprising n_i number of uniform cycles, represents a corresponding load level i. At each load level i, a part is subjected to stress components $\sigma^i_{kl}(t)$ at the time t for n_i, while the theoretical life expectancy is N_i number of cycles. Each group of constant-amplitude loading is characterized by stress amplitudes $\sigma^{i\,a}_{kl}$ and mean stresses $\sigma^{i\,m}_{kl}$. At a point P of a body subjected to any level of a sinusoidal synchronous loading, the stress components $\sigma^i_{kl}(t)$ at the time t can be expressed as follows:

$$\sigma^i_{kl}(t) = \sigma^{i\,a}_{kl}\,\sin\omega t + \sigma^{i\,m}_{kl}$$
(1)

where ω is the pulsation.

The analysis deals with replacement of the stress components $\sigma^i_{kl}(t)$ by one-dimensional equivalent stress σ^i_{eq}. For this reason, we exploit Crossland's criterion [2]. At each load level i, the equivalent stress σ^i_{eq} can be written as:

$$\sigma^i_{eq} = \xi^i_a + \alpha\,P^i_{\max}$$
(2)

Where:

- α and β are two material parameters which are determined experimentally from two alternated fatigue limits, i.e., in bending and torsion tests. One can deduce them by the following formulas:

$$\beta = t \quad ; \quad \alpha = \frac{\left(t - f/\sqrt{3}\right)}{\left(f/3\right)}$$
(3)

  f and t are the endurance limits in bending and torsion, respectively.

- ξ^i_a is the square root of the amplitude of the second invariant of the stress deviator tensor,

- $P^i_{\max}$ is the maximum value the hydrostatic stress, reached within loading cycles.

ξ^i_a and $P^i_{\max}$ represent the variables governing the fatigue process. The analysis requires the computation of the maximum equivalent stress $\sigma^i_{eq}{}^{\max}$.

At each load level i, the maximum equivalent stress σ^i_{eq} is located at the point of a part for which the equivalent stress reaches its maximum value such that :

$$\sigma^i_{eq}{}^{\max} = \max\left(\xi^i_a + \alpha\left\{P^i_{\max}\right\}\right)$$
(4)

The maximum equivalent stress $\sigma^i_{eq}{}^{\max}$, for each load level i, in the critical region of mechanic parts is *derived* from finite element analysis. For each load level i, the computation of the maximum equivalent stress $\sigma^i_{eq}{}^{\max}$ can be obtained from the manner described in our previous paper [3].

Based on the model [1] an improved nonlinear fatigue damage model is proposed. The current model reflects the fatigue damage in HCF under multiaxial loading. The cumulative damage and the remaining life can be performed, from the entire loading, through the following stepwise procedure:

- Let us start the analysis by defining the damage D_i at the ith load level as:

$$D_i = \frac{\Sigma_i^{eq} - \sigma^i{}_{eq}{}^{max}}{\tau_u - \sigma^i{}_{eq}{}^{max}}$$

(5)

Equation (5) models a nonlinear damage evolution and forms the basis of the presented fatigue damage model. In this relation Σ_i^{eq} is defined as the damage stress amplitude, at the ith load level, corresponding to the fatigue life $(N_i - n_i)$. It is determined from the S-N curve. N_i is the fatigue life associated with $\sigma^i{}_{eq}{}^{max}$. According to our previous work, the maximum equivalent stress $\sigma^i{}_{eq}{}^{max}$ is compared with the endurance limit defined from the S-N curve of fully reversed torsion test.

In order to continue the calculation, at the following $(i+1)^{th}$ load level, the damage D_i at the ith load level should be less than 1. In fact, the final failure is deemed to occur if the damage $D_i \geq 1$.

- The previous damage D_i at the ith load level, is transmitted to the current $(i+1)^{th}$ load level. Therefore, the damage D_i at the ith load level can be written in the form:

$$D_i = \frac{\Sigma_i^{eq} - \sigma^i{}_{eq}{}^{max}}{\tau_u - \sigma^i{}_{eq}{}^{max}} = \frac{\overline{\Sigma}_{i+1}^{eq} - \sigma^{i+1}{}_{eq}{}^{max}}{\tau_u - \sigma^{i+1}{}_{eq}{}^{max}}$$

(6)

Where $\overline{\Sigma}_{i+1}^{eq}$ called the damage stress amplitude, at the start of the current $(i+1)^{th}$ load level, has the ability to account for the effect of the transmission of the previous damage D_i. Based on (6) we determine the value of $\overline{\Sigma}_{i+1}^{eq}$:

$$\overline{\Sigma}_{i+1}^{eq} = \sigma^i{}_{eq}{}^{max} + D_i \left(\tau_u - \sigma^{i+1}{}_{eq}{}^{max} \right)$$

(7)

It follows that corresponding fatigue life N_{i+1}, due to the transmission of the previous damage D_i, can be obtained from the S-N curve. The remaining number of cycles to failure N_{i+1}^{RES}, at the end of the current $(i+1)^{th}$ load level, can be explicitly expressed as:

$$N_{i+1}^{RES} = N_{i+1} - n_{i+1}$$

(8)

So, the damage stress amplitude Σ_{i+1}^{eq} at the end of the current $(i+1)^{th}$ load level, associated with the remaining number of cycles to failure N_{i+1}^{RES}, is also obtained from the S-N curve. Subsequently, the cumulative damage D_{i+1}, at the end of the current $(i+1)^{th}$ load level, is formulated by the following expression:

$$D_{i+1} = \frac{\Sigma_{i+1}^{eq} - \sigma^{i+1}{}_{eq}{}^{max}}{\tau_u - \sigma^{i+1}{}_{eq}{}^{max}}$$

(9)

For the following loading blocks, this step-by-step procedure is continued until D_i equals 1. In the numerical example presented in a later section, the maximum equivalent stress σ^i_{eq} of the damaged structure is calculated using linear elastic analysis via Ansys software [4], and Matlab code [5] is then employed to perform the simulations in order to assess the cumulative damage and the remaining life.

3 Application of the proposed model

3.1 Material characterization

We propose to apply the proposed model on a carbon steel type SM 45 C according to the experiments conducted by Lee [6]. This material has the following mechanical properties: elastic modulus of 210 GPa, Poison's ratio $v = 0.3$, yield strength $\sigma_e = 638$ MPa and the *ultimate stress* $\sigma_u = 824$ MPa. The fatigue limits in fully reversed bending f_{-1} and reversed torsion t_{-1} have been obtained as : $f_{-1} = 442$ MPa, $t_{-1} = 311$ MPa. The required material properties are the S-N curves in reserved torsion and alternating bending.

3.2 Studied structure and loading

A rectangular plate with low thickness was studied. The geometry and the shape of the plate are shown in Fig. 1. For each block level i , the plate is subjected to uniaxial tensile stress σ^m_i combined with an alternating bending moment $\overrightarrow{M}_i^{(f)}$. The loading applied to the plate is shown in Fig. 2. The model is taken to be symmetric about Y axis. By taking advantage of the symmetry conditions, only one half of the specimen was modeled using the Ansys software, reducing the model size. The displacement U_X of the left vertical face is restrained. As shown in Fig. 2, the loading is decomposed into static (see Fig. 2(a)) and cyclic (see Fig. 2(b)) loadings. The right-hand side is acted upon vertical force, denoted by $\overrightarrow{F}_i^{(f)}$. Let us consider a plate loaded cyclically in a proportional manner with the external loads varying according to a sinusoidal law, i.e., $\left| \overrightarrow{F}_i^{(f)} \right| = F_i^a \sin(\omega T)$, where F_i^a is the amplitude of force load $\overrightarrow{F}_i^{(f)}$.
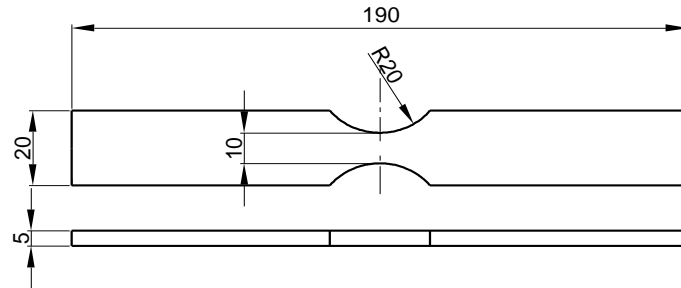
Figure 1 The geometry of the rectangular plate specimen.
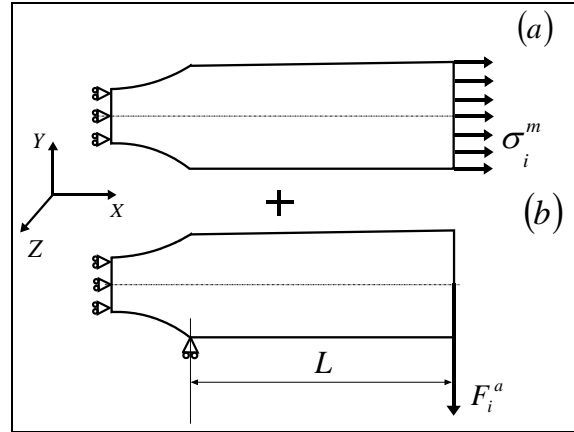
Figure 2 Modeling of the loading and the boundary conditions: static (a) and cyclic (b) loads.

The static analysis is utilized to solve the problem using the Ansys solver. The finite elements of 8-node structural solid (Plane 82) were employed.

4 Results and discussion

4.1 Effect of both static and cyclic loads on cumulative damage

4.1.1 Effect of static load on cumulative damage

In order to evaluate the effect of static load on damage accumulation, a series of calculations were conducted. For this purpose, four different uniform load-blocks for various values of uniaxial tensile stress σ_i^m (0, 10, 20, 40 and 60 MPa) were considered. For each loading, the **load force amplitude** F_i^a was kept constant $\left(F_i^a = 450\,N \right)$. First of all, knowing the values of each couple (σ_i^m, F_i^a), the maximum equivalent stress $\sigma_{\mathrm{eq}}^{i\,\mathrm{max}}$ and the predicted fatigue life N_i were computed. The values of these parameters are listed in Table 1.

Table 1: Computed maximum equivalent stress $\sigma_{\mathrm{eq}}^{i\,\mathrm{max}}$ and predicted fatigue life N_i for different one-uniform load-block with various values of uniaxial tensile stress σ_i^m (the load force magnitude F_i^a is kept constant).

Uniform load block	$F_i^a\,(N)$	$\sigma_i^m\,(MPa)$	Crossland's parameters			Predicted fatigue life N_i (cycles)
			$P_{\max}^i\,(MPa)$	ξ_a^i (MPa)	$\sigma_{\mathrm{eq}}^{i\,\mathrm{max}}\,(MPa)$	
1		0	156.2		323.8	1 044 300
2	450	10	163.9	264.8	326.7	725 900
3		40	187		335.5	334 300
4		60	202.4		341.3	231 500

After that, the cumulative damage was calculated using the proposed model. We noticed that the maximum equivalent stresses are restricted to HCF regime; the resulting lifetimes

range from $81\,254$ to 10^7 cycles. The fraction of life or cycle ratio r_i corresponding to the ith load level $(r_i = n_i / N_i)$ is used to highlight the nonlinear feature of damage evolution.

The plots in Fig. 3 illustrate the predicted cumulative damage versus fraction of life for the different uniform load-blocks. As illustrated, the traditional Palmgren-Mine's rule [6] is represented by a solid line. According to these results, we note that all the predicted curves of the model exhibit the same shape. It is noted that the curve of Palmgren-Miner's rule develops very differently of that of the current model. The main difference is that the cumulative damage, obtained by the model, progressively increases from the beginning during **the most** part of the **lifetime, after that it strongly increases** until it reaches its critical value (i.e., equal to 1) at the end of the design life. Whereas, from the Palmgren-Miner's rule, the cumulative damage curve is linear. Compared with predictions of Palmgren-Miner's law, the model estimates lower values of cumulative damage.

Examination of Fig. 3 reveals that the cumulative damage D_i increases with increasing uniaxial tensile stresses σ_i^m. It is interesting to note, for a given unit load-block, that the static load plays a significant role in determining the cumulative damage.
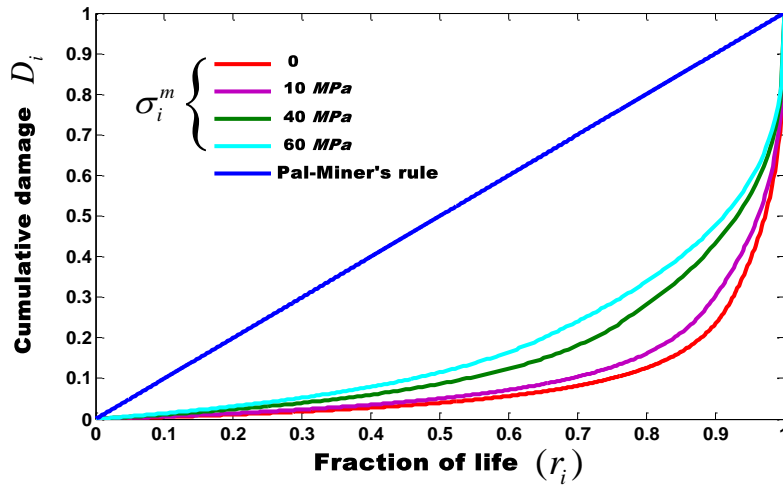
Figure 3 Predicted cumulative damage variation D_i versus cycle ratio r_i , for different one uniform load block with various values of uniaxial tensile stress σ_i^m **,** and a comparison with the Palmgren-Miner's rule.

4.1.2 Effect of cyclic load on cumulative damage

Similarly a series of calculations were conducted in order to evaluate the effect of cyclic load on cumulative damage, while the uniaxial tensile stress σ_i^m was maintained constant $(\sigma_i^m = 60\,\text{MPa})$. Four different uniform load-blocks with various values of load force magnitude F_i^a (430, 440, 450 and 460 N) are considered. The computed values of the maximum equivalent stress $\sigma^i{}_{\text{eq}}{}^{\text{max}}$ and the predicted fatigue life N_i are given in Table 2. The cumulative damage plots, given in Fig. 4, were obtained. All figures include the linear Palmgren-Miner's curve for comparison purposes.

The cumulative damage plots evolve nonlinearly with the fraction of life. As can be seen, the curves of the cumulative damage determined by the proposed model have a concave form and are always situated below Palmgren-Miner's line. At a given number of cycles, the

predicted cumulative damage is consistently found to be less than that **given** by the Palmgren-Miner's rule. It appears, for a given unit-block level, the cumulative damage D_i increases with increasing load force amplitude F_i^a .

Table 2: Computed maximum equivalent stress $\sigma^i_{eq}{}^{max}$ and predicted fatigue life N_i, for different one-uniform load-block with various values of load force magnitude F_i^a (uniaxial tensile stress σ_i^m is kept constant).

Uniform load block	F_i^a (N)	σ_i^m (MPa)	Crossland's parameters			Predicted fatigue life N_i
			$P^i{}_{max}$ (MPa)	ξ^i_a (MPa)	$\sigma^i_{eq}{}^{max}$ (MPa)	
1	430		195.5	253.0	326.9	711 900
2	440	60	198.9	258.9	334.1	369 400
3	450		202.4	264.8	341.3	231 500
4	460		205.9	270.7	348.5	161 400
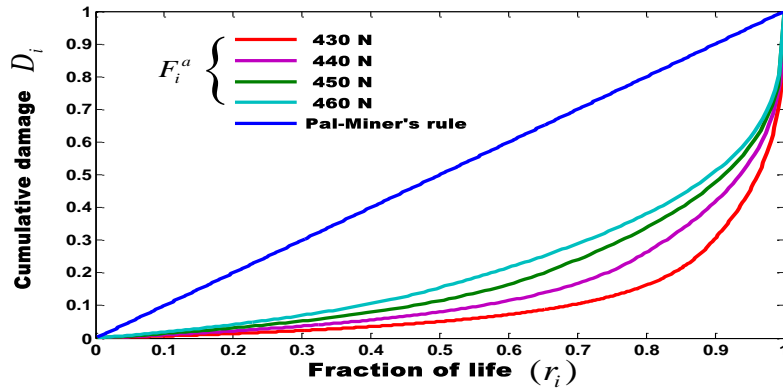
Figure 4 Predicted cumulative damage variation D_i versus cycle ratio r_i , for different one uniform load block with various values of load force magnitude F_i^a , and a comparison with the Palmgren-Miner's rule.

Indeed, the cumulative damage D_i is influenced by cyclic loading. From both loading cases, it can readily be seen from Fig. 2 and 3 that the cumulative damage D_i strongly depends upon both static and cyclic loads.

4.2 Effect of load sequence on cumulative damage and total *lifetime*

The ability of the model to account for the effect of load sequence is established in this subsection. The nonlinear cumulative damage model was applied to multi-level loading condition through sequential calculation in order to predict the resulting cumulative fatigue damage D_i and the total *lifetime*. To understand the effect of load sequence on fatigue life, we consider four-unit blocks. Each unit-block can be **achieved either** by changing the value **of** static or cyclic loads, such that :

a- Changing the value of cyclic load: four different values of load force magnitude (F_i^a = 430, 440, 450, and 460 N) were considered, while the value of the uniaxial tensile stress was kept constant ($\sigma_i^m = 60\ MPa$).

b- Changing the value of static load: four different values of uniaxial tensile stress ($\sigma_i^m = 0$, 10, 40, 60 MPa) were considered, while the value of the load force magnitude was kept constant ($F_i^a = 460$ N).

For each kind of loading described above, three different types of load histories were investigated: High-to-Low (H-L), Low-to-High (L-H) and random block-loading sequences

Each block-loading data was transformed into an associated maximum equivalent stress $\sigma^i{}_{eq}{}^{max}$, as explain in the previous sections, using the methodology described in our paper [3]. In order to evaluate and to make a comparison between different results obtained by the present model, under various load sequences, the first three *loading blocks* were chosen such that each block level i represents 25% of its corresponding lifetime ($r_i = n_i / N_i = 0.25$). In all cases, the remaining life under the fourth block was computed. Firstly, the simulation calculated the remaining life for the fourth block. After that the total lifetime, under the four load-blocks, was deduced. It is also mentioned that the total lifetime predicted by the model is influenced by the order of load blocks.

5. Conclusion

The proposed nonlinear fatigue damage accumulation model, extended to multiaxial loading, is described. The block-loading data was transformed into an equivalent constant amplitude data using the concept of maximum equivalent stress defined by Crossland's criterion. The proposed nonlinear damage theory, which includes the effects of the magnitude cyclic load, the static load and the sequence of applied fatigue loadings, allows more realistic fatigue analysis of concrete structures.

 The main aim of the present study was to determine the damage evolution and the lifetime of mechanical parts under HCF loadings. We have developed a numerical tool, based on the finite element method, in order to determine the damage evolution and the remaining lifetime. The model was tested on a carbon steel type S 45 C. The present damage model, with use of a numerical technique, was applied to a rectangular plate with low thickness under various load sequences. Three different types of load histories were investigated: High-Low (H-L), Low-High (L-H) and random block-loading sequences. The predicted curves of cumulative damage evolve nonlinearly with the number of cycles. The loading sequential effects are clearly noticeable. Compared with the expectations of the Palmgren-Miner's rule, the model predicts shorter fatigue life under H-L sequence and longer fatigue life under L-H one. The cumulative damage was found to be higher than unity when the sequence is in the L-H order and lower than unity when it is in the H-L order.

The results obtained by the proposed model confirm the findings of many researchers. It has been reported in other investigations [7-10] that the sum of fractions of life is not always equal to unity, but rather depends mainly on the load sequence. In particular, it was established that the sum of the fractions of life is greater than unity under the L-H loading sequences; on the contrary, it is less than unity under the H-L loading sequences.

It can be summarized that for a mechanical part subjected HCF loadings, the fatigue damage strongly depends on the mechanical behavior of its material, the nature of the loading with its botha parts (static and cyclic), the geometry and the shape of the structure, the number of cycles of each load-block and the type of load sequences.

References

[1] Mesmacque G, Garcia S and Amrouche A (2005). Sequential law in multiaxial fatigue: a new damage indicator. *International Journal of Fatigue* 27(4), 461-467.

[2] Crossland B (1956). Effect of large hydrostatic pressures on the torsional fatigue strength of an alloy steel. In: *Proceeding of the international conference on fatigue of metals*. London: Institution of Mechanical Engineers, pp. 138-149.

[3] *Guechichi* H, Benkabouche S, Amrouche A and Benkhettab M (2011). A high fatigue life prediction methodology under constant amplitude multiaxial proportional loadings. *Materials Science and Engineering A* 528(13-14), 4789-4798.

[4] Ansys Inc (2007). *User guide*, version 11.

[5] The MathWorks (2004). *Matlab Optimization Toolbox User Guide*, version 6.5.

[5] Lee SB (1989). Out-of-phase bending and torsion fatigue of steels. In: *Brown MW and Miller KJ (eds), Biaxial and Multiaxial Fatigue.* London: Mechanical Engineering Publications, pp. 612-634.

[6] Miner MA (1954). Cumulative damage in fatigue. *Journal of Applied Mechanics* 67, A159-164.

[7] Kujawski D and Ellyin F (1984). A cumulative damage theory for fatigue crack initiation and propagation. *International Journal of Fatigue* 6(2), 83-88.

[8] *Schijve J* (*2003).* Fatigue of structures and materials in the 20th century and the state of the art. *International Journal of Fatigue* 25(8), 679-702.

[9] Kwofie S and Rahbar N (2012). A fatigue driving stress approach to damage and life prediction under variable amplitude loading. *International Journal of Damage Mechanics* 22(3), 393-404.

[10] Risitano A and Risitano G (2013). Cumulative damage evaluation in multiple cycle fatigue tests taking into account energy parameters. *International Journal of Fatigue* 48, 214-222.

Finite Element Analysis of Out-of-plane Compressive Properties of a Novel Concept of Honeycomb Structures with Hexagonal and Auxetic (negative Poisson's ratio) topology

BOUAKBA. M [1], BEZAZI. A [2], SCARPA. F [3]

[1] Département de Génie Mécanique, Université Kasdi Merbah Ouargla, 30000 Algérie.

E-mail: bouakba.mu@univ-ouargla.dz;

[2] Laboratoire Mécanique appliquée des nouveaux matériaux (LMANM) Université 8 Mai 1945 Guelma 24000 Algérie

E-mail ar_bezazi@yahoo.com Phone: 00213 37 21 58 49 Fax: 00 213 37 20 72 68.

[3] Department of Aerospace Engineering, University of Bristol, Queens Building, University Walk, BS8 1TR Bristol, UK. E-mail: f.scarpa@bris.ac.uk

Abstract*:* This work illustrates the manufacturing and compressive testing of a novel concept of honeycomb structures with hexagonal and auxetic (negative Poisson's ratio) topology. The cellular configuration is simulated using a series of finite element models representing fullscale. The models are benchmarked against experimental results from pure compression tests. Finite element models of the honeycomb assemblies under compressive loading have been developed using nonlinear shell elements from an ANSYS code. Good agreement is observed between numerical nonlinear simulations and the experimental results.

Keywords: Lattice structures, Voronoi, Finite element analysis

1 Introduction

The mechanical and transport properties of cellular solids have been traditionally modelled using periodic unit cells representative volumes. Examples of these unit cell topologies are the hexagonal prismatic and quadrilateral centrosymmetric ones [1, 2, 5], Kelvin lattices [3, 6, 7]. The level of disorder associated to the shape and orientation of cells belonging to real open cell foams has been described numerically by making use of Voronoi diagrams. Voronoi tessellations create one-to-one optimal (i.e., minimum distance) correspondence between a point in the space and polytopes (a geometric entity delimited by segments in 2D) to guarantee the creation of six-sided polygons [4]. Voronoi diagrams have been extensively used to simulate the mechanical properties of open cell foam structures [5, 8]. The classical Voronoi tessellation (Fig. 1a) generates models related to open cell foams which show a global isotropic mechanical response under linear elastic regime [8]. However, cellular structures like the balsa wood may show a specific directionality in terms of average orientation and shape geometry of their cells, therefore providing a global anisotropic mechanical behaviour against a general Cartesian coordinates system. Moreover, polymeric open cell foams (produced in laboratory for replication or pyrolysis applications [9] do tend to show a general mechanical anisotropic behaviour due to the specific rising direction of the foam during manufacturing. The existence of anisotropic lattices with topologies inspired to disordered or Voronoi-type configurations can be nowadays reproduced using kirigami technique or other advanced manufacturing processes, making possible the study and evaluation of cellular configurations with potentially unusual deformation mechanisms [9]. Honeycomb out-of-plane compressive properties are of interest for many researchers because

they are important for the mechanical performance of sandwich panels, such as local compression and impact resistance. Bouakba *et al* [1] proposed a novel type Voronoi-lattice and study this honeycomb by FEA on in-plane mechanical properties using the ANSYS code. This work described a continued study of the out-of-plan mechanical properties. The compressive properties for this novel type Voronoi-lattice have been simulated using a full-scale representation of the honeycomb panels under compression loading. The experimental evaluations on the novel honeycomb compressive properties are implemented by doing flatwise compressive test (FCT) according to the standard ASTM C365. The sample size is 50x50x28 mm. The results are compared to the FEA results.

2 Construction Of Novel Hexagonal Cell Honeycombs Irregular.

2-1 Convex Topology

The irregular Voronoï honeycombs is known in the literature based on the subtraction perpendicular to the base of each triangle formed by the three adjacent points in a field of a point segments randomly placed in the plane (xy) Figure 1 (a) [5, 8] . Generally these points indicate the centres of the Voronoï cells. The new Voronoï cell proposed in this work is based on the use of the centres of triangles in Figure 1 (b). The coordinates of the corners of the new cell are determined by the mathematical model presented in [1]. In order to implement this model, we made the following simplifying assumptions:

1 - The points are randomly placed in the plane (xy) .

2 - Each line of these points must be parallel to an axis in the plane like any x1, y1 (figure 1b).

In the Delaunay triangulation of the two neighboring triangles construct a rhombus. The matrix point of view this corresponds to a lozenge case (i , j) .

(a)   (b)

(c)   (d)
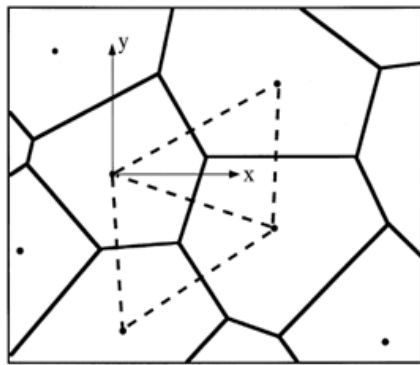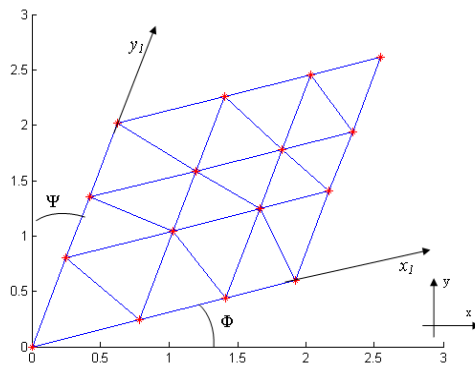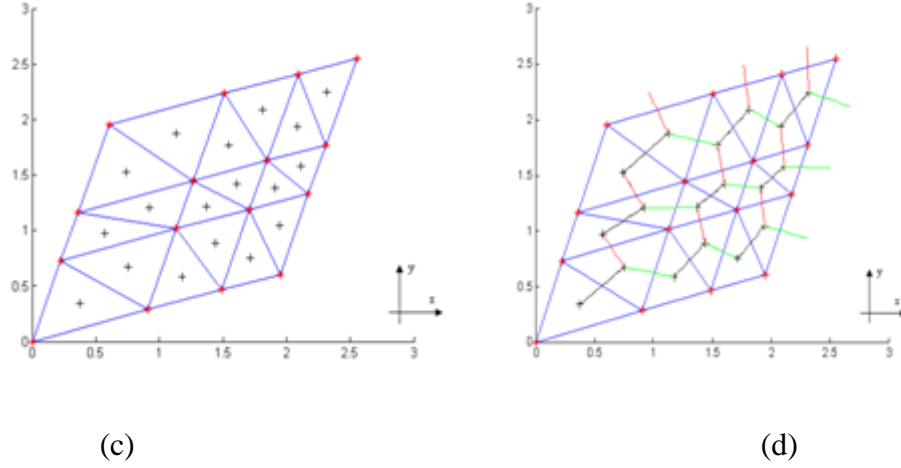
Figure 1 a) Voronoi diagram used to construct the classical Voronoi cell, b) Delaunay triangulation, (c) Contact the corners of the new irregular Voronoi cell in the (xy) plane, d) Diagram of the new cell presented in this work.

The mathematical model calculates the centers of two adjacent triangles of the same case (i, j) in Figure 1 (c). These centers form the vertices of the hexagon that materializes the proposed cell.

$$x_{\Delta\text{inf}}(i, j) = \frac{d(i, j) - b(i, j)}{a(i, j) - c(i, j)}$$

$$y_{\Delta\text{inf}}(i, j) = a(i, j)x_{\Delta\text{inf}}(i, j) + b(i, j)$$

$$x_{\Delta\text{sup}}(i, j) = \frac{h(i, j) - f(i, j)}{e(i, j) - g(i, j)}$$ (1)

$$y_{\Delta\text{sup}}(i, j) = e(i, j)x_{\Delta\text{sup}}(i, j) + h(i, j)$$

Where :

$x_{\Delta inf}$, $y_{\Delta inf}$ and $x_{\Delta sup}$ and $y_{\Delta sup}$ respectively represent the coordinates of the centre of the upper and lower triangle in the (x, y) plan for the same case *(i, j)*.

Matrices a(*i,j*), b(*i,j*), c(*i,j*), d(*i,j*), e(*i,j*), f(*i,j*), h(*i,j*),and g(*i,j*) are calculated as follows:

$$a(i, j) = \frac{(x_i - x_{i+1})\sin\Phi + 1/2(y_{j+1} - y_j)\cos\Psi}{(x_i - x_{i+1})\cos\Phi + 1/2(y_{j+1} - y_j)\sin\Psi}$$

$$b(i, j) = x_{i+1}\sin\Phi + y_j\cos\Psi - a(i, j)(x_{i+1}\cos\Phi + y_j\sin\Psi)$$

$$c(i, j) = \frac{1/2(x_{i+1} - x_i)\sin\Phi + (y_j - y_{j+1})\cos\Psi}{1/2(x_{i+1} - x_i)\cos\Phi + (y_j - y_{j+1})\sin\Psi}$$

$$d(i, j) = x_i\sin\Phi + y_{j+1}\cos\Psi - c(i, j)(x_i\cos\Phi + y_{j+1}\sin\Psi)$$

$$e(i, j) = \frac{1/2(x_i - x_{i+1})\sin\Phi + (y_{j+1} - y_j)\cos\Psi}{1/2(x_i - x_{i+1})\cos\Phi + (y_{j+1} - y_j)\sin\Psi}$$ (2)

$$f(i, j) = x_{i+1}\sin\Phi + y_j\cos\Psi - e(i, j)(x_{i+1}\cos\Phi + y_j\sin\Psi)$$

$$g(i, j) = \frac{(x_{i+1} - x_i)\sin\Phi + 1/2(y_j - y_{j+1})\cos\Psi}{(x_{i+1} - x_i)\cos\Phi + 1/2(y_j - y_{j+1})\sin\Psi}$$

$$h(i, j) = x_i\sin\Phi + y_{j+1}\cos\Psi - g(i, j)(x_i\cos\Phi + y_{j+1}\sin\Psi)$$

The diagram of the new cell is arranged in the following sequence:

- The centre of the lower triangle (i, j) is connected with the centre of the triangle top of the box (i, j).
- The centre of the upper triangle in the case (i, j) is connected with the centre of the lower triangle in the case (i, j +1).
- The centre of the upper triangle (i, j) is connected with the centre of lower triangle cell in the case (i +1, j). As shown in Figure 1 (d).

2.2 Topology auxetic (a negative Poisson's ratio)

It is possible to create re-entrant irregular Voronoï cells (Figure 2), which could provide a negative Poisson's ratio (auxetic behaviour) (Bouakba et al., 12). In this case, the first part of the equation III.2 must be converted to:

$$a(i, j) = \frac{(x_i - x_{i+1})\sin\Phi + 1/2(y_{j+1} - y_j)\cos\Psi}{(x_i - x_{i+1})\cos\Phi + 1/2(y_{j+1} - y_j)\sin\Psi}$$

(3)
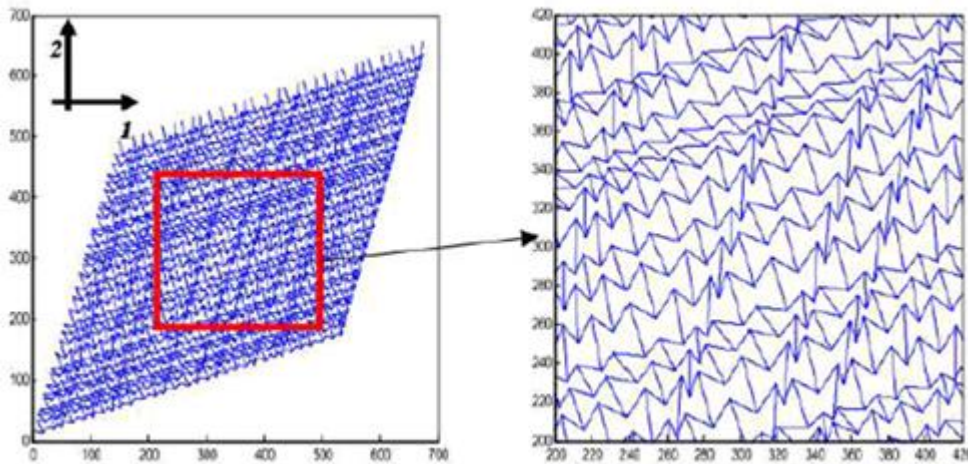
Figure 2 Re-entrant irregular Voronoï cell structures proposed.

3 Manufacturing and experimental testing

3.1 Kirigami Honeycomb Structures manufacturing process

The Kirigami manufacturing process consists in the following three steps: cutting, folding and bonding. Irregular distributions of slits are introduced within the plain carton paper using a kenf of Cutting following the patterns shown in Figure 3. The cutting lines are generated by MATLAB program based on the algorithm of the novel cell of honeycombs topology with the gauge thickness of the honeycomb walls.

The compressive properties of the novel topology along the direction parallel to the plane of the sandwich face skin are evaluated through edgewise compression tests according to the ASTM Standard ASTM C364/C364M-07 carried out on an ET testing machine. The specimen size (50 mm x 50 mm x 28 mm) satisfies the requirements of the ASTM standard, while being quite similar to the one used to dimension the specimens for flatwise compression tests. The specific machine configuration setup is the same used for the flatwise testing, with the bottom

plate fixed and the top plate moving downwards at a constant velocity of 0.5 mm/min. five specimens are tested in total, and different failure modes are observed during loading .
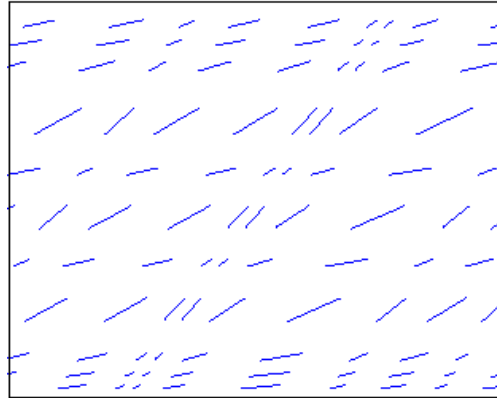
Figure 3 Cutting lines generated by MATLAB

4 Finite element models

All numerical models figure 4 are developed using the commercial code ANSYS 11.0. The out of plane compressive properties have been simulated using a full-scale representation of the honeycomb panels under compression loading. After a mesh convergence analysis, an average mesh size equal to l/4 was adopted for the SHELL63 elements.The honeycomb cell walls are modelled by using four-node three dimensional shell elements, SHELL63, in ANSYS [11]. SHELL63 has both bending and membrane capabilities. Both in-plane and normal loads are permitted. The element has six degrees of freedom at each node: translations in the nodal x, y, and z directions and rotations about the nodal x, y, and z axes. Stress stiffening and large deflection capabilities are included. A consistent tangent stiffness matrix option is available for use in large deflection analysis. The element thickness and orthotropic elastic properties are the main input data to simulate the real material. The modulus is taken as 1.1 GPa and the Poisson's ratio is set as 0.3. A Newton-Raphson nonlinear solver is used to extract the force-displacement curve F-δ.
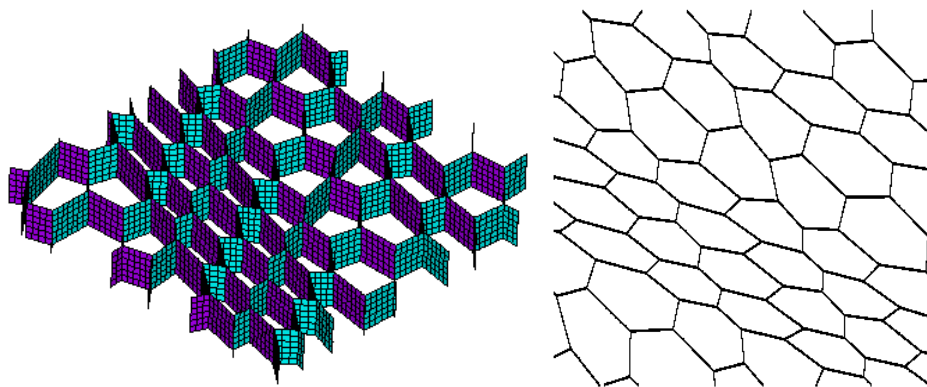
Figure 4 Full model in ANSYS code.

5 Resultats and discussions

Fig. 5 shows a typical Load-displacement curve obtained from the exprimental compressive test of the novel honeycomb lattice convex and auxetic topology.

Curve load - displacement (Figure 5) use to identify the mechanical   characteristics for the two cases studied in this work. Practically in the literature, we note that the cell size greatly affects of the out of plan Young's modulus and it has been observed through the form, we find that the out of plan Young's modulus cell is much greater than in the auxetic topology. The results confirm that for the radius auxetic topology, the elasticity limit is defeated and we note that the value of the modulus of elasticity is nearly two times big than the elasticity in the convex topology. From the viewpoint of mechanical performance structure to auxetic topology shows a yield equal to twice that produced by a convex topology. But note the contrast to the plastic limit, the factor of the plastic limit of the auxetic cell is larger than the convex. The greatest amount of energy absorbed 31%.
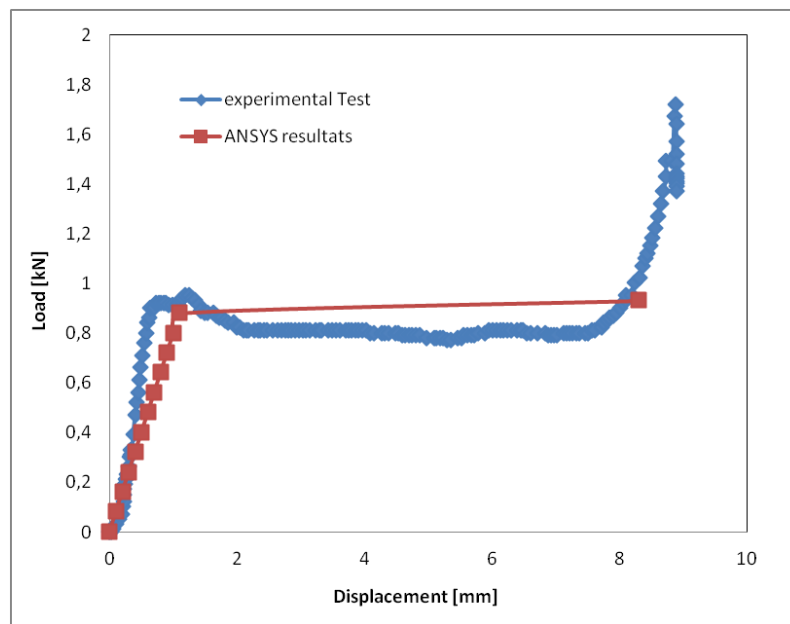
Figure 5 Load-displacement curve obtained from the experimental compressive test

The compressive deformation process can be categorized into three regions (I, II and III) based on the compressive stress-strain behaviour. The compressive stress increased almost linearly with increasing strain in region I due to the elastic buckling of cell walls, not the elastic axial shortening of cell walls. The cell walls of honeycomb composite were restrained with the neighbouring cell walls and very thin. Therefore, when the compressive deformation is performed to the honeycomb, it is more difficult to be happened by the elastic axial shortening of cell walls rather than by the elastic buckling of cell walls. When the stress-strain curve passed a maximum stress, a rapid drop of the compressive stress appeared in region II due to the onset of the plastic buckling of cell walls. The reason of a rapid drop of the compressive stress in region II is that the elastic buckling of cell walls was converted quickly to the plastic buckling of cell walls. The plastic buckling was initiated at the free walls and propagated into the ribbon. Then, the deboning fracture of cell/cell interfaces at ribbon was followed in region II. In plateau region III, the fracture resin layer on cell walls proceeded continuously. It is reasonably thought as the plastic shortening that the nearly constant load proceeded in region III with the fracture of resin layer on cell walls. The compressive stress was maintained nearly constant up to a failure in region III.

5. Conclusions

The main motivation for this study is to propose new alternative cellular cores to be used in the construction of sandwich structures, having geometries that allow the reduction of the base material.

As a result, this work presents a novel cellular structure that is proposed to be used as a core in sandwich panels. It aims to develop an FEM model for the out-of-plane effective compressive properties of the proposed cellular structure which is validated through experimental tests.

6 References

[1] Bouakba,.M., Bezazi, A., Scarpa, F., (2012). FE analysis of the in-plane mechanical properties of a novel Voronoi-type lattice with positive and negative Poisson's ratio configuration. International Journal of solide and structures.

[2] Bezazi, A., Scarpa, F., (2009). Tensile fatigue of conventional and negative Poisson's ratio open cell PU foams. *International Journal of Fatigue* 31 (3), 488–494.

[3] Choi, J., Lakes, R., (1995). Analysis of elastic modulus of conventional foams and of re-entrant foam materials with a negative Poisson's ratio. *International Journal of Mechanical Sciences* 37 (1), 51–59.

[4] Fazekas, A., Dendievel, R., Salvo, L., Brechet, Y., (2002). Effect of microstructural topology upon the stiffness and strength of 2D cellular structures. International Journal of Mechanical Sciences 44, 2047–2066. Gibson, L.J., Ashby, M.F., (1982). The mechanics of three-dimensional cellular materials. Proceedings of the Royal Society of London. A. *Mathematical and Physical Sciences* 382, 43–59.

[5] Gibson, L.J., Ashby, M.F., (1997). Cellular Solids – Structure and Properties. Cambridge Solid State Science. Cambridge University Press.

[6] Gong, L., Kyriakides, S., Jang, W.-Y., (2005). Compressive response of open-cell foams Part I: Morphology and elastic properties. *International Journal of Solids and Structures* 42 (5–6), 1355–1379.

[7] Zhu, H., Knott, J., Mills, N., 1997. Analysis of the elastic properties of open–cell foams with tetrakaidecahedral cells. *Journal of the Mechanics and Physics of Solids* 45, 319–343.

[8] Zhu, H.X., Hobdell, J.R., Windle, A.H., (2001). Effects of cell irregularity on the elastic properties of 2D Voronoi honeycombs. *Journal of the Mechanics and Physics of Solids* 49, 857–890.

[9] Zhu, H.X., Thorpe, S.M., Windle, A.H., (2006). The effect of cell irregularity on the high strain compression of 2D Voronoi honeycombs. *International Journal of Solids and Structures* 43, 1061–1078.

Numerıcal Sımulatıon of Mıxed Convectıon of Nanofluıds In A Square Cavıty With An Adıabatıc Block In The Center

Müslüm Arıcı [1], Elif Büyük Öğüt [2*] and Çağatay Kaptan [3]

[1] Kocaeli University, Mechanical Engineering Department, Kocaeli, Turkey
[2] Vocational School of Hereke, Kocaeli University, Hereke, Kocaeli, Turkey
[3] Ford Otosan, TASE Product Development Engineer, TUBITAK MAM Teknokent, Kocaeli,Turkey
([*]Corresponding author:elif.ogut@kocaeli.edu.tr)

Since heat transfer fluids such as water, oil and ethylene glycol have low thermal conductivity, nanofluids are used to enhance the heat transfer in many engineering electronic devices in recent years. In this study, a numerical simulation is carried out to investigate mixed convection of water-based nanofluids in a square cavity with insulated horizontal walls and isothermal vertical walls maintained at different temperatures and containing an adiabatic square block in the center. The top wall of cavity moves from left to right with uniform velocity. Two different nano-particles, Cu and Ag are considered in the study. The computations are performed for solid volume fractions of 0%, 5% and 10%. Grashof number is kept at a constant value of 10^4 and the Reynolds number is varied so that the Richardson number will have values of 0.1, 1 and 10. The results show that the presence of nanoparticles results in significant increase in the heat transfer rate.

Keywords: Mixed convection, nanofluid, square block

1. Introduction

In recent years, nano-particles are used for heat transfer performance improvement applications. The presence of the nano-particles in the fluids increases appreciably the effective thermal conductivity of the fluid and consequently enhances the heat transfer characteristics [1]. Therefore thermal conductivity is an important parameter in determining the heat transfer characteristics of fluids and today more than ever ultrahigh-performance heat transfer fluids are required in many industries as well as commercial applications. Since traditional fluids used for heat transfer applications such as water, mineral oils and ethylene glycol have a rather low thermal conductivity, nano - fluids with relatively higher thermal conductivities have attracted enormous interest from researchers due to their potential in enhancement of heat transfer with little or no penalty in pressure drop [2].

In recent years, many numerical studies focused on convective heat transfer and natural convection nano-fluids in closed medium have been investigated in literatures. Khanafer et al. [1] investigated numerically water-based copper nano-fluids in vertical rectangular closed medium natural convection heat transfer. According to the results, in any Grashof number, copper nano-particle volume fraction in water increases heat transfer performance. Jou and Tzeng [3] carried out a similar investigation and reported that nano-fluids usage enhances average Nusselt Number significantly. Santra et al. [4] used two different models for thermal conductivity and presented that Bruggeman model had a more accurate high thermal conductivity than Maxwell Garnett model. Hwang et al. [5] investigated aluminum based nano-fluid in rectangular closed medium heated from below side for natural convection. They reported that as nano-particle diameter increases, mean Nusselt number reduces remarkably. Oztop and Abu-Nada [6] studied natural convection numerically for various nano-particles in a cavity which consists of a high temperature left-wall, a low temperature right-wall and adiabatic other walls. In addition, the usage of nano-fluids increase heat transfer and low size nano-particles enhance heat transfer much more high size nano-particles. Ogut [7] investigated the natural heat transfer in an inclined closed square medium which consists of constant heat flux lateral walls with water-based nanofluids. The results show that the presence of nanoparticles causes a substantial increase in the heat transfer rate. The length of

the heater also affects heat transfer, the latter decreasing with an increase in the length of the heater. While the heater length is increased, the average heat transfer rate actually starts to decrease for smaller inclination angles.

Although there are a large number of numerical studies on free convection of nanofluids inside rectangular cavities with different boundary conditions in the literature, there are few studies regarding convection heat transfer in square cavities with an inside adiabatic body. Islam et al. [8] investigated numerically laminar natural and mixed-convection in a lid-driven square cavity having an isothermally heated square internal blockage for different governing parameters. The variations of the average and local Nusselt number at the blockage surface at various Richardson numbers for different blockage sizes and placement eccentricities were presented. From the analysis of the mixed convection process, it was found that for any size of the blockage placed anywhere in the cavity, the average Nusselt number does not change significantly with increasing Richardson number until it approaches the value of the order of 1 beyond which the average Nusselt number increases rapidly with the Richardson number. Mahmoodi and Sebdani [9] investigated the problem of free convection fluid flow and heat transfer of Cu–water nanofluid inside a square cavity having adiabatic square bodies at its center numerically. They showed that for all Rayleigh numbers with the exception of $Ra = 10^4$ the average Nusselt number increases with increase in the volume fraction of the nanoparticles. At $Ra = 10^4$ the average Nusselt number is a decreasing function of the nanoparticles volume fraction. Moreover at low Rayleigh numbers (10^3 and 10^4) the rate of heat transfer decreases when the size of the adiabatic square body increases while at high Rayleigh numbers (10^5 and 10^6) it increases. Apart from application of nanofluids in buoyancy driven heat transfer, free convection in cavities having an inside body has received considerable attention in the recent years due to its practical engineering applications, such as solar collectors, thermal insulation, cooling of electronic components and designing building [10].

The objective of this study is to investigate numerically mixed convection of water-based nano-fluids in a square cavity with insulated horizontal walls and isothermal vertical walls maintained at different temperatures and containing an adiabatic square block at the center. Two different nano-particles, Cu and Ag with solid volume fraction of 0%, 5% and 10% are analyzed in this study. The Grashof number is kept at a constant value of 10^4 and the Reynolds number is varied so that the Richardson number will have values of 0.1, 1 and 10.

2. Mathematical Formulation

The geometry and coordinates system for analysis are illustrated schematically in Fig. 1. The laminar natural convection of water based nano-fluid is considered in a 2D square enclosure of side length L containing an adiabatic square block of side H in the center. Horizontal walls are assumed to be adiabatic and isothermal vertical walls are maintained at different temperatures. The top wall of cavity moves from left to right with uniform velocity of U.
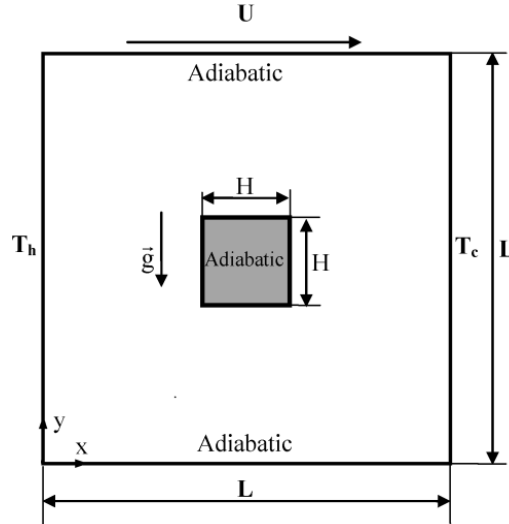
Figure 1. Physical geometry and boundary conditions

Table 1: Thermophysical properties of materials

Property	Water	Ag	Cu
ρ (kg/m3)	997.1	10500	8954
C_p (J/kgK)	4179	235	383
k (W/mK)	0.613	429	400
β_T x 10^6 (1/K)	210	19	16.7

The governing equations are presented as follows:

The continuity equation;

$$\frac{\partial u^*}{\partial x^*} + \frac{\partial v^*}{\partial y^*} = 0 \tag{1}$$

x-momentum equation;

$$\left(u^* \frac{\partial u^*}{\partial x^*} + v^* \frac{\partial u^*}{\partial y^*} \right) = -\frac{1}{\rho_{nf,0}} \frac{\partial p^*}{\partial x^*} + \frac{\mu_{eff}}{\rho_{nf,0}} \left(\frac{\partial^2 u^*}{\partial x^{*2}} + \frac{\partial^2 u^*}{\partial y^{*2}} \right) \tag{2}$$

y-momentum equation;

$$\left(u^* \frac{\partial v^*}{\partial x^*} + v^* \frac{\partial v^*}{\partial y^*} \right) = -\frac{1}{\rho_{nf,0}} \frac{\partial p^*}{\partial y^*} + \frac{\mu_{eff}}{\rho_{nf,0}} \left(\frac{\partial^2 v^*}{\partial x^{*2}} + \frac{\partial^2 v^*}{\partial y^{*2}} \right) + \frac{1}{\rho_{nf,0}} (\rho\beta)_{nf} \ g \ (T - T_C) \tag{3}$$

Energy equation;

$$\left(u^* \frac{\partial T}{\partial x^*} + v^* \frac{\partial T}{\partial y^*} \right) = \alpha_{nf} \left(\frac{\partial^2 T}{\partial x^{*2}} + \frac{\partial^2 T}{\partial y^{*2}} \right) \tag{4}$$

To convert governing equation into dimensionless form, the following parameters are used;

$$x = \frac{x^*}{L}, \ y = \frac{y^*}{L}, \ u = \frac{u^*}{\alpha_f / L}, \ p = \frac{L^2}{\rho_{fo} \alpha_f^2}, \ v = \frac{v^*}{\alpha_f / L}, \ \theta = \frac{T^* - T_C}{T_H - T_C} \tag{5}$$

In this equations u^* and v^* are dimensional form of the velocity component, p^* is dimensional pressure component, T^* is dimensional temperature, ρ_{fo} is fluid density at T_c temperature, α_f is the thermal diffusivity of fluid.

Here, the Reynolds (Re), Prandtl (Pr), Grashof (Gr) and Richardson (Ri) numbers are defined as:

$$\text{Re} = \frac{U L \rho_{f,0}}{\mu_f} \quad , \quad \text{Pr} = \frac{\mu_f}{\rho_{f,0} \alpha_f} \quad , \quad Gr = \frac{\rho_{f,0}^{\,2} \, g \, \beta_f \, L^3 (T_H - T_C)}{\mu_f^{\,2}} \quad , \quad Ri = \frac{Gr}{\text{Re}^2} \tag{6}$$

where μ is the viscosity, β is the coefficient of thermal expansion and α is the thermal diffusivity of the fluid.

The effective dynamic viscosity of the nanofluid can be presented by models for two phases mixture. In this study the Brinkman model is used.

$$\mu_{eff} = \frac{\mu_f}{(1-\phi)^{2.5}} \tag{7}$$

The density, heat capacity, thermal expansion coefficient, and thermal diffusivity of the nanofluid are as follows, respectively:

$$\rho_{nf,o} = (1-\phi)\rho_{f,o} + \phi \rho_{s,o} \tag{8}$$

$$(\rho c_p)_{nf} = (1-\phi)\rho_f c_{p_f} + \phi \rho_s c_{ps} \tag{9}$$

$$(\rho\beta)_{nf} = (1-\phi)\rho_f \beta_f + \phi \rho_s \beta_s \tag{10}$$

$$\alpha_{nf} = \frac{k_{eff}}{(\rho c_p)_{nf,o}} \tag{11}$$

In this equation Φ is the volume fraction and "nf", "f", and "s" subscripts represents nanofluid, fluid and solid particles, respectively.

For effective thermal conductivity Yu and Choi [11] model is used;

$$\frac{k_{eff}}{k_f} = \frac{k_s + 2k_f + 2(k_s - k_f)(1+\eta)^3 \phi}{k_s + 2k_f - (k_s - k_f)(1+\eta)^3 \phi} \tag{12}$$

In this model, η, which is the ratio of fluid layer thickness to the original particle radius, is fixed to 0.1.

The local Nusselt number for heated walls can be described as;

$$Nu = -\frac{k_{eff}}{k_f} \left. \frac{\partial \theta}{\partial x} \right|_{x=0} \tag{13}$$

Average Nusselt number is obtained from integration of local Nusselt number along the heated wall of the cavity:

$$Nu_a = \int_0^1 Nu \, dy \tag{14}$$

3. Numerical Solution

The aim of the study is to analyze a mixed convection by nanofluid flow and heat transfer inside a square cavity with insulated horizontal walls and isothermal vertical walls maintained at different temperatures and containing an adiabatic square block in the center adiabatic square block. In this study ANSYS Fluent 14 is employed to solve governing equations.

Momentum and energy equations are discretized by second order upwind scheme and the pressure-velocity equation is solved by SIMPLE algorithm.

The numerical code is validated with the study of Khanafer et al. [1] where heat transfer characteristics in a two-dimensional enclosed cavity filled with nanofluid by different Grashof numbers and volume fractions is investigated and Mahmoodi and Sebdani [9] where free convection heat transfer of Cu-water nanofluid inside a square cavity having adiabatic square bodies at its center was studied. The results are shown in Table 2 and Table 3. As seen from the tables, there is a high accurate agreement between present study and the benchmark studies.

Table 2: Comparison of average Nusselt number of the present study with the results of Khanefer et al. [1]

	Gr/ϕ	0.04	0.08	0.12	0.16	0.20
Present study	1000	2.07	2.19	2.30	2.43	2.57
Khanaferet al. [1]	1000	2.11	2.25	2.36	2.57	2.75
Present study	10000	4.33	4.70	4.97	5.24	5.51
Khanafer et al. [1]	10000	4.36	4.68	5.00	5.32	5.68

Table 3: Comparison of average Nusselt number of the present study with the results of Mahmoodi and Sebdani [9]

	Ra/ϕ	0.00	0.05	0.10	0.15	0.20
Present study	10000	2.00	2.09	2.10	2.23	2.27
Mahmoodi and Sebdani [9]	10000	2.00	2.10	2.15	2.20	2.30

4. Results and Discussion

The streamlines and isotherms for various Richardson numbers (Ri=0.1, 1, 10) and the solid volume fractions (ϕ=0%, 5%, 10%) with fixed Prandtl number (Pr=6.2) are presented for Cu-water nanofluids. Fig. 2 depicts the streamlines for different Richardson numbers and volume fractions of water based Cu nanofluid. As seen in the figure, streamlines are in form of eddy current in clockwise rotation direction located in the center of flow area. Due to the adiabatic square block in the center and moving top wall, a new second eddy which is in the clockwise direction is also created. As Richardson number decreases, the second eddy contracts and is dragged to top cold side of the cavity due to the shear forces effect. Besides, as Richardson number decreases the top moving wall intensifies the circulation thus force convection becomes dominant and hydrodynamic boundary layer gets thinner. As nanoparticle volume fraction increases, circulation in the flow intensifies due to the increase in transporting of energy.

Fig. 3 shows isotherms for water based Cu nanofluid with different Richardson numbers and volume fractions. After the isotherms are analyzed, there are heated flowing fluid particles upwards to top wall direction along left side wall and cooled down flowing fluid particles downwards along right side wall. Shear stress increases circulation because of top wall moving to the clockwise direction. Isotherms are more intensive at the below side of hot wall and top side of cold wall. In this way, thermal boundary layer occurs at lateral walls. Isotherms indicate a twisted characteristic around adiabatic block at the center. When the amount of nanoparticles volume fraction increases, as a result of thermal expansion increasing in the cavity, thermal boundary layers get thinner. Furthermore, heat transfer rate enhances dependent upon circulation severity with Richardson number decreasing.

The variation of local Nusselt numbers along hot wall for water based Cu nanofluids for Ri=1 is depicted in Fig. 4 for different volume fractions. As shown in the figure, isotherms are more intensive in the bottom side of the hot wall and temperature gradient decreases along the hot wall. Hence, Nusselt number reaches a maximum value in the bottom side of the hot wall and decreases along the hot wall. If volume fraction increases, local Nusselt values increases too. In contrast to non-mixed fluids, additional high thermal conductive nano-particles, heat transfer rate is increased.

Table 4 gives the average Nusselt numbers for Cu and Ag water based nanofluids at different Richardson numbers and volume fractions. The decreasing of Richardson number and circulation of shear stress enhancement increase heat transfer rate and therefore average Nusselt number increases. The average heat transfer depends strongly on the density of the nanoparticles. Therefore the enhancement in the heat transfer is more pronounced in water-Cu nanofluid comparing with water-Ag nanofluid.
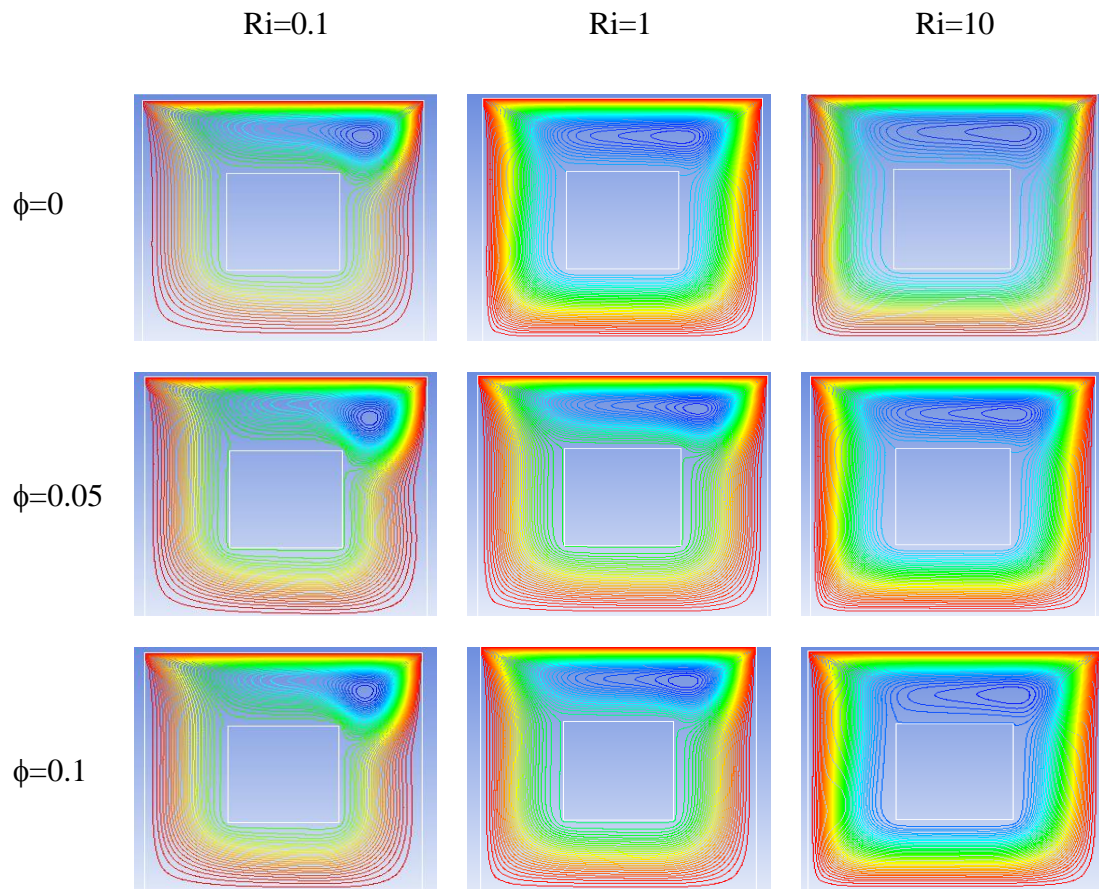
Figure 2. Streamlines of Cu – Water nanofluid in variable Ri Number and volume fraction (Gr=10^4)
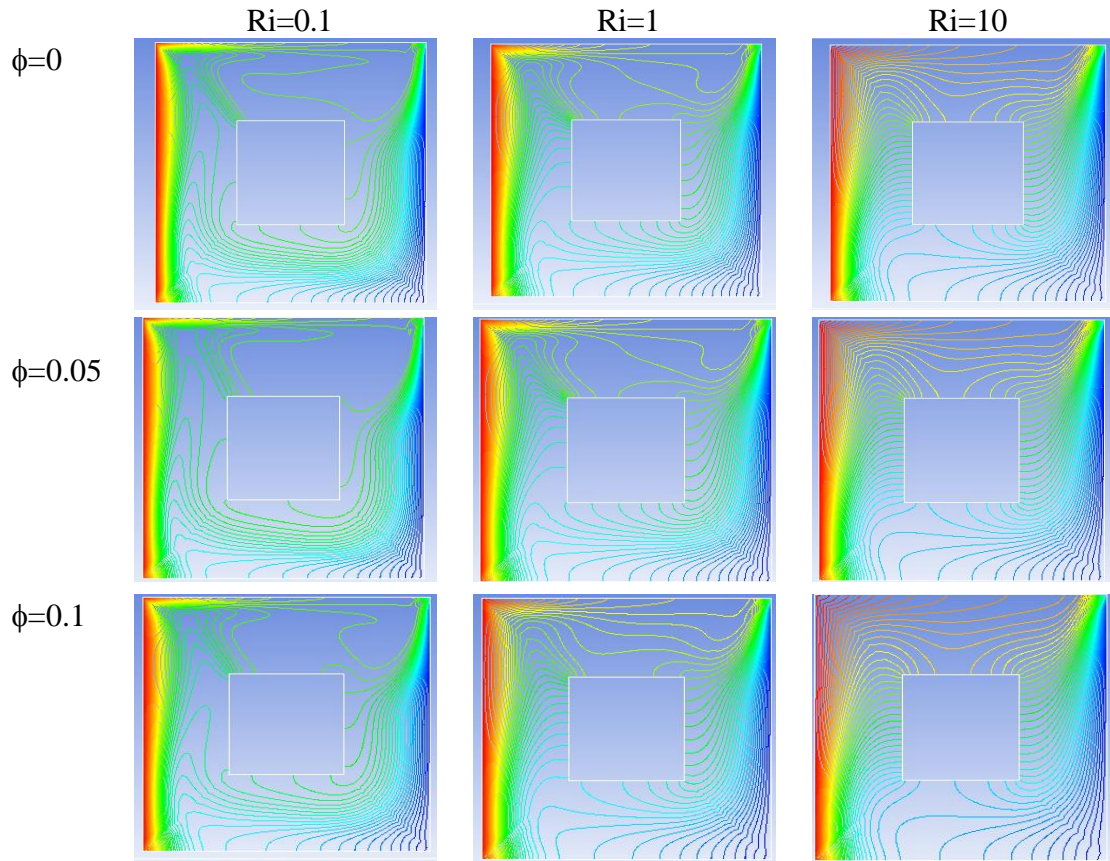
Figure 3. Isotherms of Cu – water nanofluid in variable Ri Number and volume fraction (Gr=10^4)
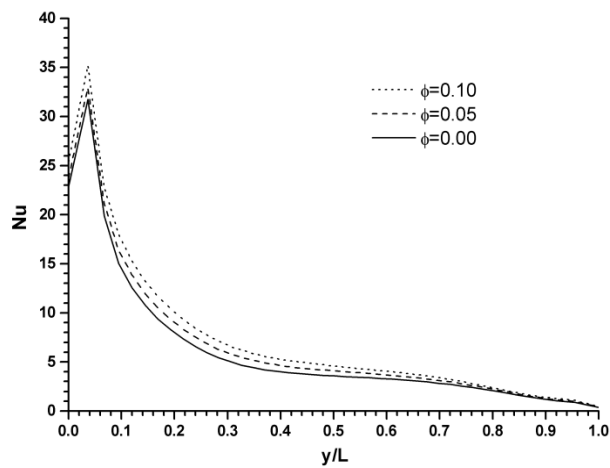
Figure 4. Variation of local Nusselt number of Cu-water nanofluid (Ri =1)

Table 4: The computed average Nusselt number for various Ri numbers and volume fractions

Nu	Cu-Water			Ag-Water		
Ri \ φ	0	0.05	0.1	0	0.05	0.1
10	5.25	5.70	5.80	5.25	5.50	5.70

1	6.70	7.40	7.58	6.70	6.98	7.36
0.1	8.55	10.50	10.63	8.55	9.62	10.19

5. Conclusions

In this study mixed convection of water-based nano-fluids in a square cavity with insulated horizontal walls and isothermal vertical walls maintained at different temperatures and containing an adiabatic square block at the center is investigated numerically. The top wall of cavity moves from left to right with uniform velocity of U. Two different nano-particles, Cu and Ag with solid volume fraction of 0%, 5% and 10% are analyzed in the study. The Grashof number is kept at a constant value of 10^4 and the Reynolds number is varied so that the Richardson number will have values of 0.1, 1 and 10.

The flow and temperature fields, as well as the heat transfer rate of the cavity are influenced by Richardson number and volume fraction. The heat transfer rate increases considerably with a decrease in the Richardson number. As nanoparticle volume fraction increases, circulation in the flow intensifies due to the increase in transporting of energy which results in increase in Nusselt number. The results show that the presence of nanoparticles in the base fluid causes a significant enhancement on heat transfer. The increase in the average heat transfer rate is more pronounced in Cu nanoparticles comparing with Ag nanoparticles.

References

[1] Khanafer, K., Vafai, K. and Lightstone, M. (2003), Buoyancy-Driven Heat Transfer Enhancement in a Two-Dimensional Enclosure Utilizing Nanofluids, *Int. J. Heat Mass Transfer*, 46, 3639–3653.

[2] Ternik,P. andRuldolf, R.(2012) Heat Transfer Enhancement for Natural Convection Flow of Water-based Nanofluidsin a Square Enclosure.*Int. J. Simul. Model* 11(1) 29-39.

[3] Jou, R.Y. and Tzeng, S.C. (2006), Numerical Research of Nature Convective Heat Transfer Enhancement Filled with Nanofluids in Rectangular Enclosures, *Int. Commun. Heat Mass Transfer*, 33, 727–736.

[4] Santra, A.K., Sen, S. and Chakraborty, N. (2008), Study of Heat Transfer Augmentation in a Differentially Heated Square Cavity using Copper–water Nanofluid, *International Journal of Thermal Sciences*, 47, 1113-1122.

[5] Hwang, K.S., Lee, J.H. and Jang, S.P.(2007), Buoyancy-driven Heat Transfer of Water-based Al2O3 Nanofluids in a Rectangular Cavity, *International Journal of Heat and Mass Transfer,* 50, 4003–4010.

[6] Oztop, H.F. and Abu-Nada, E. (2008), Numerical study of natural convection in partially heated rectangular enclosures filled with nanofluids, *International Journal of Heat and Fluid Flow*, 29, 1326-1336.

[7] Ogut, E.B. (2009), Natural convection of water-based nanofluids in an inclined enclosure with a heat source, *International Journal of Thermal Sciences*,48, 2063–2073.

[8] Islam,A.K, Sharif, M.A.R. and Carlson E.S.(2012) Mixed convection in a lid driven square cavity with an isothermally heated square blockage inside.*International Journal of Heat and Mass Transfer,* 55, 5244–5255.

[9] Mahmoodi, M. andSebdani S.M. (2012), Natural convection in a square cavity containing a nanofluid and an adiabatic square block at the center,*Superlattices and Microstructures.*52, 261-275.

[10] Tasnim, S.H. and Collins, M.R.   (2005), Suppressing natural convection in a differentially heated square cavity with an arc shaped baffle*, International Communication in Heat and Mass Transfer,*32, 94–106.

[11] Yu, W. and Choi, S.U.S. (2003), The Role of Interfacial Layer in the Enhanced Thermal Conductivity of Nanofluids: A Renovated Maxwell Model, *J. Nanoparticles Res.,*5, 167–171.

Study of The Shear Modulus of Wood-Based Layered Composites Under Static Load Using Finite Element Method

Łukasz Gołębiowski [1], Tomasz Brynk [1], Piotr Marek [2], Maciej Kowalski [3], Sławomir Krauze [3], Magdalena Jurczyk Kowalska [1]

[1] Warsaw University of Technology, The Faculty of Materials Science and Engineering, lgolebiowski@interia.eu, tbrynk@inmat.pw.edu.p, mjurczyk@meil.pw.edu.pl

[2] Warsaw University of Technology, Institute of Aeronautics and Applied Mechanics, pmarek@meil.pw.edu.pl

[3] Transport Vehicles Upholstery Manufacturer TAPS, krauze@taps.com.pl

Abstract: This article presents research on wood laminates transferring shear stress. These laminates were used for construction of railway seats. Reducing the weight of items and the required nature of the load transfer in the elements of the railway seat during service, requires the application of reinforcement in the form of continuous fibers. The multilayer laminate structure consists of interconnected layers of synthetic and natural fibers which provides rigidity and strength of the construction. Static shear strength tests with simultaneous registration of the in-plane deformation of the samples by means of Digital image Correlation (DIC) were aimed to the designation of critical shear stress and modulus of elasticity in shear. A geometric model simulating the samples used for mechanical properties testing was developed using the finite element method (FEM). The FE models were based on the criteria of strength of single layers of orthotropic composite. The FE model of a few layer wood based composite is useful for its properties optimization and for development of more efficient in large-scale simulations computational models of layered composites.

Keywords: wood-based composites, strength tests, shear modulus, digital image correlation, finite element method

1. Introduction

Plywood is very popular material in transport industry, because it is comparatively cheap, strong, and lightweight [1], [2]. Plywood is made from of thin beech wood sheets. The beech veneers are cut by rotating the trunks about its axis, so they have orthotropic properties in longitudinal (L) and tangential (T) directions of the log [3]. The proposed new type of plywood is used as a composite of a higher quality because of its resistance to cracking and breaking.

The veneers and synthetic or natural fibers are bonded together under heat and pressure with adhesives. The progressive failure of plywood, however, is complicated because of its structure as a layered fiber composite [4]. The aim of this paper is to analyse the behaviour of plywoods structures of interconnected layers of synthetic and natural fibers subjected to shear test during static loads taking into account onset and progression of damage. These analyses will be performed by using a progressive failure technique implemented in the finite element method. The accuracy of the numerical results will be assessed through the comparison between numerical and reference experimental.

2. Theoretical introduction

2.1. Pure shear stress in the inclined section

The test method presented herein includes determination of the shear modulus of wood-based structural panels associated with shear distortion in the plane of the panels. This test method is most useful for determining the modulus of rigidity of orthotropic materials for which modulus of rigidity

cannot be computed from elastic modulus and Poisson's ratios. The shear modulus obtained is that associated with shearing deformation in the plane of the plate.

State of pure shear can be represented as a special case of biaxial stress state. Assuming that the cross-section inclined at an angle of 45° to the axis of symmetry prevail only shear stress "τ" equal to the absolute value of the input stress "σ_1" and "σ_1", then in the shear planes there is equality:

$$|\sigma_1| = |\sigma_2| = \sigma = \tau \qquad (1)$$

The graphical presentation of this condition is Mohr's circle. The maximum stress shear in the planes inclined at an angle of 45 ° to the main directions are $\tau_{max} = \pm \sigma$, and the normal stresses in these directions are zero.
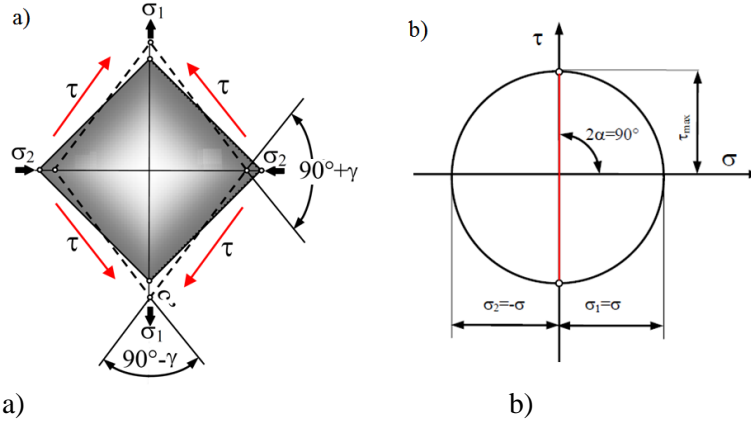
Fig. 1. The biaxial state of stresses: schematic exploration of the dependencies deformation (a), Mohr's circle (b)

The deformation of the sample of square shape is shown in Fig.1a. Since at the edges of the element there is no normal stress, the length of these edges in the deformation process does not change. Vertical diagonal is extended and horizontal diagonal is shortened. The shape of the deformation element shown is in phantom lines. The angles of the deformed element are $(90° + \gamma)$ and $(90° - \gamma)$, where γ" "is the angular deflection . In elastic strain range it can be assumed that the angular deflection "γ" is proportional to the shear stress τ.

$$\gamma = \frac{G}{\tau} \qquad (2)$$

where: G - is a factor proportional called the shear modulus

For the case of pure shear, there is no change in volume during deformation of the element but only a change in its form.

For a square like sample of length "a" and thickness "b" the relationship between shear stress "τ", a force applied "P" takes the form:

$$\tau = \frac{P}{\sqrt{a} \cdot b} \qquad$$

(3)

2.2. Load capacity of orthotropic layer - the maximum stress criterion

Determination of orthotropic layer load capacity is conceptually much more complex than for an isotropic material. For modeling layered composites diverse strength theories are widely used, most of which are defined by the main stress or strain [4] . The numerical analysis is frequently based by the criterion of maximum stress (called biaxial criterion). This criterion states that for a unidirectional composite, safe state is reached when the normal stresses "σ_1" and "σ_2" and the shear stress "τ", do not exceed the strength values in corresponding directions. It can be described the following form:

$$-X_c \leq \sigma_1 \leq X_t \qquad (4)$$
$$-Y_c \leq \sigma_2 \leq Y_t \qquad (5)$$
$$\tau \leq S_{LT} \qquad (6)$$

where: X_t - longitudinal tensile strength, X_c - longitudinal compressive strength, Y_t - transverse tensile strength, Y_c - transverse compressive strength, S_{LT} - shear strength.

Failure criteria for composite laminates are mainly analytical approximations or curve fittings of experimental results and allow the failure of a whole layer to be checked. In the case where any of the above conditions is not met, it is considered that the material may be damaged. The evolution of independent damage variables begin when the corresponding failure criterion for damage initiation is satisfied. The failure criteria of Maximum stress are used here, which involve the strength of veneer in tension and compression, in longitudinal and transverse directions, denoted as X_t, X_c, Y_t, and Y_c, respectively, as well as in-plane shear strength, S_{LT} [5].

3.Research methodology
3.1. Test material

For manufacturing new types of plywood the following components were used:
- beech veneers with thickness of 1,5 mm (Fibra spol. s r. o., Slovakia), (Fig. 2a);
- fiberglass mesh with thickness of 0,25 mm (Fig. 2b);
- flax roving with thickness of 0,32 (Safilin S.z o.o, Poland), (Fig. 2c);
- resin urea-formaldehyde "UF" (Kronocol U300, Czech Republic), UF resin is typically used in the manufacture of standard plywoods.

a)   b)   c)
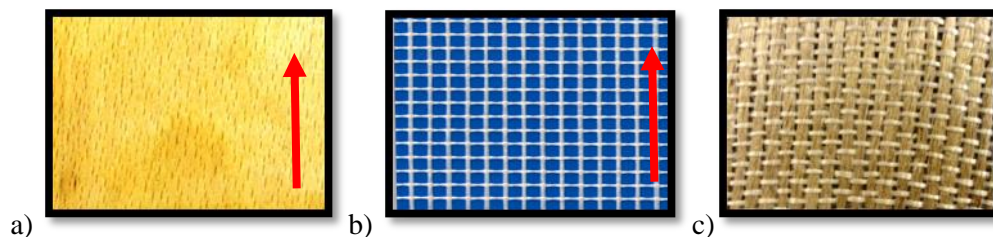
Fig. 2. The types of materials used: beech veneers with the preferred direction (a) fiberglass mesh with the preferred direction (b), flax roving (c)

3.2. Preparation of plywood

New type of plywood is manufactured by gluing the multilayer structure consisting of layers of ply veneers and synthetic and natural fibers. The plywood boards were prepared by the following procedure:
- Drying: the beech veneers were cut to the dimensions of 400 mm x 400 mm x 1,5 mm and dried to approximately 6-12wt % moisture content.
- Adhesive application: the adhesive was applied to both sides of a every second sheet of veneer using a glue applicator roller
- Lay-up: the beech veneers were arranged in a specific configuration in the 3-layer plywoods and the 3-layer plywoods reinforced with glassfiber mesh or flax roving . The types of veneers arrangement in each plywood are shown in figure 3.
- Hot-pressing: the glued plywood boards were hot-pressed at specific pressure of 1,5 MPa and temperature of 100 ºC over 15 minutes.
- Conditioning and cutting: to relieve drying stresses plywood boards were conditioned in a conditioning room maintained at a relative humidity of 60 % and temperature of 23 ºC for 6 days prior to properties evaluation. After conditioning samples were cut from each panel for testing of the required properties.
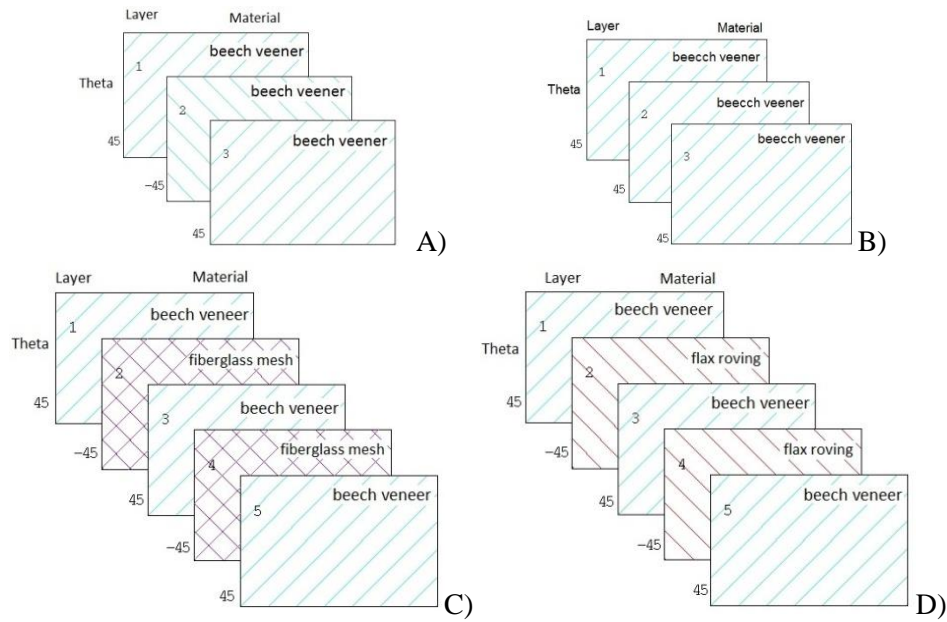
Fig. 3. Laminar configuration in plywoods: type A, B, C and D

Three types of plywoods were examined:
- ➢ type A – three adjacent layers with the grain of the beech wood arranged parallel to the adjacent layers;
- ➢ type B – three adjacent layers with the grain of the beech wood rotated relative to adjacent layers by 90 degrees;
- ➢ type C – second and fourth layer of fiberglass mesh;
- ➢ type D – second and fourth layer of flax roving.

3.3. Shear test during static load and results

The test method is primarily designed for material in which orientation of the individual fibers is parallel or perpendicular to the edge of the specimen [6] (Fig.4a).
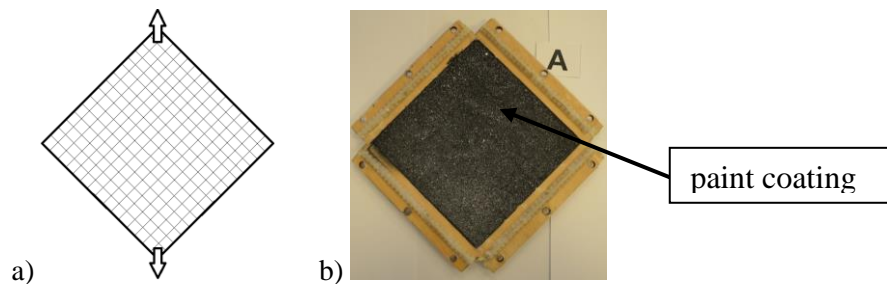
Fig. 4. Orientation of the fibers (a), the sample of type A with a paint coating (b)

The samples for testing were closed by the system shown in Fig. 5.
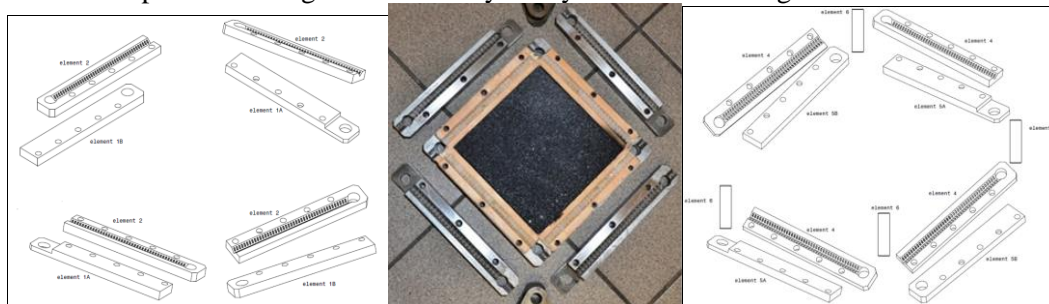
Fig. 5. Closing system

The deformation was measured by means of Digital Image Correlation (DIC) method. Digital Image Correlation (DIC) is a full-field image analysis method, based on grey value digital images, that can determine the contour and the displacements of an object under load in two dimensions [7], [8]. 2-D digital image correlation used with the camera's axis perpendicular to the object surface (Fig. 6.).

Due to rapid new developments in high resolution digital cameras for static as well as dynamic applications, and computer technology, the applications for this measurement method has broadened and DIC techniques have proven to be a flexible and useful tool for deformation analysis.

Stress measurements were carried out using static materials testing machine "Zwick/Roell Z250". This static machine operates with loads up to 250kN. Samples were loaded by a max force of +16,3kN at a 1 mm/min crosshead speed and. A photograph of testing apparatus is shown in Fig. 7.
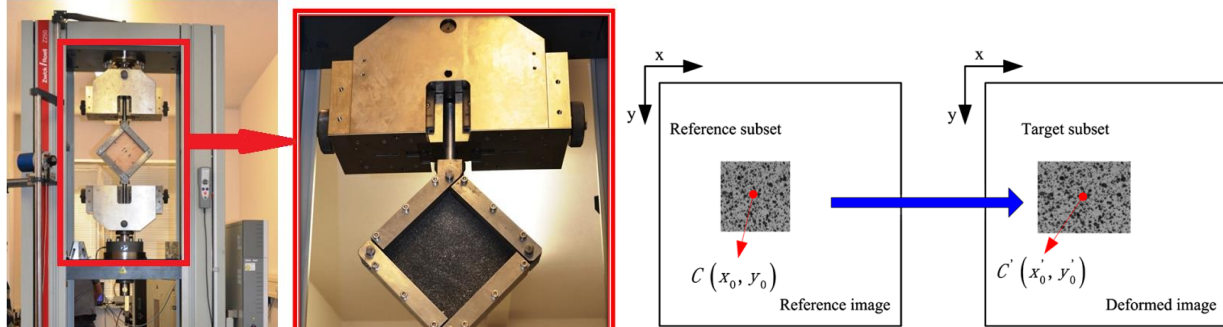
Fig. 6. Deformed evaluation
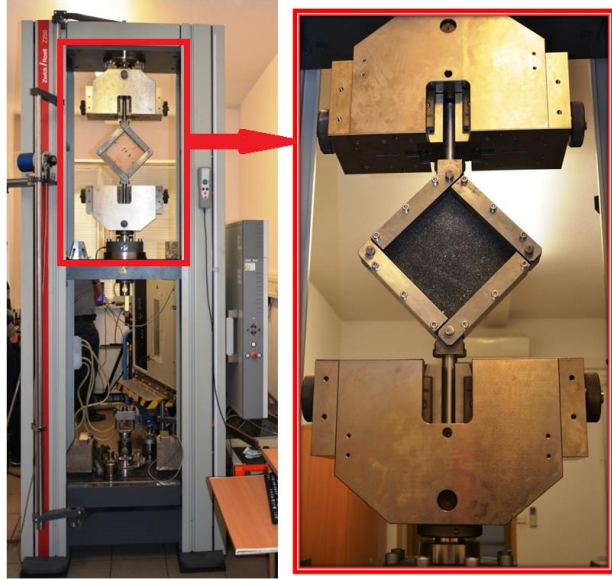
Fig. 7. Static testing machine Zwick/Roell Z250 and plane of the sample coated with a paint coating for the measurement digital image correlation.

The typical failure of the specimens is shown in Fig. 8.

Fig. 8. Typical failure of plywood specimens in sample type of A and C; the initial state and destruction

The shear tests of beech veneers in bias directions [45] of their fiber orientation show the fiber bundle rupture in shear tension and cracking along the fibers. The fractures usually happens on the entire samples surface, as it is shown in Fig. 8.

The linear correlation coefficient of the graph of $\tau = f(\gamma)$ is a measure of the shear stress modulus, as it is shown in Fig. 9.
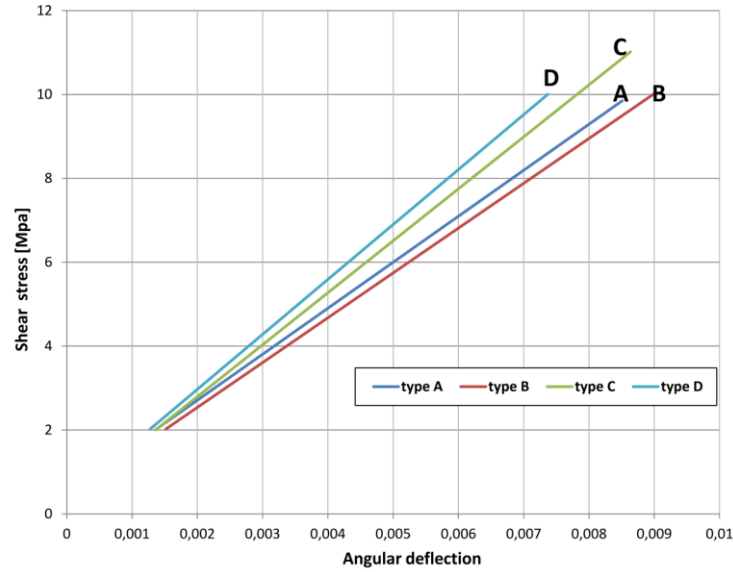
Fig. 9. The range of linear correlation (shear stress)/(angular deflection) of experimental shear test

Table 1. Material properties of plywood obtained by the strength shear test

Sample type	G (MPa)	h (mm)
A	1102	3,3
B	1079	3,3
C	1238	3,8
D	1321	3,94

In order to simulate properly the progressive failure of plywood, we need to model the mechanical behavior of its constituents. The formula for the shear modulus of individual plywood is presented below:

$$G = \frac{3G_1 h_1 + 2G_2 h_2}{3h_1 + 2h_2}$$

(7)

where: G_1 - shear modulus of beech veneer;
G_2 - shear modulus of fiberglass mesh layer;
h_1 - thickness of beech veneer;
h_2 - thickness of fiberglass mesh layer.

The shear modulus of the beech veneer G_1 was adopted from the shear strength test for simple type A and B.
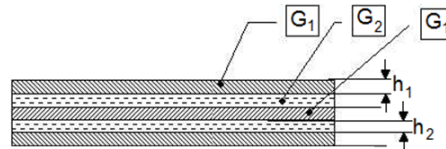
Fig. 10. Analytical model of a five-layers sample

4.   Shear test simulations and results

A geometric model simulating the samples used for testing mechanical properties was developed using the finite element method. Numerical analysis of stresses were carried out using ANSYS system. Four-nods element with six degrees of freedom type "shell 181" were used.

Calculations were performed for plywood reinforced with continuous synthetic and natural fibers, for which the material properties are presented in the Table 2. Young's modulus and Poisson's ratios were adopted from the tensile strength tests.

Table 2. Material properties adopted for the FE model

Layer	E_L (MPa)	E_T (MPa)	v_{LT}	G_{LT} (MPa)
Beech wood	15700	660	0,3	1080
Fiberglass mesh	5000	4000	0,14	2000
Flex roving	4000	400	0,3	2000

A progressive failure technique has been implemented in ANSYS. The user material routine, is used to define material stress strain relation, the mechanical constitutive behavior of materials. The accepted mechanical properties of cohesive elements and their failure parameters are chosen to correspond to the shear strength determined experimentally. The mechanical properties are given in Table 3.

Table 3. Mechanical properties of different type of layers

Layer	X_t (MPa)	X_C (MPa)	Y_t (MPa)	Y_C (MPa)	S (MPa)
Beech wood	100	-90	9	-9	18
Fiberglass mesh	136	- 80	10	-10	35
Flex roving	150	-50	9	-9	35

The numerical models plywood were conducted using one types of orientation of fibers of the layers in the loading in bias directions [-45/45] to the loading direction. The layers haven a thickness: beech veneer - 1,1mm; fiberglass - 0,25 mm; flax roving - 0,32 mm. The load capacity was tested under shear stresses.
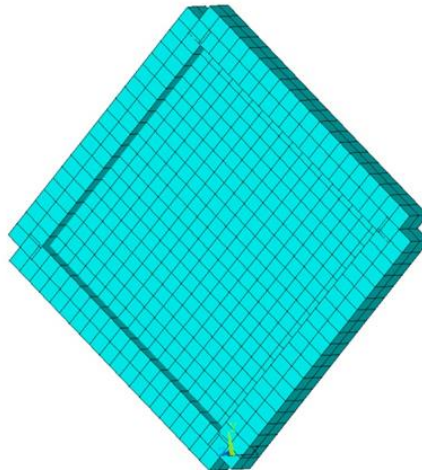
Fig. 11. Finite element mesh

Numerical results obtained using the developed procedure for the specimen are described in Fig.12-14 and have been compared with experimental results.

Table 4. Comparison between the numerical s and test experimental results

Type of simple	Final Failure Load experimental [kN]	Failure Load [kN] FEM-beech wood layer	Failure Load [kN] FEM-fiberglass layer	Failure Load [kN] FEM-flax roving layer
A	14,4	14		
B	15,9	17	18	
C	16,3	18		18,5
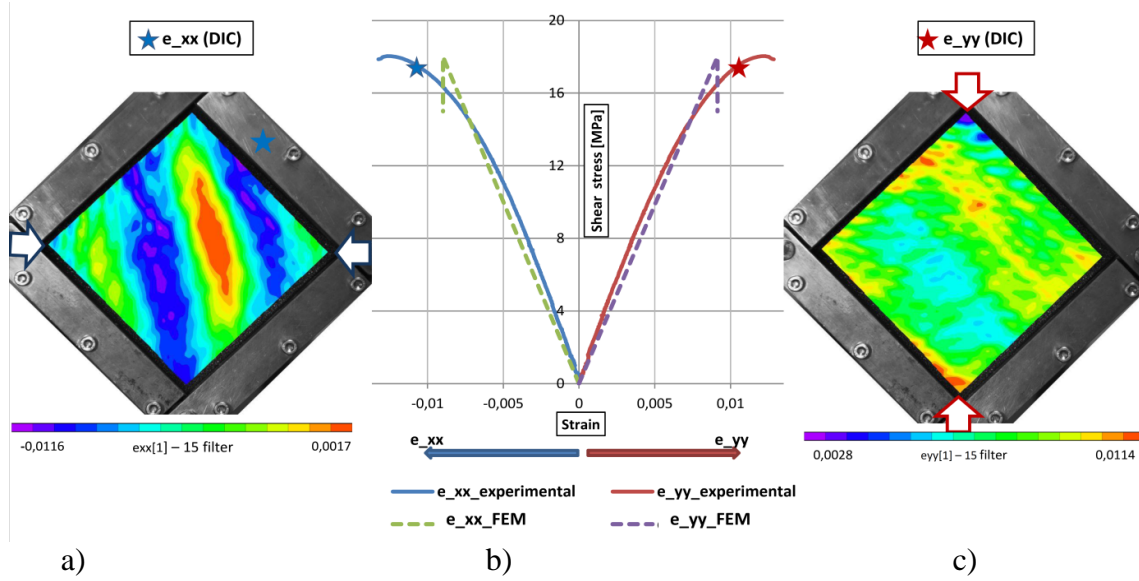
Fig. 12. The sample of type B: strain distribution in X (a) and Y (c) direction; shear stress vs strain graphs received from experimental shear test.
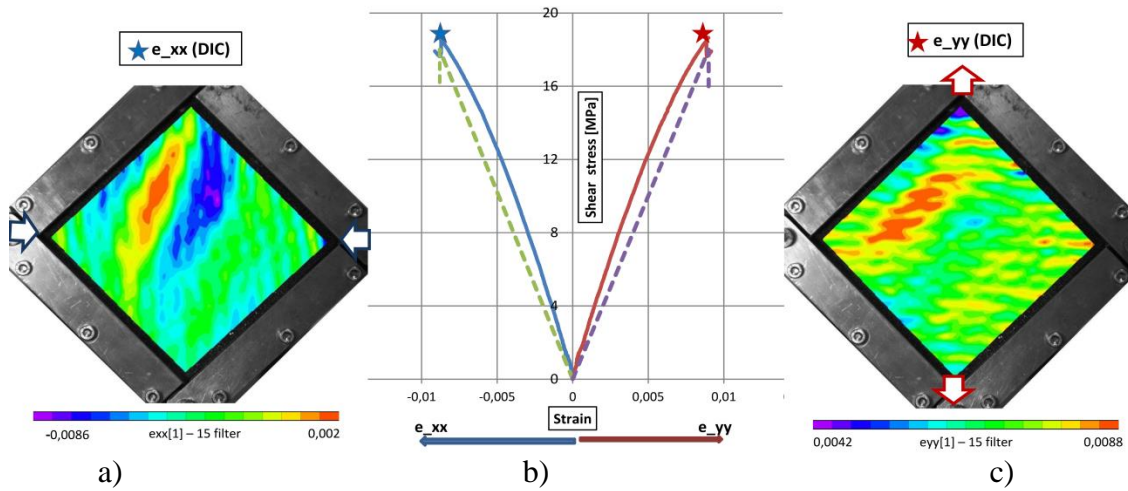
Fig. 13. The sample of type C: strain distribution in X (a) and Y (c) direction; shear stress vs strain graphs received from experimental shear test.

a)   b)   c)
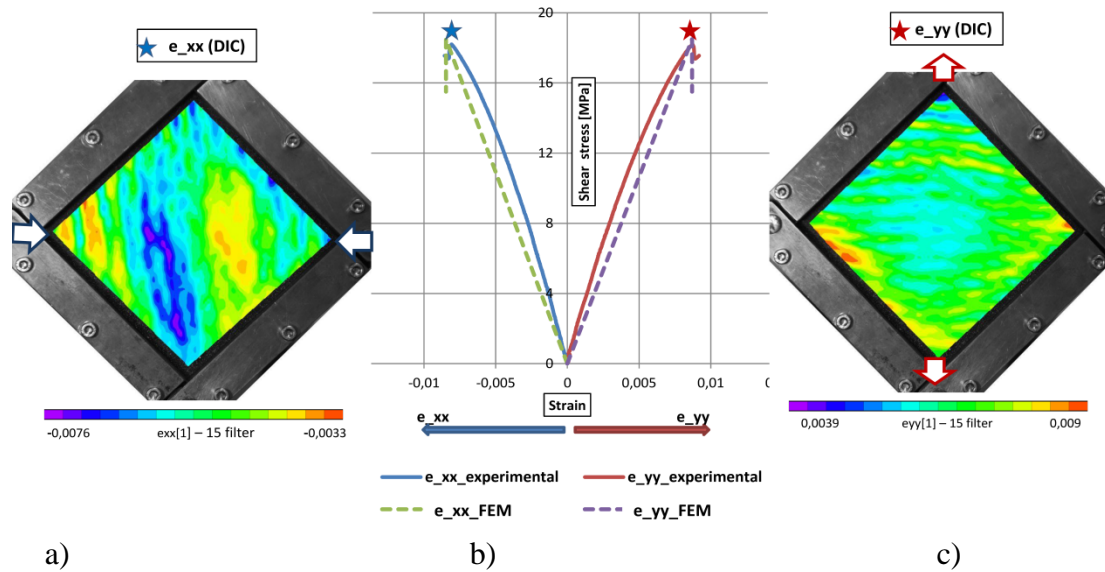
Fig. 14. The sample of type D: strain distribution in X (a) and Y (c) direction; shear stress vs strain graphs received from experimental shear test.

a)   b)   c)
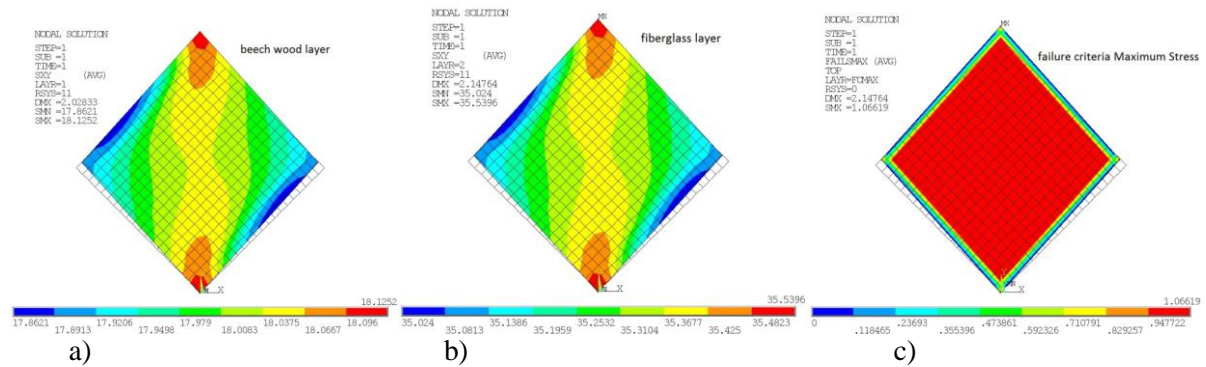
Fig. 15. The sample of type C: shear stress distribution after exceeding the load capacity of the plywood in the individual layers; beech wood layer a); fiberglass layer (b); percentage of damage at 18 kN (c)

a)   b)   c)
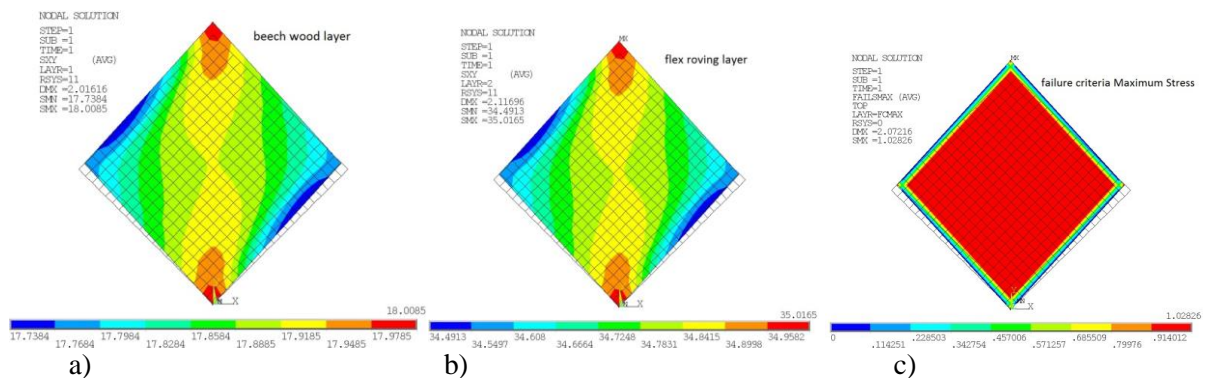
Fig. 16. The sample of type D - shear stress distribution after exceeding the load capacity of the plywood in the individual layers; beech wood layer a); fiberglass layer; percentage of damage at 18,5 kN (c)

The obtained results are very encouraging. It is possible to recognize in Fig.12-14 correspondence between the numerical results and experimental data in terms of stiffness of the structure (measured as slope of the shear stress versus strain graph).

It is worth noting that failure does places in all layers a throughout the specimen. The percentage of cracked layer computed taking into account the criterion of maximum stress is shown in Fig.15-16. In this case, the damage develops on the entire surface of the sample and propagates in the direction of the applied load.

5. Conclusions

The FE model of plywood includes failure criteria and a layer discount technique for taking into account the onset and progression of intra laminar damage. By using this model, using composite structures have been analysed and results have been compared against experimental results.
 A good agreement between the numerical results and the experimental data both in terms of global structural behaviour and failure loads has been obtained.
It can be used for optimization of plywood lay-up. The model is computationally efficient enough for shear test simulations. The FE model of plywood is capable of progressive failure investigation giving better understanding of this complex process.

6. References

 [1] RAI A., JHA C.,"Natural fibre composites and its potential as building material", Development Officer, BMTPC, New Delhi

[2] BROUWER W.D., *"Natural fibre composites saving weight and cost with renewable materials",* Centre of Lightweight Structures TUD-TNO Delf, The Netherlands

[3] IVANOV I., SADOWSKI T., *"Numerical modelling and investigation of plywood progressive failurein CT tests",* Computational Materials Science 45 (2009) 729–734

[4] GREXA, F. POUTCH, D. MANIKOVA, H. MARTVONOVA, A. BARTEKOVA, *"Intumescencein fire retardancy of lignocellulosic panels",* Polymer Degradation and Stability 82 (2003) 373–377.

[5] ŻOCHOWSKI M., JAWORSKI A., KRZESIŃSKI G., ZAGRAJEK T., "*Mechanika materiałów i konstrukcji Tom 2",* wydawnictwo: Oficyna Wydawnicza Politechniki Warszawskiej (2013) 175

[6] OCHELSKI S., *„Metody doświadczalne mechaniki kompozytów konstrukcyjnych",* Wydanie 1 WNT, (2005) 146

[7] ŠTAMBORSKÁ, M., *Application of Two-Dimensional Digital Image Correlation for Measurement of Plastic Deformations*, Transcom, 2011, ISBN 978-80-554-0375-5, p. 195-198

[8] TREBUŇA, F., ŠIMČÁK, F."*Príručka experimentálnej mechaniky",* TypoPress, Košice, 2007, ISBN 970-80-8073-816-7

Acknowledgements

Effect of Activation Temperature on Properties of Activated Carbon From Orange Peel by Zinc Chloride

Gülden Demir, Dilek Angın

Department of Food Engineering, Faculty of Engineering, Sakarya University, Esentepe Campus 54187,
Sakarya, Turkey
guldn.demir@hotmail.com, angin@sakarya.edu.tr

Abstract: Activated carbons with high surface area and pore volume are carbonaceous materials that can be produced by physical and chemical activation processes. In this study, activated carbons were prepared by chemical activation with zinc chloride ($ZnCl_2$) of the orange peel. The influence of activation temperature on the yield, surface and chemical properties of the activated carbons were investigated. This purpose, the orange peel was activated at temperatures ranging from 500 °C to 900 °C, heating rate of 5 °C min^{-1} and a $ZnCl_2$:orange peel impregnation ratio of 3:1 under nitrogen atmosphere (150 cm^3 min^{-1}). The highest BET surface area was achieved as 1779.48 m^2 g^{-1}. The chemical properties of the activated carbons were examined by proximate and ultimate analysis. As a result, it can be said that the orange peel can be effectively used as a raw material for the preparation of activated carbon with $ZnCl_2$ as activating agents. Also, the activated carbon obtained in this study can be used as a very promising adsorbent for pollution control and other applications.

Keywords: Orange peel, zinc chloride, activated carbon, characterization.

1 Introduction

Traditionally, orange peels were processed to obtain the volatile and nonvolatile fractions of essential oils and flavoring in the carbonated drinks, ice creams, cakes, air-fresheners, perfumes and cosmetic products [1]. Besides, orange peels have been reported to have germicidal, antioxidant and anti-carcinogenic properties as a remedy against breast and colon cancer, stomach upset, skin inflammation, muscle pain, and ringworm infections [2]. However, the application of these extracted constituents is limited due the overall demands for these value-added products are relatively insignificant. Therefore, it is necessary to find a rapid and easy route towards upgrading of the citrus processing biomass. Activated carbons have widely used as adsorbents because of its high adsorptive capacity. Moreover, activated carbons are usually used in the separation and purification for aqueous solutions. Hence, activated carbons have played an important role in the chemical, pharmaceutical and food industries. Activated carbons can be produced by physical or chemical activation [3]. The combination of the chemical and physical activation coverage of nitrogen adsorbed on the adsorbent surface, processes leads to the production of activated carbon with while the characteristics of the pore structure and pore specific surface properties [4]. Chemical activation involves impregnation of the raw material with chemicals such as phosphoric acid [4], potassium hydroxide, and zinc chloride [4] . Among the numerous dehydrating agents, zinc chloride in particular is the widely used chemical agent in the preparation of activated carbon. Knowledge of different variables during the activation process is very important in developing the porosity of carbon sought for a given application [4]. Activated carbons can be produced from different raw carbon resources like lignite, peat, coal, and biomass resources such as wood, sawdust, bagasse [5]. In recent years, a lot of research has been reported on activated carbons production from different precursors such as acorn shell [6], waste tea [7], rice-straw [8], pomegranate seeds [9], piassava fibers [10], char [11],etc.

Chemical activation using $ZnCl_2$ has been reported by many researchers. Several materials such as sludge [4], nuts [12], olive stone [13], pistachio shells [14], cassava peel [15], oak cups pulp [16], oil palm shell [17], and cattle manure compost [18] and have been used in the preparation of activated carbons by $ZnCl_2$ activation.

In this study, activated carbons were prepared by chemical activation with zinc chloride ($ZnCl_2$) of the orange peel. The influence of activation temperature on the yield, surface areas and chemical properties of the activated carbons were investigated. This purpose, the orange peel activated at temperatures ranging from 500 °C to 900 °C, heating rate of 5 °C min^{-1} and a $ZnCl_2$:orange peel impregnation ratio of 3:1 under nitrogen atmosphere.

2 Materials and Methods

2.1 Material

Orange peel was obtained from LİMKON Fruit Juice Factory, (Adana-TURKEY). It was dried at 103 °C for 24 h, subsequently crushed and sieved prior to activation. For an activation agent $ZnCl_2$ from MERCK chemical material was chosen.

2.2 Preparation of Activated Carbon

In this study, chemical activation of orange peel was performed using zinc chloride. The impregnation ratio was calculated as the ratio of the weight of the used orange peel to the weight of $ZnCl_2$ in solution. The orange peel was mixed with $ZnCl_2$, in a ratio ZnCl2:orange peel mass ratio of 3:1. Carbonization of the impregnated samples was carried out in a 316 stainless steel tubular reactor with a length of 90 mm and internal diameter of 105 mm (Protherm PTF 12) under nitrogen atmosphere (as Fig. 1).

Figure 1 The tubular reactor

About 10 g of the impregnated sample was placed on a ceramic crucible in the reactor and heated up to the final carbonization temperature under the nitrogen flow (150 cm^3 min^{-1}) at heating rate of 5 °C min^{-1} and held for 1 h at this final temperature. The final carbonization temperature was varied from 500 °C to 900 °C. The resulting solids after carbonization were boiled at about 90 °C with 100 mL of 1 N HCl solution for 30 min to leach out the activating agent, filtered and rinsed by warm distilled water several times until the pH value was 6-7. Finally, they were then dried at 105±3 °C for 24 h. The yield of activated carbon was calculated from the following equation:

$$\text{Yield of activated carbon} = \frac{\text{Final weight of activated carbon}}{\text{Initial weight of impregnated sample}} \times 100$$

(1)

2.3 Characterization of Activated Carbon

The contents of C, H and N of the activated carbons were measured using a CARLO ERBA model EA 1108 Elemental Analyser. The oxygen contents of activated carbons were calculated by difference. The determination of the porosity of orange peel and activated carbons were performed using physical adsorption of N_2 at 77 K (Quantachrome, NovaWin2). The surface areas were determined from nitrogen adsorption data by using Quantachrome software. Adsorption data were obtained over the relative pressure, P/Po, range from 10^{-5} to 1. The sample was degassed at 300 °C under vacuum for 3 h. The N_2 apparent surface area was calculated by using the BET (Brunauer, Emmett and Teller) equation within the 0.01–0.2 relative pressure range. Ash, volatile matter and fixed carbon contents of activated carbon were determined by the ASTM D 3174 and ASTM D 3175. Fixed carbon content was determined by difference.

3. Result and Discussion

The results of proximate and ultimate analyses of the orange peel are given in Table 1. As can be seen from the table, orange peel contains 2.8% ash, 82.7% volatile matter, and 14.5% fixed carbon. The C, H, N and O contents of orange peel were found 45.05%, 6.29%, 1.66%, 53.03%, respectively. Sulfur in orange peel was trace amounts. Also, the surface area of orange peel was determined as 0.704 m^2 g^{-1} that it was considered as a raw material for production of activated carbon.

Table 1: Proximate and ultimate analysis of orange peel

Characteristics	Orange peel
Moisture content (%)	3.7
Proximate analysis(%)	
Volatile Matter	82.7
Ash	2.8
Fixed carbon*	14.5
Ultimate analysis(%)	
Carbon	45.05
Hydrogen	6.29
Nitrogen	1.66
Sulfur	0.03
Oxygen*	53.03
BET surface area (m^2/g)	0.704

The yield is an important measure of the feasibility of preparing activated carbon from a given precursor. Activation temperature plays an important role on the yield of activated carbon. The effects of the activation temperature on the yields of activated carbon are shown in Fig. 2.

It was found out that with increasing activation temperature, the activated carbon yields decreased for impregnation ratio ($ZnCl_2$:orange peel) of 3:1 (wt%). When the activation temperature increased from 500 to 900 °C, the activated carbon yield decreased from 12.23% to 6.71%. As the temperature increases, there is a transition from the primary carbonization stage to the secondary stage. Accordingly, the chemical structure disintegrates even more as a result of which more tar is released and the activated carbon yield decreases [3].

The results of the ultimate and proximate analysis and BET (Brunauer–Emmett–Teller) surface areas of activated carbons obtained at different activation temperatures are shown in Table 2.
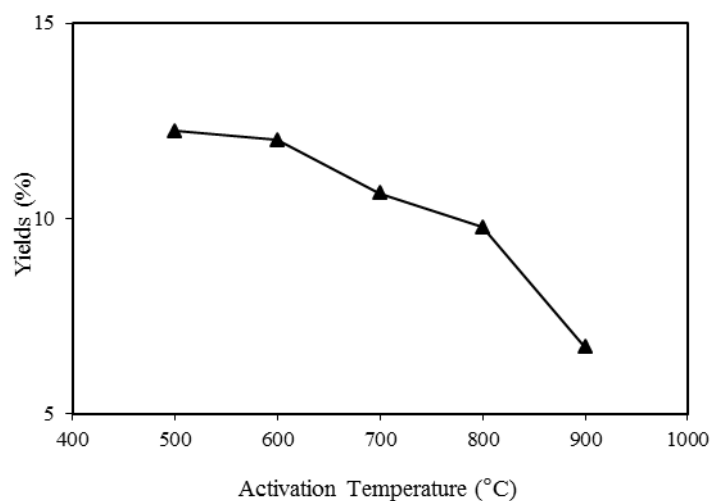
Figure 2 Effect of activation temperature on the yield of activated carbons.

Table 2: Effect of activation temperature on the surface and chemical properties of activated carbons

Characteristics	Activation Temperatures (°C)				
	500	600	700	800	900
Moisture content (%)	8.37	5.50	7.18	2.80	2.94
Proximate analysis(%)					
Volatile Matter	9.18	9.17	8.54	7.95	6.58
Ash	0.57	0.54	0.57	0.59	0.23
Fixed carbon*	90.25	90.29	90.89	91.46	93.19
Ultimate analysis(%)					
Carbon	56.57	67.41	76.75	87.96	91.92
Hydrogen	2.94	2.84	2.57	2.49	2.25
Nitrogen	0.94	0.94	1.12	0.79	0.47
Sulfur	0.08	0.12	0.10	0.11	0.16
Oxygen*	39.47	28.69	19.46	8.65	5.20
BET surface area (m^2g^{-1})	1779.48	1531.46	1471.89	1334.69	1318.68

*By difference.

The moisture contents of activated carbons obtained at different activation temperatures were observed to change between 2.80-8.37 wt.%. The volatile matter and ash contents of the activated carbons decreased with increasing activation temperature for 3:1 impregnation ratio. There was a consequent increase in the fixed carbon content of activated carbons. The ash contents of the activated carbons were low, all beings less than 1.0 wt.%. In similar studies with increasing activation temperature, fixed carbon contents of activated carbons obtained from sugar cane bagasse, pomegranate seeds, pistachio-nut shells and natural fibre textile waste were increased [19-22].

With an increase in the activation temperature from 500 to 900 °C, the carbon content of the activated carbons increased from 56.57 to 91.92 wt.%; however, the oxygen and hydrogen contents decreased from 39.47 to 5.20 wt.% and from 2.94 to 2.25 wt.%, respectively. Also, nitrogen content changed in the range of 0.47-1.12 wt.%. The carbon contents of activated carbons increased when compared to orange peel (45.05 wt.%). This trend in the elemental analysis was found similar in activated carbons produced from other precursors such as waste tea and nutshells [7-23].

In the chemical activation, the final activation temperature is important process parameters in determining the surface area of the activated carbon. When the activation temperature was increased from 500 to 900 °C, the BET surface area decreased significantly. The highest surface area was obtained at 500 °C (1779.48 m^2g^{-1}). By increasing temperature, structural ordering, pore widening and/or the coalescence of neighboring pores seem to predominate, leading to a decrease in the surface area [4].

4. Conclusion

Activated carbons were prepared from orange peel by zinc chloride ($ZnCl_2$:orange peel=3:1) activation method at different activation temperatures. According to the results of this study, it is found that the effect of activation temperature on the yield, surface and chemical properties of activated carbon were quite high. It was found that the specific surface area of the activated carbon were 1779.48 m^2g^{-1}, at a final carbonization temperature of 500 °C and at an impregnation of $ZnCl_2$:orange peel=3:1. As a result, it can be said that the orange peel can be effectively used as a raw material for the preparation of activated carbon using chemical activation procedure. In addition, the activated carbon product with high surface area obtained in this study can be used as a very promising adsorbent for pollution control and other applications.

5. References

[1]   Shiminig, L., Slavik, D., Chi-Tang, H. 2008. Polymethoxyflavones: chemistry, biological activity, and occurrence in orange peel. *Dietary Supplements (13),* 191–210.

[2] Foo, K.Y., Hameed, B.H. 2012. Preparation, characterization and evaluation of adsorptive properties of orange peel based activated carbon via microwave induced K_2CO_3 activation. *Bioresource Technology (104)*, 680-681.

[3]   Angın, D. 2013. Production and characterization of activated carbon from sour cherry stones by zinc chloride. *Fuel (115),* 804-811.

[4] Khalili, N.R., Campbella, M., Sandib, G., Golas, J. 2000. Production of micro- and mesoporous activated carbon from paper mill sludge I. Effect of zinc chloride activation. *Carbon-38,* 1905-1915.

[5] Gratuito, M.K.B., Panyathanmaporn, T., Chumnanklang, R.A., Sirinuntawittaya, N., Dutta, A. 2008. Production of activated carbon from coconut shell: Optimization using response surface methodology. *Bioresource Technology 99 (11),* 4887-4895.

[6] Saka, C. 2012. BET, TG–DTG, FT-IR, SEM, iodine number analysis and preparation of activated carbon from acorn shell by chemical activation with $ZnCl_2$. *Journal of Analytical and Applied Pyrolysis 95 (1),* 21-24

[7] Yagmur, E., Ozmak, M., Aktas, Z. 2008 . A novel method for production of activated carbon from waste tea by chemical activation with microwave energy. *Fuel 87 (15-16)*, 3278-3285.

[8] Oh, G.H., Park, C.R. 2002. Preparation and characteristics of rice-straw-based porous carbons with high adsorption capacity. *Fuel 81 (3),* 327-336.

[9] Uçar, S., Erdem, M., Tay, T., Karagöz, S. 2009. Preparation and characterization of activated carbon produced from pomegranate seeds by $ZnCl_2$ activation. *Apllied Surface Science 255 (21),* 8890-8896.

[10] Avelar, F.F., Bianchi, M.L., Gonçalves, M., Mota, E.G. 2010. The use of piassava fibers (Attalea funifera) in the preparation of activated carbon. *Bioresource Technology 101 (12),* 4639-4645.

[11] Azargohar, R., Dalai, A.K. 2008. Steam and KOH activation of biochar: Experimental and modeling studies. *Microporous and Mesoporous Materials 110 (2-3),* 413-421.

[12] Mohanty, K., Jha, M., Meikap, B.C., Biswas, M.N. 2005. Removal of chromium (VI) from dilute aqueous solutions by activated carbon developed from Terminalia arjuna nuts activated with zinc chloride. *Chemical Engineering Journal (115),* 3050-3051.

[13] Kula, İ., Uğurlu, M., Karaoğlu, H., Çelik, A. 2008. Adsorption of Cd(II) ions from aqueous solutions using activated carbon prepared from olive stone by $ZnCl_2$ activation. *Bioresource Technology (99),* 492-501

[14] Dolaş, H., Şahin, Ö., Saka, C., Demir, H. 2011. A new method on producing high surface area activated carbon: The effect of salt on the surface area and the pore size distribution of activated carbon prepared from pistachio shell. *Chemical Engineering Journal (166)*, 191-197.

[15] Pirajan, J.C.M., Giraldo, L. 2010. Study of activated carbons by pyrolysis of cassava peel in the presence of chloride zinc. *Journal of Analytical and Applied Pyrolysis (90),* 288-290.

[16] Timur, S., Kantarlı, I.C., Önenç, Ş., Yanık., J. 2010. Characterization and application of activated carbon produced from oak cups pulp. *Journal of Analytical and Applied Pyrolysis (89)*, 129-136.

[17] Hesas, R.H., Niya, A.A., Daud, W.M.A.W., Sahu, J.N. 2013. Comparison of oil palm shell-based activated carbons produced by microwave and conventional heating methods using zinc chloride activation. *Journal of Analytical and Applied Pyrolysis (105),*176-184.

[18] Qian, Q., Machida, M., Tatsumoto, H. 2007. Preparation of activated carbons from cattle-manure compost by zinc chloride activation. *Bioresource Technology (98)*, 353-360.

[19] Carrier, M., Hardie, A.G., Uras, Ü., Görgens, J., Knoetze, J.H. 2012. Production of char from vacuum pyrolysis of South-African sugar cane bagasse and its characterization as activated carbon and biochar*. Journal of Analytical and Applied Pyrolysis (96),* 24-32.

[20] Lua, A.C., Yang, T. 2004. Effects of vacuum pyrolysis conditions on the characteristics of activated carbons derived from pistachio-nut shells. *Journal of Colloid and Interface Science (276)*, 364-372.

[21] Uçar, S., Erdem, M., Tay, T., Karagöz, S. 2009. Preparation and characterization of activated carbon produced from pomegranate seeds by $ZnCl_2$ activation. *Applied Surface Science (255)*, 8890-8896.

[22] Williams, P.T., Reed, A.R. 2004. High grade activated carbon matting derived from the chemical activation and pyrolysis of natural fibre textile waste. *Journal of Analytical and Applied Pyrolysis (71),* 971-986.

[23] Aygün, A., Karakaş, S., Duman, I. 2003. Production of granular activated carbon from fruit stones and nutshells and evaluation of their physical, chemical and adsorption properties. *Microporous and Mesoporous Materials* (*66),* 189–195.

Acknowledgement

Determination of the Solid-Liquid Equilibrium of Mixtures of Sugar Alcohols for Their Use as Phase Change Materials

<u>G. Diarce</u> [1], I. Gandarias [2], S. Gómez-Cavia [1], A. García-Romero [1], J.M. Sala [3]

[1] ENEDI Research Group, Dpto. de Ingeniería Minera, Metalúrgica y Ciencia de los Materiales, Escuela Universitaria de Ingeniería Técnica de Minas y Obras Públicas, University of the Basque Country UPV/EHU, Rafael Moreno Pitxitxi 2, Bilbao, 48013, Spain. E-mail: gonzalo.diarce@ehu.es
[2] SUPREN Research Group, Dpto. de Ingeniería Química y del Medio Ambiente, Escuela Técnica Superior de Ingeniería de Bilbao, University of the Basque Country UPV/EHU, Alameda Urquijo s/n, Bilbao 48013, Spain.
[3] ENEDI Research Group, Dpto. de Máquinas y Motores Térmicos, Escuela Técnica Superior de Ingeniería de Bilbao, University of the Basque Country UPV/EHU, Alameda Urquijo s/n, Bilbao 48013, Spain.

Abstract

The use of phase change materials (PCM) based latent heat thermal energy storage (LHTES) systems can improve the energy efficiency of sustainable energies. Sugar alcohols are widespread materials that can be considered as promising candidates to be used as PCMs. However, their melting temperatures are too high to use them directly in thermal storage systems for building technologies, such as residential micro-CHP or solar thermal systems. In order to overcome this situation, eutectic mixtures of the materials were studied. The phase diagrams were calculated by the UNIFAC group contribution method. Three suitable new mixtures were identified, comprised by Erythritol and Xylitol; Erythritol and Sorbitol; and Xylitol and Sorbitol. Their melting temperatures lie within the temperature range herein sought (60-90ºC). This modeling methodology showed to be suitable and can be applied to develop new PCMs. However, the mixtures identified underwent vitrification upon cooling. Therefore, research efforts should be done to develop techniques to promote the crystallization of the materials involved.
Keywords: Phase Change Materials; Sugar Alcohols; Thermal Energy Storage; Eutectic Mixture; UNIFAC.

1. Introduction and Objectives

The continual rise in the cost of fossil fuels and their decreasing availability, combined with requirements to reduce carbon emissions, reveal the necessity for more rational and efficient energy use [1]. The use of phase change materials (PCM) based latent heat thermal energy storage (LHTES) systems can improve the energy efficiency of sustainable energies. Therefore, the development of new cost effective PCMs with larger storage density is a matter under study [2-4].

Sugar alcohols are widespread materials with melting temperatures between 90 and 200 ºC [2]. They present higher volumetric energy densities than the presently available compounds used as PCMs. Furthermore, their market price can be considered reasonable for thermal storage purposes. Hence, they are promising candidates to be used as PCMs. However, their melting temperatures are too high to be applied directly in LHTES systems for sustainable building technologies, such as domestic micro-CHP systems, or solar thermal technologies.

The melting temperature of a PCM can be tuned down by the use of mixtures of materials. Nonetheless, the determination of suitable mixtures by means of experimental methods is commonly performed by a trial-and-error procedure, which is time consuming and sometimes unfeasible. The determination of the phase equilibrium based on thermodynamics of mixtures can be a suitable way to predict the composition and thermal behavior of the mixtures, allowing in this way the development of new PCMs for LHTES applications.

Thus, the objective of the present work is double: On one hand, it is aimed to determine new mixtures of sugar alcohols with a melting temperature suitable for micro-CHP and solar thermal systems (between 60 and 90ºC). On the other hand, it is intended to demonstrate the feasibility of the employed

theoretical approach, which additionally can be employed with other type of materials to predict new PCM mixtures.

2. Materials and Methods

Binary combinations of five sugar alcohols were investigated. They were chosen according to their commercial availability. The materials employed were the following: Xylitol, Sorbitol, Erythritol, Mannitol and Galactitol. Differential Scanning Calorimetry (DSC) was used for the determination of their thermal properties.

The modeling approach employed is based on thermodynamics of solid-liquid equilibrium. In order to determine the activity coefficients for the liquid phases (the activity of the solid phases was neglected) the modified UNIFAC group contribution method was used [5]. To solve all the coupled equations involved, the Matlab (MathWorks Inc.) software was employed.

Some of the mixtures studied vitrified upon cooling. Hence, to experimentally validate the results predicted, two approaches were used. For the mixtures that recrystallized upon cooling, DSC was employed. The mixtures that underwent vitrification upon cooling could not be experimentally validated with the DSC. In these cases, the results published elsewhere [6], obtained by means of other experimental procedures, were used.

3. Results

Three eutectic mixtures suitable for medium temperature LHTES systems were predicted by means of the model. The mixture comprised by Erythritol and Xylitol showed a eutectic composition (in mole fraction, as for every composition hereafter) of 0.27 Erythritol, with a melting temperature of 83 ºC. These results were validated by DSC. The melting enthalpy of this mixture, determined through DSC, was 225000 J/kg. The mixture formed by Erythritol and Sorbitol presented a eutectic point with 0.31 Erythritol, with a melting temperature of 85.7 ºC. These results were in close agreement with the results published elsewhere. Finally, the mixture formed by Xylitol and Sorbitol, showed a eutectic point formed by 0.51 Xylitol, with a melting temperature of 75.3 ºC. Unfortunately, these results could not be validated since the mixture vitrified upon cooling, and no result published in the literature was found.

Amongst the rest of the mixtures that were studied, Mannitol and Galactitol showed a eutectic point at 156.9ºC with a eutectic composition of 0.739 Mannitol. However, it is unsuitable for the storage temperatures sought for. The rest of the mixtures did not show a significant depression in relation to the lowest melting point of the pure materials forming the mixture, and hence the use of a mixture does not present any noticeable improvement.

4. Conclusions

In order to develop new PCMs for medium temperature LHTES systems, different binary combinations of five sugar alcohols were investigated by a modeling approach. Three promising mixtures were identified, forming eutectic compositions with melting temperatures within the temperature range sougth for (60-90ºC). The modeling approach used was also validated. However, the mixtures vitrified upon cooling. Since latent thermal storage requires that repeated melting-crystallization take place in a reproducible stable manner, research efforts should be done to develop techniques to promote crystallization of the materials studied.

5. References

[1] European Commission. Directive 2010/31/EU of the European Parliament and of The Council of 19 may 2010 on the energy performance of buildings. 2010.

[2] Kenisarin M, Mahkamov K. Solar energy storage using phase change materials. Renewable and Sustainable Energy Reviews 2007;11:1913-65.

[3] Zalba B, Marín JM, Cabeza LF, Mehling H. Review on thermal energy storage with phase change: materials, heat transfer analysis and applications. Appl Therm Eng 2003;23:251-83.

[4] Zhou D, Zhao CY, Tian Y. Review on thermal energy storage with phase change materials (PCMs) in building applications. Appl Energy 2012;92:593-605.

[5] Jakob A, Joh R, Rose C, Gmehling J. Solid-liquid equilibria in binary mixtures of organic compounds. Fluid Phase Equilib 1995;113:117-26.

[6] Perkkalainen P, Halttunen H, Pitkänen I. Solid state co-crystallization of sugar alcohols measured with differential scanning calorimetry. Thermochimica Acta 1995;269–270:351-9.

 Acknowledgements

Research of The Level Of Hydration of The Low-Main Cements and Phase Composition of The Stone on Their Basis

Gulrukh Begjanova, Atabek Begjanov, Negmatov Sayibjan

State Unitary Enterprise "Fan va Taraqqiyot", Tashkent State Technical University, Uzbekistan

e-mail: polycomft2005@rambler.ru

Abstract: Low key limes of the cements are characterized by slower progress of hydration and hardening of cements oolitovogo than that of cements from low fundamental clinkers, derived from raw materials in the region of Kizilkumskogo, along with an increased number of S2S (25-52%), also contain relatively high amounts of C3a and S4AF (6.5 to 7.0 and 14.5 15.5% ÷ [1, 2] is a specific theoretical and practical study of the hydration of the cement activity in the process of formation of a cement stone.

Keywords: Polymer composition, chemical reactant, physico-chemical properties of drilling fluids.

1 Introduction

The degree of hydration of cement were studied by low definition of bound water in samples of various curing period. Their phase composition was determined to change the intensity of the diffraction reflections of source minerals and guide the martial compounds on difraktometrore DRONE-2 and a derivatografe Paulik-Paulik system-Èrdej.

Objects and methods: The low main Portland cements in starting dates are somewhat slow hardening rate of hydration process, as evidenced by the relatively low degree of hydration hydration, estimated by the amount of bound water. Its content, regardless of the values of KN, solidifying the cement paste through 1 h 20 from 8.4 to 8.8%, while in manufacturing cement, hydrated at the same time, it is 9.9%. The 3-d amount of bound water in the stone low basic cement increased to 10-11%, which is about 1.5% less than the -2.0 in stone high principal cement. The 7 d the amount of bound water in samples of cement with CN = 0.75 - 0.78 rose to 13.8 -13.6% respectively.

When the values of KN = 0.80 -0.83 by that time, the reduction of the amount of bound water -12.8 and 12.05% respectively (fig. 1). Reduction of hydration of cement when these values KN explains that the adsorption of water on the surface of the crystals of calcium, hydrosilicates and therefore cement stone, the main role is played not by silicate or alûmosilikatnaâ part of the surface, and cations (Ca2 +, A1 +). As a result of coordination molecules of water surface cations in the first coordination sphere, the strength of the surface oxygen atoms cations, mežsloevyh cations and falls, and the energy of cation with the surface even more reduced if around cations are second and subsequent coordination sphere. And in this period the water binding of calcium cations slows down.

Hardening with age, the number of water molecules in contact areas between crystalline cations Sa is growing, increasing respectively and the number of crystalline guide wars. Noted that the smaller the KH clinker, the less value of bound water in hardened cement stone. In the period from 28 to 90 days, the amount of bound water is only about 2.5 to -3%, indicating a greater flow of low hydration process of cement between 1-7 days. Therefore, increasing the strength of indicators based stone at a later date is determined not by the number of phases, the martial and guide the morphology and structural characteristics of tumors to form cement stone. The process of hydration of cement with low KN = 0.85 is quite intense and the water is spent on hydrolysis S3S and S2S (c) allocation of Sa +2, linking the water forms a Ca (OH) 2, the main diffraction reflections, which are found in the d/n = 0.263;

0.490; 0.192; 0.179 nm (fig. 2A). Its diffraction reflection at 0.263 and 0.192 nanometers are fairly intense reflections do not hydrated C_2S.
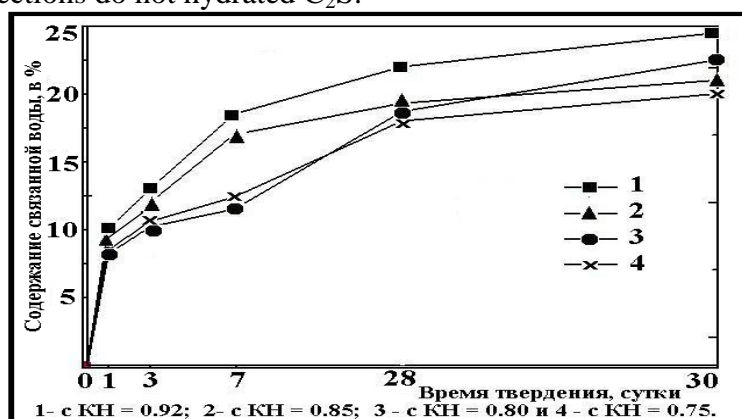
Figure 1. Water binding kinetics in the process of curing low core cements.

With the deepening of the process of hydrolysis hydration C_3S and C_2S is accelerating, as evidenced by the increase in the content of water in the samples and the growing intensity of diffraction reflections, especially when pentlandita 0.490 nm. In the period from 7 to 28 days, the process of hydration of low basic cement is the most intense diffraction reflection: the main source of clinker minerals, in particular the C_2S when d/n = 0.208; 0.278; 0.275; 0.263 nm strongly reduced, while at the same time decreases the intensity of the lines in a reduction of CA (OH) 2, showing that it is linked in the guide of his products, including a guide ro silicates of calcium. Their reflections are recorded at d/n = 0.304; 0.288; 0.249; 0.220 nm.

By that time, a small amount is also highly sulphate calcium aluminate sulphonic Po guide-erythrite with d/n = 0.583 nm. To the 90-days of intensity lines Sa (IT) 2 increases, indicating that the invasion of the hydration of the cement grains deeper layers and hydrolysis of new servings S3S, with the formation of low basic guide ro the calcium silicates. These data confirm the up-thermal analysis of main cement with low stones KN = 0.85 of various ages. From the literature it is known that high sulfate calcium sul′foalûminat Po guide produced in cement stone, unless there is a plaster.
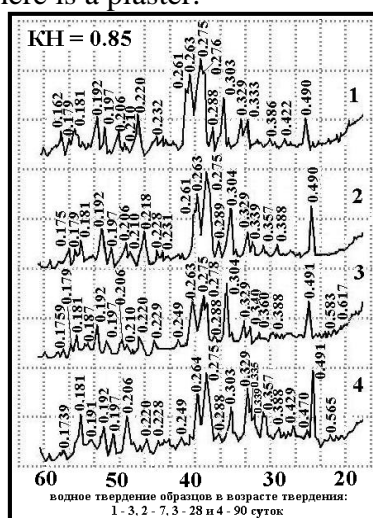
Figure 2. Difraktogrammy (a) and (b) the DTA curves of nizkoosnovnogo cement
In the absence of plaster it is perekristallizuetsâ in low-sulfate, and its recrystallization depends on the content of Alita and belita. With the increase of the recrystallization of Slavic

background. In alitovyh the process of recrystallization is over by six hours of hydration, and belitovyh-èttringit is found and after daily.

Thermal heating curves of low cement daily stone age find a photo effect sufficient intensity must also withstand the maximum, which is called total dehydration guide ro sul′foalûminatov ro aluminates, guide, guide ro tobermorita May 14 silicates and lateral tobermorit gel or° c-S-h (II). The appearance of small endothermic effects at 425 and 6400S due step nature of the dehydration of calcium aluminate and gidrosul′foalûminatov, and enough clear èkzoèffekta the 7900S-complete loss of water in the moljarnoe parity and their transition in wollastonite (fig. 2B).   The photoelectric effect when 8730S caused by dissociation of Caco3, which is present in cement stone as a result of adsorption of carbon dioxide of the air portlanditom. To 3 h èndoèffektov size increased by 425, 6500S and offset èkzoèffekta in the 7900S in higher temperatures, namely the 8000S.

If the first phenomenon is the increase in cement stone some guide ro aluminates and calcium alûmoferritov Po Guide, complete dehydration of CA (OH) 2 and partial travel guides ro silicates of calcium, the second-with complete dissociation good zakristallizovannogo Caco3. As you increase the duration of curing ranging from 28 days up to 90 days, and on the size effect in the range 100-2000 c must also withstand the maximum with markedly increases in width it is somewhat narrow, indicating that the stabilization and orderly military Guide products. The appearance and the effect when 5070S is due to dehydration, and sulphate Mono increase in èkzoèffekta in the 8000S-dehydration guide ro silicates and partial dissociation of Caco3, which judging by the size of the èndoffekta when is 9200S cement stone is a pretty large number. Thus, it is established that the process of hydration and the formation of the phase of low basic military guide cement flows as well as the highly original Portland cement with a small difference in its speed.

It is known that large hydraulic engineering concrete structures must be allocated, heat cements, which through 3 and 7 days does not exceed respectively 50 and 60 kcal/g, i.e. cements exothermic, which reduced from the normal Portland cement that are made of clinker with low content of highly neritmičnyh minerals S3S and C3a. Generally, such cementah S3S content shall not exceed 50% and C3a-not more than 8%. Therefore, based on raw materials Kizilkumskogo region low main Portland cements are cements with moderate èkzotermiej (fig. 3).
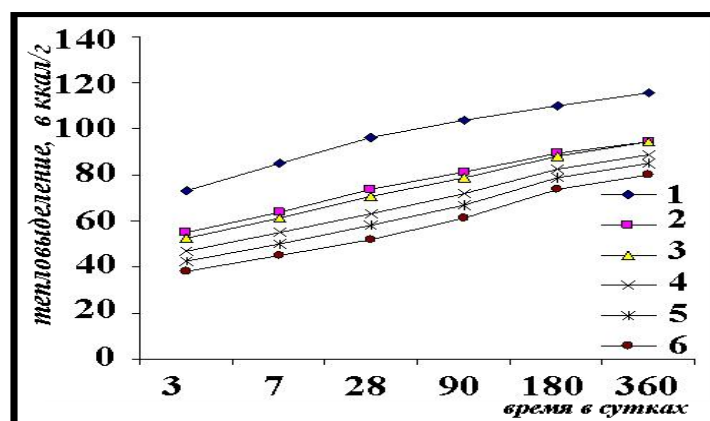
KN = 0.92 (manufacturer's clinker); 2-low basic clinker KN = 0.85; 3-KN = 0.83;
4-KN = 0.80; 5-0, 78; 6-0, 75;

Figure 3. Changing heat cements, depending on the values of KN and curing duration

Conclusion:

With decreasing values of 0.85-0.75 KN heat low basic cement gradually decreases during the whole period of hardening, for example the amount of heat generated from the low

base of cement with KN = 0.85 via 3 day at 17.99 kcal/g (24.5%) less than that of cement with KN = 0.92, and this difference increases with increasing length of hardening, reaching to 28 d 20.88 kcal/g (18.1%) This regularity and intensity of heat dissipation of the cements with lower values of KN is maintained during the whole period of hardening, which allows to recommend to use them in the manufacture of concrete external zones of massive hydraulic structures subjected to systematic freeze or thaw in fresh or brackish water.

Reference:

1. Mr. Iskandarov m.i., Begzhanov s.s., G.b. Negmatov technological aspects of fuel and energy saving during the production of Portland cement//Sun. mater. Intl. THE CPP. "Innovation-2004". -Tashkent, 2004. -P. 121-122.

2. the S.S. Begdjanova Negmatov G.B. Ruziev N.R., F.B., Atabaev Akramov e. M Prospect of manufacture in Uzbekistan energy economic knitting compositions on a low based clinker matrix//16. Internationale Baustofftagung. -Weimar. Deutschland. 2006. Band. - p. 1-1005-1010.

Possibilities of Use of Steel-Smelting Slags As Complex Raw Materials by Production of Cement Clinker

Iskandarova M. I., Mironyuk N. A., Makhmudova N. K

Research and development and test center "Strom" in case of Institute of the general and inorganic chemistry of Academy of Sciences of the Republic of Uzbekistan, Tashkent
www.strom13.00.@mail.ru; www.ionxanruz@s-link.uz

Abstract*:* In view of the fact that presence at cement of oxide of MGO magnesium at a large number (more than 5%) is undesirable, dolomite and dolomitizirovanny limestones found limited application in the cement industry as a component of a raw compound for receiving clinker**.**

Keywords: cement stone, dolomite, clinker

1 Introduction

One of the global problems requiring the urgent decision, development of rational technologies of recycling of ferrous metallurgy, including waste of steel-smelting production (Joint venture slag) is. Though their chemical and mineralogical composition testifies to suitability of application as a part of a raw compound instead of part of clay, limestone or the adjusting and active mineral component in cement, now they in cement production aren't used. In dumps of Uzmetkombinat Open joint stock company some million tons of steel-smelting (joint ventures) of slags which after magnetic separation represent calcic and magnesium aluminosilicates with rather high maintenance of carbonates and iron oxide are accumulated. In case of their use in cement production the expenditure of limestone is reduced and the klinkeroobrazovaniye is considerably accelerated when roasting. These slags represent a powdery material which doesn't require preliminary grinding and thanks to rather high hydraulic activity their introduction doesn't reduce cement brand that leads to the considerable lowering of prime cost and increase in output of additional cements to 20%. Due to scale and complex utilization of the joint venture slags the ecological situation around metallurgical productions improves.

Research technique

Phase composition of steel-smelting slags studied using a method of the X-ray phase analysis on the diffractometer DRON-2. When carrying out researches on determination of possibility of use of this slag as a part of a cement raw compound calculation of three-component raw compounds on the basis of limestone of the Balyklytau field, the loess of the Hilkovsky field carried: for clinker of cement of all-construction assignment in case of KH=0,90; n=2,2; p=1,71, and clinker for sulfate-resistant cement - KH=0,90; n=2,4; p=1,93. Thus, depending on values of KN, п and p, the maintenance of the processed joint venture slag in a raw compound made 4,03÷13,2 of %. The estimated maintenance of Al203 in % clinkers 2,73÷3,58, and % Fe203−2,10÷7,73 that provides education 3,21÷5,53 of % of C3A and 9,63÷31,34 of C4AF %. Raw compounds were exposed to roasting for study of their reaction capacity by determination the residual maintenance of Saosv in roasting products for what roasting carried out in the temperature range 1000-1450os in the laboratory silitovy furnace with exposure of 20 min. with sampling at each temperature.

Results and their discussion

As a part of the processed joint ventures slags are present: MgO periclase (d/n=0,245; 0,210; 0,149 …) nanometer; монтичеллит CaO• MgO• SiO2 (d/n=0,540; 0,387; 0,298; 0,268; 0,182) nanometer; окерманит 2CaO• MgO• 2SiO2 (d/n=0,288; 0,237; 0,228; 0,205; 0,191) nanometer; SiO2 quartz (d/n=0,426; 0,334; 0,245; 0,228; 0,221; 0,214; 0,182)

nanometer; two-calcic $2CaO \cdot Fe_2O_3$ ferrite (d/n=0,366; 0,279; 0,274; 0,268) nanometer; $SASO_3$ calcium carbonate (d/n=0,302; 0,245; 0,228; 0,209; 0,191) nanometer; minerals of the transition rows: $3CaO \cdot Al_2O_3$ and майенит $12CaO \cdot 7Al_2O_3$ (d/n=0,480 aims; 0,426; 0,408; 0,279; 0,268; 0,221; 0,214; 0,191 …) nanometer; two-water $CaSO_4 \cdot 2H_2O$ plaster (d/n=0,540 …) nanometer. The favorable mineralogical composition and high dispersibility of the joint venture slags allows to use in a complex them in production of cement as in quality a carbonate - and alyumosilikatny raw materials, and also a ferriferous mineralizer of a raw compound, and the active mineral component.

The study of kinetics of process of a klinkeroobrazovaniye of a raw compound of new composition in the specified temperature range showed that with temperature increase the speed of dissociation of $SASO_3$ with separation of Saosv, and binding last in brick minerals is strongly accelerated and its full assimilation happens in case of 1350-1420os. The maximum separation of Saosv are watched at a temperature 1000oC. With temperature increase its contents sharply decreases due to intensive binding in brick minerals. In the range 1000-1200os the maintenance of Saosv makes 44,2-25,3%, and Saosvyaz – from 36,4 to 62,6%. With temperature increase to 1300-1420os quantity Saosvyaz increases to 83,6-99,88%, and Saosv decreases to 6,4–0,12%. Roasting products at a temperature of 14500C don't contain Saosv that testifies to its full assimilation in the course of mineralogenesis. Klinkeroobrazovaniye process when roasting raw compounds with KH=0,85-0,87 comes to the end at a temperature of 13500C, and with KH=0,90-0,92 – in case of 1380-14200C. The actual maintenance of C3S in clinkers in case of KN = 0,90 - 0,92 and p-higher than 2,0, makes from 56,48 to 63,24% that is enough for support of high activity of cements on their basis, and in case of KN = 0,90 and п = 1,17, and also KN = 0,85 and п = 2,83 - respectively 45,96 and 49,49% that predicts high sulfate resistance of cements on the basis of these clinkers. The relief of a surface of a chip of experimental clinker, is provided uniformly by porous compact-grained mass with sizes of silicates of calcium 10-15 µк, алит is crystallized in the form of hexagonal prisms and tablets, and bleaches – in the form of grains of spherical and oval forms. Its contents occupies about 55-60% of lump. A small amount of an alyumoferritny phase with grains sizes 1-2 µк is distributed relatively uniformly in the form of the fine-grained films located on a surface of grains of silicates of calcium.

Normal density of cement dough on the basis of the synthesized clinkers made 25-27%, расплыв a cone made 111-112 mm. The beginning of its skhvatyvaniye came in 2 h 50 min. ÷ 2 h 58, and the end – in 4 h 45 min. ÷ 4 h 52 min. All types of test for uniformity of scope change withstood samples of cements without visible external signs. Signs of a false skhvatyvaniye of cement are absent. In 28 days of normal solidification samples has hydraulic activity in case of compression - 41,8÷43,2 of MPa that corresponds to 400 cement brand.

Inference

Recycled by JV Slag JSC Uzmetkombinat it can be used as a component of a raw compound for receiving clinker, as for cement of all-construction assignment, and sulfate-resistant cement. Thus its contents in a raw compound, depending on value of KN, makes from 6,2% to 22,3%, and he replaces partially karbonatsoderzhashchy component and completely – a ferriferous mineralizer. Roasting of raw furnace charges with the joint venture slag proceeds intensively with full assimilation of Saosv in case of 1420-1430os and formation of the brick minerals which actual contents corresponds to their estimated contents. The microstructure of the clinkers synthesized at an optimum temperature from experimental raw compounds compact-grained, it differs an accurate zakristallizovannost of grains алита and белита according to hexagonal and oval forms. Hydraulic activity of cement on the basis of experimental clinker of the optimum composition synthesized at a temperature 1420oC, makes 41,8 – 43,2 MPas that corresponds to 400 cement brand. By production of clinker saving of natural raw materials makes 10-20% of raw furnace charges of new composition,

fuel on clinker roasting - to 20% and increase of productivity of rotating furnaces - 10%. When using limestone, the loess and the processed joint venture slag production of standard clinker for cement of all-construction assignment and sulfate-resistant cement is possible.

A New Generalized Correlation of Viscosity Coefficient of Complex Hydrocarbon Mixtures in a Wide Range of Temperatures and Pressures

A.A. Gerasimov[1], B.A. Grogor'ev[2] and I.S. Alexandrov [3]

[1]Kaliningrad State Technical University, Sovietsky prospect 1, Kaliningrad, 236022, Russia,
aager_kstu@mail.ru
[2]GAZPROM VNIIGAZ, Razvilka, Leninsky Rayon, Moskovskaya oblast, 142717, Russia,
gba_41@mail.ru
[3]Kaliningrad State Technical University, Sovietsky prospect 1, Kaliningrad, 236022, Russia,
alexandrov_kgrd@mail.ru

Abstract: A new generalized correlation of viscosity coefficient of complex hydrocarbon mixtures has been developed. Experimental data used to develop the correlation included data on petroleum and gas condensates of various fields, their fractions and trade products. The generalization was performed within the framework of the extended corresponding states principle. The proposed correlation takes the reduced density and reduced temperature as variables. The density is calculated with the use of two generalized multiparameter fundamental equations of state developed by the authors and applied over a temperature range from the beginning of the hardening to 700 K with pressures up to 100 MPa. To describe the residual scaled viscosity, an optimized functional form with polynomial and exponential terms developed by the authors has been used. Complexes, that defined by the physical and chemical properties such as relative density, refractive index and the molar mass were chosen as the determining criterions of similarity. An average absolute deviation (AAD) of predictive calculation of viscosity coefficient is ± 7,0% over a temperature range from 220 K to 570 K with pressures up to 100 MPa.

Keywords: viscosity, temperature, pressure, density, petroleum, gas condensate, equation of state

1. Introduction

The data of viscosity of complex hydrocarbon systems is necessary for the calculation of the production processes, technological equipment, transport pipeline systems and so on.

The need for data has initiated numerous experimental investigations of viscosity in different laboratories around the world. However, the effective use of experimental results in the development of new fields and the introduction of new processes of organic raw materials are possible only with reliable predictive methods of calculation of viscosity. This task also devoted a considerable amount of research work. One of the latest reviews on this problem is presented in our work [1]. It should be noted that the viscosity refers to the thermal properties, for which research is connected with considerable difficulty. The main reason for this is the strong dependence of viscosity on the structure of molecules and intermolecular forces, and a very wide range of change of the viscosity in all regions of state parameters. This leads to difficulties in conducting the experiment and data fitting. As a result the accuracy of the calculation methods is considerably lower than for the other properties. And it also initiates new research.

In [1, 2] the authors presents the results of the analysis and the development of predictive calculation methods of viscosity coefficient of complex hydrocarbon mixtures. In these works an array of experimental data on viscosity is described in detail. Based on this array methods of viscosity calculation were developed and tested. The range of applicability

of the author's methods [1, 2] was limited to the value of the reduced density $\rho/\rho_c \geq 2$. This is due to the fact that for the calculation of the density the generalized local thermal equation of state of the liquid phase was used. The proposed by the authors [3] new generalized fundamental equation of state allows the calculation of all thermodynamic properties including phase equilibrium over a temperature range from the beginning of the hardening to 700 K with pressures up to 100 MPa. The use of the new generalized equation of state allowed to extend the range of applicability of the methods for calculation of viscosity and to improve their predictive accuracy.

2. Generalized Fundamental Equation of State

For the generalization, an equation in the form of the reduced Helmholtz free energy is selected

$$\frac{a(\rho,T)}{RT} = \frac{a^0(\rho,T) + a^r(\rho,T)}{RT} = \alpha^0(\delta,\tau) + \alpha^r(\delta,\tau)$$

(1)

where $a(\rho,T)$ is the Helmholtz free energy; $\alpha^0(\delta, \tau)$ is the reduced Helmholtz energy in the ideal-gas state; $\alpha^r(\delta, \tau)$ is the residual part of the reduced Helmholtz energy; $\delta = \rho/\rho_r$ is the reduced density; $\tau = T_r/T$ is the inverse reduced temperature; and ρ_r, T_r is reducing parameters. The critical parameters are used in equations as reducing parameters ($T_r = T_c$ and $\rho_r = \rho_c$). The acentric factor ω was chosen as the determining criterion of similarity.

To describe the residual part of the reduced Helmholtz energy, an optimized functional form developed by Sun and Ely [4] has been used

$$\alpha^r(\delta,\tau) = \sum_{k=1}^{6} N_k \delta^{d_k} \tau^{t_k} + \sum_{k=7}^{14} N_k \delta^{d_k} \tau^{t_k} \exp\left(-\delta^{l_k}\right)$$

(2)

The coefficients of the generalized equations of state can be defined by the following relation:

$$n_i = c_{1,i} + c_{2,i}\omega + c_{3,i}\omega^{C_{4,i}}$$

(3)

where ω is the acentric factor.

To calculate the thermodynamic properties of complex hydrocarbon mixtures containing hydrocarbons with the number of carbon atoms from five and above the two generalized fundamental equations of state were developed. The first equation describes the properties of paraffin hydrocarbons (from C_5 to C_{50}). The second equation describes the properties of cyclic hydrocarbons (naphtens and aromatic). The equations are applicable over a temperature range from the triple point to 700 K with pressures up to 100 MPa. Coefficients of equations and results of testing for complex hydrocarbon mixtures are presented in [3]. Density is calculated by numerical solution of the equation (4).

$$p = \rho RT \left(1 + \delta \left(\frac{\partial \alpha^r}{\partial \delta}\right)_\tau \right)$$

(4)

The derivatives of the ideal gas Helmholtz energy and the residual Helmholtz energy required by the equations for the thermodynamic properties are given in [10].

Thermodynamic properties are calculated within the framework of the "quasi-single-fluid models" [6]. In this approach, the mixture is treated as a pure substance. Substance identification is done on the value of the pseudocritical (hereinafter referred to as critical) properties (T_c, ρ_c) and acentric factor ω. To calculate the critical temperature, critical pressure and acentic factor the authors used the relations proposed by Kesler and Lee [7]. To calculate the critical density, the authors used the ratio proposed in [8].

Within the framework of the "quasi-single-fluid models", the mixture is a ideal solution of alkanes and cyclic hydrocarbons, featuring the same critical properties and acentric factor. Thermodynamic property Y is calculated according to the additive formula

$$Y = Y_a x_a + Y_c x_c \tag{5}$$

where Y_a, Y_c – thermodynamic property calculated from equation (1), accordingly using the coefficients for alkanes and cyclic hydrocarbons; x_a, x_c – accordingly, the proportion of alkan and cyclic structures in mixture.

x_a and x_c values were determined by $n_D - \rho - M$-method of structural group analysis [9] based on the data of the refractive index at temperature 20 ^{o}C n_D^{20}, relative density at the same temperature ρ_4^{20} and average molar mass M.

In the process of calculating thermodynamic properties from equation (1) the critical density correction was carried out on the value of the relative density ρ_4^{20} determined under laboratory conditions with high accuracy ($\sim$ 0,02 %).

3. New Correlation of Viscosity

The new generalized viscosity equation of complex hydrocarbon mixtures is given by

$$\Delta \tilde{\eta} = \exp\left[\sum_{i=1}^{5} n_i \tau_\eta^{t_i} \delta_\eta^{l_i} \exp(-\delta_\eta^{k_i}) \right] - 1 \tag{6}$$

where the scaled residual viscosity $\Delta \tilde{\eta}$ can be defined by the following relation

$$\Delta \tilde{\eta} = \left[\eta(p,T) - \eta^0 \right] \Lambda_\eta \tag{7}$$

Analysis of viscosity in various scales presented in [1, 2]. The most effective was the following

$$\Lambda_\eta = T^{-\left(\frac{1}{2}\right)} M^{-\left(\frac{1}{2}\right)} \rho^{-\left(\frac{2}{3}\right)} \tag{8}$$

For the calculation of residual viscosity $\Delta\tilde{\eta} = (\eta(p,T) - \eta^0)$ the data on the dilute gas viscosity η^o are needed. The different calculation methods of η^o are analyzed in detail in the works [1, 2]. As a result, we recommend using a simple correlation of Lee and Thodos [11].

$$\eta^0 \xi = 1,564\tau^{0,94} \tag{9}$$

where $\xi = T_c^{1/6}/M^{1/2}/P_c^{2/3}$; $\tau = T/T_c$; η^o, uPa·c; P_c, MPa.

In the generalized equation (6) $\tau_\eta = T/T_\eta$ is the reduced temperature and $\delta_\eta = \rho/\rho_\eta$ is the reduced density. As the reducing state the point on the pseudocritical isobar with a fixed value of scaled viscosity $\Delta\tilde{\eta} = 7800$ was chosen.

The scaled fixed value of residual viscosity was chosen in such a way that the temperature T_η was within the limits of the experimental investigated range. Defined by experimental data the temperature T_η was approximated by the equation (10).

$$\frac{T_\eta}{T_c} = C_0 + C_1 Y + C_2 Y^2 + C_3 Y/(K_w - 9) + C_4 K_w + C_5 \left(\frac{M}{100}\right) \tag{10}$$

where the characteristic complex of Y is given by the ratio (11)

$$Y = \frac{100\left[(n_D^{20})^2 - 1\right](n_D^{20} - \rho_4^{20})}{M\rho_4^{20}(n_D^{20} + 0,4)} \tag{11}$$

and the Watson factor $K_w = 1,2251\dfrac{T_{bv}^{1/3}}{\rho_{15}^{15}}$. T_{bv} - is the average volume boiling point temperature. The coefficients of equation (10) are given in Table 1.

Table 1: The coefficients of equation (10)

C_0	C_1	C_2	C_3	C_4	C_5
0,6592591	-0,1709597	0,1077843	-0,0721121	-0,01088077	0,0226019

The most reliable experimental data were selected in order to develop the generalized correlation. An array of data was included in the fitting procedure consisting largely of η obtained in the 1980's in the laboratory of the Grozny Petroleum Institute [12-15]. A representative array of data on viscosity consisted of the data of 41 hydrocarbon fractions of petroleum and gas origin over a temperature range 290 – 570 K and at pressures up to 50 MPa. Dynamic viscosity coefficient was determined by the flow of substances through the capillary using Golubev's capillary viscosymeter. The uncertainty of the single measurement of viscosity do not exceed 1,5 %.

Defined by experimental data the values of T_η described by equation (10) with the root-mean-square (RMS) deviation 1,23%.

The values of the coefficients of generalized equations for scaled residual viscosity where determined based on the array of experimental data, that was described above, and consisted of 41substances and contained 1105 of experimental values of η. Initially, for each

substance using the generalized equation of state (1) at temperature T_η and at pseudocritical pressure P_c the reference values of density ρ_η were determined.

The coefficients of the equation (6) are individual for each substance. For the generalization, the following relation was used

$$n_i = C_{0i} + C_{1i}Y + C_{2i}\frac{Y}{(K_w - 9)} + C_{3i}(K_w/100)^{C_{4i}} \tag{12}$$

A nonlinear optimization procedure was used to develop equation (6). The fitting procedure was described in [16]. Optimization of the coefficients and exponents of equation (6) and (12) took place simultaneously in a nonlinear form. The exponents of equation (6) and coefficients of equation (12) are given in Table 2 and Table 3.

Table 2: The exponents of generalized equation (6).

i	t	l	k
1	-0,4233	4	1
2	-1,1474	9	1
3	0,4073	6	2
4	-0,4159	1	2
5	-1,2692	11	2

Table 3: The coefficients of generalized equation (12).

i	C_0	C_1	C_2	C_3	C_4
1	8,4071346	23,413738	-430,60287	14,449930	0,15077850
2	-22,628425	-55,310165	16,361933	-142,92284	1,2212903
3	-1,8928483	-12,878272	350,73670	117,62411	1,8821112
4	17,756590	-8,1156802	91,562924	-5,7114858	-0,49601946
5	7,2611043	50,885985	-22,186015	33,947691	0,29078675

The root-mean-square deviation (RMS) for the selected array of experimental data was 7,5 %, and the average absolute deviation (AAD) was 5,4%, that is better the results, that we got in [1, 2]. It is important to note that in [1, 2] the calculation of the deviation was made in the range of applicability of the method, that is limited to the value of the reduced density $\rho/\rho c \geq 2$. Figure 1.a. present the characteristics of the uncertainties.

Figure 1.b. present the characteristics of the uncertainties for gas condensates and their fractions. We have included in the analysis the experimental values of η, that was obtained in different years in Kasnodar State Technological University over a temperature range 260 – 470 K and at pressures up to 60 MPa [17]. Total 8 gas condensates of various fields and 44 their fractions was investigated. The uncertainty of the single measurement of η in [17, 18] do not exceed 1,0 %. At the Tashkent road Institute the viscosity data was obtained for six gas condensate fields of Western Siberia and Central Asia, and for fourteen their fuel fractions. Dynamic viscosity coefficient was determined by the flow of substances through the capillary over a temperature range 290 – 470 K and at pressures up to 50 MPa. The uncertainty of the single measurement of η in [19] do not exceed 1,8 %. Total 7 gas condensates of various fields and 12 their fractions was investigated in the work of Kazarian [20] using the capillary viscosymeter over a temperature range 220 – 470 K and at pressures up to 60 MPa. The uncertainty of the single measurement of η in [20] do not exceed 2,0 %.

The root-mean-square (RMS) deviation for gas condensates was 21,5 %, and the average absolute deviation (AAD) was 17,0%. This is the 2 % less than in the [1, 2]. The

value of deviations for gas condensates and their fractions is significantly larger than for the original array containing the data of η on petroleum fractions. The reason for this is the high uncertainty of experimental data for both the η and the physical and chemical properties that are required for the calculation.

a)

b)
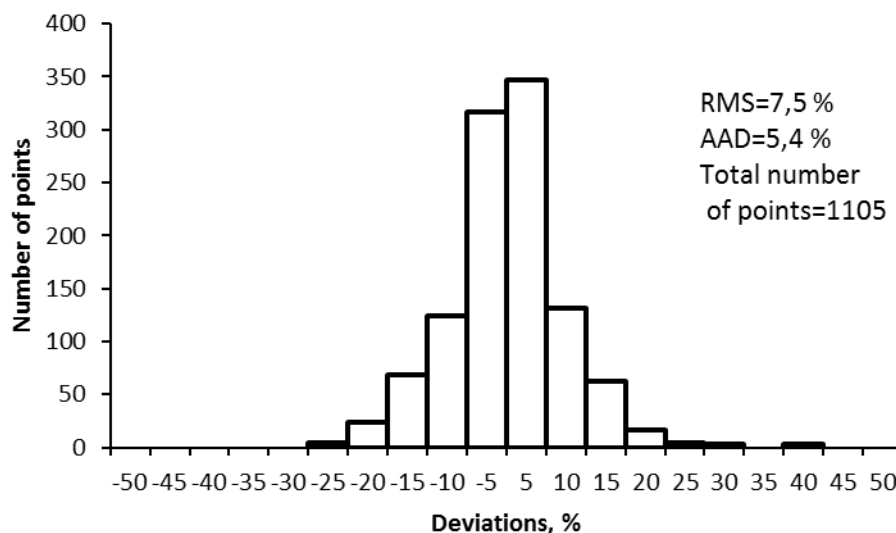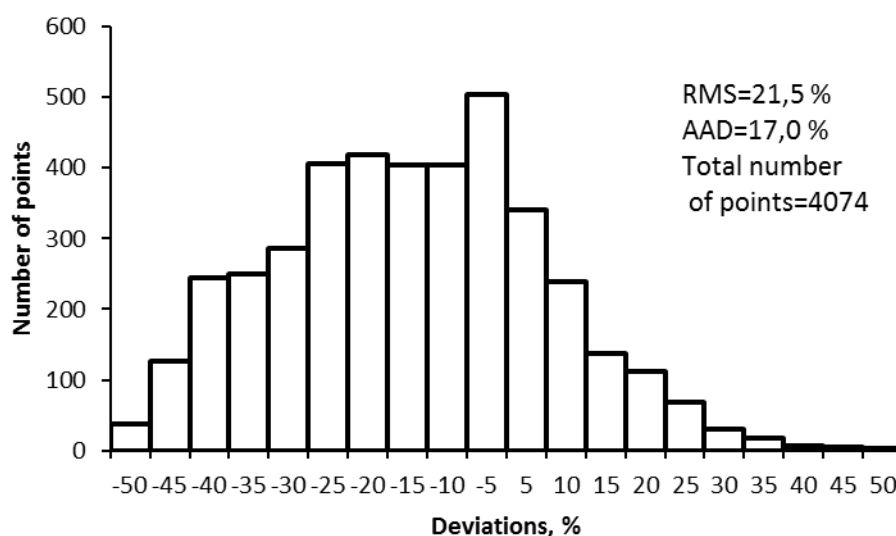
Fig. 1. Comparisons of deviations for viscosity calculated from generalized equation (6):
a) petroleums, their fractions and trade products; b) gas condensates and their fractions.

4. Conclusion

As a result of the use of generalized equations of state and effective algorithm of nonlinear optimization the new viscosity correlation for complex hydrocarbon mixtures was developed. The new correlation differs from the previous by a wider range of applicability on

temperature and pressure, by the lack of restrictions on group hydrocarbon composition of mixtures, and by more accurately predictiving viscosity.

5. References

[1] Gerasimov A.A. Analysis and development of new methods of calculation of viscosity of oil, gas condensates and their fractions / A.A. Gerasimov , B.A. Grigor'ev, E.B. Grigor'ev // Defense complex - scientific and technical progress of Russia. – 2009. – No.2. – P.73-78.

[2] Grigor'ev B.A. (2007) *Thermophysical properties and phase equlibria of gas condensates and their fractions.* Moscow Power Institute, 344 p. ISBN 978-5-383-00050-2.

[3] Grigor'ev B.A. Analysis of the application of single-fluid model for calculation of thermodynamic properties of multicomponent hydrocarbon mixtures based on the the fundamental equation of state / B.A. Grigor'ev, A.A. Gerasimov, I.S. Alexandrov // Relevant issues of studies of field hydrocarbons formations: collection of scientific articles. – Moscow, VNIIGAZ. – 2012. – 412 p.

[4] Sun L. Universal equation of state for engineering application: algorithm and application / L. Sun, J.E. Ely // Fluid Phase Equilibria. – 2004. – V.222-223. – P.107- 118.

[5] Span R. Multiparameter Equation of State: An Accurate Source of Thermodynamic Property Data/ R.Span. – Berlin: Springer, 2000. – 367 p.

[6] Grigor'ev B.A. (1999) *Thermophysical properties of petroleum, oil-products, gas condensates and their fractions.* Moscow Power Institute, 372 p. ISBN 5-7046-0483-8.

[7] Kesler M.G. Improve prediction of enthalpy of functions / M.G. Kesler, B.I. Lee // Hydrocarbon Processing. – 1976. – V.55, No.3. – P.153-158.

[8] Riazi M.R. Simplifi property predictions / M.R. Riazi, Th.E. Daubert // Hydrocarbon Processing. – 1980. – V.59, No.3. – P. 115-116.

[9] Van Nes K., Van Westen H.(1954) *Aspects of the constitution of mineral oils.* Elsevier Publishing Company. Amsterdam. 463 p. ISSN 1095-9203.

[11] Lee H. Generalized viscosyti behavior of fluids over the complete gaseous and liquid states / H. Lee, G. Thodos // Ind. Eng. Chem. Res.– 1988.– V.27, No.12.– P.2377–2384.

[12] A.S. Keramidi, *Experimental study of the dynamic viscosity coefficient of liquid paraffin hydrocarbons and oil products*, Ph. D. thesis (USSR, Grozny, 1972).

[13] D.V. Boldyrev, *Development of methods for calculating viscosity of petroleum products*, Ph. D. thesis (USSR, Grozny, 1994).

[14] Selivanov A.K. Study on the viscosity of the Mangyshlak oil and its fractions at high pressures for the information support of the unified system of thermophysical subscription / A.K. Selivanov, G.F. Metalidi, S.I. Rodchenko // Electrification and automation of oil industry objects: collection of scientific articles.- 1980.- P. 233-237.

[15] Grigor'ev B.A. Experimental study of dynamic viscosity of Malgobek oil fractions / B.A. Grigor'ev // Izv. Vyssh. Uchebn. Zaved., Neft Gaz.- 1975.- No. 5.-P. 70-92.

[16] Alexandrov I.S. A modern approach in the development of fundamental equations of technically important working substances / I.S. Alexandrov, B.A. Grigor'ev, A.A. Gerasimov // Relevant issues of studies of field hydrocarbons formations: collection of scientific articles. – Moscow, VNIIGAZ. – 2011. – 296 p.

[17] Experimental research of thermophysical properties of stable gas condensates and their fractions in liquid phase: Scientific report. / Kasnodar State Technological University: A.S. Magomadov. – Theme №112.04.14. – Krasnodar: KSTU, 1994.– 171 p.

[18] A.S. Magomadov, *Study on viscosity of gas condensates and their fractions at different temperatures and pressures*, Ph. D. thesis (USSR, Krasnodar, Krasnodar Polytechnic Institute, 1978).

[19] Mutalibov A.A. Viscosity of gas condensates and their fractions / A.A. Mutalibov, V.V. Shubin, G.N. Mahmudov, R.R. Valitov, L.N. Astaf'eva // Tables of recommended reference data. - State service of standard reference data. - R308-89.– 56 p.
[20] Kazarian V.A. (2002) *Thermophysical properties of individual hydrocarbons and gas condensates.* Moscow, "Technique", 448 p. ISBN 978-5-93969-019-5.

Acknowledgements

A New Generalized Correlation of Thermal Conductivity Coefficient of Complex Hydrocarbon Mixtures in a Wide Range of Temperatures and Pressures

B.A. Grogor'ev [1], A.A. Gerasimov [2] and I.S. Alexandrov [3]

[1]Gubkin Russian State University of Oil and Gas, Leninsky prospect 65, Moscow, 119991, Russia,
gba_41@mail.ru
[2]Kaliningrad State Technical University, Sovietsky prospect 1, Kaliningrad, 236022, Russia,
alexandrov_kgrd@mail.ru
[3]Kaliningrad State Technical University, Sovietsky prospect 1, Kaliningrad, 236022, Russia,
aager_kstu@mail.ru

Abstract: A new generalized correlation of thermal conductivity coefficient of complex hydrocarbon mixtures has been developed. Experimental data used to develop the correlation included data on petroleum and gas condensates of various fields, their fractions and trade products. The generalization was performed within the framework of the extended corresponding states principle. The proposed correlation takes the reduced density and reduced temperature as variables. The density is calculated with the use of two generalized multiparameter fundamental equations of state developed by the authors and applied over a temperature range from the beginning of the hardening to 700 K with pressures up to 100 MPa. To describe the residual scaled thermal conductivity, an optimized functional form with polynomial and exponential terms developed by the authors has been used. Complexes, that defined by the physical and chemical properties such as relative density, refractive index and the molar mass were chosen as the determining criterions of similarity. An average absolute deviation (AAD) of predictive calculation of thermal conductivity coefficient is ± 2,5% over a temperature range from 220 K to 670 K with pressures up to 100 MPa.

Keywords: thermal conductivity coefficient, temperature, pressure, density, petroleum, gas condensate

1. Introduction

The knowledge of thermal conductivity of complex hydrocarbon systems is necessary for the calculation of the production processes, technological equipment, transport pipeline systems and so on.

Among all transport properties, the thermal conductivity coefficient is investigated in detail both experimentally and theoretically. This conclusion is fair relative to the thermal conductivity of the liquid phase of petroleum, gas condensates, their fractions and trade products. In [1, 2] the authors presents the results of the analysis and the development of predictive calculation methods of thermal conductivity coefficient of complex hydrocarbon mixtures. In these works an array of experimental data on the thermal conductivity coefficient is described in detail. Based on this array methods of thermal conductivity calculation were developed and tested. The range of applicability of the author's methods [1, 2] was limited to the value of the reduced density $\rho/\rho_c \geq 2$. This is due to the fact that for the calculation of the density the generalized local thermal equation of state of the liquid phase was used. The proposed by the authors [3] new generalized fundamental equation of state allows the calculation of all thermodynamic properties including phase equilibrium over a temperature range from the beginning of the hardening to 700 K with pressures up to 100 MPa. The use of

the new generalized equation of state allowed to extend the range of applicability of the methods for calculation of thermal conductivity and to improve their predictive accuracy.

2. Generalized Fundamental Equation of State

For the generalization, an equation in the form of the reduced Helmholtz free energy is selected

$$\frac{a(\rho,T)}{RT} = \frac{a^0(\rho,T) + a^r(\rho,T)}{RT} = \alpha^0(\delta,\tau) + \alpha^r(\delta,\tau) \tag{1}$$

where $a(\rho,T)$ is the Helmholtz free energy; $\alpha^0(\delta,\tau)$ is the reduced Helmholtz energy in the ideal-gas state; $\alpha^r(\delta,\tau)$ is the residual part of the reduced Helmholtz energy; $\delta = \rho/\rho_r$ is the reduced density; $\tau = T_r/T$ is the inverse reduced temperature; and ρ_r, T_r is reducing parameters. The critical parameters are used in equations as reducing parameters ($T_r = T_c$ and $\rho_r = \rho_c$). The acentric factor ω was chosen as the determining criterion of similarity.

To describe the residual part of the reduced Helmholtz energy, an optimized functional form developed by Sun and Ely [4] has been used

$$\alpha^r(\delta,\tau) = \sum_{k=1}^{6} N_k \delta^{d_k} \tau^{t_k} + \sum_{k=7}^{14} N_k \delta^{d_k} \tau^{t_k} \exp\left(-\delta^{l_k}\right) \tag{2}$$

The coefficients of the generalized equations of state can be defined by the following relation:

$$n_i = c_{1,i} + c_{2,i}\omega + c_{3,i}\omega^{C_{4,i}} \tag{3}$$

where ω is the acentric factor.

To calculate the thermodynamic properties of complex hydrocarbon mixtures containing hydrocarbons with the number of carbon atoms from five and above the two generalized fundamental equations of state were developed. The first equation describes the properties of paraffin hydrocarbons (from C_5 to C_{50}). The second equation describes the properties of cyclic hydrocarbons (naphtens and aromatic). The equations are applicable over a temperature range from the triple point to 700 K with pressures up to 100 MPa. Coefficients of equations and results of testing for complex hydrocarbon mixtures are presented in [3]. Density is calculated by numerical solution of the equation (4).

$$p = \rho RT\left(1 + \delta\left(\frac{\partial \alpha^r}{\partial \delta}\right)_\tau\right)$$
(4)

The derivatives of the ideal gas Helmholtz energy and the residual Helmholtz energy required by the equations for the thermodynamic properties are given in [10].

Thermodynamic properties are calculated within the framework of the "quasi-single-fluid models" [6]. In this approach, the mixture is treated as a pure substance. Substance

identification is done on the value of the pseudocritical (hereinafter referred to as critical) properties (T_c, ρ_c) and acentric factor ω. To calculate the critical temperature, critical pressure and acentic factor the authors used the relations proposed by Kesler and Lee [7]. To calculate the critical density, the authors used the ratio proposed in [8].

Within the framework of the "quasi-single-fluid models", the mixture is a ideal solution of alkanes and cyclic hydrocarbons, featuring the same critical properties and acentric factor. Thermodynamic property Y is calculated according to the additive formula

$$Y = Y_a x_a + Y_c x_c \tag{5}$$

where Y_a, Y_c – thermodynamic property calculated from equation (1), accordingly using the coefficients for alkanes and cyclic hydrocarbons; x_a, x_c – accordingly, the proportion of alkan and cyclic structures in mixture.

x_a and x_c values were determined by $n_D - \rho - M$ -method of structural group analysis [9] based on the data of the refractive index at temperature 20 ^{o}C n_D^{20}, relative density at the same temperature ρ_4^{20} and average molar mass M.

In the process of calculating thermodynamic properties from equation (1) the critical density correction was carried out on the value of the relative density ρ_4^{20} determined under laboratory conditions with high accuracy ($\sim 0,02$ %).

3. New Correlation of Thermal Conductivity

The new generalized thermal conductivity equation of complex hydrocarbon mixtures is given by

$$\Delta\tilde{\lambda} = \sum_{i=1}^{5} n_i \tau_\lambda^{t_i} \delta_\lambda^{l_i} \exp(-\delta_\lambda^{k_i}) \tag{6}$$

where the scaled residual thermal conductivity $\Delta\tilde{\lambda}$ can be defined by the following relation

$$\Delta\tilde{\lambda} = \left[\lambda(p,T) - \lambda^0\right]\Lambda_\lambda \tag{7}$$

Analysis of thermal conductivity in various scales presented in [1, 2]. The most effective was the following

$$\Lambda_\lambda = T^{-\left(\frac{1}{2}\right)} M^{-\left(\frac{1}{6}\right)} \rho^{-\left(\frac{2}{3}\right)} \tag{8}$$

For the calculation of residual thermal conductivity $\Delta\tilde{\lambda} = (\lambda(p,T) - \lambda^0)$ the data on the dilute gas thermal conductivity λ^o are needed. The different calculation methods of λ^o are analyzed in detail in the work [1]. As a result, we recommend to use a simple correlation for polyatomic gases by Eiken [10]. It should be borne in mind that Eiken's correlation gives a slightly lower values of λ^o, and the modified correlation [10] – elevated. Given this fact, we

recorded the final formula as a cross between two correlations, that is very close to the formula of Thodos [10].

$$\lambda^0 \cdot 10^3 = \frac{\eta^0}{M}(16,75 + 1,15 C_v^\infty) \tag{9}$$

where λ^o, W/(m·K); η^o, uPa·c; C_v^∞ – isohoric heat capacity in the ideal-gas state, kJ/(kmol·K); M– average molar mass, kg/kmol.

To calculate the value of η^o, the authors used the ratio proposed by Lee and Thodos in [11]:

$$\eta^0 \xi = 1,564 \tau^{0,94} \tag{10}$$

where $\xi = T_c^{1/6}/M^{1/2}/P_c^{2/3}$; $\tau = T/T_c$; η^o, uPa·c; P_c, MPa;
and to calculate the ideal-gas heat capacity the authors used $n - \rho - M$ - method developed in [1].

In the generalized equation (6) $\tau_\lambda = T/T_\lambda$ is the reduced temperature and $\delta_\lambda = \rho/\rho_\lambda$ is the reduced density. As the reducing state the point on the pseudocritical isobar with a fixed value of scaled thermal conductivity $\Delta\tilde{\lambda} = 0,25$ was chosen.

The scaled fixed value of residual thermal conductivity was chosen in such a way that the temperature T_λ was within the limits of the experimental investigated range. Defined by experimental data the temperature T_λ was approximated by the equation (11).

$$\frac{T_\lambda}{T_c} = C_0 + C_1 Y + C_2 Y^2 + C_3(K_w - 10) + C_4(K_w - 10)^2 + C_5 Y(K_w - 10)$$
(11)

where the characteristic complex of Y is given by the ratio (12)

$$Y = \frac{100\left[(n_D^{20})^2 - 1\right](n_D^{20} - \rho_4^{20})}{M\rho_4^{20}(n_D^{20} + 0,4)} \tag{12}$$

and the Watson factor $K_w = 1,2251\dfrac{T_{bv}^{1/3}}{\rho_{15}^{15}}$. T_{bv} - is the average volume boiling point temperature. The coefficients of equation (11) are given in Table 1.

Table 1: The coefficients of equation (11)

C_0	C_1	C_2	C_3	C_4	C_5
0,180689	1,279527	-0,443805	0,032758	0,020290	-0,180112

The most reliable experimental data were selected in order to develop the generalized correlation. An array of data was included in the fitting procedure consisting largely of λ obtained in the 1980's in the laboratory of the Grozny Petroleum Institute [12, 13]. A representative array of data on thermal conductivity consisted of the data of eighty hydrocarbon fractions of petroleum and gas origin over a temperature range 243 – 673 K and at pressures up to 60 MPa.

The value of error for different experimental installations were 1,0 - 1,3 % at temperature 273 K, and 1,8 - 2,2 % at temperature 523 K, and 3,0 % at temperature 673 K [12, 13]. The experimental data have been agreed between both and are characterized by minimal systematic error. Defined by experimental data the values of T_λ described by equation (11) with the root-mean-square deviation (RMS) 2,54%.

The values of the coefficients of generalized equations for scaled residual thermal conductivity where determined based on the array of experimental data, that was described above, and consisted of eighty substances and contained 4582 of experimental values of λ. Initially, for each substance using the generalized equation of state (1) at temperature T_λ and at pseudocritical pressure P_c the reference values of density ρ_λ were determined.

The coefficients of the equation (6) are individual for each substance. For the generalization, the following relation was used

$$n_i = C_{0i} + C_{1i}Y + C_{2i}Y^{C_{3i}} + C_{4i}\frac{Y}{(K_w - 9)} + C_{5i}K_w \qquad (13)$$

A nonlinear optimization procedure was used to develop equation (6). The fitting procedure was described in [14]. Optimization of the coefficients and exponents of equation (6) and (13) took place simultaneously in a nonlinear form. The exponents of equation (6) and coefficients of equation (13) are given in Table 2 and Table 3.

Table 2: The exponents of generalized equation (6).

i	t	l	k
1	-0,9301	2	1
2	-0,2844	5	1
3	0,0000	7	2
4	-1,1764	3	2
5	-0,8649	1	3

Table 3: The coefficients of generalized equation (13).

i	C_0	C_1	C_2	C_3	C_4	C_5
1	-5,5373697	5,7182649	7,8139013	1,1511177	28,531293	-34,619885
2	-1,6735260	-6,7753130	2,6102832	$-1,2359813 \cdot 10^{-2}$	-0,49082253	14,950954
3	-2,4371986	0,97134763	-0,28373253	-0,23338786	0,73676059	23,649297
4	-0,94035077	-6,9501349	7,8270498	$8,4020411 \cdot 10^{-2}$	-22,258795	0,95542361
5	0,14452793	-1,8417593	2,3085567	$-9,7010118 \cdot 10^{-2}$	-6,6227901	-5,7480582

The root-mean-square deviation (RMS) for the selected array of experimental data was 2,43 %, and the average absolute deviation (AAD) was 2,25%, that is better the results, that we got in [1, 2]. It is important to note that in [1, 2] the calculation of the deviation was made in the range of applicability of the method, that is limited to the value of the reduced density $\rho/\rho c \geq 2$. Figure 1.a. present the characteristics of the uncertainties.

Figure 1.b. present the characteristics of the uncertainties for gas condensates and their fractions. We have included in the analysis the experimental values of λ, that was obtained in different years in Kasnodar State Technological University over a temperature range 230 – 470 K and at pressures up to 100 MPa [15]. The uncertainty of the single measurement of λ in [15] do not exceed 1,5 %. Total 13 gas condensates of various fields and

23 their fractions was investigated in Tashkent Road Institute over a temperature range 250 – 530 K and at pressures up to 40 MPa [16]. The uncertainty of the single measurement of λ in [16] do not exceed 3,1 %. Total 10 gas condensates of various fields and 18 their fractions was investigated in the work of Kazarian [17] using the regular mode method over a temperature range 220 – 470 K and at pressures up to 60 MPa. The four gas condensates and six straight-run fractions of gas condensate of Vuktyl field were investigated. Accuracy of data is not reported.

The root-mean-square deviation (RMS) for gas condensates was 6,2 %, and the average absolute deviation (AAD) was 5,81%. Thus, all the results are better than the results that we got in [1, 2]. The value of deviations for gas condensates and their fractions is significantly larger than for the original array containing the data of λ on petroleum fractions. The reason for this is the high uncertainty of experimental data for both the λ and the physical and chemical properties that are required for the calculation.

a)

b)
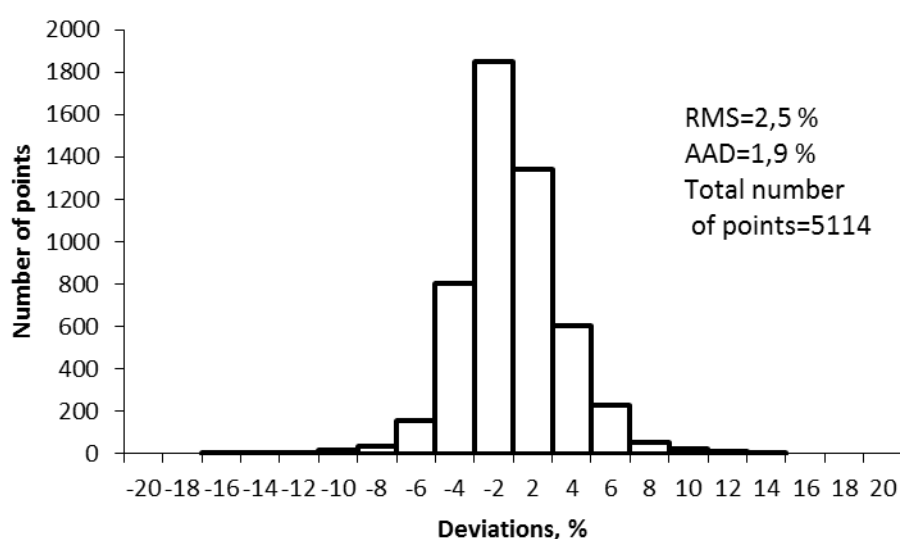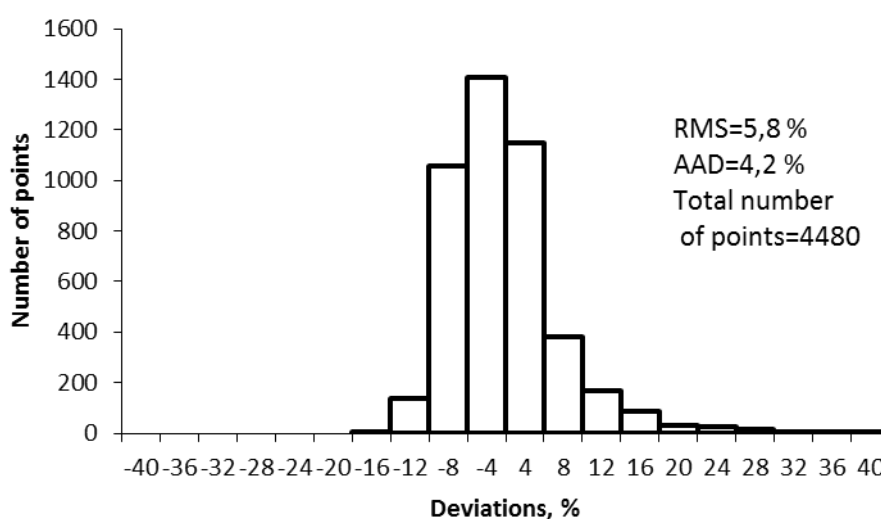
Fig. 1. Comparisons of deviations for thermal conductivity calculated from generalized equation (6):

a) petroleums, their fractions and trade products; b) gas condensates and their fractions.

4. Conclusion

As a result of the use of generalized equations of state and effective algorithm of nonlinear optimization the new thermal conductivity correlation for complex hydrocarbon mixtures was developed. The new correlation differs from the previous by a wider range of applicability on temperature and pressure, by the lack of restrictions on group hydrocarbon composition of mixtures, and by more accurately predictiving thermal conductivity.

5. References

[1] Grigor'ev B.A. (2007) *Thermophysical properties and phase equlibria of gas condensates and their fractions.* Moscow Power Institute, 344 p. ISBN 978-5-383-00050-2.
[2] Grigor'ev B.A. Analysis and development of new methods of calculation of thermal conductivity of oil, gas condensates and their fractions / B.A. Grigor'ev, A.A. Gerasimov, E.B. Grigor'ev // Defense complex - scientific and technical progress of Russia. – 2009. – No.3. – P.67-72.
[3] Grigor'ev B.A. Analysis of the application of single-fluid model for calculation of thermodynamic properties of multicomponent hydrocarbon mixtures based on the fundamental equation of state / B.A. Grigor'ev, A.A. Gerasimov, I.S. Alexandrov // Relevant issues of studies of field hydrocarbons formations: collection of scientific articles. – Moscow, VNIIGAZ. – 2012. – 412 p.
[4] Sun L. Universal equation of state for engineering application: algorithm and application / L. Sun, J.E. Ely // Fluid Phase Equilibria. – 2004. – V.222-223. – P.107- 118.
[5] Span R. Multiparameter Equation of State: An Accurate Source of Thermodynamic Property Data/ R.Span. – Berlin: Springer, 2000. – 367 p.
[6] Grigor'ev B.A. (1999) *Thermophysical properties of petroleum, oil-products, gas condensates and their fractions.* Moscow Power Institute, 372 p. ISBN 5-7046-0483-8.
[7] Kesler M.G. Improve prediction of enthalpy of functions / M.G. Kesler, B.I. Lee // Hydrocarbon Processing. – 1976. – V.55, No.3. – P.153-158.
[8] Riazi M.R. Simplifi property predictions / M.R. Riazi, Th.E. Daubert // Hydrocarbon Processing. – 1980. – V.59, No.3. – P. 115-116.
[9] Van Nes K., Van Westen H.(1954) *Aspects of the constitution of mineral oils.* Elsevier Publishing Company. Amsterdam. 463 p. ISSN 1095-9203.
[10] Poling, B.E.(2004). *The Properties of Gases and Liquids* (Revised 5th ed.). McGraw-Hill. ISBN 0071499997.
[11] Lee H. Generalized viscosyti behavior of fluids over the complete gaseous and liquid states / H. Lee, G. Thodos // Ind. Eng. Chem. Res.– 1988.– V.27, No.12.– P.2377–2384.
[12] B.A. Grigor'ev, *Study on Thermophysical properties of oils, petroleum products and hydrocarbons*, D. Sc. thesis (USSR, Grozny, 1979).
[13] G.F. Bogatov, *Thermal conductivity of individual hydrocarbons and petroleum products in the liquid state*, D. Sc. thesis (USSR, Grozny, 1992).
[14] Alexandrov I.S. A modern approach in the development of fundamental equations of technically important working substances / I.S. Alexandrov, B.A. Grigor'ev, A.A. Gerasimov

// Relevant issues of studies of field hydrocarbons formations: collection of scientific articles. – Moscow, VNIIGAZ. – 2011. – 296 p.

[15] Experimental research of thermophysical properties of stable gas condensates and their fractions in liquid phase: Scientific report. / Kasnodar State Technological University: A.S. Magomadov. – Theme №112.04.14. – Krasnodar: KSTU, 1994.– 171 p.

[16] Mutalibov A.A. Thermal conductivity of gas condensates and their fractions / A.A. Mutalibov, V.V. Shubin, G.N. Mahmudov, R.R. Valitov, L.N. Astaf'eva // Tables of recommended reference data. - State service of standard reference data. - R308-89.– 40 p.

[17] Kazarian V.A. (2002) *Thermophysical properties of individual hydrocarbons and gas condensates.* Moscow, "Technique", 448 p. ISBN 978-5-93969-019-5.

Acknowledgements

Thermophysical Characterization of a Urea Based Eutectic Mixture for Thermal Energy Storage

S. Gómez-Cavia [1], G. Diarce [1], A. Campos-Celador [2], A. García-Romero [1], J.M. Sala [3]

[1] ENEDI Research Group, Dpto. de Ingeniería Minera, Metalúrgica y Ciencia de los Materiales, Escuela Universitaria de Ingeniería Técnica de Minas y Obras Públicas, University of the Basque Country UPV/EHU, Rafael Moreno Pitxitxi 2, Bilbao, 48013, Spain. E-mail: gonzalo.diarce@ehu.es
2 ENEDI Research Group, Dpto. de Máquinas y Motores Térmicos, Escuela Universitaria de Eibar, University of the Basque Country UPV/EHU, Avda. Otaola 29, Eibar 20600, Spain.
3 ENEDI Research Group, Dpto. de Máquinas y Motores Térmicos, Escuela Técnica Superior de Ingeniería de Bilbao, University of the Basque Country UPV/EHU, Alameda Urquijo s/n, Bilbao 48013, Spain.

Summary

Eutectic mixtures of urea with other materials could be suitable materials for latent thermal storage. The mixtures could show a melting point in the domestic hot water (DHW) systems. The main advantage would be the low cost of the urea although many authors have dismissed it mainly due to its poor thermal stability.

The present article deals with the thermo analytical evaluation of the eutectic mixture based on urea and sodium nitrate in the temperature range 60-90°C. The potential application of this material is focused on thermal storage systems for cogeneration and solar ACS facilities. The material degrades with increasing temperature. However, if its degradation takes place slowly enough below 90°C, this material could be integrated in the system. That would prove the suitability of the mixture to be applied in latent heat thermal energy storage, in the specific temperature range. Therefore, the objective of this work is to determine the stability of the urea and urea based eutectic mixtures in the temperature range 60-90ºC. In the case that the stability is good enough in this temperature range, the urea mixtures could be used as PCM with a lower cost than the currently commercialized materials.

Key-words: phase change materials, PCM, thermal storage, thermal decomposition, urea mixtures

1. Introduction

The published information available about the urea and urea-based eutectic mixtures is very limited. Previous studies [1-3] report data of several eutectic compositions, their melting temperatures and enthalpies. An eutectic mixture based on 77.5% urea and 22.5% sodium nitrate, with a melting temperature of 84.5ºC was reported as a potential candidate [2,3]. This eutectic mixture was excluded as PCM because after 25 thermal cycles the material was degraded.

Several other eutectic mixtures were suggested to be suitable as PCM [1], including one mixture composed of 70.5% urea and 29.5% sodium nitrate with a melting temperature of 84ºC. However, there is no indication about thermal stability or thermal cycling. Thermal decomposition has been reported as the main drawback of these mixtures [4].

The reported results differ to a large degree from one another. The discrepancy between these results shows the necessity to continue the research in order to determine it.

The present article deals with the thermo analytical evaluation of the eutectic mixture based on urea and sodium nitrate in the temperature range 60-90°C. Several thermo physical properties of the eutectic mixture (eutectic composition and temperature, melting enthalpy, subcooling, density, thermal stability, etc) have been determined by using analytical methods. The thermal stability and the melting

and crystallization behavior have been studied by thermo analytical and spectroscopic methods. Besides, new experimental methods have been developed to determine the density of the materials in liquid state.

2. Materials and methods

Eutectic mixtures of urea and sodium nitrate were prepared. The mixtures were melted in a hot plate and then quickly crystallized to room temperature. The produced solid was subsequently milled by a planetary mill and stored in closed containers at 6ºC before producing the thermal studies.

Thermal analyses have been performed with a differential scanning calorimeter (DSC) for the determination of the melting temperature and the melting enthalpy.

In order to study the thermal cycling stability of the mixture, the sample undergoes repeated thermal cycles in the DSC. First, 100 cycled were applied to the sample, from 10ºC to 95ºC at a heating rate of 3ºC min-1. The values of the onset temperatures and the melting enthalpies were recorded and plotted. When the samples were not degraded after 100 cycles, another 100 cycle period was applied.

An experimental method to determine the relative density of liquid eutectic mixtures has been developed. The principle is based on the measurement of the weight difference between an inert body immersed in a liquid and the same body in the open air. A specific experimental set-up was prepared composed of a thermostatic bath, a weight-scale and a double jacket beaker. The same device is applied to measure the density of the sample in solid state.

3. Results

The results of the melting temperature and the melting enthalpy show a good agreement with the data published in the literature. Four samples of the eutectic composition were measured applying the same DSC method. Reproducible results were obtained (an average melting enthalpy of 155 J/g and a melting point of 84ºC). Besides, the samples showed a low subcooling.

The thermal cycling evidenced an absence of enthalpy decrease as successive melting-crystallization cycles take place. The melting temperature determined from curve-onset values neither presents a decrease over the cycling.

According to the density measurements, the urea-sodium nitrate eutectic mixture shows a larger (5%) density in liquid than in solid state.

4. Conclusions

A 70.5% urea- 29.5% sodium nitrate eutectic mixture has been studied. The determined melting temperature is 84 ºC and the melting enthalpy is 167 J/g. These results indicate that the mixture could be suitable as PCM in the working temperature range for sanitary-domestic water, i.e. 60-90ºC. The thermal stability of the mixture in this temperature range has been evaluated up to 200 cycles, concluding that the sample does not undergo thermal degradation in those testing conditions.

Larger thermal cycling is required to precisely determine the tendency towards a thermal degradation. In addition, thermal degradation kinetics are required to be studied in order to know the urea degradation rate, and evaluate the feasibility to be used as PCM for a defined period of time.

A future research topic will also include the determination of the phase diagram of the system urea and sodium nitrate, presently not avaliable in the published literature.

5. References

[1] Kauffman, K., Gruntfest, I., 1973. Congruently melting materials for thermal energy storage.

[2] Gambino.M., Gaune. P., Navabian. M., Gaune-Escard. M., Bros. J.P., 1987. Enthalpie de fusion de l´uree et de quelques melanges eutectiques a base d´uree. Thermochimica Acta. 111, 37-47.

[3] Gambino. M., Bros. J.P., 1988. Capacite calorifique de l´uree et de quelques melanges eutectiques a base d´uree entre 30 et 140ºC. Thermochimica Acta. 127, 223-236.

[4] Kamimoto. M., Sakamoto. R., Takahashi. Y., Kanari. K., Ozawa. T., 1984. Investigation of latent heat-thermal energy storage materials. II. Thermoanalytical evaluation of urea. Thermochimica Acta. 74, 281-290.

Acknowledgements

Progress in Phosphorus–Containing Polymers: Design, Structure and Properties

Tachita Vlad-Bubulac [1], Diana Serbezeanu [1], Corneliu Hamciuc [1], Ionela-Daniela Carja [1]

[1] "Petru Poni" Institute of Macromolecular Chemistry, Aleea Gr. Ghica Voda, 41A, Iasi, 700487, Romania,
E-mail: tvladb@icmpp.ro

Abstract*:* The present contribution focuses on our research in the field of phosphorus-containing macromolecular compounds, the main goals being the design, synthesis, characterization and study of the properties of new polymers containing phosphaphenanthrene heterocycle in the side chain. These polymers have been prepared by polycondensation reaction between an aromatic dichloride, aromatic bisphenols and other aliphatic diols. The complete synthetic procedure of the monomers, intermediates and polymers has been discussed. The structure of the monomers and intermediates and the basic characterization of the polymers have been performed using NMR and FTIR spectroscopy. The complete study of thermal stability, liquid crystalline behaviour, fire resistance was also done, by means of thermogravimetric analysis (TGA), FTIR-TGA measurements, differential scanning calorimetry (DSC), polarized light microscopy (PLM) etc. The structure-properties correlations have been discussed.

Keywords: phosphorus-containing polymers, thermal stability, liquid crystalline polymers

Introduction

Fully aromatic thermotropic polymers have been intensively studied due to their attractive physico-chemical properties [1]. However, these polymers possess high melting and isotropization temperatures which result in poor melt-processability [2, 3]. Thus, the current research in the field of thermotropic liquid crystalline polymers is to design and prepare aromatic polymers with low melting temperatures which allow the formation of a liquid crystalline phase bellow the temperature of polymer decomposition or isotropization.

The drawbacks of fully aromatic thermotropic polymers can be overcome by suitable design of polymers with aliphatic and aromatic moieties, introduction of bulky lateral substituent, copolymerization etc [4, 5]. Our specific interest in aromatic copolyesters containing phosphaphenanthrene bulky groups originates from the attractive properties induced by the presence of this heterocycle into the macromolecular chain: improved solubility, high thermo-oxidative stability, good adhesion, reduced birefringence, flame resistance properties etc. [6-15]. On the other hand, the utilization of flexible spacers between the calamitic mezogens is a known approach used to decrease the transition temperatures [16, 17].

The present work describes the results of polycondensation reaction of 1,6-hexanediol (**1a**), 1,12-dodecanediol (**1b**) or 2,7-dihydroxy-naphthalene (**1c**) with terephthaloyl-bis-(4-oxybenzoyl-chloride) (**2**) and two aromatic bisphenols incorporating phosphafenanthrene heterocycle, namely 2-(6-oxido-6H-dibenz<c,e><1,2>oxaphosphorin-6-yl)-1,4-benzenediol (**3a**) and 2-(6-oxido-6H-dibenz<c,e><1,2>oxaphosphorin-6-yl)-1,4-naphthalene diol (**3b**). The solubility, thermal stability and glass transition temperature of the polymers have been investigated. Mesogenic phases were observed by polarized light microscopy. Comprehensive studies on the relationship between the aliphatic/aromatic ratio, polymer liquid crystalline phase structure, flame retardancy, and thermo-oxidative stability of the copolyesters based on phosphorus-containing monomers, have been performed.

Materials and Methods

1,6-Hexanediol, 1,12-dodecanediol and 2,7-dihydroxy-naphthalene were provided from Aldrich and used as received.

Terephthaloyl-bis-(4-oxybenzoylchloride), **2**, was synthesized by treating with excess thionyl chloride, at reflux temperature, of the corresponding dicarboxylic acid that resulted from the reaction of 4-hydroxybenzoic acid with terephthaloyl chloride, according to a method presented in the literature [18]; mp.: 223-226 °C. IR (KBr, cm-1): 1780 (COCl), 1730 (COO), 1600 (aromatic), 1210 (Ph-O-OC).

2-(6-Oxido-6H-dibenz<c,e><1,2>oxaphosphorin-6-yl)-1,4-benzenediol, **3a**, was synthesized from 9,10-dihydro-9-oxa-10-phosphaphenanthrene-10-oxide (**DOPO**) and *p*-benzoquinone [19]. It was recrystalised from toluene/ethanol 1:1; m.p.: 255-256 °C. IR (KBr, cm^{-1}): 3240 (–OH), 1470 (P–Ph), 1190 (P=O), 1168 and 925 (P–O–Ph). ^{1}H-NMR (DMSO-d$_6$, ppm): δ = 10.7 (1H, s), 9.8 (1H, s), 8.24 (2H, m), 7.74 (2H, m), 7.52 (2H, m), 7.31 (3H, m), 6.91 (1H, s), 6.67 (1H, s).

2-(6-oxido-6H-dibenz<c,e><1,2>oxaphosphorin-6-yl)-1,4-naphthalene diol, **3b**, was synthesized from **DOPO** and naphthoquinone [20]. It was recrystalised from ethoxyethanol; mp. (DSC): 279-280 °C. IR (KBr, cm^{-1}): 3430 (–OH), 1470 (P–Ph), 1190 (P=O), 1165 and 925 (P–O–Ph). ^{1}H-NMR (DMSO-d$_6$, ppm): δ = 10.7 (1H, s), 9.8 (1H, s), 7.9 (2H, m), 7.8 (1H, m), 7.7 (1H, m), 7.5 (4H, m), 7.4 (1H, m), 7.3 (1H, m). 7.2 (1H, t), 7.1 (1H, t), 6.6 (1H, d).

Infrared spectra were recorded with a Specord M80 spectrometer by using KBr pellets. TGA was performed in air at 10 °C/min with a Mettler Toledo model TGA/SDTA 851. The initial mass of the samples was 3-5 mg. DSC was performed with a Mettler TA Instrument DSC 12E at a heating rate of 10 °C/min under nitrogen atmosphere. PLM investigations were performed with an Olympus BH-2 polarized light microscope fitted with a THMS 600/HSF9I hot stage, at a magnification of 200× and 400×. The mesomorphic transition temperature and disappearance of birefringence, that is, the crystal-to-nematic (T_m) and nematic-to-isotropic (T_i) transition were noted.

Results and Discussion

The copolyesters **4** and **5** have been obtained by solution polycondensation reaction of aromatic dichloride **2** with an equimolar amount of diols **1** and bisphenols **3** (Figure 1). The structures of the resulting polymers have been confirmed by spectral methods. Generally, characteristic FTIR absorption peaks appeared at 1740 cm^{-1} due to carbonyl asymmetric stretching of ester groups.

Phosphorus characteristic absorption peaks appeared at 925 cm^{-1} and 1160 cm^{-1} due to P–O–Ph groups, at 1470 cm^{-1} due to P–Ph groups and at 1205 cm^{-1} due to P=O groups, while aliphatic characteristic absorption peaks were observed at 2920 cm^{-1} and 2839 cm^{-1} due to the presence of methylene groups. Aromatic C=C bands were found at 1600 cm^{-1} and 1500 cm^{-1}, while aromatic C-H absorption was found at 3067 cm^{-1}.

The glass transition temperature (T_g) of polymers **4** and **5**, evaluated from DSC curves ranged between 83 °C and 149 °C (Table 1) being dependent on the nature of monomers **1** and/or **3**. The presence of **DOPO** pendent units into the macromolecular chain led to higher rigidity of the backbone, resulting in higher values of T_g. The polymers **4b** and **5b** incorporating 12

methylene groups per structural unit exibited the lowest values of the T_g, 83 °C and 89 °C, respectively, as a result of the increasing flexibility of the macromolecular chain.
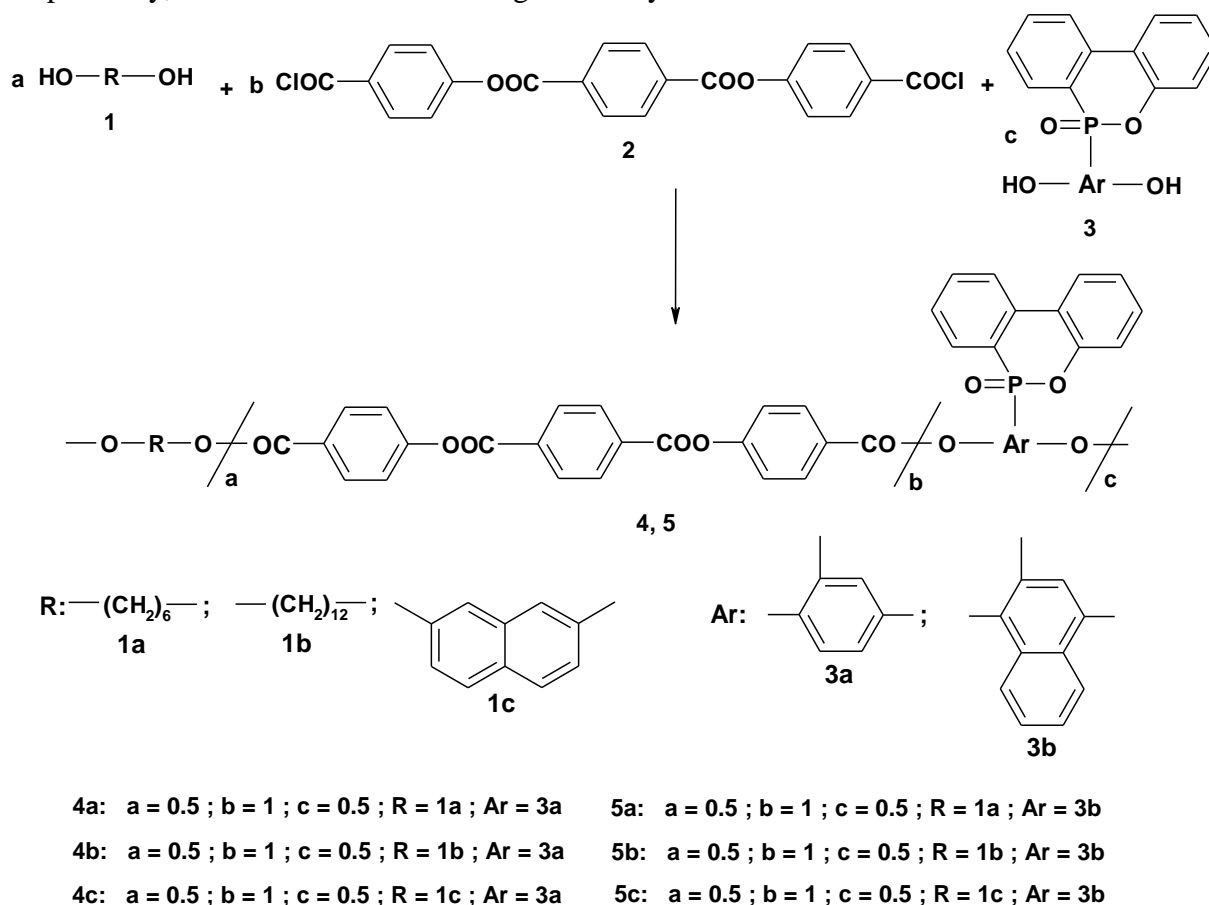
Figure 1 The preparation of polymers **4** and **5**.

The melt morphology of polymers **4** and **5** was evaluated by visual observation on a hot-stage polarized microscope. All polymers formed liquid crystalline mesophases upon heating according to observation of their optical textures on a cross-polarizing microscope. The data of mesomorphic transitions temperatures T_m and isotropisation temperature T_i are given in Table 1. Figure 2 presents different liquid crystalline textures of the sudied polymers.

The liquid crystalline behavior of the polymers **4** and **5** depended on the nature of the monomers **1** and/or **3**. The transition temperature from crystal to liquid-crystalline melt was in the range of 199 °C – 318 °C and depended mainly on the content of aliphatic CH_2-groups. The T_m and T_i of polymer **4c** were relatively higher due to the pronounced rigidity of the macromolecular chains. The introduction of naphthalene units increased the T_m and T_i values of polymers **4c** and **5c**. Significant decrease of mesomorphic transitions was observed for the polymers **4a**, **4b**, **5a** and **5b** due to the copolymerization effect and introduction of aliphatic segments with higher number of methylene groups into the macromolecular chain. Thus, the polymer **5b** based on 1,12-dodecanediol exhibited the lowest solid to LC mesophase transition (T_m = 199 °C). The isotropic transition was not clearly detected by DSC measurements in the case of the polymers **5a** and **5c** due to some thermal degradation process that took place.

Upon heating, all the LC polymer melts sheared on glass plates formed fine ordered grainy textures (Figure 2a), characteristic for nematic phases. Upon cooling from the isotropic state,

the polymer melts formed LC mesomorphic textures (Figure 2b) that by annealing developed Schlieren nematic textures (Figure 2c) or highly birefringence nematic textures (Figure 2d).

Table 1: Thermal properties of the polymers **4** and **5**.

Polymer	T_g °C	T_m °C	T_i °C	IDT °C	T_{10} °C	T_{max1} °C	T_{max2} °C	Char yield at 600 °C
4a	94	257	276	370	382	405	590	18
4b	83	234	282	387	401	421	601	11
4c	135	318	320	417	439	474	669	40
5a	102	232	-	395	405	418	603	17
5b	89	199	296	390	398	422	592	14
5c	149	222	-	381	410	466	648	36
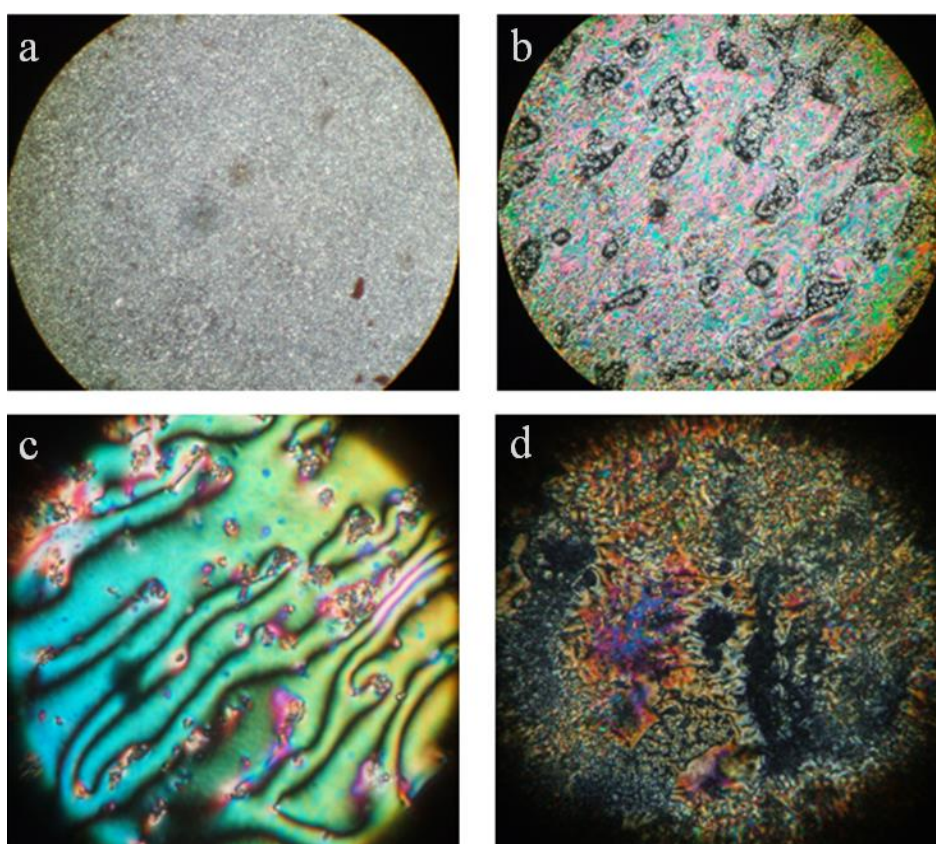
Figure 2 Optical polarized microphotographs for **5c** first heating at 265 °C (a), **5b** first cooling 281 °C (b), **5b** first cooling 280 °C (c), **5c** first heating 265 °C (d)

The thermal stability was evaluated by thermogravimetric analysis. The polymers did not show significant weight loss below 370 °C. They began to decompose in the range of 370 °C – 417 °C and they presented a 10 wt % loss in the range of 382 °C – 439 °C. From differential thermogravimetric curves of **DOPO-**containing polymers **4** and **5** it was established that the degradation process exibited two stages of thermal decomposition. The first maximum of decomposition (T_{max1}) was in the range 405 °C – 474 °C and was due to the degradation of ester units and the cleavage of **DOPO** groups which are more sensitive to thermal degradation. The second maximum of decomposition (T_{max2}) was in the range of 590 °C – 669 °C and was due to the degradation of polymer chain itself (Table 1). To further investigate the mechanism of thermal decomposition, the FTIR spectrum of the solid residue of polymer **5b**,

after heating the sample up to 460 °C with the heating rate of 10 °C/min, was examined. The value of 460 °C represents the temperature of the end of the first decomposition process, according to DTG curve.

As we disscused earlier, the most important absorption bands in the FTIR spectrum of polymer **5b** (the pristine, unheated, sample) were associated with aromatic C–H (3066 cm^{-1}, stretching vibration), aliphatic C–H (2922 cm^{-1} and 2841 cm^{-1}, asymmetric and symmetric stretching vibration), C=O (1740 cm^{-1}, stretching vibration), C–O–C ester (1260 cm^{-1} and 1001 cm^{-1}, asymmetric and symmetric stretching vibration), P–O–Ph (926 cm^{-1}, stretching vibration), aromatic C–H (760 cm^{-1}, deformation vibration caused by the 1,2-disubstituted aromatic **DOPO** heterocycle), aromatic C–H (715 cm^{-1}, deformation vibration from aromatic terephthaloyl segment) [21, 22].

By heating the sample to aproximately 25% weight loss, a decrease in intensity of the C–H aliphatic, C=O and C–O–C ester absorption bands was observed. This can be associated with thermal decomposition of the ester groups followed by the volatilization of some aliphatic moieties from the macromolecule. This process was almost complete at about 50% weight loss, when the FTIR spectrum did not exhibit the absorption bands characteristic for aliphatic structures. However, during the decomposition process, the C=O stretching vibration, did not completely vanish, but became smaller and shifted to 1730 cm^{-1}, the newer position in the spectrum being in agreement with that in polyarylates [21, 23]. At this stage it can be assumed that a transformation of the aromatic-aliphatic copolyester to an aromatic-aromatic polymer took place by volatilization, during the heating/decomposition process, of the aliphatic moieties. The other new broad absorption bands located at 1228 cm^{-1}, 1169 cm^{-1}, 1060 cm^{-1} and 733 cm^{-1} were found to be also in agreement with the formation of the aromatic-aromatic polyarylates. Another new broad absorption band centered at 1596 cm^{-1} was associated with the appearance of polyaromatic structure [24]. The organophosphorus P–Ph, P–O–Ph and P=O groups incorporated in the solid residue were distinguished by the presence of the absorption bands located at 1470 cm^{-1}, 925 cm^{-1} and 1180 cm^{-1}, respectively.

It can be concluded that in the first step of degradation, the destruction of aliphatic moieties and ester groups with an increase of phosphorus content took place. This agreed with the high char yield at high temperature. Thus, the char yield at 600 °C ranged between 11 % and 40 % (Table 1). A decrease of char yield at 600 °C was observed by introducing of aliphatic diols instead of 2,7-dihydroxy-naphthalene.

Conclusions

The polycondensation of 2-(6-oxido-6H-dibenz<c,e><1,2>oxaphosphorin-6-yl)-1,4-benzenediol or 2-(6-oxido-6H-dibenz<c,e><1,2>oxaphosphorin-6-yl)-1,4-naphthalene-diol with terephthaloyl-bis(4-oxybenzoyl-chloride), in *o*-dichlorobenzene, at high temperature resulted in liquid crystalline phosphorus-containing copolymers.

They exhibited good thermal stability, with decomposition temperature above 375 °C and glass transition temperatures in the range of 83 °C – 149 °C.

The thermotropic liquid crystalline behavior occurred upon polymer melting was observed by POM and DSC. The phosphorous-containing copolyesters were shown by POM to form liquid crystalline phases. The copolyester which had the lowest isotropization temperature was the polymer containing the longest flexible 12-methylene spacer linkage. LC copolyesters

containing shorter 6-methylene flexible spacer units or fully aromatic structural unit exhibited the most birefringent LC textures and, upon formation of the LC state, showed no isotropization temperature below °C.

References

[1] Wang, X.J., Zhou, Q. 2004. *Liquid Crystalline Polymers*, Singapore: World Scientific, 388 pages. ISBN: 9812384103.

[2] Yerlikaya, Z., Aksoy, S., Bayramli, E. 2001. Synthesis and characterization of fully aromatic thermotropic liquid-crystalline copolyesters containing m-hydroxybenzoic acid units. *Journal of Polymer Science Part A: Polymer Chemistry*, 39, 19, 3263–3277.

[3] Bhowmik, P.K., Han, H., Cebe, J.J., Burchett, R.A. 2002. Thermotropic liquid-crystalline polyesters of 4,4′-biphenol and phenyl-substituted 4,4′-biphenols with 4,4′-oxybisbenzoic acid. *Journal of Polymer Science Part A: Polymer Chemistry*, 40, 1, 141–155, 2002.

[4] Sato, M., Tada, Y., Nakashima, S., Ishikura, K.I., Handa, M., Kasuga, K. 2005. Synthesis and optical and electrochemical properties of thermotropic, liquid-crystalline, semirigid copolyesters based on 2,5-diphenyl-1,3,4-thiadiazole units. *Journal of Polymer Science Part A: Polymer Chemistry*, 43, 7, 1511–1525.

[5] Wang, Y.Z., Chen, X.T., Tang, X.D. 2002. Synthesis, characterization, and thermal properties of phosphorus-containing, wholly aromatic thermotropic copolyesters. *Journal of Applied Polymer Science,* 86, 5, 1278–1284.

[6] Levchik, S.V., Weil, E.D. 2005. Flame retardancy of thermoplastic polyesters–a review of the recent literature. *Polymer International*, 54, 1, 11–35.

[7] Balabanovich, A.I., Pospiech, D., Korwitz, A., Hausler, L., Harnish, C. 2009. Pyrolysis study of a phosphorus-containing aliphatic–aromatic polyester and its nanocomposites with layered silicates. Polymer *Degradation and Stability*, 94, 3, 355–364.

[8] Liu, Y.L., Tsai, S.H. 2002. Synthesis and properties of new organosoluble aromatic polyamides with cyclic bulky groups containing phosphorus, *Polymer*, 43, 21, 5757–5762.

[9] Sun, Y.M., Hung, A.Y.C., Wang, C.T. 2002. Studies on the synthesis and optical properties of novel blue light-emitting polymers containing phosphorus and oxadiazole structures. *Journal of Applied Polymer Science*, 85, 11, 2367–2376.

[10] Hoffmann, T., Pospiech, D., Haussler, L., Komber, H., Voigt, D., Harnisch, C., Kollann, C., Ciesielski, M., Doring, M., Perez-Graterol, R., Sandler, J., Altstadt, V. 2005. Novel Phosphorous-Containing Aromatic Polyethers – Synthesis and Characterization. *Macromolecular Chemistry and Physics*, 206, 4, 423–431.

[11] Liou, G.S., Hsiao, S.H. 2002. Synthesis and properties of aromatic poly(ester amide)s with pendant phosphorus groups. *Journal of Polymer Science Part A: Polymer Chemistry*, 40, 4, 459–470.

[12] Hamciuc, C., Vlad-Bubulac, T., Petreus, O., Lisa, G. 2007. Kinetics of thermal degradation in non-isothermal conditions of some phosphorus-containing polyesters and polyesterimides. *European Polymer Journal*, 43, 3, 980–988.

[13] Vlad-Bubulac, T., Hamciuc, C., Petreus, O., Bruma, M. 2006. Synthesis and properties of new phosphorus-containing poly(ester-imide)s. *Polymers for Advanced Technologies*, 17, 9-10, 647–652.

[14] Petreus, O., Vlad-Bubulac, T., Hamciuc, C. 2005. Synthesis and characterization of new polyesters with enhanced phosphorus content. *European Polymer Journal*, 41, 11 2663–2670.

[15] Serbezeanu, D., Vlad-Bubulac, T., Hamciuc, C., Aflori, M. 2010. Synthesis and properties of novel phosphorus-containing thermotropic liquid crystalline copoly(ester imide)s. *Journal of Polymer Science Part A: Polymer Chemistry*, 48, 23, 5391–5403.

[16] Vlad-Bubulac, T., Hamciuc, C. 2009. Aliphatic–aromatic copolyesters containing phosphorous cyclic bulky groups. *Polymer*, 50, 10, 2220–2227.

[17] Serbezeanu, D., Vlad-Bubulac, T., Hamciuc, C., Aflori, M. 2010. Structure and properties of phosphorous-containing thermotropic liquid-crystalline aliphatic–aromatic copolyesters. *Macromolecular Chemistry and Physics*, 211, 13, 1460–1471.

[18] Bilibin, A.Y., Tenkovtsev, A.V., Piraner, O.N., Skorokhodov, S.S. 1984. *Vysokomolekulyarnye Soedineniya*, A26, 2570.

[19] Wang, C.S., Shieh, J.Y. 1998. Synthesis and properties of epoxy resins containing 2-(6-oxid-6H-dibenz<c,e><1,2>oxaphosphorin-6-yl)1,4-benzenediol. *Polymer*, 39, 23, 5819–5826.

[20] Sun, Y.S., Wang, C.S. 2001. Synthesis and luminescent characteristics of novel phosphorus containing light-emitting polymers. *Polymer*, 42, 3, 1035–1045.

[21] Socrates, G. 2004. *Infrared and Raman characteristics groups frequencies: tables and charts.* 3rd ed. Chichester: John Wiley & Sons, 366 pages. ISBN: 0470093072.

[22] Thomas, L.C. 1974. *Interpretation of the infrared spectra of organophosphorus compounds.* London: Heyden, 270 pages. ISBN: 0855010347.

[23] Balabanovich, A.I. 2004. Poly(butylene terephthalate) fire retarded by bisphenol A bis(diphenyl phosphate). *Journal of Analytical and Applied Pyrolysis*, 72, 2, 229–233.

[24] Costa, L., Avataneo, M., Bracco, P., Brunella V. 2002. Char formation in polyvinyl polymers I. Polyvinyl acetate. *Polymer Degradation and Stability*, 77, 3, 503–510.

Acknowledgements

Study of Thermophysical and Mechanical Properties For New Composites Based on The Mortar and The Date Palm Wood to Use For Thermal Insulation In Buildings

Nadia Benmansour [a], Boudjemâa Agoudjil [a,*], Abdelkader Gherabli [a], Abdelhak kareche [a], Abderrahim Boudenne [b]

[a]Université El-Hadj-Lakhdar Batna, Laboratoire de Physique, Energétique Appliquée (LPEA), Batna 05000 Algérie.
[b]CERTES, Université Paris-Est Créteil, 61 Av. du Général de Gaulle, 94010 Créteil Cedex, France
*b.agoudjil@yahoo.fr

Abstract

This work focuses on the experimental study of thermophysical and mechanical properties of mortar reinforced with date palm fibers (DPF) and to the evaluation of the possibility of using this material as insulating component in buildings. The thermal and mechanical investigations were carried out on different composite samples as a function of DPF loading and sizes. The biocomposites were obtained by mixing cement, sand, and water for several palm wood fibres concentrations. Drying tests were performed in the air for 48 hours in the moulds and 28 days after moulding.

Keywords: Thermal properties, Mechanical properties, Date palm fibers, Thermal insulation, Composites.

Experimental Study

Composite Preparation

The biocomposites are obtained by mixing portlandcement(CPJ-CEMII/A32.5), sand and water for several weightconcentrations of DPF (5, 10, 15, 20, 25 and 30%). The samples are performed by mixing the fibers, cement and sand in a mixer (40 turn/minutes) during 5 minutes. The dry mixing is necessary to homogenize the mixture, so water is then added gradually. Then, the mixture is versed into cubic molds (15cm ×15cm ×15cm). Drying of the samples was performed in the open air for 48 hours in the molds and 28 days after demoulding. Three types of composites were prepared:

$MDP_{3.5mm}$: Mortar+ fine Fibers
$MDP_{6.3mm}$: Mortar + Large Fibers.
MDP_{Mix}: Mortar+ The mixture.

Measurements Methods

Thermal Conductivity of Composites

The thermal conductivity measurements were performed using a standard transient probe method based on hot wire method. The measurement is based on the analysis of temperature response of the sample to heat flow impulses.

Compressive Strength of Composites

The compressive strengthwas measured using a compression machine with standard NF EN196-1, type Controlab, precision of 0.001MPa, and loading speed of 0.5 MPa/S. All tested samples have undergone a surfacing.

Results obtained

This study shows that thethermalconductivityof mortar reinforced DPF biocomposites decreases with the increaseof the fibers DPF loading. Moreover,the increase inDPF concentrationleadsto a decrease of mechanicalproperties. However, interesting mechanical strength values were obtained at low concentration wood (5%, 10%, and 15 %). For example, for fibers content of 5%, for MDP $_{mix}$, the compressive strength reaches to 5Mpa.

Conclusion

Thus, as a conclusion, the optimum ratio of date palm fibers component is in the range of 5%-15%. For these fibers content, mechanical strength and thermal conductivity are consistent with the use of composites studied in the field of thermal insulation of buildings.

Finite Element Vibration Analysis of Epoxy Resin Reinforced with Carboxyl-Terminated Butadiene-Acrylonitrile (CTBN) Rubber

Gabriel Mansour [1], Konstantinos Tsongas [2], Dimitrios Tzetzis [3]

Abstract: A computational analysis is performed in order to investigate the vibrational behaviour of epoxy resin composites reinforced with Carboxyl-Terminated Butadiene-Acrylonitrile (CTBN) rubber. Mechanical tests were conducted for concentrations of 10, 15, 20 and 25wt% of CTBN as well as pure epoxy resin which served as a reference sample. The theoretical vibration modes of composite materials under study were calculated with the aid of finite element analysis (FEA). The FEA model simulated the samples with the various CTBN concentrations based on the properties derived from the mechanical tests. The method to evaluate the vibrational behaviour of the specimens was a cantilever beam excited into its fundamental mode by an impact force. The mechanical tests have shown a clear reduction of the modulus with the addition of CTBN, while it was evident from the results that the CTBN composites could absorb greater amounts of strain energy. The vibrational analysis results reveal that the cantilever beam reaches the highest tip deflection for the sample with 25wt% CTBN, while it demonstrates the highest rate of amplitude decrement among all tested samples. Overall, the study has shown that CTBN composites could advance the state-of-art in the field of polymeric damping, helping to ensure ductility and great amounts of energy dissipation in a wide variety of structural components and systems.

Keywords: Epoxy Resin, Carboxyl-Terminated Butadiene-Acrylonitrile, FEA, Vibrational behaviour.

1. Introduction

Vibrations are undesirable for structures due to the need for structural stability, position control, durability against fatigue, performance and noise reduction. Damping is an important modal parameter for the design of structures for which vibration control and cyclic loading are critical. Damping materials and their manufacturing technology are widely used for vibration and noise control on machine tools, rockets, missiles, satellites, airplanes, navigation equipment and electronic systems. Vibration reduction can be attained by increasing the damping capacity, which is expressed by the damping ratio and/or by increasing the stiffness, expressed by the storage modulus. The storage modulus measures the stored energy, representing the elastic portion, and the loss modulus measures the mechanical energy dissipated as heat, representing the viscous portion [1]. All engineering materials dissipate energy under cyclic load. Polymers, plastics and elastomers, dissipate much more energy per cycle than metallic materials, due to their viscoelastic character. Damping varies with different environmental effects, such as frequency, amplitude of stress, temperature, and static preload. Epoxy resins reinforced with CTBN rubber are promising damping materials for their large recoverable strain, high response and damping properties [2]. The CTBN micro-inclusions provide a sufficient reinforcement to enhance the mechanical properties of the conventional composites, due to their superior physical properties and large surface area. Adding rubber particulate (reactive liquid rubber CTBN) into polymer resin is an approach to effectively improve the damping behaviour of composites [3]. In general, embedding such inclusions, as CTBN rubber into a polymeric matrix system can effectively improve the ductility as well as the fracture toughness of the polymeric composites [4]. However, the influence of the CTBN rubber on the vibration response of epoxy base composites is rarely discussed in the literature.

[1] Associate Professor, Aristotle University of Thessaloniki, Department of Mechanical Engineering, Thessaloniki, Greece, mansour@ auth.gr
[2] PhD Student, Aristotle University of Thessaloniki, Department of Mechanical Engineering, Thessaloniki, Greece, ktsongas@ auth.gr
[3] Academic Associate, International Hellenic University, Thessaloniki, Greece, d.tzetzis@ihu.edu.gr

2. Materials and Methods

Preparation of epoxy/rubber composites

The epoxy resin that has been used to form the rubber reinforced composites was a standard diglycidyl ether of bis-phenol A/F (DGEBA/F) with an epoxide equivalent weight (EEW) of 169,7 g/eq., supplied by Gurit, UK. The reactive liquid rubber, which gives rise to the micrometer-sized spherical rubber particles upon curing of the formulation, was a carboxyl-terminated butadiene-acrylonitrile (CTBN) rubber. It was supplied as 40wt% CTBN-epoxy adduct, 'Albipox 1000' (EEW =330 g/eq), from Nanoresins, Germany. The curing agent was a 3-aminomethyl-3,5,5-trimethylcyclohexylamine (SP 115 Hardener with amine-hydrogen equivalent weight of 42,3 g/eq.), also supplied by Gurit, UK. In order to prepare a series of composites with 10–25 wt% rubber content, the SP115 epoxy resin was mechanically mixed with Albipox 1000-DGEBA/F masterbatch for 30min. The mixture was degassed for 15 min in a vacuum oven to remove the entrapped air, which then was blended with the appropriate stoichiometric amounts of SP115 Hardener (based on the amount of DGEBA and the masterbatch) for 10 min. The rubber modified resin was afterwards degassed in the vacuum oven before curing to remove any air entrapped in the mixture and then poured into a silicon mould. Finally, the resin system was room temperature cured at 24hours following 16 hours at 50º C with a ramp rate of 1ºC/min followed by cooling down to room temperature at 1ºC/min.

Tensile Tests

Tensile tests were performed at room temperature (23°C) on a Zwick Z010 (Zwick, Germany) universal testing machine at a constant crosshead speed of 1 mm/min. The measurements followed the ISO 527 testing standard using dumbbell shaped specimens. The specimens having a 4 mm thickness were fabricated using a silicone mould. The length overall of dumbbell specimens was 150 mm. The length and width of narrow section were 10 and 4 mm, respectively. E-moduli were calculated within the linear part of the tensile stress-strain curves. All presented data corresponds to the average of at least five measurements. The local microstructure of the fractured areas of the specimens was qualitatively examined using a JEOL JSM-840A scanning electron microscope (SEM).

Finite Element Analysis Model

In the current work a forced vibration analysis is studied under a time-varying disturbance applied to the structure. This involves the calculation of the effect of the vibratory force on the structure. Knowing the exciting force, the resulted motion can be computed at a number of points over a range of frequencies and it would be sufficient to describe the vibrational behaviour of the structure. The computational model implemented in order to study the vibrational response of the composite materials is a cantilever beam excited into its fundamental mode of flexural vibration by an impact force.

When the exciting force is removed, the amplitude of vibration gradually decreases with time as the vibration energy is dissipated. Based on the material parameters extracted from the mechanical tests of pure tension, the finite element model for each specimen was simulated using the commercial code ANSYS. The cantilever beam was simulated as a beam element of type BEAM188 and the inertia parameters were calculated from the cross-section of the beam. The linear cantilever beam used for the current simulation was of a total length L=120mm, width b=20mm and thickness t=5mm, shown in Fig.1.
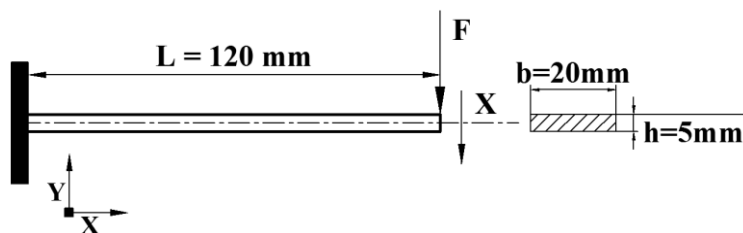
Figure 2 Cantilever beam used for the transient dynamic analysis.

3. Results and Discussion

Material Mechanical Behaviour

The stress–strain behaviour of all epoxy/rubber composites under uniaxial tension is shown in Fig. 2. The specimens with high CTBN concentrations revealed a characteristic plastic behaviour. The addition of the CTBN decreased the strength as reported in other studies [5]. The strength decrease was significant with noticeable improvement in the strain to failure, revealing a characteristic toughening effect. The synergic effects of localized cavitations at the rubber/matrix interface and plastic shear yielding in the epoxy matrix are supposed to be responsible for deformation that results in energy dissipation process which ultimately improves the toughness values of the rubber-modified epoxies. Additionally, the strength decrease can be partly explained by the fact that when concentration of the CTBN is increased, there is less available epoxy resin to sustain the uniaxial forces. Subsequently, the reduction in the strength values of CTBN-modified epoxies may be attributed to the lowering in cross-linking density of the epoxy network and justifies the high strains to failure attained.

Furthermore, it is clear that the neat resin system exhibits a brittle tensile behaviour characterized by a Young's modulus value of 3600 MPa as compared to the rubber composites. Addition of CTBN decreases the Young's modulus showing a ductile nature of the modified systems. Generally, when a rubber modifier is added to a thermoset resin, its elastomeric character authorizes a decrease in Young's modulus, significantly. This was noted when the CTBN modifier was employed in an epoxy resin by another study [6]. The percentage change of Young's modulus is up to 57%, as compared to the above reported value of the neat epoxy, upon the addition of 25wt% of CTBN. In the present case, the modification by 25wt% of CTBN permits a change of 53%. The various tensile properties for different CTBN concentrations of the rubber are formulated in Table 1. The decrease in tensile strength with rubber content can be related to stiffness of the modified network. The rubber addition decreases stiffness of the network epoxy probably due to lowering in cross-linking density.

The neat epoxy resin fractured samples showed characteristic river lines and a smooth surface as shown in Fig. 3(a). This type of fracture behaviour is typical of brittle epoxy surfaces indicating low resistance to spontaneous crack propagation which was monitored during tensile testing of specimens. All rubber toughened composites revealed a fracture surface with severely distracted patterns as shown in Figure 3(b).

The formation of these patterns is induced by areas with accumulated well-bonded rubber particles causing yielding. In addition, in contrast to the neat epoxy, the rubber reinforced specimens at the fracture area demonstrated severe micro-roughness since the addition of the elastomeric phase to the epoxy matrix significantly affects the roughness of the fracture surface and, in consequence, the balance between tough and brittle behaviour.
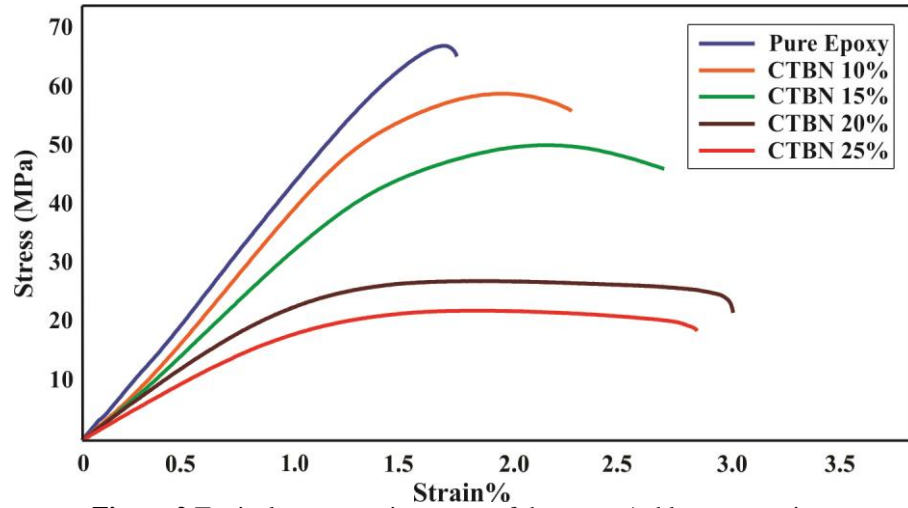
Figure 2 Typical stress-strain curves of the epoxy/rubber composites.

Table 1: Material parameters for the different CTBN concentrations.

Property	Pure Epoxy	CTBN 10%	CTBN 15%	CTBN 20%	CTBN 25%
Young's Modulus, E [MPa]	3600	3245	2630	2037	1686
Poisson's ratio, v	0.40	0.409	0.414	0.418	0.423
Density, d [g/cm^3]	1.160	1.173	1.189	1.186	1.192

Figure 3 SEM micrographs of typical fracture surfaces of a) neat epoxy resin, b) CTBN rubber toughened

epoxy.
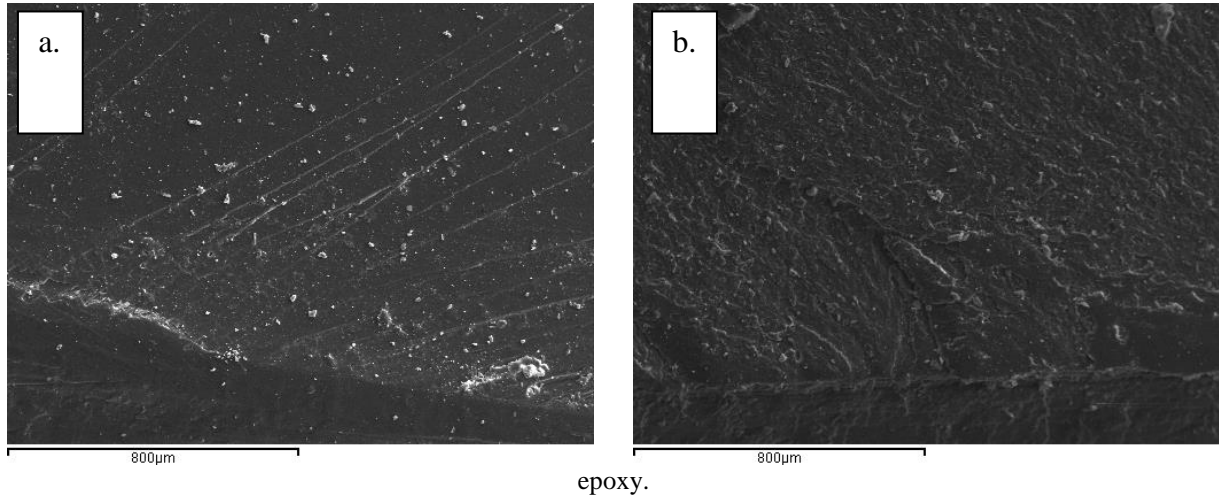
Transient Dynamic Analysis

According to the time history results of the FEA model, the displacement at the free end of the cantilever beam has been monitored for each sample (Fig.4). Obviously the attenuation rate of vibration deflection is faster when the CTBN content is higher, although the amplitude reaches greater values. The method for determining the damping ratio in the time domain is through the logarithmic decrement, which is derived from the natural logarithm of the ratio between the successive peaks in the vibration response.

The logarithmic decrement δ is defined as

$$\delta = \frac{1}{n} \ln\left(\frac{x(t)}{x(t+nT)} \right)$$

(1)

where x(t) is the amplitude at time t and x(t+nT) is the amplitude of the peak n periods away, n is any integer number of successive, positive peaks. The damping ratio ζ is then calculated by the logarithmic decrement:

$$\zeta = \frac{\delta}{\sqrt{\delta^2 + (2\pi)^2}} \approx \frac{\delta}{2\pi}$$

(2)

It is revealed that all CTBN composites exhibit better damping response than the neat epoxy resin, especially for the 25wt% that portrayed the most improved vibration behaviour. As seen in Fig.4, the free vibration of the neat epoxy, the amplitude of vibration is attenuated, reaching zero after a large number of cycles. However, it takes only a few cycles for the amplitude to approach zero when free vibration occurs for the 25wt% CTBN rubber sample.

Frequency Response Function

The solution of the vibration analysis problem can be examined as an input/output relation where the force, *F* is the input and the output is the resulted motion, *X*. The force and vibration can be represented in the frequency domain with the following relation *G* $(\omega) = X$ $(\omega) F^{-1} (\omega)$, where *G* is the frequency response function (FRF) and it has both a magnitude and phase component and if represented as a complex number, a real and imaginary component [7]. In order to obtain the structure's FRF properties from the transient vibration, the Fourier Transforms of both the excitation and the response signals were calculated. The ratio of these two functions is computed to obtain an expression from the corresponding frequency response function.

For linear systems, as a simple mass-spring-damper vibratory system, the frequency ω_n of the steady-state vibration response is equal to the frequency ω of the applied input force, with the response magnitude being dependent on the actual mechanical system. When ω/ω_n tends to 1 the amplitude of the vibration can get extremely high. This phenomenon is called resonance and the natural frequencies are obtained from the magnitude spectrum where resonance is observed (Fig.5). As seen in Fig.5, damping in a particular mode can be determined from the sharpness of each peak and is calculated in terms of damping ratio ζ given by

$$\zeta = \frac{\Delta\omega}{2\omega_n} = \frac{\omega_2 - \omega_1}{2\omega_n}$$

(3)

where ω_n is the natural frequency and ω_1, ω_2 on either side of the natural frequency where the

peak amplitude is reduced by a factor of $\sqrt{2}$.

The resulted frequency response curve as illustrated in Fig.6 shows that the peak amplitude increases for higher concentrations of CTBN, as observed in the transient analysis results. Considering the natural frequency of each sample, it decreases as the concentration of CTBN is gets higher due to the clear reduction of stiffness.
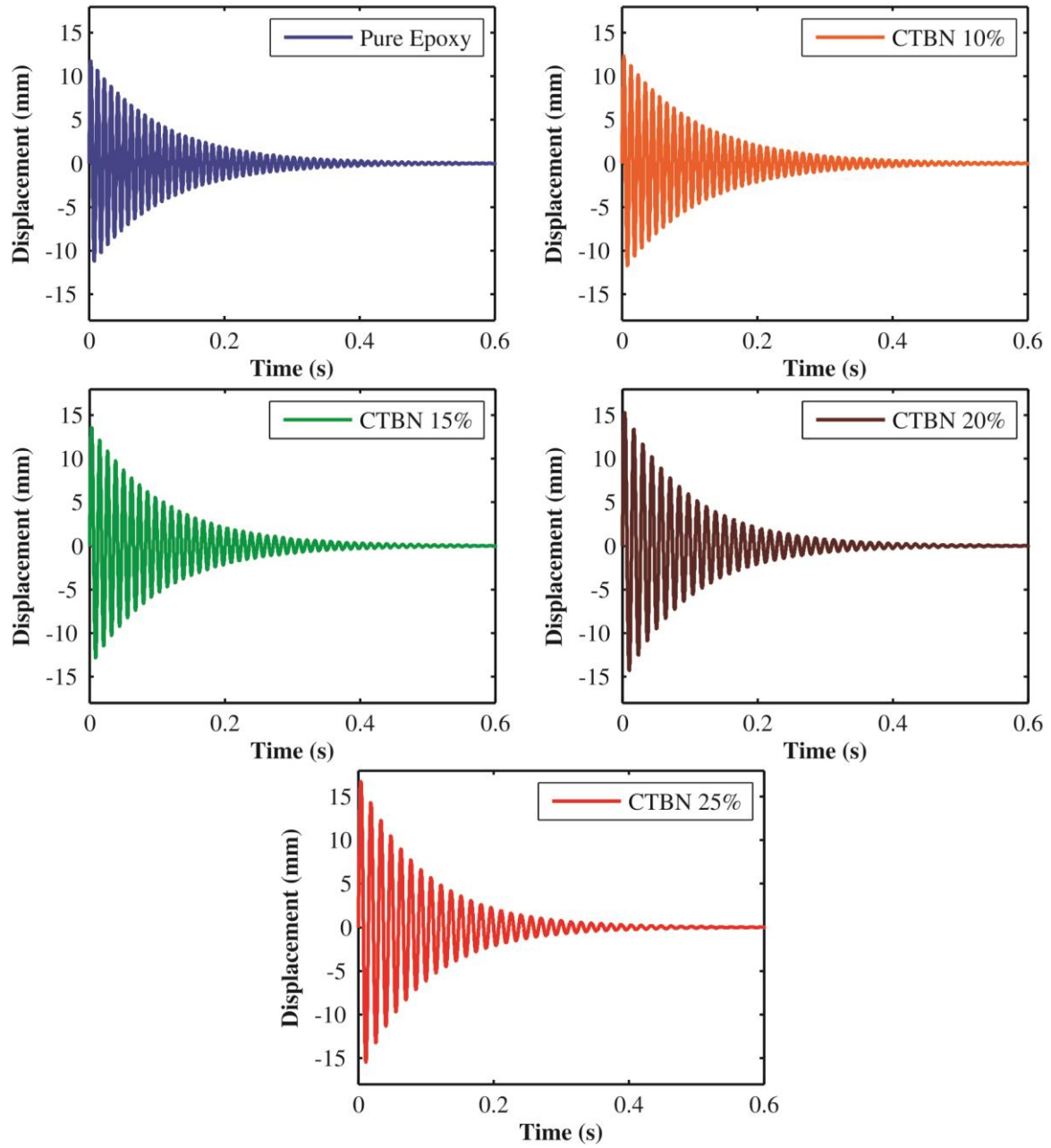
Figure 4 Forced vibration response curves with different contents of CTBN.
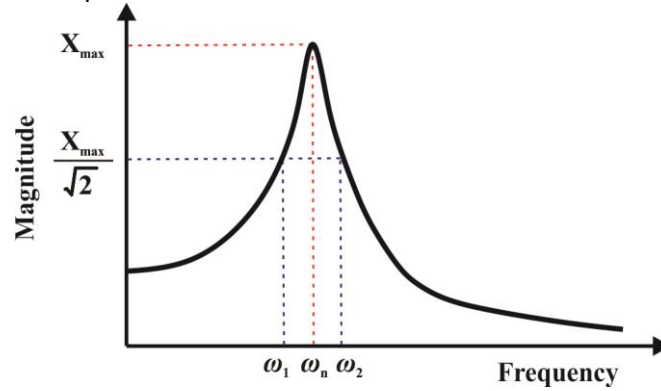
Figure 5 Magnitude of FRF of a single degree of freedom system.

151
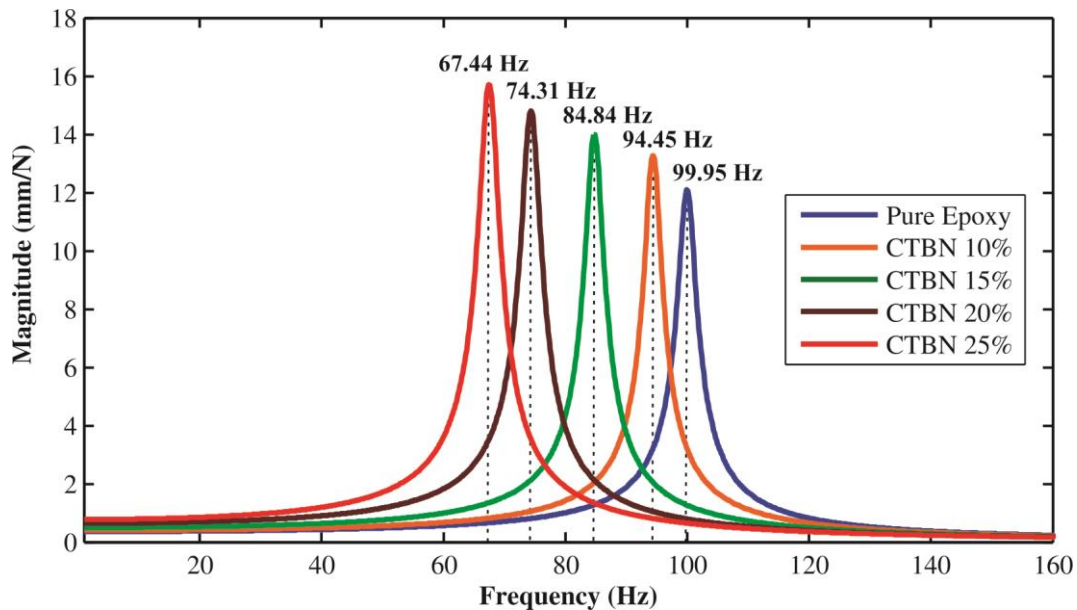
Figure 6 Magnitude curve of the epoxy/CTBN rubber composites.

The damping ratio is evaluated from both the logarithmic decrement method and the magnitude of the FRF for the different concentrations of CTBN rubber as illustrated in Fig.7. The addition of rubber in the epoxy matrix has improved the damping behaviour, while the increase seems to be almost linear. This improvement induced by the CTBN rubber particles could be attributed to their good dispersion within the epoxy as well as the reduced cross-linking density of epoxy itself. It has been also shown elsewhere that the damping properties of an epoxy resin can be modified by adding rubber particles and the FEA in the current work verifies the fact that when the epoxy is loaded with 25wt% CTBN rubber particles the highest damping value among all concentrations under study can be attained. Moreover, in Fig.7 the decrease of the natural frequency is depicted for each sample and it is considered almost linear as well.
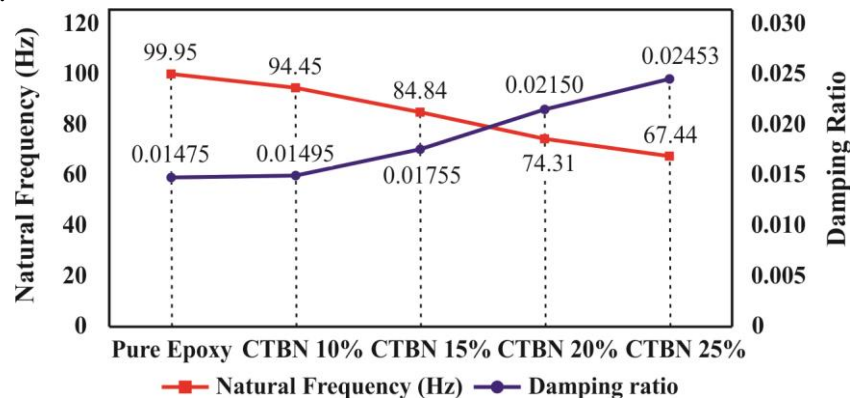
Figure 7 Natural frequency and damping ratio versus CTBN weight percentage.

4. Conclusions/Recommendations

The vibration responses of epoxy resin composites reinforced with Carboxyl-Terminated Butadiene-Acrylonitrile rubber were investigated through the use of Finite Element Method. Epoxy/rubber composites were produced and tested under uniaxial tension. The samples with high CTBN concentrations revealed a characteristic plastic behaviour, although the addition of the CTBN decreased the strength and the Young's Modulus. The strength decrease was significant with noticeable improvement in the strain to failure, revealing a characteristic toughening effect. The decrease in tensile strength with rubber content can be related to the stiffness of the modified network, while the rubber addition decreases the stiffness of the network epoxy probably due to lowering in cross-linking density. A FEA model of a

cantilever beam under a time-varying force excitation is introduced, in order to investigate the vibrational behaviour of the epoxy/ rubber composites. Time history results have shown that the attenuation rate of vibration deflection is faster when the CTBN content is higher, although the amplitude reaches greater values. The frequency response function for each composite material has been determined and fundamental parameters, as natural frequency and damping ratio were defined. Therefore, the epoxy/CTBN rubber composites are expected to have important applications as a high performance damping material. In light of the forgoing, it is suggested that a hybrid inclusion system can demonstrate enhanced damping capacity without scarifying its flexural stiffness, and thus the hybrid concept should be employed in the future design of composite materials.

5. References

[1]   Meyers, M.A., Chawla K.K. (1999). *Mechanical Behavior of Materials*. Prentice-Hall 98-103.

[2]   Jia-Lin Tsai, Nai-Ren Chang (2011). Investigating Damping Properties of Nanocomposites and Sandwich Structures With Nanocomposites. Journal of Composite Materials 2011; 45: 21 2157-2164.

[3]   Zhao X.Y., Xiang P., Tian M., Fong H., Jin R. and Zhang L.Q. (2007), *Nitrile butadiene rubber/hindered phenol nanocomposites with improved strength and high damping performance*, Polymer 2007; 48: 6056–6063.

[4]   Nigam V., Setua D.K. and Mathur G.N. (2001), *Characterization of rubber epoxy blends by thermal analysis*, J Therm Anal Calorim 2001; 64: 521–527.

[5]   Xiao K. and Ye L. (2000). *Rate-effect on fracture behavior of core-shell-rubber (CSR)-modified epoxies*. Polym Eng Sci 2000; 40: 70–81.

[6]   Thomas R, Abraham J, Thomas PS, Thomas S. (2004). *Influence of carboxyl-terminated (butadiene-co-acrylonitrile) loading on the mechanical and thermal properties of cured epoxy blends*. J Poly Sci Part B PolymPhys 2004;42:2531.

[7]   Bouzakis K. D., Mansour G. (1990). *Optimal Auslegung von Isolierelementenzur Aufstellung von werkzeug maschinen*, VDI 132 , Nr. 8, pp. 76-78.

Acknowledgments

Thermal Degradation and Burning Behavior of A Commercial Epoxy Resin Blended With an Organophosphonate

Ionela-Daniela Carja, Diana Serbezeanu, Tachita Vlad-Bubulac, Corneliu Hamciuc

"Petru Poni" Institute of Macromolecular Chemistry, Aleea Gr. Ghica Vodă 41A, Iaşi-700487, Romania

E-mail: daniela.carja@icmpp.ro

Abstract*:* Herein, a detailed characterization of the thermal properties and fire behavior of a bifunctional bisphenol-A based epoxy resin (**DGEBA**) cured with an aromatic aminic hardener (**DDM**) as a function of the weight fraction of the phosphorus flame retardant (**PFR**) was conducted. The experimental results regarding the burning behavior and thermal decomposition mechanism were compared to the reference system based on the cured epoxy resin (**DGEBA/DDM**) without the organophosphorus additive. Also, the corresponding fireproof epoxy system derived from phosphorus-modified **DGEBA** cured with **DDM** was also investigated to highlight the effect of additive on the physical properties of the rigid epoxy polymers. It was shown that with a very low content of phosphorus element, the fireproof epoxy resins exhibited significantly improved flame retardancy. A concentration of 1 wt% was enough to increase the value of the limiting oxygen index (LOI) with about 30%. The increase of the LOI value was lower in the case of the fireproof epoxy resin prepared via "reactive-type" approach then the ones obtained by physically blended with **PFR**. The thermogravimetric analysis (TGA) showed that the incorporation of **PFR** significantly increased the char yield and the thermal stability of the gradually forming phosphorus-rich carbonaceous layer at elevated temperatures. These results suggested that the main flame retardancy mechanism of the fireproof cured epoxy resins was the condensed phase mechanism.

Keywords: organophosphonate, epoxy resin, thermal degradation, flame retardancy

1. Introduction

Epoxy resins are widely used to manufacture advanced composites in various fields such as aerospace structure materials, electronic laminates, encapsulates for semiconductor and electronic devices, owing to their high strength and modulus, low shrinkage in cure, excellent chemical and solvent resistance, good thermal and electrical properties, outstanding adhesion to different substrates, easy processability under various conditions and excellent dimensional stability[1-3]. However, their use is restricted, especially in applications where high thermal stability and fire resistance are the main requirements [4]. Therefore, research efforts are underway to develop non-flammable advanced epoxy resins by adding a flame retardant promotor in their structure, either by physical blending, which implies that the flame retardant additive is dissolved into the epoxy matrix prior curing [5], or by chemical modification of the primary epoxy structure to induce inherent fire retardancy [1]. Among these two approaches, the additivation is cost effective, straightforward, less time consuming and does not require a special or sophisticated equipment for blending. Composites with poor mechanical performances can be obtained though. The development of epoxy polymers with inherent flame resistance overcomes the drawbacks related to volatility and compatibility of the additives with the epoxy matrix, but it can involve complicated organic chemistry reactions. So, the use of any of these two strategies is a matter of choice of some minimum performance requirements in a specific application field.

Phosphorus containing molecules can be incorporated into epoxy matrix as additives [5] or reactive co-reactants [6, 7] to improve their thermal properties and oxidation resistance and to reduce their flammability. Moreover, organophosphorus compounds were found to generate small amounts of smoke and less toxic gases under combustion [8]. Among various phosphorus flame retardants, the ones derived from 9,10-dihydro-9-oxa-10-phosphaphenanthrene-10-oxide (**DOPO**) have been intensively investigated due to their thermal stability, good oxidation and water resistance [2, 5, 9-11].

Herein, a detailed characterization of the thermal properties and fire behavior of a bifunctional bisphenol-A based epoxy resin (**DGEBA**) cured with an aromatic aminic hardener (**DDM**) as a function of the weight ratios of a phosphorus flame retardant additive (**PFR**) was conducted. The corresponding fireproof epoxy system derived from **DOPO**-modified **DGEBA** cured with **DDM** was also investigated to highlight the effect of additive on the physical properties of the rigid epoxy polymers. The experimental results regarding the burning behavior and thermal decomposition mechanism were compared to the reference system based on the pristine cured epoxy resin (**DGEBA/DDM**).

2. Experimental

2.1. Materials

Diglycidyl ether of bisphenol A (**DGEBA**), commercial name − ROPOXID, with an epoxy equivalent weight (EEW) of 184 – 194 g/equiv) was provided by POLICOLOR (Romania). Terephthaldicarboxaldehyde, 4,4'-diaminodiphenylmethane (**DDM**) and phenylphosphonic dichloride were purchased from Aldrich and used as received. 9,10-dihydro-9-oxa-10-phosphaphenanthrene-10-oxide (**DOPO**) was supplied by Chemos GmbH, Germany and dehydrated at 150$^{\mathrm{o}}$C for 3 h before use. 1,4-Phenylene-bis((6-oxido-6*H*-dibenz[c,e][1,2]oxaphosphorinyl)carbinol) (**1**) was synthesized by nucleophilic addition reaction of **DOPO** to the carbonyl bond of terephthaldicarboxaldehyde, as reported in the literature [5]. The phosphorus flame retardant additive (**PFR**) was obtained by solution polycondensation reaction of equimolecular amounts of **DOPO**-disubstituted diol **1** with phenylphosphonic dichloride, according to a previously published procedure [9]. **DOPO**-modified epoxy resin (**DOPO/DGEBA**) was prepared by reacting **DOPO** with **DGEBA** at 160$^{\mathrm{o}}$C for 5 h. All other reagents were used as received from commercial sources or purified by standard methods.

2.2. Preparation of the thermosets

The fireproof epoxy resins were prepared either by reacting **DGEBA** with **DOPO** at 160$^{\mathrm{o}}$C for 5 h or by symply mixing **DGEBA** with **PFR** at 120$^{\mathrm{o}}$C. The phosphorus containing epoxy resins with 1, 2 or 3 wt% atomic phosphorus were cured with the appropriate amount of DDM, in an epoxy to amine equivalent of 1 : 1. The homogeneous reaction mixtures were cured at 120$^{\mathrm{o}}$C for 2 h and postcured at 130$^{\mathrm{o}}$C for 6 h. The samples were slowly cooled to the room temperature.

2.3. Methods

FTIR spectroscopy was performed on a Bruker Vertex 70 at frequencies ranging from 4000 to 400 cm^{-1} by using KBr pellets.

The scanning electron microscopy (SEM) images were obtained with a TESLA BS 301 instrument, at 20 kV, with a magnification of 500 – 5000×.

The glass transition temperature (T_g) was determined using a Mettler-Toledo differential scanning calorimeter DSC 12 E. Approximately 5 to 8 mg of each sample were encapsulated in aluminium pans having pierced lids to allow the release of volatiles, and run in nitrogen with a heat-cool-heat profile from room temperature up to 200$^{\mathrm{o}}$C, at the heating rate of 10$^{\mathrm{o}}$C/min. Heat flow *vs.* temperature scans from the second heating cycle were plotted

and the mid-point temperature of the change in slope of the DSC signal was assigned as the T_g of the sample.

Thermogravimetric analysis (TGA) was performed on a Mettler Toledo TGA/SDTA 851^e balance, under constant air flow (20 mL/min). Approximately 3 to 5 mg of sample were heated from room temperature up to 700°C, with a heating rate of 10°C/min.

Limiting oxygen index (LOI) measurements were performed using an oxygen index instrument Qualitest according to the standard ASTMD2863-09. The minimum oxygen concentration required to support the candle-like combustion of the test specimens (90 × 6.5 × 3 mm^3) was recorded to obtained the LOI values of the thermosets.

3. Results and discussion

A series of fireproof epoxy resins were prepared via "additive-type" and "reactive-type" approaches. In the first one, the flame retardant additive **PFR** was mixed in various weight ratios with **DGEBA** at 120°C, followed by the addition of the crosslinking agent (**DDM**) and thermal treatment to prepare rigid fireproof epoxy composites. The second approach to achieve flame retardancy consisted in direct reaction of **DOPO** with **DGEBA** to obtain chemically modified epoxy polymer, **DOPO/DGEBA**, which was further treated with the appropriate amount of **DDM**. The chemical structures of the starting materials are shown in Figure 1.

Table 2 summarizes the chemical composition of the prepared rigid epoxy polymers.

flame retardant additive (**PFR**)

pristine epoxy resin (**DGEBA**)

amino hardener (**DDM**)
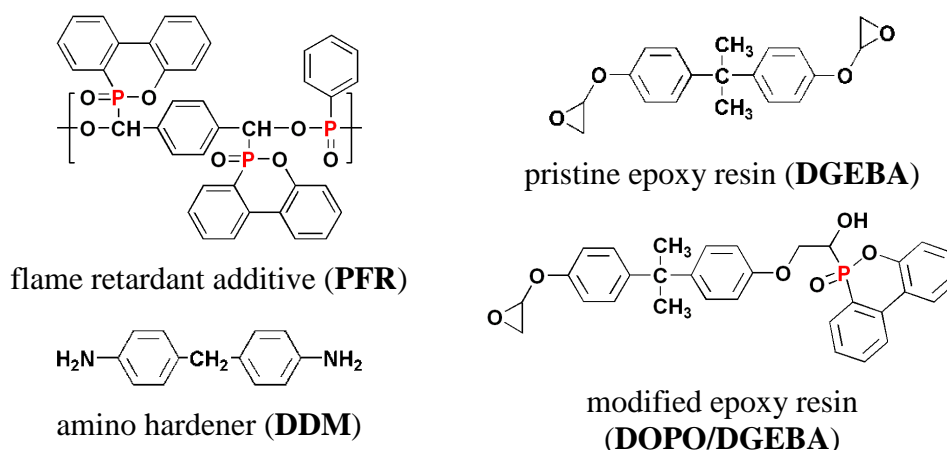
modified epoxy resin
(**DOPO/DGEBA**)

Figure 1 Chemical structure of the materials used to prepared rigid epoxy resins

Table 2: The chemical composition of different types of rigid epoxy resins

Sample code	Composition (g)				wt P* (%)
	DGEBA	PFR	DOPO	DDM	
DGEBA/DDM	75.6	0	0	20	0
PFR–DGEBA 1/DDM	75.6	7.6	0	20	1
PFR–DGEBA 2/DDM	75.6	16.6	0	20	2
PFR–DGEBA 3/DDM	75.6	27.4	0	20	3
DOPO/DGEBA/DDM	91.58	0	18.95	20	2

* theoretically determined.

FTIR spectroscopy was performed to characterize the structures of the rigid epoxy resins via the ring opening reaction between the oxirane units and the amino functional group of **DDM**. The most important signals in FTIR spectra and their attribution are given in Table 3. The absence of the characteristic absorption bands at 3056 cm^{-1}, attributed to the C–H tension of the methylene group of the epoxy ring, and at 915 cm^{-1} and 863 cm^{-1}, associated to the epoxy ring deformation confirmed the successful epoxide ring opening reaction [3, 12, 13]. All the rigid epoxy resins showed characteristic vibrations of alkyl, aryl and ether groups. The fireproof samples also presented characteristic absorption bands of phosphorus containing functional units: ~1474 cm^{-1} due to the aromatic P–C stretching vibrations, ~1203 cm^{-1} due to the aromatic P=O stretching vibrations, ~930 cm^{-1} characteristic to the aromatic P–O–C stretching vibrations and ~755 cm^{-1} associated to the deformation vibrations caused by the 1,2-disubstituted aromatic **DOPO** rings. In the case of the blended samples, a supplementary band appeared at ~1045 cm^{-1} due to the aliphatic P–O–C stretching vibrations.

Table 3: FTIR (KBr pellets, cm^{-1}) absorption bands of **DGEBA/DDM** control and fireproof epoxy resins

Band assign	DGEBA/DDM	PFR–DGEBA 1/DDM	PFR–DGEBA 2/DDM	PFR–DGEBA 3/DDM	DOPO/DGEBA/DDM
O–H or N–H str.	3400	3400	3393	3392	3400
Ar. C–H str.	3035	3034	3035	3035	3026
Aliph. C–H str.	2963; 2927; 2870	2963; 2927; 2870	2963; 2928; 2870	2963; 2928; 2870	2960; 2924; 2865
Ar. C=C str.	1610; 1510	1610; 1510	1610; 1510	1609; 1510	1600; 1501
Ar. P–C str.	–	1474	1474	1473	1475
Aliph. C–H def.	1362	1384	1362	1362	1363
Ar. C–O–C str.	1246; 1035	1246; 1035	1244; 1036	1243; 1036	1244; 1036
Ar. P=O str.	–	1203	1203	1203	1204
Aliph. P–O–C str.	–	1045	1045	1044	–
Ar. P–O–C str.	–	930	933	932	925
DOPO ring def.	–	755	755	755	756

Aliph. aliphatic, ar. aromatic, def. deformation, str. stretching

The morphology of the fractured samples surface was observed by SEM. Figure 2 shows the representative SEM micrographs of **DGEBA/DDM** control, **PFR–DGEBA 2/DDM** and **DOPO/DGEBA/DDM**. The fracture surface of **DGEBA/DDM** control was smooth, with no specific texture. In the case of the blended fireproof sample, **PFR–DGEBA**

2/DDM, the fracture surface was very dense and no obvious phase separation or gaps were observed, which means that the flame retardant additive, **PFR**, was uniformly dispersed throughout the epoxy matrix. Therefore, the blended sample exhibits good miscibility, which is a very important factor to achieving materials with high mechanical performances. As for the **DOPO/DGEBA/DDM** sample, SEM revealed a glassy and homogeneous microstructure.
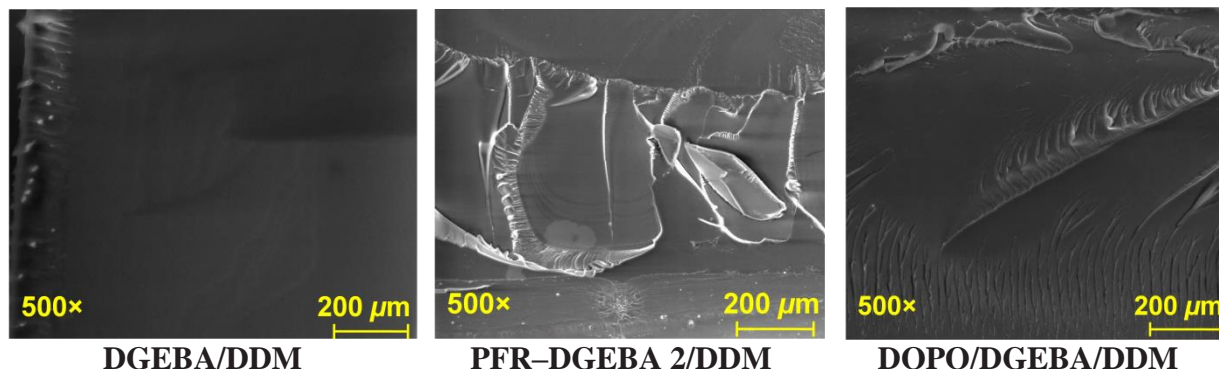

| DGEBA/DDM | PFR–DGEBA 2/DDM | DOPO/DGEBA/DDM |

Figure 2 Representative SEM micrographs of the cross section of **DGEBA/DDM** control and fireproof epoxy resins with 2 wt% atomic phosphorus, **PFR–DGEBA 2/DDM** and **DOPO/DGEBA/DDM** (SE mode, 20 kV)

The cured epoxy resins showed moderate glass-transition temperatures (T_gs), in the range of $111 - 146$°C, as it can be seen in Table 4. The introduction of **PFR** additive into the epoxy matrix monotonously decreased the T_gs values as a result of reducing the crosslinking density, behaviour typically for plasticisers [14]. When **PFR** was introduced in small amount into the epoxy matrix, only a slightly decrease of T_g value was obtained. In the case of **DOPO/DGEBA/DDM** sample, by chemically linking **DOPO** units to **DGEBA**, the T_g value decreased significantly as compared to the control sample. This is due to the reduced number of oxirane units available for the crosslinking reaction with **DDM** [15].

Table 4 Glass transition temperatures, thermogravimetric data and LOI values of the rigid epoxy resins

Sample code	T_g[1] (°C)	Stage I				Stage II				$\eta_{700°C}$[6] (%)	LOI[7] (%)
		T_{onset}[2] (°C)	T_{max}[3] (°C)	T_{endset}[4] (°C)	ΔW[5] (%)	T_{onset}[2] (°C)	T_{max}[3] (°C)	T_{endset}[4] (°C)	ΔW[5] (%)		
DGEBA/DDM	146	275	292	310	17.32	443	527	582	79.13	3.55	26
PFR–DGEBA 1/DDM	144	260	285	310	19.04	433	527	568	73.95	5.02	34
PFR–DGEBA 2/DDM	137	270	288	321	21.18	423	527	575	72.99	5.61	40
PFR–DGEBA 3/DDM	126	261	284	319	22.60	451	532	569	68.61	8.97	42
DOPO/DGEBA/DDM	111	273	333	420	50.73	502	555	620	16.12	22.00	29

[1] glass transition temperature measured by DSC; [2] thermal decomposition onset temperature; [3] thermal decomposition peak; [4] thermal decomposition endset temperature; [5] mass loss corresponding to each decomposition stage; [6] char yield measured at 700°C; [7] limiting oxygen index.

The thermo-oxidative stability of the rigid epoxy resins was investigated by TGA, with the heating rate of 10°C/min. The main thermal parameters are given in Table 4. The moisture absorption was neglected. For all the samples, the decomposition process showed a double-steps weight loss. As a common feature, the onset temperature of the fireproof samples were lower than the one corresponding to the **EP/DDM** control system, reflecting the

high susceptibility to degradation of the P–C bond in the polymer backbone [5, 16]. In the case of **PFR–DGEBA/DDM** samples, prepared via "additive-type" approach, as well as for the pristine **EP/DDM** control, the main decomposition stage was the second one, characterized by a sudden weight drop due to the vigorous gas evolution of the underlying sample ($\Delta W > 68\%$), with the maximum decomposition temperature above 527°C. By contrast, **DOPO/DGEBA/DDM** sample showed the highest emission of volatiles in the first stage and at temperature above 495°C, a relatively thermally stable char was formed during the decomposition process. Consequently, the char yield at 700°C was significantly higher as compared with those obtained for the **PFR–DGEBA/DDM** composites. Figure 3 shows comparatively the TG curves of the rigid epoxy resins.
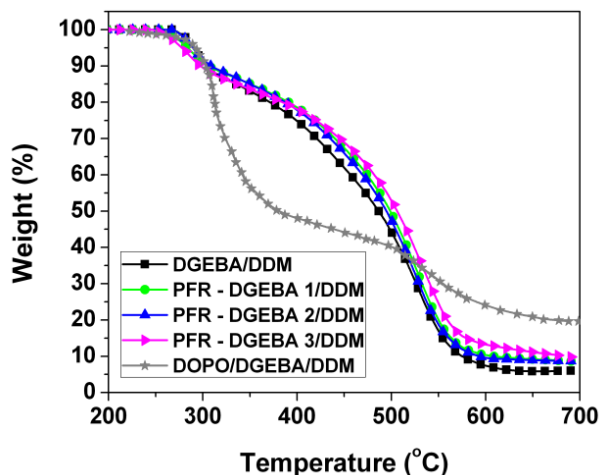
Figure 3 TG curves of the rigid epoxy resins

The flame retardant properties of the cured epoxy resins were quantitatively evaluated by measuring the LOI values, as shown in Table 4. A linear dependence was observed for the **PFR–DGEBA/DDM** composites. In addition, the LOI values increased with increasing the **PFR** content added into the epoxy matrix, reaching an increase up to 42%. These results suggest that the flame retardant additive induced good flame retardant effect to epoxy resin. This behaviour could arise from the high aromaticity of **PFR** and from the tendency of forming large amounts of char residue upon heating. Thus, a concentration of 1 wt% of phosphorus element was enough to increase the LOI value with about 30%. In the case of **DOPO/DGEBA/DDM** sample, the LOI value was lower as compared to the **PFR–DGEBA/DDM** composites, but higher then the one of the control sample, **DGEBA/DDM**.

4. Conclusion

Safe, thermally stable and fire retardant rigid epoxy resins were prepared either by simply mixing the appropriate amount of flame retardant additive, **PFR**, with a commercial epoxy resin known as ROPOXID, or by using a **DOPO**-modified epoxy resin. In both cases, **DDM** was used as aminic hardener. SEM, DSC and TGA results illustrated good dispersion of **PFR** into the epoxy matrix. Although the addition of **PFR** led to the early degradation of the composites as compared to the control sample, it increased the stability of the residual chars at elevated temperature. It was also shown that with a very low content of phosphorus element, the fireproof **PFR–DGEBA/DDM** exhibited significantly improved flame retardancy. A concentration of 1 wt% was enough to increase the LOI value with about 30%. The chemically modified epoxy resin, **DOPO/DGEBA/DDM**, showed different thermal decomposition behaviour as compared to the reference sample. By inserting the phosphorus in

the chemical structure of the epoxy resin, the rate and the pathway of the pyrolytic decomposition mechanism of the fireproof system was significantly changed.

5. References

[1] Zhang, W.; Li, X.; Li, L.; Yang, R., Study of the synergistic effect of silicon and phosphorus on the blowing-out effect of epoxy resin composites. 2012. *Polymer Degradation and Stability*, 97, 6, 1041-1048.

[2] Hamciuc, C.; Serbezeanu, D.; Carja, I.-D.; Vlad-Bubulac, T.; Musteata, V. E.; Forrat Pérez, V.; Guillem López, C.; López Buendia, A., Effect of DOPO units and of polydimethylsiloxane segments on the properties of epoxy resins. 2013. *Journal of Materials Science*, 48, 24, 8520-8529.

[3] Siddiqi, H.; Afzal, A.; Sajid, S.; Akhter, Z., Synthesis, characterization and thermal oxidative stability of rigid epoxy polymers cured from aromatic mono- and di-amines. 2013. *Journal of Polymer Research*, 20, 2, 1-10.

[4] Gu, H.; Guo, J.; He, Q.; Tadakamalla, S.; Zhang, X.; Yan, X.; Huang, Y.; Colorado, H. A.; Wei, S.; Guo, Z., Flame-retardant epoxy resin nanocomposites reinforced with polyaniline-stabilized silica nanoparticles. 2013. *Industrial & Engineering Chemistry Research*, 52, 23, 7718-7728.

[5] Wang, X.; Hu, Y.; Song, L.; Yang, H.; Xing, W.; Lu, H., Synthesis and characterization of a DOPO-substitued organophosphorus oligomer and its application in flame retardant epoxy resins. 2011. *Progress in Organic Coatings*, 71, 1, 72-82.

[6] Liu, Y. L., Epoxy resins from novel monomers with a bis-(9,10-dihydro-9-oxa-10-oxide-10-phosphaphenanthrene-10-yl-) substituent. 2002. *Journal of Polymer Science Part A: Polymer Chemistry*, 40, 3, 359-368.

[7] Artner, J.; Ciesielski, M.; Walter, O.; Döring, M.; Perez, R. M.; Sandler, J. K. W.; Altstädt, V.; Schartel, B., A novel DOPO-based diamine as hardener and flame retardant for epoxy resin systems. 2008. *Macromolecular Materials and Engineering*, 293, 6, 503-514.

[8] Schab-Balcerzak, E. 2006. Modifications of epoxy resins' properties. Bregg, R. K., Ed. Frontal Polymer Research. City: Nova Science Publishers, Inc. 2, 65-106.

[9] Carja, I. D.; Serbezeanu, D.; Lisa, G.; Vlad-Bubulac, T.; Hamciuc, C., Thermal degradation and kinetic studies of new flame-retardant phosphorus-containing polymers with liquid crystalline properties. 2014. *International Journal of Polymer Analysis and Characterization*, 19, 4, 372-382.

[10] Carja, I. D.; Serbezeanu, D.; Vlad-Bubulac, T.; Hamciuc, C.; Brumă, M., Synthesis and liquid crystalline behavior of phosphorus-containing aliphatic–aromatic copoly(ester-imide)s. 2012. *Polymer Bulletin*, 68, 7, 1921-1934.

[11] Serbezeanu, D.; Vlad-Bubulac, T.; Hamciuc, C.; Aflori, M., Synthesis and properties of novel phosphorus-containing thermotropic liquid crystalline copoly(ester imide)s. 2010. *Journal of Polymer Science Part A: Polymer Chemistry* 48, 23, 5391-5403.

[12] González González, M.; Cabanelas, J. C.; Baselga, J. 2012. Applications of FTIR on epoxy resins - identification, monitoring the curing process, phase separation and water uptake. Theophanides, T., Ed. Infrared Spectroscopy - Materials Science, Engineering and Technology. City: InTech. 13, 261-284.

[13] Nikolic, G.; Zlatkovic, S.; Cakic, M.; Cakic, S.; Lacnjevac, C.; Rajic, Z., Fast Fourier Transform IR characterization of epoxy GY systems crosslinked with aliphatic and cycloaliphatic EH polyamine adducts. 2010. *Sensors (Basel)*, 10, 1, 684–696.

[14] Su, C. H.; Chiu, Y. P.; Teng, C. C.; Chiang, C. L., Preparation, characterization and thermal properties of organic–inorganic composites involving epoxy and polyhedral oligomeric silsesquioxane (POSS). 2010. *Journal of Polymer Research*, 17, 5, 673-681.

[15] Jeng, R. J.; Shau, S. M.; Lin, J.-J.; Su, W.-C.; Chiu, Y.-S., Flame retardant epoxy polymers based on all phosphorus-containing components. 2002. *European Polymer Journal*, 38, 4, 683-693.

[16] Ge, X. G.; Wang, C.; Hu, Z.; Xiang, X.; Wang, J. S.; Wang, D. Y.; Liu, C. P.; Wang, Y. Z., Phosphorus-containing telechelic polyester-based ionomer: Facile synthesis and antidripping effects. 2008. *Journal of Polymer Science Part A: Polymer Chemistry*, 46, 9, 2994-3006.

Acknowledgements

SAC305 vs. SnPb Solder Joint Electrical and Mechanical Properties Measurements as Function of Working Temperature and Soldering Thermal Profile

Mihaela Pantazică, Gaudenţiu Vărzaru, Paul Svasta

Centre for Technological Electronics and Interconnection Techniques, "Politehnica" University of Bucharest, UPB-CETTI, Bucharest, Romania
mihaela.pantazica@cetti.ro

Abstract

The paper presents a comparative study between the electrical and mechanical properties of solder joints in case of lead-containing and lead-free alloys as function of the working temperature and the soldering thermal profile obtained through the Surface Mount Technology (SMT). The soldering method employed was Vapour Phase; two different thermal profiles have been used in order to investigate the influence of the cooling rate over the mentioned properties. For the measurement of the electrical properties, i.e. resistance of the solder joint, which deals with very low values, a more laborious methodology was used in order to eliminate the errors caused by the thermo-electric effect. For the measurement of the mechanical properties, experiments have been designed to determine the shear force of the solder joints at higher temperatures of the substrate. Both measurements have been made while keeping the surface of the test boards at different working temperatures: 198.15K, 348.15K and 398.15K.

Introduction

Many applications need electronics that operate outside the typical industrial and even beyond the standard military operating temperature ranges. These applications have special requirements for qualification and packaging. Since the introduction of the RoHS European Directive (2006), lead-containing alloys have stopped being used in the electronic industry with few exceptions like military equipment, medical equipment, aerospace and automotive fields. The more recent RoHS 2 European Directive (2013) sets out the specific date when the fields currently exempted will have to comply with the use of lead-free alloys. The designers, users and producers from these areas have to find solutions to replace the lead-containing alloys with lead-free alloys but keeping in mind the requirements for reliability and safety of such types of equipment. In order to evaluate the properties of lead-free solder joints, dedicated processes for qualification should be designed [1]. It is well known that the solder joints have three main properties: electrical, mechanical and thermal. The qualification processes for lead-free solder joints do not differ much from the ones for lead-containing solder joints. They are based on experiments designed to verify if the properties of the lead-free solder joints are as good as the properties offered by the lead-containing solder joints [2]. The values obtained for lead-free solder alloys should be at least the same as the values obtained for lead-containing solder alloys, especially for the domains specified in the RoHS 2 European Directive. The references for experiments are imposed by the environmental working conditions in the required application field of the electronic equipment. As consequence, any solder alloy must be tested through dedicated procedures for qualification and use in the application fields mentioned in the European Directive. These application fields are characterized by a large range of working temperatures and high mechanical stress levels [1]. This is yet another reason why lead-free solder alloys must assure the electrical,

mechanical and thermal properties provided by the lead-containing solder alloys, or even better, in order to replace them.

The experiments have been designed based on some previous work [1][5][6] being focused on the "Homologous Temperature" concept [3][4] in order to respond to the constraints imposed by the qualification processes for lead-free solder joints. The homologous temperature represents the ratio between the working temperature and the melting temperature of the studied solder alloy:

$$T_H = \frac{T}{T_m}$$

where T_H is the homologous temperature, T is the working temperature and T_m is the melting temperature. Figure 1 presents the variation of the strength and hardness as function of temperature for most metals. It can be observed that the mechanical properties are not significantly affected for temperatures up to $0.4T_m$. Beyond this point, the mechanical properties decrease to strain rate and creep tends to occur at a significant rate. At temperatures over $0.6T_m$, the mechanical properties are dramatically influenced, this being also the case for solder joints. In material science, the homologous temperature must not exceed the value 0.5.
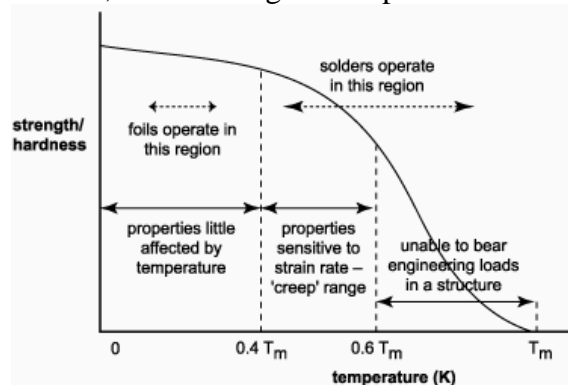
Fig.1. Strength variation with temperature [3]

The study of the electrical and mechanical properties of solder joints is closely related to the materials used to obtain those solder joints. In this case, the materials can be alloy, metal or oxide. But the most important remains the solder alloy. The concept of the homologous temperature allows the benchmarking of the mechanical strength of solder joints produced with lead-containing and lead-free solder alloys [6]. The work presented in this paper was focused on three directions: 1) a comparative study of the electrical properties of lead-containing and lead-free alloys solder joints, 2) a comparative study of the mechanical properties of lead-containing and lead-free alloys solder joints, and 3) an investigation of the influence of the process thermal profile over the electrical and mechanical properties. The tests have been performed based on experimental situations identified with the help of the 4P Soldering Model [7].

Materials and Methods

The test vehicle designed for these experiments was a daisy-chain wiring scheme connecting ten 1206 chip resistors of 0Ω; the printed circuit board substrate is the FR-4 glass epoxy laminate with a thickness of 1.6 mm and a single layer of copper (TOP) of 35 μm, electroless nickel immersion gold (ENIG) surface plating. Two solder pastes were used: from lead-containing alloys family was used the eutectic $Sn_{63}Pb_{37}$, type 3, while from lead-free the $Sn_{96.5}Ag_{3.0}Cu_{0.5}$, type 4, (SAC305).

The test vehicles were assembled using standard manufacturing process in SMT featuring the well known phases: solder paste printing, component placement, reflow soldering as well as

optical inspections after each phase. All the boards have been assembled by Vapour Phase Soldering (VPS) using a VPS Machine, SLC309, IBL, but half of them have been soldered using a thermal profile with a slow cooling rate (SCR) of 0.5K/s, and half of them have been soldered using a thermal profile with a rapid cooling rate (RCR) of 4.0 K/s. The reason for using two different thermal profiles is the already gathered knowledge that the growth of the intermetallic compound layers is influenced by the cooling rate [5].

Taking into account, for example, the military maximum working temperature the following values have been set as test temperatures: 298.15K, 348.15K and 398.15K. The paper is answering this issue with two sets of measurements, electrical and mechanical, for two types of solder pastes. Both the electrical resistance and the shear strength of solder joints have been measured by special designed tests as function of the working temperature and the soldering thermal profile [2].

The first step of the experiments has been the defining of a method to compare the solder alloys electrical properties as function of the working temperature. The electrical resistance of the solder joints has been measured in the same conditions and at the same time for all test vehicles. Indirect measurement has been carried out by using a constant current generator and measuring the drop of voltage over the solder joints. The electric circuit designed is suited for the Four Point Measurement method [5]. Since low voltage measurements are influenced by the thermoelectric effect due to the temperature differences between the instrument probe and the pad, it was adopted the Keithley Delta method for the error compensation [1][9].

The second set of the experiments has been the defining of a method to compare the solder alloys mechanical properties as function of the working temperature. The shear force strength was measured using a Multi Functional Bond Tester, Condor 70-3, XYZTEC [8]. For measurements at higher temperature a special support was built in-house using power resistors as heating element. The support was fixed on the Condor table while the temperature of the test vehicle board placed upon the support was controlled by a Data Acquisition System from thermocouples, Thermes, Physitemp Instruments.

Results and Discussion

The average electrical resistance of the analysed solder joints is presented in table 1. Figure 2 shows the variation of the measured values according to the solder paste, cooling rate and working temperature.

Tab. 1. The average electrical resistance of the analysed solder joints

Solder joint resistance [mΩ]						
Test temperature [K]	298,15		348,15		398,15	
Cooling rate	SCR	RCR	SCR	RCR	SCR	RCR
Solder paste	SAC305	1.406	1.381	2.084	1.969	2.499	2.582
	SnPb	1.169	1.388	1.892	1.957	2.146	2.282

As seen in the Table 1 and Figure 2, the electrical resistance of the solder joints obtained with SAC305 solder paste is slightly (10%...20%) higher than the case of SnPb solder paste, regardless the test temperature, for slow cooling rate; similar values were obtained for rapid cooling rate, except for 398.15K, when became higher again. For both solder pastes the electrical resistance is growing with temperature.

Tab. 2. The measured and computed values used to compare the shear strength as function of temperature

No.	Paste	T_m [K]	T_W [K]	T_H [K]	F - SCR [N]	τ_H SCR	F - RCR [N]	τ_H RCR
1	SAC305	494	298.15	0.60	94.50	1.00	93.79	1.00
2			348.15	0.70	71.67	0.76	66.94	0.71
3			398.15	0.81	48.84	0.52	49.05	0.52
4	SnPb	456	298.15	0.65	94.45	1.00	87.13	1.00
5			348.15	0.76	66.15	0.70	63.47	0.73
6			398.15	0.87	48.28	0.51	45.37	0.52

The values of the shear strength (τ) have been computed by dividing the value of the shear force by the cross-sectional area of the chip resistor 1206. The shear strength has been then normalized (τ_H) by dividing the values obtained for each test temperature to the maximum value, which corresponds here with the value obtained at room temperature. The measured and the computed values used to compare the shear strength of the lead-containing and lead-free solder joints as function of working temperature are shown in table 2. Figure 3 shows the variation of the solder joint shear strength with homologous temperature for both types of solder joints in the two analysed cases: slow cooling rate and fast cooling rate.
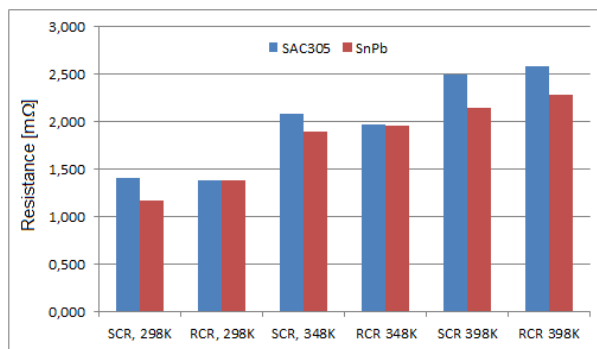
Fig. 2. Solder joint electrical resistance for different cooling rates and test temperatures
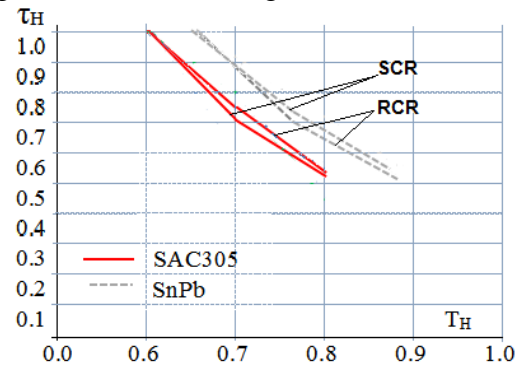
Fig. 3. The variation of the solder joint shear strength with homologous temperature

Conclusions

The measurements have shown that the electrical resistance of SAC305 solder joints is greater than the electrical resistance of SnPb solder joints at any working temperature and thermal profile, which is an disadvantage, except for rapid cooling rate at room temperature when they are practically equal. The thermal profile of the reflow process influences the electrical resistance in different ways: RCR increases the resistance for SnPb solder joint at any working temperature, while for SAC305 decreases for room and 348K, but increases for 398K.

From the mechanical properties point of view, the shear strength of SAC305 solder joints is greater than the shear strength of SnPb solder joints at any test temperature regardless the thermal profile, which is an advantage. However, the more working temperature, the less shear force strength.

A conclusion of the variation of the solder joint shear strength with homologous temperature is that the lead-free solder joint performs the same shear strength normalized value for a lower homologous temperature than SnPb; this means that it is far below the melting point

temperature, hence results a possible extended working temperature range for SAC305 than SnPb.

More experiments should be performed before drawing the conclusion that lead-free solder paste SAC305 can replace SnPb in aerospace or military systems.

References

[1] Ioan Plotog, Marian Vladescu, "Working Temperatures Influence over the Solder Joints Properties", IEEE 37th International Spring Seminar on Electronics Technology, ISSE 2014, 7-11 May 2014, Dresden, Germany;

[2] I. Plotog, Al. Marin, Laura Boanta, "Model of assembling process for electronic parts integrated in mechatronic products", The Romanian Review Precision Mechanics, Optics & Mechatronics, 2013, No. 44, ISSN 1584 – 5982;

[3] Martin Tarr, The 'homologous' temperature, www.ami.ac.uk/courses/topics/0164_homt/;

[4] J. R. Davis, Heat resistant materials, pg. 13, ASM International 1997, ISBN 0-87170-596-6;

[5] M. Branzei, F. Miculescu, A. Bibis, I. Cristea, I. Plotog, G. Varzaru, B. Mihailescu, "Lead/Lead Free Solder Joints Comparative Electrical Tests as Function of Microstructure and Soldering Thermal Profile", 2013 IEEE 19th International Symposium for Design and Technology in Electronic Packaging, SIITME 2013, 24-27 October 2013, Galati, Romania, ISBN: 978-1-4799-1555-2, pp. 255-258;

[6] I. Plotog, G. Varzaru, B. Mihailescu, M. Branzei, A. Bibis, I. Cristea, "Lead/Lead Free Solder Joints Comparative Shear Tests Function of Working Temperature and Soldering Thermal Profile", 2013 IEEE 19th International Symposium for Design and Technology in Electronic Packaging, SIITME 2013, 24-27 October 2013, Galati, Romania, ISBN: 978-1-4799-1555-2, pp. 283-286;

[7] I. Plotog, G. Varzaru, P. Svasta, "VPS technology and applications", 2010 3rd International Symposium on Electrical and Electronics Engineering, ISEEE 2010, 16-18 Sept. 2010, Galati, Romania, ISBN: 978-1-4244-8406-5, pp. 351 – 354;

[8] I. Plotog, G. Varzaru, P. Svasta, "Mechanical test assessment for electronic modules able to function in harsh conditions", 2010 3rd International Symposium on Electrical and Electronics Engineering, ISEEE 2010, 16-18 September 2010, Galati, Romania, ISBN: 978-1-4244-8406-5, pp. 355 – 358.

[9] Making Precision Low Voltage and Low Resistance Measurements, 2013 Keithley Instruments, Inc.

Modeling of the Bubble Growth Dynamics in PS/CO$_2$ Foaming System

Mostafa Salehi, <u>Mostafa Rezaei</u>[*], Mahdi Salami Hosseini

Institute of Polymeric Materials, Department of Polymer Engineering, Sahand University of Technology, P.O. Box: 51335-1996, Tabriz, Iran, Corresponding author e-mail:
rezaei@sut.ac.ir

Abstract: In foaming process, cell structure is achieved by expansion of a blowing agent in polymer melt matrix. Upon the sudden pressure drop of the foaming system with physical blowing agent, bubble nucleation starts causing the bubble to grow as gas diffuses into the bubbles. In this study, the bubble expansion in Polystyrene/CO$_2$ foaming system was modeled and compared to the experimental results. A single spherical bubble surrounded by an incompressible viscoelastic melt (upper-convected Maxwell model) was considered. To calculate concentration profile in the shell, mass diffusion equations were solved by implicit and integral methods. The predicted results show that when the gas concentration gradient near the bubble-shell interface was used to calculate the pressure inside the bubble, the predicted results were in good agreement with the experimental ones.

Keywords: Polymeric Foam; Bubble Growth Dynamics; Viscoelastic Fluid; Mass Diffusion; Polystyrene; Carbon dioxide

Introduction

Polymeric foams have a cellular structure composed of two phases; a polymeric solid and a gaseous phase. They are produced using many methods which are basically consisting of incorporating a blowing agent into polymeric matrix through a mixing process. In foaming process, cell structure is developed by expansion of a blowing agent in polymer melt. In the case of physical blowing agent, upon reducing the system pressure, bubble nucleation starts and is followed by bubble growth due to gas diffusion into the bubbles. The growth of the bubble plays an important role in the polymeric foaming dynamics and has dramatic impact on the final product properties. Generally speaking, the bubble growth process is very complicated since it consist of simultaneous mass, momentum and heat transfer between an expanding bubble and the surrounding polymeric media associated with changes in the rheological properties. In the most studies on the bubble growth field, the single bubble growth model is considered. The single bubble growth model describes the growth of a surrounded single bubble by a finite or infinite fluid [1,2 and 3].

The focus of the present study is on the bubble growth process as the second stage of the foaming process. In this work, the bubble growth processes with limited and unlimited dissolved gas available were modeled using finite difference and integral methods. The predicted results also were compared to experimental results and the integral model was modified to limit the growth of bubble.

Theory

To study the growth of a gas bubble in a finite pool of liquid, a bubble concentrically surrounded by a shell of viscoelastic melt of constant mass is considered. Fig.1 shows the configuration of the bubble and the melt shell surrounding the bubble. In this figure, R is the bubble radius, S is the outer radius of the shell, and c is the concentration of the dissolved gas in the melt. The pressure at the outer boundary of the shell is assumed to be as the applied or ambient pressure. The gas inside the bubble is assumed to behave as an ideal gas and its pressure is always greater than the ambient pressure.

Fluid around the spherical bubble is considered to be incompressible and flow assumes to be a creeping flow. Using Eq. 1 bubble pressure can be calculated and compared with calculated pressure from Eq.4. To calculate bubble pressure from Eq.1, it is needed to have normal stress around the

bubble, so the upper convected Maxwell model is used to describe the polymer viscoelastic behaviour (Eq.2 and 3). In order to calculate the bubble pressure in Eq.4, concentration gradient of blowing agent in bubble-shell interface should be known, so gas diffusion equation in shell (Eq. 5) was used to calculate the concentration distribution in shell around the bubble.
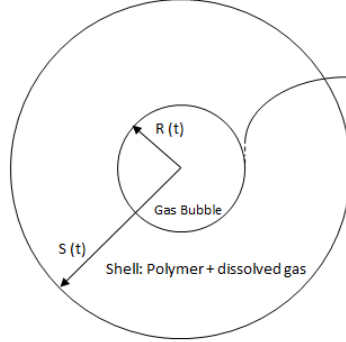
Fig. 1. Schematic view of a gas bubble and a finite melt shell to study the growth of a gas bubble

$$P_g - \frac{2\sigma}{R} - P_f + 2 \int_R^S \frac{\tau_{rr} - \tau_{\theta\theta}}{r} = 0 \tag{1}$$

$$\tau_{rr} + \lambda\left[\frac{\partial\tau_{rr}}{\partial t} + \frac{R^2\dot{R}}{r^2}\frac{\partial\tau_{rr}}{\partial r} + \frac{4R^2\dot{R}}{r^3}\tau_{rr}\right] = -4\eta\frac{R^2\dot{R}}{r^3} \tag{2}$$

$$\tau_{\theta\theta} + \lambda\left[\frac{\partial\tau_{\theta\theta}}{\partial t} + \frac{R^2\dot{R}}{r^2}\frac{\partial\tau_{\theta\theta}}{\partial r} - \frac{2R^2\dot{R}}{r^3}\tau_{\theta\theta}\right] = 2\eta\frac{R^2\dot{R}}{r^3} \tag{3}$$

$$\frac{d}{dt}(\rho_g R^3) = 3\Re TDR^2\frac{\partial C}{\partial r}|r = R \tag{4}$$

$$\frac{\partial C}{\partial t} + \frac{R^2\dot{R}}{r^2}\frac{\partial C}{\partial r} = \frac{D}{r^2}\frac{\partial}{\partial r}\left(r^2\frac{\partial C}{\partial r}\right) \quad for\ r \geq R \tag{5}$$

where, P_g is the inside pressure of the bubble, σ is the surface tension, P_f is the applied pressure, λ is the relaxation time, η is the zero-shear rate viscosity, ρ_g is the density of the gas inside the bubble and D is the mass diffusion coefficient.

In order to solve the equations 4 and 5, the integral method can be used. In this method, a polynomial concentration profile is used to describe the gas concentration profile in a thin layer. The mass balance equation is obtained by integrating the assumed polynomial profile. In the present study, two mass transfer equations of the integral method at the gas-polymer interface of a bubble are considered [4].

$$\frac{C_\infty - C}{C_\infty - C_R} = \left(1 - \frac{r - R}{\delta}\right)^2 \tag{6}$$

$$\frac{d}{dt}(P_g R^3) = \frac{6D(R_g T)(C_\infty - C_R)R}{-1 + \left\{1 + \frac{2/R^3}{R_g T}\left(\frac{P_g R^3 - P_{g_0}R_0^3}{C_\infty - C_R}\right)\right\}^{\frac{1}{2}}} \tag{7}$$

$$\frac{\dfrac{C_\infty - C}{C_\infty - C_R}}{\dfrac{r^3 - R^3}{(R + \delta)^3 - R^3}} \quad (8)$$

$$\frac{d}{dt}(P_g R^3)$$

$$= \frac{36}{5} \frac{R^4 (R_g T)^2 (C_\infty - C_R)^2}{P_g R^3 - P_{g_0} R_0^3} \quad (9)$$

Where, δ is the concentration boundary thickness, C_∞, C and C_R are the gas concentration in the outer r and R shell boundaryposition, respectively.

Numerical solution
in order to solve the ordinary and partial differential equations, 4th order Rung–Kata (RK4) and implicit finite difference methods were used, respectively. The necessary experimental parameters for modeling were extracted from literature [1]. Since in the foaming process, the bubble is growing, its boundary is changing. So trial and error method was used to calculate the radius of the growing bubble. In this study, the experimental data of the PS-CO_2 foaming system [1] were used to verify the predicted results.

Results and Discussion
Fig.2 shows the bubble growth vs. time calculated using quadratic concentration profile (QCP), in eqs. 6-7, and cubic concentration profile (CCP), in eqs. 8-9, which the predicted results are compared to the experimental results for the PS-CO_2 system reported by Leung et al. [1]. As it can be seen, if the bubble pressure is calculated using QCP, the theoretical prediction will be approached to the experimental results. As one may notice in Fig. 2, the experimental results show that the bubble grows up to an equilibrium size, whereas none of the models predict such behavior and the bubble will grow through time according to both models. This contradiction arise from the fact that in eqs. 6-9, C_∞ is consider to be constant which means that there is an infinite source of gas available for bubble to grow.
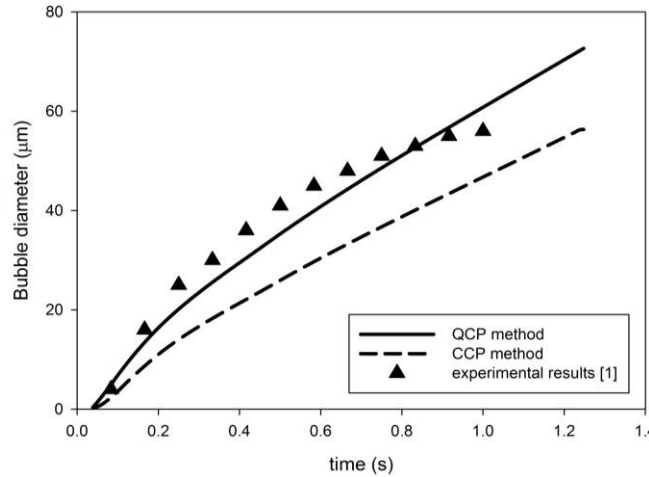
Fig. 2. comparison of the bubble growth modeling results with experimental data for PS-CO_2 foaming system

The QCP and CCP models should be modified to limit the growth of bubble. Therefore, in the present study, the gas concentration profile in the shell was obtained from the numerical solution (finite difference method) of the equation 5 and then the value of C_∞ was updated and used in equations 7 and 9.The results of the modified method are shown in Fig. 3 where the results of QCP, CCP and modified integral models are presented and compared to the experimental data. It is observed that the modified integral method can predict the steady-state stage of the bubble growth. Comparing the modified method results to experimental ones reveal that there is a remarkable difference between them. The

reason of this difference can be explained in terms of the concentration boundary thickness, δ (Eqs. 6-9). In the modified integral method, the total thickness of the shell was considered as the concentration boundary thickness. Since the concentration gradient at the interface of the bubble and shell is needed to calculate the bubble pressure, using the concentration gradient over the shell thickness instead will underestimate the required concentration gradient at the interface. But using of finite difference method and Eq. 4 as wll as the gas concentration gradient at the interface has led the results more consistent with the experiments.
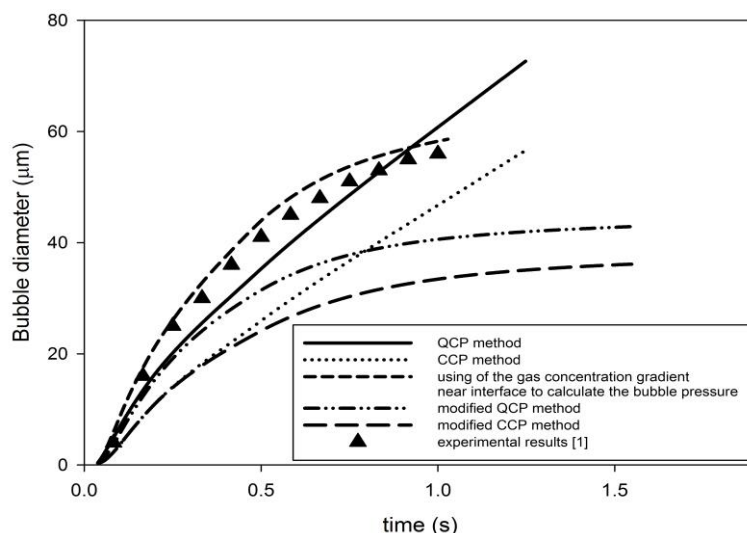
Fig. 3. comparison of the bubble growth modeling results of CCP, QCP, modified CCP and modified QCP methods with the finite difference method and experimental data for PS-CO_2 foaming system

Conclusions
In this study, the bubble growth dynamics of PS/CO_2 foaming system has been studied. In order to model the foaming dynamics, a surrounded spherical bubble by a polymeric viscoelastic shell was considered. Two integral and finite difference methods were used to obtain the gas concentration profiles in shell and the mass diffusion into the expanding bubble. The results of the integral method did not show plateau behavior at the final stages of the bubble growth, so the integral method modified with the finite difference method and the modified methods showed plateau behavior. It was shown that when the finite difference method was used, the predicted results were in good agreement with the experimental ones. Since in finite difference method, the bubble pressure was obtained through concentration gradient at bubble-shell interface, the results revealed good compliance with the experimental ones. But in integral method,the bubble pressure was obtained using concentration gradient in whole shell thickness, so the deviation from experimental results was observed for these results.

References
[1] S.N. Leung, C.B. Park, D. Xu, H.R. Li, G. Fenton, Computer simulation of bubble-growth phenomena in foaming, Ind. Eng. Chem. Res. 45 (2006) 7823–7831.
[2] A. Arefmanesh, S.G. Advani, Diffusion-induced growth of a gas bubble in a viscoelastic fluid, Rheologica Acta. 30 (1991) 274-283.
[3] H. Azimi, M. Rezaei, F. Abbasi, The effect of expansion conditions on the batch foaming dynamics of St-MMA copolymer, J Cell Plast. 48 (2012) 125-140.
[4] K. Taki, Experimental and numerical studies on the effects of pressure release rate on number density of bubbles and bubble growth in a polymeric foaming process, Chem Eng Sci. 63 (2008) 3643-3653.

Simulation of the Process of an Electro-Thermal Interaction in the Diode Laser System

V.V. Parashchuk

Stepanov Institute of Physics, National Academy of Sciences of Belarus,
E-mail: v.parashchuk@ifanbel.bas-net.by

Abstract*:* The physical-thermal characteristics of the modern thermal conducting materials, for example diamond of different types, in wide temperature range were investigated. It is shown the necessity to consider the interaction inharmoniousness of high orders of the atoms in crystals to satisfy a good agreement between calculated data with the experimental ones in definition of thermal conductivity of the materials and evaluation of the corresponding nonlinear coefficients. Spatial distribution of the thermal fields in the model with some discrete sources (elements) in the condition of electrical current flow was numerically and analytically simulated for the active region – heat transfer substrate (contact layer) system. The proposed calculation method for thermal fields allows optimizing the structure of the devices in order to increase their thermal stability.

Keywords: Power diode lasers, thermal conductivity, inharmoniousness of atoms interaction, electro-thermal interaction, diamond heatsinks.

1 Introduction

In the scope of our investigations [1-5] related to the improvement of the effectiveness of semiconductor laser diodes with the use of high effective heat transfer materials and the modifying technologies of formation of high adhesion metal layers on different surfaces based on the multifunction ion-beam and magnetron sputtering methods it is interesting to have further study of physico-thermal characteristics of these materials in general and lattice (phonon) thermal conductivity (λ_{ph}) of diamond in wide temperature range in particular. Nowadays, the theory of heat transfer by phonon is in the stage that one can not establish the strict quantitative dependence of λ_{ph} on temperature, materials structure and different effects from outside. There are some approximations based on the particular experimental data which are useful for only particular cases [6]. Therefore, in order to analyze thermal, electrical and optical processes in the real laser systems it is important to define the corresponding relationships in the form of practical ratios for general case.

It is well known, that the main source of phonon scattering are the fluctuations of the density of inharmoniousness of thermal vibrations [7,8] which leads to the thermal expansion of the medium. However, in the existing theoretical presentations the phonon heat transfer is considered only with the first pattern in the expansion string of the lattice potential energy upon the shift of atoms, which gives the main contribution and provides the inharmoniousness of energy vibrations. The analysis and comparison between the calculated and experimental data presented in this work as well as in other works (for example, [9]) show that this approximation in many cases is not enough for the appropriate description of the phenomena under consideration. The role of inharmoniousness of lattice vibrations is especially important for the nanomaterials [10].

2 Results and Discussion

2.1 Analysis of a thermal conductivity of the modern thermal conducting materials

In the frame of phenomenological approach [11,12], combining well known quantum and semi-classical models of heat transfer in solid state materials (Einstein, Debye, Frenkel models), one can show that there is a relationship in the form of ratio between the thermal conductivity coefficient λ_{ph}, temperature T and the main physical parameters of a material in consideration of interaction inharmoniousness of atoms in crystals with high orders (up to fifth order):

$$\lambda_{ph} = \frac{d_1 \, k \, R \, \rho \, \theta^3 V^2 (1+\sigma)^2}{\hbar^2 \left[\exp\left(\dfrac{\theta}{g\,T}-1\right)\right] F \, c_p (1-2\mu)^{1/2} Z^4 K}, \tag{1}$$

where factor $F = \alpha r = F(a_i, T)$, $i = 0,1,...,5$ (a_i = b, c, d, e, f) are the contributions of the inharmoniousness,

$$F = \{a^4\left(4605.9b^2 - 41453.4c + 17318\,b\,a'\right) + a^3 k\left(61412.4b^2 + 10363.3c^2 + 30399.1b\,d - \right.$$
$$-184237.2\,e - 14700\,b\,c\,a' + 103908.2\,d\,a'\big)T + a^2 k^2 \big[-134723.4b^2 c + 33162.7\,d^2 + 48362.3ce +$$
$$+ b\left(203318.9\,f - 454598.3c\,a' - 35104.9e\,a'\right) + 11701.6\,b^3\,a' - 38965.6cd\,a' + 779311.3\,f\,a'\big]T^2 +$$
$$+ a\,k^3 \big[10235.4b^4 + 92118.6e^2 + 355314.6d\,f + b\,c\left(-207266.8d + 139099.1c\,a'\right) + b^2\left(-61412.4e + \right.$$
$$+ 31360\,d\,a'\right) - 94080d\,e\,a' - 238455.7c\,f\,a'\big]T^3 + k^4 \big[f(710629.1f - 649426.1e\,a') + bc\left(-829067.3f + \right.$$
$$+ 378831.9e\,a'\right) + b^2\left(241811.3c^2 + 216475.4f\,a'\right) - 126277.3b^3 c\,a'\big]T^4\} \Big/ \{a'\big[a^2\left(70b + 131.6\,a'\right) +$$
$$+ a\,k\left(168\,d - 98.7c\,a'\right)T + k^2\left(-420b\,c + 720\,f + 109.7\,b^2 a' - 329e\,a'\right)T^2\big]^2 T\}, a' = \sqrt{\dfrac{a}{kT}}, \tag{2}$$

$a = r(1-2\mu)(1+\sigma)/(\beta Z^{5/3})$ – coefficient of quasi-elastic force, a_i – coefficients of nonlinear of different orders; σ - electrical affinity, ρ - mass density, $c_p = c_p(T)$ – thermal capacity of one kilo-molar of material, V – its volume, K – number of atoms in the molecule (unit cell of crystal), Z – coordinate number of inter-atom interaction, θ - Debye critical temperature , μ – Poisson coefficient , r – crystal lattice constant, R – gas universal constant, k – Boltzmann's constant , d_1 – constant determined by the type of diamond (the impurity density, optical and electrical properties); β - coefficient of isothermal compressing (module of bulk elasticity), related to the coefficient of thermal expansion (α), thermal capacity and some other physical quantities; g – parameter, near to the number of freedom degree of the interacted oscillators.
Analysis of the studying processes demonstrates the actuality of the phenomena of multi-particle interactions in the media under consideration – up to six phonon-phonon scatterings and phonon – electron interactions. In the frame of the developed approach, a good agreement between calculated and experimental data was received (Fig. 1). The corresponding results for one of the samples (basic objects) which are typical for three main diamond types (insert in the Fig. 1) are shown. Basing on the equations (1) and (2) one can explain the main rules of the occurring heat transfer phenomena in the solid state materials and the interaction of the corresponding processes with the medium macroscopic parameters such as behavior of the temperature dependence of λ_{ph} in the form of curve with the maximum (T_{max}) in the low temperature range and the proportionality of T_{max} with Debye temperature (θ). This dependence $\lambda_{ph}(T)$ is provided by the superposition of two processes: the interrupt decreasing of the inharmonious component of the resistance to the movement of the electrons and

phonons and the exponential decreasing of the number of phonon participated in the energy transferring processes from one point to the other.

The obtained ratios allow determining thermal conductivity of the other materials with the lattice mechanism of heat transfer based on their electrical, mechanical and the other well studied properties. This method differs from the complicated direct methods of measurement which characterized by high error degree. These results also allow estimating the values of the inharmonious interaction coefficients of high order which have important practical meaning. This can be used to create a new method to determine the indicated coefficients when majority of data about them is not known or is impossible to define by the other methods.
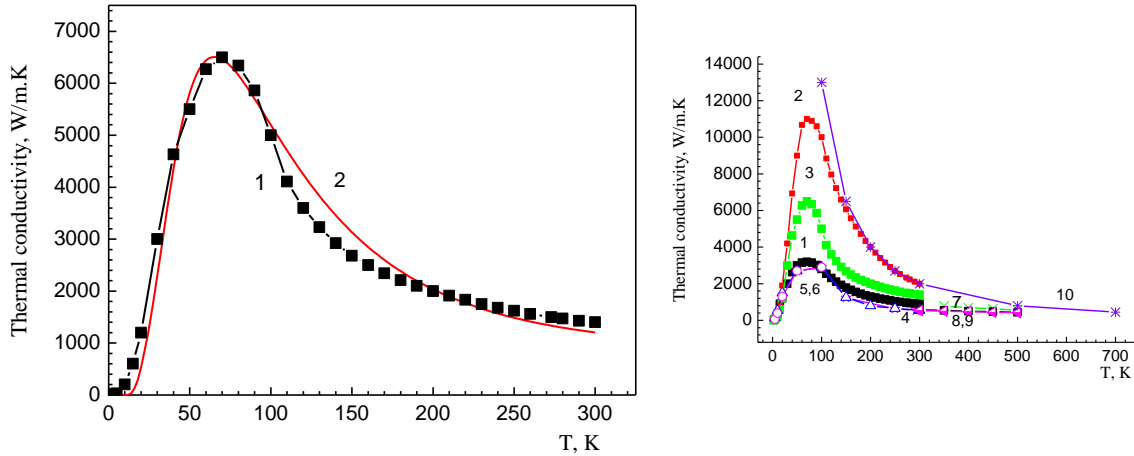

Figure 1 Dependence of thermal conductivity of diamond of type II*b*
on temperature
1 - Experimental data [6], 2 – Calculated curve with $\theta = 1850$ K, $g = 9$.
Insert: natural (1-7) and synthesized (8-10) diamonds
1, 4 - 7 - type I, 2 - type II*a*, 3 - type II*b*; N_2 concentration - $1.5 \cdot 10^{16}$
cm^3 (curve 10)

2.2 Modeling of the electro-thermal interaction process in active layer–diamond heat transfer substrate system

For further analysis of the processes under investigation the analytical spatial distributions of the thermal fields in the model of type "diode – heatsink" which is similar to the real laser system was received. This model is the modification of the studied before model [5] with the consideration of the particularities of the physico-thermal processes in the contact layers based on the three-dimensional stationary equation of thermal conductivity and the corresponding border conditions:

$$T(X,Y,z) = T_0 + ql_1l_2\left(\frac{h}{AB\lambda_2} + \frac{z-h}{ab\lambda_1}\right) + \frac{4qal_2}{\lambda_1 b\pi^2}\sum_{k=1}^{\infty}\frac{1}{k^2}\cos\left(\frac{k\pi}{a}X\right)\cos\left(\frac{k\pi}{a}\varepsilon\right)\sin\left(\frac{k\pi}{2a}l_1\right)\left[\text{th}\left(\frac{k\pi}{a}(z-h)\right) +\right.$$

$$+ \frac{\left(\frac{\lambda_1 A}{\lambda_2 a}\right) \text{th}\left(\frac{k\pi}{A}h\right)}{1+\left(\frac{\lambda_1 A}{\lambda_2 a}\right)\text{th}\left(\frac{k\pi}{A}h\right)\text{th}(\frac{k\pi}{a}(z-h))}] + \frac{4qbl_1}{\lambda_1 a\pi^2}\sum_{m=1}^{\infty}\frac{1}{m^2}\cos\left(\frac{m\pi}{b}Y\right)\cos\left(\frac{m\pi}{b}\eta\right)\sin\left(\frac{m\pi}{2b}l_2\right)\left[\text{th}(\frac{m\pi}{b}(z-h))+\right.$$

$$+ \frac{\left(\frac{\lambda_1 B}{\lambda_2 b}\right) \text{th}\left(\frac{m\pi}{B}h\right)}{1+\left(\frac{\lambda_1 B}{\lambda_2 b}\right)\text{th}\left(\frac{m\pi}{B}h\right)\text{th}(\frac{m\pi}{b}(z-h))}] + \frac{16q}{\lambda_1\pi^3}\sum_{k=1}^{\infty}\sum_{m=1}^{\infty}\frac{1}{km\sqrt{k^2/a^2+m^2/b^2}}\cos\left(\frac{m\pi}{b}Y\right)\cos\left(\frac{k\pi}{a}X\right)\times$$

$$\times\sin\left(\frac{m\pi}{2b}l_2\right)\sin\left(\frac{k\pi}{2a}l_1\right)\cos\left(\frac{m\pi}{b}\eta\right)\cos\left(\frac{k\pi}{a}\varepsilon\right)\left\{\text{th}[\sqrt{k^2\pi^2/a^2+m^2\pi^2/b^2}\cdot(z-h)]+\right.$$

$$+\frac{\lambda_1\sqrt{k^2/a^2+m^2/b^2}}{\lambda_2\sqrt{k^2/A^2+m^2/B^2}}\text{th}(\sqrt{k^2\pi^2/A^2+m^2\pi^2/B^2}\cdot h)\right\}\Big/\left\{1+\frac{\lambda_1\sqrt{k^2/a^2+m^2/b^2}}{\lambda_2\sqrt{k^2/A^2+m^2/B^2}}\times\right.$$

$$\times\text{th}(\sqrt{k^2\pi^2/A^2+m^2\pi^2/B^2}\cdot h)\cdot\text{th}[\sqrt{k^2\pi^2/a^2+m^2\pi^2/b^2}\cdot(z-h)]\right\}. \qquad (3)$$

where $\lambda_{1,2}$ - coefficients of thermal conductivity of the crystal and heatsink (substrate or contact layer), relatively; a, b, z-h and A,B, h − sizes of the indicated elements of the simulated system; $l_{1,2}$ − sizes of heat source, for example, active region of laser diode, ε and η - coordinates the heat source center, q −surface power density of heat source; T_0 − temperature at the lower surface of the heat sink (may be constant or variable value).

With the use of the solution (3) the thermal interaction between the elements (thermal sources) of laser diode structure was demonstrated. The principle of superposition is laid in the core of this model. In the figure 2 the calculated data for the case of two sources and when the heat transfer substrate (heatsink) has the typical parameters for diamond media are shown as an example.
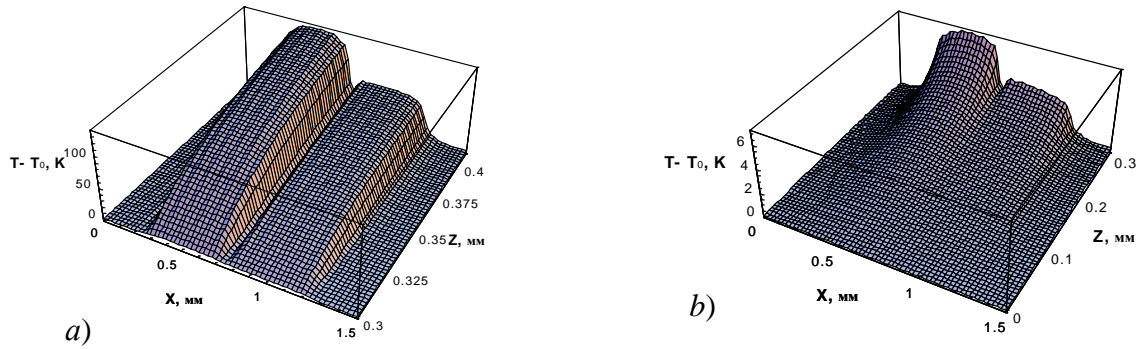
Figure 2 Distribution of the temperature field in the system of active layer (*a*) – diamond heat transfer substrate (heat sink) (*b*) in conditions of interactions of the thermal sources of different powers (P_i)

The sizes of the thermal sources 450x100 μm, active region and heat sink − 1.5×1.5×0.3 μm, the distance between the centers of the elements along X axis ε = 0.5 mm; $P_1 = 4.5, P_2 = 2.25$ W, $\lambda_1 = 1450$ W/(m·K) for heat sink, $\lambda_2 = 50$ W/(m·K) for active region; $Y = 0.75$ mm.

Consideration of the thermal interaction between the elements of the laser diode structure (for example in the laser bars), including the interaction between the inhomogeneousness of active region within one element as well as the similar interaction under the conditions of electrical current flow (electro-thermal interaction) and together with the investigated above temperature dependence of the thermal conductivity coefficient λ_{ph} allows to create the requirements for the topology of placement of the emitting and supporting elements on the crystal. This helps to improve the laser characteristics and to create new structures and systems where the principle of thermal (electro-thermal) interaction is essential. The proposed model of calculation of the three-dimensional thermal fields in the laser diode structure with the consideration of the system real topology allows to analyze its behavior in the regimes approaching to the critical one, as well as to optimize the designs of the new high power structures towards the improvement of their stability to thermal breakdown ("filamentation"). The mentioned type of instability is well known for the high power transistor structures [13]; however it is also actual in the case of laser diodes. For description of the given interaction during the deduction of the formula (4) with the border conditions the dependence of the thermal stream q on the laser diode operating current density j is taken into account as following:

$$q = Uj, \qquad j = j_0 \exp\left[\frac{e(U - rjS) - E_g}{kT}\right], \qquad (4)$$

$$E_g(T) = E_g(0) - \frac{\alpha T^2}{T + \beta}, \qquad \int_0^a \int_0^b j(x, y)dxdy = I = const, \qquad (5)$$

where U – junction p-n voltage (may be prescribed), I - fixed current through the laser diode, r – diode series resistance, $S = l_1 \times l_2$ – active region area, E_g – energy gap of the crystal, j_0 – initial current density.

Taking into account the rations (4), (5) the corresponding system of equations modeling the electro-thermal interaction processes in the single laser diodes and bars was numerically resolved under different conditions for several geometries of the active region (variants of the structure topology). In this case, the basic variant (the initial structure model), subjected to optimization from the point of view of topology, was the structure with the active region in the form of rectangular stripe with $l_1 = 0.45$ mm, $l_2 = 0.1$ mm. In the reducible results, with some exceptions we took $a = b = 1.5$ mm, $z \equiv c = 0.3$ mm, $T_0 = 0$, $U \equiv 1.52 + U\cdot0.0001$, $\varepsilon = 0.5$ mm, $\eta = 0.75$ mm.
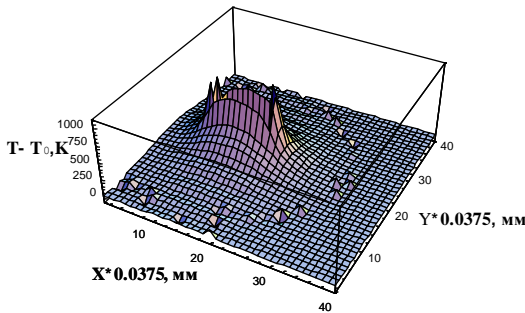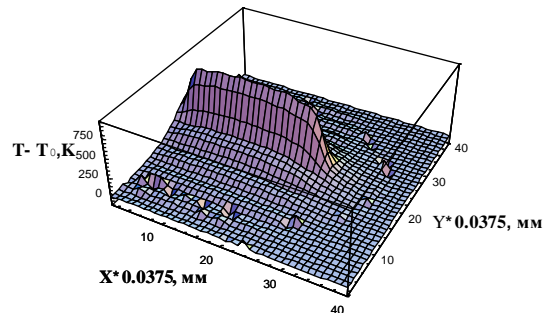
a)   *b)*

Figure 3 Electro-thermal interaction under the critical conditions for the basic variant of topology of the active region (*a*) and its diversities (*b,c*)
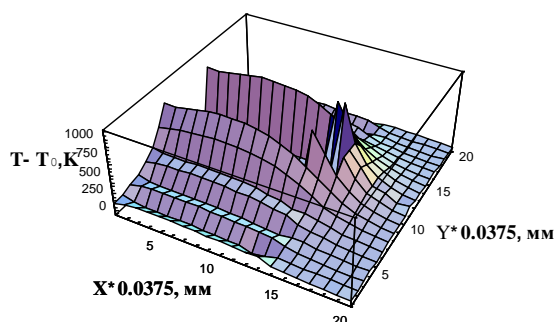$D = -10$ K^{-1}, $j_0 = 9 \cdot 10^4$ (*a,б*), $5 \cdot 10^5$ (*в*) A/см^2;
$l_1 = 0.45$ мм, $l_2 = 0.1$ мм (*a*);
$l_1 = 0.9$ мм, $l_2 = 0.05$ мм (*б,в*)

c)

With relatively small injecting (operating) current ($j_0 \sim 1 \div 150$ A/mm^2, $D = [e(U - rjS) - E_g] / k = -100 \div 100$) the weak thermal background occurs in the system and with the increase of j it is replaced by the appeared separate intensive perturbations. With the further increase of the current density the observed picture begins to remind the interaction process between the single perturbations with the formation of the more complicated spatial inhomogeneous structures. Under the certain conditions (critical regimes) there is the possibility of the transition from chaos to self-organized state and the vice versa which has an agreement with the well known results from the thermal processes [14, 15].

Under the critical conditions ($j_0 \geq 6 \cdot 10^4$ A/cm^2) sharp perturbations appear in the form of splashs and collapses ("abyss") on the background of stationary thermal field distributions (Fig. 3*a, c*) which give evidence of the formation of thermal channels or current ("filament"), similar to the data from [13].

Optimization of the geometry of the active region shows that due to the shrinkage or expansion of its width as well as its partition in smaller fragments (while the total area is unchanged) the considerable increase of the maximal scattered power ($j_{кр}$) and the structure stability for the transition to the state with the sharp inhomogeneous distribution (with filament or channels) of thermal current and temperature was achieved. Further more, the consideration of the thermal conductivity temperature dependence of active region material in correspondence with the above obtained ratios (1), (2) leads to increase about 1.5 times the value of the critical injection current density and the maximal allowed temperature in the modeling medium in spite the fact that in the corresponding region the shown dependence $\lambda_{ph}(T)$ is a decreasing function with temperature. From the calculated values it is clear that there is a possibility of structure optimization related to the spatial inhomogeneous distribution of the thermal fields and the existence of the critical points relatively to the thermal regime (hotter points). In particular, for laser diodes these are the regions near the output facets (mirrors) of the active region cavity where the shown influence of the spatial inhomogeneity is supposed to be very high.

3. Conclusion

Thermal characteristics of the modern thermal conducting materials including the thermal conductivity of diamond λ_{ph} in wide temperature range were investigated. The dependence of λ_{ph} of different types of diamond on temperature and main physical properties of the materials is established with the consideration of high order inharmoniousness of interaction of the atoms in crystals, which shows the present of the phenomena of multi-particle interactions in the investigated media. In the frame of the used approximations a good agreement between the theoretically calculated and experimental data was obtained. The received relations are

useful for confident determination of the thermal conductivities for the other materials and allow estimating their coefficients of high order inharmoniousness.

The thermal and electro-thermal interactions between the components of laser diode structures for the system "active region – thermal conducting substrate (contact layer)" were studied. It is shown that in the modeling system there is the possibility of existing of the different states: from chaos to spatial-inhomogeneous structure. The offered calculation method for the thermal fields allows the consideration of the real topology and the optimization of the device design. One also can use this method to create a new effective principle for thermal stabilization of the laser diode systems.

4. References

[1] Паращук, В.В., Рябцев, Г.И., Беляева, А.К., Безъязычная, Т.В., Баранов, В.В., Телеш, Е.В., Русаков, К.И., Vu Doan Mien, Vu Van Luc, Pham Van Truong (2010). Повышение эффективности мощных диодных лазеров при использовании алмазных теплоотводов. *Квантовая электроника*, Т.40, № 4, С. 301 – 304.

[2] Паращук, В.В., Беляева, А.К., Баранов, В.В., Телеш, Е.В., Vu Doan Mien, Vu Van Luc, Pham Van Truong. (2009). Оптимизация тепловых режимов диодных лазеров. *Известия Томского политехнического университета. Энергетика*, Т.315, №4, С.137-141.

[3] Паращук, В.В., Беляева, А.К., Баранов, В.В., Телеш, Е.В., Русаков, К.И., Vu Doan Mien, Vu Van Luc, Pham Van Truong. (2009). Формирование высокоадгезионных металлических покрытий для мощных диодных лазеров. *Вестник Брестского государственного технического университета. Физика, математика, информатика*, №5, С.102–105.

[4] Ryabtsev, G.I., Parashchuk, V.V., Belyaeva, A.K., Baranov, V.V., Telesh, E.V., Vu Doan Mien, Vu Van Luc, Pham Van Truong. (2009). Effective diamond technology for high power laser diode systems. *Abst. 5th Asian Symposium on Intense Laser Science ASILS-5* (December 2 – 5, 2009, Hanoi ,Vietnam), P.119-120.

[5] Ryabtsev, G.I., Nikeenko, N.K., Batay, L.E., Kuz'min, A.N., Parashchuk, V.V., Kotomtseva, L.A., Loiko, N.A., Sharonov, G.V., Rombak, G.I., Loiko, V.A., Holenkov, V.F., Telesh, E.V. (1999). Synthetic diamond heat sinks for high-power laser diodes. *Lithuanian Physics Journal*, Vol. 39, No.4-5, P. 389-394.

[6] Новицкий, Л.А., Кожевников, И.Г. (1975). *Теплофизические свойства материалов при низких температурах. Справочник*. – М.: Машиностроение, 216 с. (С.148); *Таблицы физических величин*. (1976). / Под ред. И.К. Кикоина, с.151; *http://www. ochem.ru*.

[7] Иоффе, А.Ф. *Физика полупроводников*. (1960). М.: Наука.

[8] Займан, Д. *Электроны и фононы*. (1962). М.: Наука.

[9] Бугай, А.Н., Сазонов, С.В. (2005). О влиянии поперечных возмущений на движение краевой дислокации. *ФТТ*, Т.47, В.4, С. 622 - 627.

[10] Кузнецов, В.М., Хромов, В.И. (2009). О роли ангармонизма решеточных колебаний в макро- и наноструктурах. *ЖТФ*, Т.79, В.6, С.156-158.

[11] Сачавский, А.Ф., Евстигнеев, В.В., Сачавская, Н.А. Единое уравнение состояния вещества. *Труды АлтГТУ им. И.И. Ползунова*. (1998). Барнаул, В.8, С. 214-222.

[12] Евстигнеев, В.В., Сачавская, Н.А., Сачавский, А.Ф. (2000). О возможности вычисления теплопроводности по другим физическим величинам. *http://elib. altstu.ru /elib/books/Files/2000-03/07/pap_07.html*.

[13] Кернер, Б.С., Осипов, В.В. (1975). Теория теплового пробоя транзистора. *Радиотехника и электроника*, Т.20, №10, С.1694-1703; (1977). Нелинейная теория неизотермического шнурования тока в транзисторных структурах. *Микроэлектроника*, Т.6, В.4, С. 337.

[14] Володин, Ю.Е., Бейбутян, В.М., Барелко, В.В., Мержанов, А.Г. (1982). "Кризис" теплообмена в системе платина – гелий. *ДАН СССР*, Т. 264, №3, С. 604 - 607.

[15] Барелко, В.В., Бейбутян, В.М., Володин, Ю.Е., Зельдович, Я.Б. (1981). Тепловые волны и неоднородные стационарные состояния в системе. In: *Автоволновые процессы в системах с диффузией* / Под ред. М.Т. Греховой, Горький: ИПФ АН СССР, С.135-148.

Acknowledgements

Recycling High Performances Concrete

A.AZZEZ RAHMANI* and M.CHEMROUK**

*Doctorate student, University of Sciences and Technology Houari Boumedien, Algeria.
**Professor, Faculty of Civil Engineering, University of Sciences and Technology Houari Boumedien, Algeria;
Email/ mchemrouk@yahoo.fr; corresponding author.

Abstract: Concrete is the world's most used construction material owing to a number of factors such as the adaptability and flexibility in use, the availability of workmanship, the relatively lower cost and the longer term maintenance. The higher rate of construction development that is witnessed today throughout the world requires an ever increasing demand in natural aggregates to supply the concrete construction industry. Yet, the available stockpiles and quarries for aggregates are no more sufficient to fulfil this need. Furthermore, the search for new aggregate extraction plants is facing multiple obstacles due to sever ecological equilibrium problems of the nature and the preservation of the natural resources of our planet. In this sense, the continuous land use for aggregate extraction and the mountains devoured represent real negative environmental impacts that should seriously be taken into consideration by the concrete construction industry. Such concrete construction industry is also affecting our nature and hence having a serious negative impact on our environment through the landfills and disposals of the demolished concrete and building rubbles resulting from the increased and varied demolition activities. Reducing such negative environmental impacts goes inevitable through the search for replacing natural aggregates to make concrete. This will certainly safeguard the ecological equilibrium of our nature and relief our environment from undesired residual waste products.
In this sense, recycling the demolished concrete into construction is an ideal replacement solution. For this objective to be achieved, the first step needed is to identify the important properties of the material required to produce a stronger and highly performing concrete using recycled aggregates. Once it will be shown that these properties can be achieved and sustained with recycled aggregates, recycled aggregate concrete will become a more viable option for a sustainable development in harmony with nature.

The present work looks at the possibilities of recycling the demolished high performances concrete as aggregates to produce new concrete. The results show that the recycled aggregates produced may be particles of an original natural aggregate covered with cement paste, particles of a stronger cement paste and particles of an original natural aggregate. Different concretes were made with substitutions of 50%, 75% and 100% of recycled aggregate respectively as coarse aggregate. The resulting concrete materials had compressive strengths and tensile strengths comparable to those of the original concrete even when 100% of recycled aggregate was used. This was thought to be due to the relatively stronger cement paste by comparison to that of ordinary concrete. Indeed, in high performances concrete, the hardened cement paste is often as strong as the aggregate itself or even more; traces of crushed aggregate particles are often observed in a crushed high performances concrete specimen. The results obtained lead to the conclusion that recycling high performances concrete as aggregates leads to a new high performances concrete without any major drop in the mechanical strengths. Recycling high performances concrete appears to be a valuable resource that has a key role in meeting the challenge of a sustainable concrete construction for a sustainable development that fulfils the needs for the current generation without endangering the opportunities for future generations to meet their particular needs.

Keywords: Compressive Strength, Tensile Strength, High Performances Concrete, Cement Paste, Aggregate, Recycling,

1 Introduction

Concrete is the most used construction material throughout the world. This building material, for which aggregates are the essential ingredient for its formulation since they occupy more

than 70% of its volume, has gained its ranking by its fabrication simplicity, its usage flexibility, its ease of concreting and its relatively better durability. The fabrication of concrete necessitates, thus, huge quantities of aggregates and their ever increasing need is further accentuated with the evolution of human comfort needs. Recycling aggregates from demolished concrete and concrete rebels becomes a viable option since it represents, on one hand, a solution for the protection of the environment from solid waste disposals and, on the other hand, a new supply source of aggregates for making concrete. Moreover, rebel materials from demolition of old building sites and from deconstructions in general are in growing quantities and are either land filled or wildly disposed off, causing a serious negative impact on the environment and a drawback for a sustainable development. The protection of our environment leads in no doubt to a sustainable development and goes inevitably through recycling demolished concrete and concrete rebels to make aggregates for new concrete.

The essential aim of the present work is the study of the rheological as well as the physic-mechanical properties of concrete made partially (50% and 75% recycled) or totally (100% recycled) of aggregates recycled from crushed high performances concrete.

2 Materials used in making concrete

The demolished high performances concrete comes from the crushing of an original high performance concrete of 75 MPa compressive strength. The natural aggregates used in making this concrete consisted of crushed calcareous stones.

The cement used consisted of a Portland cement with additives of class 42.5, that is an average compression strength of 42.5 MPa. The tested HPC fragments are then collected and crushed (see Figure 1) to produce recycled aggregates for making new concrete. The recycled crushed concrete is then sieved to give the desired sizes of aggregates needed to fabricate a new concrete.

Figure 1 : Concrete fragment crushed used to produce recycle aggregates

The Table below summarizes the grading of the natural and recycled aggregates used:

Table 1. Grading of natural and recycled aggregates used

Type	Class (mm)	Code	Origine
Natural	Granulate15- 25	GN 15/25	Crushed calcareous
	Granulate 8-15	GN 8/15	Crushed calcareous
	Granulate 3-8	GN 3/8	Crushed calcareous
	Sand 0-3	SN 0/3	Crushed calcareous
Recycled	Granulate 8-15	GR_{HPC} 8/15	Crushed HPC
	Granulate 3-8	GR_{HPC} 3/8	Crushed HPC
	Sand 0-3	SR_{HPC} 0/3	Crushed HPC

GN: Granulate Natural; GR_{BHP}: Granulate Recycled from high Performance Concrete
SN: Sand Natural; SR_{BHP}: Sand recycled from High Performance Concrete

The concrete mix of high performance concrete is given in table 2 below:

Table 2. Concrete mix for making high performance concrete

Mixing ingredients		Mixing porportions (kg /m3)
Cement		450
Silicate Fume		45
Superplasticisers		6.75 (1.5%)
Mixing Water		157.5 (W/C = 0.35)
Sand	Finer	115
	Coarser	461
Aggregates	3/8	190
	8/15	882

3. Results and Discussion

3.1 Shape and Surface texture of aggregate particles

From a visual observation, the surface texture of recycled aggregates is rougher than that of the natural ones. The recycled aggregates can be in three different shapes, namely:
1- a natural particle covered with cement paste
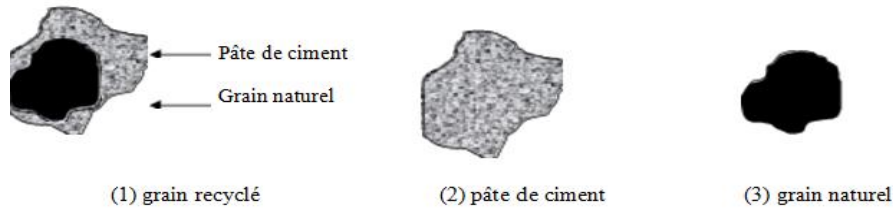2- a cement paste on its own
3- a natural particle

Figure 2 : Shape of recycled concrete aggregate

3.2 Water Absorption

Recycled aggregates absorb relatively more water than natural ones and hence care should be taken for the fresh concrete to dry out rapidly and becomes unworkable. In this sense, Debieb [1] has reported that an important absorption of water by recycled aggregates should be taken care of in order to avoid durability problems at the longer term. Louis et al [2] have argued that increased water absorption occurs at substitution rates higher than 30% of finer recycled aggregates. In the present work, the water absorption of the aggregates used, natural and recycled, is present in table 3 below:

Table 3: Water absorption of aggregates (in %)

Granulate Natural GN	Absorption (%)	HPC	Absorption (%)
GN 8/15	0.4	GR 8/15	3.97
GN 3/8	2.5	GR 3/8	6.70
SN 0/5	0.35	SR 0/5	7.30

3.3 Mechanical strength of aggregates

The mechanical strength of aggregates was appreciated in the present work through the Los Angeles test which normally gives an idea about the resistance to wear for the aggregates. The test show that the three types of aggregates described above, namely the natural granulate covered with cement paste, the hardened cement paste and the natural granulate have to a certain extent comparable strength. The results given in table 4 below illustrate that a crushed hardened cement paste could be as strong as the natural aggregate and is within the limits of producing a better resistance concrete such as that of high performance concrete. On the whole, the Los Angeles results for recycled aggregates are within the limits imposed by the French standards for making good quality concrete [3]. It is believed that the denser and compact hardened cement paste containing silicate fume as a mineral additives behaves as an aggregate when crushed.

Table 4: Hardness of Aggregates (natural and recycled) – Los Angeles Test

Granulate Natural GN	Los Angeles	Recycled HPC	Los Angeles
GN 8/15	21	GR 8/15	28
GN 3/8	25	GR 3/8	26

3.4 Properties of Fresh concrete – Workability

Workability of fresh concrete was appreciated through the slump test. The results shown in Figure 2 illustrate that concrete made with recycled high performances concrete aggregates loses its workability as the substitution ratio increases to become 100% of recycled aggregates. However, such loss is still within the acceptable limits and the use of more superplasticiers might be a solution to keep the concrete workable since a proportion of only 1.5% by weight of cement was used in the present work for both natural aggregates concrete and recycled aggregates concrete. It is to be noted that in case of compatibility with the cement used, such proportion of suplasticisers may go up to 3%.
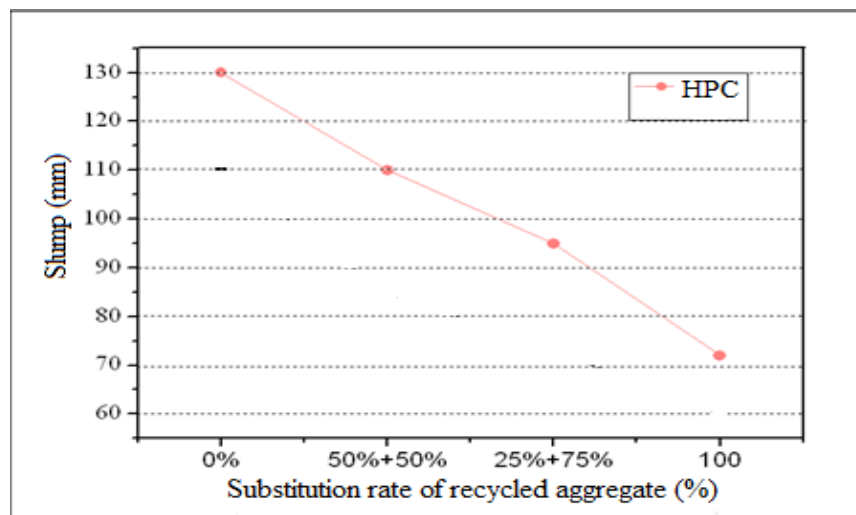
Figure 3 : Workability of fresh concrete as a function of the substitution rate of recycled high performances concrete aggregates.

The variation of the unit weight of fresh concrete with the proportion of recycled aggregates is also shown in Fig.4 which illustrates a decrease of only around 6% of the fresh density when 100% of recycled aggregates are used. This is once more due to the better quality hardened cement paste which behaves as a strong and hard aggregate particle and does not melt. The slight decrease in the density can be overcome by the use of slightly more mineral additives by comparison to the original high performance concrete.
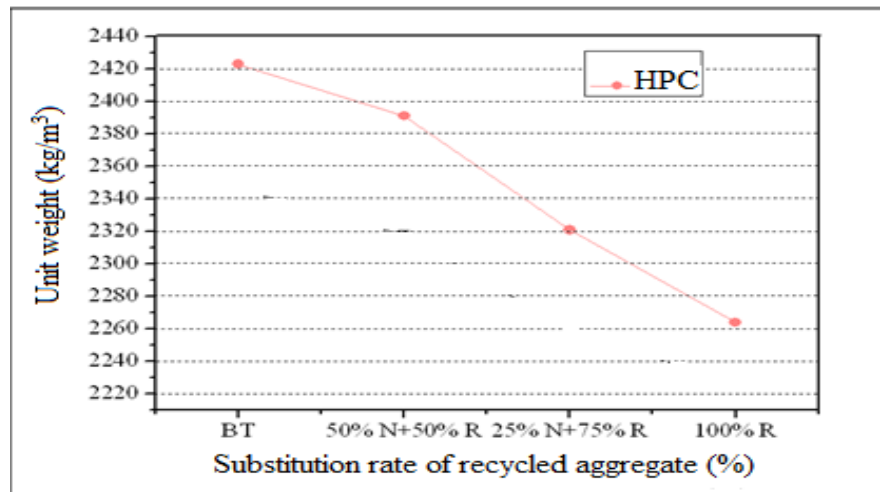
Figure 4 : Unit weight of the fresh concrete as a function of the substitution rate of recycled high performances concrete aggregates

4.4. Properties of Hardened Concrete

4.5.1. Unit Weight (density)

The variation of density of the hardened concrete material made of aggregate recycled from high performance concrete is shown in Figure 5. The figure illustrates that the density of the hardened concrete material made of 100% recycled aggregates decreases by less than 6% which is negligible and can be overcome with the use of a little extra additives.

Figure 5 : Density of the hardened concrete as a function of the substitution rate of recycled high performances concrete aggregates

4.5.2. Compressive strength

The variation of the compressive strength of concrete with the substitution rate of the recycled aggregate concrete is illustrated in Figure 6. The evolution of the strength with age was assessed at 3 days, 7 days, 14 days, 28 days and 56 days. It can be clearly seen that the strength at all ages is independent of the substitution rate of recycled aggregates and is

comparable to that of high performances concrete made of natural aggregates. A strength of almost 75 MPa is reached at 28 days of age for the four types of concretes which, in effect, vary only by the substitution rates of recycled aggregates. This is due to the better mechanical quality of aggregates recycled from high performances concrete, including the hardened cement paste aggregate particles. Such quality is exhibited through the Los Angeles of the aggregates and trough the density of the concrete made with them. This result is very beneficial for the concrete industry in a sense that high performances concrete which is known for its higher resisting qualities and relatively better longer term behaviour is also fit for a complete recycling as new aggregates in case of deconstruction and demolition without losing from its complete construction performances. Recycling high performances concrete is then a new challenge that the concrete industry will be facing and opens wider the ways for the recycling industry in the building sector.

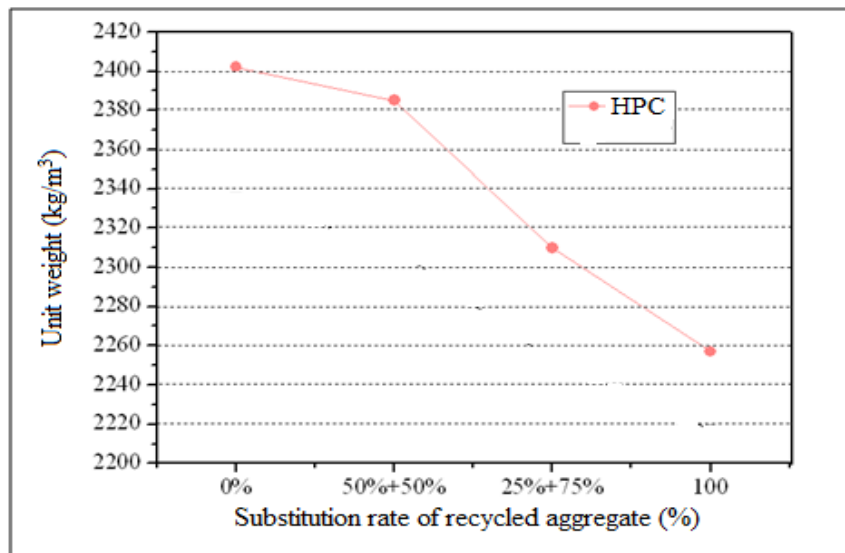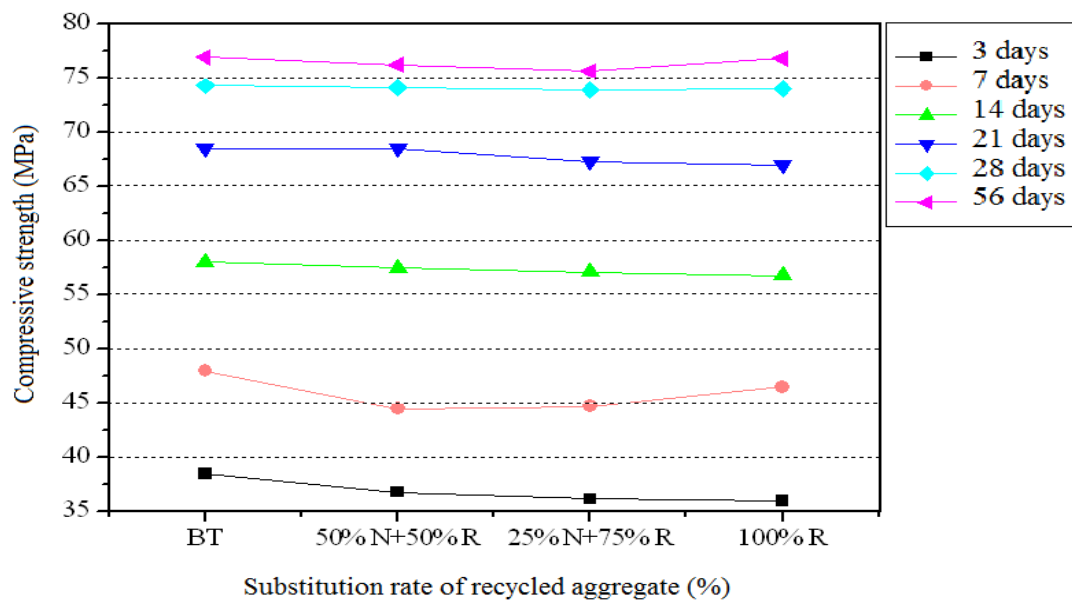Figure 6: Compressive strength of concrete as a function of the substitution rate
of recycled high performances concrete aggregates

3.5.3. Tensile Strength:

The tensile strength of concrete was measured through the splitting test carried out on concrete cubes and cylinders at 7 days, 28 days and 56 days of age respectively. The tensile strength reaches 5.2 MPa for the four types on concrete at 28 days of age, including the one made at 100% of recycled aggregates. The results illustrated in Figure 7 show clearly that recycling high performances concrete as aggregates leads to tensile strengths as equal as the original high performances concrete for all the substitution rates and at all ages. The hard quality of the cement paste of high performances concrete combined to the rougher surface of recycled aggregate particles helps obtaining a better quality bond between the recycled aggregate and the cement paste for the new concrete and hence gives a better tensile strength. The results concerning the tensile strength express once more that recycling high performances concrete as aggregates makes concrete as resistant as the original one, without any loss in the resisting qualities. The recycled cement paste of high performances concrete is as strong as the natural aggregates for making new high performances concrete.
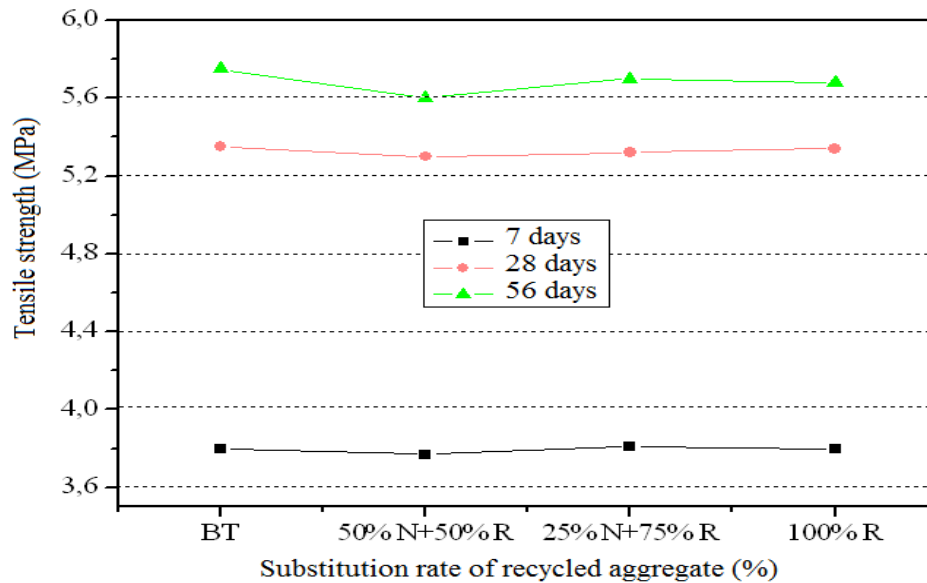
Figure 7: Tensile strength of concrete as a function of the substitution rate
of recycled high performances concrete aggregates

4. Conclusion :

Valuing recycled aggregate has a great impact on the environment in a sense that it represents a new source of supplying aggregates and hence maintain the ecological equilibrium and relief the nature from building demolition waste disposals as landfills.

The hardness of recycled high performances concrete aggregates is comparable to that of natural aggregates.

The density of concrete made of recycled high performances concrete aggregates is to a certain extent comparable to that of the natural aggregates making the original concrete. A decrease of less than 6% was recorded when a 100% of recycled aggregate was used. This slight decrease could be overcome by the use of more mineral additives.

The workability is not much influenced by the use of recycled high performances concrete; the use of more superplasticisers would certainly catch up with the recorded slight decrease.

The mechanical properties, expressed through the compressive strength and through the tensile strength, of concrete made of recycled high performances concrete aggregates are the same as those of the original high performances concrete, without any decrease. This is thought to be due to better resisting qualities of the hard cement paste of high performances concrete which behaves fully as strong aggregate.

More research work is needed on this topic to assess the validity of the present results which represent an impulse into the recycling of demolished concrete and firsthand results on recycling high performances concrete.

5. References :

[1] Debieb F (2007)., *performance et durabilité de béton à base de granulats recyclés contaminés par les chlorures et les sulfates* ; thèse de doctorat, de l'USTHB Alger, pp 168, Algérie.

[2] Louis R. and George C. (2008). *Criteria for the use of fine recycled concrete aggregates in concrete production;* Building and Environment, 31, pp. 307-316

[3] NF P 18-573 (1990). *Granulats - Essai de Los Angeles* ; French Standard.

[4] Cabral A. E. B., Dal M. and Rebeiro D. (2007). *Compressive strength and deformation modelling of recycled aggregate concrete'*; Cement & Concrete Composites 31, pp.545–560

[5] Ravindraradjah R. S. and Tam C. T. (1985). *Properties of concrete made with crushed concrete as coarse aggregates*; Magazine of Concrete Research, Vol. 37, N° 130, pp. 29-38.

An Experimental Study on the Dispersion Stability of Alumina-Water Nanofluids via Particle Size Distribution and Zeta Potential Measurements

Elif Begüm Elçioğlu [1,2], Tuba Okutucu-Özyurt [1]

[1] Department of Mechanical Engineering, Middle East Technical University,
Dumlupınar Bulvarı, No. 1, 06800, Ankara, Turkey.
[2] Eskisehir Osmangazi University, Sivrihisar Vocational School,
Mechanics Programme, Eskişehir Cad. No: 140, Sivrihisar, Eskişehir, Turkey. (ebelcioglu@ogu.edu.tr)

Abstract*:* The concept nanofluids have attracted attention due to the possibility of gaining increments in transport properties (e.g. thermal conductivity, viscosity, etc.). While such increments have been verified to some extent, their sustaining is required. Since the sustainability of the properties strongly depend on the colloidal behaviour, it is important to develop a fundamental understanding on the dispersion stability of nanofluids. This study is a demonstration of evaluating the dispersion stability of one-year old Alumina – Water nanofluids by means of the particle size distribution and zeta potential measurements. It is critical to report the thermophysical and particulate characteristics of nanofluids over certain periods, since such approach will help to foreseen the possibility of these fluids' transition to applications, as well as their feasible use in industry as heat transfer fluids. While the zeta potential results of this study indicate high electro-dynamic stability, the particle size distribution results revealed a moderately poly-dispersed (aggregated) condition of nanoparticles. However, comparison with the experimental results reported in literature showed the aggregation observed in the current study could be considered as not very critical. The authors hereby highlight the requirement of performing stability experiments periodically and frequently and give future directions on the studying nanofluids.

Keywords: nanofluid, particle size distribution, zeta potential, dispersion stability.

1 Introduction – Stability and Related Concepts

Nanofluids as mixtures of nanoparticles and base fluid(s) has been proposed by Choi and his co-workers [1] and since then, their thermophysical and heat transfer properties have been widely investigated both experimentally and theoretically. Improvements observed in those characteristics have made nanofluids to be considered as promising materials, but the data presented in literature are mostly scattered mainly due to the differences in the material preparation and handling approaches, uncontrollable experiment outcomes such as hysterezis effects, human factor, etc. In addition, instabilities resulting from the size range of the solid component of the nanofluids are complicating the topic, thus they are of great importance and should be investigated in more detail. Current context is concerned with the dispersion stability of nanofluids, therefore no introductory information of nanofluids will be given from herein.

The field nanofluids is purely multi-disciplinary, therefore a sophisticated perspective is needed. Stability of two-phase suspensions is not a straightforward concept either, and has different aspects, all in terms of different but closely related disciplines. A detailed description of stability provided by Zhu *et al.* [12] is given here to familiarize the reader to the topic. In [12], the stability of nanofluids was divided into four sections: thermodynamic stability, kinetic stability, dispersion stability and chemical stability. Nanofluids have been considered to be prone to thermodynamic, kinetic and dispersive instabilities mainly due to the high surface energies of the nanoparticles, mobility of the nanoparticles due to Brownian motion and nanoparticle aggregation- which may deteriorate the stability with time. In [12], Zhu et al.

also pointed out that two mechanisms having critical effect on nanofluid stability was aggregation and sedimentation.

The state of the literature showed that, utilizing the potential superior properties of nanofluids is only possible if and only if one can ensure a stable dispersion of nanoparticles. A highly agglomerated state of nanoparticles, which also causes the large and heavy aggregates to settle down, cannot be considered as a stable condition. As a result, the authors employed a quantitative and periodical approach to investigate the dispersion stability of the Alumina – Water nanofluids based on the particle size distribution (PSD) and zeta potential measurements.

2 The State of the Art

Some contemporary studies on nanofluid stability are overviewed here. Ghadimi *et al.* [2] reviewed the stability of nanofluids in detail, mainly based on the nanofluid preparation techniques, importance of nanofluid stability, and stability inspection instruments. Simsek *et al.* [8] also presented a comprehensive review on stability indicators, stability measurement techniques and stability enhancement methods. Herein, for the sake of simplicity, nanoparticle fraction (either by volume or weight) and nanoparticle diameter (size) are denoted with φ and d_p, respectively.

Kumar Agarwal *et al.* [4] studied the stability of Alumina (d_p=13 nm and 30 nm)–Kerosene nanofluids with φ= 0.05%-0.5 vol.%. They investigated the average d_p via Dynamic Light Scattering (DLS). Dispersion of nanoparticles was procured by bath and disruptor type ultrasonications. Visual inspections showed Alumina nanoparticles' immediate settlement in kerosene irrespective of ultrasonication conditions, while they stayed visually stable in water for a few hours after ultrasonication (for water based samples, disruptor induced ultrasonication derived higher stability). Among the oleic acid and Tween-20 LR as surfactants, the use of the former alone gave the highest stability (attributed to differences in their purities). The optimum volume fraction of oleic acid to nanoparticles was 0.3, for which no major particle settlement was visually inspected for more than 10 days. The authors concluded the stability was negatively correlated with φ. A colour change was reported for the samples ultrasonicated for more than 2 hours. DLS results showed a non-critical increase in the average d_p for increasing φ. After 2 days passing the preparation, the d_p increased by some extent- which was attributed to nanoparticle clustering- and as time approached, the average d_p at the top layers decreased as the clusters settled down. Hachey *et al.* [3] performed transient heating, steady state nanofluid stability and nanofluid hysteresis experiments on surfactant-free Alumina (d_p=10 nm)–Water and Alumina (d_p=10 nm)–Ethylene Glycol nanofluids with φ=1.0, 2.5 and 5.0 vol.% and stated that exposure of nanofluids to relatively high temperatures would inevitably reduce their stability by being a catalyst to the agglomeration process. The PSD's of the nanofluids were measured via DLS. Comparison of the PSD results between the spent (temperature exposed) and fresh nanofluids showed a flattened PSD spectrum of spent samples (attributed to the consuming of the smaller free reactants into increasingly more voluminous formations) and the authors stressed the spent nanofluids got agglomerated as a result of the isothermal heating phase, due to the increased heat energy of nanoparticles exerting a kinetic diffusion, causing enhancements in the coalescence process. They also pointed out that increased φ would decrease the stability by putting forward the statistical proximity of the neighbouring nanoparticles and compounds the speed at which coalescent reactions spread and consume nanoparticles. Nasiri *et al.* [5]

investigated the stability of single-walled, double-walled, few-walled and two types of multi-walled Carbon nanotubes with different morphologies. The authors presented a one-step process by using potassium persulfate (KPS) as oxidant to prepare water-soluble CNT's. Colloidal stability of the samples were evaluated by zeta size distribution, sedimentation imaging (the samples poured into tubes were allowed to deposit for 2 months, and then they were stirred thoroughly and PSD's were measured), and UV-VIS spectroscopy. The results showed high agglomeration/precipitation tendency of multi-walled Carbon nanotubes and highest stability of SWNT suspension among the others. Wang *et al.* [11] investigated the dispersion stability of water based TiO_2 and Al_2O_3 nanofluids produced via two-step method. Nanofluids contained SDS (sodium dodecyl sulfate) as a surfactant. They tried different concentrations of SDS as well as the addition of pH adjusters, in order to maximize the stability of those nanofluids. Stability was measured in terms of the zeta potentials and absorptivities, and results showed the water based TiO_2 and Al_2O_3 nanofluids had optimum pH values of ≈9.5 and ≈6.0, respectively, providing maximum zeta potential, and maximum stability. The optimum SDS concentrations were 0.10% and 0.14% for the water based Al_2O_3 (φ= 0.05 wt.%) and TiO_2 (φ= 0.01 wt.%) nanofluids. Pang and Kang [6] studied the stability of Al_2O_3 nanoparticles (primary d_p= 40-50 nm) dispersed in a H_2O/CH_3OH binary mixture (φ=0.1 vol.%) and GA (Gum Arabic) surfactant, via the visual inspection, Tyndall effect and of zeta potential. The researchers added NaCl in the nanofluid suspensions, in order to increase CO_2 absorbtivity (which was of the concern). They took the just-after-preparation and 1-week-later pictures to compare the nanoparticles dispersion within the base fluid. The nanoparticles were properly dispersed within the base fluid initially, resulting in a poor transmission of light, whereas the stability of nanofluids one-week-after the preparation was not as good as just-after-preparation. Addition of NaCl resulted in poorer stability, especially for the 3.5 wt% NaCl, and presence of GA as the surfactant did not help on re-establishing the stability of nanofluids. At that NaCl concentration, the zeta potential of nanofluids was approaching zero, indicating highest possibility of the nanoparticles to coagulate. In addition, the authors reported the stable life of the 0.1 vol.% nanofluids as one week, at most. Thrush [9] investigated the stability of oil based and surface functionalized Al_2O_3 (average d_p= 40-50 nm) nanofluid stability for different surfactant concentrations. Ultrasonic disrupter and ultrasonic bath were used to ensure the proper dispersion of nanoparticles, and both were successful on breaking down the aggregates. The appropriate surfactant addition step was examined, and the addition of the surfactant before the ultrasonication provided better stability (lower aggregate size) than after ultrasonication. The stable life of the nanofluids produced was between 4 to 12 days and after that period, significant deviation from the stable conditions is observed. The most stable nanofluids were containing 28:1 of oleic acid and nanoparticles. The author concluded the addition of proper surfactant and the application of proper ultrasonication method were vital to produce stable nanofluids. Addition of the surfactant PIBSA (poly-isobutylene succinic anhydride) resulted in better stability than that of the oleic acid. Schrand *et al.* [7] reported stability results for the multi-walled Carbon nanotube – Water nanofluids. The hydrophobic character of MWCNT surfaces prevents the dispersion within water and results in intensive ultrasonication even for a non-sufficient yet acceptable dispersion. The authors reported the ultrasonication done on the nanofluid samples did not help to have a long and stable life, by stressing that the MWCNT's were temporarily suspended in water.

As far as the literature survey is concerned (a small portion of it is given in this context), it can be inferred that the dispersion stability of nanofluids has been investigated in terms of both quantitative measures such as the zeta potential, absorbency, TEM analysis, PSD, etc. and sedimentation photograph capturing. While the stability was investigated in detail in some

of the studies, the field is still inconclusive in terms of longer sustainability of the stable condition of nanofluids, thus from the application perspective.

3 Material and Methodology

Information on the material of investigation and experiment procedure are given in this Section. Experiments are performed at the Polymer Research Laboratory in the Chemistry Department in Eskisehir Osmangazi University, Eskisehir, Turkey.

Experimental study is concerned with the PSD and zeta potential measurements on Alumina (Al_2O_3, d_p= 30$\pm$10 nm)–Water nanofluids of φ= 0.5, 0.25 and 0.125 vol.%. The nanofluids were purchased from NanoAmor, Inc. one year before the stability measurements. The nanofluids contained 20 wt.% (corresponding to 6.33 vol.%, conversion from weight to volume (and vice versa) is done according to the formula given in Turgut *et al.*'s [10] study) Al_2O_3 nanoparticles initially, but such concentration levels turned out to be inappropriate for stability experiments. Therefore the stock material (φ=6.33 vol.%) is diluted with water de-ionized for two times, and 0.5, 0.25 and 0.125 vol.% concentrations are prepared. Figure 1 shows the prepared samples in DLS cups (left) and zeta potential cell (right).
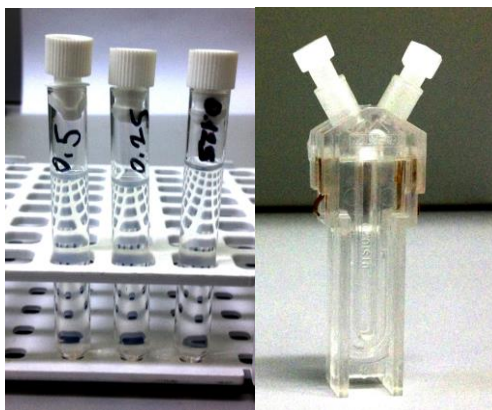

Figure 1 Nanofluid samples poured in the DLS cup (left) and disposable folded capillary zeta potential cell (right)

As can be seen in Figure 1, the DLS and zeta potential measurements require very small sample volumes. Considering the equipment used in the current study, samples of 1-2 ml have been enough for the experiments.

The PSD (via DLS) and zeta potential measurements are performed using ALV/CGS-3 compact goniometer system (Malvern Instruments, Inc, UK) and Malvern Nano ZS, respectively. The DLS measurement system is equipped with He-Ne laser at λ_0= 632.8 nm, 22 mW, photodiode detector with high quantum efficiency and an ALV/LSE–5003 multi tau digital correlator electronic system. The measurements were done with 90° constant angle scatterings on the suspensions, and the data were processed using secondary cumulant analysis. Samples also have been ultrasonicated, and for this purpose Bandelin SONOREX™ Digital 10 P Ultrasonic Bath is used. Experiments were started with zeta potential measurement and PSD measurements followed. The experiments were performed in a weekly manner in order to monitor the weekly changes in PSD.

4 Results

The zeta potential and PSD experiment results are presented herein. The zeta potential of the φ= 0.125 vol.% sample is 47.5 mV, indicating high electro-dynamic stability since its absolute value (magnitude) is higher than 30 mV [10]. The DLS measurements are performed on the φ= 0.125, 0.25 and 0.5 vol.% Al_2O_3-H_2O nanofluids. The primary particle size of the nanoparticles was provided as d_p= 30±10 nm by the manufacturer, one year ago. Therefore, this study gives information about how long the average particle size of such a nanofluid can be sustained, in terms of the PSD. The PSD's of the φ= 0.125, 0.25, and 0.5 vol.% Al_2O_3-H_2O nanofluids are measured using DLS and the variation in PSD over weeks is monitored. The impact of ultrasonication on the nanofluid stability is also evaluated.

The PSD results of φ= 0.125 vol.% Al_2O_3-H_2O nanofluid is shown in Figure 2. The first week subsequent measurements showed an increment in particle size from 30±10 nm (primary d_p) to ~ 83.6 nm (measured d_p, 1 year later) in average. The particle size augmentation could have been caused by the agglomeration of the particles.

Observation of the agglomeration of the particles in the first week, it is decided to perform an ultrasonication process to re-establish the mono-dispersed condition of the particles. The ultrasonication treatment is characterized by the ultrasonication power and ultrasonication period (duration). The ultrasonicator used has a constant power, thus different ultrasonication periods are tried. The red asterisks show the particle size values of the φ= 0.125 vol. % samples (2nd week, the first 5 runs belong to untreated samples, while the last 4 runs belong to the samples ultrasonicated for 1 hour). Comparison of the untreated and ultrasonicated samples showed a decrease in particle size at initial due to the ultrasonication, but the particle size augmentation is observed within the subsequent measurements. The PSD results shown in Figure 2 shows the influences of the 1 and 2 hour lasting ultrasonications. Observing that 1-hour ultrasonication was not sufficient (2nd week), it is decided to treat the samples with 2-hour lasting ultrasonication (3rd week), yet no significant decrease in d_p is observed.
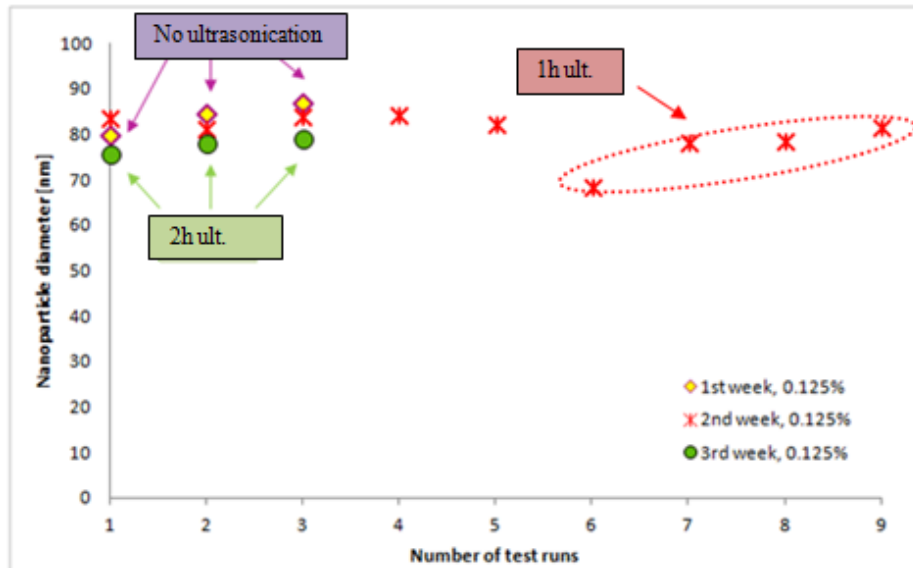

Figure 2 PSD results for the φ= 0.125 vol.% Al_2O_3-H_2O nanofluid samples treated with different sonication periods over 3 weeks.

Figure 3 shows the variation of the particle sizes of $\varphi= 0.25$ vol. % samples (untreated and ultrasonicated for 45 minutes and 1 hour). An augmentation in the d_p compared to the primary d_p is observed for this sample group, as well. Trying different ultrasonication periods over weeks showed that, the ultrasonication resulted in a decrement in particle size initially, but did not last long as the d_p approach to the initial measurements after a few minutes.
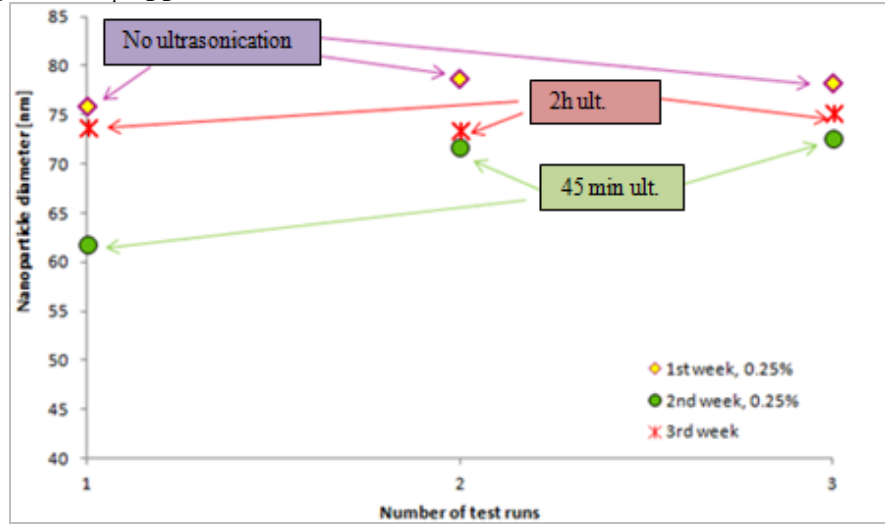

Figure 3 PSD results for the $\varphi= 0.25$ vol.% Al_2O_3-H_2O nanofluid samples treated with different sonication periods over 3 weeks.

In Figure 4, the PSD results for $\varphi= 0.5$ vol. % samples are shown. After observing that tried ultrasonications turned out to be not sufficient to decrease the d_p's to the initial for $\varphi= 0.125$ and 0.25 vol.% samples, the impact of the relaxation of the samples after ultrasonication was not studied on the $\varphi= 0.125$ and 0.25 vol.% samples. An augmentation in the d_p compared to the primary d_p value of the 0.5 vol.% sample is also observed. Comparing the particle sizes of the 1st and the 2nd week, it is seen that the ultrasonication resulted in a decrease in the d_p over a week, but the particle size turns back to the 1-week-before-value within a few minutes. In the 3rd week, the effect of the relaxation of the samples ultrasonicated for 2 hours showed the d_p is expected to turn back to the 1-week-before-value within half an hour. In the 4th week, even 5 hour ultrasonication is tried, yet, it did not give any improvement in terms of a d_p decrement.
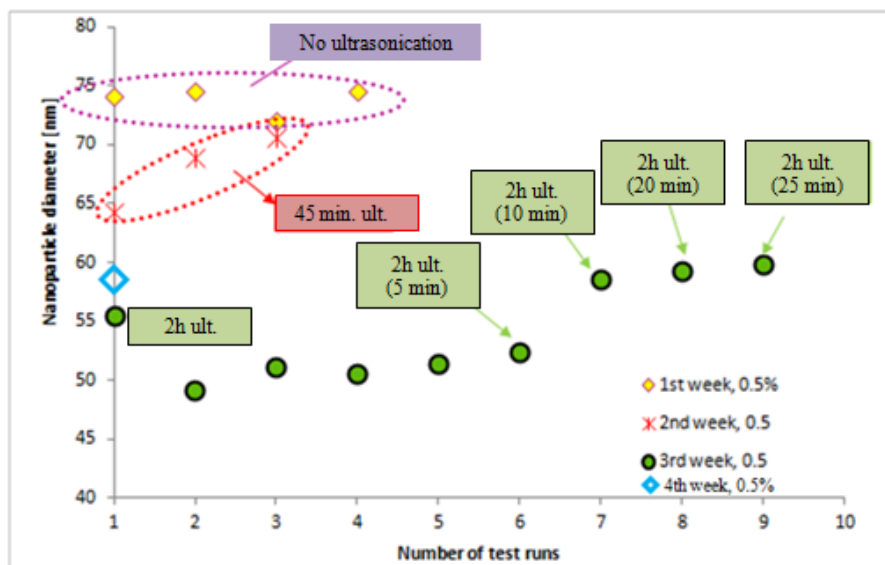
Figure 4 PSD results for the $\varphi = 0.5$ vol.% Al_2O_3-H_2O nanofluid samples treated with different sonication periods over 3 weeks.

Regarding the visual inspections, in contrary to the sedimentation related visuals reported in some studies, the nanofluids used in the current investigation do not show any nanoparticle sedimentation and/ or a gradual color change. This may be due to the nanoparticles/ nanofluids color, which is between white and gray. This finding raises the conclusion that, a nanofluid can show poly-dispersed nanoparticle condition with d_p growing twice compared to the primary value, without showing any color change or nanoparticle sedimentation. As a preliminary conclusion, it is important to perform experimentation on the other stability indicators such as the PSD and zeta potential, and not to rely on just the visual inspection, then conclude if the nanofluid is stable or not.

5 Conclusions

In this study, the time dependent PSD of Al_2O_3-H_2O nanofluids is investigated experimentally. The study gives some important conclusions and insights in some certain aspects, some stressed below.

- Stability of the examined nanofluids in terms of the particle size distribution, turned out to be not sustained over 1 year, while the studied samples did not show any evident sedimentation and/or low zeta potential corresponding to an instable particulate state, which can be due to many reasons. In literature, many instability indicators (e.g. level of agglomeration) have been used and by referring to some of those studies, in most of which the stability of nanofluids have not been investigated over a longer period as in the current study, it can be said that the stability of those nanofluids may deteriorate much further than the nanofluids of examination in the current study.

- One possible reason that the Al_2O_3-H_2O nanofluids used do not show any sedimentation may be: the concentrated stock sample received from the supplier did not have sedimentation, and it contain a surfactant. On the other hand, while the nanofluids used in the current study is visually very stable and has very high zeta potential, it has a relatively broad PSD.

- For the applications, the stable life of nanofluids should be sustained for a sufficiently long time. In literature, visual inspection seemed to be utilized a lot. Visuals may give important results, but such results may not be sufficient enough. Visual inspection can work for some cases, in which the nanoparticle settlement can be detected via the eyes, which can be possible for the nanoparticles colored different than that of the base fluid (e.g. CNT and Copper). In the studies similar to the current one, a visual inspection may not work since the Al_2O_3 nanoparticles themselves have white to grayish color.

- Particle size is an important indicator of colloidal stability and its range for nanofluids makes them unique in both advantageous and difficult-to-handle ways. The Brownian motion (which is random) of nanoparticles has been held responsible for the heat transfer enhancements obtained with nanofluids. For agglomerated nanofluids, the particles can grow a few ten times larger than the primary particles, which may result in settling down the agglomerates, and decreasing Brownian motion. Therefore, in order to take benefit from the theoretically (rarely, experimentally) obtained enhancements in heat transfer, the stability of the nanofluid of examination should be ensured, first.

- Nanofluids can be utilized in other areas than heat transfer applications, depending on the thermophysical property of relevance. Some of the thermophysical properties of nanofluids (i.e. thermal absorbtivity, thermal diffusivity, viscosity, density, etc.) are reported to be higher than those of the base fluids. Some studies have reported significant improvements in those thermophysical properties, but if the stability of the examined nanofluids is not sustained, the repeatability and applicability of those results get highly questionable.

- The flow behavior of nanofluids is highly dependent on their viscosity. A nanofluid can be a Newtonian or non-Newtonian fluid (mostly, the latter) and can have significantly different behavior than that of the base fluid used. Recent studies on stability are focused on reducing the viscosity of nanofluids by preventing the aggregate formation and developing a mono-disperse condition of nanoparticles. Reducing viscosity can result in decreased pumping power requirement to circulate the nanofluid within the system. Therefore a nanofluid having high heat transfer coefficient, low viscosity, and high stability is desired for applications.

6 Possible Future Directions

The stability is a complicated and hard-to-predict condition of nanofluids, which is of great importance in terms of fundamental research and industrial applications. Some future work suggestions are given below.

- Stability experimentation mostly requires very small sample volumes, which do not significantly affect the sample amount in other simultaneous experimentations to be performed (e.g. heat transfer). Therefore such small volumes of samples should be used for stability measurements in order to be able to state that the main measurements performed are not biased by the instabilities (agglomeration and sedimentation).

- The stability of nanofluids is an important concern and is dependent on many different parameters, such as the nanoparticle and base fluid material, nanoparticle shape, external conditions (e.g. if the nanoparticles are magnetic, external magnetic fields can affect the dispersion), nanofluid storage conditions, and etc. Therefore, more detailed efforts are needed to understand the stability of nanofluids based on the important parameters for the applications.

- As an expected fact, if a nanofluid gets deteriorated, it cannot have repeatable properties anymore. Therefore one cannot expect a nanofluid to have longer usability than its allowable shelf-life. Therefore, the nanoparticle or nanofluid suppliers in both industry and academy should provide at least a rough estimate on the shelf-life of the nanofluid, during which it can be safely used and can have repeatable properties.

7 References

[1] Choi, S.U.S., Eastman, J.A. 1995. Enhancing Thermal Conductivity of Fluids with Nanoparticles. In: *ASME International Mechanical Engineering Congress&Exposition*, November 12-17, 1995, San Francisco, CA.
[2] Ghadimi, A., Saidur, R., Metselaar, H.S.C. 2011. A Review of Nanofluid Stability Properties and Characterization in Stationary Conditions, *International Journal of Heat and Mass Transfer,* 54, 4051–4068.
[3] Hachey, M.-A., Nguyen, C.T., Galanis, N., Popa, C.V. 2014. Experimental Investigation of Al_2O_3 Nanofluids Thermal Properties and Rheology – Effects of Transient and Steady-State Heat Exposure, *International Journal of Thermal Sciences,* 76, 155-167.
[4] Kumar Agarwal, D., Vaidyanathan, A., Sunil Kumar, S. 2013. Synthesis and Characterization of Kerosene-Alumina Nanofluids, *Applied Thermal Engineering,* 60, 275-284.

[5] Nasiri, A., Shariaty-Niasar, M., Rashidi, A.M., Khodafarin, R. 2012. Effect of CNT Structures on Thermal Conductivity and Stability of Nanofluid, *International Journal of Heat and Mass Transfer,* 55, 1529–1535.

[6] Pang, C., Kang, Y.T. 2012. Stability and Thermal Conductivity Characteristics of Nanofluids (H_2O/CH_3OH + NaCl + Al_2O_3 Nanoparticles) for CO_2 Absorption Application. In: *International Refrigeration and Air Conditioning Conference.* Indiana: Paper 1190. http://docs.lib.purdue.edu/iracc/1190, 2012.

[7] Schrand, A. M., Schlager, J. J., Dai, L., Hussain, S. M. 2010. Preparation of Cells for Assessing Ultrastructural Localization of Nanoparticles with Transmission Electron Microscopy, *Nature Protocols,* 5, 744 – 757, doi:10.1038/nprot.2010.2.

[8] Şimşek, E., Elçioğlu, E.B., Okutucu-Özyurt, T. (2014), Stability of Nanofluids – A Critical Review. In: *International Symposium on Convective Heat and Mass Transfer (CONV-14)*, June 8-13, 2014, Kuşadası, Aydın, [*full paper accepted]*.

[9] Thrush, S.J. 2012. Investigation of Dispersion, Stability, and Tribological Performance of Oil-Based Aluminum Oxide Nanofluids, *Thesis* (Mechanical Engineering) – Oakland University. Rochester, 85.

[10] Turgut, A., Tavman, I., Cetin, L., Chirtoc, M., Fudym, A. 2011. Preperation and Characterization of Nanofluids Containing Alumina Nanoparticles, In: *ICHMT DIGITAL LIBRARY ONLINE, Volume 0, 2011 Issue - TMNN-2010. Proceedings of the International Symposium on Thermal and Materials Nanoscience and Nanotechnology* - 29 May − 3 June, 2011, Antalya, Turkey.

[11] Wang, X-J., Li, H., Li, X-F., Wang, Z-F., Lin, F. 2011. Stability of TiO_2 and Al_2O_3 Nanofluids, *Chin. Phys. Lett*. Vol. 28, No. 8, 086601.

[12] Zhu, H-T., Liu, S-Q., Xu, L. and Zhang, C-Y. 2007. *Preparation, Characterization and Thermal Properties of Nanofluids*, Edited by: Sabatini, D.M., Leading Edge Nanotechnology Research Developments, New York: Nova Science Publishers, Inc. Chapter 1. 5-38.

Acknowledgements

Spontaneous Polymerization Of The Tetrahydro -1,4- Oxazine With 3- Chlorine -1,2- Epoxypropane

Bored A.I., Akramov E.M.

Research and test centre "Strom" at Institute general and inorganic chemistry to Academies of the sciences of the Republic Uzbekistan

Abstract: The Open join-stock company "Angrencement" before 90-h years past centuries specialized on issue white and colour cement. For production клинкера white portland cement raw materials material served the limestone and каолиновая clay, шлам on base which had high moisture (45%). Whereas, обжиг клинкера for white portland cement was conducted under 1500-1550oC and required the greater expenses fluid fuel - a fuel oil, which in that time disastrous came short, enterprises in the beginning 1990 has stopped its activity.

Keywords*:* Polymer composition, chemical reactant, physico-chemical properties of drilling fluids.

1 Introduction

At present row action is conducted on enterprise on modernizations, technical and technological rearmament production. In this connection, gains special importance a decision on a matter, in accordance with economical use fuel-energy resource at production клинкера, for what necessary to install the possibility of the use the solid fuel in lieu thereof fluid, study the possibility of the shaping high реакционноспособных composition raw materials mixtures for reception клинкера on local raw material and техногенных departure, under обжиге which full assimilation of the oxides calcium and formation main клинкерных mineral can occur under comparatively low temperature, than the temperature обжига traditional raw materials mixtures. In this plan volcanic mountain sorts, as was it earlier noted, cause the special interest as conditional алюмосиликатное raw material with low temperature of the melting.

With provision for territorial vicinity to OOO "Angrencement" and for the reason development recommendation as far as possible use in composition of the raw materials mixtures as conditional алюмосиликатного of the component is chose габбро Akchinskogo местрождения. As карбонатсодержащего component is used limestone месторождения "Podzemgaz".

Research objects and methods

Tetrahydro-1,4-oxazine (morpholine) - colourless hygroscopic liquid; the temperature of boiling 128, 9 ^{o}C, 24,9 ^{o}C/10 mm h.g; d^{20}_4 1,0007; n^{20}_d 1,4545. 3-chlorine-1,2-epoxypropane (epichlorinehydrine) - before use the fraction has been overtaken and selected with $T_{boil.}$=390 To (0,1008 MPa); temperature of fusion is 330 K; $d=1,18_4^{20}$; $n^{20}_D=1,4381$. Ethanol (ethyl spirit) - absolutised dehydration calcium oxide, then overtaken, the selected fraction has been dehydrated in the presence of magnesium and iodine, the fraction has been overtaken and selected with $T_{boil.}$ - 351 K, fusion temperature -387,15K.

Experimental part

Synthesis of polymers on the basis of tetrahydro-1,4-oxazine with 3-chlorine-1,2-epoxypropane in the mass has been carried out as follows: 1 mole tetrahydro-1,4-oxazine is added to 1 mole of 3-chlorine-1,2-epoxypropane and 1 % of hydroquinone (from a lump of initial regents) by agitating. A reactionary mix is heated up to 50 ^{o}C within 3 hours. After reaction product time sulfuric ether is settled. The outlet makes 92 %.
The synthesised polymer represents as the powder of white colour or light pink colour.

Research of kinetic laws of spontaneous polymerisation of morpholine with epichlorinehydro has spent by the method of dilatometry. As parametre characterising speed of reaction it has been used the value of $\Delta V/V$ carried to a respective interval of time of polymerisation Δt, that is $\Delta V/V \cdot \Delta t$, where $\Delta V/V$ - relative change of the volume of solution in dilatometer in time Δt.

IR - Spectra of the initial and synthesised connections are removed on spectrophotometer marks (FTIR) model NEXUS 470. Cleanliness and individuality of the synthesised connections have been investigated by the method of **TCX** on plates «Silufol UV-254», display by iodine steams.

Discussion of results

It is revealed, that at the mixture of tetrahydro-1,4-oxazine (MPH) with 3-chlorine-1,2-epoxypropane (CHEP) both in mass, and in the environment of various organic solvents, in the range of temperatures from 10 to 50 $^{\circ}$C chemical reaction which is accompanied by the formation of water-soluble high-molecular product proceeds. The synthesised products are well dissolved in water and organic solvents.

It is experimentally established, that radical ingibitories-2,2,6,6-tetramethylpiperidile-1-oxyl, hydroquinone do not render essential inhibitory action, that is radical character of process is excluded. So, spontaneous polymerisation of MPH with ECHH consists of reactions of quaternization and polymerisations. Quaternization reaction research was not separately possible, as formed salts are instantly involved in polymerization.

Composition and the structure of synthesized products have been established by the IR-spectroscopic method and element structure has been analyzed.

The influence of various factors on the quaternization process: the nature of solvents, temperature and concentration of initial reagents has been investigated. For studying of the influence of the nature of solvent for initial speeds of polymerization the following number of solvents has been chosen: benzene, ethanol, water. The received results have shown that the speed of reaction increases with increase in the polarity of medium. For the further regular studying of kinetic features of reaction ethyl spirit that is, thus reaction proceeds in homogeneous conditions is used.

Kinetic measurements of spontaneous polymerization in the specified solvent have been spent at various temperatures (20-50 $^{\circ}$C). Experimental data show, that with rise in temperature the speed of investigated reaction increases. From the temperature dependence of speed of reaction value of effective energy of activation of process which is equal to 56,2 kDj/mole that is close to value of energy of activation of quaternization reaction in the Menshutkin reactions [2] has been defined.

Set of experimental and IR-spectral researches show, that a limiting stage found out polymerization process is Menshutkin reaction that is the reaction of the formations quaternary salts MPH with CHEP which is involved in polymerization.

Studying of influence of concentration of initial components on polymerization process shows that with increase in concentration of MPH and CHEP the speed of reaction increases. The reaction order on the concentration of MPH makes 1,1, and on the concentration of CHEP is equal to 0,9 (fig. 1).
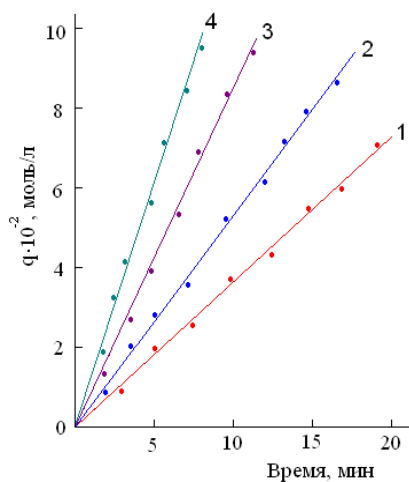
Fig. 1. Dependence of the reaction of spontaneous polymerization of MPH with CHEP from the concentration of MPH, mole/l: 1-0,25; 2-0,5; 3-0,75; 4-1,0. [CHEP] =1,0 mole/l. [Inh] = $1·10^{-4}$ mole/l. Temperature of 50 $^{\circ}$C.
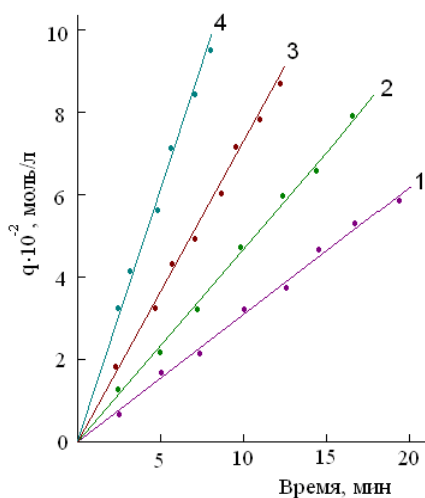
Fig. 2 Dependence of the reaction of spontaneous polymerization of MPH with CHEP from the concentration of CHEP, mole/l: 1-0,25; 2-0,5; 3-0,75; 4-1,0. [MPH] =1,0 mole/l. [Inh] = $1·10^{-4}$ mole/l. Temperature of 50 $^{\circ}$C.

Viscosity properties of the synthesized products have been studied (fig. 3). From the results of viscosimetric researches (dependence of the resulted viscosity synthesized cationic polymers in the water solution from concentration) follows, that the received polymers are typical polyelectrolytes and the resulted viscosity of the solution sharply increases in conformity at dilution (fig. 3, c.1), and introduction in the solution of polymeric electrolyte in water of low-molecular strong electrolyte 0,1 **n** PCl leads to reception usual, that is to linear dependence of the resulted viscosity on the concentration (fig. 3, c.2).
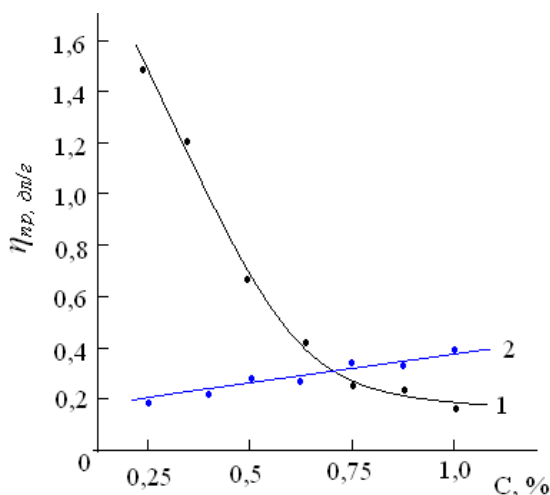
Fig. 3. Dependence of the resulted viscosity on the concentration of polymer received on the basis of MPH with CHEP in water (1) and 0,1 **n** solution PCl (2).

From results of viscosimetric researches (dependence of the resulted viscosity synthesised cationic polymers in the water solution from concentration) follows, that the received polymers are typical polyelectrolytes and the resulted viscosity of the solution sharply increases in conformity at dilution (fig. 3, c.1), and introduction in the solution of polymeric electrolyte in water of low-molecular strong electrolyte 0,1 **n PCl** leads to reception usual, that is to linear dependence of the resulted viscosity on concentration (fig. 3, c.2).

Conclusion

Thus, reaction of spontaneous polymerisation of tetrahydro-1,4-oxazine with 3-chlorine-1,2-epoxypropane in mass and in the medium of various organic solvents which has not radical nature has been investigated. Influence of the nature of solvent, temperatures and concentration of initial reagents for speed of polymerization reaction has been studied. General energy of the activation of process has been calculated and as well the order of reaction on the concentration of reacting components has been determined. The viscosity and their bactericidal properties of the received polymers have been studied.

Reference:

1. K.D.Sadikov, A.S.Smirnov, S.V.Makarenko. Synthesis of 2-morpholine-(piperdine)-3-nitroakrilytes //Magazine of organic chemistry. – V-2004. Issue 10. p-40.
2. Kneesh Ye.G., Trubchanin N.I. Methods of obtaining morpholine 3-methyle-1,2,4-triasolil-5-thioacetate, developing hepatoprotective, wound healing and antiviral activities. Patent № 2144534, RF, 2000.
3. Maksumova A.S., Ruziyev R., Djalilov A.T., Topchiyev D.A. Investigation of kinetic regularity of spontinuos reactions of polymerization N,N- dimethylaminoethylmethakrilate. //Magazine. News of institutes, series «Chemistry and chemical technology.» V –1986. Issue 2. –pp. 78-80.

Status And Perspective of Production of Cement With Use Non-Traditional Raw Materials - Volcanic Rocks of Uzbekistan

Akramov E.M Iskandarova M. I.

"Uzkurilishmateriallari's" joint-stock campaign, Tashkent, Uzbekistan

Introduction

One of the perspective directions of lowering of expenses of fuel and energy resources when roasting clinker is use of components with the high maintenance of the ferriferous and fusible components which presence as a part of a raw compound promotes increase of its reaction capacity, to lowering of temperature of roasting to 1350oC and by that – to lowering of prime cost of clinker to 25% [1-4].

Need of the cement industry of the republic for ferriferous components (mineralizers) makes about 250 thousand tons per year and in the near future will make about 500 thousand tons per year. It isn't possible to provide branch with such quantity of components due to delivery from abroad practically.

For the solution of this actual problem retrieval operations whenever possible uses of volcanic rocks as ferriferous a mineralizer and the conditional alyumosilikatny component of a raw compound are carried out by production of clinker instead of traditional components, and their huge inventories are available in the territory of Uzbekistan in close proximity to each operating cement works.

Research technique

As a mineralizer and an alyumosilikatny component of a raw compound of portlandtsementny clinker local volcanic rocks were studied: diabase-porfirity, diabase-spillity, diabase-piroksenity, andesite-porfirity, basalts, gabbro and rocks of tufoalevrolitovy composition. Composition of raw compounds with use of volcanic rocks calculated by a traditional technique. Reaction capacity of new raw compounds studied in the temperature range 1000-1400os with an interval 100oC. Completeness of process of a klinkeroobrazovaniye controlled according to the content of the free oxide of SAO calcium. Completeness of mineralogenesis checked the X-ray phase analysis by means of the diffractometer DRON-2. Durability of cements on the basis of the synthesized clinkers of optimum composition on standard samples prisms of 4x4x16 cm.

Results and their discussion

Research of chemical and mineralogical composition of rocks of different fields of Uzbekistan shows that according to the maintenance of SiO_2 they treat group of the mains the izverzhennykh of rocks, have a low melting temperature (1080-1200) about With and formation of a mobile melt in case of their use as a part of a cement raw compound. Their use instead of traditional mineralizers and the alyumosilikatnykh of components positively would be reflected in prime cost of products.

The analysis of a chemical composition of volcanic rocks showed that the content of the main oxides in them fluctuates in the following limits, % of masses: item pct - 2,10÷5,70; SiO_2 – 42,50÷56,45; Al_2O_3 – 11,50÷17,50; Fe_2O_3 – 4,25÷13,90; SAO – 4,50÷13,50; MGO – 2,80÷8,60; Na_2O – 1,50÷3,55; K_2O – 0,84÷4,50.

Temperature of their melt determined in the laboratory silitovy furnace in samples cones, except for basalt breeds, is in the following range: the beginning ~ 1100oC, the end ~ 1230oC, and for basalts – the beginning 1350oC, the end 1400oC (fig. 1). It is marked that diabase-porfirity, diabase-spillity and туфоалевролиты possess rather low melting temperatures and small intervals of the beginning and the end of melt (1130-1190) ° C with formation of a silicate melt of quite low viscosity (high flowability).
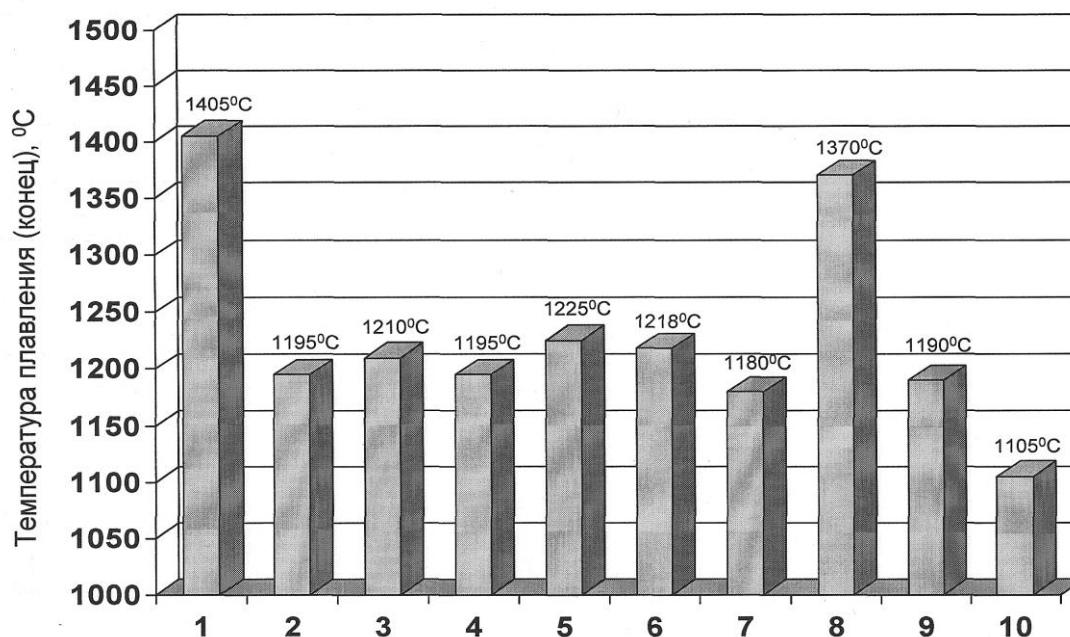
1 . Candle ends. 2 . Diabaz-spillit Pistalitausky field. 3 . Diabaz-piroksenit Belyaush-saysky field. 4 . Diabaz-piroksenit Tillyatagsky field. 5 . Andezit-porfirit Kaynarsaysky field. 6 . Diabaz-porfirit Karakhtaysky manifestation. 7 . Diabaz-piroksenit Kizilolminsky field. 8 . Basalts of the Osmansaysky and Gavasaysky field. 9 . Туфоалевролит Tashbulaksky field. 10 . Gabbro of the Akchinsky field.

It is set that process of assimilation of Saosvob when roasting the raw compounds containing volcanic rocks, proceeds intensively and the klinkeroobrazovaniye practically comes to an end at a temperature (1350-1400) ° C with formation of silicates, aluminates and алюмоферритов calcium to what the insignificant maintenance of Saosvob (less than 1% of masses) in the spekakh, burned in the laboratory silitovy furnace with exposure of 10 min. (tab. 1) testifies.   Table 1

Assimilation of Saosvob in the course of roasting of raw compounds
depending on composition and roasting temperature

№ № смесей	Содержание CaO$_{своб}$ в спеках, обожженных при температуре, ^{o}C:				
	1200	1300	1350	1400	1450
1	28,5	19,4	10,2	2,8	1,2
2	23,7	11,3	3,8	0,4	следы
3	24,6	8,4	1,2	0,1	следы
4	27,7	16,5	7,0	1,2	1,0
5	24,2	11,5	3,5	0,8	0,3
6	23,0	14,4	5,9	0,8	0,4
7	23,2	10,9	3,2	0,5	следы
8	23,7	13,2	5,6	1,3	0,7

In compositions of raw compounds the content of volcanic rocks is in limits (10-22) % of masses. In case of their 22% - number the contents in a compound the clay (alyumosilikatny) component completely is absent. It leads to formation of a liquid phase at rather low temperature of roasting. Unlike process of roasting of the traditional raw compound including limestone, a clay component and a ferriferous mineralizer in which

formation of a liquid phase (melt) in a burned material happens on the difficult mechanism at the expense of the formed minerals – more smoothly: aluminates and алюмоферритов (C3A, C4AF, C2F, etc.) being high-temperature, when roasting new raw compounds, formation of a liquid phase (melt) happens due to direct melting of volcanic rocks which contain rather high amount of the active oxides SiO2, A12O3, Fe2O3 and SAO in a look стеклофазы, silicates providing education, aluminates and алюмоферритов calcium according to energetically favorable diagrams in case of direct component interaction of a liquid phase. In the conditions of roasting of a two-component raw compound, in case of a complete elimination the kvartssoderzhashchikh of clay components, response of education silicate, the alyuminatnykh and the alyumoferritnykh of minerals happens to high speed at rather low temperature. The formed clinker is characterized by good granulation, high volume weight and activity.

The raised maintenance of MGO in volcanic rocks to (8-9) %, has no negative impact on uniformity of scope change of cement as it is a part of volcanic glass and in the course of roasting of a raw compound is in composition of a silicate melt in the form of magnesian silicates therefore in clinker the periclase won't be formed, and as a result – in case of hydrothermal and autoclave processing of cement samples there are no the internal deformations causing non-uniformity of scope change of the hardened cement stone.

Use of volcanic rocks, in particular diabase-piroksenita and diabase-porfirita allows to expel completely from composition of a raw flour two adjusting components - золоотходов and candle ends, and also partially – and clay slates. Owing to catalytic influence of volcanic rocks when roasting a raw flour temperature of the beginning of expansion of SASO3 decreases, processes of decarbonization and digestion of lime are accelerated, products of roasting are characterized by good granulation and accurate crystallization of brick minerals with heat treatment temperature drop to 1350oC. Roentgenograms of clinkers are provided by accurately expressed intensive diffraction reflections of the main brick minerals, nm: C3S (0,303; 0,297; 0,278; 0,275; 0,261; 0,218; 0,196; 0,181; 0,176) ; C2S (0,287; 0,279; 0,278; 0,275; 0,261; 0,228; 0,218; 0,196) ; C3A (0,270; 0,220; 0,196) ; C4AF (0,277; 0,266; 0,263; 0,192). Absence on roentgenograms of diffraction reflections of the intermediate phases and the free oxide of calcium testifies to completeness of processes of mineralogenesis in clinkers. High hydraulic activity of clinkers cements from which show durability in case of compression from 53,2 to 60,3 MRA also is explained by it.

The carried-out trial tests for JSC Kuvasaytsement, JSC Akhangarantsement and JSC Kizilkumtsement. real possibility of increase in productivity of furnace aggregates for (10-20) % is set when using volcanic rocks as a mineralizer and an alyumosilikatny component as in case of a dry method, and a wet method of production of clinker. In case of increase in a supply of the furnace it is necessary to regulate height of a layer of a material change of rotational speed of the furnace aggregate, by installation of the frequency transformers to the principal drives of the furnace aggregate that leads to increase of its productivity and to full combustion of fuel. Taking into account an acceleration of process of a klinkeroobrazovaniye when roasting the raw compounds containing non-traditional raw materials, the increase in productivity of rotating furnaces by their additional supply is reached.

Now the technology of receiving clinker with use the izverzhennykh of rocks is implemented on JSC Kuvasaytsement and JSC Kizilkumtsement. As a result of mastering of new technology the hour productivity of all rotating furnaces by JSC Kuvasaytsement increased to 20% (from 25,0 t/h on 30,0 t/h), the specific expenditure of gas on ton of clinker decreased by 11%, activity of clinker increased on 7,5 MRA (from 43,0 MRA to 50,5 MRA), and on JSC Kizilkumtsement increase of hour productivity of furnaces averaged 18,0% (from 114 t/h to 135 t/h), reduction of the specific expenditure of gas by clinker ton – (6-8) %, increase of activity of clinker – 8,8 MRA (from 40,5 MRA to 50,3 MRA).

Inference

High performance of the production technology of a portlandtsement with use of non-traditional raw materials – volcanic rocks of Uzbekistan as the conditional alyumosilikatny and ferriferous components which presence at a raw compound promotes lowering of temperature and an acceleration of process of roasting, increase of hydraulic activity of clinker and productivity of rotating furnaces, increase in output of cement is set. Available positive experiment on mastering of this technology allowed to recommend results of researches for JSC Kuvasaytsement and JSC Kizilkumtsement for approbation and at other cement works of the republic.

Results of industrial mastering of technology of receiving portlandtsementny clinker with use of non-traditional raw materials – volcanic rocks testify to prospects of this direction. Therefore the following stage of implementation of results of our researches is mastering of the production technology of portlandtsementny clinker on JSC Akhangarantsement and JSC Bekabadtsement with use as alyumosilikatny and ferriferous components the vulkanicheskikhkh of rocks – diabase-porfiritov of Shavazsaysky and Pistalitausky fields.

Literature

1 . Cements from basalts / under the editorship of A.A.Pashchenko. - Kiev: Naukova thought. 1983 . 192 pages.

2 . Rumyantsev of Item F. Daman A.I., YU.I. Eagles clinker synthesis at the under temperatures//11 Mezhd. meeting on chemistry and technology of cement. - M 2000. T.Z. of page 285-286.

3 . Makhmudova V. Sh., Iskandarov M. I. Cements of the low-temperature roasting from basalt breeds of Uzbekistan//Tez. докл. Mezhd.Konf. on the chemical XT 07 technology devoted to the 100 anniversary since birth Akkad. N.M.Zhavoronkova. Том.1. - Moscow. 2007 . Page 209-212.

Influence of Magnetic Field on the Morphology of the Wear of the Cutting Tool

D. NECIB [1], A. BOUCHOUCHA [2]

[1] University of Ouargla.30000, Algeria, E-mail: necib.djilani@univ-ouargla.dz; necibdjilani@yahoo.fr.

[2] Laboratory of Mechanics, Faculty of Sciences of Engineering, Mentouri Constantine University.25000. Algeria. E-mail:bouchoucha_ali1@yahoo.fr.

Abstract: This paper reports the study of the influence of a magnetic field on the morphology of the wear of the cutting tool as a function of the cutting speed during the cutting operation, and observed the weight losses (wear) and their morphologies. The wear of the cutting tool was quantified by weight loss during cutting. While carrying out experiments, we have noticed the existence of a critical value of the magnetic field intensity H = 16.5 kA.m^{-1}, for which the depth of the crater wear of cutting is minimal and the cutting edge of the cutting tool is preserved. The presence of the magnetic field in the manufacturing contact modifies completely the morphology of cutting and quality of the surface state of the cutting edge. Moreover, the increasing of the magnetic field was found to change the cutting temperature. In the present manuscript we presented the different behaviours of manufacturing observed with and without magnetic field.

Keywords: Magnetic field, tool wear, cutting process, surface quality

1. Introduction

Manufacturing by chip removal, designates the set of techniques that enable to obtain a surface via removing material using a cutting tool. This old technique is often described as a costly cutting technique due to the fact that the shaping of the material piece leads to the transformation of the noble material into waste (chips). However; it is still an important and widespread manufacture technique. In shaping the metals by cutting, the turning process, the subject of our study, represents on its own for 33 % of the field of manufacturing by chips removal. Turning plays an important role in the engineering industry, where manufacturers seek to increase production with minimum possible cost. These two objectives are limited by several parameters including the cutting tool lifetime. This has prompted researchers to improve, firstly, the quality of the material of the cutting tool, and secondly, to minimize the negative effect of the cutting speed [1]. For this, we sought to optimize the cutting tools life by a fairly new industry, which involves applying to the contact piece-tool, a magnetic field during manufacturing. Reduction of wear of a cutting tool can be obtained either by choosing the geometry and hardness of the active part of the tool, or via using a machined material that has been polished by a thermal treatment. The latter must satisfy two constraints: on one hand, a quantitative constraint which leads to the reduction of the manufactured parts cost. On the other hand, a qualitative constraint which consists in obtaining surfaces possessing optimal

geometries and micro-geometries. In 1987, V. J. Al Shits [2] studied the effect of a magnetic field applied to metal pairs and showed that its application results in a considerable modification of the plasticity of metals; that is the magnetoplastic effect. Moreover, he showed that the magnetic field can lead to the hardening of metal crystals; therefore a magnetoplastic positive effect. Nevertheless, it can lead to the softening of crystals; which is the magnetoplastic negative effect. In addition, the nature of the magnetoplastic effect depends mainly on the magnetic properties of metals [2]. In 1970 and 1971, Bagchi and Ghosh [3, 4] were the first to have studied the effect of an external electromotive force (EMF) created by a magnetic field on the wear characteristics of cutting tools in HSS on mild steel. Their results revealed an important reduction in wear and a permanent positive gain factor. In 1975 and 1977, Muju and Ghosh [5, 6, 7] presented a physical model in order to explain some obtained results during experiments carried out with a magnetized tool HSS (tool running on mild steel and brass). In their observations, they confirmed that this technique allows an increase in the lifetime of tools by about 40% as well as a reduction of the size of wear particles [5]. Furthermore, El Mansori [8, 9, 10] showed that the effect of the magnetic field on the mechanisms of friction tool-chip (position, morphology of the primary zone and of the contact tool-chip) is the reduction of the wear of the cutting tool. In 2003, O. Batainch [11] showed that this technique leads to a longer lifetime of the cutting tool of 10%, despite an increase in the interfacial temperature during manufacturing. These recent studies showed that the application of the magnetic field is concentrated at the superficial layer of material, which can modify its mechanical behavior at the tribology of the contact tool-chip.

The main objective of this paper is to determine the influence of a magnetic field on the wear morphology of a cutting tool. In addition, we seek to link the damage mechanisms of the cutting tool with the thermo-mechanical stress at the interface tool-chip-piece in the case of manufacturing with and without magnetic field. The discussion of results is mainly based on microscopic observations of the active tip of the tool and the profile of the cutting surface, as well as on the state of the surface of the cutting tool.

2. Experimental Procedure

2.1 Description of tests and the experimental

The international standard DIN ISO 3685 [1] was used for wear tests of long duration carried out to assess the lifespan of tools in P25 at different cutting speeds. By using a microbalance accurate to 100μg, weight difference before and after each cutting operation allowed evaluation of the weight loss (W). Longitudinal turning operations relative to the different

tests were realized on round specimens of non-alloy steel of grade XC38, 65 mm diameter, 500 mm in length (the machined length is lc = 300 mm) and hardness 52 HRC. An 8 mm in diameter centering hole is made to ensure rigid fixation of the part (piece) between the two points. A lathe (Fig. 1), of a power of 9.5 kW, mounted on a pin, was used for the cutting operations. The inserts used (Fig. 2) are removable of a rhombic form made of metallic carbide of grade P25 (type CCMT09T308E-73) with a ray of rounding corresponding to 80°. The insert tightening torque is fixed at 3 Nm. The insert holder, of reference SCLC2020K09 (D4010T) [12] and designation SCLCR/L2525M12 is fitted with a tightening screw of the insert.

The experimental setup shown schematically in Figure 1, includes mainly:

1. An infrared camera
2. A metallic carbide removable insert of a rhombic form (cutting tool)
3. The part to be manufactured (the workpiece)
4. An Ammeter.
5. A regulator of a voltage to an alternative courant used to vary the magnetic field by changing the current applied to the coil
6. A coil of 1600 turns and a resistance equal to 3.9 Ω, serving to the creation of a magnetic field inside the tool
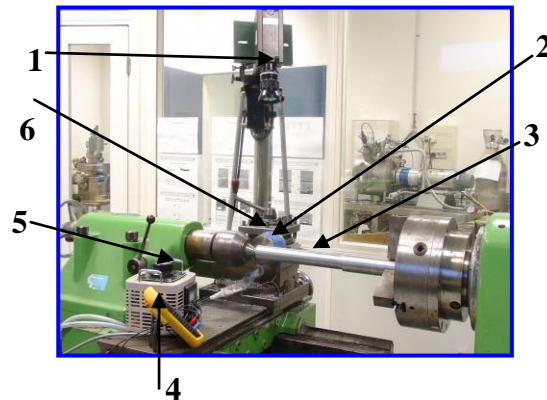
Figure 1 Experimental apparatus
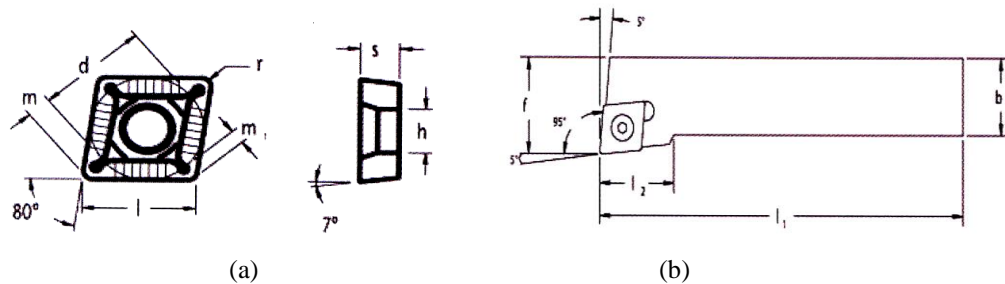
| (a) | (b) |
Figure 2 Forms and dimensions of the carbide insert and tool holder

2.2 Dimensions of inserts, geometry of the active part and body of the cutting tool

The insert is fixed by screws and is positioned in the direction where exercising the cutting efforts (Table 1). The cutting tests were performed without lubrication, with an advance f = 0.125 µm.tr^{-1}, a depth of cut ap = 0.5 mm, cutting speeds Vc = 6, 17, 48, 82 and 136 m.min^{-1}, intensities of magnetic field H = 5.5, 16.5 and 28.5 kA.m^{-1} and a cutting time (Tc), 14 min for each pass. Images of the scanning electron microscopy (SEM) were performed using a JEOL 5600 LV SEM operating at a voltage of 20 kV in secondary electron mode. An infrared thermography camera brand ESCIL operating during cutting operations has permitted determining the temperature between the cutting tool and work-piece (manufactured part).

Dimensions of the insert [mm]	r	d	I	s	h	m	m$_1$
	0,8	9,52	9,57	3,97	4,40	2,20	1,21
Dimensions of the tool holder [mm]	b		L$_1$		L$_2$		
	25		150		25		
Angle of the flank face [°]	5						

Table 1: Dimensions of the insert and tool holder

3. **Results and Discussion**

3.1 Influences of Magnetic Field on the Tool Wear

The cutting edge of the tool, which constitutes the active element by which the deformation work is carried out, is subjected to very severe mechanical and thermal strains, which cause its wear and degradation. This is studied as a function of cutting parameters. Figure 3 illustrates the evolution of wear as a function of the cutting speed when H is fixed (for each curve). Examination of Figure 3a reveals that the weight loss is maximal in the absence of magnetic field and corresponds to 400 µg. The wear is frontal (VB) and reached 0.3 mm. In contrast, the loss decreased down to 300 µg for H = 5.5 KA.m^{-1} (Fig. 3b). When H = 16.5 KA.m^{-1} (Fig. 3c), the weight loss decreased to 100 µg and is far from the value of VB = 0.3 mm (wear criterion NFE66505). Finally, when H = 28.5 KA.m^{-1} (Fig. 3d), the weight loss is about 300 µg. This value is due to the cutting speed, which increases the tool wear. This wear, which is of mechanical nature, is due to permanent or cyclical stresses as well as to the action of friction. In this case, their severity is accentuated by significant thermal effects, which tend to degrade the resistance qualities of the cutting material.
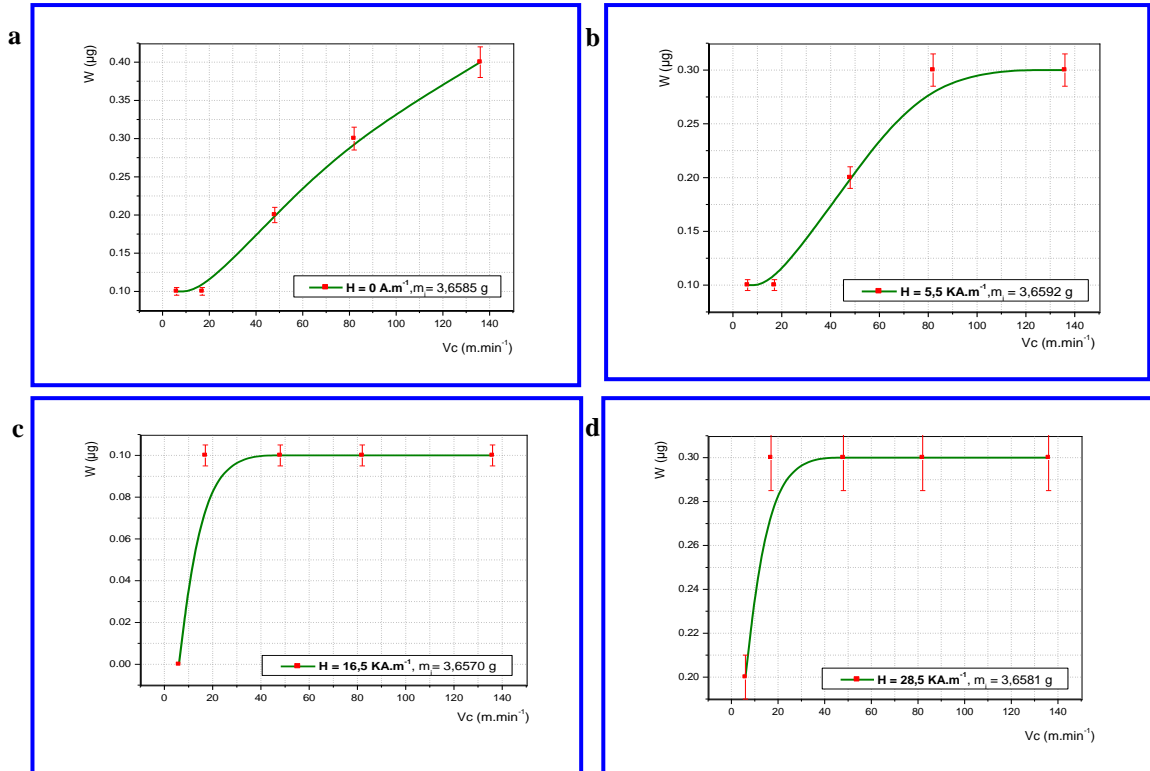
Figure 3 Evolution of mass loss (wear) depending on the cutting speed: (a) $H = 0$ A.m^{-1}, (b) $H = 5.5$ KA.m^{-1}, (c) $H = 16.5$ KA.m^{-1} and (d) $H = 28.5$ KA.m^{-1}

3.2 Influence of the Magnetic Field on the Roughness of the Cutting Edge of the Cutting Tool

Analysis by SEM does not enable to assess the profile of the cutting surface. It is therefore necessary to complete the observations of the attack surface of the cutting tool by analyzing the state of the surface after manufacturing with and without magnetic field. Using an interferential microscope Taly Surf ICC, we measured the morphology, roughness and cutting surface profile (contact surface). Figure 4 shows the morphology and cutting surface profile. The section of the chip removed during manufacturing without a magnetic field is much larger than that in the presence of a magnetic field. The shallow depth of the profile in magnetized contact confirms the small crater wear compared to that obtained without magnetic field. Examination of Figure 4a proves that the roughness of the cutting surface is maximal in the absence of a magnetic field and is equal to 1.53 µm, and the depth of the crater wear is equal to 31.1µm due to the specific pressure of chips on the attack face of the cutting edge. Contrary, in the presence of the magnetic field the state of surface decreases up

to 0.305μm and the depth of the crater wear is reduced to 2.22μm. Applying the magnetic field around the contact of manufacturing slightly decreases the crater wear of the cutting tool and improves the state of the surface of the cutting edge. These effects are due to the hardening of the contact surfaces by the increase of dislocations due to the magnetic field [7] and the magnetization of the contact surfaces. The previous Figure 4 shows the state of surface with and without the magnetic field. In the absence of the magnetic field, the delaminated particles of the cutting surface generates a very rough surface (H = 0 Am^{-1}). Application of the magnetic field demonstrates that there is no formation of the white layer (H= 5.5, 16.5 and 28.5 KA.m^{-1}) and that the cutting surface remains always smooth .The movement of dislocations toward the interface [7] generates a hardening of the contact surface (tool-piece) and the weakening of the contact junctions and increases the transfer of particles of the chip by adherence at the contact level. These effects allow having a slight softening of wear in the presence of the magnetic field, which slightly reduces the wear of the cutting tool, and modifies the mode of wear and improves the state of surface of the cutting edge in the magnetized contact.
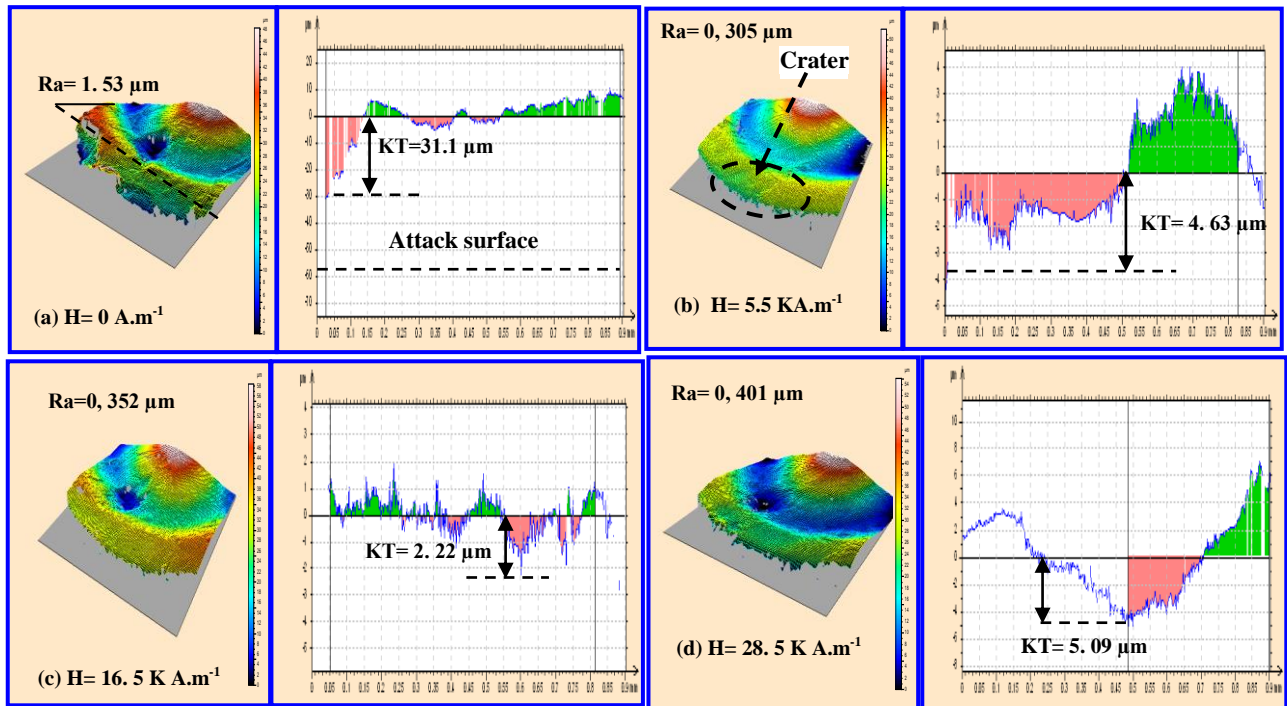
Figure 4 Morphology and profile of the wear of the cutting tool

3.3 Influence of the Magnetic Field on the Morphology of the Surface of the Cutting Edge

Examination of figure 5 allows to identify the wear patterns developed on the tool. A first area called the running in of the cutting edge is characterized by flank wear. Then, a crater wear is

recorded on the bevel of this edge, and then appears on the same edge a wear by plastic deformation. In practical terms, the frontal wear is the most important, because it conditions simultaneously the surface of the manufactured part (work piece) and the dimensional precision (Fig. 5a). Figures 5a and 5b show that crater wear appears much sooner when the cutting speed increases. This phenomenon is particularly related to the cutting increased temperature which favors wear by diffusion. Figure 5d shows the presence of chips that have been adhered on the cutting surface. Indeed, when the chip slides over the clearance face (rake face) of the cutting tool, an intense friction engenders the increase of the localized temperature of mergers and micro-weldings. This may result in bonding of certain particles of the chip on the rake face of the cutting tool [13, 14, 15]. The damage to this later is low in the presence of a magnetic field (Figs. 5b, 5c and 5d) (noting that this later causes only a low wear of crater type). However, in the absence of magnetic field, the crater wear becomes significant, when a frontal wear and a plastic deformation wear appear on the rounding of the cutting edge.
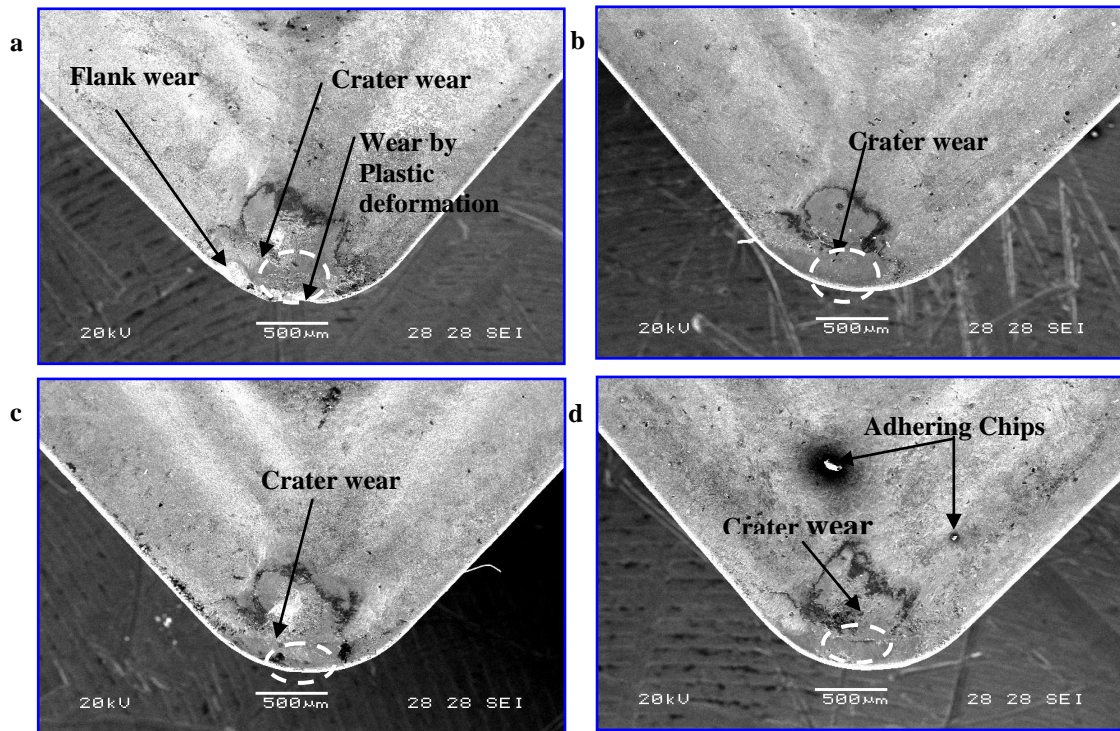
Figure 5 SEM observations of the tip rounding of the tool: ap = 0.5 mm, f = 0.125 mm.rev^{-1}, lc = 300 mm, (a) H = 0 A.m^{-1}, (b) H = 5.5 KA.m^{-1},(c) H = 16.5 KA.m^{-1} and (d) H = 28.5 KA.m^{-1}

3.4 Influence of Magnetic Field on the Cutting Temperature

The average temperature T_m of the cutting tool obtained using an infrared thermographic camera is usually measured on the upper surface of the chip (the temperature is not that of the interface because the contact tool-piece is inaccessible). Infrared imagery of Figure 6 shows

the distribution of thermal field in the cutting area around the cutting tool and chip. When we increase the applied parameters (Vc and H), the temperature at the interface increases. This elevation is not only due to the raise of cutting speed, but also to the effects of magnetization and Joule effect, created by the currents Foucault generated by the variable magnetic field in the rotating part [8,11]
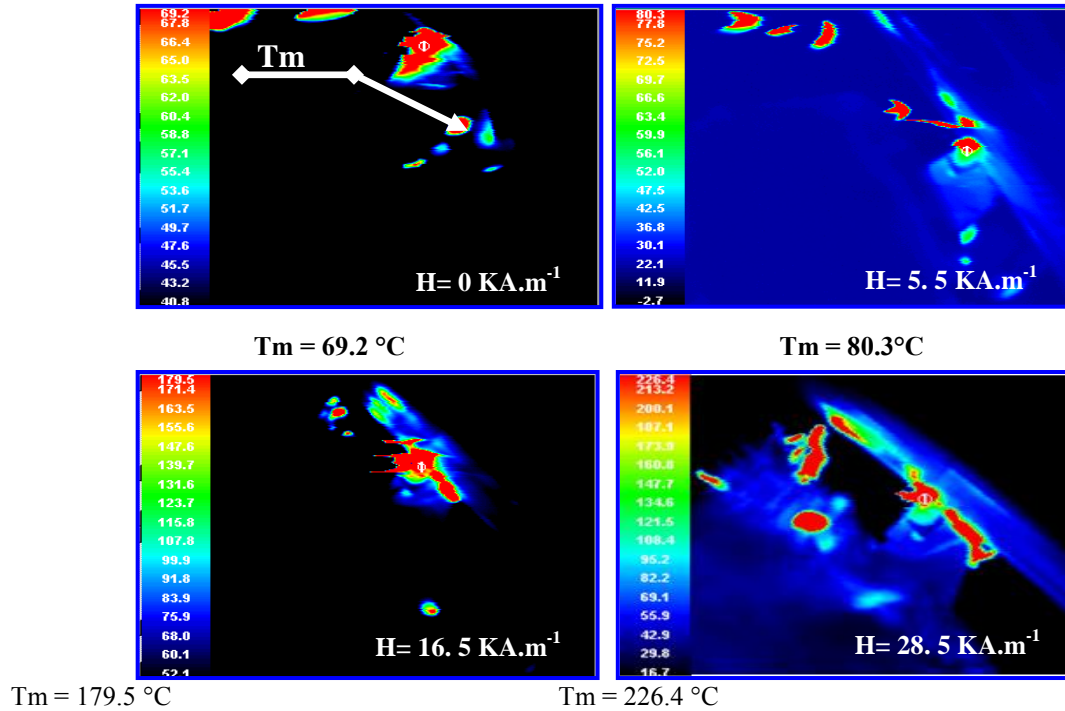
Figure 6 Distribution temperature at the interface along cutting: Vc = 136 m.min^{-1}

4. Conclusion

This paper has enabled us to provide responses to certain questions related to manufacturing and the wear of a cutting tool in a magnetic field. Experimentally, after a comparison with results obtained in manufacturing, it appears clearly that the magnetic assistance has several impacts on manufacturing and the morphology of cutting. Thus, we can notice its influence on:

1. The improvement of the cutting surface roughness at the interface and the decrease of the depth of the crater wear KT.
2. Reducing the wear of cutting tools.
3. Changing patterns of the wear of cutting tools.
4. The increase of temperature that contributes to changing the profile type of the manufacturing chip.

It stand out therefore that applying a magnetic field to cutting tools appears as simple, effective and inexpensive solution to increase their shelf life and thereby contribute to the optimization of the production tool.

4. References

[1] Padilla, P (1986), *Mechanical production*, pp.136-145. Ed. Dunod Paris ISBN 2-04-016467-7.

[2] Al'shits, V.L (1990), pp. 597, Sov. Phys. Crystallogr 35 ISSN 0038-5638.

[3] Bagachi, P.K (1970), *Effect of magnétisation on the wear characteristics of cutting tools*, pp. 264-269. Indian J. Technology ISSN 0019-5669.

[4] Bagachi, P.K (1971), *Mechanisms of cutting tool wear in the presence of a magnetic field*, pp.165-168. Indian J. Technology ISSN 0019-5669.

[5] Muju, M.K (1977), *Effect of magnetic field on wear*, ASME Publication 75-PTG-5.

[6] Muju, M.K (1977), *Effect of magnetic field on wear model of adhesive wear in the presence of a magnetic field-I*, *Wear* 41, pp. 103-116.

[7] Muju, MK (1980), Effect of a magnetic field on diffusive wear of cutting tools, pp. 49-58. Wear 58 ISSN 0043-1648.

[8] ElMansori, M (2004), *Improving surface wearing of tools by magnetization when cutting dry*, pp. 566-571. Surface & Coatings Technology 188–189 ISSN 0294-8972.

[9] ElMansori, M (2006), *Magnetic Field Effects in machining Processes and on manufactured part mechanical characteristics*, pp. 136-145. Journal of Manufacturing Science and Engineering 128 ISSN 1087-1357.

[10] ElMansori, M (2003), *Reduction of tool wear in metal cutting using external electromotive*, pp. 472-477. Surface and Coatings Technology 163-164 ISSN 0294-8972.

[11] Bataineh, O (2003), *Effect of pulsed magnetic treatment on drill wear*, pp.190-196. Journal of Materials Processing Technology 134 ISSN 0294-0136.

[12] International Norm ISO 9001-2000 (2000), (F), *Manufacturing and distribution of precision cutting tools*. pp. 35, 36 and 126, Turning. Ref. 359 CATF.V1. www.stellram.com.

[13] Caubet, JJ (1964), *Theory and practical industrial of friction*, pp. 94-99. Dunod-Technip, Paris.

[14] Zaidi, H (2007), *Magnetotribology of ferromagnetic/ferromagnetic sliding couple*, pp.1518-1526. Wear 263 ISSN 0043-1648

[15] Chin, KJ (2001), *Tribological behavior and surface analysis of magnetized sliding contact XC48 steel / XC48 steel*, pp. 470-476. Wear 250 ISSN 0043-1648.

Structural And Optical Properties of Tin Oxide Thin Films Prepared by Spray Ultrasonic Technique

Hamza Bendjedidi , Abdallah Attaf, Souhir Semmari, Salah Yahiaoui, Khira Ben Nacer, H.Nadjette and Hannane Saidi

Laboratoire de Physique des Couches Minces et Applications, Université de Biskra, BP 145 RP, 07000 Biskra, Algérie
E-mail : ab_attaf@univ-biskra.dz

ABSTRACT :

Transparent conducting SnO_2 films were fabricated by employing an inexpensive, simplified spray ultrasonic technique using an ultrasonic generator at deferent substrate's temperatures (300, 350, 400, 450 °C). The structural studies reveal that the SnO_2 films are polycrystalline (at 350, 400, and 450 °C) with preferential orientation along the (200) and (101) plane, and amorphous at 300 °C. The crystallite size of the films was found to be in the range of 20-50 nm. The optical transmittance in the visible range and the optical band gap are 75% and 3.9 eV respectively. The films thicknesses were varied between 466 nm and 1840 nm. This simplified Ultrasonic spray technique may be considered as a promising alternative to conventional spray for the massive production of economic SnO_2 films for solar cells, sensors and opto-electronic applications.

KEYWORDS : tin oxide, thin films, spray ultrasonic, structural properties, optical properties.

1. Introduction

Metal oxide semiconductors such as SnO_2, In_2O_3, CdO and ZnO have been used in the opto-electronic devices mostly for flat panel displays, photovoltaic devices, gas sensors and heat reflecting mirrors because of their suitable band gaps of 2.8–4.2eV, n-type conductivity and other useful characteristics [1]. Tin oxide thin films are transparent and conductive, and are particularly useful when good transparency in the visible range and good electrical conductivity are simultaneously required [2]. SnO_2 films have high chemical stability and physical strength. SnO_2 films can also be used in energy conversion systems. This material could find application in semiconductor electrode for hydrogen based photo-electrochemical conversion and solar cells. SnO_2 thin film can be prepared by a number of methods, such as CVD [3- 4], sputtering [5-6], spray pyrolysis [7-8], plasma and sol–gel methods [9], each of which had advantages and disadvantages. The preparation of SnO_2 films have been well established by spray

ultrasonic technique. This technique is simple, inexpensive and permits easy deposition in the atmospheric condition. The optical and structural properties of spray deposited SnO_2 films have also been well studied [10-11], due to the greater interest of SnO_2 thin films.

The main accomplishment of this work is to characterize the SnO_2 films (structural and optical characterisation) deposited by spray ultrasonic process, the film's properties dependence from the film deposition conditions and substrate temperatures. This is an important parameter for understanding the nature of thin film and its uses for required applications.

2. Experimental Procedure

Tin oxide thin films were prepared by spraying an alcoholic solution contains Tin Chloride Hydrat $SnCl_2$-$2H_2O$ and CH_4O on glass substrates with deferent temperatures using ultrasonic spray process. Substrates were cleaned and degreased in successive

with Acetone, propanol, and distilled water. The films were deposited with a procurser molarity of 0.1 mol/l, and we have varied the temperature from 300 to 450 °C in atmospheric pressure. The films were characterized by means of structural and optical techniques. The films thickness was calculated from the interferences fringes obtained transmittance spectra by the UV–VIS–NIR transmittance. The X ray diffraction studies were carried out using a D8 ADVANCED BRUKER diffractometer with copper anode having a wavelength λ = 1.5418A°, the crystallite size were estimated to study the effect of the temperature. The UV–VIS–NIR tran-smittance measurements were performed PerkinElmer LAMBDA1050 UV/VIS/NIR Spectrometer in the spectral range 300–1500 nm.

3. Results and discussion
3. 1. Structural properties

The X-ray diffraction patterns for SnO_2 films deposited at 300, 350, 400, and 450°C are shown in Fig.1. It can be found that films deposited at 300°C were nearly amorphous whereas for higher temperatures, the amorphous background was dimin-ished and diffraction peak (110) of standard SnO2 powder revealed for all samples as mentioned by other research-ers [12-15]. The While films deposited at higher temperatures exhibit five peaks. Since all peaks are sharp, it is evident that the films deposited at 350, 400 and 450°C are polycrystalline in nature. In all films the half width of the Bragg peaks decreases and displays gradual change in the preferred orientation from (1 0 1) to (2 0 0) plane with increase in the substrate temperature from 350 to 500 °C [16].
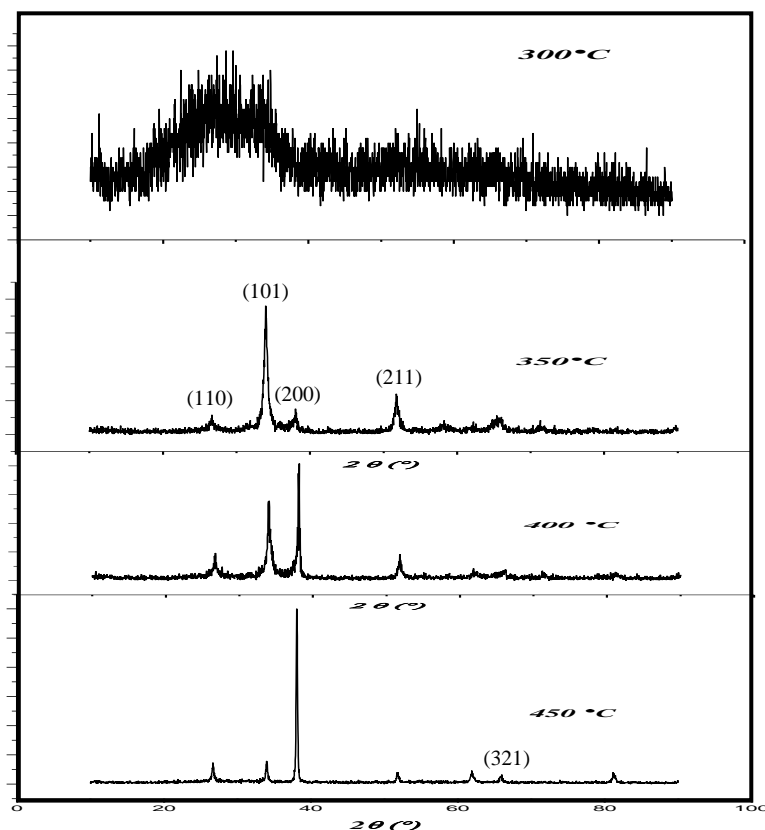
Figure 1: X-ray diffraction pattern of SnO_2 films prepared at various substrate temperatures.

In order to determine the variation of the crystallite size with increasing substrate temperatures the size of the crystallites oriented along (101) plane is calculated using Scherrer's formula [17-18]

$$D = \frac{(0.94 \times \lambda)}{\Delta\theta_{hkl} \times \cos\theta_{hkl}} \tag{1}$$

Where D is the size of cristallite, $\Delta\theta_{hkl}$ the broadening of diffraction line measured at half its maximum intensity in radians and λ is wavelength of X-rays (1.54 A°). The calculated values of crystallite size are given in fig2. It can be seen that substrate temperature has an effective influence on the crystallite size, which increases from 21 to 50 nm. The increase of crystallite size is due to the fact that the substrate temperatures higher than 300°C during deposition are usually relatively high enough to provide sufficient ther-mal energy for recrystallization. Hence, crystallization process improved and the smaller crystallites agglomer-ated with increasing substrate temperature to cause a change in crystallite size distribution towards larger crystallites. This result is in agreement with those of other researchers [16, 19-20].
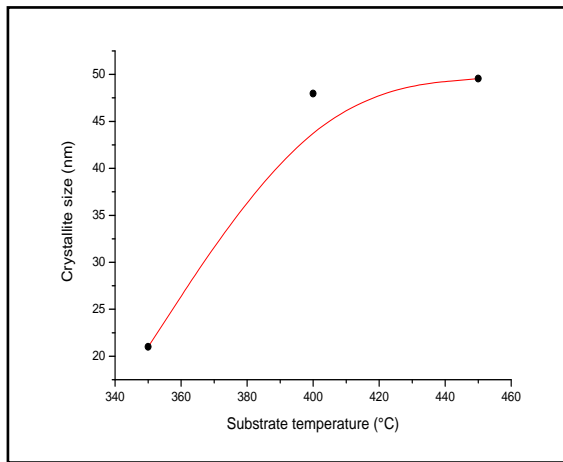
Figure 2: Dependence of the crystallite size vs. substrate temperatures

3. 2. Optical properties:

The optical transmission spectrum for SnO2 films deposited at 300, 350, 400, and 450 °C are shown in Fig. 2. Shows the variation of transmittance with respect to wavelength of SnO_2 thin films deposited at various substrate temperatures. The average transmission in the visible region has been found to be ranging from 60% to 75% depending upon the substrate temperature. An increase in transmission is observed with increase in temperature. At lower temperatures, i.e. at 350 °C, relatively lower transmission is due to the formation of milky films and that is because of incomplete decomposition of the sprayed droplets. In general, in the visible region of the spectrum, the transmission is high (high enough to observe interference fringes). It is due to the fact that the reflectivity is low and there is no (or less) absorption due to transfer of electrons from the valence band to the conduction band owing to optical interference effects, it is possible to maximize the transmission of thin film at particular region of wavelengths[20-21].
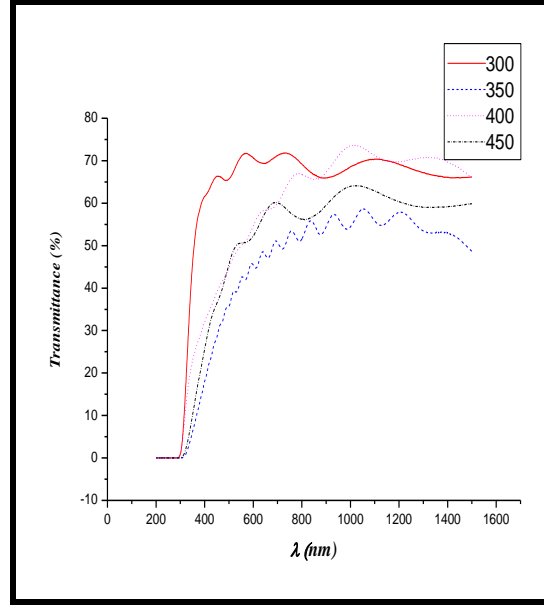
Figure 3: the transmittance spectra of SnO_2 films prepared at various substrate temperatures.

We have used the pattern of transmission in the transparent region with successive minima and maxima to evaluate the thickness of the SnO_2 films. The thickness d of the films can be calculated from the following equations [21-22]:

$$N1,2 = 2S.\frac{(T_M - T_m)}{T_M.T_m} + \frac{S^2 + 1}{2} \qquad (2)$$

$$n_{1,2} = \left(N_{1,2} + (N_{1,2}^2 - S^2)^{1/2}\right)^{1/2} \qquad \begin{matrix}(3)\\(4)\end{matrix}$$

$$d = \frac{\lambda_1\lambda_2}{2(n_1\lambda_2 - n_2\lambda_1)}$$

Where d is the film's thikness, T_M and T_m are maxima and minima transmittance respectively, n, s are the film and glass refractive indice respectively.

The films optical band gap has been determined on the basis of UV–VIS transmission measurements. The band gap (Eg) is determined by extrapolating the straight line portion of the plot to the energy axis. The intercept on energy axis gives the value of band gap energy Eg for all the samples. The obtained optical band gap values lie in the range 3.92–3.98 eV.

In fig.4 we have reported the variation of film thickness as function of temperature.
It shows that the film thickness decreases almost linearly with substrate temperature, owing to increased evaporation rate of the initial product with rise in substrate temperature leading to the diminished mass transport towards the substrates [16].
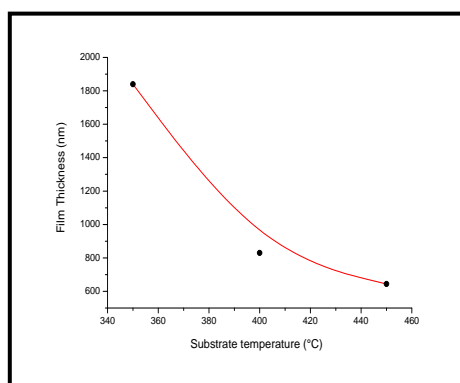
Figure 4: Dependence of thickness vs. substrate temperatures

the variation of band gap Eg as the function of substrat temperature is shown in fig 5.
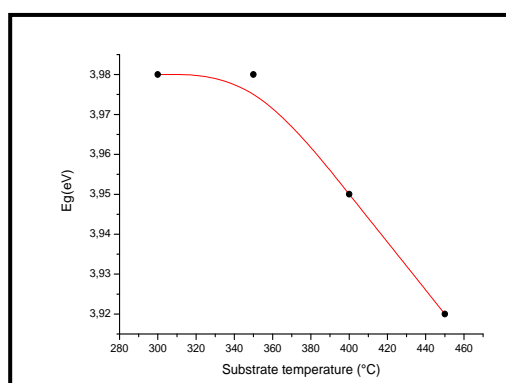
Figure 5: Dependence of Eg vs. substrate temperatures

The obtained energy gap values are in good agreement with other literature reports [23-25]. It is found that the band gap energy decreases with increasing substrate temperature. The values of band gap lie in the range of 3.92–3.98eV taking into account the experimental errors; these values of band gap indicate that the SnO_2 films had direct band gap energy [26]. This result can be attributed to the decrease of grain boundaries as scattering centers. In fact, the increase of substrate temperature improves crystallinity and increases average crystallite size which results in decreasing grain boundaries; therefore band gap energy decreases [14].

4. Conclusion

Highly transparent films of Tin oxide have been prepared by an ultrasonic spray CVD process. Films deposited at temperature higher than 350°C and having thicknesses greater than 530 nm are identified as polycrystalline Tin Oxide. The increase of temperature to the range 350–450°C improves the films crystallinity and enhances the grain size. The transmission in the visible and infrared regions of deposited films was found to be weakly affected by temperature deposition between 300 and 450°C, the films transmittance exceeds 75%. The optical band gap values ranges: 3.92–3.98 eV for films deposited at different temperatures.

5. References :

[1] C.H. Yang, S.C. Lee, and S.C. Chen; *Mater. Sci. Eng*. **B 129,** (2006), 154.
[2] W. Fliegel, G.Behr, J. Werner, G. Krabbes; *Sens. Actuators* **B 18/19,** (1994), 474.
[3] G. Sanon, A. Rajrup; *Thin Solid Films* **190,** (1990), 287.
[4] Y. Liang, H. Zheng, B. Fang, Materials Letters108(2013)235–238
[5] C. Agashe, S.S. Major; *Mater. Sci*. **31,** (1996), 2965.

[6] T. Jäger, B. Bissig, M. Döbeli, A.N. Tiwari, Y.E. Romanyuk, Thin Solid Films 553 (2014) 21–25.

 [7] I.S. Mulla, H.S. Soni, V.J. Rao, A.P.B. Sinha; *J. Mater. Sci*. **21,** (1986), 1280.

[8] B. Barış, Physica B 438(2014)53–59.

[9] Rani S., Puri N.K., Roy S.C., Bhatnagar M.C., Kanjilal D.; *Nucl. Instrum. Methods Phys. Res* **B 266** (2008) 1987.

[10] S. Rani, S.C. Roy, N. Karar, M.C. Bhatnagar; *Solid State Commun* **141** (2007) 214.

[11] N. Bhardwaj, S. Kuriakose, S. Mohapatra, Journal of Alloys and Compounds 592 (2014) 238–243

[12] R. Ferro, J.A. Rodriguez, *Mater. Sci. Eng*. **B87** (2001), 83.

[13] H. Sefardjella, B.Boudjema, A.Kabir, G.Schmerber, Journal of Physicsand Chemistry of Solids 74(2013)1686–1689.

[14] M. Zadsar, H.RezaFallah, M.HajiMahmoodzadeh, A.Hassanzadeh, M.G.Varnamkhasti, Materials Science in Semiconductor Processing 15 (2012) 432–437.

[15] D. Miao, Q. Zhao, Sh. Wu, Zh. Wang, X. Zhang, X. Zhao, Journal of Non-Crystalline Solids 356 (2010) 2557–2561.

[16] P.S. Patil , S.B. Sadale, S.H. Mujawar, P.S. Shinde, P.S. Chigare, Applied Surface Science, 253 (2007) 8560-8567.

[17] B.D. Cullity, Elements of X-ray Diffraction, A. W. Pub. Comp. Inc, (1978), p. 99–106.

[18] M.R. Yang, S.Y. Chu, R.C. Chang, Sensors and Actuators B 122 (2007) 269–273.

[19] R.R. Kasar, N.G. Deshpande, Y.G. Gudage, J.C. Vyas, Ramphal Sharma, Physica B 403 (2008) 3724–3729.

[20] V.M. Nikale, N.S. Gaikwad, K.Y. Rajpure, C.H. Bhosale, J. Mater. Chem. Phys. 78 (2003) 363.

[21] O.S. Heavens, G. Hass, R.E. Thun, Physics of Thin Films, Academic Press, New York, (1964), p. 203.

[22] J.C. Manifacier, J. Gasiot, J.P. Fillard, Journal of Physics E 9 (1976) 1002–1004.

[23] K.L. Chopra, S. Major, D.K. Pandya, Thin Solid Films 102 (1983) 15.

[24] Ian Y.Y. Bu, Ceramics International 40 (2014) 3445–3451

[25] E. Benamara, M. Rami, C. Messaoudi, D. Sayah, A. Ennaoui, Solar Energy Materials and Solar Cells 56 (1999) 125*D*139.

[26] C.Wang, Journal of Photo-chemistry and Photobiology 168 (2004) 47–52.

Molarity Effect on The Optical And Structural Properties of Sprayed Indium Oxide Thin Films

Hanane SAIDI, Abdallah ATTAF, Mabrouka BOUBECHE, Aicha CHENNOUFI, Malika NOUADJI, Souhir SEMARI and Hamza BENDJEDIDI

Laboratoire des Matériaux Semi-conducteurs et Métalliques, Université de Biskra, BP 145 RP, 07000 Biskra, Algérie
E-mail: Saidih77@yahoo.fr

Abstract: Transparent conductive Indium oxide (In_2O_3) thin films were deposited on glass substrates by ultrasonic spray technique. The study was in one series by varying the molarity from 0,05 to 0,3 mol/l at substrate temperature 400°C. To investigate the influence of precursor molarity on structural, optical and electrical properties of indium oxide thin films, several characterizations were carried out such as: XRD to determine the grains size and the stress, SEM for microstructural study and to determine films thickness, EDS to assure chemical composition of the films and UV-Vis-Nir Spectroscopy for optical studies like the absorption coefficient, the optical gap, the disorder and the refraction index. The results of both characterizations are presented in this report.

Keywords*: Indium* oxide, TCO, Ultrasonic Spray, optical and structural properties.

1. Introduction:

Indium oxide belong among transparent conducting oxides are widely used in various applications thanks to their low resistivity, high optical transparency and wide band gap. These applications include using in solar applications the transparent electrodes in various optoelectronic devices [1], liquid crystal displays [2], light-emitting diodes [3], the barrier layers in tunnel junctions [4], the active layers of gas sensors [5] or the material for ultraviolet lasers [6]. Therefore, there have been a lot of works on investigations of their growth conditions and studying their properties in dependence on the synthesis methods ranging from such as evaporation, sputtering, chemical pyrolysis to metal organic chemical vapour deposition [6–8], thermal oxidation [9] pulsed laser deposition (PLD) [10–12], atomic-layer epitaxial growth [13], spin coating [14] and the sol–gel method [15]. In_2O_3 thin films have a good adherence to the substrate surface and high chemical inertness [16]. The material properties, described in the literature often differ considerably from each other. One important reason for this is that the preparation conditions aredifferent and consequently the oxidation state of the samples is different.In_2O_3 can appear in two stable modifications as body centred (bcc) cubic (a=10.118 Å) and rhombohedral (rh) (a=5.478 Å and c=14.51 Å) (crystallographic data are taken from [17]). They can be stabilized by choosing appropriate deposition conditions or synthesis methods [18-20]. The band gap of both is currently a subject of discussion and it seems to be that this material

exhibits indirect transitions [21]. The values for the indirect and direct gaps of the cubic phase are between 2.1 to 3.1 eV and between 3.1 to 3.7 eV [22-24]. In the case of the rhombohedral In_2O_3 phase the indirect gap was estimated to be in the range from 3.0 to 3.3 eV, whereas the direct gap can be expected 3.3 and 3.4 eV [23, 24].

2. Experimental Procedure :

Indium oxide thin films were prepared by spraying an alcoholic solution containing indium chloride $InCl_3$ on glass substrates using ultrasonic spray process, substrates were degreased in successive rinses with acetone, ethanol, and distilled water for 5 min. the films were deposited in 400°C, and we have varied the precursor molarity from 0,05 to 0,3 mol/l in atmospheric pressure.

The films were characterized by means of morphological, structural, optical and electrical methods. The surface morphology of the films was observed using a JEOL, model JSM 6301F Scanning Microscopy by field effect and the films thickness were calculated from the obtained micrographs. The X ray diffraction studies were carried out using a D8 ADVANCED BRUKER diffractometerwith copper anode having a wavelength $\lambda = 1.5418A°$, the crystallite size were estimated to study the effect of the molarity. The UV−VIS−NIR transmittance measurements were performed PerkinElmer LAMBDA1050 UV/VIS/NIR Spectrometer in the spectral range 300−1500 nm. The electrical conductivity of the films was determined by two-point probe method at the temperature 25°C. The type of the semiconductor was determined from Hall measurements at room temperature.

3. Results and discussion:

3.1. Structural properties of In_2O_3 thin films:

Different micrographs obtained by SEM are presented in Figure 1
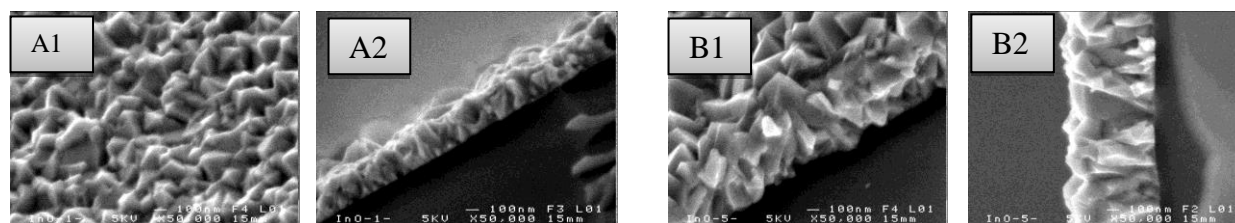
Figure1: micrographs SEM, A: for 0,05 mol/l B: for 0,1 mol/l

The growth rates were estimated using the figures 1 and figure 2 presents its variation on function of molarity

,,
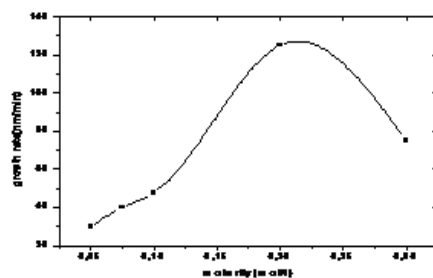
Figure 2: Molarity influence in the growth rate of In$_2$O$_3$ thin films.

As we can show an augmentation in growth rate until 125 nm/min (saturation of substrate).Then, it starts in decrement to 75, 2 nm/min.

Figure 3 shows EDS analysis results that assure the chemical composition of In$_2$O$_3$ films, the atomic and weight percentages of the element present in the films, our films are composited from O and In atoms in addition to *Cl* whish come from the precursor, Si and Fe from the substrate, N from the air. In atomic percentage augments with the increment of molarity.
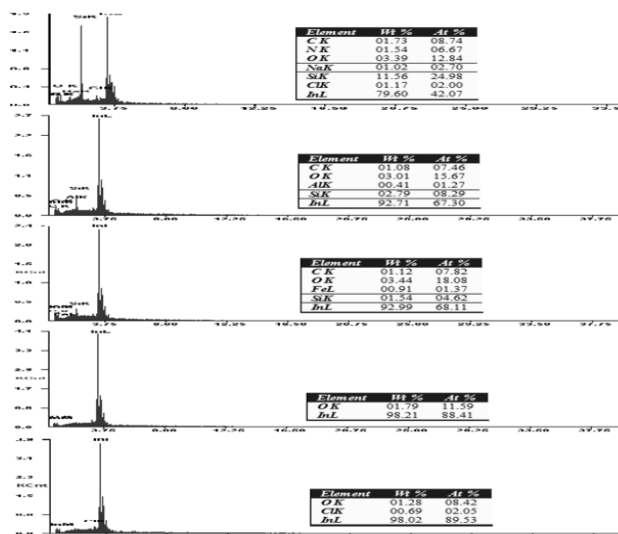
Figure 3: EDS analysis results

The X ray diffraction spectra are presented in Figure 4
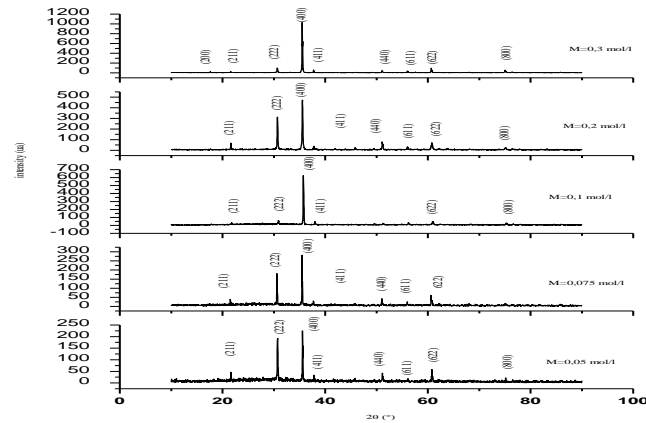
Figure 4: Evolution of the spectra of X-rays diffraction of In$_2$O$_3$ thin films for all molarities

The important orientation is along the plan (400) has intensive important peak in all the films that increases according to the increment of molarity by shifting in the diffraction's angle and its maximum is around the angle 2θ=37, 99° for m=0,3mol/l. The second important orientation (222) has unsteady intensities, its maxima is around the angle 2θ=30, 7° for m=0, 2 (mol/l), and the others have small values. In addition to many plan with weak intensities. The mean crystallite size *D* was calculated from the (400) diffraction peak using Sheerer's formula:

$$D = \frac{(0,94 \times \lambda)}{\Delta\theta_{hkl} \times \cos\theta_{hkl}} \qquad (1)$$

Its variation with molarity is illustrated in figure 5, its values is between 47 and 74 nm it is obtained for 0,075mol/l.
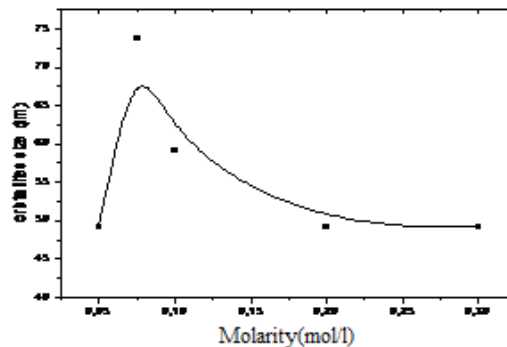
Figure 5: Molarity effect on the grains size

3.2 Optical properties:

Figure 7 shows the optical transmittance curves as a function of the wavelength for the In_2O_3 films deposited at 400°C with different molarities. The films deposited by 0,1 mol/l exhibit a high optical transmittance (greater than 80%) in the visible region and the infrared one. The average optical transmittance increase with the molarity until 0,1 mol/l, then it in decrement. Furthermore, the absorption edge shifts towards shorter wavelength, suggesting a widening of the energy band-gap with increasing of molarity from 0,05 to 0,1 mol/l.
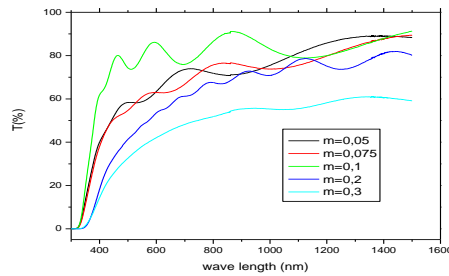
Figure 7: Molarity effect in the transmittance of In_2O_3 thin films.

The optical band gap (Eg) of the films was determined from the optical transmittance data using Tauc's relation [25]:

$$\alpha(h\upsilon) = A\ (h\upsilon - E_{00})^n \qquad (2)$$

Where n depend on the kind of optical transition that prevails. Here $n = 1/2$, as In_2O_3 films are directly allowed n-type degenerate semiconductors. The optical bang gap is obtained by plotting $(\alpha h\upsilon)^2$ versus the photon energy ($h\upsilon$) and by extrapolating of the linear region of the plots to zero absorption ($(\alpha h\upsilon)^2 = 0$) (figure8). It increased from 3,646 to 3,938 eV
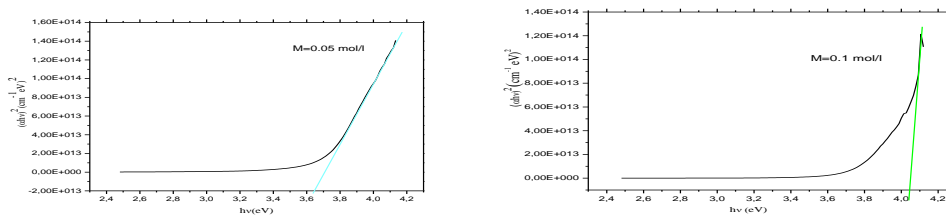
Figure 8: **variations of $(\alpha h\upsilon)^2$ on function of hv.**
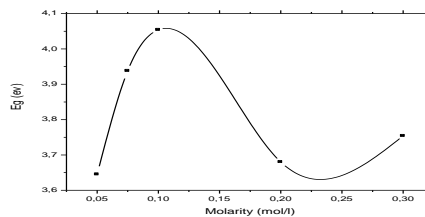
Figure 9: **Molarity effect on E_g values**

It is also assumed that the absorption coefficient near the band edge shows an exponential dependence on photon energy and this dependence is given as follows [26],

$$\alpha = \alpha_0 \exp\frac{h\upsilon}{E_u} \qquad (3)$$

Where α_0 is a constant and E_{00} is Urbach energy interpreted as the width of the tails of localized states, associated with the amorphous state, in the forbidden gap.

The $ln(\alpha)$ vs. photon energy plots for In$_2$O$_3$ thin films are shown in Figure 10 The values of E_{00} obtained from this figure are plotted on function of molarity in figure 11. It is believed that the exponential dependence of a on photon energy may arise from random fluctuations of the internal fields associated with the structural disorder in many materials. We find that E$_{00}$ increases with the increment of molarity and its values between 0.280 and 0.5 eV.
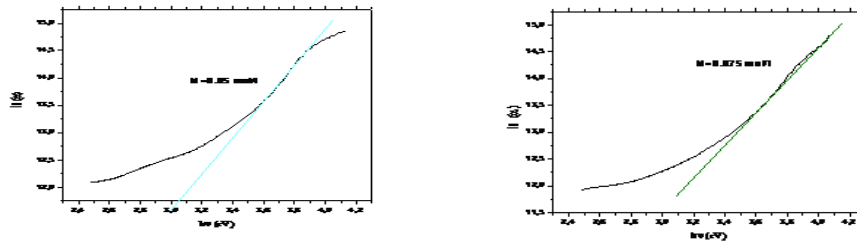
Figure 10: Variations of Ln (α) on function of hν
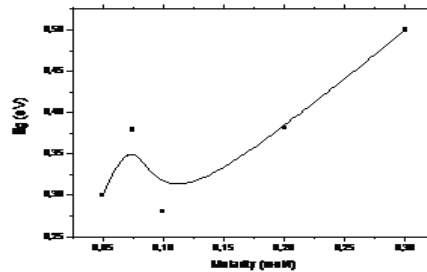
Figure 11: Molarity effect in the disorder E$_{00}$

The transmission curves present a series of maximum (noted T$_M$) and minimum (Tm) of the envelope of interference, are now considered to be continuous functions of λ. For any λ, T$_M$ has a correspondent value Tm .The refractive index is calculated by:

$$n = \left[N + (N^2 - s^2)^{1/2} \right]^{1/2} \qquad (4)$$

Where N is defined as

$$N = \frac{2s(T_M - T_m)}{T_M T_m} + \frac{(s^2 + 1)}{2} \qquad (5)$$

Following this method, we have derived values for the refractive index n which have been found to be in the range 1,45 – 1,46.

4. Conclusion:

The effect of the precursor's molarity on the crystalline state, composition, surface morphology, optical properties and electrical conductivity of indium oxide films grown by ultrasonic spray technique are investigated.. The morphological studies using SEM, as showed that the films are rough with different grains sizes and the thickness was around 300 to 1250 nm. X-ray diffraction analysis reveals a polycrystalline nature (cubic phase) for all the films those are deposited at Ts = 400, it is observed that the grains size is varied between ~ 49.174 and 73.736 nm. EDS results gives an increase in indium weight percentage with increase in molarity.

The optical characterization on the range of 300 nm with 1500 nm showed that our films are transparent with a value about 50 % to 85 %. Also, interference fringes are present in the area of strong transparency indicating that our films have rough surfaces. The fall of transmittance between 300 nm and 400 nm shows that the films absorb the light ultra violet, there is a strong transmittance in the visible range and near infra-red, this properties, leaves some suggest applications of these films in the bread of the Windows, as protective against the sunbeams, the optical gap, we found that it is varied between 3.646 eV and 4.046 eV, and the values found of disorder are between 0.28 eV and 0.50 eV.

Reference:

[1] K. Hara, T. Horiguchi, T. Kinoshita, K.Sayama, H. Sogihara, H. Arakawa, Sol.Energy Mater. Sol Cells 64, 115(2000).
[2] C. Falcony, J. R. Kirtley, D. J. Dimaria, T. P.Ma, T. C. Chen, J. Appl. Phys. 58 (1985)3556.
[3] J. Lao, D. Huang Wang, Ren. Zhifeng, Adv.Mater. 16 (2004) 65.
[4] J. Xu, Y. Chen, J. Shen. Mater, Lett, (2008), 1363.
[5] M. Ali , Ch. Y. Wang, C. C. Röhlig, V.Cimalla, Th. Stauden, O. Ambacher, Sens.Actuator B (2008) 467–472.
[6] P. Malar, B. CH. Mohanty, A.K. Balamurugan, S. Rajagopalan, A. K. Tyagi, S. Kasiviswanathan, Surf Interface Anal 37 (2005), 281.
[7] D. Beena, K. J. Lethy. R. Vinodkumar . V. P. mahadevan, V. Ganesan, D. M. Phase, S. K. Sudheer, Applied Surface Science 255 (2009), 8334.
[8] G.Korotcenkov, V. Bridzari, M. Ivanov, A. CerneavschI, J. Rodriguez, A. Cirera, A. Cornet. J. Morante, Thin Solid Films 479 (2005), 38.
[9] V.D. Das, S. Kirupavathy, L. Damodare, N. Lakshminarayan, J. Appl. Phys. 79 (1996)8521.
[10] Y. Yamada, N. Suzuki, T. Makino, T. Yoshida, J. Vac. Sci. Technol. A18 (2000) 83.
[11] D. Zhang, C. Li, S. Han, X. Liu, T. Tang, W. Jin, C. Zhou, Appl. Phys. Lett. 82 (2003)112.

[12] R.K. Gupta, K. Ghosh, S.R. Mishra, P.K. Kahol, J. Optoelectron. Adv. Mater. 9 (2007)2211.

[13] T. Asikainen, M. Ritala, W.-M. Li, R. Lappalainen, M. Leskel ä, Appl. Surf.Sci.112(1997) 231.

[14] A. Gurlo, M. Ivanovskaya, A. Pfau, U. Weimar, W. Göpel, Thin Solid Films 307(1997) 288.

[15] S. Naseem, I.A. Rauf, K. Hussain, Thin Solid Films 156 (1988) 161.

[16] P. Prathap, G. Gowri Devi, Y.P.V. Subbaiah, K.T. Ramakrishna Reddy, V. Ganesan, Curr. Appl. Phys. 8 (2008) 120.

[17] ICDD PDF-2 Data base, JCPDS-Int. Center for Diffraction Data, Pensylvania, 1994.

[18] Ch.Y. Wang, V. Cimalla, H. Romanus, Th. Kups, G. Ecke, Th. Stauden, M. Ali, V. Lebedev, J. Pezoldt, O. Ambacher, Appl. Phys. Lett. 89 (2006) 011904.

[19] Ch.Y. Wang, Y. Dai, J. Pezoldt, B. Lu, Th. Kups, V. Cimalla, O. Ambacher, Cryst. Growth & Design 8 (2008) 1257.

[20] B. Yaglioglu, H.-Y.Yeom, D. Paine, Appl. Phys. Lett.86 (2005) 261908.

[21] R.L. Weiher, R.P. Ley, J. Appl. Phys. 37 (1966) 299.

[22] S.Zh. Karazhanov, P. Ravindram, P. Vajeeston, A. Ulyashin, T.G. Finstand, H.Fjellvag, Phys. Rev. B 76 (2007) 075129.

[23] F. Fuchs, F. Bechstedt, Phys. Rev. B 77 (2008)155107.

[24] P.D.C. King, T.D. Veal, F. Fuchs, Ch.Y. Wang, D.J. Payne, A. Bourlange, H. Zhang, G.R. Bell, V. Cimalla, O. Ambacher, R.G. Engdell, F. Bechstedt, C.F. McConville, Phys.Rev. B 79 (2009) 205211.

[25] J. Tauc, Amorphous and Liquid Semiconductors, Plenum Press, New York, 1974.

[26] F. Urbach, PhysRev. **92**, 1324 (1953).

Calibration of Moisture Sensor for the Monitoring of Temperature-Moisture Regime in Volcanic Tuffs (Natural Rock Dwellings) in BrhlovceVillage (Slovakia)

Vlastimil Boháč [1], Viliam Vretenár [1], Danica Fidríková [1], Lenka Kralovičová [2], Tatiana Durmeková [2], Ján Vlčko [2]

[1] Institute of Physics, Slovak Academy of Sciences, Dúbravská cesta 9, 84511 Bratislava, Slovakia
[2] Department of Engineering Geology, Faculty of Natural Sciences, Comenius University in Bratislava, Mlynská dolina, 842 15 Bratislava, Slovakia
*Corresponding author's Tel: +421-2-5941-0577, E-mail: vlastimil.bohac@savba.sk

Abstract: The underlying research is based on in-situ monitoring of the temperature-moisture regime of natural rock mass /volcanic tuffs/. Temperature-moisture regime is the control parameter that influences deterioration process of rock massive. Depending on thermodynamic conditions, the moisture sensor utilizes changes of thermal conductivity of porous structure when pores are filled by air/vapor, water or ice. The relationship between thermophysical properties and water content in certain pore material needs to be known. Therefore it's necessary to calibrate the moisture sensor and determine change of thermal conductivity of tuff pore material in dry and water saturated states in the temperature range that is typical for the climate of Brhlovce locality. The calibration is carried out in a temperature range of different degrees of moisture content.

The construction of moisture probe is based on hot ball sensor in combination with rock cylinder made of tuff and assembled in a proper way. The probe can be used for the measurement in quasi steady-state regime or in transient regime. The new probes were calibrated in transient regime that is more sensitive for the properties change and the results improved accuracy of measurement. The difference in thermal conductivity of dry and moisture saturated sates is about 50% that gives big sensitivity for relative changes of moisture content. The four probes were constructed and calibrated for the in-situ monitoring of temperature and moisture at the four distances from the surface within the range of depths from 10 cm up to 190 cm. The results are discussed.

Keywords: Moisture sensor, thermal properties, monitoring, preservation of historical monuments.

1 Introduction

Porous rock materials in natural conditions are exposed to the climate changes and thus the deterioration processes start up in time. The mentioned processes are caused by phenomena of sun radiation, precipitation and evaporation, freezing and thawing.

The water phases found in pores (gas, liquid, solid) cause the mentioned phenomena mainly. The resulting thermal conductivity of a porous material is a function of the content of pores.

The problem of moisture content and transport phenomena in porous materials are in high interest of building industry as well as in the area of preservation of historical buildings and monuments. The recent methods are based on various principles, like the measurement of electrical resistivity, microwave techniques with measurement of permittivity, measurement of relative air humidity in material cavities or drilled holes. The problem is in monitoring of moisture at different depths of rock massive in the free nature or the masonry surface of building that are exposed to climate changes. In our case the moisture probes are placed at the depths of 10, 38, 58, 90 and 190cm from the free rock surface. It is problematic to place any other kind of probes at these depths. The solution of the problem is to use the laboratory

calibrated moisture probes based on rock cylindrical bodies drilled out directly from the monitored place in rock dwellings in Brhlovce preserved as historical heritage. The hot ball probe is inserted into a small cylinder of tuff (Figure 1).

2 Theories

The principle of hot ball probe is based on generation of the heat pulse in the step-wise form and recording the temperature response to this heat pulse. Model of the hot ball method assumes a constant heat flux q from the empty sphere of radius r_b (radius of hot ball probe) into the infinitive medium that starts to be generated for times $t > 0$ (Figure 1 right). Then the temperature distribution within the medium is characterized in [1, 2].
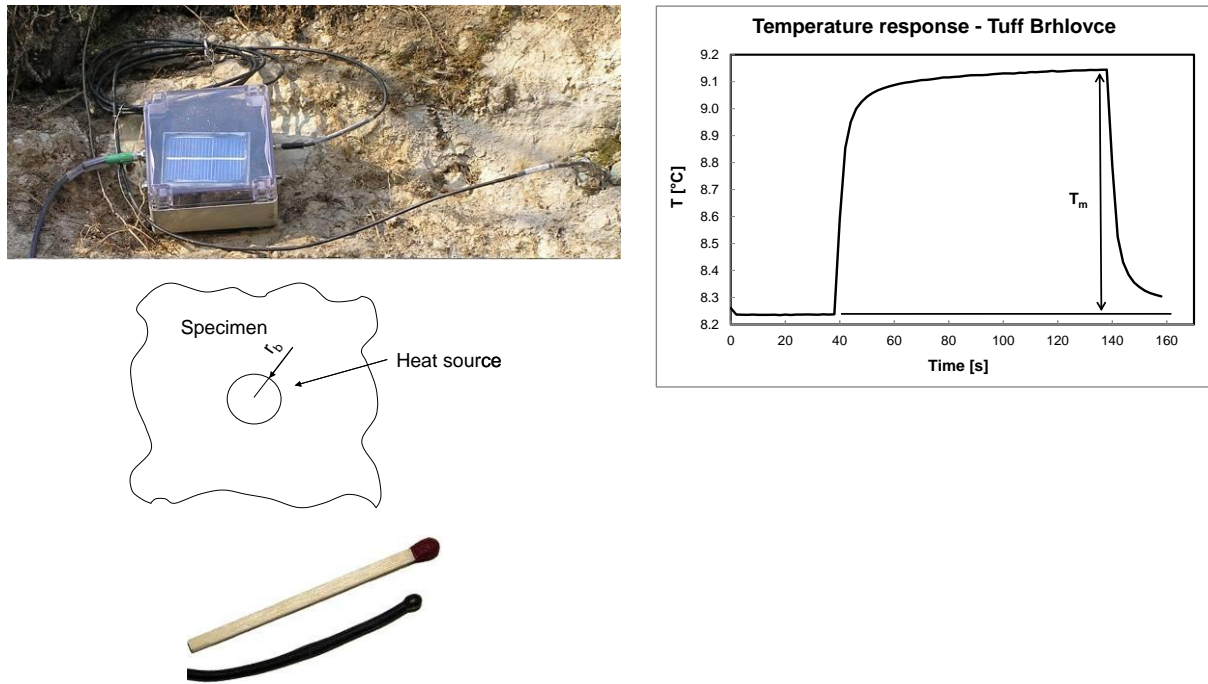
Figure 1. RTM-solar version of electronic instrument (processor, A/D converter and memory for data storage) in connection with the hot ball arranged as moisture probe (up), model of the hot ball (down left) and probe real size picture (down right). An example of the temperature response measured for tuff (right).

The solution of the partial differential equation that describe the heat conduction for this experimental technique and describe the shape of temperature response (Fig. 1), is described according the equation (1) derived for the initial $T(0, r) = 0$ and the boundary condition

$$-\lambda \frac{\partial T}{\partial r}\bigg|_{r=r_0} = ql(t)$$

$$T(r,t) = \frac{q}{4\pi\lambda r}\left\{erfc\left(\frac{r-r_b}{2\sqrt{\alpha t}}\right) - \exp\left(\frac{r-r_b}{r_b} + \frac{\alpha t}{r_b^2}\right)erfc\left(\frac{r-r_b}{2\sqrt{\alpha t}} + \frac{\sqrt{\alpha t}}{r_b}\right)\right\}$$

$$\mathrm{erfc(x)} \equiv 1 - \frac{2}{\pi}\int_0^x \exp(-\zeta^2)d\zeta$$

(1)

where *erfc(x)* is the complementary error function and λ is thermal conductivity, κ is thermal diffusivity of the surrounding medium, q is heat flux, λ is thermal conductivity. The long-time approximation ($t \to \infty$) solution of function (1) was derived as the working relation of the

measuring method and the equation (2) is used for the case of steady state measurement regime

$$T_m = \frac{q}{4\pi r_0 \lambda} \qquad (2)$$

Thus for the thermal conductivity λ we can write

$$\lambda = \frac{q}{4\pi r_b T_m} \qquad (3)$$

where T_m is the stabilized value of the temperature. The thermophysical parameters are calculated from the temperature response by fitting procedure using model (1) or calculated from maximum (2).

3 Experiments

Tuff is the rock material having high porosity (40-60%). The thermal conductivity is changing with fluctuation of water content in pores. The laboratory calibration within the range of dry and water saturated material sets the maximum range present in nature rock massive. The Hot ball probes were calibrated in different baths before inserting to the stone cylinder. This primary calibration is used to obtain the basic probe parameters to calculate thermal conductivity and thermal diffusivity from the temperature response.

Figure 2. Moisture sensor with wire connections to RTM solar before inserting into rock massif.

For the study there were selected the cores from drilling of holes for placing the moisture sensors. The cylinders carved in tuff from Brhlovce rock dwellings having diameter 32 mm were drilled out in a middle and hot ball probe having 2.5 mm in diameter was inserted into a centre of such a hole in rock cylinder and cables were supported by cage made of nickel wires (Fig. 2.). The reason for the choice of the lithological rock types was the existence or the preparation of monitoring procedure on the temperature - moisture regime, and related laboratory research as well.

Volcanoclastic tuffs from Brhlovce belong to complex of andesite neovolcanism. In terms of descriptive characteristics of the material the color is light grey, the grain size is ranging from 0.063 to 2.0 mm, and has the porous structure with cryptopcrystallic matrix. Physical properties of tuff from Brhlovce locations are the following: specific gravity – 2.569 g.cm^{-3}, volume density – 1.500 g.cm^{-3}, porosity – 31.8 %, water absorption – 16.4 % and uniaxial compression strength – 17 MPa.

3.1 Calibration procedures

The hot ball probe is calibrated in liquid media having different but known value of thermal diffusivity, in this case the water and glycerol, so one can calculate thermal conductivity from measured temperature response characteristics according a given equations 1÷3.

Series of hand-made Hot-ball sensors were tested for reliability and calibrated in bath liquids of water and glycerol to have two calibration points for thermal conductivities in a range of thermal conductivity values that will be measured by probe. This procedure shows also the sensitivity of the probe to thermal conductivity changes.

The research was focused on the study of moisture regime of tuff stone with hot ball probe. Such a probe is inserted in a core from drilling of holes (usually carved in a form of cylinder of porous tuff stone) and moisture sensor is ready (Fig. 2.). It is important to use the same tuff stone drilled out from massive to have the same thermophysical properties and the same porosity as the surroundings in hole where the moisture sensor will be arranged.

The first condition was to start with the drying the specimen that was kept at the temperature 104°C and weighting to determine the dry state. This state is defined as the 0% of moisture in the sample. Into a dry stone cylinder the hot ball probe was inserted to make a moisture sensor. Thus the next type of calibration has to be done for the use of the probe as a moisture sensor. The measured value of heat flux and temperature maximum q/T_m inside the moisture sensor represents thermal conductivity that is changing in dependency of moisture content. The probe sensitivity should be high enough to register the moisture content change during moisturizing process in between dry and moisture saturated state (from 0 up to 100 % of moisture content). This change is measured as the difference of λ. The difference – the maximum and minimum values of λ is the sensitivity and in the case of this probe it was about 0.5 $Wm^{-1}K^{-1}$. These probes were calibrated just at the temperature range from -20 up to 40°C. This calibration serves for calculation of thermal conductivity from temperature response calculated by fitting procedure.

After calibration the moisture sensors were inserted in the tuff massif at Brhlovce. Previously manufactured sensors were used for the in-situ monitoring started from October 31st 2011 [4]. The reason for their recent replacement by recently calibrated sensors is better accuracy of new ones that are able to offer all thermophysical parameters by fitting procedures. The old probe was not temperature calibrated, but the results show us how to improve methodology of the measurement of the thermal conductivity temperature dependence in regard with moisture content by this type of sensors.

For the next future, monitoring in tuff massive in depths at 10, 38, 67 and 190 cm with the new series of probes was started to run. Such moisture sensors were calibrated in dependence of temperature in both – the dry and moisture saturated regime. The new probes have the sensitivity 0.5 $Wm^{-1}K^{-1}$ calculated for dry and saturated state in a given temperature range. For different moisture content a linear dependency is valid, so one can recalculate measured values of λ to the moisture content from this calibration. The dry-moisture calibration was performed in laboratory conditions for the range of temperatures from -20 up to 40 °C.

3.2 Calibration results

The first calibration was carried out on moisture probes dried at 105 °C till the constant weight. Constant weight was below maintenance of using silica gel in re-closable bags.

The second calibration was done for water-saturated condition when stone cylinder was packed using Parafilm. Drying process and the saturation of the samples by water was carried out according to the applicable technical standard [3].

Humidity sensors (rock bodies with hot ball probe) exposed to temperatures from -20 °C up to +40 °C in the thermostat controlled chamber RTB 1.02. Measurements of thermal conductivity at stabilized temperatures were performed every hour inside rock bodies to keep enough time for temperature stabilization in between the heat pulses. Temperature in the chamber was set in several steps to 25, 40, 17, 10, -13, -8, -5, -1 and the back to 25 °C to check the repeatability as well as the state of water saturation. The given temperatures were always lasts for 24 hours to get perfect stability of results. An experiment was conducted on cylindrical test samples (moisture sensors) of length 32 mm and diameter 20 mm with built-in hot-ball probe. Overall, the samples were calibrated in heating-freezing-heating cycle.

Subsequently, the experimental results were statistically processed. Result of the calibration experiment is shown in Fig. 4. The figure represent the calibrated values of thermal conductivity calculated by fitting procedure from (1) that is changing in dependency of temperature for the materials studied in dry and moisture saturated conditions during freezing-thawing cycle. The temperature dependency of measured mean values of thermal conductivity of rock in dry as well in water saturated state is linear. The calibrated temperature dependency of the thermal conductivity for the moisture saturates state is negative for the temperatures above 0 and negative for the temperatures below the freeze point (Fig. 3.). Besides this probe a next 3 probes were calibrated simultaneously.
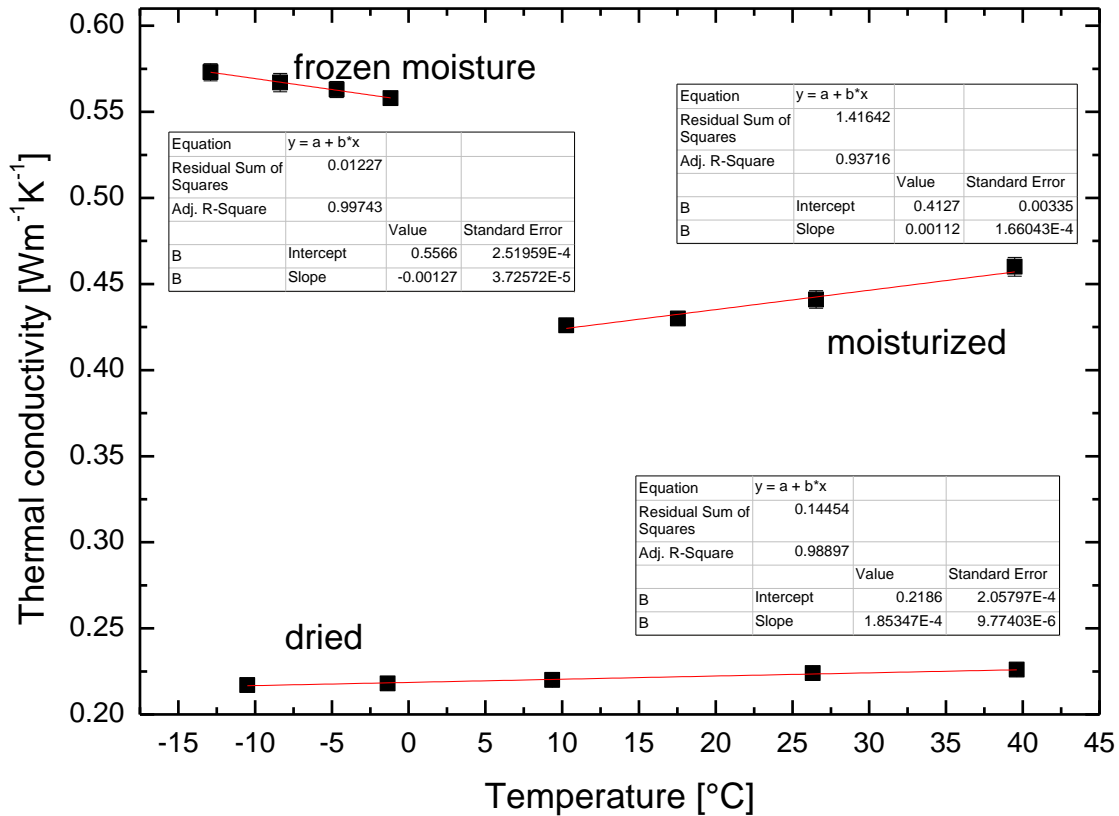
Figure 3. Temperature dependency of λ calculated from (1) by fitting procedure. Data were measured for tuff in dry and water saturated conditions within the temperature range from -13 up to 40°C. Data were statistically averaged for a given temperature. The tuff cylinder for moisture sensor was drilled out from the massif depth of 184-190cm.

The values of thermal conductivity λ in the case of water saturated probes are much higher than the dried one. The high difference in the values of the thermal conductivity for the dry and reached water-saturated state of tuff also proves its high water absorption (45-65%).

According to the difference of thermal conductivity in dry and water saturated conditions at different temperatures it was confirmed the relationship between water absorption and

increase of thermal conductivity for the positive temperatures. For the temperatures below the freezing point the monitoring of moisture content change is more complicated, as the frozen water will probably block the next diffusion of the water as well as the snow precipitation is expected for in-situ measurement at this temperatures.

The moisture sensor data collected within three years are in the Fig. 4 and Fig. 5. as a temperature dependency of measured parameter q/Tm as well as the in time dependency that reflects the thermal conductivity changes according (3) and thus the change of moisture content. Data in Fig. 5. and Fig. 6. illustrates the time changes within this three years period.
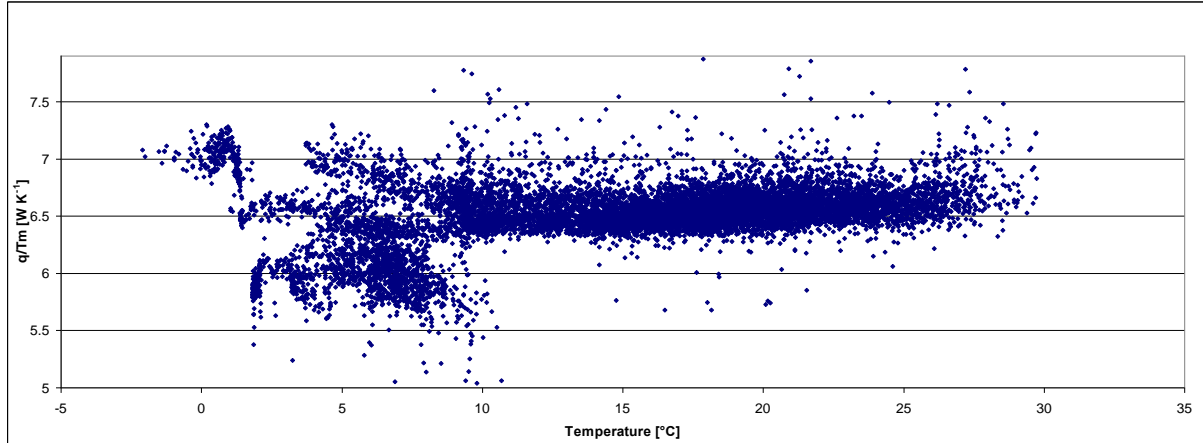
Figure 4. The sensitivity scale of old probe in q/T_m. Data collected during monitoring in 10 cm of depth in massif are given in the temperature range monitored in Brhlovce locality. This sensor was not temperature calibrated.
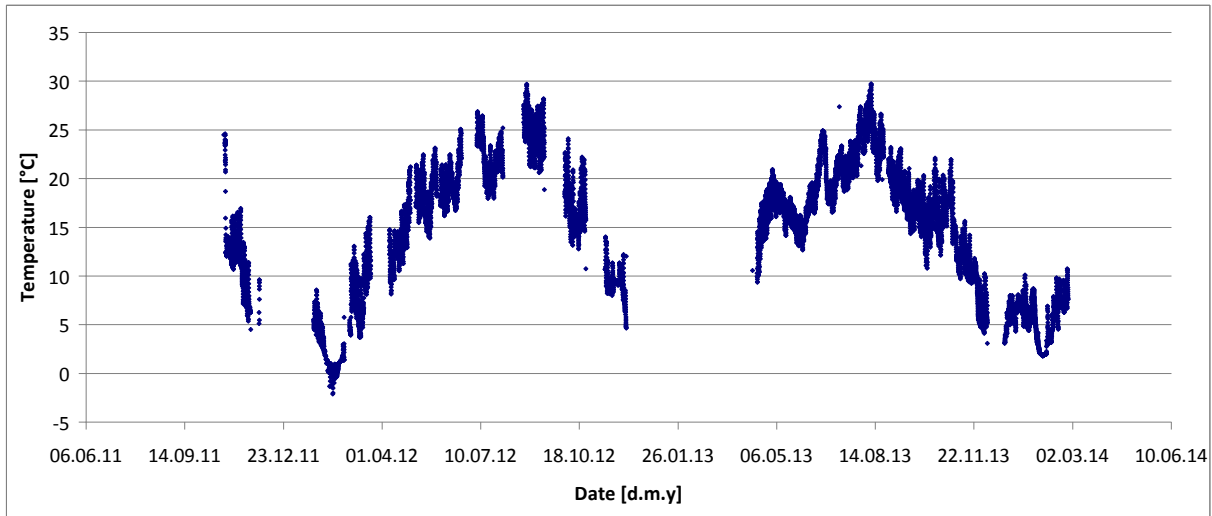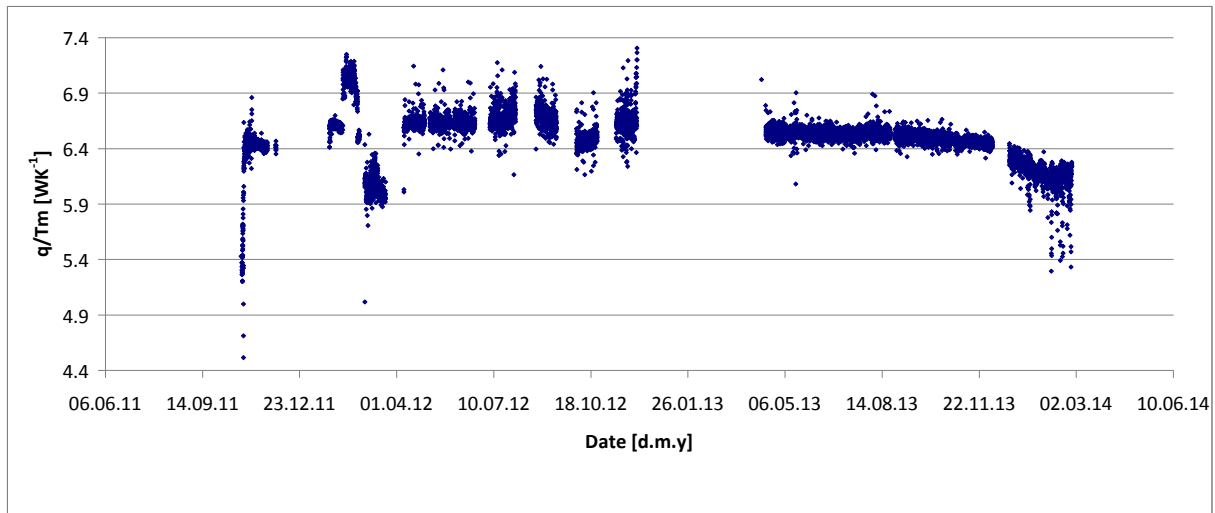
Figure 5. Data collected in time period of three years from locality Brhlovce [4]. Upper part show temperature changes during this seasons and corresponding values of q/Tm adequate to moisture changes.

4 Conclusions

The calibration data on temperature change in dependency for the moisture sensors made of tuff stone cylinders in dry and moisture saturated states were presented temperature. The thermal conductivity values which correspond to change of moisture content in moisture probes were measured for calibration purposes in measurement chamber RTB 1.02 [5]. Four moisture sensors will be placed into the tuff massif at locality in Brhlovce rock for the purpose of in situ monitoring of temperature – moisture regime. This kind measurement is necessary for the geology engineers to calculate the deterioration risks as there were some collapses of the rock marquis appeared over the dwellings in years 2011 - 2013 [4]. The data values of q/T_m 0 raised from 3.6 up to 6.9 W K^{-1} were measured at the temperature range 16-25 °C. At the initial three days of monitoring the rapid increase is evident and gives an image on difference between the dry and probably near-moisture saturated state. The values above value of 6.9 are higher due to positive temperature dependency of thermal conductivity and seem to give apparently higher moisture content over 100%, what is not true. This fact was the reason of temperature calibration of new probes.

For the calibrated moisture sensors the variation of λ with variation of moisture content as a parameter, the temperature dependency was found. Based on observed physical properties such as porosity, water absorption and thermal conductivity of studied materials; it can be assumed relationship between water absorption and increases of thermal conductivity. The experiment was carried out for the needs of correlations between laboratory and field research. This experiment will be helpful in monitoring the moisture in field research, because values of thermal conductivity are defined in extreme dry and wet conditions. On the basis of the experiment we could better eliminate linear increase in thermal conductivity due to the increase of temperature and thus determine the actual moisture in rock massif from the equations obtained by linear fit in dry and moisture saturated state as well as in the case of moisture frozen state. All new calibrated moisture probes will be inserted into a massif and monitoring of moisture content in next period should start. In this way we would be able get more accurate data and better possibility for calculation of moisture content from measured values of thermal conductivity. The data measured by new probes have a laboratory limit that was found at calibration for dry and moisture saturated state. Nevertheless, the data measured by old probe on Fig. 5. should be revised after the recalibration of old probe under the same methodology like new ones.

5 References

[1] Carslaw, H.S. & Jaeger, J.C. 1986. Conduction of heat in solids, Oxford, Clarendon Press, Second edition, p. 348.

[2] Kubičár, Ľ., Vretenár, V., Štofanik & V. Boháč, V. 2010. Hot-Ball Method for Measuring Thermal Conductivity, International Journal of Thermophysics, 31, 10, p. 1904-1918.

[3] EN 13755: 2008. Natural stone test methods. Determination of water absorption at atmospheric pressure.

[4] Ekkertová, P., Šimková, I., Brček, M., Durmeková, T. & Boháč, V. 2012. Influences of temperature change and moisture content on the thermal conductivity of rocks. Thermophysics 2012 - Conference Proceedings, 17th International Meeting of Thermophysical Society, 31st October to 2th November 2012, Podkylava, Slovak Republic, org. Institute of Physics, Slovak Academy of Science in Bratislava, Printed by: Brno University of Technology, Faculty of Chemistry, ISBN: 978-80-214-4599-4, p.33-40.

[5] Patent No.SK 285834 B6, producer www.transientms.com

Acknowledgements

References - alphabetical order

Carslaw, H.S. & Jaeger, J.C. 1986. Conduction of heat in solids, Oxford, Clarendon Press, Second edition, p. 348.

Ekkertová, P., Šimková, I., Brček, M., Durmeková, T. & Boháč, V. 2012. Influences of temperature change and moisture content on the thermal conductivity of rocks. Thermophysics 2012 - Conference Proceedings, 17th International Meeting of Thermophysical Society, 31st October to 2th November 2012, Podkylava, Slovak Republic, org. Institute of Physics, Slovak Academy of Science in Bratislava, Printed by: Brno University of Technology, Faculty of Chemistry, ISBN: 978-80-214-4599-4, p.33-40.

EN 13755: 2008. Natural stone test methods. Determination of water absorption at atmospheric pressure.

Kubičár, Ľ., Vretenár, V., Štofanik & V. Boháč, V. 2010. Hot-Ball Method for Measuring Thermal Conductivity, International Journal of Thermophysics, 31, 10, p. 1904-1918.

Patent No.SK 285834 B6, producer www.transientms.com

Deformation of Super Alloys at Elevated Temperatures

M. Oktay ALNIAK

Bahçeşehir University, Industrial Engineering Dept., 34353 İstanbul, *oktay.alniak@eng.bahcesehir.edu.tr*

ABSTRACT

Material parameters affecting the material structures can be used for modeling the deformation behavior of super alloys. Thermo-mechanical processes are applied to P/M super alloys for consolidation. Stress-strain relationship can be established by the factors such as strain, strain rate, grain size, temperature and structural parameters. A new deformation model is suggested in this work by means of searching the compatibility of experimental results and analytical studies. In this study, P/M Rene´ 95 super alloy was used as experimental material and micro-thermo-mechanical behaviors were investigated under constant strain rates at elevated temperatures.

Keywords: P/M Rene´ 95, super alloy, modeling, strain rate, modeling of constitutive equation.

1. INTRODUCTION

Modeling of deformation mechanisms of engineering materials can be expressed by constitutive equations. These are useful for calculation and estimation of strength of material subjected to hot or cold deformation or extrusion operations. Some factors affecting materials' yield stress could be grouped as direct or indirect. While direct factors are said to be as deformation, deformation rate, and temperature; indirect factors may be chemical and metallurgical composition of the material, grain size, and history of the material.

Modeling of deformation mechanisms of engineering materials can be expressed by constitutive equations. These are useful for calculation and estimation of strength of material subjected to hot or cold deformation or extrusion operations. Some factors affecting materials' yield stress could be grouped as direct or indirect. While direct factors are said to be as deformation, deformation rate, and temperature; indirect factors may be chemical and metallurgical composition of the material, grain size, and history of the material.

2. EXPERIMENTAL STUDY

Behaviour of Rene 95 at elevated temperatures, at constant strain rates:

A theoretical formulation was investigated considering some parameters affecting stress and strain relations such as deformation rate, absolute temperature, activation energy, grain size, for super alloys, Rene´95. After consolidation of material at hot isostatic pressure, tests were carried out at elevated temperatures such as 1050 ^{0}C, 1100 ^{0}C. A new model constitution equation for Rene´ 95 super alloys were investigated by taking into account the stress, deformation, deformation rate, material parameters and structural changes.

The changes in microstructure induced by plastic deformation in hot isostatically pressed (HIPed) P/M Rene 95 under isothermal conditions are discussed. Results of the constant true strain rate compression tests are presented for initially fine (7 µm) and coarse (50 µm)grained compacts deformed at temperatures of 1050 $^{\circ}$C, 1075 $^{\circ}$C and 1100 $^{\circ}$C and at strain rates in the range from 10^{-4} s^{-1}to 1s^{-1}. Under these test conditions, both the fine and coarse-grained compacts recrystallize and their grain size are refined during flow. This grain refinement gives rise to softening in both materials. Ultimately, their microstructures transform into the same equiaxed fine-grained microduplex structure at which point their flow strength becomes identical. Continued deformation at that point produces no further change in grain size or flow strength. Under this steady state regime of deformation, the microduplex grain size and flow strength are independent of the original microstructure but are conditioned by the strain rate at a given temperature. The steady state grain size increases whereas the steady flow strength decreases with a decrease in strain rate and/or an increase in temperature.

Stress-Strain relations of Rene 95 at constant strain rates:
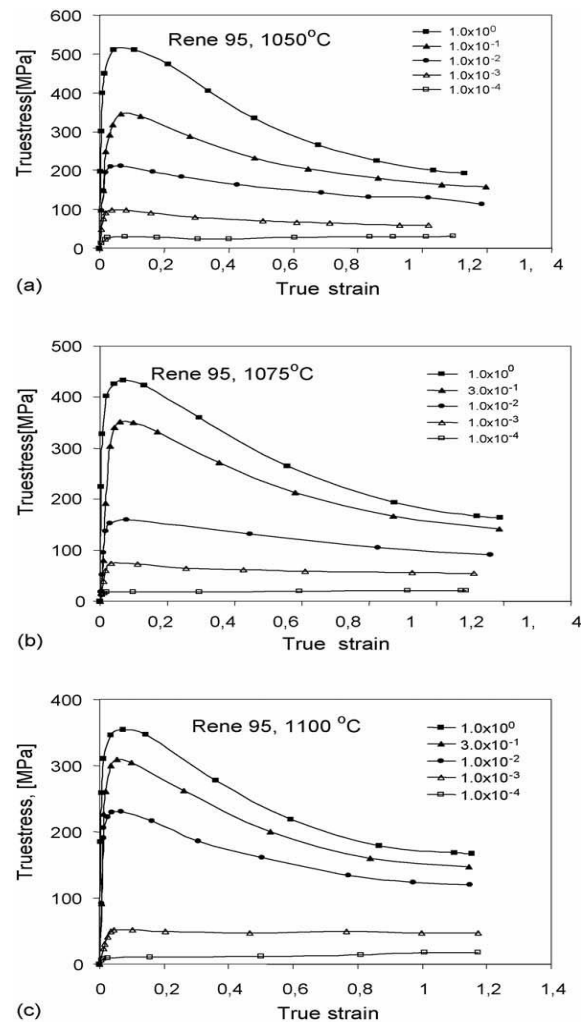
Figure 1: Constant true strain rate flow curves for the as-hipped P/M Rene 95 compacts showing the effect of applied strain rate at the three test temperatures examined in this work.

Change of strain rate sensitivity factor due to elevated temperatures:
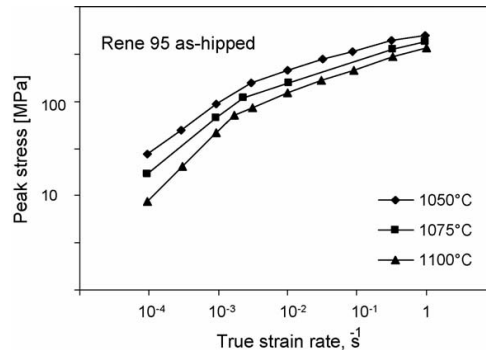
Figure 2: Variation in the peak flow strength of the hipped P/M Rene 95 fine grained compacts as a function of strain rate (log–log plot).
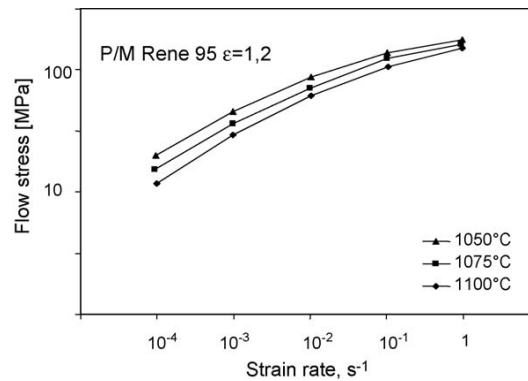
Figure 3: Variation in flow stress of the P/M Rene 95 compacts at a strain of 1.2 as a function of strain rate at the three test temperatures.

True stress- true strain relationship at elevated temperatures:
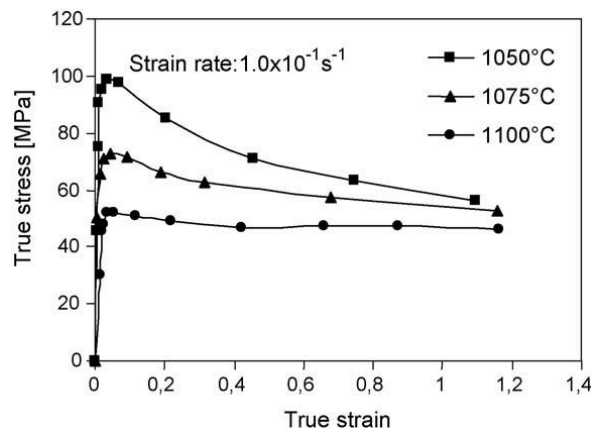
Figure 4: Constant true strain rate flow curves for the as-hipped P/M Rene 95 compacts showing the effect of test temperature on the flow behavior at identical strain rates

Microstructural changes due to elevated temperatures and at different strain rates:
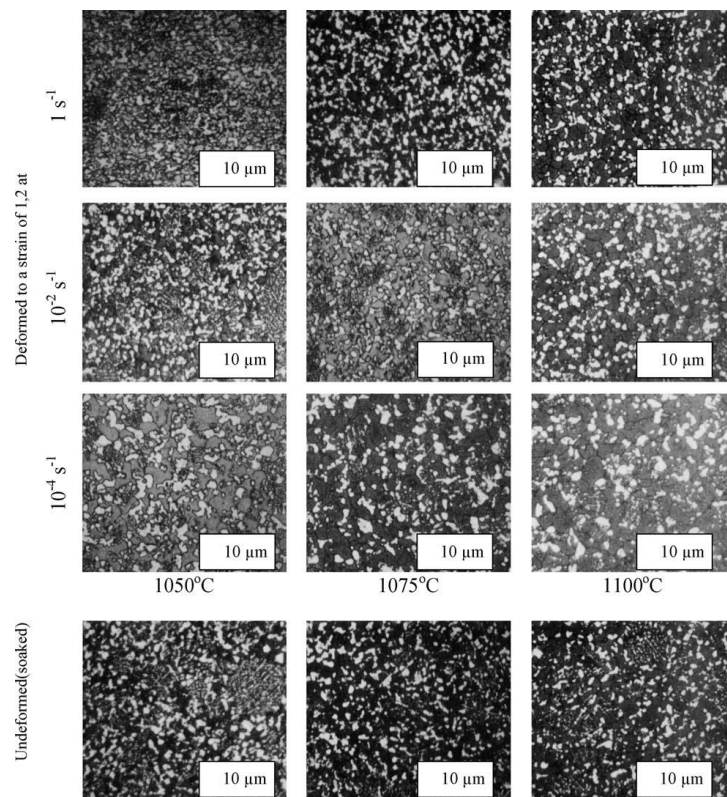
Figure 5: Effect of forging temperature and strain rate on the microstructure of the as-hipped fine-grained P/M Rene 95 compacts after a true strain of 1.2 corresponding to a 70% reduction in height of the compression test piece.

The microstructures of undeformed specimens soaked for 20 min at the three test temperatures are also shown for compression

4. EQUATION'S FOR DEFORMATION MECHANISMS OF POWDER METALLURGY

Material parameters can be used for description of deformation mechanisms. A function can be composed of the parameters like of the some structural parameters of materials such as microstructure, transformations of grains, stress, strain deformation, temperature and transformations rate.

The idea of developing new models depending on these parameters had been constituted basic of this research for modeling of powder metallurgy super alloys.

In modeling of super alloys that was obtained by constant pressure and temperature at the same deformation. To obtain of the constitutive equations, ıt can be faced complex situations

because of fine grain size of this materials, microstructure of material change during the deformation, effects of the diffusional flow which is occurred in high temperature and deformation rate. Deformation mechanisms of grains can be reviewed for this kind of study. One of the deformation mechanisms is motion of dislocation glide. The component in Eq.1 can be represented by a dislocation glide/climb controlled creep equation like the following form. [Alniak and others, 1988]

$$\dot{\varepsilon}_{mdg} = A' \frac{D_V \mu b}{kT} (\frac{\sigma - \sigma_0}{\mu})^4 \tag{1}$$

Another deformation mechanism may be originated from grain boundary slide. Grain boundaries' slides are important for the super alloys. Grain boundary sliding mechanism in a rather low deformation rate as a factor contribute to the deformation also GITTUS model is used to modeling of super alloys deformation.

$$\dot{\varepsilon}_{gbs/G} = 53.4 \frac{D_B \mu b}{kT} (\frac{b}{\lambda})^2 (\frac{\sigma - \sigma_i}{\mu})^2 \tag{2}$$

The deformation models that defines fine grained super alloys' (between 2 and 9 micron) deformation mechanism at related deformation rates were offered in this study. There may be three different deformation mechanisms at these deformation rates:

$$\dot{\varepsilon}_{(10^{-4}S^{-1} \sim 10^{-2}S^{-1})} = \dot{\varepsilon}_{gbs}$$
$$\dot{\varepsilon}_{(10^{-2}S^{-1} \sim 10^{-0}S^{-1})} = \dot{\varepsilon}_{mdg} \tag{3}$$
$$\dot{\varepsilon}_{(10^{-4}S^{-1} \sim 10^{0}S^{-1})} = \dot{\varepsilon}_{gbs} + \dot{\varepsilon}_{mdg}$$

At 1050°C, at a wide deformation strain rates between 10^{-4} S^{-1} and 10^{0} S^{-1} the constitution equation of Rene´ 95 could be written as below:

$$\dot{\varepsilon} = 53,4 \frac{D_B}{kT} (\frac{b}{\lambda})^2 (\frac{\sigma - \sigma_i}{\mu})^2 + A' \frac{D_B}{kT} (\frac{\sigma - \sigma_0}{\mu})^4 \tag{4}$$

This constitutive equation give appropriate results for P/M 713 LC and RENE´ 95 super alloys. Also in this work, material parameters had been used by modified and results of test have ensured accuracy of theoretic formulation. [Immarigeon and others,1989]

In a research carried in constant deformation rate at 1100 ^{0}C high temperature; diffusion mechanism might be considered as a factor of deformation such as dislocation movements

and mechanism of grain boundary slides. Namely, diffusional flow contributes deformation mechanisms.

The constitutive equation of Rene´ 95 is then written as follows between 10^{-4} S^{-1} and 10^{0} S^{-1} at $1100^{0}C$.

$$\dot{\varepsilon} = \dot{\varepsilon}_{mdg} + \dot{\varepsilon}_{gbs/G} + \dot{\varepsilon}_{gbs/AV} \tag{5}$$

Regarding Ashby's and Veral's work, general constitutive equation is expressed as in the following manner.

$$\dot{\varepsilon} = 53,4 \frac{D_B}{kT} (\frac{b}{\lambda})^2 (\frac{\sigma - \sigma_i}{\mu})^2 + A' \frac{D_B}{kT} (\frac{\sigma - \sigma_0}{\mu})^4 + \frac{100\Omega}{kT\lambda^2} (\frac{0.72\Gamma}{\lambda}) D_V (1 + \frac{3.3\delta}{\lambda} \frac{D_B}{D_V}) \tag{6}$$

This proposal was made as the first time and may be accepted as the constitutive equation of RENE´ 95. This equation is based on material parameters and used atomistic models. This equation has been obtained from three different deformation mechanism's super position. The theoretical results obtained from the constitutive equation has confirmed by the experimental data. [Alnıak, 1990]

Recently completed researches dealing with high temperature effects on deformation of materials also reviewed by this study. Ongoing studies suggest new methods to be applied to gain new features for aeronautical applications. Some comparisons are made between test results. Weakening of strength of materials is observed by the effects of elevated temperatures. [Ning, 2013]

Temperature, grain size, diffusion mechanisms are also found as the effects of influencing deformation mechanisms and strength as well as the constant strain rates. [Zhang, 2013]

5. CONCLUSIONS

RENE´ 95 alloys were tested in high temperature experiments like 1050 ^{0}C and 1100 ^{0}C after they were consolidated in constant pressure. The new two models were offered using the stress, deformation, deformation rate relationships. Modified material parameters according to test temperatures are the following. This paper expresses whole evaluation of Rene 95 super alloy' plastic deformation at elevated temperatures considering both experimental results, and satisfied models for elevated temperatures depending upon material and test parameters. This is also one of the early studies on the subject. The results and methodology of this study are accepted as an example for the newest ones. Some studies of super alloys were completed

recently dealing with elevated temperatures for plastic deformation, but a mathematical model were not studied.

ε	true strain, $\ln(h/h_0)$ where h_0 is initial specimen height
$\dot{\varepsilon}$	true strain rate
$\dot{\varepsilon}_S$	strain rate in soft regions of model material
$\dot{\varepsilon}_R$	strain rate in hard regions of model material
F	volume fraction of soft recrystallized material
σ	flow stress
σ_P	peak flow strength
σ_{SS}	steady state flow strength
σ_0	back stress due to intragranular
σ_i	internal stress due to grain boundary ledges
m	strain rate sensivity of flow strength
P	grain size sensivity of flow strength
Q	activation energy
R	gas constant
T	absolute temperature in K
$C(S, \dot{\varepsilon})$	structure and strain rate dependent time constant
t	time
n	time exponent
A, A'	experimentally established material constants
$\dot{\varepsilon}_{gbs}$	rate equation for grain boundary sliding
$\dot{\varepsilon}_{gbs}/AV$	ibid (Ashby and Verall mechanism)
$\dot{\varepsilon}_{gbs}/G$	ibid (Gittus mechanism)
$\dot{\varepsilon}_{mdg}$	rate equation for intragranular flow by dislocation creep (motion of dislocation within grains)
D_V	volume diffusion coefficient
D_B	grain boundary on interphase boundary diffusion coefficient
Γ	grain boundary energy
b	Burgers' vector
μ	shear modulus
k	Boltzmann's Constant
λ	initial grain size
d	as-worked steady state grain size number of steady state grain layers in partially recrystallized spherical grain model

Table 1: Symbols

Symbol	Parameter	Value
A'	Power law creep constant	a
A' (1323K)	Power law creep constant at 1323 K	4.7×10^3
A' (1373K)	Power law creep constant at 1373 K	9.3×10^3
B (m)	Burgers vector	1.7×10^{-10}
K (MN m/K)	Boltzmann's constant	1.38×10^{-29}
μ (MN/m^2)	Shear modulus	b
μ (1323 K)(MN/m^2)	Shear modulus at 1323 K	5.0×10^4
μ (1373 K)(MN/m^2)	Shear modulus at 1373 K	3.5×10^4
D_v (m^2/s)	Volume diffusion coefficient	c
D_v (1323 K)(m^2/s)	Volume diffusion coefficient at 1323 K	1.1×10^{-17}
D_v (1373 K)(m^2/s)	Volume diffusion coefficient at 1373 K	3.2×10^{-17}
σ_i(MN/m^2)	Back stress due to grain boundary ledges	<1 [19]
D_B (m^2/s)	Boundary diffusion coeff	d
D_B (1323) (m^2/s)	Boundary diffusion coefficient at 1323 K	2.1×10^{-11}
D_B (1373) (m^2/s)	Boundary diffusion coefficient at 1373 K	3.6×10^{-11}
Ω (m^3)	Atomic volume	1.1×10^{-29}
δ (M)	Boundary thickness ~ $2b$	3.0×10^{-10}
Γ (J/m^2)	Boundary energy	0.1
R (J/mol/K)	Gas constant	8.3143
Q_V (kJ/mol/K)	Activation energy for volume diffusion	318
Q_B (kJ/mol/K)	Activation energy for boundary diffusion	159

Table 2: Calculated And Modified Values Of Parameters And Constants

5. ACKNOWLEDGMENTS

6. REFERENCES

[1] ALNIAK, O., MORPHY, D.D., TERADA, T., KOUL, A.K., IMMARIGEON, J.P., "Laboratory Technical Report LTR-ST-1637", National Research Council, Canada, Eylül 1988

[2] IMMARIGEON, J.P. ,KOUL,A.K., ALNIAK, O., MORPHY, D., TERADA, T., "Constitutive Relation For The Modelling of Flow Behaviour of P/M Rene 95 Under Isothermal Forging Conditions" NRC, NAE, Canada, 1989

[3] ALNIAK, O. "Constitutive Equations of Plastic and Super Plastic Materials Behavior, The deformation of P / M super - alloys at elevated temperatures and microstructure changes modeling " Phd Thesis, Gazi University, 1990, Ankara

[4] NING, Y.Q. " Structural-gradient-materials produced by gradient temperature heat treatment for dualproperty turbine disc/ Alloys and Compounds Manuscript Draft", School of Materials Science and Engineering, Northwestern Polytechnical University, Xi'an 710072, P.R. China, 2013

[5] ZHANG, M.J. et al. "School of Materials Science and Engineering/ Materials Science & Engineering A Manuscript Draft" Northwestern Polytechnical University, Xi'an 710072, P.R. China, 2013

A premature Failure of a Super-heater Tubing in a Power utility Unit

Elarbi O. Khalil,

University of Tripoli, P.O.Box 13292,Tripoli-Libya,
E-mail: ekhalil9@yahoo.com

Abstract

Boiler tube failures continue to be a major cause of boiler forced outages. This paper presents the failure investigation of a superheater tubing material, and describes some mechanisms by which materials may fail at high temperature service. Samples were collected from one of the oil-fired power plants in Tripoli after five years of service. The as received super-heater tube showed considerable bulging at the fracture location. Collected failed samples were undergone several experimental examinations including visual inspection, thickness measurement, chemical analysis, and micro-structural evaluation.

Based on the results of this investigation, it is believed that the tube has failed as a result of ductile stress over-load failure caused by rapid short-term overheating. In this situation, the tube metal-temperature is extremely elevated from a lack of cooling steam flow through the tube. This has been assisted by presence of internal oxide scale deposit on inner tube surface which leads to higher than design operating temperatures. The internal oxide deposit could have been formed by the carry-over of a bad quality steam which brings suspended or dissolved solids (hardness). As a result, creep expansion thinned the tube wall and creep rupture resulted in failure by ductile stress over-load at elevated temperature.

Keywords- superheater, oil-fired boiler, overheating, rupture, oxidation

Introduction:

There is increased need for power generation to meet the needs of growing population and economy. Moreover, the reliability of electrical supply is essential particularly during the summer peak months. In Libya, a large part of electric power is generated in steam power stations; in which boilers are used to heat water and produce steam. In boiler operation, tube failures in various locations continue to be a prime cause of forced outages in electric power production. The resulting downtime normally causes production losses due to reduced steam output. These losses far exceed actual repair & maintenance costs incurred during normal shutdown[1].

The boiler tube failures are related to a number of effects[2,3,4,5] not limited to but including: (1) waterside corrosion, which results from fouled heat transfer surfaces in presence of active corrodent. Typical examples include: stress corrosion, caustic corrosion attack, H-damage and galvanic attack.

(2) thermal effects: such as rapid overheating, long-term overheating, and thermal stress. A single incident or a small number of incidents exposes the tube to an excessively high temperature (hundreds of degrees above normal) to the point where deformation or yielding occurs.

(3) external (or fire-side) corrosion: this is caused by deposition of alkali-sulfate salts on external tube surfaces and causes high temperature or ash erosion.

To reduce failure incidences boiler tube materials, especially in critical pressure parts such as piping, headers and super-heaters, have to be strong with considerable resistance to fireside and steam side corrosion. Masuyama [2] demonstrated that most advanced steels show allowable stresses that are nearly 2 to 3 times higher than those of conventional steels, e.g, steel ASME - T22 with 2-1/4Cr 1-Mo steel. According to Masuyama, four generation of ferritic steels have evolved since 1960 to the last decade(2000 – 2010) . The first generation of these steels had creep rupture strength of 60 MPa(10^5 hr service at a maximum

245

temperature of 565 ^{o}C) while the emerging grades with increased amounts of W and addition of Co achieved up to 180 MPa(10^5 hr service at a maximum temperature of 650 ^{o}C)

There is continual need to up-grade the material of construction in order to achieve higher efficiency. The recent trend is to use steels working at higher temperatures above 600 ^{o}C. An example of such steel is the high-Cr martensitic steel which is characterized by large thermal conductivity and smaller thermal expansion compared with austenitic steels or Ni-base super-alloys. The increased efficiency is achieved by the increase in steam parameters, namely temperature and pressure of the steam.To extend boiler tube service life, plant operators employ several methods for testing resistance of protection against wear, corrosion and to raise the creep strength [6,7]. Wear susceptible portions of boiler tubing has been protected by weld cladding using inconels, stainless steel, or chromium carbide composites. The objective of this work is to explain the reasons for a superheater tubing failure case and describe some mechanisms by which materials may fail at high temperature service. As the metal temperature raises up, new deformation mechanisms start to operate. The equilibrium number of vacancies increases and the strength of the metals starts to decline. Among degradation mechanisms due to thermal effects, overheating in particular constitutes a major cause for boiler tube failures. Thielsch & Cone [8] noted that The localized nature of the overheating is a consequence of the fact that deposits do not form uniformly with time. The deposits, occur in locations of high heat flux or in places where physical "drop out" of suspended solids is more likely occurs, such as sloped tubes. These deposits insulate the metal from the cooling effects of the water, resulting in reduced heat transfer into the water and increased metal temperatures.

Preliminary and Visual Examination:

The failed piece of tube (300 mm long) was received from an oil-fired boiler for electric power generation operating at 9 MPa pressure and carrying steam at 315 ^{o}C. The tubing material was specified to 2.25 inch (57 mm) outside diameter, with 0.188 inch (4.7 mm) minimum wall thickness as per ASTM A106 GradeB. The tube has been in service for 5 years. It was stated that the failed tube section was collected from the superheater section of unit-5 boiler. Table (1) shows the details and operating conditions of high temperature superheater tube. The material used for this superheater part is steel A106 Grade B seamless carbon steel for high temperature service.

Table (1) Material Specification and Operating Conditions of Superheater Tube

Material	ASTM A106 GradeB
Diameter, OD (mm)	57
Min.Thickness (mm)	4.7
Super-heated steam flow (t/h)	2250
Super-heated steam temperature (^{o}C)	510
Super-heated steam pressure (bar)	9

A set of wall thickness measurements was conducted on the tube circumference as shown below in figure(1) at the fracture site and at about 150 mm away from the fracture location. Figure(2) depicts the as received super-heater tube conditions. It showed considerable bulging at the fracture site.
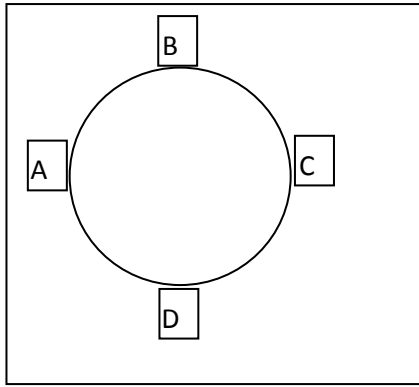
Figure(1) Locations of metal loss measurements

Figure(2) Close-up view of ruptures superheater tube

Metallography&Chemical Analysis:

the failed tube was sectioned at and away from the fracture site for metallographic examination. The samples were prepared for metallographic examination in accordance with ASTM E3. Etching was performed in accordance with ASTM E407 in Nital solution. Then, samples were examined using an optical microscope. The purpose of the micro-examination was to identify the micro-constituents of the tube material and confirm any metallurgical changes that might happened during service exposure. Micro-structural examination was further used to identify the nature of internal or external damage to tube surfaces. A specimen was cut from the tube and analyzed for its chemical composition using ElvaX portable ED XRF spectrometer available at the Industrial Research Centre (Tajora)

Discussion of Results :

Considerable wall thinning was noted at the fracture site as can be seen in figure (2). The average tube wall thickness in the fractured area is 3.44 mm while the thickness 250 mm away from fracture is 4.77 mm. Approximately 73% reduction of wall thickness was recorded at the fracture location. The reduction in wall thickness was significant at the fracture location. Inspection of the ruptured tube at the fracture site revealed a thin-lip rupture with brownish thin layer of oxide film on inner tube surfaces. There was no evidence of pitting. The outer surfaces of the tube exhibited a general oxidized condition. The inner surfaces of tube were also in an oxidized state along with some black deposits. Table (2) gives the metal loss at and away from the fracture site.

Table(2) Detection of tube wall thinning at and away from the fracture site

Location	Average Wall thickness (mm)	
	At fracture	Away from fracture
A	3.98	4.92
B	2.14	4.93
C	3.49	4.56
D	4.15	4.68

The microstructure of the ruptured tube away from the ruptured site consisted of pearlite in a equiaxed ferrite matrix, typical of low carbon steel, as shown in Figure (3). On the other hand, the microstructure at the fracture location is deformed ferrite plus pearlite grains; Figure (4) with some spherodized carbides. This latter microstructure normally forms due to prolonged heating under the transformation temperature for steel 723 ^{o}C. In other words, the tube has suffered excessive overheating. The rupture edges were relatively thin. Grain elongation and

ductile voids were evident in the microstructure adjacent to the rupture location. The results for chemical analysis are presented in table(3) where it may be seen that the failed tube did meet the specified chemical requirements of ASTM A106 Grade B. Micro-examination also revealed the presence of uniform layer of dark scale on
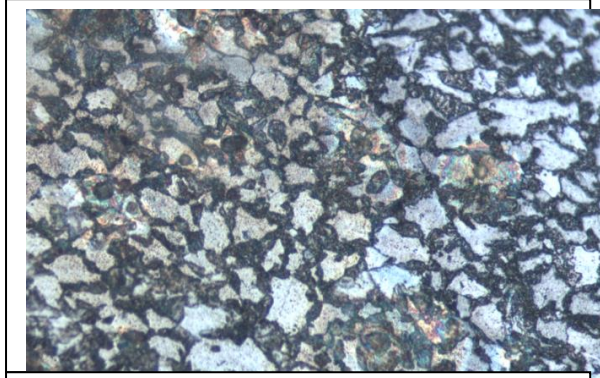

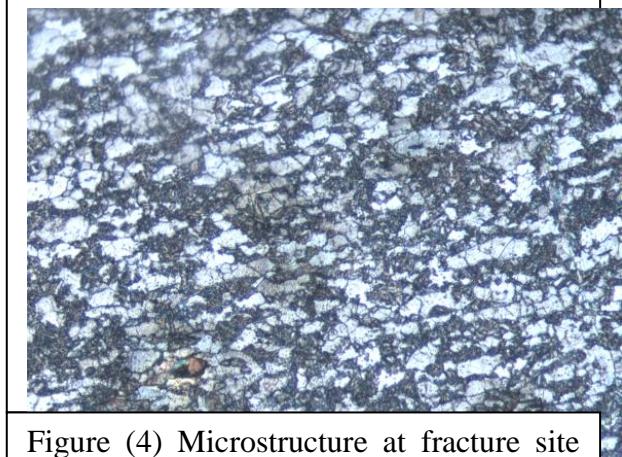Figure (3) Microstructure away from fracture showing pearlite in equiaxed ferrite matrix. (2% nital etch) (500X)

Figure (4) Microstructure at fracture site showing deformed ferrite & pearlite grains. (2% nital etch) (500X))

the steam side of tube surface. While dependent upon heat flux for a particular boiler unit, one mil(0.025 mm) of inside scale will typically increase the operating temperature by $\sim 2\ ^{o}C$ [9].

Table (3) Chemical composition(wt.%) of failed tube as measured by XRF spectrometer.

Element	C	Mn	Si	S	P	Cr	Mo	Ni	Fe
Wt.%	0.27	0.83	0.30	0.029	0.031	0.25	0.11	0.10	balance

In this work, the analyzed boiler produces steam that is superheated to 510 ^{o}C at the inlet of the turbine. For such design, the steam flow has to be intense to permit the heat absorption from the tube, avoid deformation because of high temperature. Visual inspection of internal tube surfaces also revealed the presence of internal oxidized condition with some dark deposited layer. This evidence further supports the prediction of possible tube overheating. When formed, oxide layers act as barrier to heat transfer. As the thickness of the oxide layer increases, the tube temperature increases. In the work conducted by Asrar et al [5], it was found that The strength of carbon steel remain nearly constant up to about 454 ^{o}C. Above this temperature, steel begins to lose its strength rapidly. If the tube metal temperature is gradually increased beyond this level, it will plastically deform and then rupture. The approximate time to rupture is a function of the hoop stress (related to internal pressure and tube dimension) and the operating temperature. Similar observation was made by Viswanathan and Sarver [6] who found that Overheating is caused by attached deposit in internal tubes which is carried over by flow of bad quality steam which bring suspended solid or dissolved solid (hardness). The hardness can be carried over with steam because separation process of steam-water mixture cannot be executed perfectly in steam drum. Deposits can be removed by adding chemical injection (phosphate) in steam drum to make hardness be soluble, then the next step is to discharge it through in blow down process. Dooley and McNaughton [10] used the ration of the tube wall loss(y) to the thickness of scale on the inside tube surface(x) to distinguish between fireside corrosion and creep damage. They stated if y/x is greater than 5, fireside

corrosion is the most probable cause of failure. But if the ration (y/x) is < 3 creep damage is the main cause. In our investigation, no signs of fireside corrosion were observed on external tube surfaces and the (y/x) ration was about 3. At the location where extensive wall thinning there was no heavy oxide/ash accumulation on fireside of tube as can be seen in figure(1). Failure in superheater tubes may also occur during bad start up process. If combustion temperature is increased rapidly without adjusting water and steam balance flow, the superheater will feel overheating in short term because there isn't steam flow which has function as cooler. Steam flow through superheater tubes act as cooler because temperature of steam is lower than radiant temperature due to combustion. So start up procedure shall be established to perform good combustion. Based on the above results and From the characteristic features of the fracture appearance, it is believed that the tube has failed as a result of ductile stress over-load failure caused by rapid short-term overheating. In this situation, the tube metal-temperature is extremely elevated from a lack of cooling steam flow through the tube. As a result, creep expansion thinned the wall and creep rupture resulted in failure by ductile stress over-load at elevated temperature. Similar failure cases have been reported in the literature [3,4,5,11] on different types of steels.

CONCLUSION:

Sudden tube rupture is a serious problem because it may cause damage to other components in the system; such as erosion of furnace side walls by escaping steam and overheating of other tubes due to interrupted fluid circulation. In the present failure case, it is believed that the tube has failed as a result of ductile stress over-load failure caused by rapid short-term overheating. In this situation, the tube metal-temperature is extremely elevated from a lack of cooling steam flow through the tube. As a result, creep expansion thinned the wall and creep rupture resulted in failure by ductile stress over-load at elevated temperature. The analysis of the failed superheater tube material indicated the presence of oxide scale on inner tube surface which further supports the possible occurrence of excessive overheating.

References

[1] Neves D, et al. *Stress and Integrity Analysis of Steam Superheater Tubes of a High Pressure Boiler*. Materials Research, 2004; 7 (1): 155-161

[2]Masuyama F. *New Developments in Steels for Power Generation Boilers*. in Advanced Heat Resistant Steels for Power Generation, R. Viswanathan and J.W. Nutting, Editors, IOM Communication ltd., London, 1999; 33-48

[3] Husain A, Habib K. *Investigation of Tubing Failure of Superheater boiler from Kwait Desalination Electrical Power Plant*. Desalination, 2005; (183): 203-208

[4] Dooley B, Chang P. *The Current State of Boiler Tube Failures in Fossil Plants*. Power Plant Chemistry, 2000;2(4): 197-203

[5]Asrar N, Malik A, Ahmed S. *Overheating and Fuel ash Corrosion Failures of Boiler Tubes in SWCC Power Plants O & M*, SWCC, Al-Jubail, sept.29 – Oct.3, 1997: 1411 – 1428

[6] Viswanathan R, Sarver J, Tanzosh J. Boiler *Materials for Ultra-supercritical Coal powered Steamside Oxidation*. J. of Materials Engineering & Performance, 2006;15(3): 255-274

[7] Valente T. Fireside Corrosion of Superheater Materials in Chlorine Containing Flue Gas. J. of Materials Engineering & Performance, 2001;10(5): 608-613

[8] Thielsch H, Cone F. *Superheater and Reheater Outlet Header Inspections, Failures and Repairs – Scheduled and forced Outage Consideration*. 8th Annual Outage "Best Practices" Conference, Aug.26 – 28, 2002, Clearwater, Florida: 1 – 65

[9] Labuda E, Cline D, Shields K. *Fireside Corrosion in Coal and Oil-fired Units: Failure Mechanisms & Methods of Prevention*.NACE Corrosion Conference 2000, Paper No. 00234: 1 - 18

[10] Dooley W, McNaughton W. *Boiler Tube Failures: Theory and Practice*. Pleasant Hill, CA: EPRI, 1996,(3) :33.1 – 34.10

[11] Annual Book of ASTM Standards,Vol. 03.02 Wear and Erosion; Metal Corrosion. American Society for Testing and Materials, Philadelphia, PA 2002

HOW TO OPTIMIZE DATA QUALITY OF THERMOPHYSICAL PROPERTIES OF NICKEL BASED SUPERALLOYS

W. Hohenauer; D. Lager

E-Mail: wolfgang.hohenauer@ait.ac.at

AIT Austrian Institute of Technology GmbH, ENERGY Department,
Donau-City-Straße 1, A-1220 Wien, Austria

Keywords: Thermophysical Properties, Uncertainty, Sample-Crucible Interaction, Oxygen Trapping

Abstract

Nickel based superalloys are representatives of a huge class of materials, showing significant chemical reactions with air constituents – specially oxygen. Worse: oxygen acts as a catalyst in reactions with usual lining materials in technological processes and measurement crucibles. Thus the measurement of thermo-physical properties of materials like these is definitely challenging, and the mentioned chemical interactions become reason for faulty measurements, so far they are ignored during the measuring process.

This contribution focusses on the measurement of the basic set of thermo-physical properties: thermal expansion, specific heat and thermal diffusivity. Thermal conductivity is determined as the product of these quantities. For measurements a push rod dilatometer, a dynamic scanning calorimeter and a laser flash device were used. From technical measurement reasons the application of OTS components (OTS = Oxygen Trapping System) in measurement devices is recommended to minimize distorting effects as parasitic reaction enthalpies or corrosion of crucibles. An elementary physical background is given and methods how to optimize measurement procedures are shown. Last but not least a concept to formulate the uncertainty of the measured data is proposed, which allows separate equipment related effects and limitations caused from the chosen mathematical examinations from sample related effects. The thermo-physical properties of a typical representative of a Nickel based superalloy are qualitatively given from ambient temperatures up to some 1600°C.

Introduction

Nickel based superalloys are representatives of a huge class of materials showing significant chemical reactions with air constituents – specially oxygen. Worse: oxygen acts as a catalyst in reactions with usual lining materials in technological processes and measurement crucibles. Thus the measurement of thermo-physical properties of materials like these is definitely challenging and the mentioned chemical interactions become reason for faulty measurements, so far they are ignored during the measuring process. Possible corrosion driven effects on conventional Al_2O_3 liner are illustrated with the left image of Fig. 1. Simultaneously to the material–liner interactions, various alloy oxidation happens. Thus the application of an Oxygen Trapping System (OTS) is meaningful from this point of view too. Titanium based devices operate sufficiently at temperatures above some 700°C. The effective application of an OTS is demonstrated impressively on the right image of Fig. 1: no significant corrosion of the liner happen, the surface of the molten – and re-solidified – sample shows the inversion of the surface roughness from the mechanical machining of the liner. Unfortunately OTS cannot be inserted e.g. in dilatometers. And, whenever applying a push rod dilatometer to measure thermal expansion in a liquid phase, no sufficient gas exchange inner the container – necessary to impede the molten material – can be achieved. Resulting corrosion effects are demonstrated in Fig. 2. As a consequence from this one has to suspect that no sufficient expansion measurements can be achieved whenever sample induced corrosion of the container happens: initial liquid phases will glue the pistons of the container device similar to a brazing effect and the resulting "loss" of molten phase leads to an ambiguous detection of the expansion behaviour in the melting range, quite different to the measured expansion behaviour of the solid when measured under the significantly more inert gas conditions of a solid state measurement (Fig. 3 – left image). Concerning the measurement of the thermal diffusivity, comparably comfortable measuring conditions might be met. Applying a laser flash device with an improved gas system, some 10^{-5} mbar can be achieved. Measurements in the melting regime are typically done in sapphire container. When a repeated pumping and subsequent flashing with inert gases (He) is done, sufficient chemical conditions are achieved and chemically induced artefacts can be minimized (Fig. 3 – right).
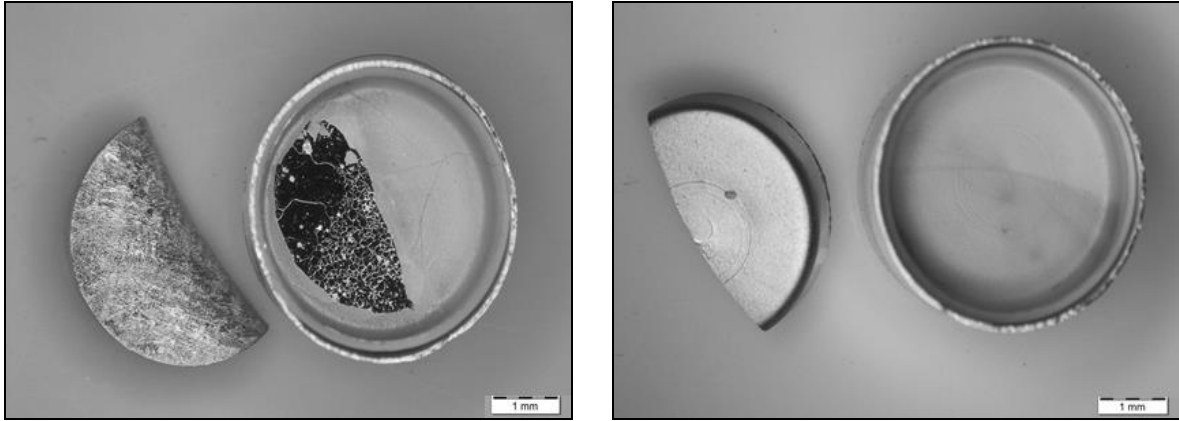
Fig. 1: DSC crucible with Al2O3 liner and Ni based superallpy sample after measurement
         left: 3 evacuation runs at ~5 x 10-2 mbar and Ar flushing
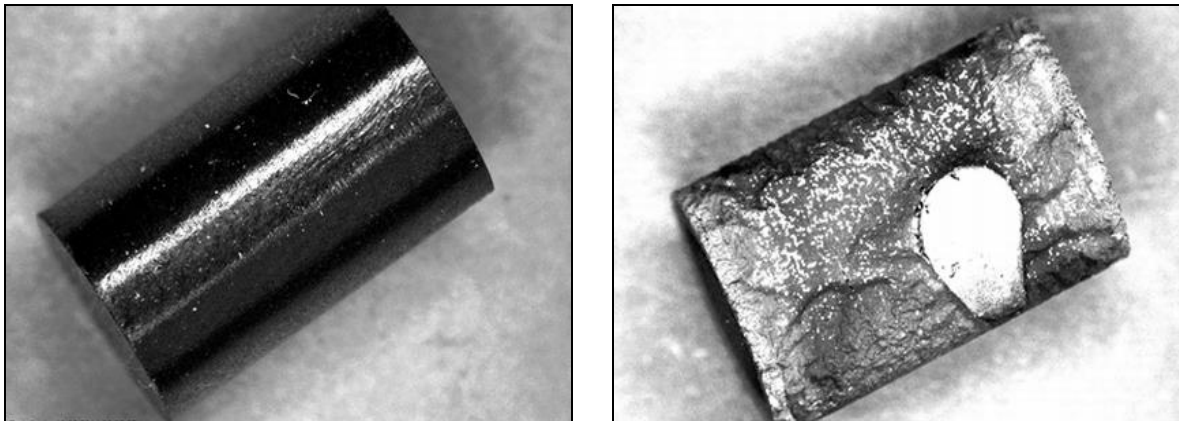   right: 3 evacuation runs at ~5 x 10-2 mbar and Ar flushing using a OTS application

Fig. 2: Dilatometer sample: left: d = 4,5 mm, L_0 = 10 mm before measurement, right after measurement in a
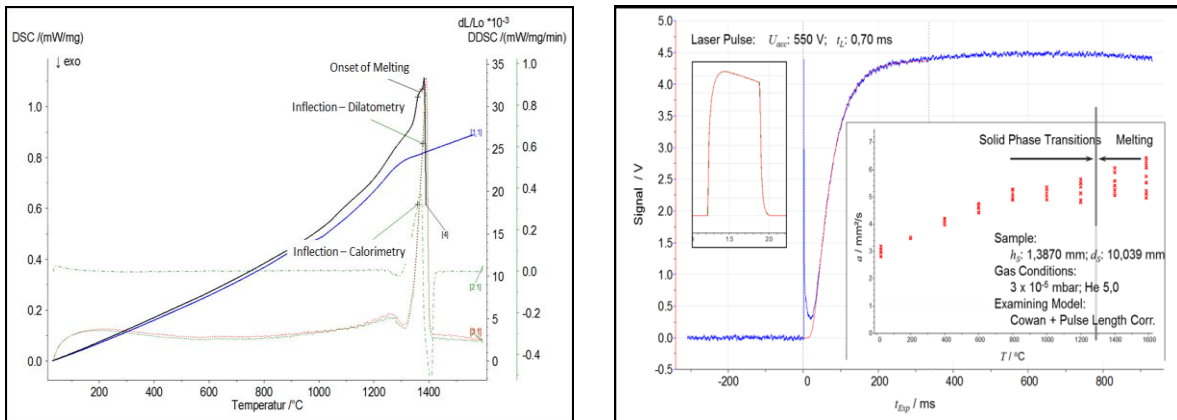 Al_2O_3 container after 3 evacuation runs at ~5 x 10^{-2} mbar and He flushing

Fig. 3: Raw data of an expansion measurement (left) and of a measurement of tehrmal diffusivity (right).
         Left: siginificant deviation between a conventional solid state measurements (black curve) and the
         measurement in a Al_2O_3 container to measure up to molten phases (blue curve)
         Right: typical transient temperature response of a flash measurement

Experimental

This contribution focusses on the measurement of the basic set of thermo-physical properties: thermal expansion, specific heat and thermal diffusivity[1]. Thermal conductivity is presented as the product of these quantities. For measurements a push rod dilatometer NETZSCH DIL 402C, a dynamic scanning calorimeter NETZSCH DSC

404C and a laser flash device NETZSCH LFA 427 were used. DSC measurements were performed by use of an OTS component (OTS = Oxygen Trapping System). Inert gas conditions were applied (DSC: Ar, DIL, LFA: He). Applied heating rates were 2 K/min in the DIL and 20 K/min in the DSC. Type S sensors were used. Liners were mainly manufactured from Al_2O_3 or sapphire. Dilatometer measurements were done with Y_2O_3 containers too: no significant differences in the chemical behaviour could be detected.

Physical Back Ground and Uncertainty Concept

Physical back ground is the thermal balance of a body, the theory of specific heat, and the phenomenology of thermal expansion. It is to be noticed that a thermally inert material behavior is assumed to ensure conservative conditions. An advanced concept to construct uncertainties of measurement results is deduced from the recommendations of the GUM[2]. Aim is to separate sample related effects (*SSU*) from those traceable back to the measurement devices (*ESU*) and the examining mathematical models (*MSU*)[3]. An overview is given in Fig. 4.
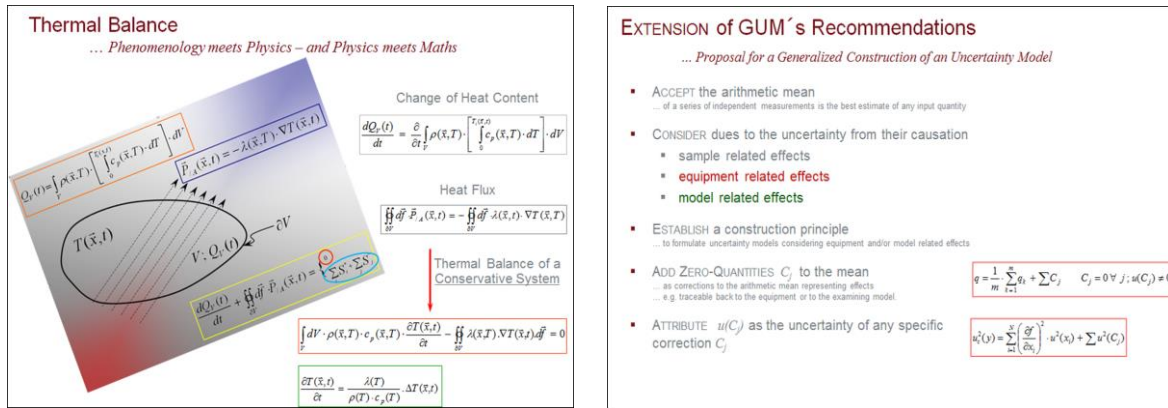
Fig. 4: Physical back ground and uncertainty concept

Results

The thermo-physical properties of a typical representative of a Nickel based superalloy are qualitatively given in a temperature range from ambient temperatures up to 1600 °C. SSU, ESU and MSU are represented.

Specific Heat $c_p(T)$: Based on sufficient raw data, apparent specific heat(= superposition of specific heat and enthalpy effects) and specific heat is given (Fig. 5). An optimized representation of the specific heat is calculated fom a $c_p(T)$ mastercurve – modifying a sapphire curve to fit measured data.
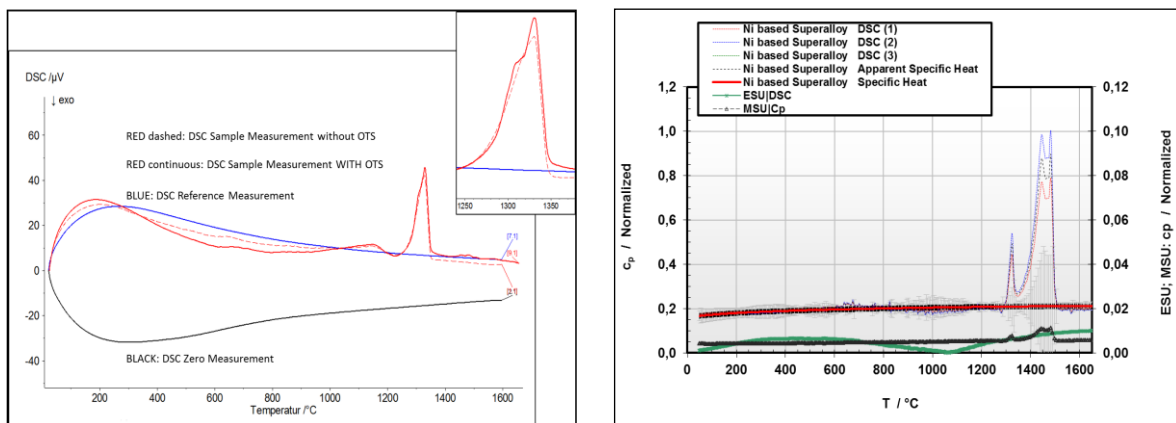
Fig. 5: Comparison of DSC data from measurements with and without use of an OTS system (left) and resulting specific heat data from an OTS improved DSC device (right)

Thermal Expansion $\Delta L/L_0(T)$, $CTE(T)$: Based on solid state measurements and DSC data, the onset of melting was used to adjust results from liquid state measurements. That way results from both expansion regimes could be merged to a suitable presentation of the thermal expansion behaviour (Fig. 6). Notice that *ESU(CTE)* – and $u_c(CTE)$ therefore – shows a singularity at the reference temperature (20°C) from principal reasons!

253
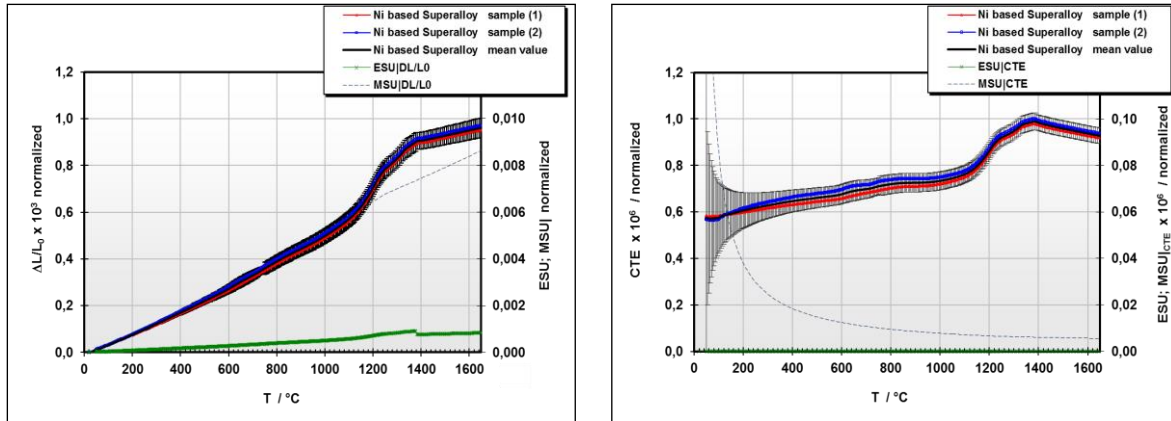
Fig. 6:   *Thermal expansion and linear coefficient of thermal expansion*

Thermal diffusivity *a(T) and thermal conductivity λ(T):* Based on sufficient raw data of the thermal response of the material Cowan-Model was applied to examine thermal diffusivity. No heat pulse correction was necessary. Near 800°C and at temperatures above 1200°C phase reactions are detected. This consequences in increased uncertainty levels. Thermal conductivity was calculated as the product of thermal density, specific heat and thermal diffusivity (Fig. 4 and Fig. 7).
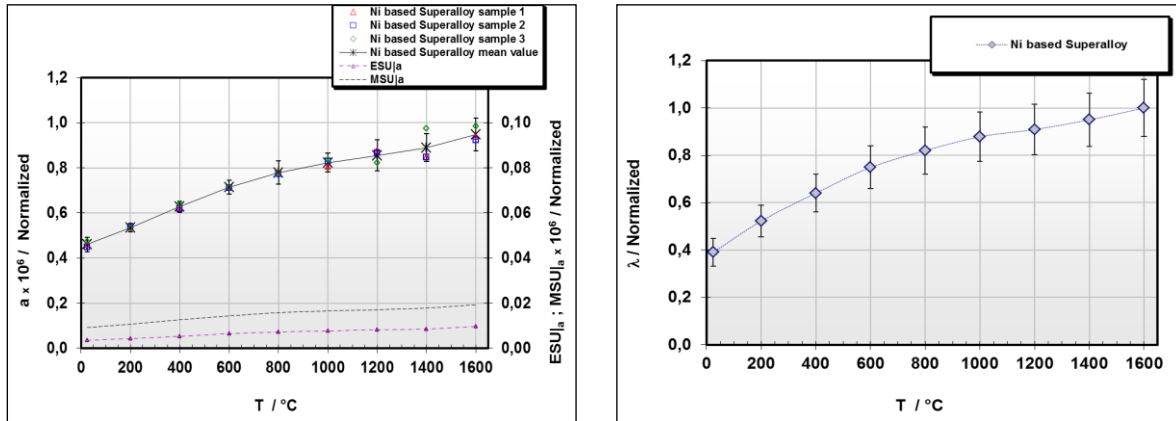
Fig. 7:   *Thermal diffusivity and thermal conductivity*

Conclusions

The thermo-physical properties of a typical representative of a Nickel based superalloy are qualitatively given in a temperature range from ambient temperatures up to some 1600°C. Optimized measuring procedures can be achieved by use of a OTS system (DSC measurements). Dilatometric results are constructed from conventional measurements in solid state and measurements in Al_2O_3 containers. Effective melting onset is detected from DSC results and carefully observed solid state dilatometry. Flash data were used to examine thermal diffusivity. Thermal conductivity is calculated from density, specific heat and thermal diffusivity. An extended uncertainty concept is used: sample related uncertainty contributions (*SSU*), equipment related uncertainty contributions (*ESU)* and uncertainty contributions related to the examining mathematical model (*MSU)* are represented.

References

1   K.D. Maglitsch, A. Cezairliyan, V.E. Peletsky, Compendium of Thermophysical Property Measurement Methods, Plenum Press 1992, Vol 2, (1992)

2   ENV 13005; Guide to the expression of uncertainty in measurement (1999)

3   W. Hohenauer; A Proposal to reduce GUM's Recommendations to Practice in Flash Methods, Proc. Thermophysics 2013, pp 18-23, Slovac Academy of Science in Bratislava (2013)

Investigation of Polyethylene/Graphite Composites and Their Electrical, Thermal and Mechanical Properties

[a] **Igor Novák,** [a, b] **Igor Krupa,** [c] **Ismail H. Tavman,** [a] **Ivan Chodák,** [a, d] **Anton Popelka and** [a] **Marian Valentin**

[a]Polymer Institute, Slovak Academy of Sciences, 845 41 Bratislava, Slovakia,
[b]Center for Advanced Materials, QAPCO Polymer Chair, Qatar University, Doha, Qatar
[c]Dokuz Eylul University, Mechanical Engineering Department, 35397 Tinaztepe
Buca, Izmir, Turkey
[d]Center for Advanced Materials, Qatar University, Doha, Qatar
E-mail: igor.novak@savba.sk

Abstract

Electrical conductivity, thermal conductivity and ultimate mechanical properties, namely elongation at break and stress at break of low and high density polyethylene/graphite composites were investigated in this paper. Percolation concentration at about 11 vol.% of the filler was found. The degree of crystallinity of polyethylene matrix did not have an significant influence neither the percolation concentration nor electrical conductivity of composites. DSC measurement indicated that filler has no significant influence on the change of degree of crystallinity of polyethylene matrices. The thermal conductivity of filled high-density polyethylene is higher then thermal conductivity of filled low-density in the whole concentration range due to higher degree of crystallinity of high density polyethylene. The nonlinear behavior was observed for the dependency stress at break versus filler content. After initial decrease in stress at break, a reinforcing effect was observed. The reinforcing effect was more pronounced for high-density polyethylene matrix.

Introduction

Polymer/graphite composites have long been used in structural, aerospace and sporting goods applications (1–3). Electrically conductive polymeric composites are often used as heating elements, temperature-dependent resistors and sensors, self-limiting electrical heaters and switching devices, antistatic materials for electromagnetic interference shielding of electronic devices (4). The importance of thermal conductivity (5–8) in polymer composites is associated with the need for appreciable levels of thermal conductance in circuit boards, heat exchangers, appliances, and machinery (5). The of information on thermal conductivity of materials is also necessary for modeling of optimum conditions during materials processing, as well as for a analysis of transport of heat in materials during practical applications. Physical behavior of filled polyethylene filled with synthetic graphite particles, namely electrical conductivity, thermal conductivity and ultimate properties was investigated in this paper.

Experimental

Two grades of polyethylene were used as the matrix, namely low density polyethylene Bralen RA 2–19 (MFI = 1.7 g/10 min, density = 0.916 g/cm^3, particle size <50 umikrons) from Slovnaft, Slovakia, high density polyethylene Stamylan HD 9089 V (MFI = 8 g/10 min, density = 0.963 g/cm^3) (DSM, The Netherlands), while graphite (EG-10, synthetic graphite, SGL Carbon, UK) was used as the filler.

The blends were prepared by mixing both components in a 50 m mixing chamber of Brabender Plasticorder PLE 331 at 170 ◦C (LDPE) or 200 ◦C (HDPE) for 10 min at the mixing speed 35 rpm. The dog-bone specimens with a working area 35mm×3.6mm×1mm were cut from the slabs. The mechanical properties were measured at RT using an Instron 4301 universal testing machine (England) at deformation rate 10 mm/min at RT. For the electrical conductivity measurements the prepared composites were compression molded using a laboratory press Fontijne 200 (The Netherlands) at 180 or 200 °C for 2 min under 22.5 kN/cm2. The thickness of the compression molded samples was about 0.2 mm. The volume electrical conductivity in polymer composites was measured according to ASTM D 257. Three-electrode electrometer arrangement was used for the dc-measurement of the resistance. The voltage level used varied in the range 0.1–500V. For thermal conductivity measurements the specimens with 50mm diameter and 10mm thick have been compression molded at 170 or 200 ◦C for 5 min with subsequent cooling under the pressure down to room temperature. The thermal conductivity was measured using multipurpose apparatus (Isomet, Applied Precision, Slovakia) for non-steady state measurement of thermal properties. The data are calculated automatically from a time dependence of the thermal flow in the material.

Results and discussion

Electrical conductivity
The dependency of electrical conductivity of composites LDPE/graphite and HDPE/graphite composites on the filler content is shown in Figure 1. It is seen that around 11 vol. % of the filler, the sharp increase of electrical conductivity was observed in both cases.
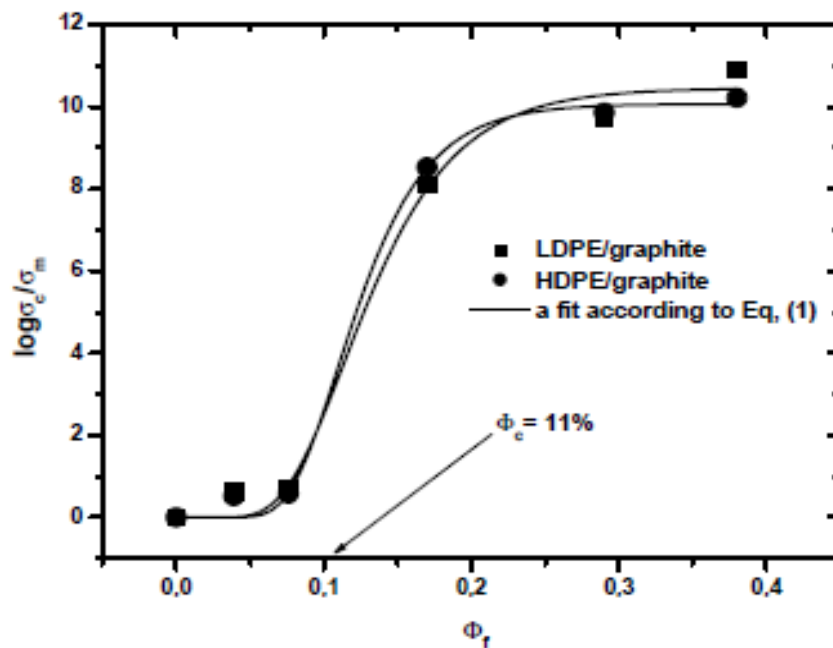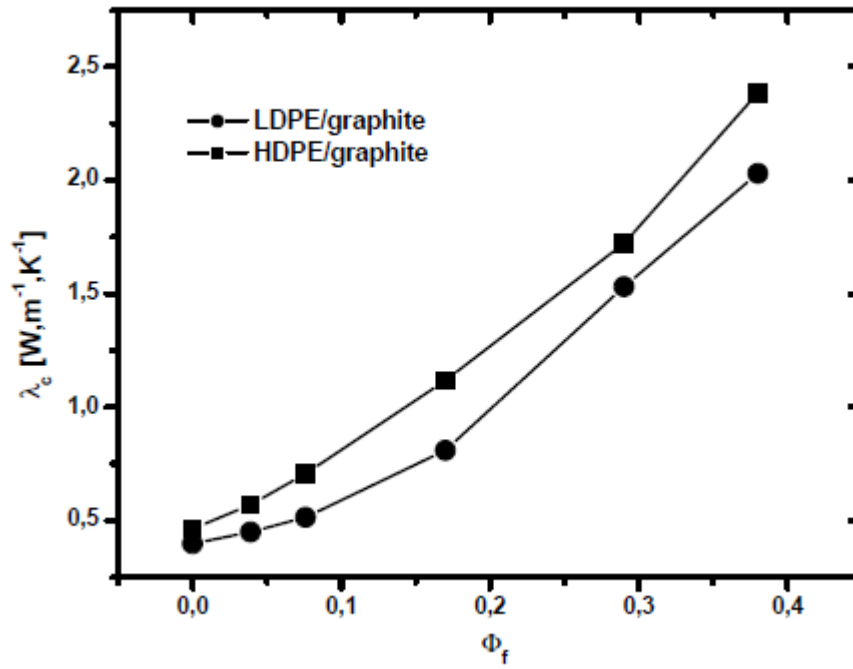

Figure 1. Electrical conductivity (σ_c/σ_m) of the graphite filled LDPE (squares) and HDPE (circles) as a function of the volume filler content (φ_f). Straight line = curve fitting according to Eq. (1).

This concentration is generally called percolation concentration. In this case infinite cluster of particles is formed within a polymeric matrix. This cluster penetrates throughout the sample and represents a conductive way for a movement of electrons throughout the sample. From

this concentration of the filler the material dramatically changes its electrical conductivity and becomes conductive. Since in a real situation only limited number of experimental points is available, we arbitrary identified a percolation threshold as an inflexion point in an empirical fitting curve. For a fitting of experimental data we suggested Eq. (1):

$$\log\left(\frac{\sigma_c}{\sigma_m}\right) = B(1 - e_f^{-a\phi})^n$$

(1)

where B, a, n are adjustable parameters, σ_c is electrical conductivity of composites, σ_m is electrical conductivity of polymeric matrix and φ_f is volume portion of filler.

Thermal conductivity

The thermal conductivity of LDPE, HDPE/graphite composites versus graphite content is shown in Figure 2. It is seen that the thermal conductivity of composites nonlinearly increases with an increase in graphite content. The thermal conductivity of filled HDPE is higher than thermal conductivity of filled LDPE due to higher degree of crystallinity of HDPE matrix. Generally, the most inorganic fillers have much higher thermal conductivity, then polymers and therefore their incorporation in the material leads to an increase in thermal conductivity of composites. Unfortunately, a prediction of thermal conductivity of filled polymers is very difficult and depends on geometry and orientation of filler particles in the matrix, concentration of the filler, ratio between thermal conductivity of the filler and thermal conductivity of the matrix. On the base of these factors, many different models have been already developed, but none of them has general validity (5), since the most of the model are derived for regular shape of particles, flakes or fibers as well as uniform distribution of their size. In our case, particles of the graphite are irregularly shaped and their size exhibit relatively broad size distribution.

Mechanical properties

The dependence of elongation at break on the graphite content is shown in the Figure 3. This dependency is displayed in semi logarithmic scale, due to big differences among values. A steep decrease of elongation at break with an increase in graphite content was observed for both investigated systems.
The initial elongation at break of virgin LDPE decreased from 554% to 4%, when 60 wt.% of graphite was used. The same is true for HDPE, where initial elongation at break decreased from 1610 to 2% at the same filler content. The steepest decrease was observed at the lowest used concentration of the filler (1 wt.%). Elongation at break of LDPE filled with 1 wt.% of graphite was found of 70% and elongation at break of HDPE filled with 1 wt.% of the graphite had the value of 27%. Generally, a decrease of elongation at break with an increase in the filler content is always observed. For description of this behavior, a few models have been suggested, Nielsen's model (9, 10) given by Eq. (2) being the most known:

$$\frac{\varepsilon_{b,c}}{\varepsilon_{b,m}} = 1 - \phi_f^{1/3}$$

(2)

where $\varepsilon_{b,c}$, $\varepsilon_{b,m}$ is elongation at break of composite or matrix, respectively and φ_f is a volume portion of the filler.

Figure 2. Thermal conductivity (λc) of the graphite filled LDPE (squares) and HDPE (circles)
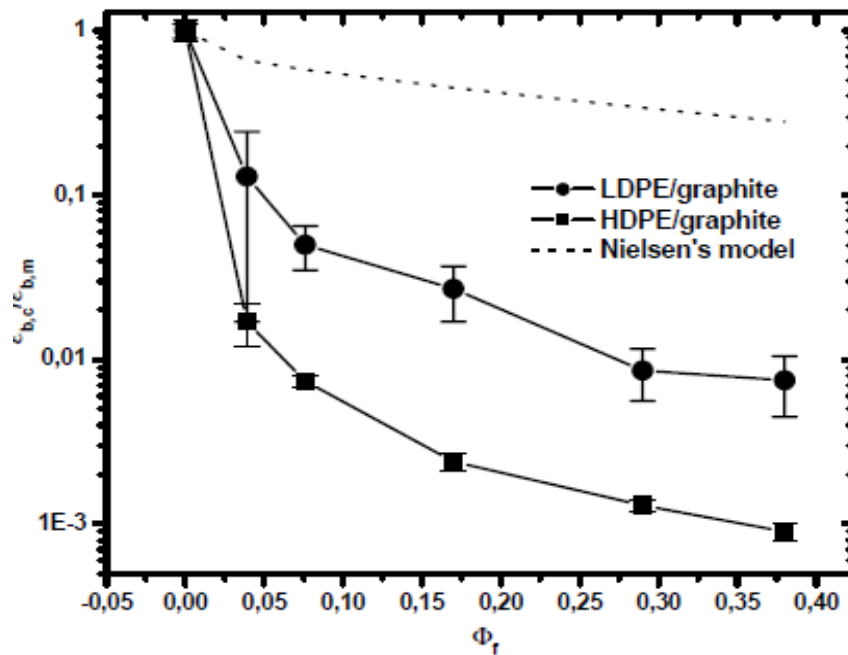as a function of the volume filler content (φf).

Figure 3. Elongation at break ($\varepsilon_{b,c}/\varepsilon_{b,m}$) of the graphite filled LDPE (squares) and HDPE
(circles) as a function of the volume filler content (φ_f). Dotted line = Nielsen's
model.

The use of Nielsen's model is correct only if a deformation is homogeneous. In the case of
polyethylene, a neck is created during drawing and therefore stretching is not homogeneous.
The presence of defects in front of the neck has a critical influence on the drawability.

Conclusion

The electrical conductivity measurements indicated percolation concentration at about 11 vol.% for both polymer systems. The degree of crystallinity of polyethylene matrix does not significant influence neither the percolation concentration nor electrical conductivity of composites. The thermal conductivity measurements of composites showed their nonlinear increase with the increase in graphite content. The thermal conductivity of filled HDPE is higher compared to thermal conductivity of filled LDPE due to higher degree of the crystallinity The sharp decrease of elongation at break with an increase in graphite content for both investigated systems were observed. This decrease is much sharper than a decrease, expected according to Nielsen's model. Very irregular shape of particles of our graphite, which consist of many sharp edges (potential stress concentrators) is more probably responsible for this behavior. The nonlinear behavior was observed for the dependency stress at break versus filler content. The presence of a filler results in both an easier initiation of crack formation via stress concentration on the filler surface on the one hand and in a decrease of chain mobility due to polymer-filler interactions resulting in lower deformability of the material on the other hand.

Acknowledgements

References

[1] T.A. Ezquerra, M. Kulescza, F.J. Balta-Calleja, Synth. Metals **41** (1991) 915.
[2] J. Navarro, A. Roig, P. Noguera, F. Vicente, J. Vilaplana, J. López, J. Mater. Sci. **29** (1994) 4064.
[3] M. Blaszkiewicz, D.S. McLachlan, R.E. Newnham, Polym. Eng. Sci. **32** (1992) 421.
[4] C. Klason, D.H. McQueen, Kubát, Macromol. Symp. **108** (1996) 247.
[5] D.B. Bigg, Adv. Polym. Sci. **119** (1995) 1.
[6] I. Krupa, I. Chodák, Eur. Polym. J. **37** (2001) 2159.
[7] W. Thongruang, R.J. Spontak, M. Balik, Polymer **43** (2002) 2279.
[8] W. Thongruang, R.J. Spontak, M. Balik, Polymer **43** (2002) 3717.
[9] I. Chodák, I. Krupa, J. Mater. Sci. Lett. **18** (1999) 1457.
[10] I. Novák, I. Krupa, I. Chodák, Synth. Met. **131** (2002) 93.

Thermal Conductivity of Epoxy Resin Cross-Linking

[a] Igor Novák, [b] Ludovít Kubičár, [b] Carlos Calvo Anibarro, [b] Viliam Vretenár, [c] Peter Dieška, [d] Ismail H. Tavman, [a] Ivan Chodák

[a]Polymer Institute, Slovak Academy of Sciences, 845 41 Bratislava, Slovakia,
[b]Institute of Physics, Slovak Academy of Sciences, 845 11 Bratislava, Slovakia
[c]Faculty of Electrical Engineering and Information Technology, Slovak University of Technology, 812 19 Bratislava, Slovakia
[d]Dokuz Eylul University, Mechanical Engineering Department, 35397 Tinaztepe, Buca, Izmir, Turkey
E-mail: igor.novak@savba.sk

Abstract

In the presence of selected cross-linking agents epoxy resins are able to polymerize creating a three dimensional (3D) net. During cross-linking different physical processes in epoxy resin can be detected, mainly formation of polymer chains and 3D net formation. A new thermal conductivity sensor was used for detection of the cross-linking process., that is based on the hot-ball method for determination the thermal conductivity and recognizes the polymerization processes. This paper is devoted to study of cross-linking process in the system diglycidylether of bisphenol A (BADGE) epoxy resin modified with aromatic reactive diluent, where the curing rate was controlled by temperature and cross-linking agent (boron trifluoride).

Introduction

The differences between standard and transient methods are based on the varieties of specimen sizes, measuring time, and measured parameters number (1). Improvements in the methodology of transient methods and the use of up-to-date electronic elements led to the construction of portable instruments and monitoring systems significantly simplifying the operation (2, 3). The needle probe (3) and the hot-bridge [4] sensor have been most frequently used in portable instruments. The hot-ball sensor in a two-component configuration (as a heat source and thermometer fixed apart from each other) has been recently published (5, 6). The sensor is based on the spherical symmetry of the temperature field. This contribution is devoted to application of the hot-ball sensor in a single-function configuration for curing process of epoxy resin monitoring (7-11) based on of bisphenol A diglycidyl ether (BADGE) cross-linking by boron trifluoride complex with mono ethylamine (BTF–MEA). The characteristic process of cross-linking, i.e., the transition fluid/solid state was investigated.

Experimental

Material
BADGE epoxy resin (Spolchemie, Czech Republic) and BTF–MEA complex (Synpo, Czech Republic) were used for experimental purposes.

Instrumentation
A set of the instruments was used for monitoring of the curing process: temperature stabilized chamber of instruments RT 1.02 (Transient MS), a vessel filled by the studied epoxy reaction mixture and an RTM monitoring system (Transient MS). A copper vessel with inside

diameter and height of 20 mm was placed in the temperature-controlled chamber. The hot-ball sensor was fixed in the center of the vessel. The monitoring procedure consists of the following: the temperature of the chamber was set to the curing temperature. The reaction mixture (resin and cross-linking agent) was poured into the vessel at room temperature. Room-temperature values of the thermal conductivity of the reaction mixture were taken by an RTM 1.01 instrument. Then the vessel was fixed in the chamber heated to 70 $^\circ$C and then the monitoring was started.

The analysis of the *thermal conductivity* λ will be started on the basis of the well-known formula used in a gas that for insulations reads:

$$\lambda_{ph} = (1/3)\bar{v}_G C_V \bar{l} \tag{1}$$

where C_V is the harmonic part of the heat capacity, $\bar{v}_G$ is the mean phonon group velocity and $\bar{l}$ is the average mean free path of phonons that is usually used in experimental analysis. For *thermal diffusivity* can be witten:

$$a = (1/3)\bar{v}_G \bar{l} \tag{2}$$

Hot ball construction

A hot ball sensor can be constructed of single component like thermistor, and RTD resistance. One component configuration requires a more sophisticated electronic as the component should generate a constant heat rate and simultaneously it should measure its temperature change. Our approach is to separate these functions into two components to limit mutual interference (patent pending). A hot-ball sensor has been constructed consisting of two elements, a heater and a thermometer. Both elements are fixed in the ball using epoxy resin. The hot-ball diameter ranges from 1.8 to 2.3 mm. A simple instrument was constructed that consists of a data logger, a microcontroller connected with A/D converter for temperature measurement and a D/A converter in connection with current source for heat generation. The instrument can be pre-programmed through USB channel by a PC computer.
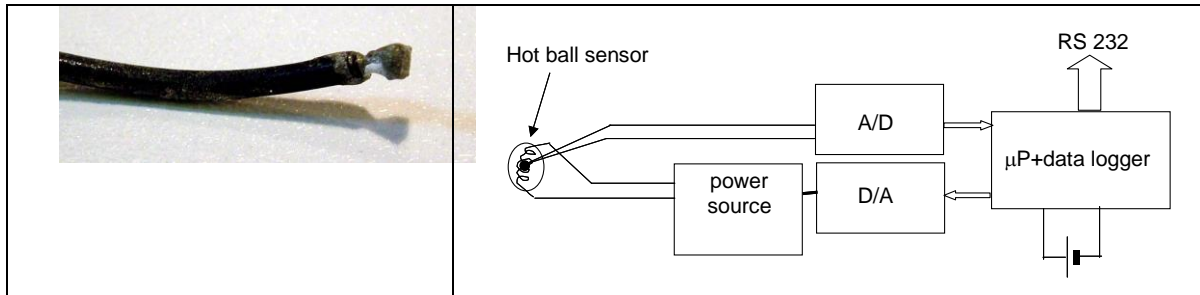
Figure 1. Photo of hot ball sensor (left) and the scheme of the instrument RTM for monitoring thermal conductivity.

Thermal properties measurement

Instrument RT 1.02 (Figure 2, right) (Transient MS) was used for monitoring of the curing process together with the vessel filled by the studied suspension (Figure 2, left).
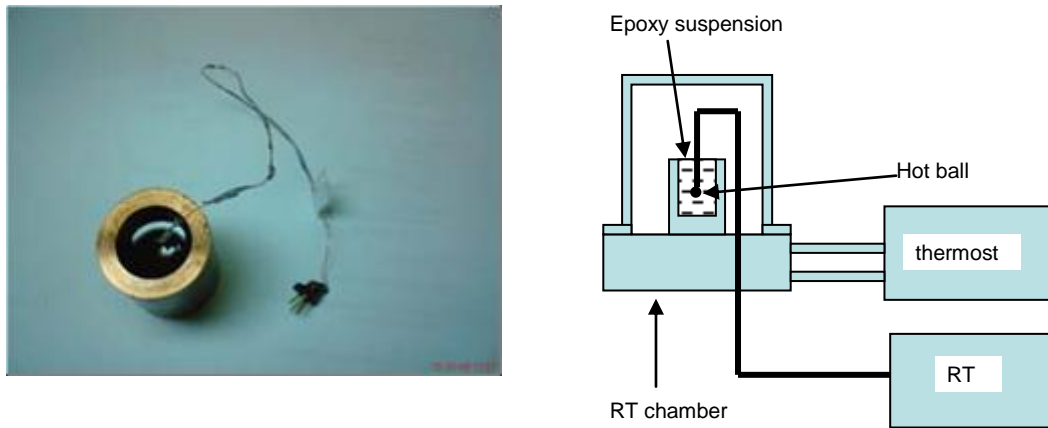
Figure 2. Experiment scheme (right) and epoxy filled vessel with fixed hot ball (left).

The vessel made of copper with both inside diameter and height of 20 mm was fixed in the instrument. The sensor for measurement of thermal conductivity (Figure 2, left) was fixed in the center of the vessel. The monitoring procedure consists of the following: The temperature of the chamber of the instrument RT 1.02 was preheated on the level of the curing temperature. The epoxy suspension (resin and hardener) was mixed together and poured into the vessel at room temperature. The room temperature values of the thermal conductivity of suspension were taken by RTM 1.01 instrument. Then the vessel was fixed into the heated chamber of the RT 1.02 and the monitoring started, using instrument RTM 1.01. A heat output $q = 9$ mW and measuring time $t = 600$ s was used for monitoring regime.
Characteristics of studied epoxy ChS Epoxy 513 are given in Table 2.

Table 2. Characteristics of investigated epoxy system

Epoxy resin	ChS Epoxy 513
Hardener	Boric trifluoride
Molecular weight [g/mol]	800
Viscosity [mPa.s]	23

Detail temperature plot is shown in Figure 3 to find how good isotherm was reached during the curing process. The desired measuring regime requires a negligible reaction rate in comparison to the measuring time. However a small temperature increase was found during curing process that indicates an exothermic reaction. A detailed inspection of this temperature increase indicates that formation of blocks is accompanied by heat production, i.e. an exothermic reaction.
The curing of epoxy acrylate resin ChS Epoxy 513 mixed with complexes of boron trifluoride (BF_3) proceeds according to a cationic polymerization mechanism. The BF3 amine complex is a latent catalyst, that is, it is inactive at room temperatures and requires elevated temperatures to be activated. Above a certain temperature, in our case 70 ^{o}C, the amine complexes cause rapid cross-linking. A detailed study of the curing process has shown that formation of blocks and cross-linking can be distinguished using our measuring technique. The formation of blocks immobilizes the configuration regroupings of polymeric chains. As a result a strong reduction of configuration entropy is caused. Cross-linking, in a fact, is based on the same type of reaction like formation of blocks. The only difference is that formation of blocks runs among the polymer chains and cross-linking among the blocks. Cross-linking of blocks increases viscosity and thus the shear module is growing. Characteristic data of the curing process are given in Table 2.
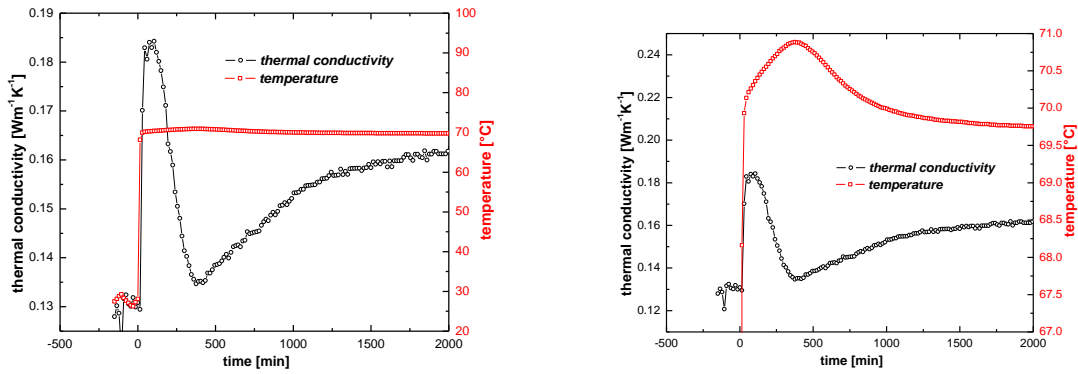
Figure 3. Thermal conductivity and temperature of the ChS Epoxy 513 as a function of temperature during curing process (left).

Table 2. Characteristics data of epoxy system curing process specified in Table 1.

Epoxy	Curing temperature [°C]	$\lambda_{room\ T}$ [W m^{-1} K^{-1}]	λ_{min} [W m^{-1} K^{-1}]	λ_{final} [W m^{-1} K^{-1}]	Time of curing [min]
ChS Epoxy 513	70	0.13	0.135	0.162	1600

Conclusion

A new transient method modification, the hot ball method for thermal conductivity measuring has been discussed. This method is based on delivering constant heat by a heat source in the form of a ball into the non-limited surrounding medium for times t > 0. A hot ball sensor has been constructed consisting of two elements a heater and a thermometer. Both elements are fixed in a ball by epoxy resin. Diameter of the ball ranges within 2÷2.3 mm. A simple instrument based on data logger in connection with the microcontroller was used to realize monitoring regime. A working equation of the hot ball based on a model of the empty sphere in a non-limited surrounding medium has been found. Main disturbing effects of the measuring process are listed. Irregularities of the hot ball and the contact with the surrounding medium represent the most significant contribution to the measuring error. Calibration procedure using a set of materials was used to eliminate data shift caused by disturbing effects. Calibration was performed in the thermal conductivity range from 0.026 to 0.5 W m K. Application of the hot ball method for epoxy resin curing, using boric compound BF3, has been presented. The curing process was monitored by measuring thermal conductivity. Two stages of the curing process was detected, namely formation of blocks and cross-linking. While former causes drop of heat capacity due to vanishing of configuration entropy, the latter one increases thermal diffusivity due to growth of phonon velocity and its free path. The former immobilizes structural units, the latter forms chemical bonds that are responsible for growth of elastic constants. A competition of these two parameters yields the final value of thermal conductivity.

Acknowledgements

References

[1] J. Krempaský, Meranie termofyzikálnych veličín (Vyd. SAV, Bratislava, 1969), p. 1–288 (in Slovak).

[2] Ľ. Kubičár and V. Boháč, in: Proceedings of 24th Int. Conf on Thermal Conductivity, 12th Int. Thermal Expansion Symposium, October **26-29** (1997), 135.

[3] N. Lockmuller, J. Redgrove, Ľ. Kubičár, High Temp. High Press. **35-36** (2003/2004) 127.

[4] U. Hammerschmidt, W. Sabuga, Int. J. Thermophys. **21** (2000) 1255.

[5] Ľ. Kubičár, V.Vretenár, V. Štofanik,· V. Boháč, Int. J. Thermophysics 2008, 145.

[4] J. Krempaský, Meranie termofyzikálnych veličín (Vyd. SAV, Bratislava, 1969) 1 (in Slovak).

[5] Ľ. Kubičár and V. Boháč, in: Proc. of 24th Int. Conf on Thermal Conductivity, 12th Int. Thermal Expansion Symposium, October **26-29** (1997) 135.

[6] Haifeng Zhang, Liqun He, Shuxia Cheng, Zaiteng Zhai, Dayong Gao, Meas. Sci. Technol. **14** (2003) 1396.

[7] G. Grimvall: Thermophysical properties of materials. North-Holland (1986) 3.

[8] Ľ. Kubičár, V. Vretenár and V. Boháč: Study of Phase Tran Method, Solid State Phenomena **138** (2008) 3.

[9] R.O. Pohl, X. Liu and E. Thompson: Rev. Mod. Phys. **74** (2002) 991.

[10] R E Smith and C. H. Smith, Journal of Applied Polymer Science, **31** (1986) 929.

[11] T Spychaj, J. A. Soroka and A Bledzky, Journal of Thermal Analysis, **29** (1984) 965.

The Effect of Thermal Cycles on the Mechanical Properties of High Density Polyethylene (HDPE) and Graphite/HDPE composites

Kutlay SEVER [1], Ismail H. TAVMAN [2], Mehmet SARIKANAT [3], Yoldaş SEKİ [4], İsmail ÖZDEMİR [1], Alpaslan TURGUT [2]

[1] İzmir Katip Çelebi University, Departmant of Mechanical Engineering, Çiğli, İzmir
[2] Dokuz Eylül University, Departmant of Mechanical Engineering, Buca, İzmir
[3] Ege University, Departmant of Mechanical Engineering, Bornova, İzmir
[4] Dokuz Eylül University, Departmant of Chemistry, Buca, İzmir

Abstract

In this study, the Graphite/HDPE composites having different graphite content were prepared by melt blending. The graphite content was in the range of 2 to 30 wt%. To investigate the effect of thermal cycles on the mechanical properties of HDPE and graphite/HDPE composites, HDPE and each composite samples were subjected to the thermal cycle processes for 100, 200 and 400 times between temperatures of $85^{o}C$ and $-25\ ^{o}C$. The moduli of HDPE and HDPE/GR composites at the end of each thermal cycle at 100, 200 and 400°C increased.

Introduction

With the increased use of polymeric composites in many industrial areas, it is necessary to understand the mechanical behavior of the composites having cyclic temperature changes. The effect of temperature on the stiffness of polymers is probably most important with regard to the design and use of polymers for load bearing engineering applications[1].

The primary objective of this paper is to determine the effect of thermal cycles on the mechanical properties of HDPE and graphite/HDPE.

Materials

High density polyethylene (HDPE- I-668) having density of 0.968 g/cm3 and melt flow rate of 5.8 g/10 min was supplied by Petkim A.Ş., İzmir. Graphite powder with an average particle size of 400 nm and purity of 99.9% was purchased from Nanostructured and Amorphous Materials, Inc.-Houston, USA.

Composite Preparation

The composites were prepared by melt blending in a chamber of a Brabender Plasticoder PLE 331 mixer. Graphite powder and HDPE were mixed for 15 minutes at a screw speed of 35 rpm and temperature of 180 ^{0}C. Different compositions having various graphite content have been prepared. The graphite content was in the range of 2 to 30 wt%. After the composite preparing step, the mixture obtained was taken out. Afterwards, after passing through the rollers and the mixture was solidified. Then, each mixture was put in a mold and thin sheets of 1 mm were obtained by compression moulding for 5 min at 120 °C under 40 kPa in a hot press.

Thermal cycles of Composites

Firtsly, composites were heated to a maximum temperature of 85 ^{o}C and hold for 5 seconds in temperature of 85°C. Then they were cooled at a minimum temperature of −25 ^{o}C and hold for 5 seconds in temperature of −25°C. The thermal cycle processes were repeated 100, 200 and 400 times for each composite samples.

Tensile Test

Tensile tests were performed on Shimadzu Universal testing machine at a fixed crosshead speed of 3 mm min-1. Samples were prepared according to ASTM D 638.

Mechanical Properties

Tensile strength, Young modulus and elongation at break of high density polyethylene (HDPE) and high density polyethylene/graphite (HDPE/GR) composites were shown in Table 1. Increases in tensile stress and Young modulus of the HDPE matrix after graphite is incorporated into HDPE were determined. The Young modulus of the HDPE/GR composites increased continuously with increasing graphite content. An improvement of about 136% in Young modulus was investigated with an addition of 20 wt.% of graphite. However, the highest tensile strength was obtained with 4 wt.% graphite. At this loading, 42.3 %

enhancement in tensile strength was observed. Obviously, graphite has reinforcing effect. Besides, the degree of increase in each mechanical property after thermal cycle processes was different for HDPE and the composites. When the thermal cycle processes were repeated 100, 200 and 400 times for HDPE, the most effect for tensile stress of the HDPE was observed after thermal cycle of 100 times. Namely, tensile strength of the HDPE increased by 17.7 %. It is interesting to note that the elongation break value of the HDPE decreased from 912.7 to 15.6 %. However, when the thermal cycle processes were repeated 400 times for HDPE, the most effect for Young modulus of the HDPE was investigated after thermal cycle of 400 times. That increase was 180.4 %. The variations of mechanical properties with increase in number of thermal cycles were shown in Figure 1-2. The moduli of HDPE/GR composites at the end of each thermal cycle at 100, 200 and 400°C increased. When the number of thermal cycles increases to 400 cycles, the Young modulus of the HDPE90/GR10 composites increased by % 56.5. The most effect on the modulus was observed for HDPE90/GR10 composites. We note that the composites of this study did not show any variation in the tensile stress when tested in thermal-cycling.

[1] S. Bal, D. Mahesh, T.K. Sen and B.C. Ray, Effect of Changing Environments on Microstructure of HDPE Polymer, Journal of Minerals & Materials Characterization & Engineering, Vol. 6, No.1, pp 1-16, 2007

Acknowledgments

Sample name	weight fractıon (%)	number of thermal cycles	Maks.tensile stress (Mpa)	Young Modulus (Gpa)	elongation at break (%)
HDPE	0	0	23,31±1,41	0,56±0,04	912,65±62,43
	0	100	27,43±0,30	0,75±0,08	15,61±0,55
	0	200	27,12±1,12	1,17±0,13	15,15±0,70
	0	400	26,68±0,12	1,57±0,16	14,36±0,80
HDPE96/GR4	4	0	33,18±1,46	0,67±0,06	380,52±26,75
	4	100	34,16±1,67	0,72±0,05	21,36±1,35
	4	200	34,84±2,41	0,80±0,04	19,63±1,01
	4	400	33,98±1,82	0,84±0,03	18,05±1,53
HDPE90/GR10	10	0	32,74±1,51	1,08±0,05	34,42±4,63
	10	100	32,15±2,20	1,11±0,04	9,63±0,24
	10	200	32,46±2,76	1,41±0,04	7,56±0,36
	10	400	32,34±1,69	1,69±0,03	6,12±0,21
HDPE80/GR20	20	0	28,46±1,87	1,32±0,04	24,32±0,12
	20	100	28,40±1,09	1,42±0,05	8,95±0,16
	20	200	28,58±2,10	1,63±0,04	8,62±0,13
	20	400	28,72±2,24	1,84±0,39	8,55±0,21
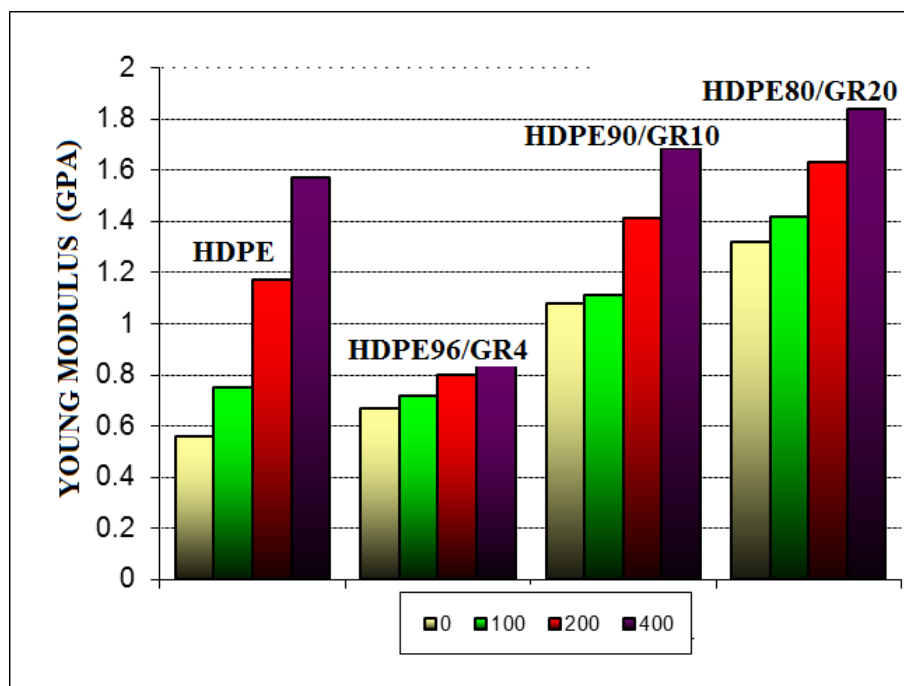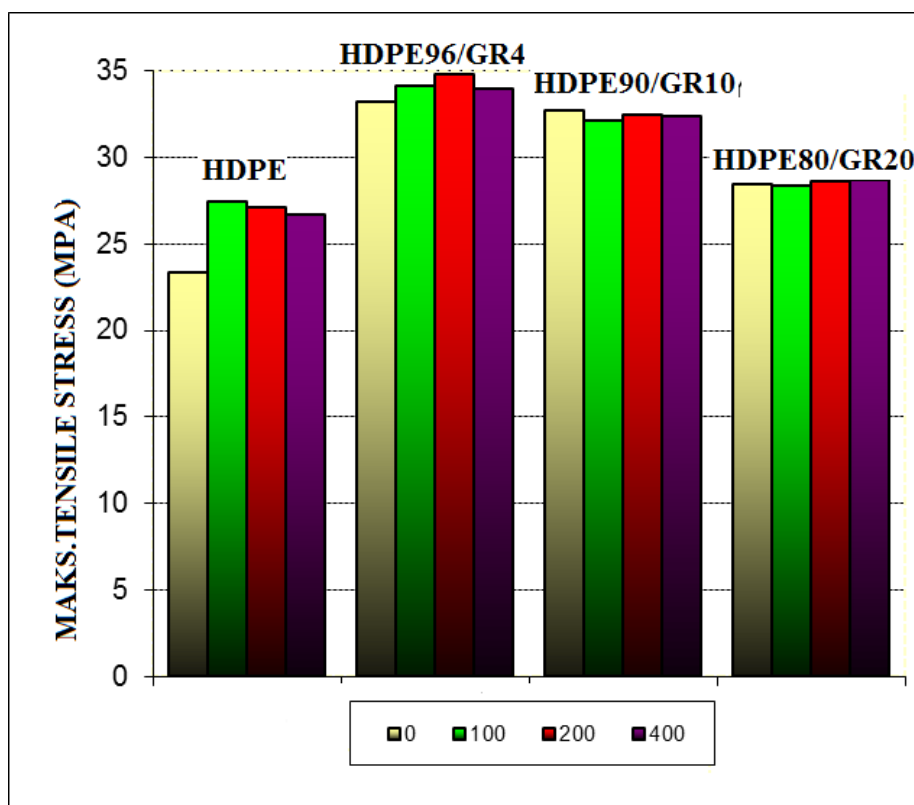
Influence of Thermal Cycling on Tensile Properties of Expanded Graphite/High Density Polyethylene Nanocomposites

Mehmet SARIKANAT [1], Kutlay SEVER [2], Yoldaş SEKİ [3], Ismail H. TAVMAN [4], Alpaslan TURGUT [4], İsmail ÖZDEMİR [2],

[1] Ege University, Departmant of Mechanical Engineering, Bornova, İzmir
[2] İzmir Katip Çelebi University, Departmant of Mechanical Engineering, Çiğli, İzmir
[3] Dokuz Eylül University, Departmant of Chemistry, Buca, İzmir
[4] Dokuz Eylül University, Departmant of Mechanical Engineering, Buca, İzmir

Abstract

In this study, expanded graphite (EG) /high density polyethylene (HDPE) nanocomposites having concentrations of 2–20 wt.% were prepared by the melt-mixing process. EG5 and EG50 flakes have 5–7 µm in diameter and 40–55 µm in diameter, respectively. HDPE matrix and the nanocomposites were subjected to the thermal cycle for 200 times between temperatures of -30 ^{o}C and 90 ^{o}C. After thermal cycling, the tensile properties of HDPE matrix and the nanocomposites were investigated. The tensile strengths and Young moduli of HDPE and EG/HDPE nanocomposites after thermal cycling of 200 times increased. It was found that HDPE showed the best modulus enhancement after thermal cycling.

Materials

High density polyethylene (HDPE BP 5740 3VA) having a melting enthalpy of 199 J/g and a melting temperature of 129.3 ^{o}C was obtained from British Petrol (UK). EG5 and EG50 as expanded graphite fillers were used. EG5 having particle sizes of 5–7 µm in diameter and EG50 having 40–55 µm in diameter were provided by SGL Technologies GMBH (Germany). Real density of the fillers is 2.25 g/cm3.

Composite Preparation

The nanocomposites were prepared by melt mixing in a Brabender Plasticorder PLE 331 mixer (Germany) at temperature of 180 oC and a screw speed of 35 rpm for 15 min. EG/HDPE nanocomposites having various expanded graphite concentrations (wt%) were prepared. The graphite content was in the range of 2 to 20 wt%. Afterwards, compression

molding was applied to the polymer based materials the at 180 °C under 45 kPa for 1 min in a hot press(Fontijne 200, The Netherland) for forming sheets of 1 mm in thickness.

Thermal cycling Process

In thermal cycling process, HDPE and the nanocomposites were heated to a maximum temperature of 90oC and hold for 5 seconds in this temperature. Then they were cooled at a minimum temperature of −30oC and hold for 5 seconds in this temperature. The thermal cycle process were repeated 200 times for HDPE and each nanocomposite sample.

Tensile Test

Tensile tests were carried out on universal testing machine (Shimadzu Autograph AG-G, Japan) at a crosshead speed of 1 mm min^{-1}. Tensile test samples were prepared according to ASTM D638 standard.

Mechanical Properties

Variations in tensile strength and Young's modulus of HDPE and EG-HDPE composites after thermal cycling were presented in Table 1. Table 1 shows that values of tensile strengths and Young modulus of HDPE and EG/HDPE nanocomposites increased with thermal cycling of 200 times. The tensile strength of HDPE increased from 23.01 MPa to 27.12 MPa. For EG/HDPE nanocomposites, the most increase in tensile strength was obtained for HDPE/EG5 (90/10). The tensile strength of HDPE/EG5 (90/10) nanocomposite increased from 31.55 MPa to 34.26 MPa. While the increments was about 8.6 % for HDPE/EG5 (90/10), the increments was about 17.9% for HDPE.

While the Young modulus of HDPE is 510 MPa, it increased to 1170 MPa after thermal cycling. For EG/HDPE nanocomposites, the most increase in Young modulus were obtained for HDPE/EG5 (98/2) composite. After thermal cycling, the Young modulus of HDPE/EG5 (2/98) nanocomposite increased from 0.418 GPa to 0.623 GPa. Namely, while increase in Young modulus of HDPE/EG5 (98/2) was about 49 %, increase in Young modulus of HDPE

was 129.4%. Variations in Young modulus of EG/HDPE nanocomposites after thermal cycling were less.

Acknowledgments

Table 1. Tensile strengths and Young's moduli of HDPE and EG-HDPE nanocomposites after thermal cycling

Sample	Tensile strength (MPa)		Young Modulus (GPa)	
	0	200 cycle	0	200 cycle
HDPE	23.01	27.12	0.51	1.17
HDPE/EG5 (98/2)	35.71	37.52	0.418	0.623
HDPE/EG5 (90/10)	31.55	34.26	0.526	0.754
HDPE/EG5 (80/20)	28.72	30.12	0.745	0.812
HDPE/EG50 (98/2)	34.95	35.16	0.858	1.265
HDPE/EG50 (90/10)	33.22	34.86	1.214	1.435
HDPE/EG50 (80/20)	29.86	32.18	1.634	1.834

Artificial Conglomeration on The Basis of The Low-Temperature Sulfoalyuminatny Cements Modified by The Composition Component "Metakaolin-Fosfoangidrit"

Atabayev F.B.

Research and development and test center "Strom" in case of Institute of the general and inorganic chemistry of Academy of Sciences of the Republic of Uzbekistan, Tashkent

Abstract: In the conditions of the sharp growth of a share of the private sector in construction when are erected one - two - three - and multi-storey residential, public, office buildings, are imposed to their design and architectural design special requirements in the plan not only reliability and longevity, but also architectural expressiveness, production of the modern construction materials of finishing assignment according to energetically favorable technological diagrams with use of local natural and technogenic raw material resources is required.

Keywords: Polymer composition, chemical reactant, physico-chemical properties of drilling fluids.

1 Introduction

Thus special attention needs to be paid to a question of the organization of production of the white and color cements providing a combination national architectural traditions and the modern color in design of facades of objects under construction. In this regard, now in Uzbekistan research and development operations on development of effective compositions, optimization of production of the appropriate brands and sorts of decorative cements with complex use of local mineral raw material and technogenic resources, including a phosphite and local kaolinic clays as they represent huge raw potential for production of decorative cements and composition knitting materials are widely unrolled. Now in dumps of the chemical companies of the republic more than 100 million phosphite which is of interest as valuable raw materials to production of different construction materials and products are accumulated. The favorable chemical composition the kaolinizirovannykh of breeds also allows their complex use as as a principal component of a raw compound for receiving clinker of white cement, and the active mineral component to it. In this operation results of researches on development composition knitting finishing assignment on the basis of the cements low-temperature the sulfoalyuminatnykh modified by the composition mineral component "metakaoline-фосфоангидрит" are provided.

Objects and methods: In operation as a matrix the clinker synthesized by roasting in case of 1250-1300os to a compound of limestone, kaolinic clay and a phosphite is used sulfoalyuminatno-silicate (SAB). For obtaining the composition component "metakaoline-фосфоангидрит" the compound of kaolinic clay and a phosphite in the ratio 1:1, 1:2, 1:3, 2:1, 3:1 subjected thermoactivations in case of 700-750os with exposure of 1 hour. The level of substitution of SAB of clinker on composition "metakaoline - фосфоангидрит" made 10-30%. Durability composition knitting in case of compression determined on samples cubes by the sizes of edges of 1,41 cm of composition 1:0 in 3, 7, 28, 90 and 160 days of solidification, hydration kinetics, the composition of new growths and genesis of formation of an artificial conglomeration researched the RFA and SEM methods.

It is set that joint introduction фосфоангидрита (Fa) and metakaoline (Мк), depending on a component ratio and a dose of the entered component, differently influences process of solidification and hydraulic activity the sulfokompozitsionnykh of the knitting: in case of the maintenance of 6-7% of Fa and 4-8% of Me process of solidification of SAB of cement is a little decelerated that to 3 days leads to lowering of activity of a being created aggregate of an order on 2,0 MPas, and then the set of durability is accelerated, as a result aggregate durability on 2-3 MPas exceeds durability of the initial SAB of cement. With age curings bigger hardening of a sulfovyazhushchy aggregate is watched still: by 3rd and 6 months its durability respectively on 4,54-8,04 MPas and 1,38-8,04 MPas is higher, than at a matrix.

Changeover of 20% by the sulfoklinkerny component composition component including 10% for Fa and 10% of MK has no essential impact on process of solidification of SAB of cement: durability of samples remains at the level of a matrix. Change of a ratio of components of this component towards reduction of the maintenance of Fa and corresponding increase in Mk (Fa's 8% + 12% of MK) promotes deceleration of process of solidification and lowering of initial durability сульфокомпозита to 9,82 MPas. However as a result of an acceleration of process of hydration and solidification in the subsequent periods it is characterized by higher rates of durability (19,12 MPas), than at a matrix (16,06 MPas). Such high rate of a set of durability showed this composition of composition also in case of the long solidification: to the 3rd and the 6th months durability of samples respectively on 5,43 and 3,58 MPas exceeded matrix indexes.

The raised dosage of composition "metakaolin-fosfoangidrit" in SAB cement, irrespective of a ratio of ingredients, sharply decelerates solidification process in initial periods, and, with increase in quantity of Mk due to Fa's corresponding reduction, the speed of a set of durability of samples during 3-28 days is decelerated, and by 3rd and 6 months process of solidification is intensified and сульфокомпозит, the containing 30% of the composition component including 5-10% for Fa and 20-25% for Mk possesses the same durability, as at samples from cement SAB. The optimum dose of composition "metakaoline - фосфоангидрит", providing the highest rates сульфокомпозита, makes 10-20%, and the ratio of Fg and Mk in the initial compound of the composition component shall is in limits 1:1 and 1,5:1. In case of such contents of the component strengthening indexes of samples steadily raise and by 6 months almost by 1,5 times exceed matrix indexes.

Primary products of hydration composition knitting, containing the component "metakaolin-фосфоангидрит", are гидросульфоалюминаты calcium, probably two-water plaster and C3AH6 which make a crystalline frame of skeletal structure of the being created artificial conglomeration which speed of formation depends on a level of saturation of the reactionary environment ions of Sa2 +, Al3 +, SO42-: skeletal forms of crystals, as we know, are found in that case when a supply of a growing crystal happens by diffusion in strongly viscous solution, as it is possible in case of big saturation. The microstructure of the aggregate containing metakaoline and фосфоангидрит, is formed by acicular crystals эттрингита and short fibers of C-S-H, the dense structures of lamellar C-S-H and the bound crystalline hydrate new growths.

The favorable combination of minerals of sulfoalyuminatny clinker (C4A3 Ŝ, C5S2 Ŝ), фосфоангидрита (With Ŝ) and the metakaoline (Al2O3.SiO2), being in a high-reactionary status, provides high supersaturation of the reactionary environment by ions of A13+, Sa2 +, to SO2-and the intensive new growth which crystalline products to 7 days chaotically settle down in all volume of the being hydrated environment, then continue to grow together with each other, creating parallely oriented units which in process of the growth and a sequential lamination will form the monolithic structure providing high physicomechanical and construction and technical properties сульфоконгломерата which strength indices by 1,5-2 times are exceeded by durability of sulfoalyuminatno-belite cement (rice).
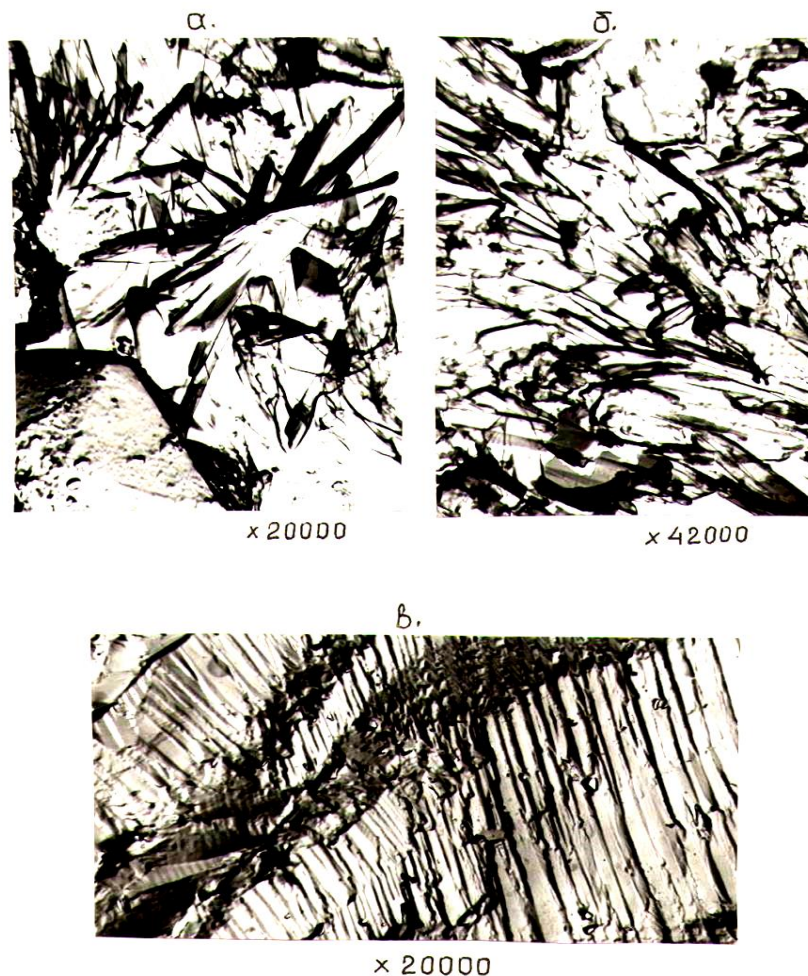
Composition: 70% of SAB clinker + 30% of the component
with a ratio of Mk: Fa = 1:1
**Structure of a surface of a chip сульфоконгломерата through
7 days of solidification**

Inference

Thus, developed power - and the resource-saving technology, thanks to creation of conditions for directional formation of phase composition and a microstructure artificially a conglomeration on the basis of non-traditional composition composition knitting, provides complex use of two large-tonnage waste – a phosphite and kaolinic clay as a component сырьевойсмеси by production of sulfoalyuminatno-silicate clinker, and the composition active mineral component in case of its grinding with receiving the sulfokompozitsionnykh the vyazhushchykh of decorative assignment in which the developing construction industry of Uzbekistan is in great need. The offered method is effective as in respect of increase of operational reliability, improving of depth of tone decorative knitting, and lowerings of expenses of energy resources on their production, therefore - product cost and improvement of industrial ecology.

Low Velocity Impact Response of Sandwich Composites With Different Core Thicknesses

Aidel Kadum Jassim AL-SHAMARY [1], Ramazan KARAKUZU [2], Okan ÖZDEMİR [3]

Department of Mechanical Engineering, Dokuz Eylul University,
E-mail: adel_kadum500@yahoo.com

Abstract

Due to their excellent mechanical properties over metallic materials, structural sandwich composites are commonly used in various engineering applications like aerospace, automotive and wind turbine blades and so on. Sandwich composites used in these applications are often subjected to transverse impact loads resulting in different damage modes. Since these damage modes can cause significant decrease in the composite stiffness, the impact properties of sandwich composites have been investigated by many researchers.

In the present work, sandwich composite plates were manufactured by using vacuum assisted resin infusion molding (VARIM). E-glass fabrics 0/90 having density of $300g/m^2$ as a reinforcing material and Epoxy ARALDITE LY 1564 SP resin and ARADUR 3487B hardener as a matrix material were used. The stacking sequence of sandwich composites was considered as [0/90/0/core/0/90/0] and AIREX PVC foam core in three different core thicknesses (5, 10 and 15mm) was selected as a core material.

It is seen from the contact force-deflection curves that there are two peaks at higher impact energy levels which demonstrate the failure of upper and bottom face sheets, respectively. Also, the contact force values decrease by increasing the core thickness while maximum deformation values increase by increasing the core thickness. According to photos of cross section area, the fiber cracks, matrix cracks and delamination between face sheets and core material were observed.

Keywords: PVC foam, core thickness, sandwich composite, low velocity impact

1. Introduction

 Sandwich composite is increasingly used in the various constructional applications including aerospace vehicles, wind turbine blades, complex aircraft and automobile parts because of high mechanical strength and bending stiffness etc. which is obtained from E-glass as reinforcement fibers bonded to the lightweight core material with different thickness.

Atas & Sevim [1] carried out experimental investigation for impact response of sandwich composite panels between PVC foam core and balsa wood core and investigated the repeated and the single impact responses for the specimens. They used various impact energies in the experiments, and damage process was analyzed from cross-examining, load-defection curves,

the damaged specimens and energy profile diagrams. After that they observed damages as like fiber cracks at the top and bottom face sheets, delamination between glass and epoxy, and shear fractures.

The investigation of the effects of a small mass impact on the sandwich composites plates was studied by Christopherson et al. [2]; they used foam-filled honeycomb cores that supported to small mass impact. Carbon fiber was used as reinforcement in the skins. They investigated the effect of different laminate configuration during impact loading. They determined the damage by down for strength connected with the impact event.

Bending of sandwich composite is analyzed by Kheirikhah et al. [3], they used three dimensional finite element methods, elastic core and two skins (with shape memory alloy wires) to analyze the sandwich composite. Numerical results show bending behavior is improved by using the shape memory alloy wires in the face sheets.

In this paper [4], Olsson investigated impact response and impact damage by using Engineering mode on the sandwich composites. Impact behavior depends on the impactor mass by using different methods, impactor mass sometimes is lager or smaller than mass of impacted panel.

Composite sandwich plate is used to study dynamic response by a rigid ball, this work well-done by Lee et al [5], they put two separate plates however the core has transverse shear and normal stiffness to find deformations under load of two faces. The finite element methods were used to discretize the sandwich plate in the numerical study. The results of dynamic strain theoretical analysis are compared with strain gage measurement ones.

Authors in [6] used four types of core thicknesses of 3D-sandwich with and without foam filling between the same fabric densities (face sheets) to study impact damage in the sandwich composites and low velocity impact properties. They used 32J and 48J energy levels to conduct impact test. Time to load, peak load, absorbed energy and energy to load are found. They also analyzed the compressive strength and impact damage.

In their study [7], low velocity impact behavior in numerical and experimental was studied by using finite element software and vacuum assisted resin transfer molding (E-glass and

carbon). E-glass and carbon were selected to manufacture specimens composite in experimental study however in the numerical study LS-DYNA was used in order to compare the results with experimental study.

2. Experimental Study

2.1. Material description

E-glass fabrics 0/90 having density of 300 g/m^2 were used as a reinforcing material however AIREX PVC foam C.71.55 was chosen as a core material with different thicknesses 5mm, 10mm and 15mm. Epoxy ARALDITE LY 1564 SP resin and ARADUR 3487B hardener were used as matrix material. The ratio of the resin and hardener was 3/1.

2.2. Fabrication of specimen

Stacking sequences of sandwich composites were [0º/90º/0º/5mm/0º/90º/0º], [0º/90º/0º/10mm/0º/90º/0º] and [0º/90º/0º/15mm/0º/90º/0º]. Figure1. Explains the Schematic drawing of components of VARIM process, Vacuum assisted resin infusion molding (VARIM) was used in order to manufacture the samples at 80 °C during 8 hours as seen from the Figure.2. Then the temperature is decreased slowly to room temperature. Sandwich composites consist of six layers and core with various thickness 5mm, 10mm and 15mm.
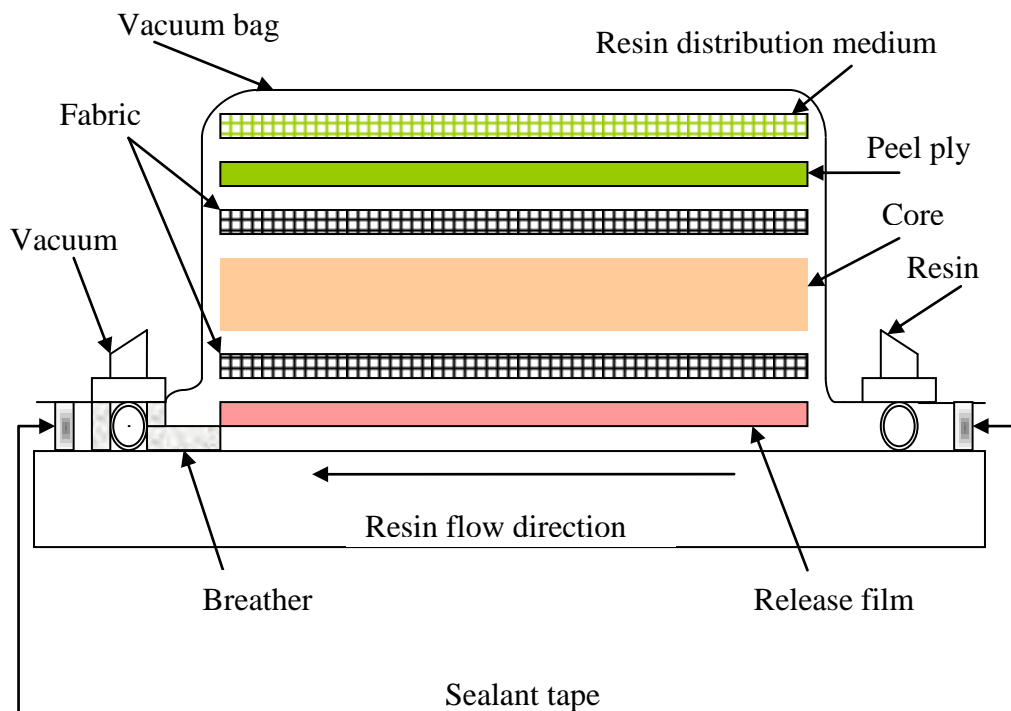
Figure1. Schematic illustration of sandwich composites
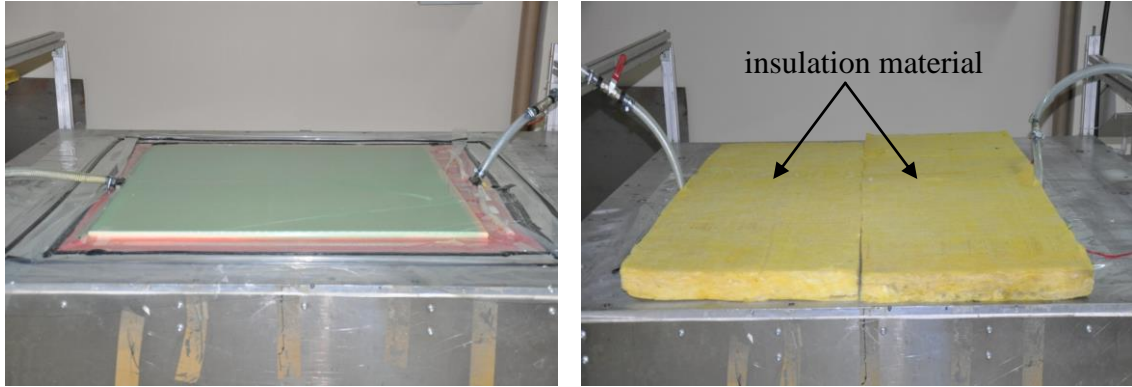
Figure2. Sandwich composite plates were manufactured by using vacuum assisted resin infusion molding (VARIM).

2.3 Testing of impact

Low velocity impact tests were performed by using CEAST 9350 with High-Energy System (Fractovis Plus) impact testing machine Figure3. All specimens were subjected to impact loading in order to investigate the impact behavior of the sandwich composite by using different energies (10, 15, 20, 25, 30, 35, 40, 50) J. The specimen was prepared dimensions of 100x100 mm as shown in the Figure 4. By using DS-250/1300 wet cutting machine. The specimen is fixed by fixture with 76 mm inner diameter, pneumatically. The impactor has hemispherical nose, 12.7 mm diameter and mass of 5 kg. Force transducer has maximum loading up to 22.4 kN.

(a)
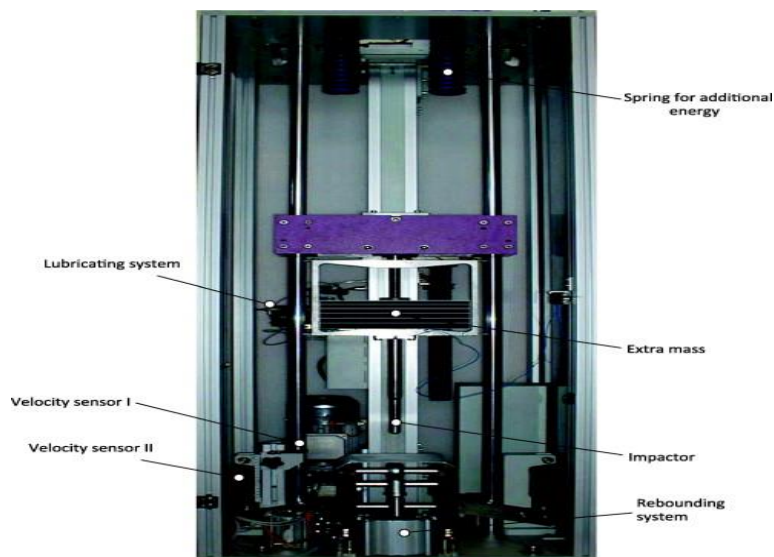
(b)

Figure 3 (a) Fractovis Plus impact testing machine with data acquisition system (DAS) (b) upper part of the testing machine.
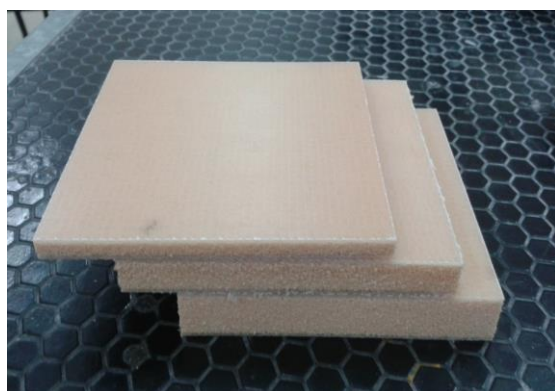
Figure 4 Sandwich composites with thicknesses of 5 mm, 10 mm and 15 mm

3. Result and discussion

3.1 Contact force-deflection

As seen from the Figure 5. Contact force-deflection curves for specimens of the sandwich composite which impacted at 10J, 20J, 35J, and 50J energies for three types of sandwich composite with core material thickness 5mm, 10mm, and 15mm. The results show that bending stiffness increases by increasing core material thickness at low impact energy in general, the curves have one peak by using 10J energy its meaning the impactor return of the top layer after impact the specimens, rebounding case occurs at cores material thickness 5mm and 10mm but at 15mm core material thickness the penetration case occurs, and the deflection increases more than 5mm, and 10mm cores material thickness as shown in the Figure 5.a.

The curves have two peaks for three types of samples sandwich composites which have differ cores material thickness, rebounding case occurs in 5mm and 10mm cores material thickness at bottom layer and the contact force at second peak increases more than the first peak in 5mm core material thickness because of the stiffness increases when impact test happening, however in 15mm core curve depicts penetration case because of the impactor permeates to top layer, core and bottom layer, respectively. And stops in the specimens, the contact force in the second peak less than the first peak and the contact force decreases by increasing the core material thickness but deflection increases by increasing the core material thickness at 20J energy such as explained in the Figure 5.b.

Contact force-deflection curves are mountain-like shape for all the curves and have two peaks because of the impactor perforates to the specimens; perforation case occurs at 5mm and 10mm. The contact force at second peak is bigger than the first peak in 5mm core material thickness, while penetration cases occurs in 15mm core material thickness, the first and second peaks worth were nearly the similar at 10mm and 15mm. On the contrary, deflection is different because of the thickness at 15mm is bigger than 10mm, the contact force decreases by increasing the core material thickness. However, deflection increases by increasing the core thickness by using 35J impact energy in the Figure 5.c.

As seen from the Figure 5.d perforation case occurs for all samples of sandwich composite with different core material thicknesses which have two peaks, the curve clearly shows that core material thickness does not seem clear at 5mm due to small core material thickness however the specimens be more rigid at 5mm core material thickness. On the contrary, at 10 mm and 15mm core material thicknesses which seem clear as shown, on the other hand, contact force decreases by increasing the core thickness but deflection increases by increasing the core thickness by using impact loading 50J.
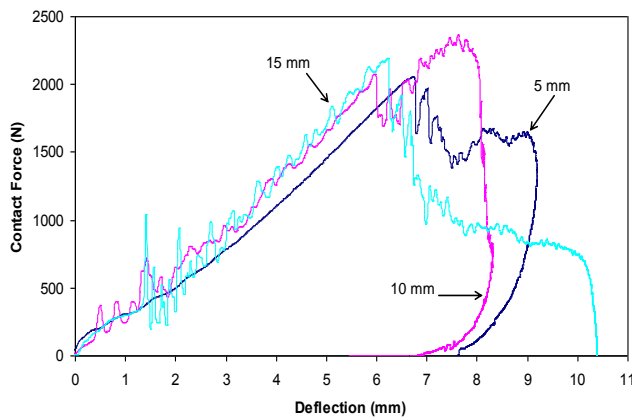
(a)
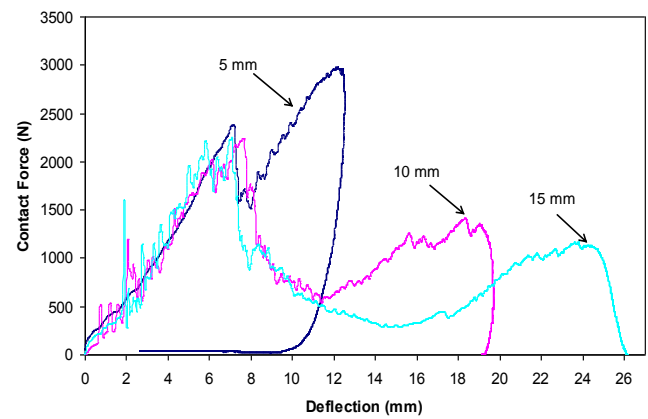
(b)
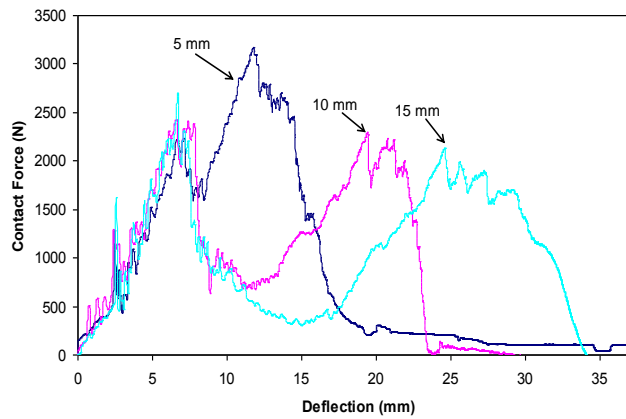
(c)
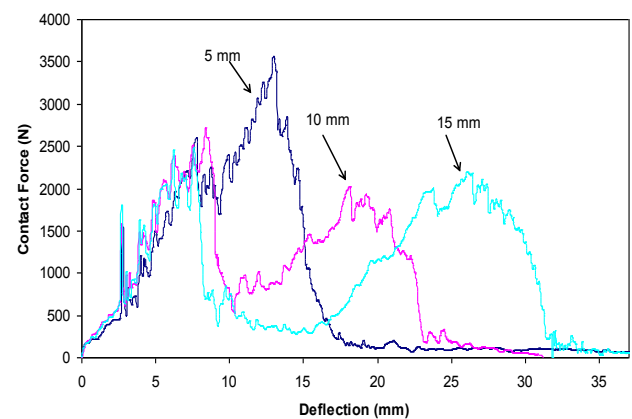
(d)

Figure 5 Contact force-deflection diagram for specimens the sandwich composite which impacted by (a) 10J (b) 20J (c) 35J and (d) 50J.

3.2. Absorbed energy-impact energy curves

Energy profile diagram represents absorbed energy versus impact energy as shown in the Figure 6. For three types of specimens the sandwich composite, the energy profile diagram explains difference between three types of the core material thicknesses which consist from 5mm, 10mm, and 15mm core material thickness.

The penetration threshold starts in 25J at 5mm and 15mm cores material thickness while rebounding threshold occurs in 20J at 10mm core material thickness and the perforation threshold occurs in 30J energy at 5mm core material thickness, occurs in 25J impact energy at 10mm core however, in 35J energy at 15mm core material thickness.
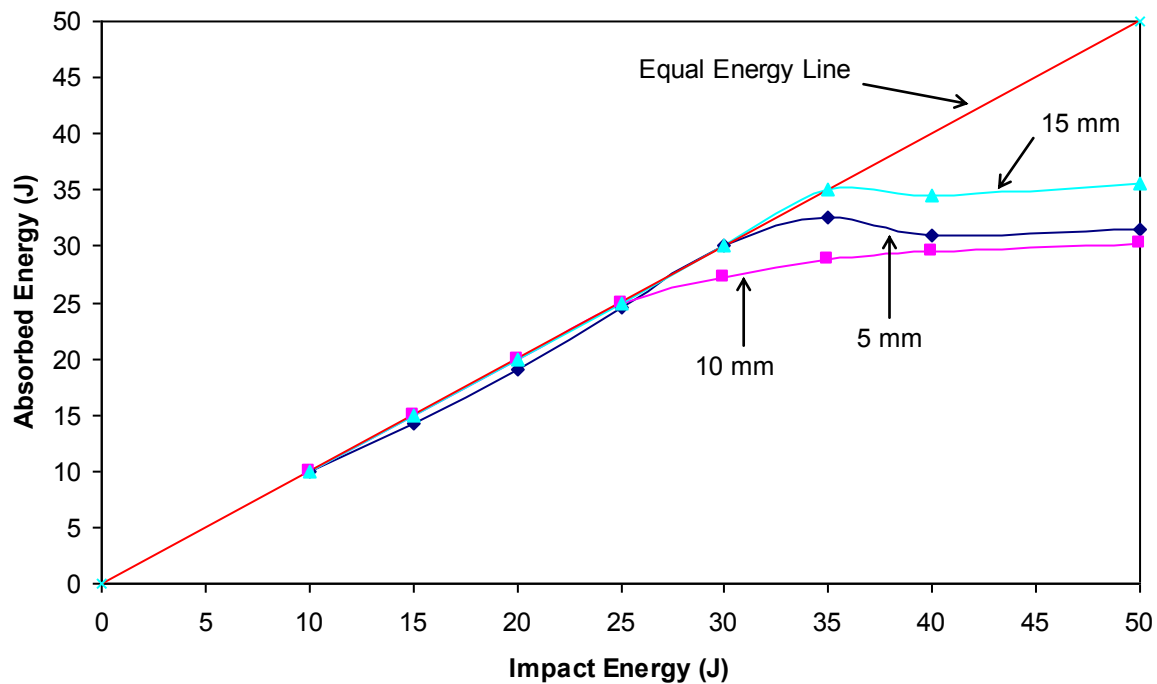
Figure 6 the energy profile diagram

4. Mechanism of damage

By visual inspections of top and bottom layers for specimen's sandwich composites, the damage mechanism like delamination occurs by using 10J impact energy only in top layers, and there is no damage in bottom layers as shown in the Figure 7. By increasing impact energy to 20J the delamination increases in top layers and occurs in the bottom layers. Under

the 35J impact energy the matrix cracks and delamination occur at top and bottom layers and fiber breakage, delamination area increase. At 50J impact energy, damages mechanism occur like matrix cracks, fiber breakage and delamination in the top and bottom layers as seen in the Figure 8.
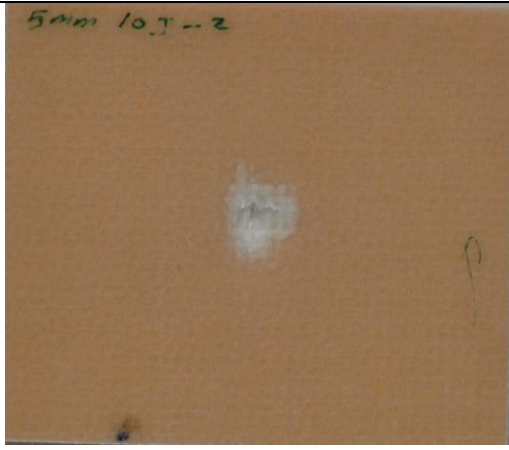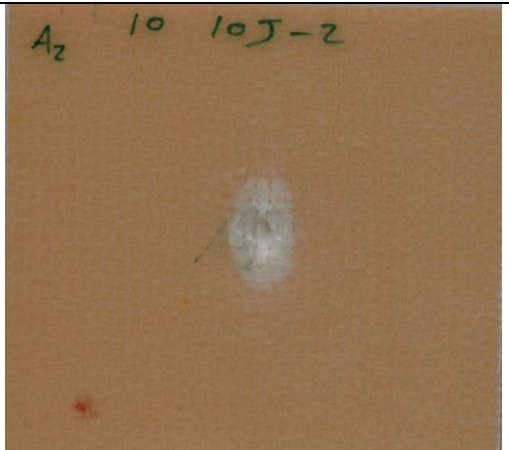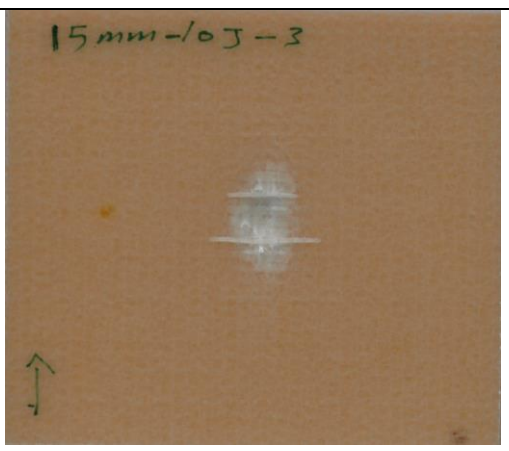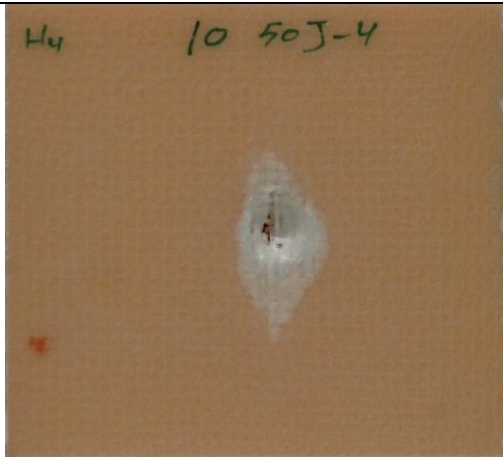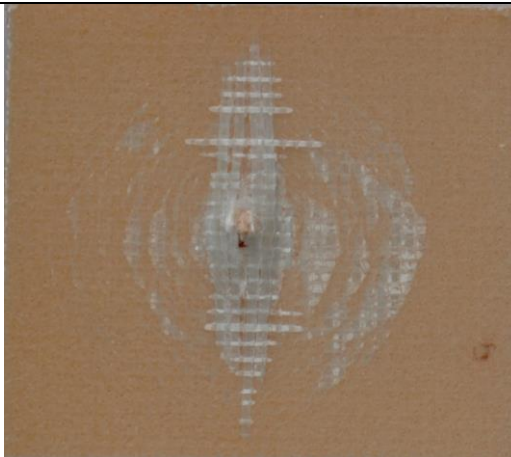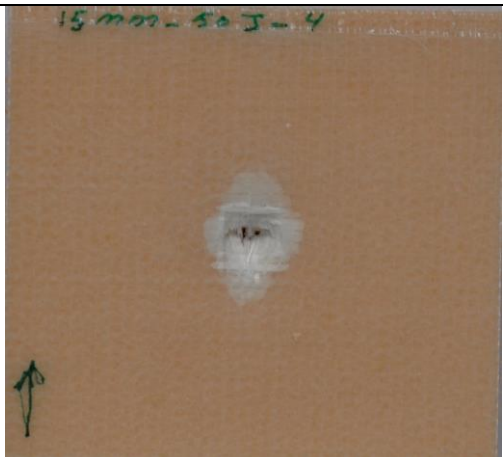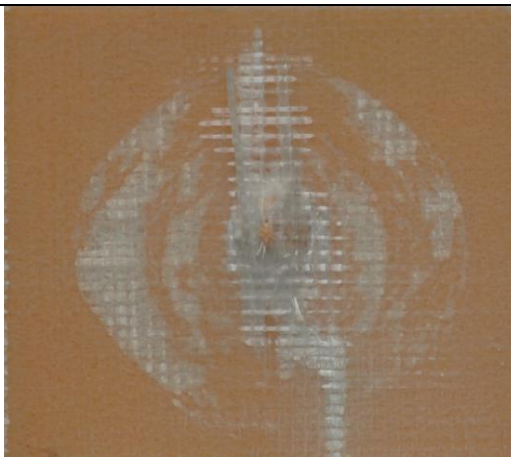
Core thickness	Top layers	Bottom layers
5mm		
10mm		
15mm		

Figure 7 Damages of impacted specimens for 10J impact energy.

Core thickness	Top	Bottom
5mm		
10mm		
15mm		

(b)

Figure 8 Damages of impacted specimens for 50J impact energy

5. Conclusions

In this study, the specimens of sandwich composite were manufactured in order to investigate in impact behavior experimentally. Low velocity impact tests were performed CEAST 9350 with High-Energy System (Fractovis Plus) impact testing machine. The results show that absorbed energy is more significant by influence core material thickness on structure sandwich composites, absorbed energy gains by increasing core thickness and the contact force values decrease by increasing the core thickness while deflection values increase by increasing the core thickness. All the sandwich composites were used in this paper have been manufactured in the Composite Research Laboratory of Dokuz Eylul University in Izmir.

6. References

[1] Atas, C., & Sevim, C. (2010). *On the impact response of sandwich composite with cores of balsa wood and PVC foam*. Composite structures, 93, 40-48

[2] Christopherson, J., Aagaah, MR., Jazar, GN., & Mahinfalah, M. (2005). *An investigation on the effect of a small mass impact on sandwich composite plates*. Composite Structures, 67, 299-306.

[3] Gautam s. Chandekar and Ajit D. Kalkar (2014) *experimental and numerical investigation of textile hybrid composites subjected to lo velocity impact loading*. Hindawi Publishing Corporation ID 325783, 14 pages.

[4] Karahan, M., Gul, H., Ivens, J., & Karahan, N. (2012). *Low velocity impact characteristics of 3D integrated core sandwich composites*. Textile Research Journal, 82, 945-962.

[5] Kheirikhah, M.M., Khadem, M., Farahpour, P. (2012). *Bending Analysis of soft core sandwich plates with embedded shape memory alloy wires using three-dimensional finite element method*. Proceedings of the institution of mechanical engineers part l-journal of material s-design and applications, 226.186-202.

[6] Lee, L.J., Huang, K.Y., & Fann, Y.J. (1993). *Dynamic-Response of composite sandwich plate impacted by a rigid Ball*. Journal of Composite Materials, 27, 1238-1256.

[7] Olsson, R. (2002*). Engineering Method for Prediction of Impact Response and damage in sandwich panels.* Journal of Sandwich Structures and Materials, 4, 3-29.

Thermal Analysis of Bipolar Microelectronic Devices

Mustafa Aydemir *,1, Müslüm Arıcı *,2, Hasan Karabay *,3

*Mechanical Engineering Department, Kocaeli University, Umuttepe Campus, 41380 Kocaeli, Turkey
[1]musty.aydemir@gmail.com, [2]muslumarici@kocaeli.edu.tr, [3]hkarabay@kocaeli.edu.tr

Abstract: Deep Trench Isolation (DTI) wells have crucial importance in bipolar microelectronic devices since they serve as heat insulator to reduce parasitic capacitance and crosstalk. However, under self-heating effect of bipolar devices, DTI wells may cause temperature increase near the heat source region which results in a decrease in performance of bipolar devices. In this study, the effect of the DTI length and heat source on temperature distribution near heat source region is investigated numerically for trench isolated devices. It is shown that trenches restrict to dissipate heat over the lateral sides which cause sharp temperature gradients in the trench isolated region. Hence, temperature increases with increasing trench length. As heat generation increases, temperature increases significantly. The effect of the trench length on the temperature distribution increases at higher heat generation.

Keywords: Deep Trench Isolation, trench length, bipolar device

1 Introduction

The demand to enhance the performance of transistors has been increasing in recent decades. High power transistors have some obstacles to obtain high performance, sustainable and reliable working conditions. Due to high current, power dissipation rises significantly and junction temperature increases. Bipolar transistors that are typical high power transistors are surrounded by electrical insulator to reduce cross talk interference and parasitic capacitances which is called Deep Trench Isolation (DTI) [1,2]. There is a trade-off between transistor secondary effects (such as crosstalk and parasitic noise) and thermal effects to obtain best depth of DTI wells since junction temperature increases fast due to low thermal conductivity of DTI materials. DTI wells strongly restrict lateral spreading of the heat flow. In the literature there are different approaches for the location of the heat source. It is reported in [3,4] that thermal response of emitter current change is more obvious than other parts of transistor, so emitter region is assumed to be heat source. However, base-collector depletion region is assumed to be heat source in [5,6]. In this study, the latter approach is used. DTI wells are filled either by fully silicon dioxide [7] or by thin silicon dioxide layer within polysilicon [8] which is used in this study. Position of the heat generation region depends on the design of transistors. In this study, the effect of different lengths of the DTI wells and different heat source powers on temperature gradients near the heat source of the transistor is investigated which is crucial for the performance of the transistor.

2 Problem Descriptions and Numerical Method

The schematic geometry of the problem is depicted in Figure 1. The problem is assumed to be steady state and two dimensional and the height and length of the chip are assumed to be 50 μm and 70 μm, respectively. The detail of the DTI wells and transistor region which is the primary interest of this study is also presented in Figure 1. It is assumed that heat source with sizes of 1 μm x 1 μm is in the middle of the DTI wells and located 1 μm beneath of top boundary. The thermal properties of the transistor and DTI wells are given in Table 1.
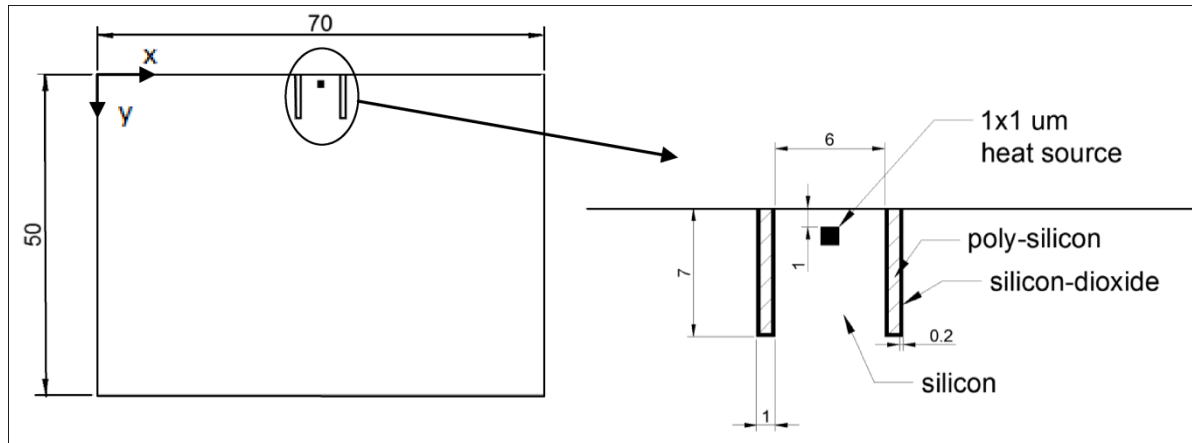
Figure 1 Schematic geometry of the problem

Table 1: Thermal properties of materials

Material	Thermal conductivity [W/mK]	Heat capacity [J/kgK]	Density [kg/m^3]
Silicon (Si)	148	730	2300
Silicon-Dioxide (SiO_2)	1.4	1000	2200
Poly-Silicon ($poly-Si$)	125	753	2330

The lateral sides of the device are assumed to be adiabatic and bottom side to be constant temperature due to contacting chip package. Heat generation is assumed to be uniform. It is also assumed that there is no effect of convection hence upper boundary condition can be assumed to be adiabatic since Biot number (which is hL_c/k where h is convection coefficient of fluid, k is thermal conductivity and L_c is characteristic length) is much less than unity. Governing equation is solved by Fluent ANSYS. The program is validated with the result of Walkey et al. [5] where temperature distribution of fully oxide filled trenches for 2 mW of 1 µm x 1 µm area of heat source is examined. They assumed that top and lateral sides are adiabatic and temperature at the bottom is 300 K. As shown in Figure 2, the isotherms are nearly the same.
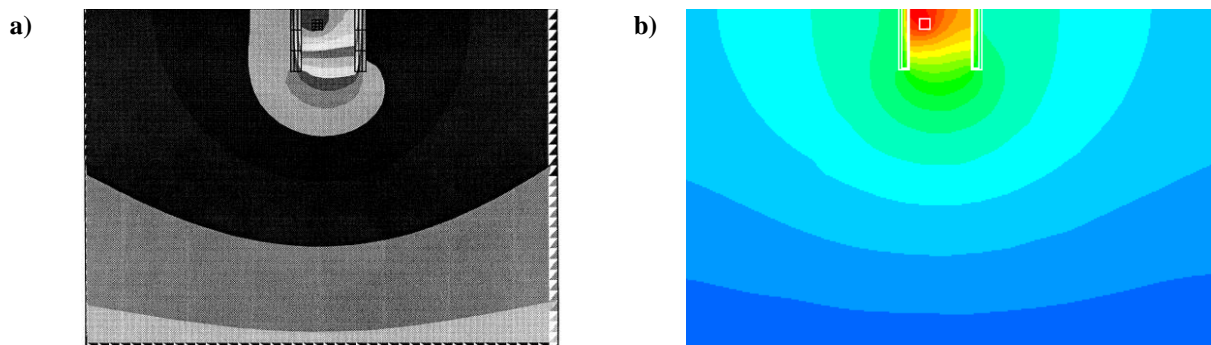
a)

b)

Figure 2 Isotherms for numerical simulations a) Walkey et al. [5], b) the present study

In this study, the effect of trench length which differs from 3 µm to 9 µm with 1 µm increments and heat source which varies from 0.5 mW to 3 mW with 0.5 mW increments on the temperature gradient near the heat source is investigated.

3 Results and Discussion

Temperature contour for 7 μm of DTI length and 1.5 mW of heat generation is shown in Figure 3. It is seen from the figure that temperature gradient is very small near the bottom while sharp temperature gradients in the trench isolated region is observed since trenches restrict to dissipate heat over the lateral sides.
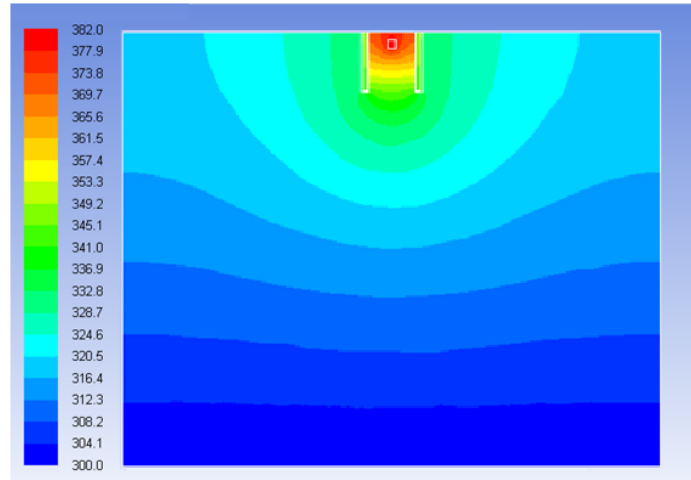

Figure 3 Temperature contour for 7 μm DTI length and 1.5 mW of heat generation

Figure 4 shows temperature variation in DTI-substrate contact interfaces for different trench lengths and different heat source powers. As seen in the figure, the outer temperature is almost constant due to low thermal conductivity of silicon dioxide and poly-silicon materials. However, the temperature at the inner surfaces varies significantly and decreases almost linearly except the edges of the trenches. As trench length increases, outer surface temperature decreases and inner surface temperature increases which results in a larger temperature difference between inner and outer surfaces of the DTI wells. Hence, a nearly one-dimensional heat flow is observed between the DTI wells which reveals the assumption of considering the DTI wells as adiabatic in [4, 5, 9].

Figure 5 represents temperature variation in the vertical centerline of the transistor working area for three different trench lengths and heat source powers. As seen in the figure, the maximum temperature occurs at the heat source, as expected. Beyond the heat source, temperature decreases as y increases. The decrease in temperature for larger trenches is almost linear since the trenches behave like thermal barrier. As the heat generation increases, temperature increases significantly. The difference between temperatures for different trench lengths also increases with increasing heat generation.
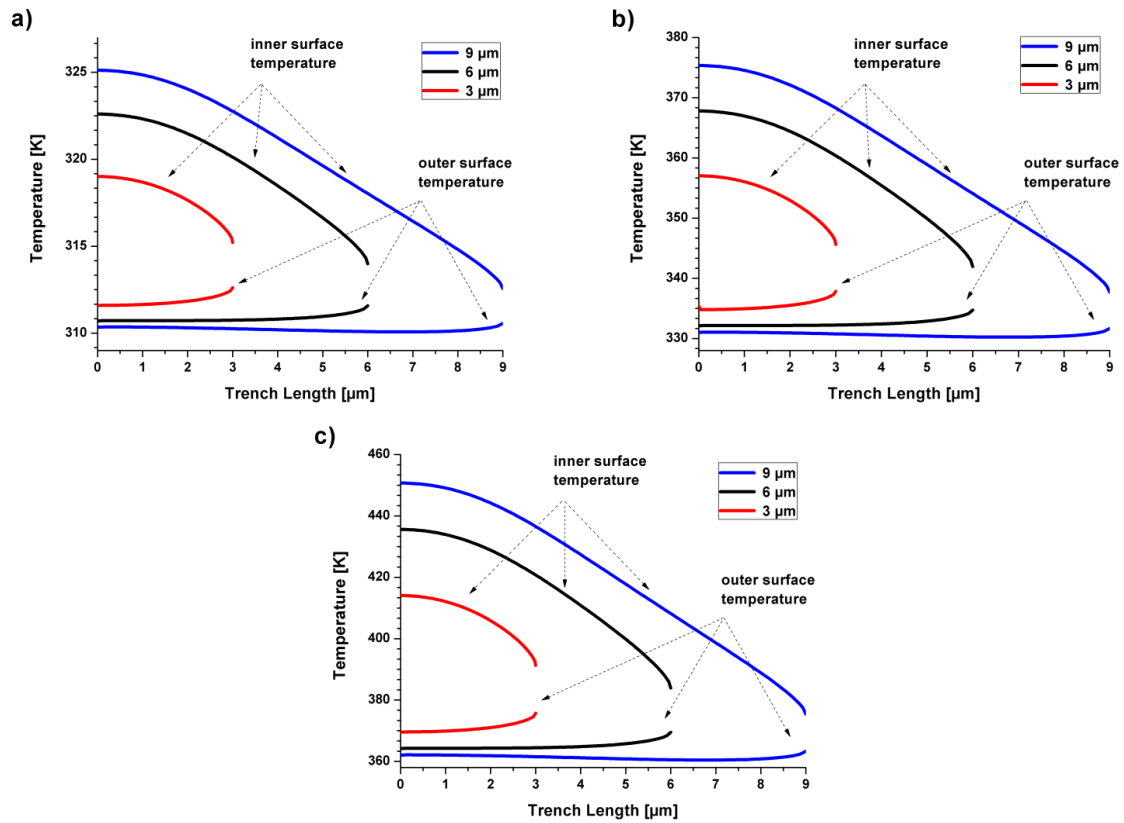
Figure 4 Temperature variations at the inner and outer surfaces of DTI wells a) 0.5 mW, b) 1.5 mW, c) 3.0 mW
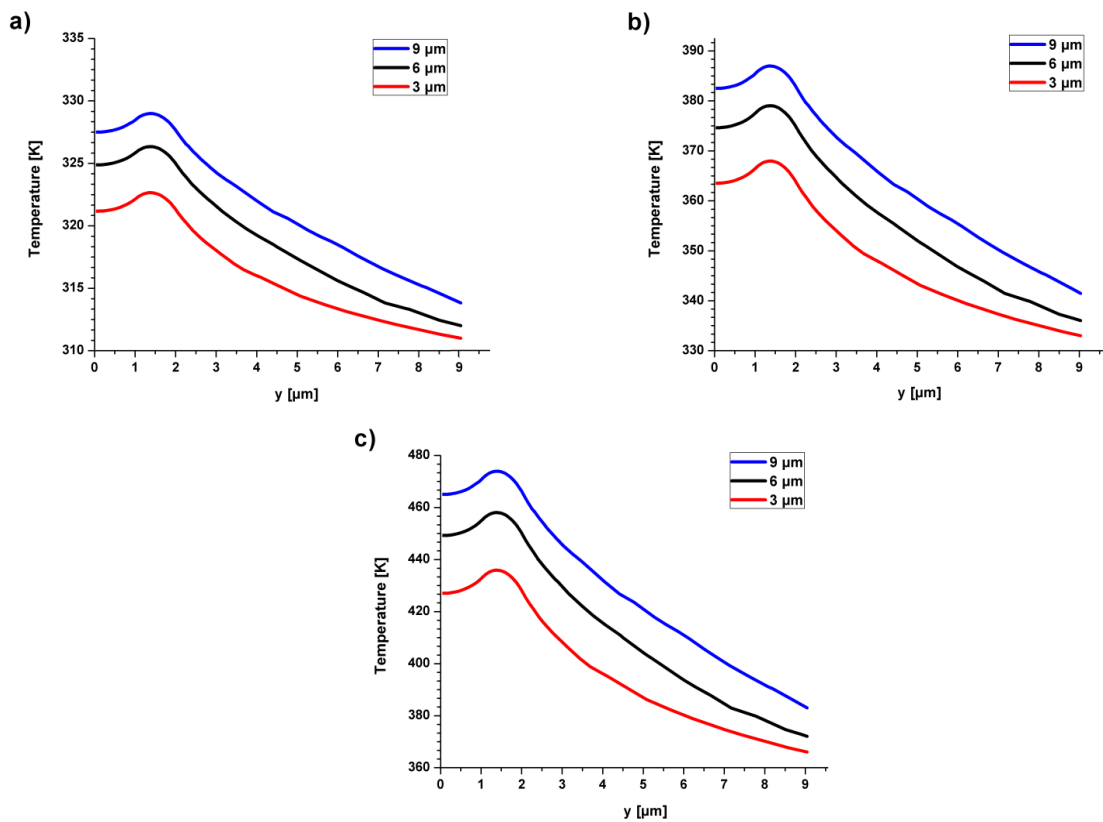

Figure 5 Temperature variation in the vertical centerline of the transistor working area for various trench lengths
a) 0.5 mW of heat source b) 1.5 mW of heat source c) 3.0 mW of heat source

The observed maximum temperature in the device is depicted in Figure 6 for all trench lengths and heat generations investigated in this study. As seen in the figure, maximum temperature increases almost linearly for each heat generation. The effect of trench length on the maximum temperature increases as the heat generation increases. For instance, while maximum temperature increases 6 K (from 323 K to 329 K for trench length of 3 μm and 9 μm, respectively) for heat generation of 0.5 mW, it increases 38 K for heat generation of 3.0 mW.
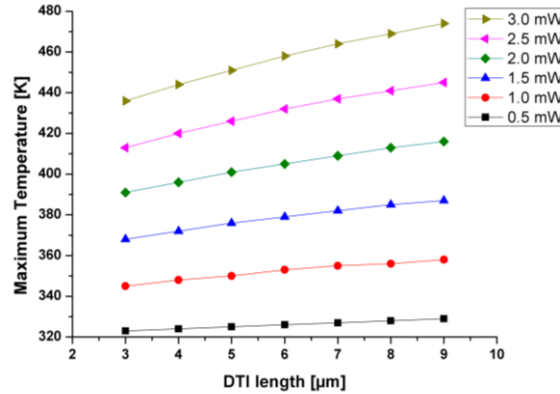

Figure 6 DTI lengths and maximum temperature change curve.

4 Conclusions

Deep Trench Isolation (DTI) wells have crucial importance in bipolar microelectronic devices since they serve as heat insulator to reduce the parasitic capacitance and crosstalk. In this study, the effect of the DTI length on temperature distribution near the heat source region is investigated for different heat generations. It is shown that trenches restrict to dissipate heat over the lateral sides which cause sharp temperature gradients in the trench isolated region. Hence, temperature increases with increasing trench length. As heat generation increases, temperature increases significantly. The effect of the trench length on the temperature distribution increases at higher heat generation.

5 References

[1] Harame DL, Comfort JH, Cressler JD, Crabbé EF, Sun JYC, Meyerson BS, Tice T, 1995, Si/SiGe Epitaxial-Base Transistors – Part II: Process Integration and Analog Applications. *IEEE Transaction on Electron Devices*, 42, 469–482.
[2] Forsberg M, Björmander C, Johansson T, Ko T, Liu W, Vellaikal M, Cheshire A, 2000, Shallow and deep trench isolation for use in RF-Bipolar ICs. *IEEE*, 212–215
[3] Marano I, D'Alessandro V, Rinaldi N, 2009, Analytical modeling and numerical simulations of the thermal behavior of trench-isolated bipolar transistors. *Solid-State Electronics*, 53, 297–307.
[4] Joy RC, Schlig ES, 1970, Thermal Properties of Very Fast Transistors. *IEEE Transactions on Electron Devices*, 17, 586-594.
[5] Walkey DJ, Smy TJ, Marchesan D, Tran H, Schröter M, 2000, A scalable thermal model for trench isolated bipolar devices. *Solid-State Electronics*, 44, 1373-1379.
[6] Walkey DJ, Smy TJ, Marchesan D, Tran H, Schröter M, 2000, Prediction of Thermal Resistance in Trench Isolated Bipolar Device Structures. *IEEE BCTM* 12.3.
[7] Harame DL, Comfort JH, Cressler JD, Crabbe EF, Sun JYC, Meyerson BS, Tice T, 1995, Si/SiGe Epitaxial-Base Transistors- Parts I: Materials, Physics and Circuits, *IEEE Transaction on Electron Devices,* 42, 455-468.
[8] Ohue E, Oda K, Hayaui K, Washio KA, 1998, A 7.7-ps CML using selective-epitaxial SiGe HBTs, *IEEE BCTM 5.3*, 97-100.
[9] Vanhoucke T, Hurkx GAM, 2006, A New Analytical Model for the Thermal Resistance of Deep-Trench Bipolar Transistors. *IEEE Transactions on Electron Devices*, 53, 1379-1388

Influence of Concentration on Thermal and Mechanical Properties of Elastomeric Polyamide Blends for Industrial Applications

A.R. Caramitu [1], T. Zaharescu [1], V. Tsakiris [1], L. Avadanei [2], S. Mitrea [1]

[1]National Institute for R&D in Electrical Engineering, ICPE-CA, Bucharest, Romania,
[2]SC ICEFS COM SRL Savinesi, Romania
E-mail: alina_caramitu@icpe-ca.ro

Abstract

This research is the basic part of a detailed study concening the preparation of cable insulation having improved mechanical and thermal performances. The paper presents the various PA6-based blends with EPDM (ethylene-propylene-diene terpolymer), Exxelor (medium viscosity semi-crystaline ethylene copolymer functionalized with maleic anhydride), Lotader (random terpolymer of ethylene, ethyl acrylate and maleic anhydride), Marfran (mixture polypropylene, polyethylene and polyethylene vinyl acetate) and SEBS (styrene-ethylene/butyl-styrene block copolymer). The mixing proportions cover the following PA6/elastomer ratios: 100/0, 90/10, 80/20 for EPDM, 100/0, 95/5, 90/10 and 80/20 for Exxelor, Lotader, Marfran. Tensile and bending mechanical tests, as well as three-point bending strength determinations were achieved on these compositions. Starting from the thermal endurance tests the possibility of successful using of PA6/elastomers compounds in the same conditions as PA6 basic material may ne economically considered.

I.INTRODUCTION

The necessity of materials with certain properties, which allow the operation under hard conditions, requires the compounding of different categories of polymers. In the case of polyamides, the decrease in the softening temperature simultaneously with the increase in material viscosity may be achieved by blending with various elastomers due to the reduction of interfacial tension [1]. The degree of cohesion between the two phases of polyamide blends depends strongly on the type of elastomer, because polar moieties induce a tighter interaction [2]. The engineering materials containing polyamides present satisfactory behavior related to thermal resistance [3, 4] or radiation resistance [5]. However, the presence of elastomers in the blends of polyamides increases the performances of products because of the intermolecular bridges established between oxygen or nitrogen atoms and protons belonging to unlike molecules [6]. The basic material of compounds determines the main characteristics, but they may be modified according to the further application by the mixing with proper component which turns the behavior towards the desired range.

The modification of polyamide-6 has been a practical purpose through which foreseen properties are gained in several alternatives. The compatibilization of PA-6 with ABS [7] produces composites, where the components can be bonded by means of nanotubes. The blending of PA 6 with nanostructured fluoroelastomer [8] leads to an improved material, whose tensile strength is higher relative to neat polyamide. The presence of maleic anhydride as compatibilizer loaded in PP/PA-6 systems [9] generates a very stable material with intermolecular bridges emphasized by FTIR records. The blending of maleated EPDM with polyamide 6 is a proper alternative for the production of improved behavior material [10], where the interaction between compounded phases keep the tightly. Even though ethylene-propylene elastomers (EPDM and EPR) are not miscible with polyamide 6, it was demonstrated their processing at higher temperatures between 270 and 310 °C is possible

because the value of interaction parameter from Flory-Huggins equation becomes favorable [11].

The present paper presents the compatibilization effects on the technical behavior of polyamide 6 blends, where various elastomers are minor components maximum load being 20 wt/wt%. The selection of these materials (EPDM, Exxelor, Lotader, Marfran and SEBS) was done based on the similarity in the skeleton structures, but the differences of chemical compositions cause the dissinmilarities in the measured functional properties. The presence of oxygen differently bonded in the secondary components determines some particular features in connection with the electron atraction and intermolecular interactions. The material answer to the mechanical charges reflects the contribution of minor component.

II.   MATERIALS AND METHODS

II.1 Materials

PA 6-based compounds were been obtained by mixing process, which includ four different elastomers: EPDM, Exxelor, Lotader and Marfran. They present hydrocarbon skeletons or functionalized structures. The elastomer loadings were 100:0, 90:10, 80:20 for PA 6: EPDM formulations and 100:0, 95:5; 90:10, 80:20 for PA6: Exxelor/Lotader/Marfran dual composites.

- PA 6 from RADICI Italy (Radipol®S100-004 PA 6 standard viscosity) with the following characteristics: flow index (ISO 1133) at 230°C and 250°C, and 2.16 kgf: 34.88 and 95.185 g/10 min, respectively; melt density at 230°C and 250°C, and 2.16 kgf: 1.044 and 1.005 g/cm^3, respectively; ash content: 0.588%.

- Ethylene propylene diene terpolymer grafted with maleic anhydride (EPDM-*g*-MA type Nordel IP 3745P - Dow Chemical Company) with the following characteristics: density (ASTM D792): 0.87 g/cm^3; melt index (ASTM D-1238 190°C, 2.16 kg) : <0.5; T$_g$: - 44 °C [12].

- Ethylene propylene copolymer functionalized with maleic anhydride (EP-*g*-MA tip Exxelor VA 1801 – Exxon Mobil Chemical) with the following characteristics: density 0.880 g/cm^3; flow index (ISO 1133) 9 g/10 min.

- Ethylene-acrylic ester terpolymer-maleic anhydride (Lotader 4720-Arkema) with the following characteristics: melt index (ASTM D1238) 7 g/10min, tensile strength at break 5.5 MPa (ASTM D 638), elongation at break 800 % (ASTM D 638); Ethylene-acrylic ester content : 30%; maleic anhydride content : 0.3%.

- Styrene-ethylene/butylene-styrene block copolymer (SEBS type Marfran SK6-47 DC - Franceschetti Elastomeri) with the following characteristics: tensile strength 19.1 MPa (DIN 53504), elongation 815 % (DIN 53504), shore D hardness : 45 (DIN 53505).

II.2. Equipment and methods

The polyamidic compounds were obtained using a two screws Brabender extruder: characterized by the ratio L/D 40 the maximum working temperature: 450°C, screw speed: 600-800 rpm

•the test samples were prepared in an injection machine Dr. BOY 35 type, (Germany) with the following features: screw diameter 28 mm; ratio L/D 18.6; calculated injection capacity: 59 cm^3; maximum pressure inside the material: 2200 bar; temperature control zones: 240/250/260/270/260; real injection capacity min 500 mm;

•mechanical tests (tensile and three points bending strength) were performed using the

equipment for determining static tensile strength of materials, LFM 30kN (model Walter & His AG, Switzerland), with the main technical characteristics: nominal force: 30 kN. This equipment allows the measurement of tensile and three bending points strength;

• thermal endurance appraisals were carried out using the oven MEMMERT (Germany) at temperatures between 180 and 220°C and an analytical balance (A & D Instruments type, Japan) error ±0.1 mg.

II.3. Estimation of thermal endurance based on mass loss criterion

Thermal endurance praxis based on IEC 60216/3-2011 standard was accomplished at different temperatures (neat technological limits) for 5,000 hours followed by the extrapolation of results at 20,000 hours [13]. The determination of temperature index from 5000 to 20000 hours was based on statistical calculation. The levels of thermal stress and life time of materials keep certain requirements: minimum temperature exposure: 180^0C, maximum temperature exposure 220^0C; first testing temperature should not exceed 20°C over the estimated operating temperature of each material. The degradation criterion is the mass loss (end of life corresponds to 30% mass loss). The temperature regime program is presented in Table 1.

Table no.1

Testing temperature (^{O}C)	Exposure duration (hours)
180	120
200	72
220	24

II.4. Determination of mechanical characteristics

Determination of tensile and bending characteristics was performed according to ISO: 527-2:2000 for the determination of static tensile strength of materials, LFM model 30kN having nominal force of 30 kN allowing measurements of tensile strength, compression and bending.

III RESULTS AND DISCUSSION
III.1 Estimation of thermal endurance based on mass loss criterion

Table 2 presents the thermal aging results, which shows the calculated temperature indices (TI), while in the regression for each compound is presented in Fig 1. It is found that the temperature indices are quite close for all studied compounds. This can be explained by the presence of polyamide as the major component. However, it can be observed a slight increase of the temperature index for PA6 +20 EPDM and PA6+10 Lotader compounds (relative to PA6).

Table no. 2

Compound	TI_{20000}	TI_{5000}
PA6	161	179
PA6+10 EPDM	161	179
PA6+20 EPDM	162	181
PA6+5 Exxelor	162	180
PA6+10 Exxelor	158	177
PA6+20 Exxelor	161	179
PA6+5 Lotader	161	180
PA6+10 Lotader	162	180
PA6+20 Lotader	161	180
PA6+5 Marfran	161	180
PA6+10 Marfran	161	180
PA6+20 Marfran	161	180

IT$_{20000}$=161(PA6, PA6/10,30EPDM, PA6/20EXXELOR, PA6/5, 20LOTADER;
PA6/5,10,20 MARFRAN); 162(PA6/20EPDM, PA6/10LOTADER), 158(PA6/10EXXELOR),
IT$_{5000}$=179(PA6, PA6/10EPDM, PA6/20EXXELOR), 177(PA6/10EXXELOR),
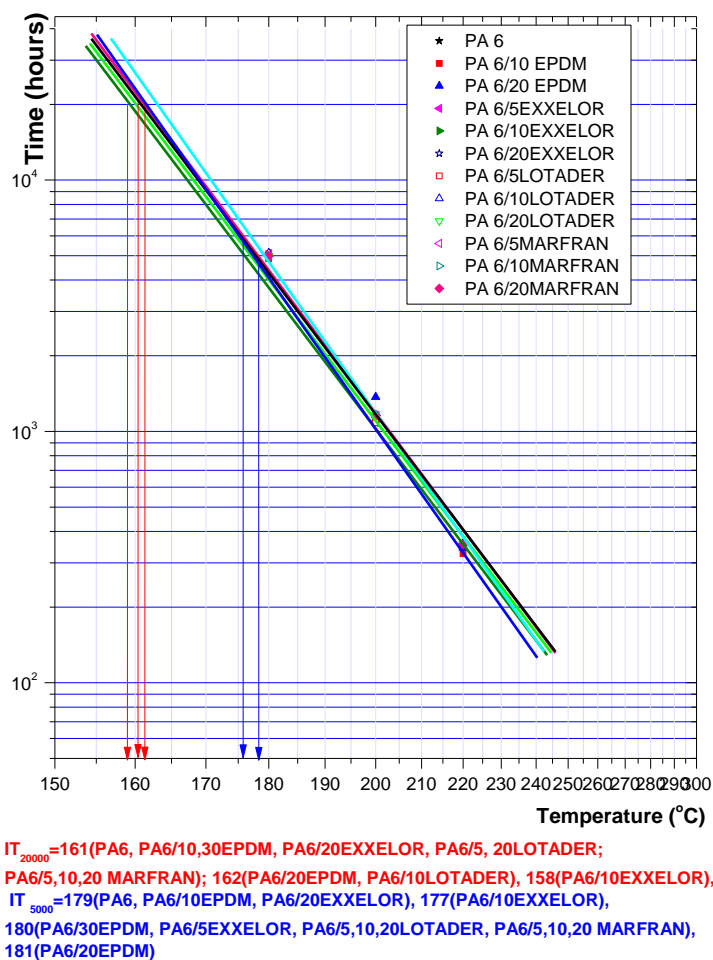180(PA6/30EPDM, PA6/5EXXELOR, PA6/5,10,20LOTADER, PA6/5,10,20 MARFRAN),
181(PA6/20EPDM)

Fig. 1 Regression for each compound

III.2. Determination of mechanical characteristics

III.2.1. Tensile strength

The experimental results obtained on all compounds based on PA6 with different elastomers namely EPDM, Exxelor, Lotader and Marfran are presented in the Fig. 2 (a-c).

(a)

(b)

(c)
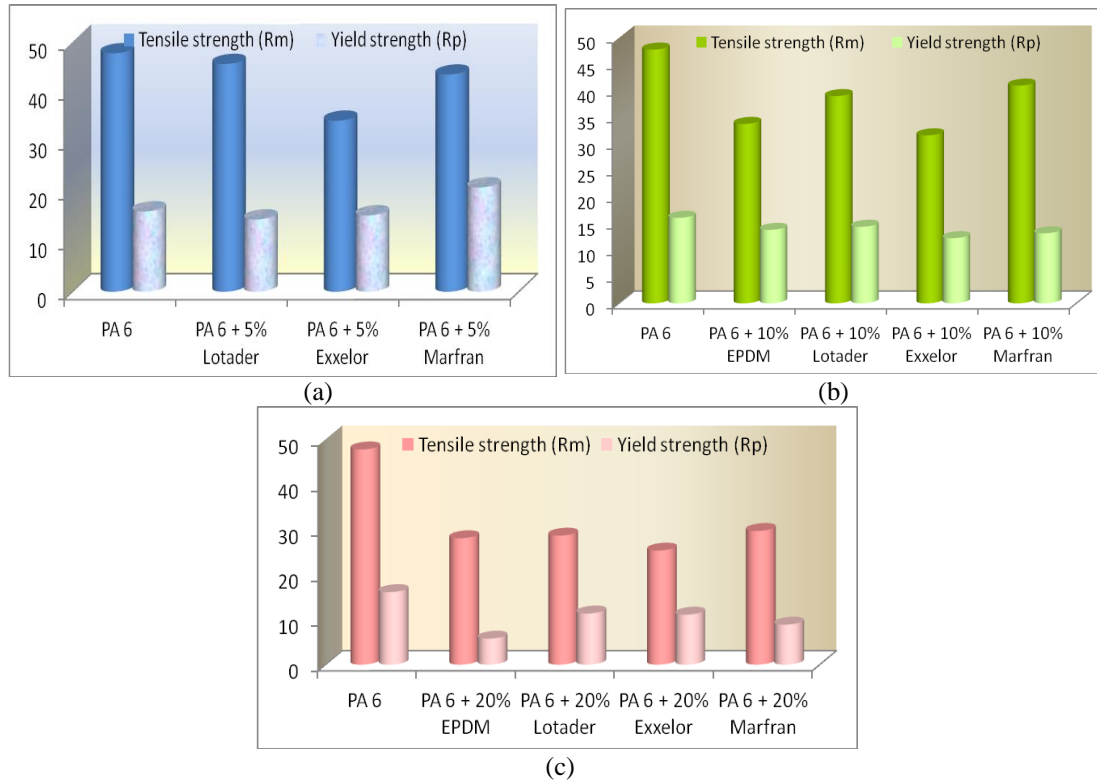
Fig.2. Comparative tensile strength for (a) PA 6/5Lotader/5Exxelor/5Marfran, (b) PA 6/10EPDM/10Lotader/10Exxelor/10Marfran, (c) PA 6/20EPDM/20Lotader/20Exxelor/20Marfran
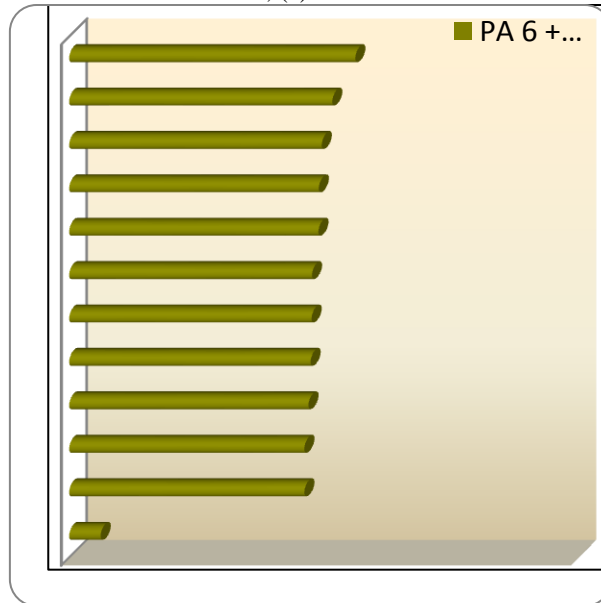

Fig. 3 Comparative elongation for all studied compounds

For all studied compounds, increasing the addition of elastomer load in PA6 matrix is accompanied by a decrease in tensile strength (Rm) (fig.3). Also can be seen that yield strength shows the highest values for PA6. This can be explained by the fact that the degree of stiffness of the matrix decreases with the addition of elastomer so, the deformability of the compounds increases when increases the elastomer rate.

The reason of achieving of these compounds based on P A6 was to establish an optimal solution from the point of vieew of mechanical withstand, but also from the point of view of further machining of polyamide as cable insulation. As is known, polyamide is very rigid thatfor the reason of supplementig of these several percents of elestomers was to decrease

stiffness. Fallowing these tests, was established that through supplementing of these elastomers percents it encrease the elasticity. It is established that the best elasticity properties are exhibit the compounds with the highest percent of elastomer. So, it is possible to establish a classification from the point of view of elasticity as fallow: PA6/5 Exxelor < PA 6 <PA6/10 EPDM<PA6/20 EPDM<PA6/5 Lotader<PA6/5 Marfran<PA6/10 Exxelor<PA6/10 Marfran <PA6/10 Lotader< PA 6/20Marfran< PA6/20Exxelor<PA6/20Lotader.

III.2.1.1. PA6/EPDM Compounds

A signifiant decreasing (41%) of the mechanical strength was observed for the PA6/EPDM receipt having added the highest percent of EPDM (20%).

Also, increasing the elastomer rate, allows to the decreasing of yield strength ($R_{p0.2}$-64% for PA6/20 EPDM) and to the increasing of elongation with only 1.02% related to PA6 matrix.

Adding ten or twenty percents of EPDM has no influence on terms of elongation (A), but allows to a decreasing of the value of modulus of elasticity with 19% and respectively 47%, compared with PA6 matrix.

It would be expected that the structural differences between the components of studied blends, polyamide and ethylene-propylene diene elastomer bring about somewhat dissimilar behavior, but the elasticity of macromolecules seems to be closed to each other.

III.2.1.2. PA6/Exxelor Compounds

A signifiant decreasing (47%) of the mechanical strength was observed for the PA6/Exxelor receipt having added the highest percent of Exxelor (20%). In terms of mechanical strength, the optimum composition is PA6/5Exxelor.

The yield strength ($R_{p0.2}$) values decrease dramatically, when the rate of elastomer increases (5% for PA6/5Exxelor, 23% for PA6/10Exxelor and 31% for PA6/20Exxelor).

The addition of 5% Exxelor to PA6 causes higher values of elongation (A) with around 24% in respect with PA6 matrix. The highest value of elongation (25%) was obtained by the adding 20% Exxelor in the PA6.

III.2.1.3. PA6/Lotader Compounds

A signifiant decreasing (40%) of the mechanical strength was observed for the PA6/Lotader formulation containing the highest percent of Lotader (20%). The best mechanical strength was found on the sample PA6/5 Lotader.

The sharp decrease in the yield strength ($R_{p0.2}$) values of samples consisting of polyemide 6 and Lotader decrease also dramatically was noticed, when the content of elastomer increases (10% for PA6/5Lotader, 10.5% for PA6/10Lotader and 29% for PA6/20Lotader).

The presence of 5% Lotader in PA6, brought about higher values of elongation (**A%**) with around 1.5%, in comparison with uncompounded PA6 matrix. The highest value of elongation (333%) was obtained by adding 20% Lotader in the PA 6.

III.2.1.4. PA6/Marfran Compounds

The experimental results show that the adding of Marfran elastomer influences by the decreasing mechanical strength (R_m) for all receipts (9% for PA6/5 Marfran, 14% for PA6/10 Marfran and 37% for PA6/20 Marfran) compared with PA6 matrix. The optimum mechanical strength was found for PA6/5Marfran.

The yield strength ($R_{p0.2}$) values decrease also dramatically, when the amount of elastomer increases. (7% for PA6/5Marfran, 18% for PA6/10 Marfran and 45% for PA6/20 Marfran).

The presence of 5% Marfran elastomer leads to higher values of elongation (A%) with around 1.5% in respect with pristine PA6, while 10 percents of added elastomer improves the value of (A%) with 3.5% and 20 percents of added elastomer improves the value of (A%) with 4% relative to neat PA 6.

The general view on evolution of tensile tests indicates that the optimum receipt for each compound is: PA6/10EPDM; PA6/5Exxelor; PA6/5Lotader and PA6/5Marfran. From the analysis on the mechanical features of all studied materials the sequence describing the decrease in tensile stength is: Rm PA6>Rm PA6/5Lotader>Rm PA6/5Marfran>Rm PA6/10Marfran>Rm PA6/10Lotader>Rm PA6/5Exxelor>Rm PA6/10 EPDM>Rm PA6/10Exxelor>Rm PA 6/20Marfran>Rm PA6/20 Lotader>Rm PA6/20EPDM >PA6/20Exxelor.

For the application of PA6/elastomer compounds, the most convenient choice would be PA6/5Lotader.

III.2.2. Bending strength

In the Fig. 4 (a-c) below are presented the results of bending tests performed on all type of studied compounds. These results are explained by the compound consistancies, which lighlights the conribution of oxygen atoms to the interaction between the two types of components for each pair of blends. The presence of maleic anhydride improves the mechanical features, while the lack of oxygen in SEBS does not exhibit any contribution to the enlarging mechanical answer.
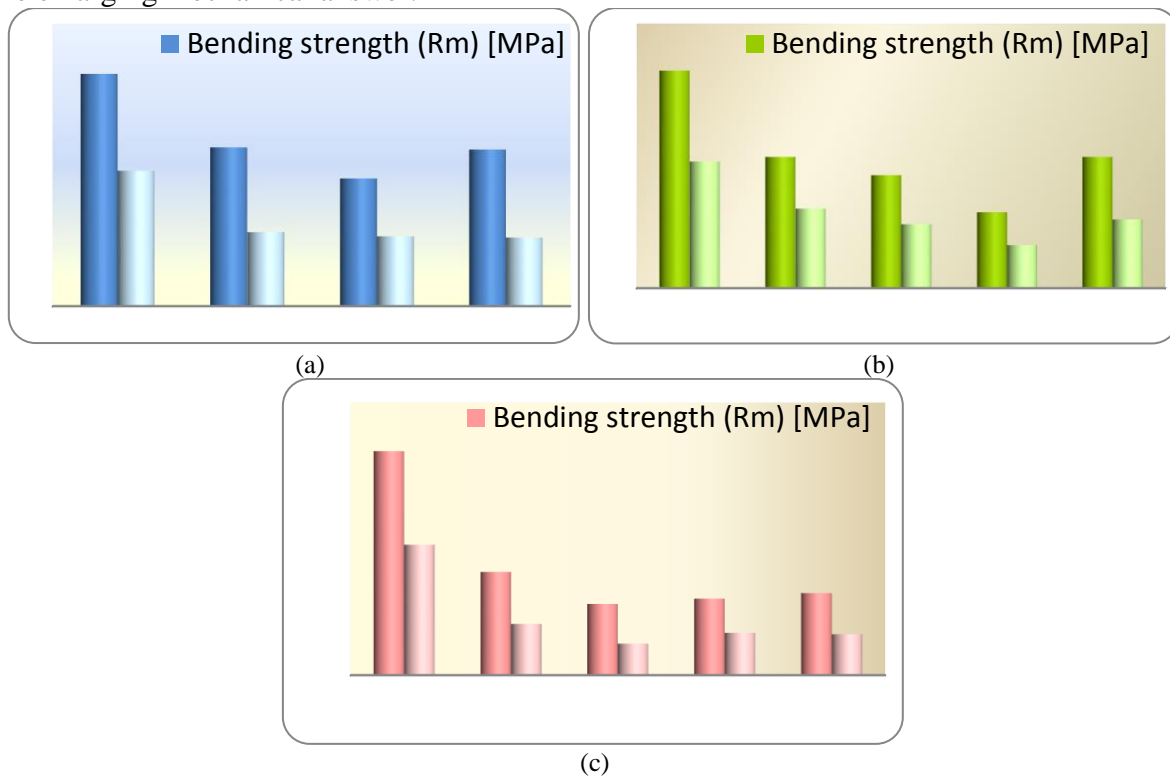

(a)

(b)

(c)

Fig.4. Comparative bending strength, yield strength and Young modulus for (a) PA 6/5Lotader/5Exxelor/5Marfran, (b) PA 6/10EPDM/10Lotader/10Exxelor/10Marfran, (c) PA 6/20EPDM/20Lotader/20Exxelor/20Marfran

The obtained values indicate that generally, for all studied compounds, increasing the addition of elastomer in PA6 matrix, allows to a decreasing of bending strength.

III.2.2.1. PA6/EPDM Compounds

A signifiant decreasing (53%) of the bending strength was observed for the PA6/EPDM receipt having added the highest percent of EPDM (20%). Increasing the elastomer rate, allows to the decreasing of bending strength with 23% (for PA6/10 EPDM).

The bending strength, yield strength and Young modulus decreases uniformly with the addition of elastomer.

III.2.2.2. PA6/Exxelor Compounds

A signifiant decreasing (66%) of the bending strength was observed for the PA6/Exxelor receipt having added the highest percent of Exxelor (20%). Increasing the elastomer rate, allows also to the decreasing of bending strength with 45% (for PA6/5Exxelor) and 65% (for PA6/10Exxelor). In terms of mechanical strength, the optimum composition is PA6/5Exxelor.

Adding 20% of Exxelor elastomer allows to decreasing of yield strength value with 68 % related to the PA6 matrix.

III.2.2.3. PA6/Lotader Compounds

A signifiant decreasing (68%) of the bending strength was observed for the PA6/Lotader formulation containing the highest percent of Lotader (20%). Increasing the elastomer rate, allows also to the decreasing of bending strength with 32% (for PA6/5Lotader) and 48% (for PA6/10Lotader).

Adding 20% of Lotader elastomer allows to decreasing of yield strength value with 76 % related to the PA6 matrix.

III.2.2.4. PA6/Marfran Compounds

The experimental results show that the adding of Marfran elastomer influences by the decreasing bending strength (R_m) for all receipts (39% for PA6/5 Marfran, 40% for PA6/10 Marfran and 63% for PA6/20 Marfran) compared with PA6 matrix.

Adding 20% of Marfran elastomer allows to decreasing of yield strength value with 69 % related to the PA6 matrix.

Between all studied materials, can be done thew follow clasification: Rm PA6>Rm PA6/5Lotader>RmPA6/5Marfran>RmPA6/10EPDM>RmPA6/10Marfran>RmPA6/5Exxelor >RmPA6/10Lotader>RmPA6/20EPDM>RmPA6/20Marfran>RmPA6/10Exxelor>RmPA6/ 20Exxelor>Rm PA6/20Lotader.

IV. CONCLUSIONS

The thermal endurance tests accomplished on PA6/elastomer blends have demonstrated that equivalent values of mechanical properties were obtained due the compound consistacies, PA 6 is major component of each compound). In terms of thermal endurance the PA6/20 EPDM receipt is the best choice. The larger differences between these formulations will be obtained during the determination of oxidation strength.

After mechanical tests, the optimal compound consisting of PA6/5 Lotader (wt/wt) receipt can be crecommended for the production of electrical insulation for cables and wires.

V. REFERENCES

1. Tanrattanakul, V., Sungthong, N., Raska, P. (2008). *Polym. Testing* 27, 794-800.
2. Modic, M. J., Pottick, L. A. (1993). *Polym. Eng. Sci*. 33, 819-826.
3. Jurkowski, B., Olkhov, Y. A., Kelar, K., Olkhova, O. M. (2002). *Eur. Polym. J*. 38, 1229-1236.
4. Ohlsson, B., Hassander, H., Törnell, B. (1998). *Polymer* 39, 6705-6714.
5. Burillo, G., Adem, E., Nuñoz, E., Vásquez, M. (2013). *Radiat. Phys. Chem*., 84, 140-144.
6. van Puyvelde, P., Oommen, Z., Koets, P., Groeninckx, G., Moldenaers, P. (2003). *Polym. Eng. Sci.* 43, 71-77.

7. Meincke, O., Kaempfer, D., Weickmann, H, Fridrich, Ch., Vathauer, M., Warth, H. (2004). *Polymer* 45, 739-748.
8. Banerjee, S. S., Bhowmick, A. K. (2013). *Polymer* 54, 6561-6571.
9. Roeder, J., Oliveira R. V. B., Gonçalves, M. C., Soldi, V., Pires, A. T. N. (2002). *Polym. Testing* 21, 818-821.
10. Vieira, I., Severgnini. V. L. S., Mazera, D. J., Soldi, M. S., Pinheiro, E. A., Pires, A. T. N., Soldi, V. (2001). *Polym. Degrad. Stab*. 74, 151-157.
11. Tomova, D., Kressler, J. Radusch, H.-J. (2000). *Polymer* 41, 7773-7783.
12. Technical Information ─ Product Selection Guide NORDEL™ Hydrocarbon Rubber.
13. CEI 216 Guidelines for the determination of thermal endurance properties of electrical insulating materials.

Acknowledgements

Computational Thermal Properties of Building Super Insulting Materials / Recent Advances

D. Baillis [1], R. Coquard [2]

[1]Laboratoire de Mécanique des Contacts et des Solides (LAMCOS), UMR CNRS / INSA Lyon 5514, 20 rue des Sciences,69621 Villeurbanne Cedex,, France. Email : dominique.baillis@insa-lyon.fr
[2] Société (EC2-MODELISATION) ; 66, boulevard Niels Bohr, 69603 Villeurbanne CEDEX, France. Email: remi.coquard@ec2-modelisation.fr

A model for estimating the total heat transfer inside new cellulose-based aerogels has been investigated. The model accounts for the characteristic solid matrix at the nanometric scale by using a cellular representation of the nanofoam porous structure. The radiation-conduction heat transfer is taken into account. Previous analytical correlation for the fluid phase is used to model the conduction heat transfer in gas. New analytical formulations based on mean free path theory combined with phonon tracking approach are proposed to model the conduction heat transfer in the solid phase at the nanometric scale. The contribution of radiation heat transfer is obtained from Rayleigh scattering approach combined to the Rosseland approximation.
Relations obtained are expected to be useful for researchers aiming at developing new insulating organic aerogels since they permit to determine conduction-radiation equivalent conductivity as a function of cell dimensions, phonon and optical properties of cellulose.

Keywords: aerogel, nanofoam, cellular structure, heat transfer, modelling

1. Introduction

These last years, the need for a reduction of energy consumption in building sector has led to a growing interest in theoretical modelling of the thermal radiative and conductive properties of insulating materials. As examples we can cite the works on extruded polystyrene foam [1], polystyrene and polyurethane foams [**2**],[3], expanded polystyrene foams [4], [5], fibrous media [6]-[11] and super insulating materials such as silica nanoporous matrices [12]-[19].

Conventional insulation materials for buildings are macroporous media used at atmospheric pressure: mostly polymeric foams (polystyrene, polyurethane...) or mineral fibers. They are commonly used to improve the thermal insulation of a building envelope. Their impact on the energy consumption increases together with the insulation layer thickness. However, when this thickness is limited to few centimeters, which is common in urban areas where the living space is rare and expensive, the impact of insulation is limited. In conventional insulation materials, the main heat transfer is due to gaseous conduction in the porous volume. The thermal conductivity of standing still air ($25 mW/(m.K)$ at standard conditions) is thus a limit for this kind of insulation materials.

Super insulation materials are defined as materials with a thermal conductivity below 25 mW/(m.K). To get such a low conductivity, the gaseous conduction is decreased thanks to the Knudsen effect. Most of the recent researches in this field have focused on silica-based super-insulating materials. The materials developed are thermally very efficient and, in this regard, are extensively studied as heart of Vacuum Insulating Panels (VIP) as discussed in the review paper []. The pore size in these materials is greatly reduced (submicronic pore size). However,

the main constraint on the generalisation of their use in the building sector is due to their mechanical fragility.

To remedy these deficiencies, one of the most promising solutions lies in the hybridisation of the silica super-insulating materials with environmentally-friendly binders having high insulating performances. Very recent works have led to the formulation of organic aerogels obtained from cellulose as precursors. The elaboration process and the structural characterisations of these porous cellulose-based materials have been described in recent studies [21], [212]. From the analyses of Scanning Electron Microscope (SEM) pictures, it appears that a cellular porous structure with open-cell can represent the real porous nanostructure (Fig.1 a). The porous and solid structures of these aerogels have been investigated using Hg porosimetry and synchrotron radiation Small Angle X-ray Scattering (SAXS) to obtain Pore Size Distributions (PSD) and Chord Length Distributions (CLD) of the solid phase, respectively. They exhibit a submicronic pore size while the solid phase characteristic size is around several nanometers or tenths of nanometers. Therefore, they are subjected to "Knudsen effects" due to the confinement of the gas leading to a substantial reduction of the gas conductivity and thus to high insulating performances. Moreover, the very small characteristic size of their solid phase certainly implies that the macroscopic Fourier law of heat conduction cannot be rigorously applied to these materials since the phonon transport at the local nanometric scale is affected by the presence of the solid-fluid interface.

a)   b)
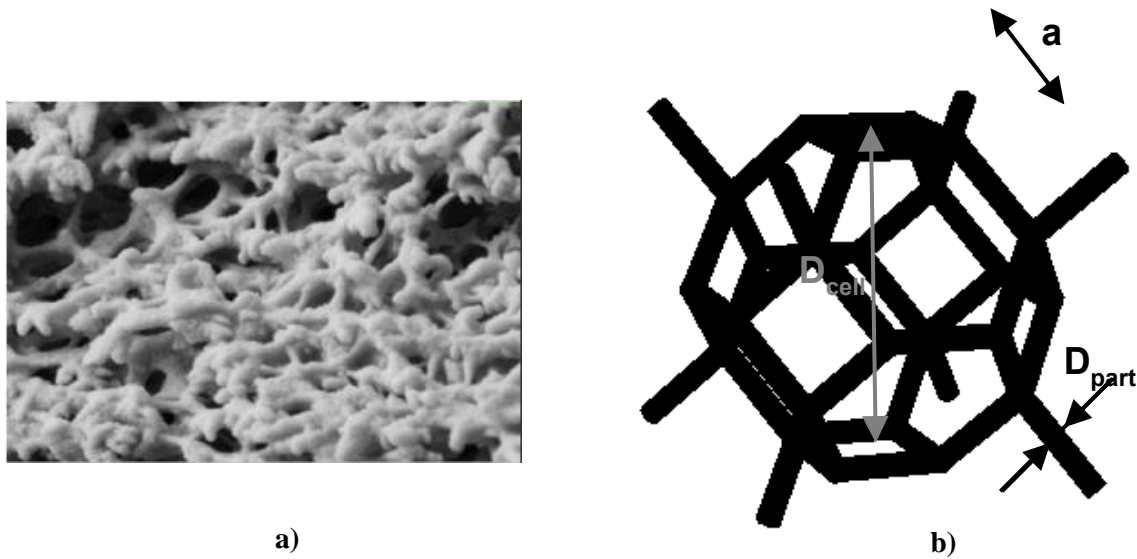
Figure 1: Illustration of the representative structure retained : a) SEM pictures of cellulose aerogels (elaborated by Mines ParisTech) ; b) tetrakaedecahedron open-cell with circular cylindrical struts

An adequate theoretical description of the structure is not an easy task. To overcome this problem, most of the approaches used for simulating the thermophysical properties of cellular foams are based on idealized cellular structures. Cellular foam structure is often represented by polyhedral cells.

Similarly to usual insulating open cell foams, in the present work, the open cells of cellulose aerogel are represented by tetrakaedecahedron and the struts are assumed cylindrical with circular cross-section (Fig. 1. b). The solid phase is assumed to be entirely comprised in the cell struts (open-cell). Considering these approximations, the structure is characterised using only two parameters: the cell diameter D_{cell} and porosity ε (or solid fraction f_v), since the

diameter D_{part} of the cylindrical struts can be related to D_{cell} and ε. The relation $\varepsilon = F(D_{part}, D_{cell})$ is obtained numerically by generating tetrakaedecahedron cellular structures made of struts with circular cross sections with variable ratio D_{part}/D_{cell} and computing the corresponding porosities.

A power law permits to fit very accurately the evolution computed numerically since the mean error made when using analytical relation (1) is lower than 0.7% for the range of solid fractions $f_v \in [0.005, 0.3]$:

$$(1 - \varepsilon) = f_v \approx 8.4761 \times \left(\frac{D_{part}}{D_{cell}}\right)^{1.973} \Leftrightarrow \frac{D_{part}}{D_{cell}} \approx \left(0.11798 \times (1 - \varepsilon)\right)^{0.50684} \qquad (1)$$

Using this simplified representation of the porous morphology at the nanometric scale, we modelled the total heat transfer inside cellulose aerogels. In the present work, a special emphasis is put on the derivation of analytical effective thermal conductivity models for estimating the total heat transfer inside cellulose-based aerogels. New simple analytical relations permit to determine the equivalent thermal conductivity as a function of cell dimensions, phonon properties and optical properties of solid phase. They are useful to optimize such materials and their manufacturing process from a thermal point of view.

2. Heat transfer model and results

For super-insulating materials, the radiative heat transfer contribution can be determined using equivalent radiative conductivity k_r while heat conduction contribution through the solid and fluid phase can be represented by an effective thermal conductivity k_c [0]. For aerogels with high porosity ($\varepsilon \approx 0.9$), the fluid phase can be considered as a continuous phase which connects directly the hot and cold regions with no considerable bottle-necks in the heat flow path. Therefore, the contribution of the fluid phase is usually expressed in the form $\varepsilon.k_f$. On the other hand, the solid phase could not be considered as a solid block connecting the heat source to the heat sink. The conductive flux rather results from flows through small contact areas connecting different zones in contact. Therefore, it is not possible to relate simply the solid contribution, denoted as k_{solid}, to the porosity and conductivity of cellulose $k_{cellulose}$ alone since the structural parameters of the solid matrix also play a role. We can write:

$$k_c = \varepsilon.k_f + k_{solid}$$
(2)

To quantify heat conduction in the fluid phase, Kaganer's correlation [223] is currently applied and has been largely used in preceding studies dealing with heat transfer in super-insulating materials.

As regards heat conduction in the solid phase of nanostructured materials, first models governing the phonon transport were essentially applied to silicon, gallium or aluminium in the micro-electronic field [234]- [302] and more recently to silica for super insulating materials used for building application [313].

Some of them are based on Molecular Dynamics (MD) we can cite Domingues et al. [256] and Mahajan et al. [27]. MD simulations are promising and give rise to a growing interest. However, their major drawback concern the high computation costs and time required when dimensions of several nm or tenth of nm are considered. This is prohibitive in view of parametric studies.

Other numerical methods have been developed to model the heat transfer at nanometric scale when macroscopic laws are invalid. The most common one consists in solving the Boltzmann equation governing the phonon transport inside nano-structured materials. The classical approach for the resolution of the Boltzmann Equation is to resort to Monte Carlo (MC)

procedures. Mazumder and Majumdar [234], Lacroix et al. [] and Baillis and Randrianalisoa [280], [291] have solved the Boltzmann equation via MC procedure and have computed the thermal conductivity of very thin silicon films. They have shown that it gets lower than the macroscopic conductivity when the thickness of the film is the same order of magnitude as the phonon mean free paths. Then, the method has been applied to predict the effective thermal conductivity of nanostructured porous media such as silicon–based materials [302] and silica-based materials [313]. MC procedures for the numerical solution of the BTE are suitable approaches to perform realistic (such as 3D) simulation of thermal conduction, however, they require an important numerical effort and are time-consuming thus usually restricted to low-dimensional systems.

In the study [324], an hybrid model based on combination of analytical and phonon-tracking approaches was proposed to predict thermal conductivity of porous nanostructured materials. It was applied to predict the thermal conductivity of etched meso-porous silicon, having fractal-like open pore structure, and annealed porous silicon, characterized by spherical closed-pores. Compared to more advanced prediction approaches such as the direct MC methods and Molecular Dynamic simulations, the hybrid model [32] presents a numerical advantage in term of computation time and numerical efforts.

In this current work, we propose to generalize the hybrid model developed in [34] to cellular nanostructured porous materials in order to deduce new analytical relation for the solid conduction contribution, k_{solid}. This analytical solution is derived from the exact solution of the BTE in the diffusion regime and is based on the mean-free-path theory.

Concerning radiative contribution, several attempts have been carried out to estimate the radiative properties of nanoporous materials, especially nanostructured silicas. Lallich et al. [18,19] computed the radiative properties of silica nanoporous particles thanks to the Mie theory, in order to estimate the non-gray Rosseland radiative conductivity. The scatterers were not the nanoparticles but aggregates of nanoparticles that are constituted during the manufacturing process of the powders. The authors pointed out that in the small wavelength range (wavelength lower than 1 μm), a satisfactory solution using the Mie theory applied to a spherical scatterer (representing the aggregate) can never be obtained. It is due to the fact that the Mie theory does not take into account the nanostructure of the aggregates. They have used Discrete Dipole Approximation improving the modeling results in the small wavelength range. An alternative model was proposed by Dombrovsky et al. [17] for the determination of the radiative properties of nanoporous silicas. The silica primary nanoparticles were not isolated in a nanoporous silica powder, they are collected in stable aggregates. These aggregates were assimilated to hollow microspheres with a wall thickness equal to the nanoparticles diameter. The radiative conductivity was calculated by using the analytical equation of Rayleigh scattering for hollow spherical particles.

Regarding the radiative heat transfer in aero-cellulose, considering the very small dimensions of the solid structure, we propose to use analytical relations obtained from Rayleigh scattering applied to cylinder struts forming tetrakaedecahedron cell of aero-cellulose.

The results obtained by the current theoretical models have been confronted with conductivity measurements on different aero-cellulose samples. The conductivities were measured by a direct method using a μ-fluxmeter device specially developed by CSTB for measuring samples with very small dimensions (noted "μF" on Fig. 1). The structural properties of these samples (samples noted A to E) have also been characterized experimentally by Hg porosimetry. The pore size distributions (PSD) of the samples produced obtained from Hg

porosimetry measurements allow us to evaluate $<t_p>$ while the porosity (ε) was estimated by pycnometry or by the classical weighting method considering that the bulk density of cellulose $\rho_{cellulose} \approx 1600$ kg/m^3. It should be noted that, in the samples developed, a proportion of the total pore volume could have larger pore size than those accounted for in the PSD obtained by Hg porosimetry (p_{psd}). The proportion of macropores is thus $p_{macro.} = 1 - p_{psd}$. These structural properties are summarized on Table I. We also indicate in this Table the density of the aerogel (ρ), the mean pore size $\langle t_p \rangle$, the cell diameter (D_{cell}) of the corresponding cellular structure used for the representation of the porous morphology.

Sample	Solid Phase	ρ (kg/m^3)	ε	$<t_p>$ (nm)	D_{cell} (nm)
A	cellulose	166	0.897	47.8	44.7
B	cellulose	142	0.912	95.8	84.1
C	cellulose	128	0.921	57.2	48.1
D	cellulose	177	0.890	60.4	58.0
E	cellulose	207	0.871	99.6	101.9

Table I: Characteristics of the aero-cellulose samples studied

The equivalent thermal conductivities predicted by our model using these structural properties and assuming diffuse ($p_s=0$) or specular ($p_s=1$) reflection of phonons are compared with the measured conductivities on Fig. 1. One can notice a good agreement, the relative discrepancies being always lower than 15%.
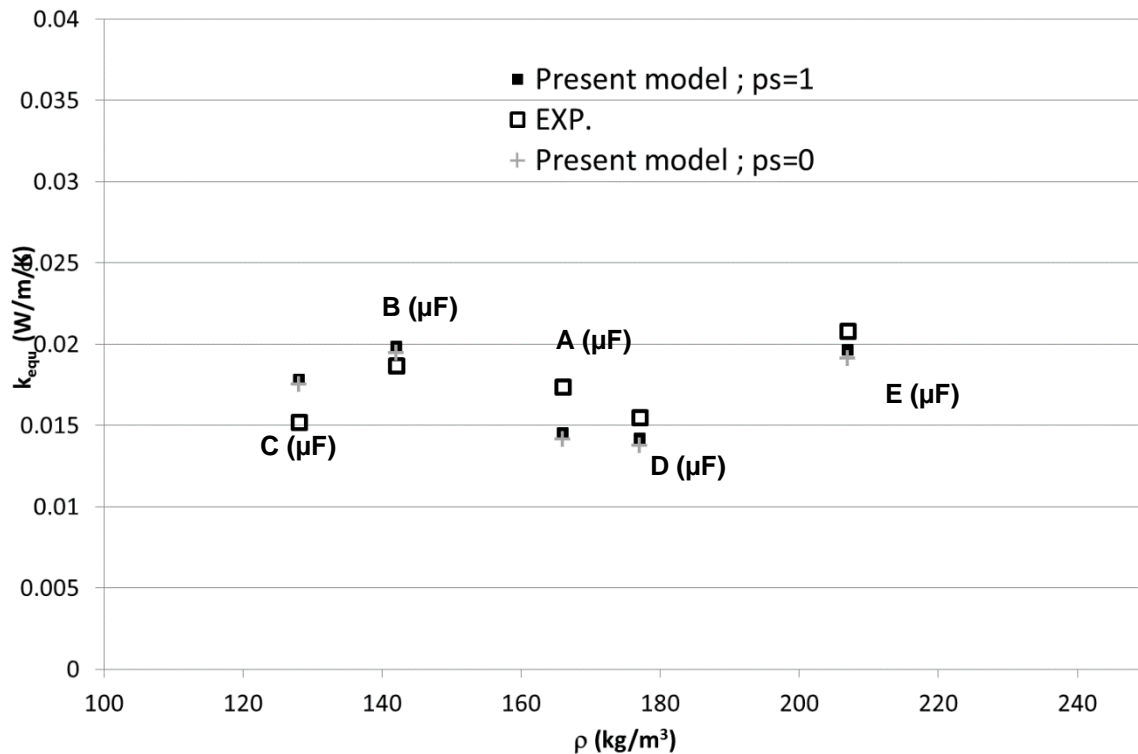
Figure 1: Comparison of the equivalent conductivities measured and computed for the aerocellulose samples A to E (μF : from μ-Fluxmeter)

305

3. Conclusion

Innovative cellulose-based aerogels (aero-cellulose) are currently under development in view of their hybridisation with nanostructured silica-based materials. The final goal is to obtain an environmentally-friendly composite material with high insulating properties (super-insulation) and enhanced mechanical resistance (compared to current silica-based superinsulators) in order to remedy the major weak point of current silica-based superinsulators. The interesting thermal behaviour of the aero-cellulose has already been partially demonstrated experimentally through pore size characterisations and conductivity measurements. However, an exhaustive knowledge of the mechanisms responsible for the total heat transfer through the nano-structured cellulose matrix and pores remains of primary importance for the optimisation of their structures.

Therefore, we have developed theoretical tools which account for both heat conductions in the fluid phase and in the solid phase at the local nanometric scale and thermal radiation propagation through the solid matrix. An ideal solid structure has been retained to represent the shape of the cellulose matrix : open-cell material with tetrakaedecahedron shape made of cylindrical struts.

4. References

[1] Kaemmerlen, A., Vo, C., Asllanaj, F., Jeandel, G. and Baillis. D. (2010) Radiative properties of extruded polystyrene foams: Predictive models and experimental results, *J. Quant. Spectr. Radiat. Transfer*, 111(6): 865-877.

 [2] Kuhn, J., Ebert, H.P., Arduini-Schuster, M.C., Büttner, D. and Fricke, J. (1992) Thermal transport in polystyrene and polyurethane foam insulations, *Int. J. Heat Mass Transfer*, 35(7): 1795-1801.

[3] Placido, E., Arduini-Schuster, M.C., and Kuhn, J. (2005) Thermal properties predictive model for insulating foams, *Infrared Phys. Tech.*, 46(3): 219-231.

[4] Coquard, R. and Baillis, D. (2006) Modeling of heat transfer in low-density EPS foams, *ASME J. Heat Transfer*, 128(6): 538-549.

[5] Coquard, R., Baillis, D. and Quenard, D. (2009) Radiative properties of expanded polystyrene foams, ASME J. Heat Transfer, 131(1): paper 012702.

[6] Boulet, P., Jeandel, G. and Morlot, G. (1993) Model of radiative transfer in fibrous media - Matrix method, *Int. J. Heat Mass Transfer*, 36(2): 4287–4297.

[7] Cunnington, G.R. and Lee, S.-C. (1996) Radiative properties of fibrous insulations: theory versus experiment, *J. Thermophys. Heat Transfer*, 10(3): 460–466.

[8] Marschall, J. and Milos, F.S. (1997) The calculation of anisotropic extinction coefficients for radiation diffusion in rigid fibrous ceramic insulations, *Int. J. Heat Mass Transfer*, 40(3): 627–634.

[9] Lee, S.C and Cunnington, G.R (2000)Conduction and radiation heat transfer in high-porosity fiber thermal insulation, *J. Thermophys. Heat Transfer*, 14(2): 121–136.

[10] Heino, J , Arridge, S., Sikora, J. and Somersalo, E. (2003) Anisotropic effects in highly scattering media, *Physical Review E* 68 paper 031908.

[11] Kamdem Tagne, H.T and Baillis, D. (2005) Radiative heat transfer using isotropic scaling approximation: Application to fibrous medium, *ASME J. Heat Transfer*, 127(10): 1115–1123.

[12] Quenard D. and Sallée H., (2005) "Micro-nano porous materials for high performance thermal insulation", Proceedings of the 2nd International Symposium on Nanotechnology in Construction, Euskalduna Palace Bilbao - Spain ,13th - 16th November.

[13] Rettelbach T., Sauberlich J., Korder S. and Fricke J., (1995) "Thermal conductivity of IR-opacified silica aerogel powders between 10 K and 275 K", J. Phys. D: Appl. Phys. Vol. 28, Issue 3, pp 581-587

[14] Caps R., Heinemann U., Ehrmanntraut M., Fricke J., (2001) 'Evacuated insulation panels filled with pyrogenic silica powders : properties and applications', High Temperatures- High pressures, 33, 151-156

[15] Caps R., Fricke J., (2000) "Thermal Conductivity of Opacified Powder Filler Materials for Vacuum Insulations", International Journal of Thermophysics, Vol. 21, n°2,

[16] Schwab H., Heinemann U., Beck A., Ebert H.P. and Fricke J., (2005) " Dependence of Thermal Conductivity on Water Content in Vacuum Insulation Panels with Fumed Silica Kernels", Journal of Building Physics, Vol. 28, No. 4, , pp. 319-326

[17] Dombrovsky, L., Lallich, S., Enguehard, F., Baillis, D. (2010) An effect of "scattering by absorption" observed in near-infrared properties of nanoporous silica *Journal of Applied Physics*., 107(8), DOI: 10.1063/1.3374473 (8 pages).

[18] Lallich, S., Enguehard, F. and Baillis, D. (2009) Experimental determination and modeling of the radiative properties of silica nanoporous matrices. *Journal of Heat Transfer*, 131(8), pp. 1-12

[19] Lallich, S., Enguehard, F., Baillis, D. (2008) Radiative properties of silica nanoporous matrices *International Journal of Thermophysics,* 29 (4) , pp. 1395-1407
Thermal radiation properties of highly porous cellular foams

[20] Bouquerel M., Duforestel T., Baillis D. and Rusaouen G., (2012) "Heat transfer modeling in vacuum insulation panels containing nanoporous silicas—A review", *Energy and Buildings*, Volume 54, , pp. 320-336

[201] Fischer F., Rigacci A., Pirard R., Berthon-Fabry S. and Achard P., (2006) "Cellulose-based aerogels", *Polymer*, Volume 47, N° 22, pp. 7636–7645

[212] Sescousse R., Gavillon R., and Budtova T., (2011) "Aerocellulose from cellulose–ionic liquid solutions: Preparation, properties and comparison with cellulose–NaOH and cellulose–NMMO routes", *Carbohydrate Polymers*, Volume 83, N°4, , pp. 1766–1774

[22] Kaganer M. G., (1969) "Thermal Insulations in Cryogenic Engineering", Israel Program for Scientific Translations,.

[23] Mazumder S. and Majumdar A., (2001) "Monte Carlo Study of Phonon Transport in Solid Thin Films Including Dispersion and Polarization", ASME J. Heat Transfer 123 749–759.
[24] Chantrenne, P., Raynaud, M., Baillis, D., Barrat, J.L. (2003) Study of phonon heat transfer in metallic solids from molecular dynamic simulations Microscale Thermophysical Engineering 7 (2) , pp. 117-136

[256] Domingues G., Volz S., Joulain K., and Greffet J.J., (2005) "Heat Transfer between Two Nanoparticles Through Near Field Interaction", Physical Review Letters PRL 94, 085901

[26] Domingues G., Rochais D., Volz S., (2008) "Thermal contact resistance between two nanoparticles", Journal of Computational and Theoretical Nanoscience, Volume 5, Number 2, February , pp. 153-156

[27] Mahajan S.S. and Subbarayan G., (2007) "Estimating thermal conductivity of amorphous silica nanoparticles and nanowires using molecular dynamics simulations", Physical Review E, 76, 056701

[29] Lacroix D., Joulain K. and Lemonnier D., (2006) "Monte Carlo simulation of phonon confinement in silicon nanostructures: Application to the determination of the thermal conductivity of silicon nanowires" Applied Physical Letters PPLIED 89, 103104

[28] Randrianalisoa J. and Baillis D., (2008) "Monte Carlo Simulation of Steady-State Microscale Phonon Heat Transport Heat conduction in submicron crystalline materials ," ASME J. Heat Transfer, 130, 072404, July.

[29] Baillis D. and Randrianalisoa J. (2009), "Prediction of thermal conductivity of nanostructures: Influence of phonon dispersion approximation," International Journal of Heat and Mass Transfer, Vol. 52, Issues 11-12, May, pp. 2516-2527.

[30] Randrianalisoa J. and Baillis D., (2008) "Monte Carlo simulation of cross-plane thermal conductivity of nanostructured porous silicon films," Journal of Applied Physics, 103, 053502

[31] R. Coquard, D. Baillis, V. Grigorova, F. Enguehard, D. Quenard; P. Levitz, (2013) "Modeling of the Conductive Heat Transfer through Nano-structured Porous Silica Materials", Journal of Non-Crystalline Solids, Volume 363, 1 March, Pages 103-115

[32] Randrianalisoa, J., Baillis, D. (2009) "Combined analytical and phonon-tracking approaches to model thermal conductivity of etched and annealed nanoporous silicon" Advanced Engineering Materials11 (10), pp. 852-861

Acknowledgements

CO_2 Solubility in Ionic Liquids at High Pressures and Wide Range of Temperatures

Rena Hamidova [2], Javid Safarov [1,2], Astan Shahverdiyev [2], Egon Hassel [1]

[1] Lehrstuhl für Technische Thermodynamik, Universität Rostock, Germany.
[2] Department of Heat and Refrigeration Techniques, Azerbaijan Technical University, Baku, Azerbaijan.
E-mail: javid.safarov@uni-rostock.de

Over the last 100 years a number of so called greenhouse gases have shown an increasing concentration in the atmosphere. at the end of the last century, because of the intensive development of instruments, remote methods and extensive application of isotopic methods in earth sciences, independent proofs of current climate heating were obtained. The main cause for this is attributed by common scientific belief to the continued increase of greenhouse gas concentrations in our atmosphere over the last century. One of the most important greenhouse gases at the present time is carbon dioxide. The continued burning of fossil fuels has and will continue to increase carbon dioxide (CO_2) in the atmosphere.

Ionic liquids (ILs) are regarded as environmentally-benign solvents due to their immeasurably low vapor pressure. Recently, significant progress has been made in the application of ILs as alternative solvents for CO_2 capture due to their unique properties, a broad range of liquid temperatures, excellent thermal and chemical stabilities and selective dissolution of certain organic and inorganic materials. The prediction of gas solubility in ILs is a fundamental step toward the development of simulation tools to aid in the process calculations prior to industrial applications.

The experiments to determine the high pressure solubility of CO_2 in IL's at various temperatures are performed in a stainless steel measuring cell in equilibrium by using the isochoric method. The installation consists of three main parts: a) gas reservoir, b) stainless steel measuring (equilibrium) cell, c) Electronic tracking system box.

The wall of gas reservoir consists of two parallel 19 mm Kömacel (Germany) expanded plastic slab materials with a vacuum in between them. Such insulated wall system is a very high protection against heat exchange between the outside and inside of reservoir. In the inside of the gas reservoir have the aluminum heating plate and three high pressure gas balloons [two of them with 150 cm^3 (Swagelok, Germany) and one with 300 cm^3 (HPS, Germany)]. Beside the balloons, the gas reservoir consists of pressure transducers (PAA33X-V-100, Omega Engineering inc., 0-100 bar, Newport Electronics GmbH, Germany), PT100 thermometer (1/5 DIN Class B, Temperatur Messelemente Hettstedt GmbH, Germany), and an emergence (overflow) valve (R3A, Swagelok, Germany). The heating is done by eight parallel connected hot foils (100 X 200 mm 24 V ca. 20 W, Conrad Electronic SE, Germany) in the back side of the heating plate.

Experiments were carried out in four different pressure steps: in the first step, the maximum possible pressure (about 5 MPa) is created in the gas reservoir. The other steps with maximum pressure are: second - about 3 MPa, third – about 1.5 MPa, and finally – about 0.5 MPa. Experimental temperatures ranging from T=413.15 K to T=273.15 K in decrements of 20 K at selected pressures controlled by a PC with the LabVIEW program.

The temperature dependency of Henry's law constant was calculated and the average deviation of the Henry's law constant is always better than ±1%. Thermodynamic properties of solution such as the free energy of solvation $\Delta_{sol}G$, enthalpy of solvation $\Delta_{sol}H$, entropy of solvation $\Delta_{sol}S$ and heat capacity of solvation $\Delta_{sol}c_p$ were calculated at various temperatures T to evaluate the solute-solvent molecular interactions.

The measured CO_2 solubility results in IL as a function of temperature at the various pressures are fitted to virial equation using the mole fraction dependence.

Keywords: Solubility, Ionic liquid, Equilibrium, Henry's constant.

Thermophysical Properties of Butanol-1 at Pressures Up To 200 Mpa

Bahruz Ahmadov [1], Javid Safarov [2,3], Saleh Mirzayev [1], Astan Shahverdiyev [2], Egon Hassel [3]

[1] Department of Industrial ecology and safety of habitability, Baku, Azerbaijan.

[2] Lehrstuhl für Technische Thermodynamik, Universität Rostock, Germany.

[3] Department of Heat and Refrigeration Techniques, Azerbaijan Technical University, Baku, Azerbaijan.

E-mail: javid.safarov@uni-rostock.de

The use of various alcohols as alternative to conventional gasoline and diesel fuels is increased dramatically. The successful using of 1-butanol as a fuel in an internal combustion engine is actually during the last years. 1-butanol has longer hydrocarbon chain causes and it to be fairly non-polar. In this case, 1-butanol more similar to gasoline than it is to ethanol. 1-butanol has been demonstrated to work in vehicles designed for use with gasoline without modification [1].

Today, the fuel injection systems for diesel engines reach pressures approximately up to 160 MPa for auto transport systems. Future systems are targeting even higher pressures in excess of 200-300 MPa. The one question in this filed: the possible number of injections per cycle during such extreme high pressures can be expanding and the time of one injection can be reduced. From another side, under such high pressure conditions, it is necessary to have the thermophysical properties of the fuel. Because, they can increase many times its atmospheric levels. Upon injection of the fuel in the cylinder, the large depressurization of the fuel results in a significant gradient of the viscous properties of the fluid [2]. The density, viscosity, speed of sound, heat capacity etc. are the main thermophysical properties for the study of such processes.

In this work, we present the thermophysical properties of 1-butanol at high pressures and wide range of temperature. The temperature interval was increased up to T=263.15 K and pressure up to 140 MPa. The experimental (p,ρ,T) results are helpful to extrapolate the temperature up to T=253.15 K and pressure up to 200 MPa using the constructed equation of state.

An equation of state for fitting of the (p,ρ,T) data has been developed as a function of pressure and temperature to calculate the various thermophysical properties of 1-butanol, such as isothermal compressibility, isobaric thermal expansibility, differences in isobaric and isochoric heat capacities, thermal pressure coefficient, internal pressure, heat capacities, speed of sound.

Keywords: Density, 1-butanol, Alternative fuel, Equation of state.

Literature:

1. http://en.wikipedia.org/wiki/Butanol_fuel
2. Duncan, A.M., Ahosseini, A., McHenry, R., Depcik, C.D., Stagg-Williams, S.M., Scurto, S.M. High-Pressure Viscosity of Biodiesel from Soybean, Canola, and Coconut Oils, Energy Fuels 2010, 24, 5708–5716.

Thermophysical Properties of Azerbaijan and Turkish Water Resources

Misirkhan Talibov [1], Lala Azizova [2], Sevinc Babayeva [3], Anar Ahmadov [1], <u>Javid Safarov</u> [1,4], Mahir Bashirov [1], Astan Shahverdiyev [1], Egon Hassel [4]

[1] Department of Heat and Refrigeration Techniques, Azerbaijan Technical University, Baku, Azerbaijan.
[2] Department of Industrial ecology and safety of habitability, Azerbaijan Technical University,
Baku, Azerbaijan.
[3] Department of Heat Power Engineering, Azerbaijan State Oil Academy, Baku, Azerbaijan.
[4] Lehrstuhl für Technische Thermodynamik, Universität Rostock, Germany.
E-mail: javid.safarov@uni-rostock.de

Azerbaijan and Turkey possesses rich water (geothermal, mineral and river water) resources. Various thermal water resources of these countries has temperatures up to ~140 °C. Mainly, these resources potentially use for bottled water production, medicinal purposes, for spas and health clinics that utilize the waters to treat arthritis, dysfunction of the nervous system and skin diseases. But they can be also used for: thermal heat, for warming soil, hotbeds and hothouses with the aim of early and rapid growth of vegetables and fruits (40-50 °C). In this filed, Turkey have more knowledge and there are many alternative energy installations already installed in the country. There are some installed energy equipments in Azerbaijan also and this work developing speedily.

Kura river starting in north-eastern Turkey, it flows through Turkey to Georgia, then to Azerbaijan, where it receives the Aras River as a right tributary, and enters the Caspian Sea. Pollution of the river from the territory of the neighbouring states creates an environmental tension. Mineralisation of the water of the Kura river raises till 800-1200 mg in the connecting part of Araz and Kura rivers is 35-50 per cent more compared to its medium current. Density of polluted water of Kura river is max. 9 times more than sanitary norms.

To use the water resources for the alternative energy source, also in daily life requires the investigation of the chemical and thermophysical properties of a wide range of parameters. In this work, we present the chemical and thermophysical properties of geothermal, mineral and river water resources of both countries using the various installations (Spectrometer, Chromatography, Densimeter, Viscometer, DSC calorimeter etc.)

The samples were filtered and degassed slowly using the vacuum system. To stop vaporisation of pure water, the vacuum procedure was very slow (the groove of the flask valve, which held the sample, was very slightly opened). These investigations have been examined for the first time.

An empiric equation of state for fitting of the (p,ρ,T) data of these water samples has been developed as a function of pressure and temperature. The molecular weight of thermal waters was analysed. The fitting of properties of water resources are discussing. The equation of state is used for the calculation of the thermophysical properties of IL, such as isothermal compressibility, isobaric thermal expansibility, thermal pressure coefficient, internal pressure, isobaric and isochoric heat capacities, speed of sound and isentropic expansibility.

Keywords: Geothermal water, River, Density, Viscosity, Speed of sound.

Thermophysical Properties of Ionic Liquids With [NTf$_2$]$^-$ Anions

Javid Safarov [1,2], Astan Shahverdiyev [2], Egon Hassel [1]
[1] Lehrstuhl für Technische Thermodynamik, Universität Rostock, Germany.
[2] Department of Heat and Refrigeration Techniques, Azerbaijan Technical University, Baku, Azerbaijan.
E-mail: javid.safarov@uni-rostock.de

Typical ILs have a stable liquid range of over 300 K and have a very low vapor pressure at room temperature. As well known the ILs have been suggested as potentially "green" replacements for conventional organic solvents since they are nonvolatile (negligible vapor pressure), nonflammable, thermal stable, and recyclable. While scientific and technological interest in the properties of room-temperature ILs and their mixture with other fluids are rapidly increasing.

One of the most important advantages of ionic liquids is their physical-chemical properties and the phase behavior of the systems based on the ILs can be tuned/controlled by tailoring their structures. To do this, however, it is crucial to assume that ILs are the solvents of which the local structural (i.e., electronic and steric) features may be correlated with their physical-chemical properties and then deal with the effect of their cation and anion structures in altering the abovementioned properties and phase behavior.

A homological series of the 1-alkyl-3-methylimidazolium bis(trifluoromethanesulfonyl)imides or [C$_n$mim][NTf$_2$] where n= 2, 4, 6, 8 is the *even* chain length of the alkyl-imidazolium cation has been the most frequently investigated class of aprotic ionic liquids. In contrast, thermodynamic data on the representatives of this family with the odd alkyl chain-length, where n= 3, 5, 7, are practically absent in the literature, probably because the precursors for synthesis of these ionic liquids are hardly commercially available.

In this case, we have tried to find the community between even and odd alkenes number ionic liquids 1-C$_N$mim-3-methylimidazolium (N=2, 3, 4, 5, 6, 7, 8) with [NTf$_2$]$^-$ anion using the molecular weight of ionic liquid. For this purpose, the (p,ρ,T) data of even alcohol number ionic liquids with bis(trifluoromethylsulfonyl)imide [NTf$_2$]$^-$ anions ([EMIM][NTf$_2$], [BMIM][NTf$_2$], [HMIM][NTf$_2$] and [OMIM][NTf$_2$] at T = (273.15 to 413.15) K and pressures up to p =140 MPa are reported with an estimated experimental relative combined standard uncertainty of $\Delta\rho/\rho = \pm(0.01$ to $0.08)$ % in density. The measurements were carried out with a newly constructed Anton-Paar DMA HPM vibration-tube densimeter, which based on the dependence of the period of oscillation of a unilaterally fixed U - tube (Hastelloy C - 276) on its mass. This mass consists of the U - tube material and the mass of the fluid filled into the U - tube.

The temperature in the measuring cell where the U – tube is located is controlled using a thermostat (F32 - ME Julabo, Germany) with an error of ±10 mK and is measured using the (ITS-90) Pt100 thermometer (Type 2141) with an experimental error of ±15 mK. Pressure is measured by pressure transmitters P-10 and HP-1 (WIKA Alexander Wiegand GmbH & Co., Germany) with a relative uncertainty of (0.1 and 0.5) % respectively, of the measured value.

An empiric equation of state for fitting of the (p,ρ,T) data of ionic liquids has been developed as a function of pressure, temperature and molecular weight of ionic liquids. The fitting using the group contributions will discussed. This equation is used for the calculation of the thermophysical properties of IL, such as isothermal compressibility, isobaric thermal expansibility, thermal pressure coefficient, internal pressure, isobaric and isochoric heat capacities, speed of sound and isentropic expansibility.

The literature (p,ρ,T) values of [C$_3$MIM][NTf$_2$] were compared with our calculated values and good agreement was obtained.

Keywords: Density, vibration tube densimeter, equation of state, thermal properties.

Density of Bosporus Seawater

Abzar Mirzaliyev [1], <u>Javid Safarov</u> [1,2], Astan Shahverdiyev [1], Egon Hassel [1]

[1] Department of Heat and Refrigeration Techniques, Azerbaijan Technical University, Baku, Azerbaijan.

[2] Lehrstuhl für Technische Thermodynamik, Universität Rostock, Germany.

E-mail: javid.safarov@uni-rostock.de

The Bosporus is a strait that forms part of the boundary between Europe and Asia. The world's narrowest strait used for international navigation, the Bosporus connects the Black Sea with the Sea of Marmara, after this connection Mediterranean Sea. These area located in the high ship navigation. The Bosporus, as connection between these water basins, play important role for international ship transport. of course, such intensive transportation play also negative role to ecology and atmosphere of this region. The one of biggest city of the world, Istanbul, located directly in the both side of strait. The daily life of 12 million people of this city also connected with Bosporus. The correct regulation of sanitary sewer system in Istanbul play important role for the water quality of Bosporus. Istanbul's wastewater consisted many pumping systems, pre-treatment and biological wastewater treatment plants. Most part of treated wastewaters is discharged into the Bosporus and small part to flow to Black Sea.

At the result of these discussions, it is to be seen, that the study of water quality of the Bosporus is very important. We studied three water sample taken from south, middle and north parts of Bosporus. The main interest was to study the changing of water quality from distances. at the first, the chemical analysis of Bosporus water was studied. After this, the density, viscosity, speed of sound, vapour pressure etc. thermophysical properties analysing. In this work, the chemical analysis and density measurements are presented.

The chemical analysis of these samples (cations and anions) were analysed using the IRIS Intrepid II Optical Emission Spectrometer and DX 100 ion chromotography.

The density measurements were carried out using the Anton-Paar DMA HPM vibration-tube densimeter, which based on the dependence of the period of oscillation of a unilaterally fixed U - tube (Hastelloy C - 276) on its mass. The temperature in the measuring cell where the U – tube is located is controlled using a thermostat (F32 - ME Julabo, Germany) with an error of ± 10 mK and is measured using the (ITS-90) Pt100 thermometer (Type 2141) with an experimental error of ± 15 mK. Pressure is measured by pressure transmitters P-10 with a relative uncertainty of 0.1 % respectively, of the measured value.

An empiric equation of state for fitting of the (p,ρ,T) data of water samples of Bosporus has been developed as a function of pressure, temperature and salinity of water. This equation is used for the calculation of the thermophysical properties of samples, such as isothermal compressibility, isobaric thermal expansibility, thermal pressure coefficient, internal pressure etc.

Keywords: Seawater, Bosporus, Density.

Simulation of Convection Heat Transport in Open-Cell Metal Foam

Ahmed S. Suleiman and Nihad Dukhan

Department of Mechanical Engineering University of Detroit Mercy
4001 W. McNichols Rd.Detroit, MI 48334 USA,
ndukhan@att.net

Abstract: In this paper a large domain made up of numerous idealized geometrical cells in the flow direction is used to simulate heat transfer due to air flow in open-cell metal foam. The large number of cells avoided periodicity issues and ensured minimal or no size and entrance effects. The flow and heat transfer equations are solved directly at the pore scale; and the temperature fields are obtained for various approach velocities using a commercial package. The details of the geometrical modeling and simulation are given. The commercial foam simulated has 20 pores per inch and porosity of 91.5%. The simulation shows a clear thermal-development region. To validate the simulation results and the modeling approach, direct comparisons to analytical local fluid temperatures from the solution of volume-average two-equation model in the thermally fully-developed region from the literature are presented. Good agreement between the simulation and analytical results are displayed.

Keywords: Unit Cell; Simulation; Metal Foam; Convection

Nomenclature

c specific heat of fluid ($J.kg^{-1}.K^{-1}$)
h convection heat transfer coefficient ($W.m^{-2}.K^{-1}$)
k effective thermal conductivity ($W.m^{-1}.K^{-1}$)
q"   heat flux ($W.m^{-2}$)
T temperature (K)
u volume-averaged pore velocity ($m.s^{-1}$)
$\mathbf{u}$ fluid velocity vector
x axial coordinate along flow direction (m)
z vertical coordinate perpendicular to flow direction (m)

Greek

ε porosity (dimensionless)
ρ density of fluid ($kg.m^{-3}$)

Subscripts

f   fluid
s   solid
w   wall

Introduction

Convection heat transfer in open-cell metal foam [1] is gaining more interest. For heat transfer, the foam is attractive because of the high conductivity of the solid phase and the large surface area per unit volume. This is in addition to the vigorous mixing of the flowing fluid and continuous destruction of boundary layers, which enhances convection between the solid and the fluid phases.

The internal morphology of open-cell foam is complex. Exact solutions of transport equations, including all pertinent effects, are extremely difficult. Detailed numerical analysis

at the microscopic level can assist in better understanding intricacies of the complex temperature fields inside metal foam. In order to solve the governing equations, an idealized geometrical model of the internal structure of the foam is crucial. Many studies attempted to model the geometry of open-cell metal foam by defining a representative elementary volume (rev) that captures the relevant characteristics of these materials. For example, du Plessis et al. [2] represented the foams by a set of rectangular prisms and Boomsma et al. [3] represented the cell of the foam by a tetrakaidecahedron (six 14-sided polyhedra having 12 pentagonal and two hexagonal faces, and two pentagonal dodecahedra), and used a 'periodic' unit that consisted of eight such cells.

Krishnan et al. [4] simulated flow and heat transfer in open-cell metal foam using a single ideal body center cube (bcc) unit cell. They assumed fully-developed flow and invoked periodicity. Karimian and Straatman [5] used a unit cell based on interconnected sphere-centered cubes to represent the internal structure of foam. They used two such cells in the flow direction and assumed fully-developed laminar flow. Periodic boundary conditions were imposed at the inlet and outlet.

Bai and Chung [6] used a sphere-center Kelvin structure to simulate fluid flow in metal foam by studying two kinds of cells: an interior cell (away from a confining wall) and a boundary cell in order to assess interactions with a solid boundary. A single unit cell was used in the simulation. Horneber et al. [7] used a single and multiple Kelvin cells to simulate flow in a metal-foam reactor. Constant inlet velocity was imposed and constant outlet pressure was prescribed. Results showed that the single cell case always produced higher pressure as compared to the case of multiple cells. The authors confirmed the presence of entrance and exit effects that could not be captured by simulating a single cell.

Kopanidis et al. [8] carried out numerical simulations for the conjugate flow and heat transfer in open-cell metal foam. They used a cell geometry that was obtained by minimizing surface energy. The computational domain consisted of 10 cells. Both laminar and turbulent flows were investigated for 10- and 20-pore-per-inch (ppi) metal foam. Boundary conditions included fixed inlet velocity and fixed inlet-outlet pressure difference, noting that the former represented the entrance region of a larger foam domain, while the latter represented fully-developed flow conditions.

The current work presents details of obtaining a bcc cell, and links the cell to the morphology of actual metal foam. The unit cell is similar to Kelvin's cell, which was believed to have minimum surface area-to-volume ratio compared to other geometries [4,9], until 1994, when Weaire and Phelan [10] provided a counter example having a slightly lower surface area. The bcc geometry is relatively simple and easier in terms of meshing compared to others used in the literature [3,8].

Unlike many other modeling studies which considered a domain of only one cell [4,6], or few cells [3,5], the current study employs a large number of cells in order to insure fully-developed conditions and to avoid the issue of periodicity and size effect. Another improvement provided by the current study is the direct and meaningful validation of the simulation results using the well-accepted volume-average analytical solution.

Unit Cell

The internal structure of commercial aluminum foam is formed by connecting solid ligaments to form cells and open windows (pores, Figure 1).
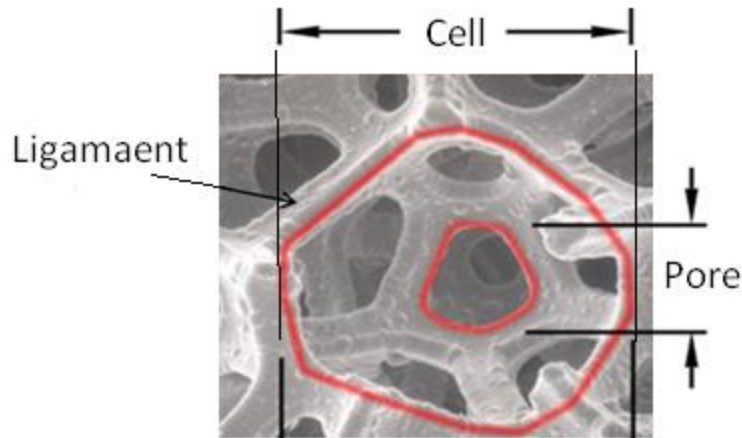
Figure 1 Internal Structure of Open-Cell Metal Foam

For simulation this geometry is idealized as follows. Consider a cube of side length a_1. Fifteen equal spheres of radius R are subtracted from the cube as shown in Figure 2. The distance between the centers of the central sphere and a polar sphere after overlapping is adjusted to be a_1. The distance a_1 is related to the number of pores per inch (ppi), which is a common industrial designation. Open-cell 10-ppi commercial aluminum foam on average has 5 central spheres in one linear inch.
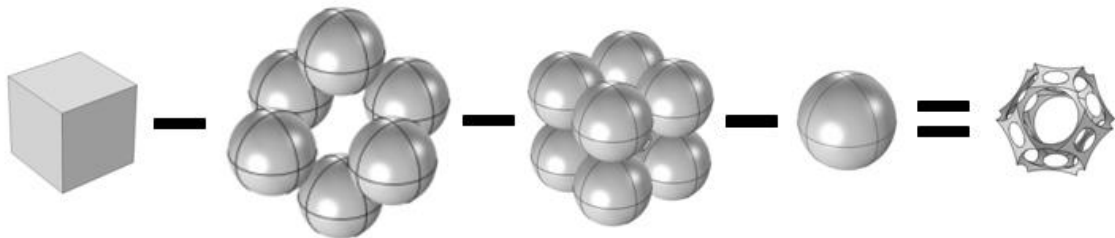
Figure 2 Generating the Idealized Unit Cell by Subtraction Spheres at Cube's Faces, Vertices and Center

The steps of Figure 2 for obtaining the idealized cell geometry can be easily performed in a Computer-Aided-Design (CAD) package. This geometry along with the sphere-subtraction method produces a cell diameter and a pore diameter within 3.3% and 15.0% of averaged measured values for commercial aluminum foam [11], respectively. In addition, the sphere-subtraction method produces the triangular shape of the cross-section of the ligaments, as can be found in actual high-porosity foam.

Simulation

Convection heat transfer simulations were carried out in COMSOL. A 20-ppi foam domain having a length of 83.8 mm in the flow direction and a height of 38.1 was simulated. Due to symmetry, this domain represents flow and heat transfer between two heated parallel plates separated by a distance of 76.2 mm. There were a total of 495 cell- 33 cells in the flow direction and 15 cells perpendicular to the flow direction. Attached to this domain was a one-mm-thick wall (to apply a heat flux). This solid wall is shown at the bottom of the insert in

Figure 3. To save on computational cost exploiting symmetry, the thickness of the domain was half a cell, as shown in Figure 3. The fluid domain (air) was obtained by subtracting the solid domain from an imaginary channel surrounding the total domain, Figure 3.
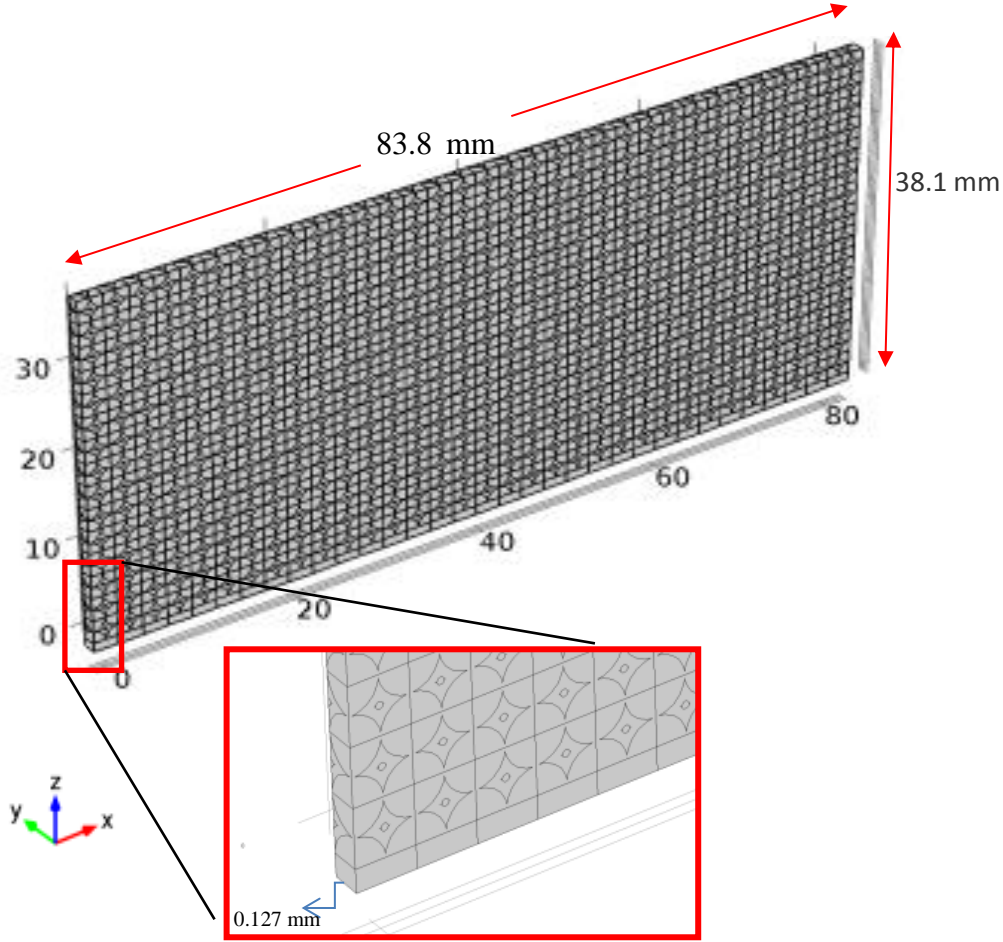
Figure 3 The Computational Domain

Continuity, Navier-Stokes and the energy equations (for the solid and fluid phases) were solved using a built-in function called Solver in COMSOL. These equations are

$$\rho \nabla . \mathbf{u}. = 0 \tag{1}$$

$$(\mathbf{u}.\nabla).\mathbf{u} = \nabla.\left[-pI + \mu\left(\nabla\mathbf{u} + \{\nabla\mathbf{u}\}^T\right)\right] + F \tag{2}$$

$$\nabla.\left(k_f \nabla T_f\right) = \rho\, c\, \mathbf{u}\, \nabla T_f \tag{3}$$

$$\nabla.\left(k_s \nabla T_s\right) = 0 \tag{4}$$

where $\mathbf{u}$ is the fluid velocity vector, p is the pressure, μ is the fluid viscosity, ρ is the fluid density and F represents body forces. T is the temperature and the subscripts f and s refer to the fluid and solid phases, respectively. k is the thermal conductivity and c is the specific heat of the fluid. It must be noted here that during the solution steps of COMSOL Solver, the software ensures that both the temperature and heat flux are continuous at the solid-fluid interface. In this manner Eqs. (3) and (4) are indeed coupled.

317

The following exterior boundary conditions were used:

$$\text{at } y = H \qquad \frac{\partial \mathbf{u}}{\partial y} = 0 \qquad\qquad\qquad (5a)$$

$$\text{at } y = H \qquad \frac{\partial T_f}{\partial y} = \frac{\partial T_s}{\partial y} = 0 \qquad\qquad\qquad (5b)$$

$$\text{at } y = 0 \qquad \mathbf{u} = 0 \qquad\qquad\qquad (6a)$$

$$\text{at } y = 0 \qquad -k_f \frac{\partial T_f}{\partial y} = -k_s \frac{\partial T_s}{\partial y} = q'' \qquad\qquad\qquad (6b)$$

At the entrance, various values for a constant fluid velocity (0.1, 0.15 and 0.2 m/s) were imposed one at a time, along with a constant temperature of 295.15 K. At the outlet, constant fluid pressure of 0 bar was used. The wall heat flux was 8495 W/m^2. At the internal surface of the solid phase of the foam, zero fluid velocity (no-slip) was imposed. The flow was assumed to be laminar, steady and incompressible. Air was the working fluid with a density of 1.2 kg/m^3 and a viscosity of 1.814x10^{-5} Pa.s. The range of entrance velocity produced Reynolds numbers well within the laminar flow regime in porous media.

The computational domain was meshed using tetrahedral elements. A finer mesh was applied to areas on the porous cell surface to account for anticipated large gradients in these areas. Mesh generation with a total 5,370,251 degrees of freedom produced 3,953,369 elements. The simulation took five hours and 31 minutes for each flow-velocity case on a 64-bit operating system, with a processor operating at 3.40 GHz and 31.7 GB of usable RAM.

To ensure mesh independence, the same computational domain was spatially discretized using three meshes of varying refinement. The three different unstructured-tetrahedral-element coarse, medium and fine meshes were generated using built-in mesh-generating functions in COMSOL. They consisted of 1,168,547, 3,953,369 and 6,826,533 elements, respectively. For the same entrance velocity of 0.2 m/s, the influence of the mesh density on three particular parameters was considered, namely, average surface pressure at the entrance, local air temperatures along the flow direction at 0.127 cm from the heated wall and local air velocities (x-component) as a function of z at 6.225cm from the entrance. There was little difference between the results obtained by the medium and fine meshes for all three parameters. The medium mesh was chosen for all subsequent studies.

Results

The temperature of air as it passed through the heated domain is shown in Figure 4. The temperature of air increases as it continuously absorbs heat from the heated wall. Close to the inlet and far from the heated wall, the temperature is similar to inlet air temperature of 295 K. Close to the heated wall and farther away from the inlet, the temperature increases gradually to a maximum of about 350 K. This behavior is expected and is consistent with the physics of heat transfer in a channel.
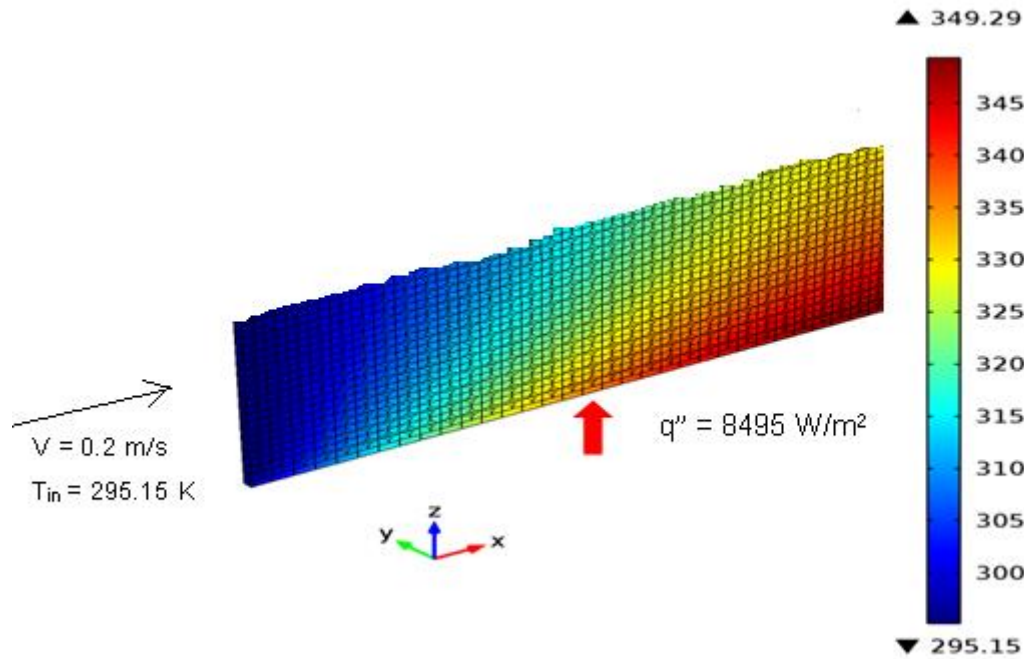
Figure 4 Color Plot of Air Temperature along Simulation Domain

A plot of the wall temperature as a function of the flow direction is shown in Figure 5. For each velocity, the wall temperature exhibits development: it increases as the distance from the entrance increases with a decreasing slop. The rate of increase (the slope) seems to become constant at about x = 7.5 cm indicating thermal full development. This trend in the wall temperature of heated metal foam is similar to what is presented in [12]. Similar trends were observed experimentally in [13] for a foam cylindrical system heated with a constant heat flux.
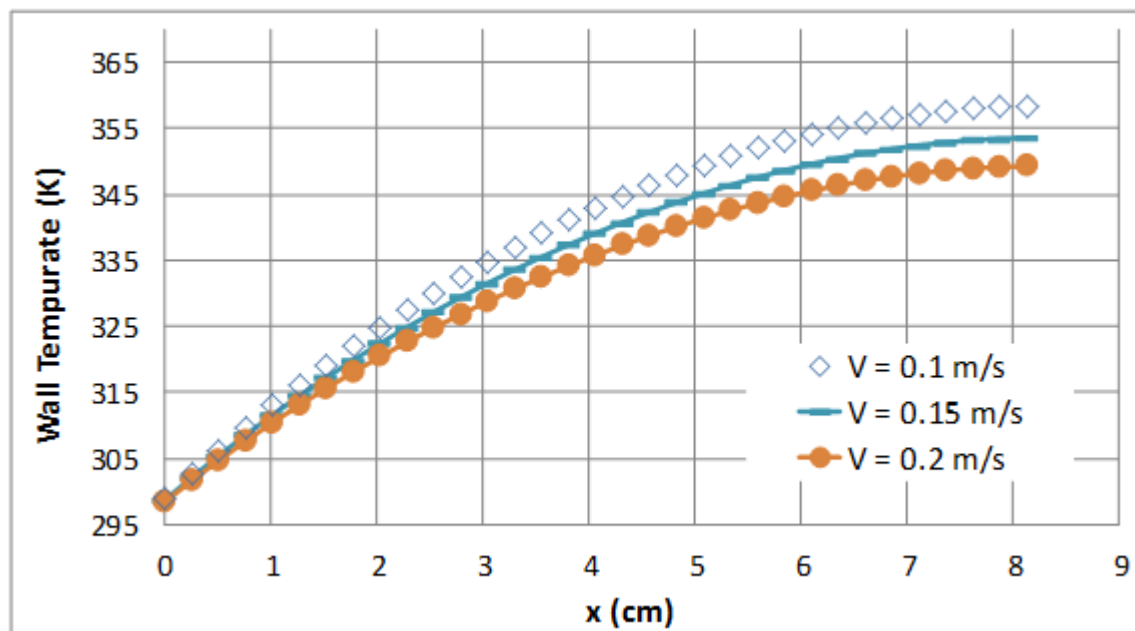
Figure 5 Wall Temperature as a Function of Flow Direction

The entry length shows little or no dependence on the velocity (or flow Reynolds number) due to the small changes in velocity. Recent studies alluded to the entrance region for flow in metal foam [7,8].

Analytical Validation

The simulation approach is validated using the volume-averaged solution of the two-energy-equation analytical model. The relatively simple case for Darcy-Brinkman flow through a porous medium occupying the space between two heated parallel plates is amenable to analytical solution given in [14].

Figures 6, 7 and 8 show a comparison between the fluid temperature obtained by simulation and the prediction of the volume-average solution. For this comparison, the simulation temperatures were taken in the fully-developed region, i.e., at an axial location x = 7.62 cm. The temperatures were obtained at the center of each cell: y = 0.
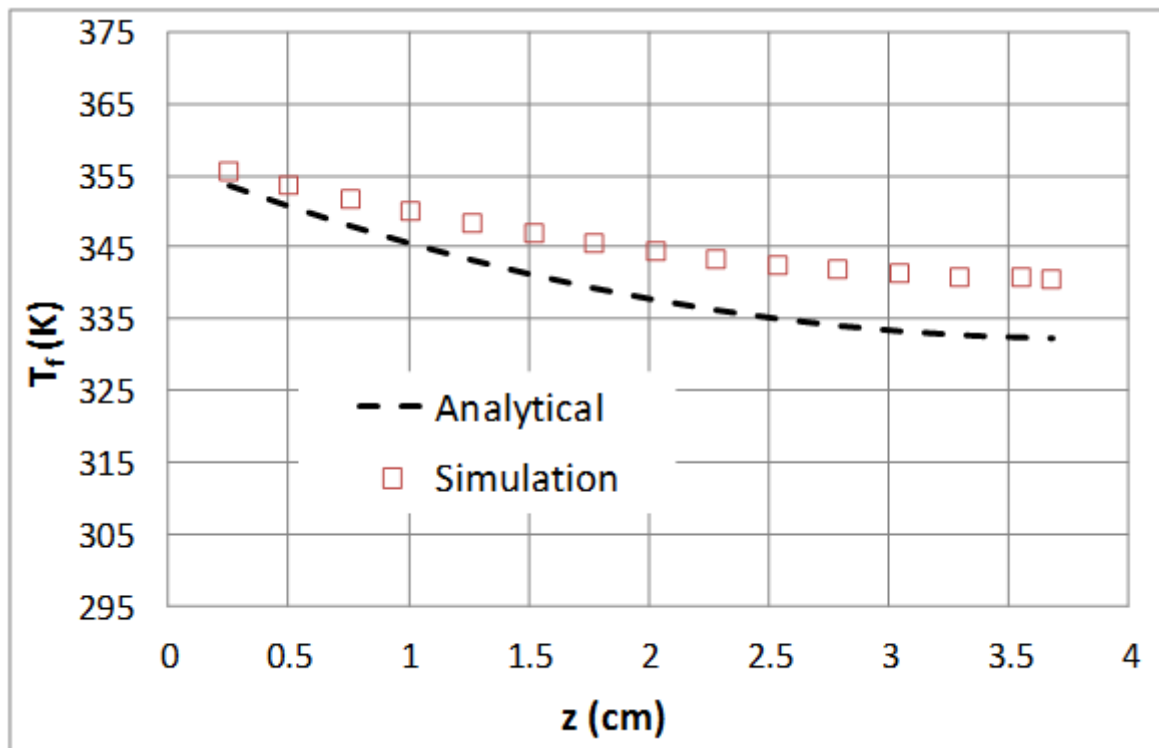
Figure 6 Simulation and analytical fluid temperatures for entrance velocity = 0.1 m/s
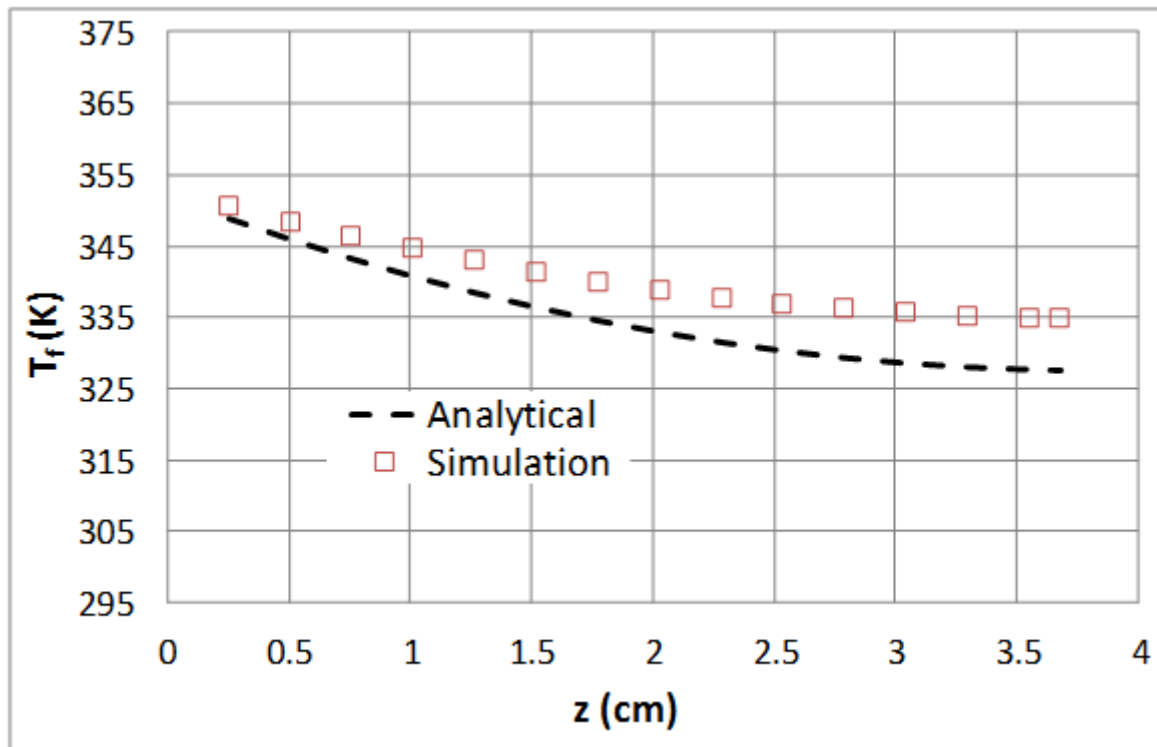
Figure 7 Simulation and analytical fluid temperatures for entrance velocity = 0.15 m/s
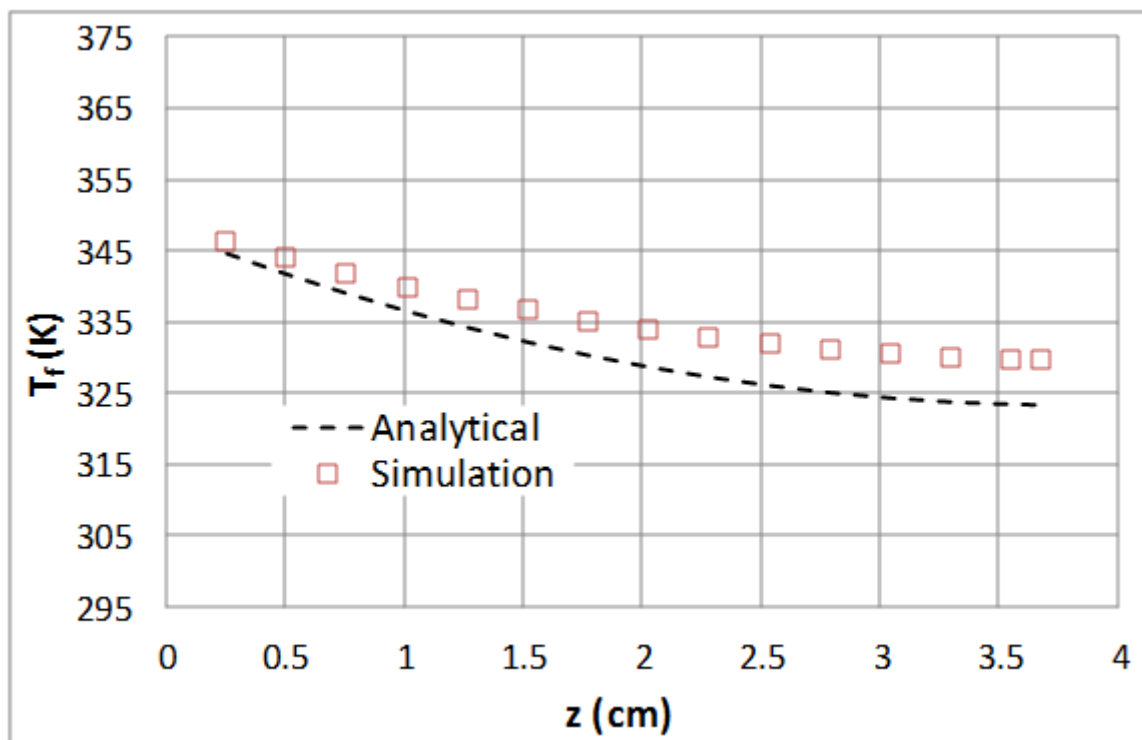
Figure 8. Simulation and analytical fluid temperatures for entrance velocity = 0.2 m/s

The simulation and analytical temperature curves are relatively close to each other, with the difference being small close to the heated wall (z = 0) and increasing as the distance from the heated wall increases. Nonetheless, the maximum difference between the two temperatures is less than 2.5% for the velocity of 0.1 m/s (Figure 6). The analytical solution is seen to consistently predict a lower temperature for all cases. Interestingly, similar occurrence was

found by Dukhan et al. [13]: the volume-average analytical solution predicted lower fluid temperature than experimentally-obtained local fluid temperatures for a heated cylinder filled with similar aluminum foam.

Conclusion

Simulation of convective heat transfer inside commercial metal foam was conducted on a large domain composed of numerous idealized cells. The idealized cell geometry was based on a body center cube. The governing equations were solved at the microscopic level. Results clearly showed thermal development. For validation, fluid temperatures in the thermally fully-developed region were compared to their analytical counterparts. Very good agreement between the analytical and simulation fluid temperatures was displayed. However, the analytical solution of the volume-averaged energy equations seemed to slightly and consistently under-predict the fluid temperature.

References

[1] Dukhan, N., Editor. 2013: *Metal Foam: Fundamentals and Applications*. DESTech, Lancaster, PA.
[2] P. du Plessis, A. Montillet, J. Comiti, J. Legrand, Pressure Drop Prediction for Flow through High Porosity Metallic Foams, *Chemical Engineering Science*, 49(21) (1994) 3545–3553.
[3] K. Boomsma, D. Poulikakos, Y. Ventikos, Simulations of Flow Through Open Cell Metal Foams Using an Idealized Periodic Cell Structure, *Int. J. Heat Fluid Flow*, 24(6) (2003) 825–834.
[4] S. Krishnan, J. Y. Murthy, S. V. Garimella, Direct Simulation of Transport in Open-Cell Metal Foam, *J. Heat Transfer*, 128(8) (2006) 793-799.
[5] S. A. M. Karimian, A. G. Straatman, CFD Study of the Hydraulic and Thermal Behavior of Spherical-Void-Phase Porous Materials, *Int. J. Heat Fluid Flow*, 29(1) (2008) 292–305.
[6] M. Bai, J. N. N. Chung, Analytical and Numerical Prediction of Heat Transfer and Pressure Drop in Open-Cell Metal Foams, *Int. J. Thermal Sciences*, 50(6) (2011) 869–880.
[7] T. Horneber, C. Rauh, A. Delgado, Fluid Dynamic Characterization of Porous Solids in Catalytic Fixed-Bed Reactors, *Microporous and Mesoporous Materials*, 154 (2012) 170–174.
[8] A. Kopanidis, A. Theodorakakos, E. Gavaises, D. Bouris, 3D Numerical Simulation of Flow and Conjugate Heat Transfer Through a Pore Scale Model of High Porosity Open Cell Metal Foam, *Int. J. Heat Mass Transfer*, 53(12) (2010) 2539–2550.
[9] K. A. Brakke, The Surface Evolver, *Experimental Mathematics*, Vol. 1, No. 2 (1992), 141-165.
[10] D. Weairea & R. Phelana, A counter-example to Kelvin's conjecture on minimal surfaces, *Philosophical Magazine Letters*, Volume 69, Issue 2, 1994, pages 107-110. DOI:10.1080/09500839408241577
[11] ERG Materials and Aerospace, http://www.ergaerospace.com, accesses June 2013.
[12] V. V. Calmidi, R. L. Mahajan, Forced Convection in High Porosity Metal Foams, *J. Heat Transfer*, 122 (2000) 557-565.
[13] N. Dukhan, M. A. Al-Rammahi, A. S. Suleiman, Fluid Temperature Measurements Inside Metal Foam and Comparison to Brinkman–Darcy Flow Convection Analysis, *Int. J. Heat Mass Transfer*, 67 (2013) 877–884.
[14] H. J. Xu, Z. G. Qu, W. Q. Tao, Thermal Transport Analysis in Parallel-Plate Channel Filled with Open-Celled Metallic Foams, *Int. J. of Heat Mass Transfer*, 38 (2011) 868-873.

Experimental Characteristics of Oscillating Liquid Flow in Metal Foam: Effect of Flow Displacement

Özer Bağcı [1], Nihad Dukhan [2,*], and Mustafa Özdemir [1]

[1] Makina Fakültesi
Istanbul Technical University
Gümüşsuyu, 34437, Istanbul, Turkey
[2] Department of Mechanical Engineering
University of Detroit Mercy, Detroit, MI 48334, USA
(*Corresponding author: ndukhan@att.net +313 993 3285)

Abstract: Characteristics of oscillating water flow in open-cell metal foam were obtained experimentally. The foam had 20 pores per inch and a porosity of 87.6%. Three flow displacements 74.35, 97.2 and 111.53 mm were applied at the flow frequency of 0.116 Hz. Steady-state experiment was also conducted and the permeability and form/inertial drag coefficient were obtained. The range of flow velocity covered Darcy and Forchheimer flow regimes. The effect of flow displacement on important variables is presented and discussed. The appropriately defined friction factor and the Reynolds number for steady-state and oscillating flows were calculated, with the friction factor for oscillating flow being higher. The current results were compared to other studies from the literature employing oscillating air and water in various kinds of porous media.

Keywords: Metal foam; Oscillating flow; Porous media; Friction factor; Kinetic Reynolds number

Nomenclature

α	constant, Eq. (5)
β	constant, Eq. (5)
$\tilde{\alpha}$	correlation constant, Eq. (10)
$\tilde{\beta}$	correlation constant, Eq. (10)
A	cross-sectional area of test section (m^2)
D	inner diameter of test section (mm)
f	friction factor for steady flow $= \dfrac{2(\Delta p/L)D}{\rho\, u^2}$
f_{max}	oscillating flow friction factor $= \dfrac{2(\Delta p_{max}/L)D}{\rho u_{max}^2}$
F	Forchheimer coefficient
K	permeability (m^2)
L	length of porous medium (m)
p	static pressure (kPa)
Re	Reynolds number for steady flow $= \dfrac{\rho u D}{\mu}$
Re_{max}	Reynolds number for steady flow $= \dfrac{\rho \omega D x_{max}}{2\mu}$
Re_{ω}	kinetic Reynolds number $= \dfrac{\rho \omega D^2}{\mu}$
t	time (s)
u	average velocity (m/s)
x_{max}	maximum flow displacements (mm)

Greek

Δ change

ε porosity

μ viscosity (Pa.s)

ν flow frequency (Hz)

ω angular frequency (rad/s)

ρ density (kg/m^3)

Introduction

Open-cell metal foams are relatively a new class of porous media made from several metals and alloys. The foams are highly porous, permeable, thermally-conductive and contain large surface area per unit volume. All these properties make metal foams very attractive for heat transfer enhancement designs, and other applications [1].

Oscillating flow and heat transfer in porous media is a phenomenon that occurs in many engineered systems, e.g., heat pipes, regenerators (e.g. in Stirling engines and cryocoolers), cooling designs of nuclear power plants and reciprocating internal combustion engines. Oscillating and pulsating fluid flow and heat transfer in traditional porous media (spherical particles, granular beds and mesh screens) have received considerable attention. See for example, Kim et al. [2], Gue et al. [3], Sozen and Vafai [4] Hsu et al. [6] Byun et al. [5] and Dai and Yang [7]. Khodadadi [8] provided an analytical solution for oscillatory flow through a porous channel bounded by two solid walls for two limiting cases: highly inertial and highly viscous flow. For the first case, the velocity and pressure gradient had a phase shift of 90o and there was a channeling effect: the velocity profiles exhibited maxima next to the solid wall.

Zhao and Cheng [9] experimentally investigated pressure drops due to oscillatory air flow through a woven-screen packed column. The average pressure drop for the oscillatory flow was several times higher than that for steady flow. Cha et al. [10] investigated oscillating flow of helium through typical porous fillers for pulse-tube and Stirling-cycle cryocooler regenerators (e.g. mesh screens, foam metal, stacked micro-porous nickel disks), both experimentally and using CFD. They reported a phase shift between the inlet and outlet pressures of the porous media that increased with increasing frequency.

Pamuk and Özdemir [11] experimentally investigated oscillating water flow in two sets of mono-sized packed steel balls. The porosity of the first set was 36.9%, while it was 39.1% for the other. It was shown that the permeability and inertial coefficient for oscillating flow were greater than their steady-state counterparts. Pamuk and Özdemir [12] presented experimental heat transfer results using the same porous media subjected to oscillating flow of water.

Published results concerning oscillating flow in metal foam are scarce. Leong and Jin [13] experimentally investigated oscillating air flow through a channel filled with open-cell metal foam. They showed that the oscillating flow characteristics in the foam were governed by the hydraulic-ligament-diameter-based kinetic Reynolds number and the dimensionless flow displacement amplitude. The effect of the kinetic Reynolds number on the pressure drop and flow velocity was more significant. There was a small phase difference between the velocity and the pressure drop. As compared to oscillating flow in wire screens, the maximum friction factor was generally lower for the case of metal foam.

In a different study, Leong and Jin [14] studied heat transfer due to oscillating air flow through a channel filled with 40 pore-per-inch aluminum foam experimentally. The pressure drop and flow velocity increased with increasing oscillating frequency and varied almost sinusoidally. In a third investigation, Leong and Jin [15] conducted experiments to study the heat transfer performance of metal foam heat sinks subjected to oscillating flow of air. The aluminum foams had 10, 20 and 40 pores per inch. Profiles of the pressure drop increased with increasing foam's pore density. The maximum pressure drops and velocities increased with increasing kinetic Reynolds number, i.e., the dimensionless oscillating frequency.

As indicated by Pamuk and Özdemir [11], all experimental studies in the literature concerning oscillating flow and heat transfer in porous media (including metal foam) used gas, mostly air, as the working fluid. Oscillating flow of water in metal foam has not been presented. The purpose of this study is to investigate the characteristics of oscillating water flow in open-cell metal foam. The ultimate purpose is to enhance fundamental understanding of oscillating flow phenomenon in metal foam in terms of increased pressure drop (or pumping power), effect of frequency, effect of stroke length, flow regimes, scales and pertinent non-dimensional numbers, etc.

Experiment

Figure 1 is a schematic of the experimental setup. The test section 1 is an aluminum alloy (6061-T6) pipe having inner diameter of 50.80 mm and length of 305 mm. Commercial open-cell aluminum foam having 20 pores per inch (ppi) and porosity of 87.6% is brazed to the inside surface of the pipe.

The test section is connected to two 51.4-mm-diameter 200-mm-long Polyethylene tubes 2 at its two ends; pressure taps are drilled on these tubes. The outlets of the Polyethylene tubes are connected to stainless steel pipes 3 32 mm in diameter and 110 cm in length. The ends of these tubes are connected to an oscillating flow apparatus 6-10 via hoses 5. The oscillation generator is a double-acting cylinder which is connected to an electrically driven motoreductor by means of a flywheel and a crank arm. Inner diameter of hydraulic cylinder is 50 mm and the diameter of the piston installed inside it is 32 mm. The maximum stroke obtainable by this mechanism is 200 mm. Rotational speed of the 7.5-kW motoreductor is controlled via a variable speed AC-drive (6.99-20.97 rpm). Additionally, an adjustment system mounted on the flywheel allows changes in stroke.

The pressure at the inlet and outlet of the test section is measured by Keller models PR-23R and PA-21Y piezoresistive transmitters. PR-23R is able to measure gauge pressure up to 0.100 bars, while PA-21Y measures pressures up to 2.5 bars. The transmitters are connected to a data logger 11. They provide 2-10 V as direct-current signals, which are converted to actual pressure values using a linear relation between voltage and pressure.

For steady-state pressure measurements, the set-up can be easily converted to unidirectional flow arrangement using control valves 4. For this case water is supplied from a constant-head elevated tank (not shown). For a given run, control valves are adjusted and water is allowed to flow into the foam until steady state is reached. A valve at the inlet provides fine control over the mass flow rate. For a fixed valve opening (flow rate), water exiting the test section is captured in a collecting tank over a known period of time. The mass flow rate and the average flow velocity are determined.

For oscillating flow testes, the set-up is switched to a closed system fully charged with water and connected to the oscillating generator. In order to avoid entraining air, the whole system is vacuumed down to 700 mmHg absolute. Heavily-filtered water is allowed to flow in from taps at the two ends of the piston 6. As air bubbles are removed from the system through the purger 13.
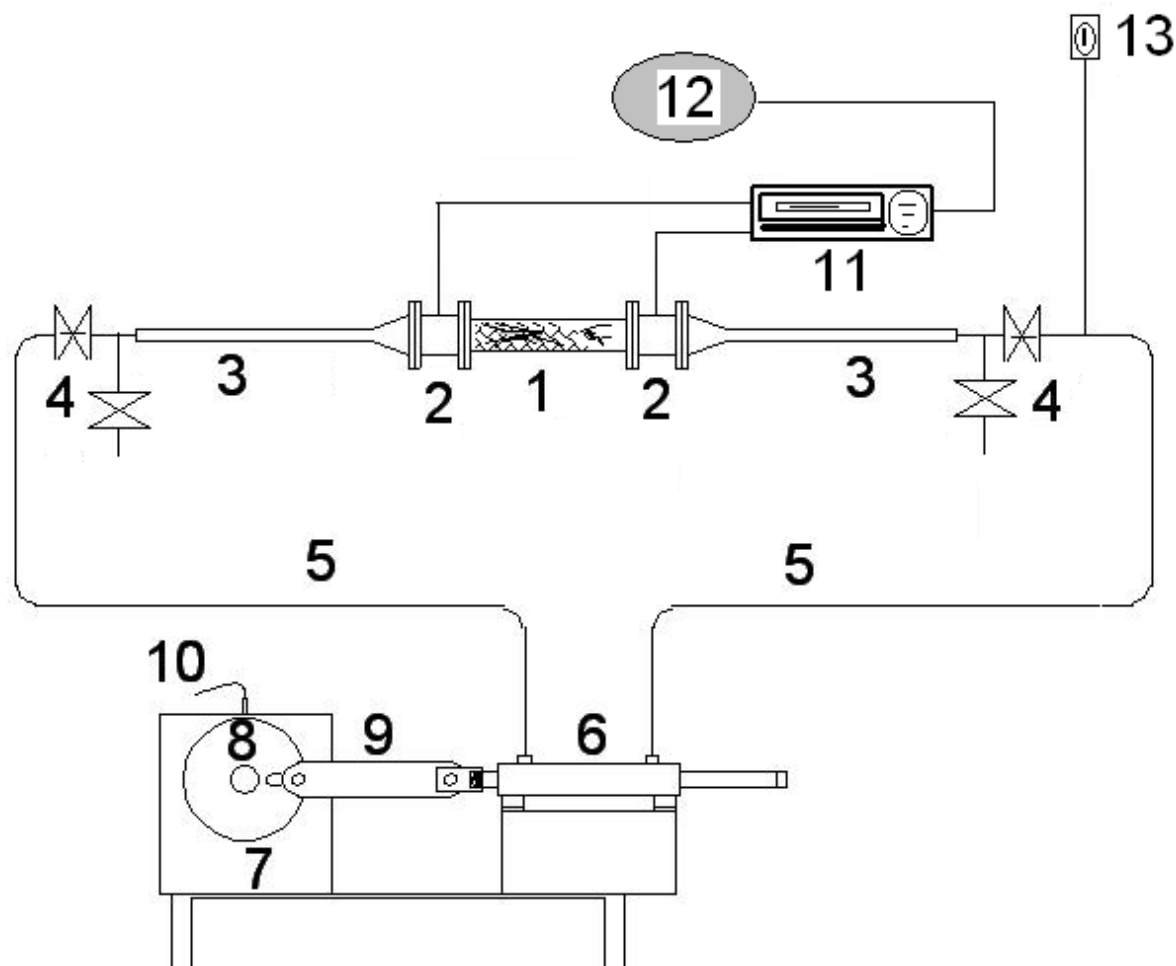
Figure 1 Schematic of Experimental Setup: 1.Test Section (metal foam), 2. Polyethylene tube, 3. Steel pipe of 32-mm in diameter, 4. Separating valves, 5. Connecting hoses, 6. Oscillation Generator, 7. Motoreductor, 8. Flywheel, 9. Crank Arm, 10. Inductive Proximity Sensor, 11. Data logger, 12. Computer, 13. Air Purger.

For a given oscillating flow run, the stroke length of the piston is set to a desired value, the oscillating generator is switched on, and the oscillating frequency is ramped to the targeted value. After the system stabilizes (up to 10 minutes), a Keithley 2700 XLINX data acquisition system, communicates with the data logger and records two pressure signals from the two pressure transmitters and one signal from a clicker. This clicker touches a bump on a flywheel (part of the oscillation system) once per cycle, and it is used to calculate the angular speed. The above is repeated for stroke lengths (displacement of piston) 130 mm, 170mm and 195 mm, and line frequency 5 Hz.

Uncertainty in the reported data includes error in the directly-measured quantities, e.g., dimensions and frequency; and propagated error in derived quantities, [16]. The

uncertainties in length and diameter of the metal foam tube were 0.33% and 0.04%, respectively. As for pressure measurements, the transmitters had an error band of ±1% of full scale. These values were provided by the manufacture and included effects of linearity, hysteresis and repeatability. The uncertainties in the angular frequency and maximum fluid displacement are estimated as 0.43% and 0.51%, respectively.

2.1 Data Reduction

For oscillating flow, maximum fluid displacements are related to the displacements of the piston: 130 mm, 170 mm and 195 mm according to conservation of mass, and the fact that water is an incompressible fluid. The maximum flow displacements (x_{max}) at the entrance of the metal foam are calculated from the ratio of the cross-sectional areas of piston and entrance of porous channel as

$$x_{max} = \frac{2RA_p}{A} \tag{1}$$

where R, A_p and A are flywheel radius, cross-sectional areas of double acting cylinder and metal-foam pipe, respectively. This gives 74.35 mm, 97.23 mm and 111.53 mm for x_{max}.

For each displacement, line frequency is set at 5 Hz by a servo drive of motor. Actual flow frequency is linearly proportional to line frequency. The motoreductor operates at 69.7 rpm at 50 Hz line frequency.

The piston displacement is actually equal to the fluid displacement since the fluid is incompressible. Hence, at the entrance of the foam, the fluid displacement x_m varies with angular frequency ω and time t according to

$$x_m(t) = \frac{x_{max}}{2}(1 - \cos \omega t) \tag{2}$$

The cross-sectional mean fluid velocity in the channel is

$$u(t) = u_{max} \sin \omega t \tag{3}$$

where $u_{max} = \omega x_{max}/2$.

Results and Discussion

In Figure 2 the average velocity through the foam is superimposed on the pressures at the inlet and outlet for the case of x_{max}= 97.23 mm for the frequency of 0.232 Hz. The two pressures are not in phase. The phase shift between the inlet pressure and flow velocity is approximately 36o, and between the outlet pressure and flow velocity the shift is about 212°. Pamuk and Özdemir [11] reported no phase shift between the pressures and flow velocity for oscillating water flow in packed spheres. Khodadadi [8] reported a phase shift of 90° between the velocity and pressure gradient based on his analytical solution. Zhao and Cheng [9] also reported a phase shift between pressure drop and velocity for air flow in screens; this phase shift increased with frequency. The channeling effect (flow velocity exhibiting maxima next to the solid wall) reported by Khodadadi [8] could be responsible in part for this phase shift.

The interactions of inertia and acceleration effects combined with sudden flow reversal also have some influence.

In Figure 2, the dotted lines represent the flow velocity at which the Forchheimer regime starts for the steady-state case. What this means is that flow changes regimes between Darcy and Forchheimer more than once within a given period. Regime changes indicate frictional resistance changes; this phenomenon adds to the complexity of the phenomenon at hand.

The effect of maximum fluid displacement on the pressure at the inlet of the foam is shown in Figure 3. As expected there is a positive correlation between the displacement and the inlet pressure. The pressure exhibits a periodic behavior with the period being longer for shorter displacements.

The effect of maximum fluid displacement on pressure drop across the foam is shown in Figure 4 for various frequencies. For the low frequency of 0.116 Hz, the pressure drop is periodic and has equal amplitudes above and below the zero line. The behavior of the pressure drop for the low frequency of 0.116 Hz is consistent with what was obtained by Pamuk and Özdemir [11] for water flow in packed spheres, Leong and Jin [13,14] for air flow in metal foam and by Zhao and Cheng [9] for air flow in a packed bed of woven screens.
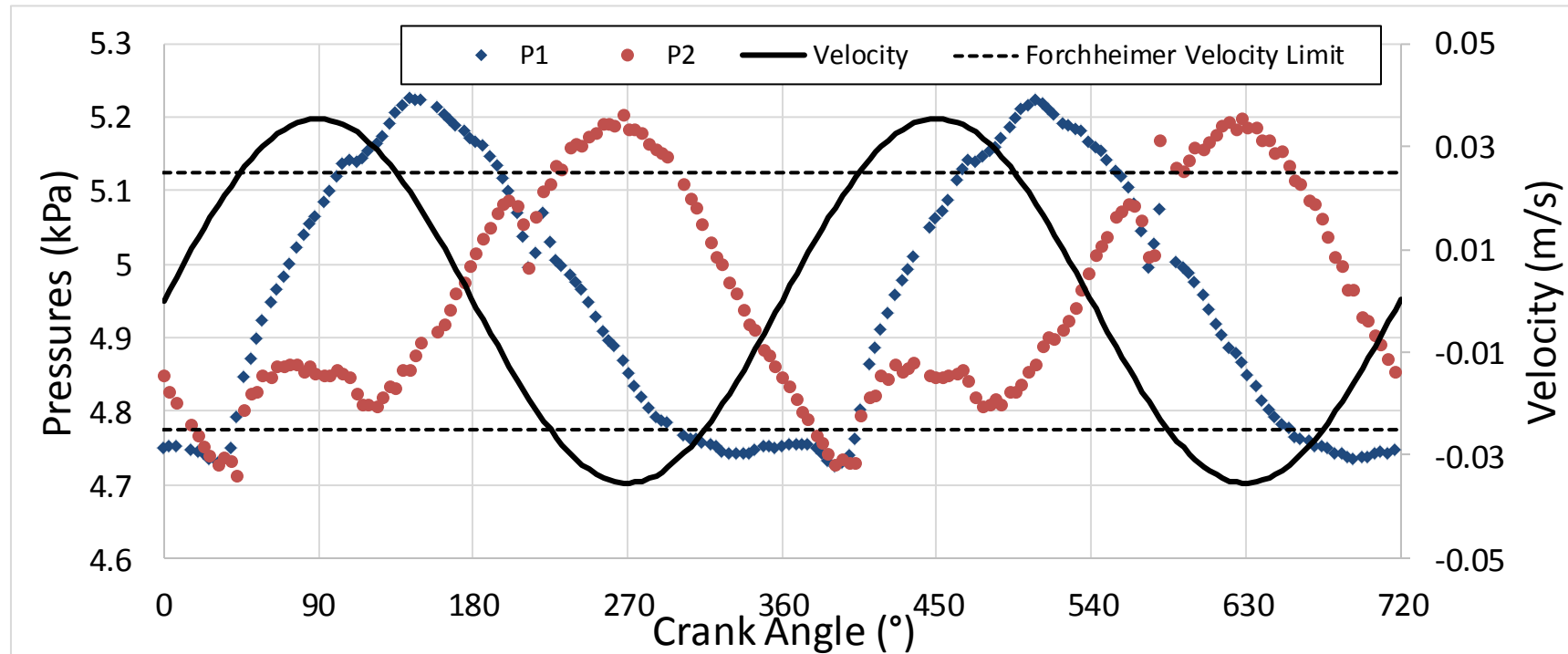
Figure 2 Temporal pressures at inlet and outlet and average flow velocity for x_{max} = 97.23 mm and ν = 0.116 Hz
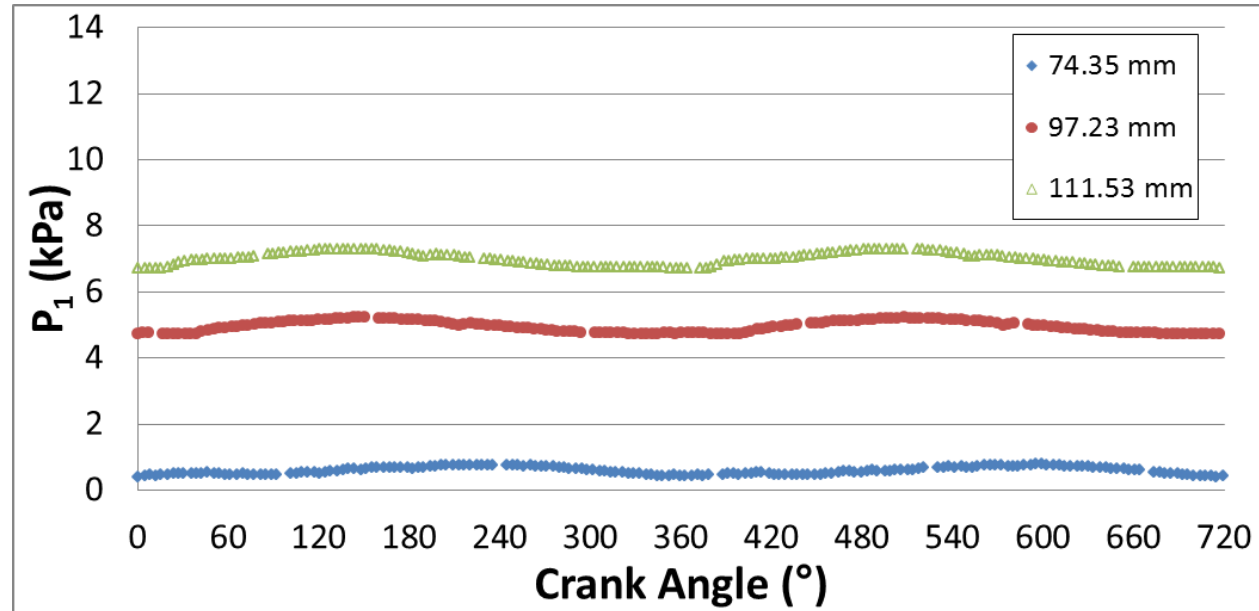
Figure 3 Temporal pressure at inlet- Effect of displacement for ν = 0.116 Hz
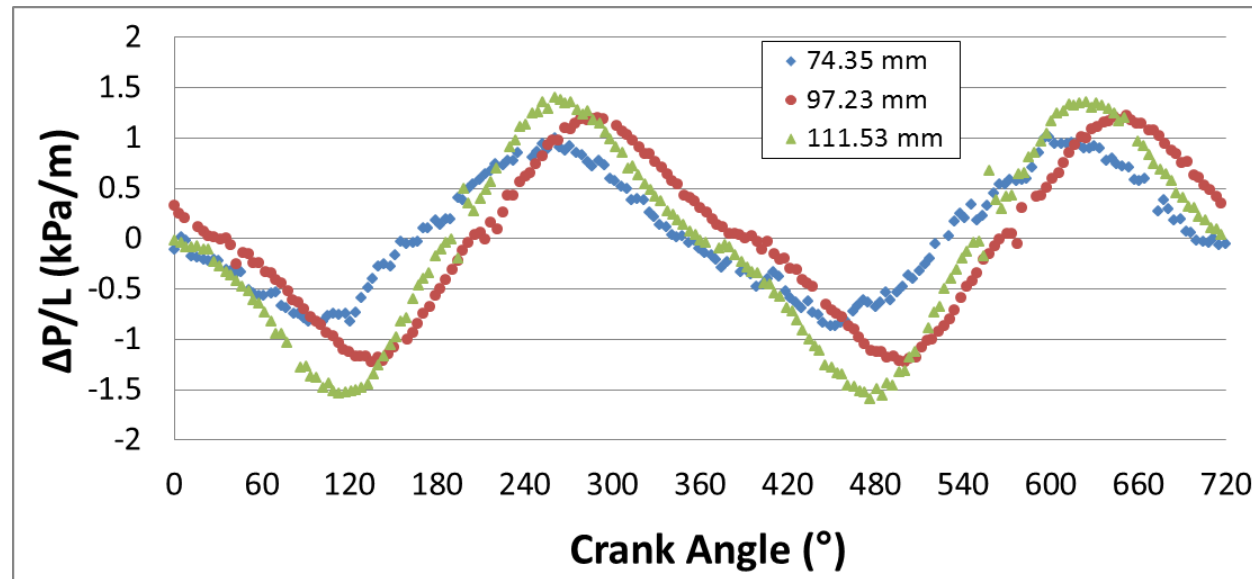
Figure 4 Pressure drop as a function of crank angle- Effect of displacement: ν= 0.116 Hz

Figure 3 is a plot of the steady-state pressure drop over length vs. average velocity. The trend is typical for pressure drop in porous media: the pressure drop increases in quadratic fashion with velocity. Quadratic curve fit of the data is shown with a high correlation factor R^2.
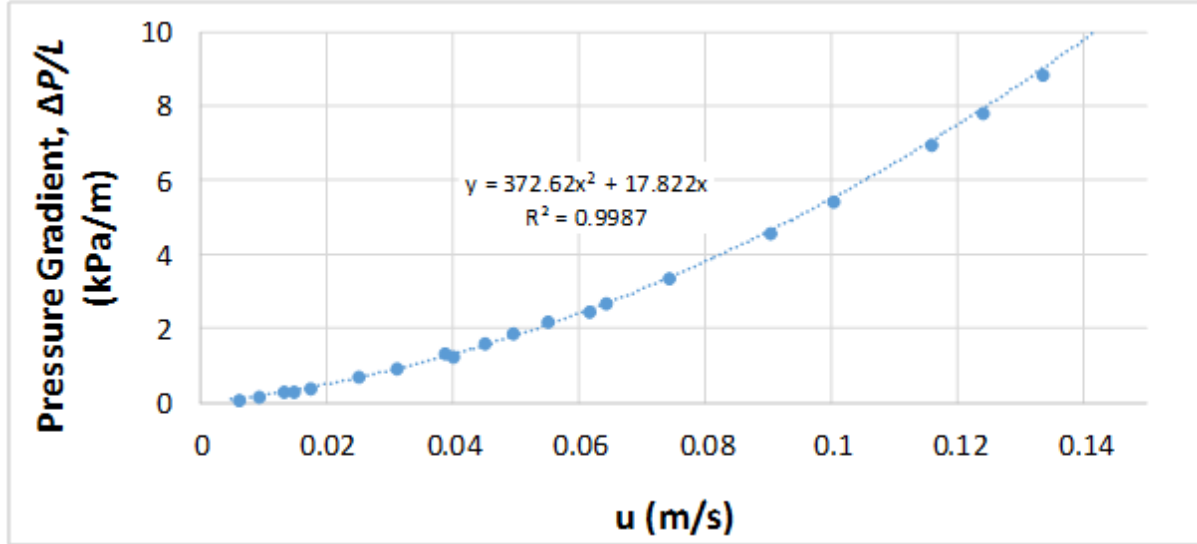
Figure 5 Pressure drop per unit length versus average velocity for steady-state flow

The second-order Forchheimer equation is:

$$\frac{\Delta p}{L} = \frac{\mu}{K} u + \frac{\rho F}{\sqrt{K}} u^2 \qquad (4)$$

where Δp is the static pressure drop, L is the length of the porous medium in flow direction, μ is the fluid viscosity, K is the permeability of the porous medium, u is the superficial velocity, ρ the density of the fluid and F is the Forchheimer coefficient. By matching the curve-fit equation in Figure 3 to the Forchheimer equation, the permeability and Forchheimer coefficient are obtained as listed in Table 1.

Table 1: Permeability and Forchheimer coefficient for steady-state test

Permeability, $K \times 10^8 (\text{m}^2)$	13.15
Forchheimer Coefficient, F	0.110

For steady-state unidirectional flow in packed beds, Dybbs and Edwards [17] experimentally confirmed that the friction factor behaved according to

$$f = \alpha \left(\frac{1}{\text{Re}} \right) + \beta \qquad (5)$$

where $f = 2(\Delta p/L)D/\rho u^2$, $\text{Re} = \rho u D/\mu$ and α and β are adjustable parameters. Here D is the tube diameter.

For oscillating flow the friction factor is based on the maximum velocity, u_{max} and maximum pressure gradient, Δp_{max} according to

$$f_{max} = \frac{2(\Delta p_{max}/L)D}{\rho u_{max}^2}$$ (6)

The kinetic Reynolds number is defined as

$$Re_{\omega} = \frac{\rho \omega D^2}{\mu}$$ (7)

where ω is the angular frequency. The Reynolds number based on maximum displacement is defined as

$$Re_{max} = \frac{\rho \omega D x_{max}}{2\mu}$$ (8)

The relationship between these two Reynolds is

$$Re_{max} = x_{max} Re_{\omega}/2D$$ (9)

Table 2 Correlation coefficients for steady and oscillating flow

	α, $\tilde{\alpha}$	β, $\tilde{\beta}$
Steady State Flow	88,428	39
Oscillating Flow	145,144	33

It is only possible to obtain one value for the friction factor for oscillating flow since there is only one frequency considered in the current study. The friction factor for oscillating flow lies above that for steady flow, as expected, and as was obtained for the case of air flow in packed woven screens by Zhao and Cheng [9], for water flow in packed spheres by Pamuk and Özdemir [11] and for air flow in metal foam by Leong and Jin [13]. Compared to the spheres of Pamuk and Özdemir [11] the difference between steady and oscillating friction factors is more pronounce in the case of metal foam.

The behavior of oscillating-flow friction factor correlates with Re_{max} according to

$$f_{max} = \tilde{\alpha}\left(\frac{1}{Re_{max}}\right) + \tilde{\beta}$$ (10)

with the correlation coefficients $\tilde{\alpha}$ and $\tilde{\beta}$ given in Table 2, albeit from one point. A similar correlation to Eq. (11) was obtained by Zhao and Cheng [9] for air flow in packed woven screens, by Pamuk and Özdemir [11] for water flow in packed spheres and by Leong and Jin [13,14] for air flow in metal foam. For oscillating water flow in metal foam, the friction factor at the current frequency lied above oscillating air flow in metal flow of Leong and Jin [13] and below water flow in packed spheres [11].

Conclusion

Characteristic of oscillating water flow in commercial open-cell metal foam were experimentally acquired and presented for three flow displacements at one frequency. The following statements can be made:

- The pressure drop increases with flow displacement.
- There was a phase shift between the inlet and outlet pressures and flow velocity.

When compared to other studies at approximately the same frequency, the following was found:

- The fiction factor for the case of oscillating water flow in metal foam was higher than that for air flow.
- The friction factor for oscillating water flow in packed spheres was higher than that for flow in the high-porosity metal foam of the current study.

References

[1] Dukhan, N., Editor. 2013: *Metal Foam: Fundamentals and Applications*. DESTech, Lancaster, PA, pp. xiv.
[2] Kim, S.Y., Kang, B.H., Hyuan, J.M., Heat transfer from pulsating flow in a channel filled with porous media, *Int. J. Heat Mass Trans*, 37 (1994) 2025-2033
[3] Gue, Z.X., Kim, S.Y., Sung, H.J., Pulsating flow and heat transfer in a pipe partially filled with a porous medium, *Int. J. Heat Mass Trans*, 40 (1997) 4209-4218
[4] Sozen, M. and Vafai, K., Analysis of oscillating flow compressible flow through a packed bed, *Int. J. Heat Fluid Flow*, 12 (1990) 130-136
[5] Byun, S.Y., Ro, S.T., Shin, J.Y., Son, Y.S., Lee, D.-Y., Transient thermal behavior of porous media under oscillating flow condition, *Int. J. Heat Mass Trans*, 49 (2006) 5081-5085
[6] C.-T. Hsu, H. Fu and P. Cheng, 1999, On Pressure-Velocity Correlation of Steady and Oscillating Flows in Regenerators Made of Wire Screens, *Journal of Fluids Engineering*, 121, pp. 52-56
[7] Dai, Q. and Yang, L., LBM numerical study on oscillating flow and heat transfer in porous media, *Applied Thermal Engineering*, 54 (2013) 16-25
[8] J. M. Khodadadi, 1991, Oscillatory fluid flow through a porous medium channel bounded by two impermeable parallel plates, *Journal of Fluids Engineering*, 113, pp. 509-511
[9] T.S. Zhao and P. Cheng, 1996, Oscillatory pressure drops through a woven-screen packed column subjected to a cyclic flow, *Cryogenics*, 36, pp. 333-341
[10] J.S. Cha, S.M. Ghiaasiaan and C.S. Kirkconnell, 2008, Oscillatory flow in microporous media applied in pulse-tube and Stirling-cycle cryocooler regenerators, *Experimental Thermal and Fluid Science*, 32, pp. 1264-1278
[11] M.T. Pamuk and M. Özdemir, Friction factor, permeability and inertial coefficient of oscillating flow through porous media of packed balls, *Experimental Thermal and Fluid Science*, 38 (2012) 134-139
[12] Pamuk and Özdemir, Heat transfer in porous media of steel balls under oscillating flow, *Experimental Thermal and Fluid Science*, 42 (2012) 79-92
[13] Leong, K.C. and Jin, L.W., Characteristics of oscillating flow through a channel filled with open-cell metal foam, *Int. J. Heat Fluid Flow*, 27 (2006) 144-153
[14] Leong, K.C. and Jin, L.W., An experimental study of heat transfer in oscillating flow through a channel filled with an aluminum foam, *Int. J. Heat Mass Trans*., 48 (2005) 243-253
[15] Effect of oscillating frequency heat transfer in foam heat sinks of various pore density, *Int. J. Heat Mass Trans,* 49 (2006) 671-681
[16] Figliola, R., Beasley, D. (2000). *Theory and Design for Mechanical Measurements*. John Wiley and Sons, New York, pp. 149-163.
[17] Dybbs, A., Edwards, R. V. (1984) *A new look at porous media fluid mechanics – Darcy to turbulent*, in Fundamentals of Transport Phenomena in Porous Media, J. Bear and M. Y. (Eds.) Corapcioglu. Martinus Nijhoff Publishers, NATO ASI Series, Series E. The Hague.

Acknowledgement

INDEX

SPONSORS

SILVER SPONSORS

BRONZ SPONSORS